Signal Design for Modern Radar Systems

Mohammad Alaee-Kerahroodi
Mojtaba Soltanalian
Prabhu Babu
Bhavani Shankar

Signal Design for Modern Radar Systems

Mohammad Alaee-Kerahroodi
Mojtaba Soltanalian
Prabhu Babu
M. R. Bhavani Shankar

To my lovely wife Zeynab, and my wonderful son Ali

Mohammad Alaee-Kerahroodi

To the memory of my father,
and all those who held my hands and helped me grow

Mojtaba Soltanalian

To all my teachers

Prabhu Babu

To all those from whom I have learnt

M. R. Bhavani Shankar

Contents

Page

Chapter 1 Introduction **1**
1.1 Practical Signal Design 2
1.1.1 The Why 2
1.1.2 The How 3
1.1.3 The What 4
1.2 Radar Application Focus Areas 6
1.2.1 Designing Signals with Good Correlation Properties . 6
1.2.2 Signal Design to Enhance SINR 7
1.2.3 Spectral Shaping and Coexistence with Communications 7
1.2.4 Automotive Radar Signal Processing and Sensing for Autonomous Vehicles 8
1.3 What this Book Offers 8
References 10

Chapter 2 Convex and Nonconvex Optimization **17**
2.1 Optimization Algorithms 17
2.1.1 Gradient Descent Algorithm 18
2.1.2 Newton's Method 18
2.1.3 Mirror Descent Algorithm 19
2.1.4 Power Method-Like Iterations 20
2.1.5 Majorization-Minimization Framework 20
2.1.6 Block Coordinate Descent 22
2.1.7 Alternating Projection 23
2.1.8 Alternating Direction Method of Multipliers 25
2.2 Summary of the Optimization Approaches 26
2.3 Conclusion 27

References . . . 28

Chapter 3 PMLI **31**
3.1 The PMLI Formulation . . . 32
3.1.1 Fixed-Energy Signals . . . 32
3.1.2 Unimodular or Constant-Modulus Signals . . . 33
3.1.3 Discrete-Phase Signals . . . 33
3.1.4 PAR-Constrained Signals . . . 33
3.2 Convergence of Radar Signal Design . . . 34
3.3 PMLI and the Majorization-Minimization Technique: Points of Tangency . . . 35
3.4 Application of PMLI . . . 35
3.4.1 A Toy Example: Synthesizing Cross-Ambiguity Functions . . . 35
3.4.2 PMLI Application with Dinkelbach's Fractional Programming . . . 39
3.4.3 Doppler-Robust Radar Code Design . . . 43
3.4.4 Radar Code Design Based on Information-Theoretic Criteria . . . 48
3.4.5 MIMO Radar Transmit Beamforming . . . 50
3.5 Matrix PMLI Derivation for (3.71) and (3.75) . . . 60
3.6 Conclusion . . . 61
3.7 Exercise Problems . . . 61
References . . . 62

Chapter 4 MM Methods **67**
4.1 System Model . . . 67
4.2 MM Method . . . 70
4.2.1 MM Method for Minimization Problems . . . 70
4.2.2 MM Method for Minimax Problems . . . 71
4.3 Sequence Design Algorithms . . . 72
4.3.1 ISL Minimizers . . . 73
4.3.2 PSL Minimizers . . . 100
4.4 Numerical Simulations . . . 114
4.5 Conclusion . . . 120
4.6 Exercise Problems . . . 120
References . . . 122

Chapter 5 BCD Method **125**

5.1 The BCD Method . . . 125
5.1.1 Rules for Selecting the Index Set . . . 128
5.1.2 Convergence of BCD . . . 129
5.2 BSUM: A Connection Between BCD and MM . . . 131
5.3 Applications . . . 132
5.3.1 Application 1: ISL Minimization . . . 133
5.3.2 Application 2: PSL Minimization . . . 139
5.3.3 Application 3: Beampattern Matching in MIMO Radars 146
5.4 Conclusion . . . 152
5.5 Exercise Problems . . . 152
References . . . 153
Appendix 5A . . . 156
Appendix 5B . . . 157
Appendix 5C . . . 158

Chapter 6 Other Optimization Methods 159
6.1 System Model . . . 159
6.1.1 System Model in the Spatial Domain . . . 160
6.1.2 System Model in the Spectrum Domain . . . 160
6.2 Problem Formulation . . . 161
6.3 Optimization Approach . . . 162
6.3.1 Convergence . . . 166
6.3.2 Computational Complexity . . . 167
6.4 Numerical Results . . . 168
6.4.1 Convergence Analysis . . . 168
6.4.2 Performance Evaluation . . . 169
6.4.3 The Impact of Similarity Parameter . . . 171
6.4.4 The Impact of Zero Padding . . . 173
6.5 Conclusion . . . 173
References . . . 173
Appendix 6A . . . 175

Chapter 7 Deep Learning for Radar 179
7.1 Deep Learning for Guaranteed Radar Processing . . . 182
7.1.1 Deep Architecture for Radar Processing . . . 183
7.1.2 Numerical Studies and Remarks . . . 187
7.2 Deep Radar Signal Design . . . 189
7.2.1 The Deep Evolutionary Cognitive Radar Architecture . 192
7.2.2 Performance Analysis . . . 193

7.3 Conclusion . . . 196
7.4 Exercise Problems . . . 197
References . . . 197

Chapter 8 Waveform Design in 4-D Imaging MIMO Radars 201
8.1 Beampattern Shaping and Orthogonality . . . 202
8.1.1 System Model . . . 204
8.1.2 Problem Formulation . . . 206
8.2 Design Procedure Using the CD Framework . . . 207
8.2.1 Solution for Limited Power Constraint . . . 210
8.2.2 Solution for PAR Constraint . . . 212
8.2.3 Solution for Continuous Phase . . . 213
8.2.4 Solution for Discrete Phase . . . 213
8.3 Numerical Examples . . . 214
8.3.1 Contradictory Nature of Spatial and Range ISLR . . . 215
8.3.2 Trade-Off Between Spatial and Range ISLR . . . 216
8.3.3 The Impact of Alphabet Size and PAR . . . 218
8.4 Conclusion . . . 220
8.5 Exercise Problems . . . 220
References . . . 220
Appendix 8A . . . 222
Appendix 8B . . . 226
Appendix 8C . . . 227
Appendix 8D . . . 227
Appendix 8E . . . 229

Chapter 9 Waveform Design for Spectrum Sharing 231
9.1 Scenario and Signal Model . . . 232
9.1.1 Communication Link and CSI . . . 234
9.1.2 Transmit Signal Model . . . 234
9.1.3 Signal Model at Targets . . . 236
9.1.4 Backscatter Signal Model . . . 237
9.1.5 Clutter Model . . . 239
9.1.6 Signal Model at ACV . . . 240
9.1.7 CSI Exploitation . . . 241
9.2 Performance Indicators . . . 242
9.2.1 ACV SNR Evaluation . . . 243
9.2.2 SCNR at JRCV . . . 243
9.3 Waveform Design and Optimization Formulation . . . 244

9.3.1 Design Methodology . . . 244
9.3.2 Optimization Problem for ACV . . . 245
9.3.3 Formulation of JRC Waveform Optimization . . . 247
9.3.4 Solution to the Optimization Problem . . . 248
9.3.5 JRC Algorithm Design . . . 252
9.3.6 Complexity Analysis . . . 252
9.3.7 Range-Doppler Processing . . . 254
9.4 Numerical Results . . . 255
9.4.1 Convergence Behavior of the JRC Algorithm . . . 256
9.4.2 Performance Assessment at the Radar Receiver . . . 257
9.4.3 Performance Assessment at the Communications Receiver . . . 261
9.4.4 Trade-Off Between Radar and Communications . . . 261
9.5 Conclusion . . . 264
References . . . 265
Appendix 9A . . . 267
Appendix 9B . . . 268
Appendix 9C . . . 269

Chapter 10 Doppler-Tolerant Waveform Design 271
10.1 Problem Formulation . . . 272
10.2 Optimization Method . . . 275
10.3 Extension of Other Methods to PECS . . . 281
10.3.1 Extension of MISL . . . 281
10.3.2 Extension of CAN . . . 282
10.4 Performance Analysis . . . 285
10.4.1 ℓ_p Norm Minimization . . . 285
10.4.2 Doppler-Tolerant Waveforms . . . 288
10.4.3 Comparison with the Counterparts . . . 288
10.5 Conclusion . . . 293
References . . . 294
Appendix 10A . . . 297

Chapter 11 Waveform Design for STAP in MIMO Radars 301
11.1 Problem Formulation . . . 301
11.2 Transmit Sequence and Receive Filter Design . . . 305
11.2.1 Optimum Filter Design . . . 305
11.2.2 Code Optimization Algorithm . . . 306
11.2.3 Discrete Phase Code Optimization . . . 310

11.2.4 Continuous Phase Code Optimization 311
11.3 Numerical Results 312
11.4 Conclusion 318
References 318

Chapter 12 Cognitive Radar: Design and Implementation 321
12.1 Cognitive Radar 323
12.2 The Prototype Architecture 324
12.2.1 LTE Application Framework 324
12.2.2 Spectrum Sensing Application 325
12.2.3 MIMO Radar Prototype 326
12.3 Experiments and Results 334
12.4 Performance Analysis 341
12.5 Conclusion 347
References 347
Appendix 12A 349
Appendix 12B 352

Chapter 13 Conclusion 353
13.1 Computational Efficiency 354
13.2 Waveform Diversity 355
13.3 Performance Trade-Off 355

About the Authors 359

Index 363

Foreword

Transmit signal design plays a key role in enhancing classical radar operations including detection, classification, identification, localization, and tracking. It refers to the signal adaptation over a number of dimensions, including spectral, polarization, spatial, and temporal. In modern radar contexts, waveform optimization is coupled with the advent of MIMO architectures that make the design problems more and more challenging but with amazing sensing performance improvements.

The main goal of this book is to highlight relevant problems in radar waveform design and motivate several approaches leveraging the application of nonconvex optimization principles. In this respect, the book focuses on key applications and discusses a variety of optimization techniques including majorization minimization, coordinate descent, and power method-like iterations applied to radar signal design and exploitation. To further bring the optimization closer to an implementation for real systems, practical constraints, such as finite energy, unimodularity (or constant-modulus), and finite or discrete-phase (potentially binary) alphabet, are accounted for.

This is an excellent reference and complements some further books available in the open literature about waveform diversity and optimization theory for waveform design. In this respect, it could be useful to students, scientists, engineers, and practitioners who need a rigorous and academic point of view on the topic.

Professor Antonio De Maio
Dipartimento di Ingegneria Elettrica e delle Tecnologie dell'Informazione,
Universita degli Studi di Napoli "Federico II," Napoli, Italy
November 2022

Chapter 1

Introduction

Man-made sensing systems such as radar and sonar have been a vital part of our civilization's advancement in navigation, defense, meteorology, and space exploration. In fact, "The strongest signals leaking off our planet are radar transmissions, not television or radio. The most powerful radars, such as the one mounted on the Arecibo telescope (used to study the ionosphere and map asteroids) could be detected with a similarly sized antenna at a distance of nearly $1,000$ light-years."[1] It is thus no surprise that signal processing and design problems for active sensing have been of interest to engineers, system theorists, and mathematicians in the last 60 years.

In the last two decades, however, the radar world has been revolutionized by significant increase in the computational resources—an ongoing revolution with considerable momentum. Such advances are enabling waveform design and processing schemes that can be adaptive (also referred to as cognitive, or smart) while maintaining extreme agility in modifying information collection strategy based on new measurements, and/or modified target or environmental parameters. Nevertheless, the static use of a fixed waveform reduces efficiency due to limited or no adaptation to the dynamic environment as well as vulnerability to electronic attacks, thus highlighting the need for multiple and diverse waveforms exhibiting specific features. These novel waveform design and processing schemes have also opened new avenues for enhancing robustness in radar detection and estimation, as well as coexistence in networked environments with limited

1 Seth Shostak, American astronomer and director of Search for Extraterrestrial Intelligence (SETI) Institute.

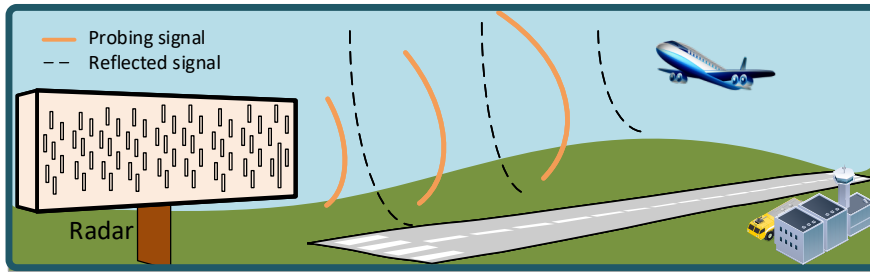

Figure 1.1. An illustration of a simplistic radar setup. Useful information about the target is extracted from the backscattered signal.

resources such as a shared spectrum—all leading to increased adaptivity, agility, and reliability.

1.1 PRACTICAL SIGNAL DESIGN

1.1.1 The Why

Note that the goal of waveform design for radar is to acquire (or preserve) the maximum amount of information from the desirable sources in the environment, where, in fact, the transmit signal can be viewed as a medium that collects information. An illustrative example is the simple radar setup depicted in Figure 1.1: An active radar emits radio waves (referred to as radar signals or waveforms) toward the target. A portion of the transmitted energy is backscattered by the target and is received by the radar receiver antennas. Thanks to the known electromagnetic wave propagation speed, the radar system can estimate the location of the target by measuring the time difference between the radar signal transmission and the reception of the reflected signal.

Radar waveform design and processing have a crucial role not only in efficiently collecting the target information but also in fulfilling the above promises of adaptivity, agility, and reliability: The waveform design usually deals with various measures of quality (including detection/estimation and information-theoretic criteria), while incorporating practical requirements such as that the employed signals must belong to a limited signal set. This

diversity of design metrics and signal constraints lays the groundwork for many interesting research projects in waveform optimization.

Waveform design for next-generation radar is also a topic of great interest due to the growing demands in increasing the number of antennas/sensors in different radar applications. As a focal example, the realization of the potential of multiple-input multiple-output (MIMO) radars [1, 2], which employ several antennas at the radar station, has attracted a significant interest to waveform design and diversity. Currently, high-resolution MIMO radar sensors operating at 60, 79, and 140 GHz with sometimes finer than 10 cm range resolution are becoming integral in a variety of applications ranging from automotive safety and autonomous driving [3–5] to infant and elderly health monitoring [6]. Unlike a standard phased-array (PA) radar, a MIMO radar can transmit multiple probing signals that can be distinct. The resulting waveform and spatial diversity provide MIMO radar with superior capabilities in comparison to the traditional radar settings [7, 8]. Indeed, waveform diversity has made MIMO radars a low-cost alternative for adding more antenna elements, making them ideal for mass manufacturing. Particularly in the emerging scenario of self-driving automotive applications, with the goal of enhancing safety and comfort, high spatial resolution is achieved using the MIMO virtual arrays which is obtained by having sparse transmit/receive antenna arrays and maintaining orthogonality between the transmit waveforms. To achieve waveform orthogonality, time division multiplexing (TDM)-, binary phase code multiplexing (BPM)-, and Doppler division multiplexing (BPM)-MIMO are implemented and industrialized, which improve sensor performance in discriminating objects. By using code division multiplexing (CDM)-MIMO to create waveform orthogonality, the next generation of ultra high-resolution 4D imaging automotive radars may be able to achieve large number of virtual antenna elements, providing additional high-resolution information for object identification, classification, and tracking.

1.1.2 The How

It is evident from the above discussion that efficient waveform design algorithms are instrumental in realizing future advanced radar systems. Therefore, there should be no surprise that while radar research has been around for a relatively long time, it is still a very active area—due to the existence of many interesting but yet unsolved problems.

Research in the area of waveform design for active sensing is focused on the design and optimization of probing signals in order to improve target detection performance, as well as the target location and speed estimation [9, 10]. To this end, the waveform design problems are often formulated as an optimization problem with a certain metric that represents the quality objective, along with the constraint set of the transmit signals. Among others, the most widely used signal quality objectives include auto and cross correlation sidelobe metrics (see [11–13]), mean-square error (MSE) of estimation (see [14, 15]), signal-to-noise ratio (SNR) of the processed signals (see [16–18]), information-theoretic criteria (see [19–21]), and excitation metrics (see [22]). Due to implementation and technological considerations, the transmit signals should also comply with certain constraints. Other than reliability requirements, such constraints typically include (finite) energy, unimodularity (or being constant-modulus) [23], peak-to-average power ratio (abbreviated as PAPR or PAR), and finite or discrete-alphabet (e.g., being integer, binary, or from m-ary constellation, also known as roots-of-unity [10, 12, 24–26]).

The signal design problems lie in the interplay of different metrics and different constraints; see Figure 1.2. The exciting fact supported by the above discussion is that the set of metrics and constraints are so diverse that they pave the way for a large number of interesting problems in waveform design—many of which are shown to be NP-hard (indicating an overwhelming complexity), whereas the complexity of many other such problems is unknown to this date, and they are generally deemed to be difficult. Briefly speaking, the most interesting challenges in dealing with radar waveform design can be summarized as below.

Some signal constraints are difficult to deal with.	$\rightarrow$	**How do we *handle* signal constraints?**
Agility is required for the future cognitive radars.	$\rightarrow$	**How to do we do the above *efficiently*?**

1.1.3 The What

This book will be essentially focused on agile waveform design and processing for modern radar systems. Note that, due to the associated complexity

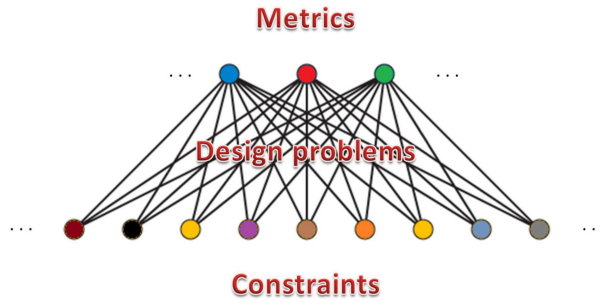

Figure 1.2. Diversity of problems in radar waveform design and processing due to various signal quality metrics and constraints.

and hardware considerations, many waveform design algorithms could not be practically implemented for several decades in the mid-twentieth century. Although the implementation of such algorithms is somewhat versatile at this point, there are still many developments in the field that require a fresh look and novel methodologies:

1. **The problem dimensions are increasing rapidly and significantly**. This is due to several factors including a considerably increased number of antennas, as well as the exploitation of larger probing waveforms in order to achieve a higher range/resolution for target determination.

2. **The designs are becoming real-time** (see the literature on cognitive radar [27–29]). In such scenarios, the sensing system has to design/update the waveforms on the spot to cope with new environmental and target-scene realizations.

3. **New approaches and requirements are emerging**. For instance, compressive sensing-based approaches are likely important contributors

to new radar systems with high performance, while low-resolution sampling for low-cost, large-scale array processing becomes a requirement to be considered.

As indicated earlier, the waveforms must be designed to comply with implementation considerations. The radar transmit subsystems usually have certain limitations when it comes to the properties of the signals that they can transmit (with small perturbation). To facilitate a better accuracy of transmission, as well as to simplify the transmission units, signal constraints are typically considered.

1.2 RADAR APPLICATION FOCUS AREAS

In order to highlight the practical use of the optimization algorithms presented in this book, we typically apply them on signal design problems of significant interest to the radar community. We provide the reader with some examples below.

1.2.1 Designing Signals with Good Correlation Properties

In single-input single-output (SISO)/PA radar systems, a longstanding problem is effective radar pulse compression (intrapulse waveform design), which necessitates transmit waveforms with low autocorrelation peak sidelobe level (PSL) and integrated sidelobe level (ISL) values. PSL shows the maximum autocorrelation sidelobe of a transmit waveform. Depending on how the constant false alarm rate (CFAR) detector is set, a false detection or a miss detection may occur. Similar principle applies to ISL, where the energy of autocorrelation sidelobes should be low to mitigate the deleterious effects of distributed clutter. For example, in solid state-based weather radars, ISL must be small to enhance reflectively estimation and hydrometer classifier performance. A few recent publications on waveform design with small correlation sidelobes can be found in [30–41].

PSL/ISL reduction is more difficult in MIMO radar systems because the cross-correlation sidelobes of the transmitting set of sequences must also be addressed. Small cross-correlation sidelobe values enable the MIMO

radar receiver to differentiate the transmitted waveforms and exploit waveform diversity to construct the virtual array [42–46]. Furthermore, waveform diversity is a useful tool for upcoming 4D imaging automobile radars that must transmit a number of beam patterns at the same time [47].

1.2.2 Signal Design to Enhance SINR

While enhancing the correlation properties of transmit waveforms is an effective tool towards improving the performance of radar systems, such an approach does not fully exploit the target and environmental information available to the system. In contrast, the signal to interference-plus-noise ratio (SINR) maximization provides excellent opportunities for data exploitation (and, in most cases, subsume the good correlation metrics) [48–54]. Particularly, it is essential to develop low-cost waveform design and processing algorithms for a diverse set of metrics and a variety of emerging problems including cases with large-scale antenna arrays, signal-dependent interference, signal similarity constraints, and joint filter designs.

The SINR maximization is coupled with transmit beam pattern shaping that involves steering the radiation power in a spatial region of desired angles, while reducing interference from sidelobe returns to improve target detection. There exists a rich literature on waveform design for SINR enhancement and beam pattern shaping following different approaches with regard to the choice of the variables, the objective function, and the constraints; kindly refer to [54–60] for details. An interesting approach to enhance detection of weak targets in the vicinity of strong ones is the design of waveforms with a small integrated sidelobe level ratio (ISLR) [57, 58] in the beam or spatial domain. This can be achieved by imparting appropriate correlation among the waveforms transmitted from different antennas [56].

1.2.3 Spectral Shaping and Coexistence with Communications

Spectrum congestion has become an imminent problem with a multitude of radio services like wireless communications, active radio frequency (RF) sensing, and radio astronomy vying for the scarce usable spectrum. Within this conundrum of spectrum congestion, radars need to cope with simultaneous transmissions from other RF systems. Spectrum sharing with communications is thus a highly plausible scenario given the need for high bandwidth in both systems [61, 62]. While elaborate allocation policies are in

place to regulate the spectral usage, the rigid allocations result in inefficient spectrum utilization when the subscription is sparse. In this context, smart spectrum utilization offers a flexible and a fairly promising solution for improved system performance in the emerging smart sensing systems [63, 64].

The interfered bands, including those occupied by communications, are not useful for the radar system, and traditional radars aim to mitigate these frequencies at their receivers. To avoid energy wasted due to transmissions on these bands while pursuing coexistence applications, research into the transmit strategy of spectrally shaped radar waveforms has been driving coexistence studies since the last decade [64–73]. In fact, it is possible to radiate the radar waveform in a smart way by using two key elements of the cognition: spectrum sensing and spectrum sharing [74–76]. Further, it is possible to increase the total radar bandwidth and consequently improve the range resolution by combining several clear bands together [65, 77].

1.2.4 Automotive Radar Signal Processing and Sensing for Autonomous Vehicles

The radar technology exhibits an unmatched performance in a variety of vehicular applications, due to excellent resolving capabilities and immunity to bad weather conditions in comparison with visible and infrared imaging techniques. An important avenue for development in the area is to enhance resolvability with lower processing bandwidths and to reduce the cost of vehicular radars for advanced safety. Such an approach will enable mass deployment of advanced vehicular safety features.

The vast repertoire of vehicular radar applications has been made possible by continuous innovations towards achieving improved signal design and processing. Note that while sensing systems can be used outside of the vehicle to detect pedestrians, cars, and natural object, which results in a lower risk of accidents, they can also be used inside the car to monitor the passengers' situation and medical conditions, including heartbeats and breathing [6, 78–82].

1.3 WHAT THIS BOOK OFFERS

Focusing on solid mathematical optimization foundations, we will embark on an educational journey through various optimization tools that have

been proven useful in modern radar signal design along with practical examples. The journey begins with a survey of convex and nonconvex optimization formulations as well as commonly used off-the-shelf optimization algorithms (Chapter 2). From its birth in the seminal works of Minkowski, Carathéodory, and Fenchel, convexity theory has made enormous contributions to the mathematical tools applied in various engineering areas. In mathematical optimization, the theory and practice of convex optimization have been a paradigm-shifting force, to the extent that convex versus nonconvex is now the most pertinent classification for optimization problems—a classification that once was based on linearity versus nonlinearity [83]. Due to practical signal constraints, it is no surprise, however, that many radar signal design problems occur to be nonconvex, which is deemed to be the more difficult class of problems to deal with.

Local optimization algorithms are the central part of our toolkit to tackle nonconvex optimization problems that emerge in radar signal design. We continue our journey with introducing several particularly effective local optimization algorithms in the context of radar, namely, power method-like iterations, majorization-minimization methods, and variations of coordinate descent (Chapters 3 to 5). A key feature of such local optimization methods is their inherent ability to circumvent the need for costly matrix inversions (e.g., inverting a Hessian matrix) within the optimization process, while providing an opportunity to enforce practical signal constraints. Other relevant optimization techniques are discussed in Chapter 6. In practice, a variety of presented techniques may be used in tandem to achieve the signal design goals. We finalize our discussion of signal design techniques by looking at the application of the widely sought-after deep learning approaches in the context of radar signal design and processing (Chapter 7). In particular, we present a powerful methodology that can benefit from traditional local optimization algorithms (like those in Chapters 2 to 6) as blueprints for data-driven signal design and processing, in such a way to enable exploiting the available data/measurements in order to enhance the radar performance.

Due to their computational efficiency and incorporation of practical needs of modern radar systems, the presented mathematical optimization tools have an untapped potential not only for a pervasive usage in modern radar systems but also to foster a new generation of radar signal design and processing paradigms. As such, in Chapters 8 to 11, we will go through a number of emerging applications of significance, that is, high-resolution

and 4D imaging MIMO radars for automotive applications, waveform design for spectrum sharing, designing Doppler-tolerant waveforms, and optimal transmit signal design for space-time adaptive processing (STAP) in MIMO radar systems. In particular, the role of mathematical optimization techniques for signal design in such applications will be highlighted. Chapter 12 is devoted to a cognitive radar prototype that takes advantage of the commonly used universal software radio peripheral (USRP). Such prototypes can benefit the interested reader by helping with a practical and real-time evaluation of the proposed signal design and processing algorithms.

Finally, Chapter 13 presents the concluding remarks by the authors and puts forth some avenues for future research and development.

References

[1] E. Fishler, A. Haimovich, R. Blum, D. Chizhik, L. Cimini, and R. Valenzuela, "MIMO radar: an idea whose time has come," in *Proceedings of the 2004 IEEE Radar Conference (IEEE Cat. No.04CH37509)*, pp. 71–78, 2004.

[2] J. Li and P. Stoica, *MIMO Radar Diversity Means Superiority*, ch. 1, pp. 1–64. Wiley-IEEE Press, 2009.

[3] J. Hasch, E. Topak, R. Schnabel, T. Zwick, R. Weigel, and C. Waldschmidt, "Millimeter-wave technology for automotive radar sensors in the 77 GHz frequency band," *IEEE Transactions on Microwave Theory and Techniques*, vol. 60, no. 3, pp. 845–860, 2012.

[4] S. M. Patole, M. Torlak, D. Wang, and M. Ali, "Automotive radars: A review of signal processing techniques," *IEEE Signal Processing Magazine*, vol. 34, no. 2, pp. 22–35, 2017.

[5] F. Engels, P. Heidenreich, M. Wintermantel, L. Stäcker, M. Al Kadi, and A. M. Zoubir, "Automotive radar signal processing: Research directions and practical challenges," *IEEE Journal of Selected Topics in Signal Processing*, vol. 15, no. 4, pp. 865–878, 2021.

[6] G. Beltrão, R. Stutz, F. Hornberger, W. A. Martins, D. Tatarinov, M. Alaee-Kerahroodi, U. Lindner, L. Stock, E. Kaiser, S. Goedicke-Fritz, U. Schroeder, B. S. M. R., and M. Zemlin, "Contactless radar-based breathing monitoring of premature infants in the neonatal intensive care unit," *Scientific Reports*, vol. 12, p. 5150, Mar. 2022.

[7] W. Melvin and J. Scheer, *Principles of Modern Radar: Advanced Techniques*. The Institution of Engineering and Technology, 2012.

[8] J. Li and P. Stoica, *MIMO Radar Signal Processing*. John Wiley & Sons, Inc., Hoboken, NJ, 2009.

[9] B. Ottersten, M. Viberg, P. Stoica, and A. Nehorai, *Exact and Large Sample Maximum Likelihood Techniques for Parameter Estimation and Detection in Array Processing*. Springer, 1993.

[10] M. Soltanalian, *Signal Design for Active Sensing and Communications*. Uppsala, Sweden: Uppsala Dissertations from the Faculty of Science and Technology, Acta Universitatis Upsaliensis, 2014.

[11] S. W. Golomb and G. Gong, *Signal Design for Good Correlation: For Wireless Communication, Cryptography, and Radar*. Cambridge University Press, 2005.

[12] H. He, J. Li, and P. Stoica, *Waveform design for active sensing systems: a computational approach*. Cambridge University Press, 2012.

[13] M. Soltanalian and P. Stoica, "Computational design of sequences with good correlation properties," *IEEE Transactions on Signal Processing*, vol. 60, no. 5, pp. 2180–2193, 2012.

[14] M. Soltanalian, B. Tang, J. Li, and P. Stoica, "Joint design of the receive filter and transmit sequence for active sensing," *Signal Processing Letters, IEEE*, vol. 20, no. 5, pp. 423–426, 2013.

[15] P. Stoica, H. He, and J. Li, "Optimization of the receive filter and transmit sequence for active sensing," *IEEE Transactions on Signal Processing*, vol. 60, no. 4, pp. 1730–1740, 2012.

[16] M. M. Naghsh, M. Soltanalian, P. Stoica, M. Modarres-Hashemi, A. De Maio, and A. Aubry, "A Doppler robust design of transmit sequence and receive filter in the presence of signal-dependent interference," *IEEE Transactions on Signal Processing*, vol. 62, no. 4, pp. 772–785, 2014.

[17] A. De Maio, Y. Huang, M. Piezzo, S. Zhang, and A. Farina, "Design of optimized radar codes with a peak to average power ratio constraint," *IEEE Transactions on Signal Processing*, vol. 59, no. 6, pp. 2683–2697, 2011.

[18] M. Soltanalian and P. Stoica, "Designing unimodular codes via quadratic optimization," *IEEE Transactions on Signal Processing*, vol. 62, pp. 1221–1234, Mar. 2014.

[19] F. Gini, A. De Maio, and L. Patton, *Waveform design and diversity for advanced radar systems*. The Institution of Engineering and Technology, 2012.

[20] M. M. Naghsh, M. Modarres-Hashemi, S. ShahbazPanahi, M. Soltanalian, and P. Stoica, "Unified optimization framework for multi-static radar code design using information-theoretic criteria," *IEEE Transactions on Signal Processing*, vol. 61, no. 21, pp. 5401–5416, 2013.

[21] Z. Zhu, S. Kay, and R. S. Raghavan, "Information-theoretic optimal radar waveform design," *IEEE Signal Processing Letters*, vol. 24, no. 3, pp. 274–278, 2017.

[22] E. Hidayat, M. Soltanalian, A. Medvedev, and K. Nordström, "Stimuli design for identification of spatially distributed motion detectors in biological vision systems," in *13th International Conference on Control Automation Robotics & Vision (ICARCV)*, pp. 740–745, IEEE, 2014.

[23] O. Aldayel, V. Monga, and M. Rangaswamy, "Tractable transmit MIMO beampattern design under a constant modulus constraint," *IEEE Transactions on Signal Processing*, vol. 65, no. 10, pp. 2588–2599, 2017.

[24] N. Levanon and E. Mozeson, *Radar Signals*. New York: Wiley, 2004.

[25] A. L. Swindlehurst and P. Stoica, "Maximum likelihood methods in radar array signal processing," *Proceedings of the IEEE*, vol. 86, no. 2, pp. 421–441, 1998.

[26] N. A. Goodman, P. R. Venkata, and M. A. Neifeld, "Adaptive waveform design and sequential hypothesis testing for target recognition with active sensors," *IEEE Journal of Selected Topics in Signal Processing*, vol. 1, no. 1, pp. 105–113, 2007.

[27] S. Haykin, "Cognitive radars," *IEEE Signal Processing Magazine*, vol. 23, pp. 30–40, Jan. 2006.

[28] R. A. Romero and N. A. Goodman, "Cognitive radar network: Cooperative adaptive beamsteering for integrated search-and-track application," *IEEE Transactions on Aerospace and Electronic Systems*, vol. 49, no. 2, pp. 915–931, 2013.

[29] W. Huleihel, J. Tabrikian, and R. Shavit, "Optimal adaptive waveform design for cognitive MIMO radar," *IEEE Transactions on Signal Processing*, vol. 61, no. 20, pp. 5075–5089, 2013.

[30] P. Stoica, H. He, and J. Li, "New algorithms for designing unimodular sequences with good correlation properties," *IEEE Transactions on Signal Processing*, vol. 57, no. 4, pp. 1415–1425, 2009.

[31] P. Stoica, H. He, and J. Li, "On designing sequences with impulse-like periodic correlation," *IEEE Signal Processing Letters*, vol. 16, no. 8, pp. 703–706, 2009.

[32] J. Song, P. Babu, and D. Palomar, "Optimization methods for designing sequences with low autocorrelation sidelobes," *IEEE Transactions on Signal Processing*, vol. 63, pp. 3998–4009, Aug 2015.

[33] J. Song, P. Babu, and D. P. Palomar, "Sequence design to minimize the weighted integrated and peak sidelobe levels," *IEEE Transactions on Signal Processing*, vol. 64, no. 8, pp. 2051–2064, 2016.

[34] L. Zhao, J. Song, P. Babu, and D. P. Palomar, "A unified framework for low autocorrelation sequence design via Majorization-Minimization," *IEEE Transactions on Signal Processing*, vol. 65, pp. 438–453, Jan. 2017.

[35] J. Liang, H. C. So, J. Li, and A. Farina, "Unimodular sequence design based on alternating direction method of multipliers," *IEEE Transactions on Signal Processing*, vol. 64, no. 20, pp. 5367–5381, 2016.

[36] M. Alaee-Kerahroodi, A. Aubry, A. De Maio, M. M. Naghsh, and M. Modarres-Hashemi, "A coordinate-descent framework to design low PSL/ISL sequences," *IEEE Transactions on Signal Processing*, vol. 65, pp. 5942–5956, Nov. 2017.

[37] J. M. Baden, B. O'Donnell, and L. Schmieder, "Multiobjective sequence design via gradient descent methods," *IEEE Transactions on Aerospace and Electronic Systems*, vol. 54, no. 3, pp. 1237–1252, 2018.

[38] R. Lin, M. Soltanalian, B. Tang, and J. Li, "Efficient design of binary sequences with low autocorrelation sidelobes," *IEEE Transactions on Signal Processing*, vol. 67, no. 24, pp. 6397–6410, 2019.

[39] M. Kumar and V. Chandrasekar, "Intrapulse polyphase coding system for second trip suppression in a weather radar," *IEEE Transactions on Geoscience and Remote Sensing*, vol. 58, no. 6, pp. 3841–3853, 2020.

[40] S. P. Sankuru, P. Babu, and M. Alaee-Kerahroodi, "UNIPOL: Unimodular sequence design via a separable iterative quartic polynomial optimization for active sensing systems," *Signal Processing*, vol. 190, p. 108348, 2022.

[41] C. A. Mohr, P. M. McCormick, C. A. Topliff, S. D. Blunt, and J. M. Baden, "Gradient-based optimization of pcfm radar waveforms," *IEEE Transactions on Aerospace and Electronic Systems*, vol. 57, no. 2, pp. 935–956, 2021.

[42] B. Friedlander, "Waveform design for MIMO radars," *IEEE Transactions on Aerospace and Electronic Systems*, vol. 43, no. 3, pp. 1227–1238, 2007.

[43] H. He, P. Stoica, and J. Li, "Designing unimodular sequence sets with good correlations; including an application to MIMO radar," *IEEE Transactions on Signal Processing*, vol. 57, pp. 4391–4405, Nov. 2009.

[44] M. Alaee-Kerahroodi, M. Modarres-Hashemi, and M. M. Naghsh, "Designing sets of binary sequences for MIMO radar systems," *IEEE Transactions on Signal Processing*, vol. 67, pp. 3347–3360, July 2019.

[45] W. Fan, J. Liang, G. Yu, H. C. So, and G. Lu, "MIMO radar waveform design for quasi-equiripple transmit beampattern synthesis via weighted l_p-minimization," *IEEE Transactions on Signal Processing*, vol. 67, pp. 3397–3411, Jul. 2019.

[46] W. Huang, M. M. Naghsh, R. Lin, and J. Li, "Doppler sensitive discrete-phase sequence set design for MIMO radar," *IEEE Transactions on Aerospace and Electronic Systems*, pp. 1–1, 2020.

[47] E. Raei, M. Alaee-Kerahroodi, and M. B. Shankar, "Spatial- and range- ISLR trade-off in MIMO radar via waveform correlation optimization," *IEEE Transactions on Signal Processing*, vol. 69, pp. 3283–3298, 2021.

[48] A. Aubry, A. DeMaio, A. Farina, and M. Wicks, "Knowledge-aided (potentially cognitive) transmit signal and receive filter design in signal-dependent clutter," *IEEE Transactions on Aerospace and Electronic Systems*, vol. 49, no. 1, pp. 93–117, 2013.

[49] M. M. Naghsh, M. Soltanalian, P. Stoica, M. Modarres-Hashemi, A. De Maio, and A. Aubry, "A Doppler robust design of transmit sequence and receive filter in the presence of signal-dependent interference," *IEEE Transactions on Signal Processing*, vol. 62, no. 4, pp. 772–785, 2014.

[50] G. Cui, H. Li, and M. Rangaswamy, "MIMO radar waveform design with constant modulus and similarity constraints," *IEEE Transactions on Signal Processing*, vol. 62, no. 2, pp. 343–353, 2014.

[51] A. Aubry, A. De Maio, and M. M. Naghsh, "Optimizing radar waveform and Doppler filter bank via generalized fractional programming," *IEEE Journal of Selected Topics in Signal Processing*, vol. 9, no. 8, pp. 1387–1399, 2015.

[52] L. Wu, P. Babu, and D. P. Palomar, "Cognitive radar-based sequence design via SINR maximization," *IEEE Transactions on Signal Processing*, vol. 65, no. 3, pp. 779–793, 2017.

[53] Z. Cheng, Z. He, B. Liao, and M. Fang, "MIMO radar waveform design with PAPR and similarity constraints," *IEEE Transactions on Signal Processing*, vol. 66, no. 4, pp. 968–981, 2018.

[54] L. Wu, P. Babu, and D. P. Palomar, "Transmit waveform/receive filter design for MIMO radar with multiple waveform constraints," *IEEE Transactions on Signal Processing*, vol. 66, no. 6, pp. 1526–1540, 2018.

[55] P. Stoica, J. Li, and Y. Xie, "On probing signal design for MIMO radar," *IEEE Transactions on Signal Processing*, vol. 55, no. 8, pp. 4151–4161, 2007.

[56] D. R. Fuhrmann and G. S. Antonio, "Transmit beamforming for MIMO radar systems using signal cross-correlation," *IEEE Transactions on Aerospace and Electronic Systems*, vol. 44, pp. 171–186, Jan. 2008.

[57] H. Xu, R. S. Blum, J. Wang, and J. Yuan, "Colocated MIMO radar waveform design for transmit beampattern formation," *IEEE Transactions on Aerospace and Electronic Systems*, vol. 51, no. 2, pp. 1558–1568, 2015.

[58] A. Aubry, A. De Maio, and Y. Huang, "MIMO radar beampattern design via PSL/ISL optimization," *IEEE Transactions on Signal Processing*, vol. 64, pp. 3955–3967, Aug 2016.

[59] W. Fan, J. Liang, and J. Li, "Constant modulus MIMO radar waveform design with minimum peak sidelobe transmit beampattern," *IEEE Transactions on Signal Processing*, vol. 66, no. 16, pp. 4207–4222, 2018.

[60] X. Yu, G. Cui, L. Kong, J. Li, and G. Gui, "Constrained waveform design for colocated MIMO radar with uncertain steering matrices," *IEEE Transactions on Aerospace and Electronic Systems*, vol. 55, no. 1, pp. 356–370, 2019.

[61] L. Zheng, M. Lops, Y. C. Eldar, and X. Wang, "Radar and communication coexistence: An overview: A review of recent methods," *IEEE Signal Processing Magazine*, vol. 36, no. 5, pp. 85–99, 2019.

[62] K. V. Mishra, M. R. Bhavani Shankar, V. Koivunen, B. Ottersten, and S. A. Vorobyov, "Toward millimeter-wave joint radar communications: A signal processing perspective," *IEEE Signal Processing Magazine*, vol. 36, no. 5, pp. 100–114, 2019.

[63] H. Griffiths, L. Cohen, S. Watts, E. Mokole, C. Baker, M. Wicks, and S. Blunt, "Radar spectrum engineering and management: Technical and regulatory issues," *Proceedings of the IEEE*, vol. 103, no. 1, 2015.

[64] C. Aydogdu, M. F. Keskin, N. Garcia, H. Wymeersch, and D. W. Bliss, "Radchat: Spectrum sharing for automotive radar interference mitigation," *IEEE Transactions on Intelligent Transportation Systems*, vol. 22, no. 1, pp. 416–429, 2021.

[65] M. J. Lindenfeld, "Sparse frequency transmit-and-receive waveform design," *IEEE Transactions on Aerospace and Electronic Systems*, vol. 40, no. 3, pp. 851–861, 2004.

[66] H. He, P. Stoica, and J. Li, "Waveform design with stopband and correlation constraints for cognitive radar," in *2010 2nd International Workshop on Cognitive Information Processing*, pp. 344–349, 2010.

[67] W. Rowe, P. Stoica, and J. Li, "Spectrally constrained waveform design [SP tips tricks]," *IEEE Signal Processing Magazine*, vol. 31, no. 3, pp. 157–162, 2014.

[68] P. Ge, G. Cui, S. M. Karbasi, L. Kong, and J. Yang, "A template fitting approach for cognitive unimodular sequence design," *Signal Processing*, vol. 128, pp. 360 – 368, 2016.

[69] A. R. Chiriyath, B. Paul, G. M. Jacyna, and D. W. Bliss, "Inner bounds on performance of radar and communications co-existence," *IEEE Transactions on Signal Processing*, vol. 64, no. 2, pp. 464–474, 2016.

[70] M. Labib, V. Marojevic, A. F. Martone, J. H. Reed, and A. I. Zaghloui, "Coexistence between communications and radar systems: A survey," *URSI Radio Science Bulletin*, vol. 2017, no. 362, pp. 74–82, 2017.

[71] B. Tang and J. Li, "Spectrally constrained MIMO radar waveform design based on mutual information," *IEEE Transactions on Signal Processing*, vol. 67, no. 3, pp. 821–834, 2019.

[72] S. H. Dokhanchi, B. S. Mysore, K. V. Mishra, and B. Ottersten, "A mmwave automotive joint radar-communications system," *IEEE Transactions on Aerospace and Electronic Systems*, vol. 55, no. 3, pp. 1241–1260, 2019.

[73] A. Aubry, A. De Maio, M. A. Govoni, and L. Martino, "On the design of multi-spectrally constrained constant modulus radar signals," *IEEE Transactions on Signal Processing*, vol. 68, pp. 2231–2243, 2020.

[74] M. S. Greco, F. Gini, and P. Stinco, "Cognitive radars: Some applications," in *2016 IEEE Global Conference on Signal and Information Processing (GlobalSIP)*, pp. 1077–1082, 2016.

[75] S. Z. Gurbuz, H. D. Griffiths, A. Charlish, M. Rangaswamy, M. S. Greco, and K. Bell, "An overview of cognitive radar: Past, present, and future," *IEEE Aerospace and Electronic Systems Magazine*, vol. 34, no. 12, pp. 6–18, 2019.

[76] M. Alaee-Kerahroodi, E. Raei, S. Kumar, and B. S. M. R. R. R., "Cognitive radar waveform design and prototype for coexistence with communications," *IEEE Sensors Journal*, pp. 1–1, 2022.

[77] D. Ma, N. Shlezinger, T. Huang, Y. Liu, and Y. C. Eldar, "Joint radar-communication strategies for autonomous vehicles: Combining two key automotive technologies," *IEEE Signal Processing Magazine*, vol. 37, no. 4, pp. 85–97, 2020.

[78] C. Li, J. Cummings, J. Lam, E. Graves, and W. Wu, "Radar remote monitoring of vital signs," *IEEE Microwave Magazine*, vol. 10, no. 1, pp. 47–56, 2009.

[79] C. Gu, C. Li, J. Lin, J. Long, J. Huangfu, and L. Ran, "Instrument-based noncontact Doppler radar vital sign detection system using heterodyne digital quadrature demodulation architecture," *IEEE Transactions on Instrumentation and Measurement*, vol. 59, no. 6, pp. 1580–1588, 2010.

[80] A. Lazaro, D. Girbau, and R. Villarino, "Analysis of vital signs monitoring using an IR-UWB radar," *Progress In Electromagnetics Research*, vol. 100, pp. 265–284, 2010.

[81] C. Li, J. Ling, J. Li, and J. Lin, "Accurate Doppler radar noncontact vital sign detection using the RELAX algorithm," *IEEE Transactions on Instrumentation and Measurement*, vol. 59, no. 3, pp. 687–695, 2010.

[82] F. Engels, P. Heidenreich, A. M. Zoubir, F. K. Jondral, and M. Wintermantel, "Advances in automotive radar: A framework on computationally efficient high-resolution frequency estimation," *IEEE Signal Processing Magazine*, vol. 34, no. 2, pp. 36–46, 2017.

[83] S. Boyd and L. Vandenberghe, *Convex Optimization*. Cambridge University Press, 2004.

Chapter 2

Convex and Nonconvex Optimization

Optimization plays a crucial role in the performance of various signal processing, communication, and machine learning applications. The synergy between these applications and optimization has a history, going back to the invention of linear programming (LP) [1]. However, with the advancements in technology, the underlying optimization problems have become much more complicated than LPs. Broadly, such optimization problems can be grouped into two major classes: convex and nonconvex problems [2]. Convex problem generalizes the LP formulation and incorporates optimization problems wherein both the objective function and the constraint sets are convex. In contrast, when the objective function or any of the constraints are not convex, the resulting problem becomes nonconvex. In addition to being convex or nonconvex, the underlying optimization problems may also be nonsmooth. Such problems are even more challenging to solve since the objective function in this case is not continuously differentiable.

2.1 OPTIMIZATION ALGORITHMS

Let us begin by considering the following generic optimization problem:

$$\underset{\mathbf{x}\in\chi}{\text{minimize}}\ f(\mathbf{x}) \tag{2.1}$$

where $f(\mathbf{x})$ is the objective function and χ is the constraint set. Historically, several optimization algorithms have been proposed to solve the problem at hand. To give a brief overview of such optimization algorithms, let us begin

with the classical gradient descent (GD) algorithm. Nowadays, gradient-based methods have attracted a revived and intensive interest among researchers for radar waveform design applications [3–6]. This method is also commonly used in machine learning (ML) and deep learning (DL) to minimize a cost or loss function (e.g., in a linear regression).

2.1.1 Gradient Descent Algorithm

Suppose the objective function $f(\mathbf{x}) : \mathbb{R}^{m\times 1} \rightarrow \mathbb{R}$ is continuously differentiable. Then the gradient descent algorithm arrives at the optimum of an unconstrained problem by taking steps in the opposite direction of the gradient of the objective function $f(\mathbf{x})$, that is,

$$\mathbf{x}^{k+1} = \mathbf{x}^k - \alpha^k \nabla f(\mathbf{x}^k) \tag{2.2}$$

where $\mathbf{x}^k$ is the value taken by $\mathbf{x}$ at the kth iteration, and α^k is the iteration-dependent step size and is usually found by line search methods. Also, $\nabla f(\mathbf{x})$ represents the gradient of the function $f(\mathbf{x})$. One of the main disadvantages of gradient-based methods is their slow convergence speed. However, with proper modeling of the problem at hand, combined with some key ideas, it turns out that it is possible to build fast gradient schemes for various classes of problems arising in different applications, particularly waveform design problems [5].

2.1.2 Newton's Method

Another classical optimization algorithm is the Newton's method, which additionally exploits the second-order information of the objective function to arrive at the minimizer:

$$\mathbf{x}^{k+1} = \mathbf{x}^k - \alpha^k (\nabla^2 f(\mathbf{x}^k))^{-1} \nabla f(\mathbf{x}^k) \tag{2.3}$$

where $\nabla^2 f(\mathbf{x})$ represents the Hessian matrix of the function $f(\mathbf{x})$. When compared to the gradient descent method, the Newton's method is reported to have a faster convergence [7]. This is because the Newton's method exploits the second-order information of the objective function and therefore approximates the objective function in a better manner when compared

with the gradient descent. However, by comparing (2.2) and (2.3), one can observe that the Newton's method involves computing the inverse of the Hessian matrix at every iteration. This makes the Newton's method computationally expensive when compared with the gradient descent algorithm. Nonetheless, both the optimization algorithms assume the objective function to be continuously differentiable and, thus, cannot be applied to solve a nonsmooth optimization problem.

2.1.3 Mirror Descent Algorithm

Mirror descent algorithm (MDA) [8] can be used to tackle a nonsmooth convex optimization problem wherein the objective function $f(\mathbf{x})$ is convex, but not continuously differentiable. In particular, MDA solves an optimization problem of the following form:

$$\begin{aligned} &\underset{\mathbf{x}}{\text{minimize}}\ f(\mathbf{x}) \\ &\text{subject to}\ \ \mathbf{x} \in \chi \end{aligned} \tag{2.4}$$

where χ denotes the constraint set, which is assumed to be convex and MDA generally requires that the subgradient of the objective is computable. Before going into the details of MDA, we define the following distance metric with respect to a function $\mathbf{\Phi}$:

$$\mathbf{B}_{\mathbf{\Phi}}(\mathbf{x}, \mathbf{y}) = \mathbf{\Phi}(\mathbf{x}) - \mathbf{\Phi}(\mathbf{y}) - \nabla^T \mathbf{\Phi}(\mathbf{y})(\mathbf{x} - \mathbf{y}) \tag{2.5}$$

where the function $\mathbf{\Phi}$ is a smooth convex. Note that, for the choice of $\chi \to \mathbb{R}^m$ and $\mathbf{\Phi}(\mathbf{x}) = \frac{1}{2}\|\mathbf{x}\|_2^2$, we get $\mathbf{B}_{\mathbf{\Phi}}(\mathbf{x}, \mathbf{y}) = \frac{1}{2}\|\mathbf{x} - \mathbf{y}\|_2^2$. Another choice of the function $\mathbf{\Phi}$ could be either a unit simplex or the entropy function which is defined as: $\mathbf{\Phi}(\mathbf{x}) = \sum_{j=1}^{m} x_j \log x_j$. The MDA algorithm employs function in (2.5) to solve (2.4) by solving the following subproblem at each iteration of the algorithm:

$$\mathbf{x}^{t+1} = \underset{\mathbf{x} \in \chi}{\arg\min}\ g(\mathbf{x}^t)^T \mathbf{x} + \frac{1}{\beta^t} \mathbf{B}_{\mathbf{\Phi}}(\mathbf{x}, \mathbf{x}^t) \tag{2.6}$$

where $g(\mathbf{x}^t)$ denotes the subgradient of $f(\mathbf{x})$ at $\mathbf{x}^t$ and $\beta^t > 0$ is step size.

2.1.4 Power Method-Like Iterations

As the name suggests, similar to the well-known power method, power method-like iterations (PMLI) can be applied for efficient solution approximation in signal-constrained quadratic optimization problems. However, PMLI is a generalized form of the power method that enables the accommodation of various signal constraints, in addition to the regularly used fixed-energy constraint. Consider a quadratic optimization problem of the generic form:

$$\begin{aligned} \underset{\mathbf{x}}{\text{maximize}} \quad & \mathbf{x}^H \mathbf{R} \mathbf{x} \\ \text{subject to} \quad & \mathbf{x} \in \Omega \end{aligned} \tag{2.7}$$

where $\mathbf{R}$ is positive definite and Ω is the signal constraint set containing signal with a fixed energy. A monotonically increasing objective of this quadratic problem can be obtained by updating $\mathbf{x}$ iteratively, via solving the following nearest-vector problem at each iteration:

$$\begin{aligned} \underset{\mathbf{x}^{(i+1)}}{\text{minimize}} \quad & \left\| \mathbf{x}^{(i+1)} - \mathbf{R}\mathbf{x}^{(i)} \right\|_2 \\ \text{subject to} \quad & \mathbf{x}^{(i+1)} \in \Omega \end{aligned} \tag{2.8}$$

whose solution can be represented using the projection operator $\mathbf{\Gamma}(\cdot)$ into the set Ω, that is,

$$\mathbf{x}^{(i+1)} = \mathbf{\Gamma}\left(\mathbf{R}\mathbf{x}^{(i)}\right) \tag{2.9}$$

where i denotes the iteration number. The derivations and applications of PMLI will be discussed in detail in Chapter 3.

2.1.5 Majorization-Minimization Framework

The majorization-minimization (MM) algorithm is a powerful optimization framework from using which we can derive iterative optimization algorithms to solve both convex and nonconvex problems. The idea behind the MM algorithm is to convert the original problem into a sequence of simpler problems to be solved until convergence. To explain this framework, let us

begin by considering the following generalized optimization problem:

$$\underset{\mathbf{x}\in\chi}{\text{minimize}}\ f(\mathbf{x}) \tag{2.10}$$

where $f(\mathbf{x})$ is assumed to be a continuous function. We would like to emphasize here that the above problem can take any of the following forms: convex, nonconvex, smooth, or nonsmooth. Furthermore, the constraint set χ can be either a convex or a nonconvex set. The MM-based algorithm solves the problem in (2.10) in two steps. In the first step, it constructs a surrogate function $g(\mathbf{x}|\mathbf{x}^t)$ which majorizes the objective function $f(\mathbf{x})$ at the current iterate $\mathbf{x}^t$. Then in the second step, the surrogate function is minimized to get the next iterate, that is,

$$\mathbf{x}^{t+1} \in \underset{\mathbf{x}\in\chi}{\arg\min}\ g\left(\mathbf{x}|\mathbf{x}^t\right) \tag{2.11}$$

The above two steps are repeated at every iteration, until the algorithm converges to a stationary point of the problem in (2.10). The majorization step combines the tangency and the upper bound condition, that is, a function $g(\mathbf{x})$ would be a surrogate function only if it satisfies the following conditions:

$$\begin{aligned} g\left(\mathbf{x}^t|\mathbf{x}^t\right) &= f\left(\mathbf{x}^t\right) \\ g\left(\mathbf{x}|\mathbf{x}^t\right) &\geq f\left(\mathbf{x}\right) \end{aligned} \tag{2.12}$$

It is worth pointing out that an objective function $f(\mathbf{x})$ can have more than one surrogate function $g(\mathbf{x})$. The convergence rate and computational complexity of the MM-based algorithm depends on how well one constructs the surrogate function. To achieve lower computational complexity, the surrogate function must be elementary and easy to minimize. However, the speed of convergence of the MM algorithm depend on how closely the surrogate function follows the shape of the objective function. Consequently, the success of the MM algorithm depends on the design of the surrogate function. To design a surrogate function, there are no fixed steps to follow. However, there are guidelines for designing various surrogate functions, which can be found [9, 10]. The derivations and applications of MM will be discussed in detail in Chapter 4.

2.1.5.1 Convex Concave Procedure

An optimization approach named convex concave procedure (CCP) or Difference of Convex (DC) programming [11] focuses on solving problems that take the following form:

$$\begin{aligned} &\underset{\mathbf{x}}{\text{minimize}}\ f_0(\mathbf{x}) - h_0(\mathbf{x}) \\ &\text{subject to}\ f_i(\mathbf{x}) - h_i(\mathbf{x}) \leq 0,\ i = 1, 2, \cdots, m \end{aligned} \tag{2.13}$$

where $f_i(\mathbf{x})$ and $h_i(\mathbf{x})$ denote some smooth convex functions. Note that the problem in (2.13) is convex only when $h_i(\mathbf{x})$ are affine functions; otherwise it is nonconvex in nature. To achieve a stationary point of the problem (2.13), the CCCP technique solves the following subproblem at each iteration:

$$\begin{aligned} &\underset{\mathbf{x}}{\text{minimize}}\ f_0(\mathbf{x}) - \left(h_0(\mathbf{x}^t) + \nabla h_0(\mathbf{x}^t)^T \left(\mathbf{x} - \mathbf{x}^t\right)\right) \\ &\text{subject to}\ f_i(\mathbf{x}) - \left(h_i(\mathbf{x}^t) + \nabla h_i(\mathbf{x}^t)^T \left(\mathbf{x} - \mathbf{x}^t\right)\right) \leq 0,\ i = 1, 2, \cdots, m \end{aligned} \tag{2.14}$$

The CCCP arrives at an iterative sequence by replacing each $h_i(\mathbf{x})$ in (2.13) by its tangent plane passing through $\mathbf{x}^t$.

2.1.5.2 Expectation Maximization Algorithm

Expectation maximization (EM) is an iterative approach, every iteration of which involves the following two steps: the expectation step and the maximization step [12]. In the expectation step, the conditional expectation of log likelihood function of complete data is arrived and in the next step, the conditional expectation computed in the previous step is maximized to arrive at the next iteration. The abovementioned two steps are repeated until the process converges. The EM algorithm has been widely used in the field of statistics to estimate the parameters of the maximum likelihood function. However, the main drawback of EM is that it involves computation of conditional expectation of complete data log likelihood function, which in some cases is not straightforward to calculate.

2.1.6 Block Coordinate Descent

When the objective of the optimization problem is separable in the variable blocks, then an approach known as the block coordinate descent (BCD) [13]

can be employed to solve the underlying optimization problem. At every iteration of BCD, minimization is performed with respect to one block by keeping the other blocks fixed at some given value. This usually results in subproblems that are much easier to solve than the original problem. Consider the following block-structured optimization problem:

$$\begin{array}{ll} \underset{\mathbf{x}_n}{\text{minimize}} & f(\mathbf{x}_1, \ldots, \mathbf{x}_N) \\ \text{subject to} & \mathbf{x}_n \in \mathcal{X}_n, \; \forall n = 1, \ldots, N \end{array} \tag{2.15}$$

where $f(.) : \prod_{n=1}^{N} \mathcal{X}_n \rightarrow \mathbb{R}$ is a continuous function (possibly nonconvex, nonsmooth), each $\mathcal{X}_n$ is a closed convex set, and each $\mathbf{x}_n$ is a block variable, $n = 1, 2, \ldots, N$. The general idea of the BCD algorithm is to choose, at each iteration, an index n and change $\mathbf{x}_n$ such that the objective function decreases. Thus, by applying BCD at every iteration i, N optimization problems, that is,

$$\begin{array}{ll} \underset{\mathbf{x}_n}{\text{minimize}} & f(\mathbf{x}_n; \mathbf{x}_{-n}^{(i)}) \\ \text{subject to} & \mathbf{x}_n \in \mathcal{X}_n \end{array} \tag{2.16}$$

will be solved, where, at each $n \in \{1, \ldots, N\}$, $\mathbf{x}_n$ is the current optimization variable block, while $\mathbf{x}_{-n}^{(i)}$ denotes the rest of the variable blocks. The index n can be updated in a cyclic manner using the Gauss-Seidel rule. Other update rules that can be used in BCD are the maximum block improvement (MBI) and the Gauss-Southwell rule [14, 15]. Note that the alternating minimization method is also known as the BCD approach when the number of blocks in the optimization variables is two. If we optimize a single coordinate instead of a block of coordinates, the BCD method simplifies to the coordinate descent (CD) approach. The derivations and applications of BCD will be discussed in detail in Chapter 5.

2.1.7 Alternating Projection

If the underlying minimization problem has multiple constraint sets (all of which are convex), the alternating projection (AP) or projection onto convex sets (POCS) approach [16, 17] can be used to solve it. The steps involved in AP are illustrated in the following. To begin, consider the following

example:

$$\begin{aligned} &\underset{\mathbf{x}}{\text{minimize}} \ \|\mathbf{x}-\mathbf{y}\|_2^2 \\ &\text{subject to } \ \mathbf{x} \in C_1 \cap C_2 \end{aligned} \tag{2.17}$$

where C_1 and C_2 are assumed to be some convex sets (as a simple case, we have assumed only two convex sets but the approach can be easily extended to more than two sets). The minimization problem in (2.17) seeks for the point $\mathbf{x}$ that is closer to $\mathbf{y}$ and also lies into the intersection of the two sets. Let $\mathcal{P}_{C_1}(\mathbf{x})$ and $\mathcal{P}_{C_2}(\mathbf{x})$ denote the orthogonal projection of $\mathbf{x}$ onto the convex sets C_1 and C_2, respectively. Then, according to alternating projection, given an estimate, the alternating projection algorithm first compute $\mathbf{z}^{t+1} = \mathcal{P}_{C_1}(\mathbf{x}^t)$ and then, using $\mathbf{z}^{t+1}$, determine $\mathbf{x}^{t+1} = \mathcal{P}_{C_2}(\mathbf{z}^{t+1})$ which will be used in the next iteration. Hence, the alternating projection computes a sequence of iterates $\mathbf{x}^t$ by alternatingly projecting between the two convex sets C_1 and C_2. However, as mentioned in [18], the alternating projection approach has very slow convergence. An improvement of the alternating projection method is the Dykstra's projection [19, 20] which finds a point nearest to $\mathbf{y}$ by adding few correction vectors $\mathbf{p}^k$ and $\mathbf{q}^k$ before every orthogonal projection step, that is, for the initialize values $\mathbf{p}^0 = 0$ and $\mathbf{q}^0 = 0$, the steps of Dykstra's method involve the following steps, which are repeated until convergence:

$$\begin{aligned} \mathbf{z}^t &= \mathcal{P}_{C_1}(\mathbf{x}^t + \mathbf{p}^t) \\ \mathbf{p}^{t+1} &= \mathbf{x}^t + \mathbf{p}^t - \mathbf{z}^t \\ \mathbf{x}^{t+1} &= \mathcal{P}_{C_2}(\mathbf{z}^t + \mathbf{q}^t) \\ \mathbf{q}^{t+1} &= \mathbf{z}^t + \mathbf{q}^t - \mathbf{x}^{t+1} \end{aligned} \tag{2.18}$$

Note for the implementation of both AP and the Dykstra's method, we must know how to compute the projection onto the convex sets. In the last two decades or so, an optimization algorithm named the interior point method [2] was widely used and that algorithm can solve a wide variety of convex problems. For instance, apart from solving the linear programming problems, the interior point method can solve many other convex optimization problems like quadratic, second-order cone, and semidefinite programming problems. However, the downside of the interior point approach is that at the every iteration of the interior point method, Newton's method has to be employed to solve a system of nonlinear equations, which

is noted to be time-consuming and, as a result, the interior point method-based algorithms are generally not scalable to solve problems with large dimensions [21].

2.1.8 Alternating Direction Method of Multipliers

Recently, an iterative optimization algorithm named alternating direction method of multipliers (ADMM) [22] has been introduced to solve a wide variety of optimization problems that can take the following form:

$$\begin{aligned} &\underset{\mathbf{x}_1,\,\mathbf{x}_2}{\text{minimize}}\; g_1(\mathbf{x}_1) + g_2(\mathbf{x}_2) \\ &\text{such that} \quad \mathbf{A}\mathbf{x}_1 + \mathbf{B}\mathbf{x}_2 = \mathbf{c} \end{aligned} \tag{2.19}$$

where $g_1(\cdot)$ and $g_2(\cdot)$ denote some convex functions, and $\mathbf{A}$, $\mathbf{B}$, and $\mathbf{c}$ denote some matrices and a vector, respectively. From (2.19), it can be seen that ADMM solves optimization problems with objective functions that are separable in two variables. Therefore, to solve a given optimization problem via ADMM, one might need to introduce new extra variables such that the optimization problem admits a form as in (2.19). Formulating the augmented Lagrangian for (2.19), we obtain:

$$\begin{aligned} L_\rho(\mathbf{x}_1, \mathbf{x}_2, \boldsymbol{\lambda}) =& g_1(\mathbf{x}_1) + g_2(\mathbf{x}_2) + \boldsymbol{\lambda}^T (\mathbf{A}\mathbf{x}_1 + \mathbf{B}\mathbf{x}_2 - \mathbf{c}) \\ &+ \frac{\gamma}{2}\|\mathbf{A}\mathbf{x}_1 + \mathbf{B}\mathbf{x}_2 - \mathbf{c}\|_2^2 \end{aligned} \tag{2.20}$$

where $\gamma > 0$ denotes the penalty parameter and $\boldsymbol{\lambda}$ denotes the Lagrangian multiplier. ADMM solves the problem in (2.19) in an iterative manner, that is, the primal variables ($\mathbf{x}_1$ and $\mathbf{x}_2$) are updated first by alternatingly minimizing the Lagrangian in (2.20) with respect to one variable while keeping the other fixed and vice versa. In the end, the dual variable is updated using the primal variables obtained in the previous step of the algorithm. The iterative steps involved in ADMM are summarized below:

$$\begin{aligned} \mathbf{x}_1^{t+1} &= \arg\min_{\mathbf{x}_1} L_\rho(\mathbf{x}_1, \mathbf{x}_2^t, \boldsymbol{\lambda}^t) \\ \mathbf{x}_2^{t+1} &= \arg\min_{\mathbf{x}_2} L_\rho(\mathbf{x}_1^{t+1}, \mathbf{x}_2, \boldsymbol{\lambda}^t) \\ \boldsymbol{\lambda}^{t+1} &= \boldsymbol{\lambda}^t + \gamma(\mathbf{A}\mathbf{x}_1^{t+1} + \mathbf{B}\mathbf{x}_2^{t+1} - \mathbf{c}) \end{aligned} \tag{2.21}$$

The proof of convergence for ADMM seeking the minimizer of problem (2.19) can be found in [22]. Interestingly, if we consider the extension of the problem (2.19) to three optimization variables, although it looks straightforward to implement the steps shown in (2.21), there are no concrete convergence guarantees available [23]. Consequently, this hinders the extension of the ADMM algorithm to handle additional constraints.

2.2 SUMMARY OF THE OPTIMIZATION APPROACHES

A summary of commonly used optimization algorithms is given below.

- Gradient descent can handle smooth convex and nonconvex objective functions. It requires selection of optimal step size at every iteration. Some of its applications are adaptive filtering [24] and parameter tuning in neural networks [25].
- Newton's method can handle both convex and nonconvex objective functions. At every iteration of the algorithm, it requires inverting a square matrix; which finds the iteration-dependent step size. Some of the applications are portfolio management [26] and logistic regression [25].
- MDA is applicable to both convex and nonconvex problems, it can also handle nonsmooth functions and nonconvex constraint sets. It requires selection of optimal step size at every iteration. One of the applications is in the reconstruction of positron emission tomography (PET) images [27].
- BCD is applicable to both convex and nonconvex problems. It is used when the optimization variable can be split into blocks. Some applications are non-negative matrix factorization [28] and linear transceiver design for communication systems [15].
- The alternating projection approach is used to solve optimization problems when the orthogonal projection of a given point onto the desired convex set is computable. Also, recently, the AP approach has been used to solve problems with nonconvex sets [29]. Some applications of AP are signal restoration [30], image denoising [31], and transmission tomography [32].

- Dykstra's projection is used when the orthogonal projection of a given point onto the desired convex set is computable. Some applications include image reconstruction from projections [33] and atomic-norm based spectral estimation.
- CCP is used to solve optimization problems when the cost function and constraints can be modeled as difference of convex functions. Multimatrix principal component analysis, and floor planning [11] are few applications where the DC approach is used.
- EM is used to solve MLE problems with hidden variables. Some applications of EM are the parameter estimation in Gaussian mixture model [34] and K-distribution [35].
- ADMM is applicable when the cost function is separable in the optimization variables. Some applications of ADMM include the estimation of sparse inverse covariance matrix and Lasso [22].

2.3 CONCLUSION

In the following, we discuss various factors that should be considered while deciding which optimization approach could be used to solve the optimization problem in hand:

- Optimization frameworks that yield algorithms, that avoid expensive operations such as huge matrix inversions at every iteration should be preferred. Furthermore, in the case of the multivariate optimization problem, the approach should exploit the block variable nature and should be able to split the parameters and optimize which will pave way for a parallel update of the parameters.
- The optimization approach should leverage any structure in the problem, that is, instead of solving the original complicated nonconvex problem, one can optimize a series of simpler problems to arrive at a stationary point of the original nonconvex problem.
- The optimization procedure should be a general framework and encompass many other optimization algorithms (like the MM approach covers the approaches like EM, CCP, and the proximal gradient descent algorithm).

- Some optimization algorithms, such as the gradient descent algorithm, require the user to tune the optimal step size, which can be seen as a drawback of the approach as the tuning of the hyper-parameter may not be easy and straightforward. However, optimization approaches like MM are independent of hyperparameter tuning.
- Another desirable feature for optimization approaches is their monotone nature of decreasing the objective through the course of iterations. For instance, through (2.11) and (2.12), it can be seen that the sequence of points $\{\mathbf{x}^t\}$ generated by the MM procedure will monotonically decrease the objective function:

$$f(\mathbf{x}^{k+1}) \leq g(\mathbf{x}^{k+1}|\mathbf{x}^k) \leq g(\mathbf{x}^k|\mathbf{x}^k) = f(\mathbf{x}^k) \tag{2.22}$$

  This is an important feature as it ensures natural convergence and the resultant algorithm is also stable. Moreover, under some mild assumptions, these algorithms can be easily proven to converge to a stationary point of the optimization problem [15].

References

[1] A. Ben-Tal and A. Nemirovski, *Lectures on Modern Convex Optimization: Analysis, Algorithms, and Engineering Applications*. SIAM, 2001.

[2] S. Boyd and L. Vandenberghe, *Convex Optimization*. Cambridge University Press, 2004.

[3] C. Nunn and L. Welch, "Multi-parameter local optimization for the design of superior matched filter polyphase pulse compression codes," in *Record of the IEEE 2000 International Radar Conference [Cat. No. 00CH37037]*, 2000, pp. 435–440.

[4] B. Friedlander, "Waveform design for MIMO radars," *IEEE Transactions on Aerospace and Electronic Systems*, vol. 43, no. 3, pp. 1227–1238, 2007.

[5] J. M. Baden, B. O'Donnell, and L. Schmieder, "Multiobjective sequence design via gradient descent methods," *IEEE Transactions on Aerospace and Electronic Systems*, vol. 54, no. 3, pp. 1237–1252, 2018.

[6] C. A. Mohr, P. M. McCormick, C. A. Topliff, S. D. Blunt, and J. M. Baden, "Gradient-based optimization of PCFM radar waveforms," *IEEE Transactions on Aerospace and Electronic Systems*, vol. 57, no. 2, pp. 935–956, 2021.

[7] J. Nocedal and S. Wright, *Numerical Optimization*. Springer Science & Business Media, 2006.

[8] A. Beck and M. Teboulle, "Mirror descent and nonlinear projected subgradient methods for convex optimization," *Operations Research Letters*, vol. 31, no. 3, pp. 167–175, 2003.

[9] Y. Sun, P. Babu, and D. P. Palomar, "Majorization-minimization algorithms in signal processing, communications, and machine learning," *IEEE Transactions on Signal Processing*, vol. 65, no. 3, pp. 794–816, 2017.

[10] D. R. Hunter and K. Lange, "A tutorial on MM algorithms," *The American Statistician*, vol. 58, no. 1, pp. 30–37, 2004.

[11] T. Lipp and S. Boyd, "Variations and extension of the convex–concave procedure," *Optimization and Engineering*, vol. 17, no. 2, pp. 263–287, 2016.

[12] A. P. Dempster, N. M. Laird, and D. B. Rubin, "Maximum likelihood from incomplete data via the em algorithm," *Journal of the Royal Statistical Society: Series B (Methodological)*, vol. 39, no. 1, pp. 1–22, 1977.

[13] S. J. Wright, "Coordinate descent algorithms," *Mathematical Programming*, vol. 151, no. 1, pp. 3–34, 2015.

[14] B. Chen, S. He, Z. Li, and S. Zhang, "Maximum block improvement and polynomial optimization," *SIAM Journal on Optimization*, vol. 22, no. 1, pp. 87–107, 2012.

[15] M. Razaviyayn, M. Hong, and Z.-Q. Luo, "A unified convergence analysis of block successive minimization methods for nonsmooth optimization," *SIAM Journal on Optimization*, vol. 23, no. 2, pp. 1126–1153, 2013.

[16] H. H. Bauschke and J. M. Borwein, "On projection algorithms for solving convex feasibility problems," *SIAM Review*, vol. 38, no. 3, pp. 367–426, 1996.

[17] C. L. Byrne, "Alternating minimization and alternating projection algorithms: A tutorial," *Sciences New York*, pp. 1–41, 2011.

[18] D. Henrion and J. Malick, "Projection methods for conic feasibility problems: applications to polynomial sum-of-squares decompositions," *Optimization Methods & Software*, vol. 26, no. 1, pp. 23–46, 2011.

[19] J. P. Boyle and R. L. Dykstra, "A method for finding projections onto the intersection of convex sets in hilbert spaces," in *Advances in Order Restricted Statistical Inference*. Springer, 1986, pp. 28–47.

[20] R. L. Dykstra, "An algorithm for restricted least squares regression," *Journal of the American Statistical Association*, vol. 78, no. 384, pp. 837–842, 1983.

[21] F. A. Potra and S. J. Wright, "Interior-point methods," *Journal of Computational and Applied Mathematics*, vol. 124, no. 1-2, pp. 281–302, 2000.

[22] S. Boyd, N. Parikh, E. Chu, B. Peleato, J. Eckstein *et al.*, "Distributed optimization and statistical learning via the alternating direction method of multipliers," *Foundations and Trends in Machine learning*, vol. 3, no. 1, pp. 1–122, 2011.

[23] C. Chen, B. He, Y. Ye, and X. Yuan, "The direct extension of admm for multi-block convex minimization problems is not necessarily convergent," *Mathematical Programming*, vol. 155, no. 1-2, pp. 57–79, 2016.

[24] R. Arablouei, S. Werner, and K. Dougancay, "Analysis of the gradient-descent total least-squares adaptive filtering algorithm," *IEEE Transactions on Signal Processing*, vol. 62, no. 5, pp. 1256–1264, 2014.

[25] C. M. Bishop, *Pattern Recognition and Machine Learning*. Springer, 2006.

[26] A. Agarwal, E. Hazan, S. Kale, and R. E. Schapire, "Algorithms for portfolio management based on the newton method," in *Proceedings of the 23rd International Conference on Machine Learning*, 2006, pp. 9–16.

[27] S. Rose, E. Y. Sidky, and C.-M. Kao, "Application of the entropic mirror descent algorithm to TOF PET image reconstruction," in *2014 IEEE Nuclear Science Symposium and Medical Imaging Conference (NSS/MIC)*, 2014, pp. 1–3.

[28] Y. Xu and W. Yin, "A block coordinate descent method for regularized multiconvex optimization with applications to nonnegative tensor factorization and completion," *SIAM Journal on Imaging Sciences*, vol. 6, no. 3, pp. 1758–1789, 2013.

[29] J. A. Tropp, I. S. Dhillon, R. W. Heath, and T. Strohmer, "Designing structured tight frames via an alternating projection method," *IEEE Transactions on Information Theory*, vol. 51, no. 1, pp. 188–209, 2005.

[30] A. Levi and H. Stark, "Signal restoration from phase by projections onto convex sets," *JOSA*, vol. 73, no. 6, pp. 810–822, 1983.

[31] M. Tofighi, K. Kose, and A. E. Cetin, "Denoising using projection onto convex sets (pocs) based framework," *arXiv preprint arXiv:1309.0700*, 2013.

[32] J. A. O'Sullivan and J. Benac, "Alternating minimization algorithms for transmission tomography," *IEEE Transactions on Medical Imaging*, vol. 26, no. 3, pp. 283–297, 2007.

[33] Y. Censor and G. T. Herman, "On some optimization techniques in image reconstruction from projections," *Applied Numerical Mathematics*, vol. 3, no. 5, pp. 365–391, 1987.

[34] R. A. Redner and H. F. Walker, "Mixture densities, maximum likelihood and the EM algorithm," *SIAM Review*, vol. 26, no. 2, pp. 195–239, 1984.

[35] W. J. Roberts and S. Furui, "Maximum likelihood estimation of k-distribution parameters via the expectation-maximization algorithm," *IEEE Transactions on Signal Processing*, vol. 48, no. 12, pp. 3303–3306, 2000.

Chapter 3

PMLI

To achieve agility in constrained radar signal design, an extremely low-cost quadratic optimization framework, referred to as PMLI, was developed in [1–3], and can be used for a multitude of radar code synthesis problems. The importance of PMLI stems from the fact that many waveform design and processing problems can be transformed directly to (or as a sequence of) quadratic optimization problems. Several examples of such a transformation will be provided in this chapter.

As evidence of its wide applicability, the reader will observe that PMLI subsumes the well-known power method as a special case. In contrast, since PMLI can handle various signal constraints (many of which cause the signal design problems to become NP-hard), it opens new avenues for practical radar signal processing applications requiring computational efficiency, such as in high-resolution settings with longer radar codes and large amounts of data collected for processing. Due to these unique properties, the PMLI have been already used in tens of technical publications; see, e.g., [4–18]. Nevertheless, there is an untapped potential for PMLI to breed a new generation of agile algorithms for waveform design and adaptive signal processing.

3.1 THE PMLI FORMULATION

Consider a quadratic optimization problem of the generic form:

$$\begin{aligned} \max_{\mathbf{x}} \quad & \mathbf{x}^H \mathbf{R} \mathbf{x} \\ \text{s. t.} \quad & \mathbf{x} \in \Omega \end{aligned} \tag{3.1}$$

where $\mathbf{R}$ is positive definite and Ω is the signal constraint set containing waveforms with a fixed energy. Although (3.1) is NP-hard for a general signal constraint set [1, 19], a monotonically increasing objective of (3.1) can be obtained by updating $\mathbf{x}$ iteratively by solving the following nearest-vector problem at each iteration:

$$\begin{aligned} \min_{\mathbf{x}^{(s+1)}} \quad & \left\| \mathbf{x}^{(s+1)} - \mathbf{R}\mathbf{x}^{(s)} \right\|_2 \\ \text{s. t.} \quad & \mathbf{x}^{(s+1)} \in \Omega \end{aligned} \tag{3.2}$$

Equivalently, this solution can be represented using the projection operator $\mathbf{\Gamma}(\cdot)$ into the set Ω, that is,

$$\mathbf{x}^{(s+1)} = \mathbf{\Gamma}\left(\mathbf{R}\mathbf{x}^{(s)}\right) \tag{3.3}$$

where s denotes the iteration number. One can continue updating $\mathbf{x}$ until convergence in the objective of (3.1), or for a fixed number of steps, say, S. It was already shown in [1] that the proposed iterations provide a monotonic behavior of the quadratic objective, no matter what the signal constraints are. In addition, one can easily ensure the positive definiteness of $\mathbf{R}$ by a simple diagonal loading, which results in an equivalent waveform design problem. In the following, we will consider several widely used signal constraints and derive the projection operator $\mathbf{\Gamma}(\cdot)$ for those cases.

3.1.1 Fixed-Energy Signals

This is a special case in which the iterations in (3.3) boil down to a simple power method, namely,

$$\mathbf{x}^{(s+1)} = \frac{\sqrt{N}}{\|\mathbf{R}\mathbf{x}^{(s)}\|_2} \left(\mathbf{R}\mathbf{x}^{(s)}\right) \tag{3.4}$$

where the energy of the waveform $\mathbf{x}$ is assumed to be equal to its length N.

3.1.2 Unimodular or Constant-Modulus Signals

Each entry of $\mathbf{x}$ is constrained to be on the unit circle. The PMLI can then be cast as:

$$\mathbf{x}^{(s+1)} = \exp\left(j \arg\left(\mathbf{R}\mathbf{x}^{(s)}\right)\right) \tag{3.5}$$

which simply sets the absolute values of $\mathbf{R}\mathbf{x}^{(s)}$ to one and keeps the phase arguments.

3.1.3 Discrete-Phase Signals

Suppose each entry of $\mathbf{x}$ is to be drawn from the M-ary set,

$$\Omega_M = \left\{ \exp\left(\frac{j2\pi m}{M}\right) : \; m = 0, 1, \cdots, M-1 \right\} \tag{3.6}$$

In this case the projection operator is given as

$$\mathbf{x}^{(s+1)} = \exp\left(j\mathbf{\Phi}_M\left(\arg\left(\mathbf{R}\mathbf{x}^{(s)}\right)\right)\right) \tag{3.7}$$

where the operator $\mathbf{\Phi}_M(.)$ yields the closest M-ary phase vector with entries from the set $\{\frac{2\pi m}{M} : \; m = 0, 1, \cdots, M-1\}$.

3.1.4 PAR-Constrained Signals

In many applications, unimodularity (equivalent to having a unit PAR) is not required and one can consider a more general PAR constraint, namely,

$$\text{PAR} = \frac{N \left\|\mathbf{x}\right\|_\infty^2}{\left\|\mathbf{x}\right\|_2^2} \leq \gamma \tag{3.8}$$

to design $\mathbf{x}$. In such cases, a PAR-constrained $\mathbf{x}$ can be obtained iteratively by solving

$$\begin{aligned} \min_{\mathbf{x}^{(s+1)}} \quad & \left\| \mathbf{x}^{(s+1)} - \mathbf{R}\mathbf{x}^{(s)} \right\|_2 \\ \text{s.t.} \quad & \left| \mathbf{x}_k^{(s+1)} \right| \leq \sqrt{\gamma}, \;\; 1 \leq k \leq N \\ & \left\| \mathbf{x}^{(s+1)} \right\|_2^2 = N \end{aligned} \tag{3.9}$$

whose globally optimal solution is obtained via the low-cost recursive algorithm suggested in [23].

The above derivations provide additional evidence for the simplicity of PMLI in the implementation stage. Due to their structure, PMLI is also a perfect candidate for unfolding into deep neural networks [24, 25], since its iterations can be characterized by a linear step, followed by a possibly non-linear operation—paving the way for further application of deep learning in radar signal design and processing. This aspect is further discussed in Chapter 7.

3.2 CONVERGENCE OF RADAR SIGNAL DESIGN

While local optimization algorithms typically ensure a monotonic behavior of the optimization objective and eventually its convergence through the optimization process, the PMLI formulation provides useful guarantees on the convergence of the waveform itself. In fact, it was shown in [1] that

$$\mathbf{x}^{(s+1)\,H} \mathbf{R}\, \mathbf{x}^{(s+1)} - \mathbf{x}^{(s)\,H} \mathbf{R}\, \mathbf{x}^{(s)} \geq \sigma_{\min}(\mathbf{R}) \, \|\mathbf{x}^{(s+1)} - \mathbf{x}^{(s)}\|_2^2 \tag{3.10}$$

where $\sigma_{\min}(.)$ denotes the minimum eigenvalue of the matrix argument. This implies that, for a positive definite $\mathbf{R}$, a convergence in the objective $\mathbf{x}^H \mathbf{R} \mathbf{x}$ directly translates into a convergence for the radar signal $\mathbf{x}$. Note that a unique solution is assumed, as usually happens in practical applications—with the exception of signal design problems involving several signals of similar quality. In such cases, a convergence to any of the performance-equivalent solutions would be desirable.

3.3 PMLI AND THE MAJORIZATION-MINIMIZATION TECHNIQUE: POINTS OF TANGENCY

Since the MM technique will be discussed in the next chapter, it would be useful to discuss the connections between the two approaches. Although the original PMLI derivations in [1–3] rely on a different mathematical machinery than MM, a strong connection between the two approaches exists. In fact, it can be shown that the iterations of PMLI can also be derived according to an MM perspective as follows: Problem (3.1) can be equivalently recast into a minimization problem with the objective function $-\mathbf{x}^H\mathbf{R}\mathbf{x}$. Recall that $\mathbf{R}$ is supposed to be positive definite, then the first-order Taylor expansion of $-\mathbf{x}^H\mathbf{R}\mathbf{x}$ provides a majorizer to the mentioned objective; see Chapter 4 for more details. Thus, the subproblem to be solved at the sth iteration of MM is

$$\begin{aligned} \min_{\mathbf{x}^{(s+1)}} \quad & -\operatorname{Re}\left(\mathbf{x}^{(s+1)\,H}\mathbf{R}\,\mathbf{x}^{(s)}\right) \\ \text{s.t.} \quad & \mathbf{x}^{(s+1)} \in \Omega \end{aligned} \tag{3.11}$$

which is further equivalent to problem (3.2) given that $\mathbf{x}$ is a signal with a fixed energy, meaning that the value of $\|\mathbf{x}^{(\mathbf{s+1})}\|_{\mathbf{2}}$ is fixed.

3.4 APPLICATION OF PMLI

To help the reader, various examples of PMLI deployment will be presented in the following.

3.4.1 A Toy Example: Synthesizing Cross-Ambiguity Functions

The radar ambiguity function represents the two-dimensional response of the matched filter to a signal with time delay τ and Doppler frequency shift f [26, 27]. The more general concept of cross-ambiguity function occurs when the matched filter is replaced by a mismatched filter. The cross ambiguity function (CAF) is defined as

$$\chi(\tau, f) = \int_{-\infty}^{\infty} u(t)v^*(t+\tau)e^{j2\pi ft}dt \tag{3.12}$$

where $u(t)$ and $v(t)$ are the transmit signal and the receiver filter, respectively (with the ambiguity function obtained from (3.12) using $v(t) = u(t)$). In particular, $u(t)$ and $v(t)$ are typically given by pulse coding:

$$u(t) = \sum_{k=1}^{N} x_k p_k(t), \quad v(t) = \sum_{k=1}^{N} y_k p_k(t) \tag{3.13}$$

where $\{p_k(t)\}$ are pulse-shaping functions (such as the rectangular pulses), and

$$\boldsymbol{x} = (x_1 \cdots x_N)^T, \ \ \boldsymbol{y} = (y_1 \cdots y_N)^T \tag{3.14}$$

are the code, and the filter vectors, respectively. The design problem of synthesizing a desired CAF has a small number of free variables (i.e., the entries of the vectors $\boldsymbol{x}$ and $\boldsymbol{y}$) compared to the large number of constraints arising from two-dimensional matching criteria (to a given $|\chi(\tau, f)|$). Therefore, the problem is generally considered to be difficult and there are not many methods to synthesize a desired (cross) ambiguity function. Below, we describe briefly the cyclic approach of [28] for CAF design that can benefit from PMLI-based optimization.

The problem of matching a desired $|\chi(\tau, f)| = d(\tau, f)$ can be formulated as the minimization of the criterion [28],

$$g(\boldsymbol{x}, \boldsymbol{y}, \phi) = \int_{-\infty}^{\infty} \int_{-\infty}^{\infty} w(\tau, f) \left| d(\tau, f) e^{j\phi(\tau, f)} - \boldsymbol{y}^H \boldsymbol{J}(\tau, f) \boldsymbol{x} \right|^2 d\tau df \tag{3.15}$$

where $\boldsymbol{J}(\tau, f) \in \mathbb{C}^{N \times N}$ is given, $w(\tau, f)$ is a weighting function that specifies the CAF area of interest, and $\phi(\tau, f)$ represent auxiliary phase variables. It is not difficult to see that, for fixed $\boldsymbol{x}$ and $\boldsymbol{y}$, the minimizer $\phi(\tau, f)$ is given by $\phi(\tau, f) = \arg\{\boldsymbol{y}^H \boldsymbol{J}(\tau, f) \boldsymbol{x}\}$. For fixed $\phi(\tau, f)$ and $\boldsymbol{x}$, the criterion g can be written as

$$\begin{aligned} g(\boldsymbol{y}) &= \boldsymbol{y}^H \boldsymbol{D}_1 \boldsymbol{y} - \boldsymbol{y}^H \boldsymbol{B}^H \boldsymbol{x} - \boldsymbol{x}^H \boldsymbol{B} \boldsymbol{y} + \text{const}_1 \\ &= (\boldsymbol{y} - \boldsymbol{D}_1^{-1} \boldsymbol{B}^H \boldsymbol{x})^H \boldsymbol{D}_1 (\boldsymbol{y} - \boldsymbol{D}_1^{-1} \boldsymbol{B}^H \boldsymbol{x}) + \text{const}_2 \end{aligned} \tag{3.16}$$

where $\boldsymbol{B}$ and $\boldsymbol{D}_1$ are given matrices in $\mathbb{C}^{N \times N}$ [28]. Due to practical considerations, the transmit coefficients $\{x_k\}$ must have low PAR values. However, the receiver coefficients $\{y_k\}$ need not be constrained in such a way. Therefore, the minimizer $\boldsymbol{y}$ of $g(\boldsymbol{y})$ is given by $\boldsymbol{y} = \boldsymbol{D}_1^{-1} \boldsymbol{B}^H \boldsymbol{x}$. Similarly, for fixed

$\phi(\tau, f)$ and $\boldsymbol{y}$, the criterion g can be written as

$$g(\boldsymbol{x}) = \boldsymbol{x}^H \boldsymbol{D}_2 \boldsymbol{x} - \boldsymbol{x}^H \boldsymbol{B}\boldsymbol{y} - \boldsymbol{y}^H \boldsymbol{B}^H \boldsymbol{x} + \text{const}_3 \tag{3.17}$$

where $\boldsymbol{D}_2 \in \mathbb{C}^{N\times N}$ is given [28]. If a unimodular code vector $\boldsymbol{x}$ is desired, then the optimization of $g(\boldsymbol{x})$ is a unimodular quadratic program (UQP), as $g(\boldsymbol{x})$ can be written as

$$g(\boldsymbol{x}) = \begin{pmatrix} e^{j\varphi}\boldsymbol{x} \\ e^{j\varphi} \end{pmatrix}^H \begin{pmatrix} \boldsymbol{D}_2 & -\boldsymbol{B}\boldsymbol{y} \\ -(\boldsymbol{B}\boldsymbol{y})^H & 0 \end{pmatrix} \begin{pmatrix} e^{j\varphi}\boldsymbol{x} \\ e^{j\varphi} \end{pmatrix} + \text{const}_3 \tag{3.18}$$

where $\varphi \in [0, 2\pi)$ is a free phase variable. Such a UQP can be tackled directly by employing PMLI.

In the following, we consider the design of a thumbtack CAF [26–31]:

$$d(\tau, f) = \begin{cases} N & (\tau, f) = (0, 0) \\ 0 & \text{otherwise} \end{cases} \tag{3.19}$$

Suppose $N = 53$, let T be the time duration of the total waveform, and let $t_p = T/N$ represent the time duration of each subpulse. Define the weighting function as

$$w(\tau, f) = \begin{cases} 1 & (\tau, f) \in \Psi \backslash \Psi_{ml} \\ 0 & \text{otherwise} \end{cases} \tag{3.20}$$

where $\Psi = [-10t_p, 10t_p] \times [-2/T, 2/T]$ is the region of interest and $\Psi_{ml} = ([-t_p, t_p]\backslash\{0\}) \times ([-1/T, 1/T]\backslash\{0\})$ is the mainlobe area that is excluded due to the sharp changes near the origin of $d(\tau, f)$. Note that the time delay τ and the Doppler frequency f are typically normalized by T and $1/T$, respectively, and as a result, the value of t_p can be chosen freely without changing the performance of CAF design.

The synthesis of the desired CAF is accomplished via the cyclic minimization of (3.15) with respect to $\boldsymbol{x}$ and $\boldsymbol{y}$. A Björck code is used to initialize both vectors $\boldsymbol{x}$ and $\boldsymbol{y}$. The Björck code of length $N = p$ (where p is a prime number for which $p \equiv 1 \pmod 4$) is given by $\boldsymbol{b}(k) = e^{j(\frac{k}{p})\arccos\left(1/(1+\sqrt{p})\right)}$, $0 \le k < p$, with $(\frac{k}{p})$ denoting the Legendre symbol. Figure 3.1 depicts the normalized CAF modulus of the Björck code (i.e., the initial CAF) and the obtained CAF using the UQP formulation in (3.18) and the proposed method. Despite the fact that designing CAF with a unimodular transmit vector $\boldsymbol{x}$ is a rather difficult problem, PMLI is able to efficiently suppress the CAF sidelobes in the region of interest.

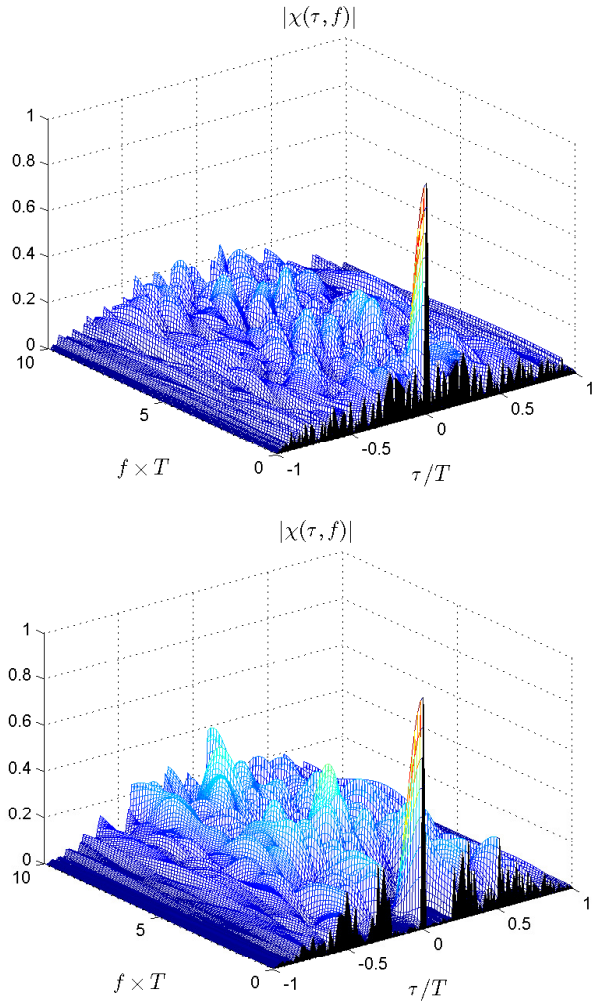

Figure 3.1. The normalized CAF modulus for (top) the Björck code of length $N = 53$ (i.e., the initial CAF), and (bottom) the UQP formulation in (3.18) and the PMLI-based design.

3.4.2 PMLI Application with Dinkelbach's Fractional Programming

The PMLI approach can be used to optimize the radar SNR or MSE objectives. Consider a monostatic radar that transmits a linearly encoded burst of pulses. In a clutter-free scenario, the observed baseband backscattered signal $\boldsymbol{y}$ for a stationary target can be written as (see, e.g., [32]):

$$\boldsymbol{y} = a\boldsymbol{s} + \boldsymbol{n} \tag{3.21}$$

where a represents channel propagation and backscattering effects, $\boldsymbol{n}$ is the disturbance/noise component, and $\boldsymbol{s}$ is the unimodular vector containing the code elements.

Under the assumption that $\boldsymbol{n}$ is a zero-mean complex-valued circular Gaussian vector with known positive definite covariance matrix $\mathbb{E}[\boldsymbol{n}\boldsymbol{n}^H] = \boldsymbol{M}$, the signal to noise ratio (SNR) is given by [33],

$$\text{SNR} = |a|^2 \boldsymbol{s}^H \boldsymbol{P} \boldsymbol{s} \tag{3.22}$$

where $\boldsymbol{P} = \boldsymbol{M}^{-1}$. Therefore, the problem of designing codes optimizing the SNR of the radar system can be formulated directly as a UQP.

Of interest is the fractional objective cases that occur in mismatched filtering. In particular, the MSE of the radar backscattering coefficient (α_0) estimation may be expressed as [34],

$$\text{MSE}(\widehat{\alpha}_0) = \frac{\boldsymbol{w}^H \boldsymbol{R} \boldsymbol{w}}{|\boldsymbol{w}^H \boldsymbol{s}|^2} = \frac{\boldsymbol{s}^H \boldsymbol{Q} \boldsymbol{s} + \mu}{\boldsymbol{s}^H \boldsymbol{W} \boldsymbol{s}} \tag{3.23}$$

where $\boldsymbol{W} = \boldsymbol{w}\boldsymbol{w}^H$ with $\boldsymbol{w}$ being the mismatched filter (MMF),

$$\boldsymbol{R} = \beta \sum_{0<|k|\leq(N-1)} \boldsymbol{J}_k \boldsymbol{s}\boldsymbol{s}^H \boldsymbol{J}_k^H + \boldsymbol{M} \tag{3.24}$$

$$\boldsymbol{Q} = \beta \sum_{0<|k|\leq(N-1)} \boldsymbol{J}_k^H \boldsymbol{w}\boldsymbol{w}^H \boldsymbol{J}_k \tag{3.25}$$

the matrix operators $\{\boldsymbol{J}_k\}$ are the shifting matrices defined by

$$[\boldsymbol{J}_k]_{l,m} = [\boldsymbol{J}_{-k}^H]_{l,m} \triangleq \delta_{m-l-k} \tag{3.26}$$

with $\delta_{(.)}$ denoting the Kronecker delta function, $\boldsymbol{M}$ is the signal-independent noise covariance matrix, β is the average clutter power, and $\mu = \boldsymbol{w}^H \boldsymbol{M} \boldsymbol{w}$.

We observe that both the numerator and denominator of (3.23) are quadratic in $\boldsymbol{s}$. To deal with the minimization of (3.23), we exploit the idea of fractional programming [35]. Let $a(\boldsymbol{s}) = \boldsymbol{s}^H \boldsymbol{Q} \boldsymbol{s} + \mu$, $b(\boldsymbol{s}) = \boldsymbol{s}^H \boldsymbol{W} \boldsymbol{s}$, and note that, for MSE to be finite, we must have $b(\boldsymbol{s}) > 0$. Moreover, let $f(\boldsymbol{s}) = \text{MSE}(\widehat{\alpha}_0) = a(\boldsymbol{s})/b(\boldsymbol{s})$ and suppose that $\boldsymbol{s}_\star$ denotes the current value of $\boldsymbol{s}$. We define $g(\boldsymbol{s}) \triangleq a(\boldsymbol{s}) - f(\boldsymbol{s}_\star) b(\boldsymbol{s})$, and $\boldsymbol{s}_\dagger \triangleq \arg\min_{\boldsymbol{s}} g(\boldsymbol{s})$. It is straightforward to verify that $g(\boldsymbol{s}_\dagger) \leq g(\boldsymbol{s}_\star) = 0$. Consequently, we have that $g(\boldsymbol{s}_\dagger) = a(\boldsymbol{s}_\dagger) - f(\boldsymbol{s}_\star) b(\boldsymbol{s}_\dagger) \leq 0$, which implies

$$f(\boldsymbol{s}_\dagger) \leq f(\boldsymbol{s}_\star) \tag{3.27}$$

as $b(\boldsymbol{s}_\dagger) > 0$. Therefore, $\boldsymbol{s}_\dagger$ can be considered as a new vector $\boldsymbol{s}$ that decreases $f(\boldsymbol{s})$. Note that for (3.27) to hold, $\boldsymbol{s}_\dagger$ does not necessarily have to be a minimizer of $g(s)$; indeed, it is enough if $\boldsymbol{s}_\dagger$ is such that $g(\boldsymbol{s}_\dagger) \leq g(\boldsymbol{s}_\star)$.

For a given MMF vector $\boldsymbol{w}$, and any $\boldsymbol{s}_\star$ of the minimizer $\boldsymbol{s}$ of (3.23), we have (assuming $\|\boldsymbol{s}\|_2^2 = N$):

$$g(\boldsymbol{s}) = \boldsymbol{s}^H (\boldsymbol{Q} + (\mu/N)\boldsymbol{I} - f(\boldsymbol{s}_\star)\boldsymbol{W}) \boldsymbol{s} = \boldsymbol{s}^H \boldsymbol{T} \boldsymbol{s} \tag{3.28}$$

where $\boldsymbol{T} \triangleq \boldsymbol{Q} + (\mu/N)\boldsymbol{I} - f(\boldsymbol{s}_\star)\boldsymbol{W}$. Now, let λ be a real number larger than the maximum eigenvalue of $\boldsymbol{T}$. Then the minimization of (3.23) with respect to (w.r.t.) unimodular $\boldsymbol{s}$ can be cast as the following UQP:

$$\begin{aligned} \max_{\boldsymbol{s}} \quad & \boldsymbol{s}^H \widetilde{\boldsymbol{T}} \boldsymbol{s} \\ \text{s.t.} \quad & |s_k| = 1, \;\; 1 \leq k \leq N \end{aligned} \tag{3.29}$$

in which $\widetilde{\boldsymbol{T}} \triangleq \lambda \boldsymbol{I} - \boldsymbol{T}$ is positive definite. The PMLI-based approach to (3.29) is referred to as the CREW(cyclic) algorithm [34]. Due to the application of PMLI, CREW(cyclic) can also deal with other common signal constraints such as a more general PAR constraint.

We examine the performance of CREW(cyclic) by comparing it with three methods previously devised in [36]; namely CAN-MMF, CREW(gra), and CREW(fre). The CAN-MMF method employs the CAN algorithm in [29] to design a transmit sequence with good correlation properties. As a result, the design of the transmit waveform is independent of the receive filter. Note that no prior knowledge of interference is used in the waveform design of CAN-MMF. CREW(gra) is a gradient-based algorithm for

minimizing (3.83), which can only deal with the unimodularity constraint. Moreover, a large number of iterations is needed by CREW(gra) until convergence and, in each iteration, the update of the gradient vector is time-consuming. CREW(fre) is a frequency-based approach that yields globally optimal values of the spectrum of the transmit waveform as well as the receive filter for a relaxed version of the original waveform design problem, and hence, in general, does not provide an optimal solution to the latter problem. Like CAN-MMF, CREW(fre) can handle both unimodularity and PAR constraints. Moreover, it can be used to design relatively long sequences due to leveraging FFT operations.

We adopt the same simulation settings as in [36]. Particularly, we consider the following interference (including both clutter and noise) covariance matrix:

$$\mathbf{\Gamma} = \sigma_J^2 \mathbf{\Gamma}_J + \sigma^2 \boldsymbol{I} \tag{3.30}$$

where $\sigma_J^2 = 100$ and $\sigma^2 = 0.1$ are the jamming and noise powers, respectively, and the jamming covariance matrix $\mathbf{\Gamma}_J$ is given by $[\mathbf{\Gamma}_J]_{k,l} = q_{k-l}$ where $\Big(q_0\, q_1\, \cdots\, q_{N-1}\, q_{-(N-1)}\, \cdots\, q_{-1}\Big)$ can be obtained by an inverse FFT (IFFT) of the jamming power spectrum $\{\eta_p\}$ at frequencies $(p-1)/(2N-1)$, $p \in \{1, \cdots, 2N-1\}$. We set the average clutter power to $\beta = 1$. The Golomb sequence is used to initialize the transmit code $\boldsymbol{s}$ for all the algorithms.

As the first example, we consider a spot jamming located at a normalized frequency $f_0 = 0.2$, with a power spectrum given by

$$\eta_p = \begin{cases} 1, & p = \lfloor (2N-1) f_0 \rfloor \\ 0, & \text{elsewhere,} \end{cases} \quad p = 1, \cdots, 2N-1 \tag{3.31}$$

Figure 3.2 shows the MSE values corresponding to CAN-MMF, CREW (fre), CREW(gra), and CREW(cyclic), under the unimodularity constraint, for various sequence lengths. In order to include the CREW(gra) algorithm in the comparison, we show its MSE only for $N \leq 300$ since CREW(gra) is computationally prohibitive for $N > 300$ on an ordinary PC. Figure 3.2 also depicts the MSE values obtained by the different algorithms under the constraint PAR ≤ 2 on the transmit sequence. One can observe that CREW(cyclic) provides the smallest MSE values for all sequence lengths. In particular, CREW(cyclic) outperforms CAN-MMF and CREW(fre) under both constraints. Due to the fact that both CREW(gra) and CREW(cyclic) are MSE optimizers, the performances of the two methods are almost identical under the unimodularity constraint for $N \leq 300$. However, compared

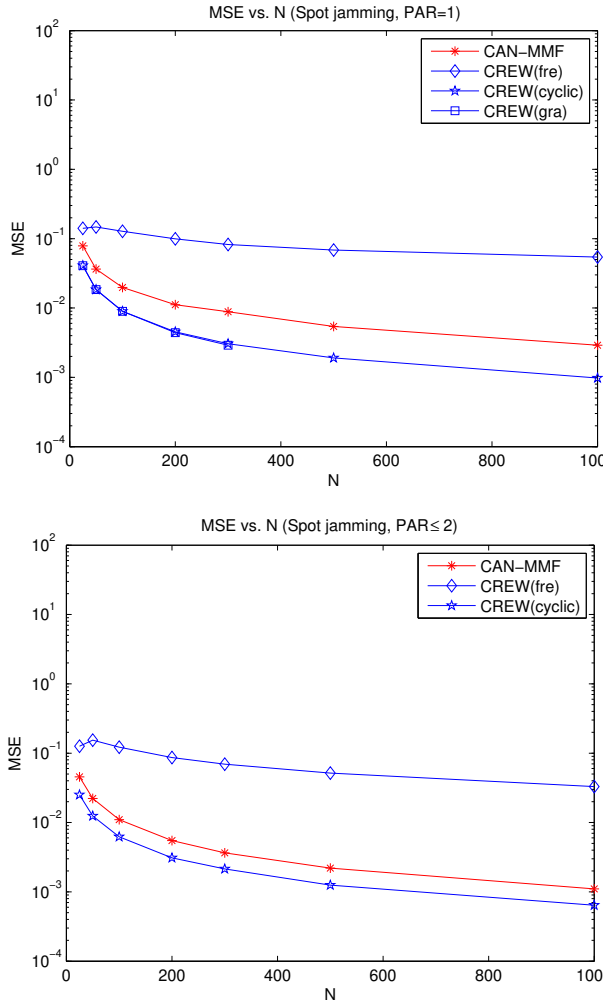

Figure 3.2. MSE values obtained by the different design algorithms for a spot jamming with normalized frequency $f_0 = 0.2$, and the following PAR constraints on the transmit sequence: (top) PAR $= 1$ (unimodularity constraint), and (bottom) PAR ≤ 2.

to CREW(gra), the CREW(cyclic) algorithm can be used to design longer sequences (even more than $N \sim 1,000$) due to its relatively small computational burden. Furthermore, CREW(cyclic) can handle not only the unimodularity constraint but also more general PAR constraints.

3.4.3 Doppler-Robust Radar Code Design

In the moving target scenario, the discrete-time received signal $\boldsymbol{r}$ for the range-cell corresponding to the time delay τ can be written as [37, 38]:

$$\boldsymbol{r} = \alpha\, \boldsymbol{s} \odot \boldsymbol{p} + \boldsymbol{s} \odot \boldsymbol{c} + \boldsymbol{n} \tag{3.32}$$

where $\alpha = \alpha_t e^{-j\omega_c \tau}$, $\boldsymbol{s} \triangleq [s_0 \quad s_1 \quad \dots \quad s_{N-1}]^T$ is the code vector (to be designed), $\boldsymbol{p} \triangleq [1 \; e^{j\omega} \quad \dots \quad e^{j(N-1)\omega}]^T$ with ω being the normalized Doppler shift of the target, $\boldsymbol{c}$ is the vector corresponding to the clutter component, and the vector $\boldsymbol{n}$ represents the signal-independent interferences. A detailed construction of $\boldsymbol{c}$ and $\boldsymbol{w}$ from the continuous variables $c(t)$ and $n(t)$ can be found in [37].

Using (3.32), the target detection problem can be cast as the following binary hypothesis test:

$$\begin{cases} \mathrm{H}_0: & \boldsymbol{r} = \boldsymbol{s} \odot \boldsymbol{c} + \boldsymbol{n} \\ \mathrm{H}_1: & \boldsymbol{r} = \alpha \boldsymbol{s} \odot \boldsymbol{p} + \boldsymbol{s} \odot \boldsymbol{c} + \boldsymbol{n} \end{cases} \tag{3.33}$$

Note that the covariance matrices of $\boldsymbol{c}$ and $\boldsymbol{w}$ (denoted by $\boldsymbol{C}$ and $\boldsymbol{M}$) can be assumed to be a priori known (e.g., they can be obtained by using geographical, meteorological, or prescan information) [39, 40]. For a known target Doppler shift, using the derivation in [41, Chapter 8] in the case of (3.33) yields the GLR detector:

$$\left| \boldsymbol{r}^H \left(\boldsymbol{M} + \boldsymbol{S}\boldsymbol{C}\boldsymbol{S}^H \right)^{-1} (\boldsymbol{s} \odot \boldsymbol{p}) \right|^2 \underset{\mathrm{H}_1}{\overset{\mathrm{H}_0}{\lessgtr}} \eta \tag{3.34}$$

where η is the detection threshold and $\boldsymbol{S} \triangleq \mathrm{Diag}(\boldsymbol{s})$. In the sequel, we refer to $\boldsymbol{S}$ as the *code matrix* associated with the code vector $\boldsymbol{s}$. The performance of the above detector is dependent on the GLR SNR [41, Chapter 8], that is

$$|\alpha|^2 (\boldsymbol{s} \odot \boldsymbol{p})^H \left(\boldsymbol{M} + \boldsymbol{S}\boldsymbol{C}\boldsymbol{S}^H \right)^{-1} (\boldsymbol{s} \odot \boldsymbol{p}) \tag{3.35}$$

It is interesting to observe that the GLR SNR is invariant to a phase-shift of the code vector $\boldsymbol{a}$, that is the code vectors $\boldsymbol{s}$ and $e^{j\varphi}\boldsymbol{s}$ (for any $\varphi \in [0, 2\pi]$) result in the same value of the GLR SNR. The code design for obtaining the optimal GLR SNR can be dealt with by the maximization of the following GLR performance metric:

$$\begin{aligned}(\boldsymbol{s}\odot\boldsymbol{p})^H\left(\boldsymbol{M}+\boldsymbol{S}\boldsymbol{C}\boldsymbol{S}^H\right)^{-1}(\boldsymbol{s}\odot\boldsymbol{p}) \\ =\mathrm{tr}\left\{\boldsymbol{S}^H(\boldsymbol{M}+\boldsymbol{S}\boldsymbol{C}\boldsymbol{S}^H)^{-1}\boldsymbol{S}\boldsymbol{p}\boldsymbol{p}^H\right\} \\ =\mathrm{tr}\left\{\left((\boldsymbol{S}^H\boldsymbol{M}^{-1}\boldsymbol{S})^{-1}+\boldsymbol{C}\right)^{-1}\boldsymbol{p}\boldsymbol{p}^H\right\}\end{aligned} \tag{3.36}$$

To improve the detection performance of the system when the target Doppler shift ω is known, it is required that the metric in (3.36) be maximized for the given ω. However, the target Doppler shift (ω) is usually unknown at the transmitter. In such cases, the detector of (3.34) will no longer be applicable. The optimal detector for the detection problem in (3.33) in cases where ω is unknown is obtained by considering prior pdf of ω. Due to the fact that there exists no closed-form expression for the performance metrics of the optimal detector in this condition, we consider the following design metric:

$$\mathrm{tr}\left\{\left(\boldsymbol{S}^{-1}\boldsymbol{M}\boldsymbol{S}^{-H}+\boldsymbol{C}\right)^{-1}\boldsymbol{W}\right\} \tag{3.37}$$

where $\boldsymbol{W} = \mathbb{E}\{\boldsymbol{p}\boldsymbol{p}^H\}$ w.r.t. ω over any desired interval $[\omega_l, \omega_u]$ ($-\pi \leq \omega_l < \omega_u \leq \pi$). The reason for selecting this metric is that it can be shown that maximizing the above metric results in the maximization of a lower bound on the J-divergence associated with the detection problem. It is worth mentioning that the pdf of ω and the values of ω_l and ω_u can be obtained in practice using a priori knowledge about the type of target (e.g., knowing if the target is an airplane, a ship, or a missile) as well as rough estimates of the target Doppler shift obtained by prescan procedures.

To optimize the design metric under an energy constraint, we consider the following problem:

$$\begin{aligned}\max_{\boldsymbol{S}}\ \ &\mathrm{tr}\left\{\left(\boldsymbol{S}^{-1}\boldsymbol{M}\boldsymbol{S}^{-H}+\boldsymbol{C}\right)^{-1}\boldsymbol{W}\right\} \\ \text{s.t.}\ \ &\boldsymbol{S}\in\Omega,\end{aligned} \tag{3.38}$$

where Ω denotes the unimodular constraint signal set. In the following, we discuss the CADCODE-U framework of [37] to tackle (3.38), where U stands for unimodular signals. A solely energy-constrained signal version of the algorithm can also be found in [37], which is simply referred to as CADCODE.

We begin by observing that as $\boldsymbol{W} \succeq \boldsymbol{0}$, there must exist a full column-rank matrix $\boldsymbol{V} \in \mathbb{C}^{N\times\delta}$ such that $\boldsymbol{W} = \boldsymbol{V}\boldsymbol{V}^H$ (particularly observe that $\boldsymbol{V} = [\boldsymbol{w}_1\ \boldsymbol{w}_2\ ...\ \boldsymbol{w}_\delta]$ yields such decomposition of $\boldsymbol{W}$). As a result,

$$\begin{aligned}\mathrm{tr}\left\{\left((\boldsymbol{S}^H\boldsymbol{M}^{-1}\boldsymbol{S})^{-1}+\boldsymbol{C}\right)\boldsymbol{W}\right\} &= \mathrm{tr}\left\{\boldsymbol{S}^H(\boldsymbol{M}+\boldsymbol{S}\boldsymbol{C}\boldsymbol{S}^H)^{-1}\boldsymbol{S}\boldsymbol{W}\right\}\\ &= \mathrm{tr}\left\{\boldsymbol{V}^H\boldsymbol{S}^H(\boldsymbol{M}+\boldsymbol{S}\boldsymbol{C}\boldsymbol{S}^H)^{-1}\boldsymbol{S}\boldsymbol{V}\right\}\end{aligned} \tag{3.39}$$

Let $\boldsymbol{\Theta} \triangleq \theta\boldsymbol{I} - \boldsymbol{V}^H\boldsymbol{S}^H(\boldsymbol{M}+\boldsymbol{S}\boldsymbol{C}\boldsymbol{S}^H)^{-1}\boldsymbol{S}\boldsymbol{V}$, with the diagonal loading factor θ chosen such that $\boldsymbol{\Theta} \succ \boldsymbol{0}$. Note that the optimization problem (3.38) is equivalent to the minimization problem

$$\begin{aligned}\min_{\boldsymbol{S}}\ \ &\mathrm{tr}\{\boldsymbol{\Theta}\}\\ \text{s.t.}\ \ &\boldsymbol{s}\in\Omega\end{aligned} \tag{3.40}$$

Now define

$$\boldsymbol{R} \triangleq \begin{bmatrix}\theta\boldsymbol{I} & \boldsymbol{V}^H\boldsymbol{S}^H\\ \boldsymbol{S}\boldsymbol{V} & \boldsymbol{M}+\boldsymbol{S}\boldsymbol{C}\boldsymbol{S}^H\end{bmatrix} \tag{3.41}$$

and observe that for $\boldsymbol{U} \triangleq [\boldsymbol{I}_\delta\ \ \boldsymbol{0}_{N\times\delta}]^T$, we have

$$\boldsymbol{U}^H\boldsymbol{R}^{-1}\boldsymbol{U} = \boldsymbol{\Theta}^{-1} \tag{3.42}$$

To tackle (3.40), let $g(\boldsymbol{S},\boldsymbol{Y}) \triangleq \mathrm{tr}\{\boldsymbol{Y}^H\boldsymbol{R}\boldsymbol{Y}\}$ with $\boldsymbol{Y}$ being an auxiliary variable, and consider the following minimization problem:

$$\begin{aligned}\min_{\boldsymbol{S},\boldsymbol{Y}}\ \ &g(\boldsymbol{S},\boldsymbol{Y})\\ \text{subject to}\ \ &\boldsymbol{Y}^H\boldsymbol{U}=\boldsymbol{I}\\ &\boldsymbol{S}\in\Omega\end{aligned} \tag{3.43}$$

For fixed $\boldsymbol{S}$, the minimizer $\boldsymbol{Y}$ of (3.43) can be obtained using result 35 in [42, p. 354] as

$$\boldsymbol{Y} = \boldsymbol{R}^{-1}\boldsymbol{U}(\boldsymbol{U}^H\boldsymbol{R}^{-1}\boldsymbol{U})^{-1} \tag{3.44}$$

However, for fixed $\boldsymbol{Y}$, the minimization of $g(\boldsymbol{Y}, \boldsymbol{S})$ w.r.t. $\boldsymbol{S}$ yields a UQP w.r.t. $\boldsymbol{s}$; see [37] for details. Consequently, PMLI can be employed for the task of code design.

It is straightforward to verify that at the minimizer $\boldsymbol{Y}$ of (3.43),

$$g(\boldsymbol{Y}, \boldsymbol{S}) = \mathrm{tr}\{\boldsymbol{\Theta}\} \tag{3.45}$$

From this property, we conclude that each step of the cyclic minimization of (3.43) leads to a decrease of $\mathrm{tr}\{\boldsymbol{\Theta}\}$. Indeed, let $f(\boldsymbol{S}) = \mathrm{tr}\{\boldsymbol{\Theta}\}$ and note that

$$\begin{aligned} f\left(\boldsymbol{S}^{(k+1)}\right) &= g\left(\boldsymbol{Y}^{(k+2)}, \boldsymbol{S}^{(k+1)}\right) \\ &\leq g\left(\boldsymbol{Y}^{(k+1)}, \boldsymbol{S}^{(k+1)}\right) \\ &\leq g\left(\boldsymbol{Y}^{(k+1)}, \boldsymbol{S}^{(k)}\right) = f\left(\boldsymbol{S}^{(k)}\right) \end{aligned} \tag{3.46}$$

where the superscript k denotes the iteration number. The first and the second inequalities in (3.46) hold true due to the minimization of $g(\boldsymbol{S}, \boldsymbol{Y})$ w.r.t. $\boldsymbol{Y}$ and $\boldsymbol{S}$, respectively. As a result, CADCODE-U converges to a local optimum of (3.38).

Numerical results will be provided to examine the performance of the proposed method as compared to the alternatives discussed in [37]. Throughout the numerical examples, we assume that the signal-independent interference can be modeled as a first-order auto-regressive process with a parameter equal to 0.5, as well as a white noise at the receiver with variance $\sigma^2 = 0.01$. Furthermore, for clutter we let

$$C_{m,k} = \rho^{(m-k)^2}, \ 1 \leq k, l \leq N \tag{3.47}$$

with $\rho = 0.8$. Note that the model in (3.47) can be used for many natural clutter sources [43]. We also set the probability of false alarm (P_{fa}) for the GLR detector to 10^{-6}.

Herein we consider an example of code design for a Doppler shift interval of $[\omega_l, \omega_u] = [-1, 1]$. We use the proposed algorithm to design optimal codes of length $N = 16$. The results are shown in Figure 3.3. The goodness of the resultant codes is investigated using two benchmarks: (1) the upper bound on the average metric that is not necessarily tight [37], and (2) the average metric corresponding to the uncoded system (using the transmit code $\boldsymbol{s} = \mathbf{1}$).

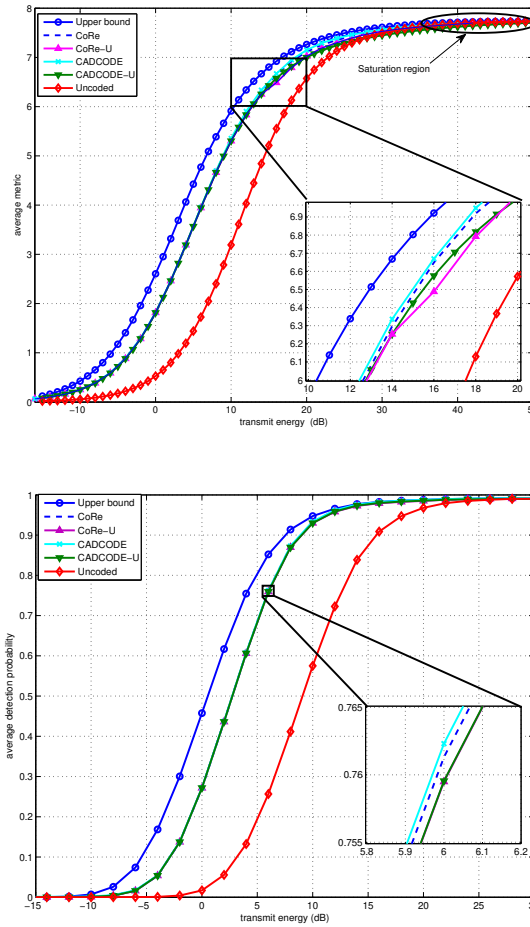

Figure 3.3. The design of optimized Doppler-robust radar codes of length $N = 16$ using the PMLI-based CADCODE-U method in comparison with CADCODE and CORE design algorithm alternatives discussed in [37]. (top) The average metric for different methods as well as the uncoded system (with $\boldsymbol{s} = \mathbf{1}$) versus the transmit energy. (bottom) The average detection probability associated with the same codes (as in the top subfigure) with $|\alpha|^2 = 5$ versus the transmit energy.

It can be observed from Figure 3.3 that, as expected, a coded system employing CADCODE or CADCODE-U outperforms the uncoded system. It is also practically observed that the performance obtained by the randomly generated codes is similar to that of the all-one code used in the uncoded system. Moreover, Figure 3.3 reveals that the quality of the codes obtained via constrained designs is very similar to that of unconstrained designs. However, there are minor degradations due to imposing the constraints. We also observe a performance saturation phenomenon in Figure 3.3 with increasing transmit energy. A more detailed discussion of the performance saturation phenomenon can be found in [37].

3.4.4 Radar Code Design Based on Information-Theoretic Criteria

The information-theoretic design presents an opportunity to study an example of the application of PMLI alongside the MM technique, which will be discussed extensively in the next chapter.

In multistatic scenarios, the interpretation of the detection performance is not easy in general and the expressions for detection performance may be too complicated to be amenable to utilization as design metrics (see, e.g., [44, 45]). In such circumstances, information-theoretic criteria can be considered as design metrics to guarantee a type of optimality for the obtained signals. For example, in [45] a signal design approach for the case of multistatic radars with one transmit antenna was proposed where a concave approximation of the J-divergence was considered as the design metric. MI has been considered as a design metric for nonorthogonal MIMO radar signal design in [46] for clutter-free scenarios. A problem related to that of [46] has been studied in [47] where Kullback-Leibler (KL) divergence and J-divergence are used as design metrics. In [48], KL-divergence and MI have been taken into account for MIMO radar signal design in the absence of clutter. Information-theoretic criteria have also been used in research subjects related to the radar detection problem. The authors in [49] studied the target classification for MIMO radars using minimum mean-square error (MMSE) and the MI criterion assuming no clutter. Reference [50] employed Bhattacharyya distance, KL-divergence, and J-divergence for signal design of a communication system with multiple transmit antennas, which presents similarities with radar formulations. MI has also been used to investigate the effect of the jammer on MIMO radar performance in clutter-free situations in [51].

In the following, we provide a unified PMLI-based framework for multistatic radar code design in the presence of clutter. Although closed-form expressions for the probability of detection and the probability of false alarm of the optimal detector are available, the analytical receiver operating characteristic (ROC) does not exist. As such, we employ various information-theoretic criteria that are widely used in the literature (see, e.g., [46, 48, 50])—namely, Bhattacharyya distance ($\mathcal{B}$), KL-divergence ($\mathcal{D}$), J-divergence ($\mathcal{J}$), and MI ($\mathcal{M}$), as metrics for code design. In particular, we express these metrics in terms of the code vector and then formulate the corresponding optimization problems.

We will cast the optimization problems corresponding to various information-theoretic criteria mentioned earlier under a unified optimization framework. Namely, we consider the following general form of the information-theoretic code optimization problem:

$$\begin{aligned} \max_{\boldsymbol{s},\lambda_k} \ & \sum_{k=1}^{N_r} f_{\mathcal{I}}(\lambda_k) + g_{\mathcal{I}}(\lambda_k) \\ \text{s.t.} \ & \lambda_k = \sigma_k^2 \boldsymbol{s}^H (\sigma_{\text{c},k}^2 \boldsymbol{s}\boldsymbol{s}^H + \mathbf{M}_k)^{-1} \boldsymbol{s} \\ & \boldsymbol{s} \in \Omega \end{aligned} \tag{3.48}$$

where $\mathcal{I} \in \{\mathcal{B}, \mathcal{D}, \mathcal{J}, \mathcal{M}\}$, $f_{\mathcal{I}}(.)$ and $g_{\mathcal{I}}(.)$ are concave and convex functions for any $\mathcal{I}$, respectively, and Ω represents the unimodular signal set. More precisely, we have that [4]:

$$\begin{cases} f_{\mathcal{B}}(\lambda_k) = \log(1 + 0.5\lambda_k), & g_{\mathcal{B}}(\lambda_k) = -\frac{1}{2}\log(1+\lambda_k), \\ f_{\mathcal{D}}(\lambda_k) = \log(1 + \lambda_k), & g_{\mathcal{D}}(\lambda_k) = \frac{1}{1+\lambda_k} - 1, \\ f_{\mathcal{J}}(\lambda_k) = 0, & g_{\mathcal{J}}(\lambda_k) = \frac{\lambda_k^2}{1+\lambda_k}, \\ f_{\mathcal{M}}(\lambda_k) = \log(1 + \lambda_k), & g_{\mathcal{M}}(\lambda_k) = 0. \end{cases}$$

The solution $\boldsymbol{s} = \boldsymbol{s}_\star$ of (3.48) can be obtained iteratively by solving the following UQP at the $(l+1)$th iteration:

$$\begin{aligned} \min_{\boldsymbol{s}} \ & \boldsymbol{s}^H \left(\sum_{k=1}^{N_r} \phi_{k,\mathcal{I}}^{(l)} \boldsymbol{M}_k^{-1} \right) \boldsymbol{s} - \Re \left(\left(\sum_{k=1}^{N_r} \boldsymbol{d}_{k,\mathcal{I}}^{(l)} \right)^H \boldsymbol{a} \right) \\ \text{s.t.} \ & \boldsymbol{s} \in \Omega, \end{aligned} \tag{3.49}$$

where the positive constant $\{\phi_{k,\mathcal{I}}^{(l)}\}$ and the vectors $\{\boldsymbol{d}_{k,\mathcal{I}}^{(l)}\}$ depend on $\mathcal{I} \in \{\mathcal{B}, \mathcal{D}, \mathcal{J}, \mathcal{M}\}$, whose closed-form expressions may be found in [4]. To tackle the code design problem, a PMLI-based design approach referred to MaMi was proposed in [4], which is considered for our evaluations.

We present a numerical example to examine the performance of MaMi. In particular, we compare the system performance for coded and uncoded (employing the code vector $\boldsymbol{s} = \sqrt{E/N}\,\mathbf{1}$ with E denoting the transmit energy) scenarios. We assume a code length of $N = 10$, the number of receivers $N_r = 4$, variances of the target components given by $\sigma_k^2 = 1$ (for $1 \leq k \leq 4$), and variances of the clutter components given by $(\sigma_{\mathrm{c},1}^2, \sigma_{\mathrm{c},2}^2, \sigma_{\mathrm{c},3}^2, \sigma_{\mathrm{c},4}^2) = (0.125, 0.25, 0.5, 1)$. Furthermore, we assume that the kth interference covariance matrix $\boldsymbol{M}_k$ is given by $[\boldsymbol{M}_k]_{m,n} = (1 - 0.15k)^{|m-n|}$. The ROC is used to evaluate the detection performance of the system using analytical expressions for P_d and P_{fa} (see eqs. (32)-(34) in [44]).

Figure 3.4 shows the ROCs associated with the coded system (employing the optimized codes) with no PAR constraint and with PAR $= 1$ as well as the uncoded system for $E = 10$. It can be observed that the performance of the coded system outperforms that of the uncoded system significantly. A minor performance degradation is observed for unimodular code design as compared to the unconstrained design. This can be explained using the fact that the feasibility set of the unconstraint design problem is larger that that of the constrained design.

3.4.5 MIMO Radar Transmit Beamforming

This example is particularly interesting because it represents an application of PMLI on radar signals that take a matrix form instead of the usual vector structure.

Consider a MIMO radar system with M antennas and let $\{\theta_l\}_{l=1}^{L}$ denote a fine grid of the angular sector of interest. Under the assumption that the transmitted probing signals are narrowband and the propagation is nondispersive, the steering vector of the transmit array (at location θ_l) can be written as

$$\boldsymbol{a}(\theta_l) = \left(e^{j2\pi f_0 \tau_1(\theta_l)}, e^{j2\pi f_0 \tau_2(\theta_l)}, \ldots, e^{j2\pi f_0 \tau_M(\theta_l)}\right)^T \tag{3.50}$$

where f_0 denotes the carrier frequency of the radar and $\tau_m(\theta_l)$ is the time needed by the transmitted signal of the m^{th} antenna to arrive at the target location θ_l.

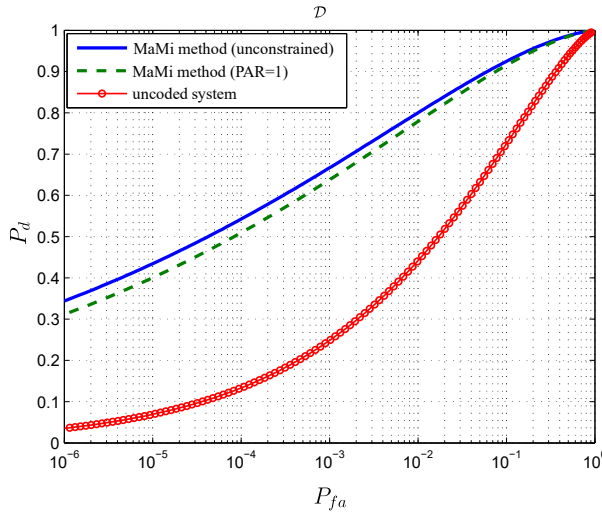

Figure 3.4. ROCs of optimally coded and uncoded systems.

In lieu of transmitting M partially correlated waveforms, the transmit beamspace processing (TBP) technique [52] employs K orthogonal waveforms that are linearly mixed at the transmit array via a weighting matrix $\boldsymbol{W} \in \mathbb{C}^{M\times K}$. The number of orthogonal waveforms K can be determined by counting the number of significant eigenvalues of the matrix [52]:

$$\boldsymbol{S} = \sum_{l=1}^{L} \boldsymbol{a}(\theta_l)\boldsymbol{a}^H(\theta_l) \tag{3.51}$$

The parameter K can be chosen such that the sum of the K dominant eigenvalues of $\boldsymbol{S}$ exceeds a given percentage of the total sum of eigenvalues [52]. Note that usually $K \ll M$ (especially when M is large) [52], [53]. Let $\boldsymbol{\Phi}$ be the matrix containing K orthonormal TBP waveforms, namely,

$$\boldsymbol{\Phi} = (\boldsymbol{\varphi}_1, \boldsymbol{\varphi}_2, \ldots, \boldsymbol{\varphi}_K)^T \in \mathbb{C}^{K\times N}, \quad K \leq M \tag{3.52}$$

where $\boldsymbol{\varphi}_k \in \mathbb{C}^{N\times 1}$ denotes the kth waveform (or sequence). The transmit signal matrix can then be written as $\boldsymbol{S} = \boldsymbol{W}\boldsymbol{\Phi} \in \mathbb{C}^{M\times N}$, and thus, the

transmit beam pattern becomes

$$\begin{aligned} P(\theta_l) &= \|\boldsymbol{S}^H \boldsymbol{a}(\theta_l)\|_2^2 \\ &= \boldsymbol{a}^H(\theta_l)\boldsymbol{W}\boldsymbol{\Phi}\boldsymbol{\Phi}^{\boldsymbol{H}}\boldsymbol{W}^{\boldsymbol{H}}\boldsymbol{a}(\theta_l) \\ &= \boldsymbol{a}^H(\theta_l)\boldsymbol{W}\boldsymbol{W}^H\boldsymbol{a}(\theta_l) \\ &= \|\boldsymbol{W}^H\boldsymbol{a}(\theta_l)\|_2^2 \end{aligned} \tag{3.53}$$

Equation (3.53) sheds light on two different perspectives for radar beam pattern design. Observe that matching a desired beam pattern may be accomplished by considering $\boldsymbol{W}$ as the design variable. By doing so, one can control the rank (K) of the covariance matrix $\boldsymbol{R} = \boldsymbol{S}\boldsymbol{S}^{\boldsymbol{H}} = \boldsymbol{W}\boldsymbol{W}^{\boldsymbol{H}}$ through fixing the dimensions of $\boldsymbol{W} \in \mathbb{C}^{M\times K}$. This idea becomes of particular interest for the phased-array radar formulation with $K = 1$. Note that considering the optimization problem with respect to $\boldsymbol{W}$ for small K may significantly reduce the computational costs. However, imposing practical signal constraints (such as discrete-phase or low PAR) while considering $\boldsymbol{W}$ as the design variable appears to be difficult. In such cases, one can resort to a direct beam pattern matching by choosing $\boldsymbol{S}$ as the design variable.

In light of the above discussion, we consider beam pattern matching problem formulations for designing either $\boldsymbol{W}$ or $\boldsymbol{S}$ as follows. Let $P_d(\theta_l)$ denote the desired beam pattern. According to the last equality in (3.53), $P_d(\theta_l)$ can be synthesized exactly if and only if there exist a unit-norm vector $\boldsymbol{p}(\theta_l)$ such that

$$\boldsymbol{W}^H\boldsymbol{a}(\theta_l) = \sqrt{P_d(\theta_l)}\boldsymbol{p}(\theta_l) \tag{3.54}$$

Therefore, by considering $\{\boldsymbol{p}(\theta_l)\}_l$ as auxiliary design variables, the beam pattern matching via weight matrix design can be dealt with conveniently via the optimization problem:

$$\min_{\boldsymbol{W},\alpha,\{\boldsymbol{p}(\theta_l)\}} \sum_{l=1}^{L} \left\| \boldsymbol{W}^H\boldsymbol{a}(\theta_l) - \alpha\sqrt{P_d(\theta_l)}\boldsymbol{p}(\theta_l) \right\|_2^2 \tag{3.55}$$

$$\text{s.t.} \qquad (\boldsymbol{W}\odot\boldsymbol{W}^*)\mathbf{1} = \frac{E}{M}\mathbf{1} \tag{3.56}$$

$$\|\boldsymbol{p}(\theta_l)\|_2 = 1,\ \forall\, l \tag{3.57}$$

where (3.56) is the transmission energy constraint at each transmitter with E being the total energy and α is a scalar accounting for the energy difference

between the desired beam pattern and the transmitted beam. Similarly, the beam pattern matching problem with $\boldsymbol{S}$ as the design variable can be formulated as

$$\min_{\boldsymbol{S},\alpha,\{\boldsymbol{p}(\theta_l)\}} \sum_{l=1}^{L} \left\| \boldsymbol{S}^H \boldsymbol{a}(\theta_l) - \alpha \sqrt{P_d(\theta_l)} \boldsymbol{p}(\theta_l) \right\|_2^2 \tag{3.58}$$

$$\text{s.t.} \qquad (\boldsymbol{S} \odot \boldsymbol{S}^*)\mathbf{1} = \frac{E}{M}\mathbf{1} \tag{3.59}$$

$$\|\boldsymbol{p}(\theta_l)\|_2 = 1, \ \forall\, l \tag{3.60}$$

$$\boldsymbol{S} \in \Psi \tag{3.61}$$

where Ψ is the desired set of transmit signals. The above beam pattern matching formulations pave the way for an algorithm (which we call Beam-Shape) that can perform a direct matching of the beam pattern with respect to the weight matrix $\boldsymbol{W}$ or the signal $\boldsymbol{S}$, without requiring an intermediate synthesis of the signal covariance matrix.

3.4.5.1 Beam Shape: Direct Shaping of the Transmit Beam Pattern

We begin by considering the beam pattern matching formulation in (3.55). For fixed $\boldsymbol{W}$ and α, the minimizer $\boldsymbol{p}(\theta_l)$ of (3.55) is given by

$$\boldsymbol{p}(\theta_l) = \frac{\boldsymbol{W}^H \boldsymbol{a}(\theta_l)}{\|\boldsymbol{W}^H \boldsymbol{a}(\theta_l)\|_2} \tag{3.62}$$

Let $P \triangleq \sum_{l=1}^{L} P_d(\theta_l)$. For fixed $\boldsymbol{W}$ and $\{\boldsymbol{p}(\theta_l)\}$ the minimizer α of (3.55) can be obtained as

$$\alpha = \Re \left\{ \left(\sum_{l=1}^{L} \sqrt{P_d(\theta_l)} \boldsymbol{p}^H(\theta_l) \boldsymbol{W}^H \boldsymbol{a}(\theta_l) \right) / P \right\} \tag{3.63}$$

Using (3.62), the expression for α can be further simplified as

$$\alpha = \left(\sum_{l=1}^{L} \sqrt{P_d(\theta_l)} \left\| \boldsymbol{W}^H \boldsymbol{a}(\theta_l) \right\|_2 \right) / P \tag{3.64}$$

Now assume that $\{\boldsymbol{p}(\theta_l)\}$ and α are fixed. Note that

$$\begin{aligned} Q(\boldsymbol{W}) &= \sum_{l=1}^{L} \|\boldsymbol{W}^H \boldsymbol{a}(\theta_l) - \alpha\sqrt{P_d(\theta_l)}\boldsymbol{p}(\theta_l)\|_2^2 \\ &= \text{tr}(\boldsymbol{W}\boldsymbol{W}^H\boldsymbol{A}) - 2\Re\{\text{tr}(\boldsymbol{W}\boldsymbol{B})\} + P\alpha^2 \end{aligned} \tag{3.65}$$

where $\boldsymbol{S}$ is as defined in (3.51), and

$$\boldsymbol{B} = \sum_{l=1}^{L} \alpha\sqrt{P_d(\theta_l)}\boldsymbol{p}(\theta_l)\boldsymbol{a}^H(\theta_l) \tag{3.66}$$

By dropping the constant part in $Q(\boldsymbol{W})$, we have

$$\widetilde{Q}(\boldsymbol{W}) = \text{tr}(\boldsymbol{W}\boldsymbol{W}^H\boldsymbol{A}) - 2\Re\left\{\text{tr}(\boldsymbol{W}\boldsymbol{B})\right\} \tag{3.67}$$

$$= \text{tr}\left(\begin{pmatrix} \boldsymbol{W} \\ \boldsymbol{I} \end{pmatrix}^H \underbrace{\begin{pmatrix} \boldsymbol{A} & -\boldsymbol{B}^H \\ -\boldsymbol{B} & \boldsymbol{0} \end{pmatrix}}_{\triangleq \boldsymbol{C}} \underbrace{\begin{pmatrix} \boldsymbol{W} \\ \boldsymbol{I} \end{pmatrix}}_{\triangleq \widetilde{\boldsymbol{W}}} \right).$$

Therefore, the minimization of (3.55) with respect to $\boldsymbol{W}$ is equivalent to

$$\min_{\boldsymbol{W}} \quad \text{tr}\left(\widetilde{\boldsymbol{W}}^H\boldsymbol{C}\widetilde{\boldsymbol{W}}\right) \tag{3.68}$$

$$\text{s.t.} \ \ (\boldsymbol{W} \odot \boldsymbol{W}^*)\boldsymbol{1} = \frac{E}{M}\boldsymbol{1} \tag{3.69}$$

$$\widetilde{\boldsymbol{W}} = \left(\boldsymbol{W}^T \ \boldsymbol{I}\right)^T \tag{3.70}$$

As a result of the energy constraint in (3.69), $\widetilde{\boldsymbol{W}}$ has a fixed Frobenius norm, and hence a diagonal loading of $\boldsymbol{C}$ does not change the solution to (3.68). Therefore, (3.68) can be rewritten in the following equivalent form:

$$\max_{\boldsymbol{W}} \quad \text{tr}\left(\widetilde{\boldsymbol{W}}^H\widetilde{\boldsymbol{C}}\widetilde{\boldsymbol{W}}\right) \tag{3.71}$$

$$\text{s.t.} \ \ (\boldsymbol{W} \odot \boldsymbol{W}^*)\boldsymbol{1} = \frac{E}{M}\boldsymbol{1} \tag{3.72}$$

$$\widetilde{\boldsymbol{W}} = \left(\boldsymbol{W}^T \ \boldsymbol{I}\right)^T \tag{3.73}$$

where $\widetilde{\boldsymbol{C}} = \lambda \boldsymbol{I} - \boldsymbol{C}$, with λ being larger than the maximum eigenvalue of $\boldsymbol{C}$. In particular, an increase in the objective function of (3.71) leads to a decrease of the objective function in (3.55). Although (3.71) is nonconvex, a monotonically increasing sequence of the objective function in (3.71) may be obtained (see Section 3.5 for a proof) via a generalization of the PMLI, namely:

$$\boldsymbol{W}^{(t+1)} = \sqrt{\frac{E}{M}}\, \eta\left(\begin{pmatrix} \boldsymbol{I}_{M\times M} \\ \boldsymbol{0} \end{pmatrix}^T \widetilde{\boldsymbol{C}}\, \widetilde{\boldsymbol{W}}^{(t)} \right) \tag{3.74}$$

where the iterations may be initialized with the latest approximation of $\boldsymbol{W}$ (used as $\boldsymbol{W}^{(0)}$), t denotes the internal iteration number, and $\eta(\cdot)$ is a row-scaling operator that makes the rows of the matrix argument have unit-norm.

Next, we study the optimization problem in (3.58). Thanks to the similarity of the problem formulation to (3.55), the derivations of the minimizers $\{\boldsymbol{p}(\theta_l)\}$ and α of (3.58) remain the same as for (3.55). Moreover, the minimization of (3.58) with respect to the constrained $\boldsymbol{S}$ can be formulated as the following optimization problem:

$$\max_{\boldsymbol{S}} \qquad \text{tr}\left(\widetilde{\boldsymbol{S}}^H \widetilde{\boldsymbol{C}} \widetilde{\boldsymbol{S}}\right) \tag{3.75}$$

$$\text{s.t.} \quad (\boldsymbol{S} \odot \boldsymbol{S}^*)\boldsymbol{1} = \frac{E}{M}\boldsymbol{1} \tag{3.76}$$

$$\widetilde{\boldsymbol{S}} = \left(\boldsymbol{S}^T \boldsymbol{I}\right)^T,\ \boldsymbol{S} \in \Psi \tag{3.77}$$

with $\widetilde{\boldsymbol{C}}$ being the same as in (3.71). An increasing sequence of the objective function in (3.75) can be obtained via PMLI by exploiting the following nearest-matrix problem (see Section 3.5 for a sketched proof):

$$\min_{\boldsymbol{S}^{(t+1)}} \quad \left\| \boldsymbol{S}^{(t+1)} - \begin{pmatrix} \boldsymbol{I}_{M\times M} \\ \boldsymbol{0} \end{pmatrix}^T \widetilde{\boldsymbol{C}}\, \widetilde{\boldsymbol{S}}^{(t)} \right\|_F \tag{3.78}$$

$$\text{s.t.}\ \ (\boldsymbol{S}^{(t+1)} \odot \boldsymbol{S}^{*\,(t+1)})\boldsymbol{1} = \frac{E}{M}\boldsymbol{1},\ \ \boldsymbol{S}^{(t+1)} \in \Psi \tag{3.79}$$

Obtaining the solution to (3.78) for some constraint sets Ψ such as real-valued, unimodular, or p-ary matrices is straightforward, namely,

$$\boldsymbol{S}^{(t+1)} = \begin{cases} \sqrt{\frac{E}{M}}\,\eta\left(\Re\left\{\widehat{\boldsymbol{S}}^{(t)}\right\}\right), & \Psi = \text{real-values matrices} \\ e^{j\arg\left(\widehat{\boldsymbol{S}}^{(t)}\right)}, & \Psi = \text{unimodular matrices} \\ e^{j\mathcal{Q}_p\left(\arg\left(\widehat{\boldsymbol{S}}^{(t)}\right)\right)}, & \Psi = p\text{-ary matrices} \end{cases} \tag{3.80}$$

where

$$\widehat{\boldsymbol{S}}^{(t)} = \begin{pmatrix} \boldsymbol{I}_{M\times M} \\ \boldsymbol{0} \end{pmatrix}^T \widetilde{\boldsymbol{C}}\,\widetilde{\boldsymbol{S}}^{(t)} \tag{3.81}$$

Furthermore, the case of PAR-constrained $\boldsymbol{S}$ can be handled efficiently via the recursive algorithm devised in [54].

Note that the considered signal design formulation does not take into account the signal and beam pattern auto/cross-correlation properties that are of interest in some radar applications using match filtering. Nevertheless, numerical investigations show that the signals obtained from the proposed approach can also have desirable correlation/ambiguity properties presumably due to their pseudorandom characteristics. We refer the interested reader to [55–60] for several computational methods related to (MIMO) signal design with good correlation properties.

We now provide several numerical examples to show the potential of Beam-Shape in practice. Consider a MIMO radar with a uniform linear array (ULA) comprising $M = 32$ antennas with half-wavelength spacing between adjacent antennas. The total transmit power is set to $E = MN$. The angular pattern covers $[-90^\circ, 90^\circ]$ with a mesh grid size of 1° and the desired beam pattern is given by

$$P_d(\theta) = \begin{cases} 1,\ \theta \in [\widehat{\theta}_k - \Delta, \widehat{\theta}_k + \Delta] \\ 0,\ \text{otherwise} \end{cases} \tag{3.82}$$

where $\widehat{\theta}_k$ denotes the direction of a target of interest and 2Δ is the chosen beamwidth for each target. In the following examples, we assume 3 targets located at $\widehat{\theta}_1 = -45^\circ$, $\widehat{\theta}_2 = 0^\circ$, and $\widehat{\theta}_3 = 45^\circ$ with a beamwidth of 24° ($\Delta = 12^\circ$). The results are compared with those obtained via the covariance

matrix synthesis-based (CMS) approach proposed in [55] and [61]. For the sake of a fair comparison, we define the mean square error (MSE) of a beam pattern matching as

$$\text{MSE} \triangleq \sum_{l=1}^{L} \left| \boldsymbol{a}^H(\theta_l) \boldsymbol{R}\, \boldsymbol{a}(\theta_l) - P_d(\theta_l) \right|^2 \tag{3.83}$$

which is the typical optimality criterion for the covariance matrix synthesis in the literature (including the CMS in [55] and [61]).

We begin with the design of the weight matrix $\boldsymbol{W}$ using the formulation in (3.55). In particular, we consider $K = M$ corresponding to a general MIMO radar, and $K = 1$, which corresponds to a phased array. The results are shown in Figure 3.5. For $K = M$, The MSE values obtained by Beam-Shape and CMS are 1.79 and 1.24, respectively. Note that a smaller MSE value was expected for CMS in this case, as CMS obtains $\boldsymbol{R}$ (or equivalently $\boldsymbol{W}$) by globally minimizing the MSE in (3.83). However, in the phased-array example, Beam-Shape yields an MSE value of 3.72, whereas the MSE value obtained by CMS is 7.21. Such a behavior was also expected due to the embedded rank constraint when designing $\boldsymbol{W}$ by Beam-Shape, while CMS appears to face a considerable loss during the synthesis of the rank-constrained $\boldsymbol{W}$.

Next we design the transmit signal $\boldsymbol{S}$ using the formulation in (3.58). In this example, $\boldsymbol{S}$ is constrained to be unimodular (i.e. $|\boldsymbol{S}(k,l)| = 1$), which corresponds to a unit PAR. Figure 3.6 compares the performances of Beam-Shape and CMS for two different lengths of the transmit sequences, namely $N = 8$ and $N = 128$. In the case of $N = 8$, Beam-Shape obtains an MSE value of 1.80 while the MSE value obtained by CMS is 2.73. For $N = 128$, the MSE values obtained by Beam-Shape and CMS are 1.74 and 1.28, respectively. Given the fact that $M = 32$, the case of $N = 128$ provides a large number of degrees of freedom for CMS when fitting $\boldsymbol{S}\boldsymbol{S}^H$ to the obtained $\boldsymbol{R}$ in the covariance matrix synthesis stage, whereas for $N = 8$ the degrees of freedom are rather limited.

Finally, it can be interesting to examine the performance of Beam-Shape in scenarios with large grid size L. To this end, we compare the computation times of Beam-Shape and CMS for different L, using the same problem setup for designing $\boldsymbol{S}$ (as the above example) but for $N = M = 32$. According to Figure 3.7, the overall CPU time of CMS is growing rapidly as L increases, which implies that CMS can hardly be used for beamforming

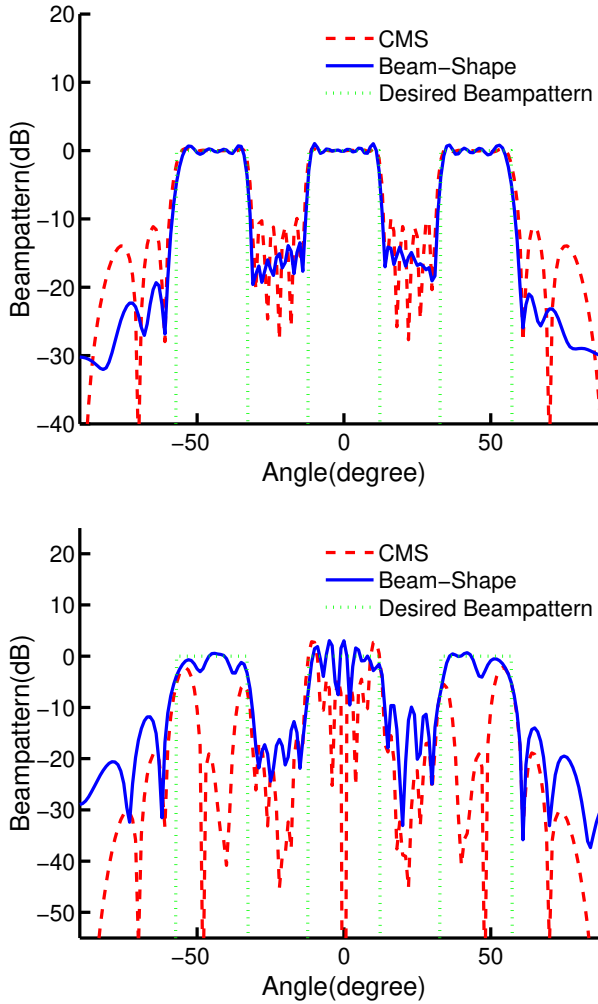

Figure 3.5. Comparison of radar beam pattern matchings obtained by CMS and Beam-Shape using the weight matrix $\boldsymbol{W}$ as the design variable: (top) $K = M$ corresponding to a general MIMO radar, and (bottom) $K = 1$, which corresponds to a phased array.

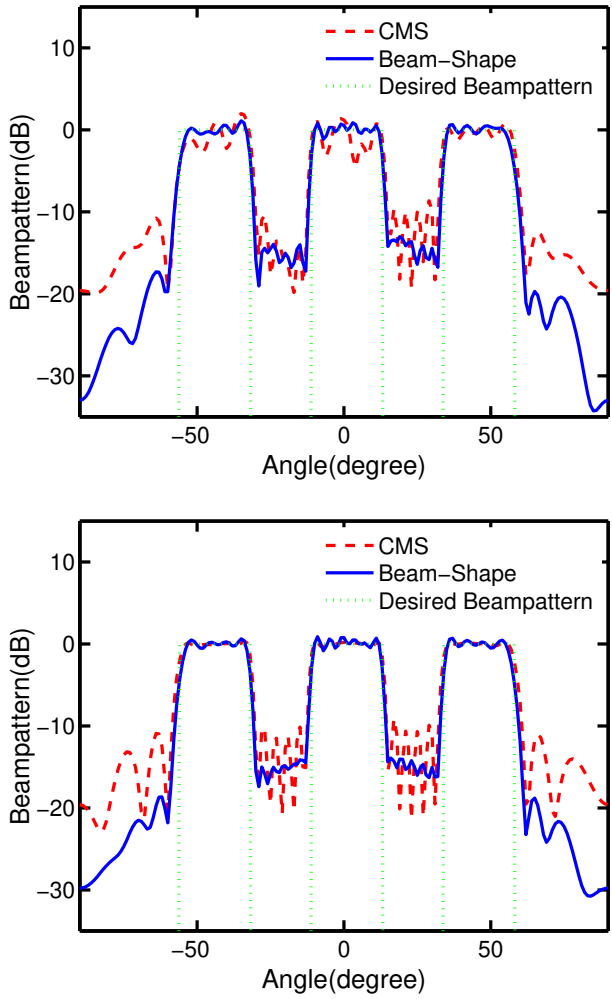

Figure 3.6. Comparison of MIMO radar beam pattern matchings obtained by CMS and Beam-Shape using the signal matrix $\boldsymbol{S}$ as the design variable: (top) $N = 8$, and (bottom) $N = 128$.

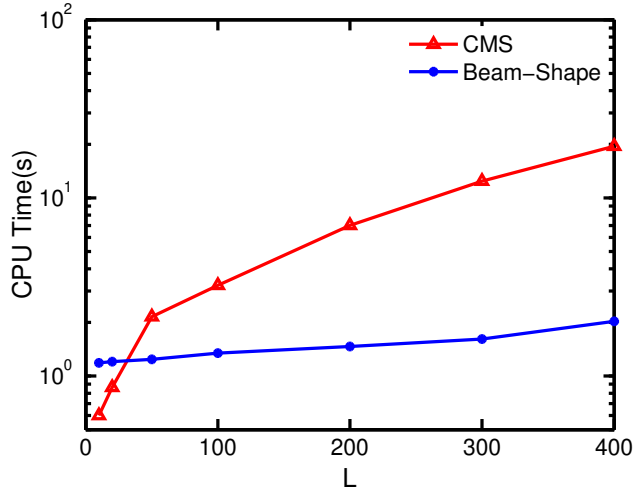

Figure 3.7. Comparison of computation times for Beam-Shape and CMS with different grid sizes L.

design with large grid sizes (e.g., $L \gtrsim 10^3$). In contrast, Beam-Shape runs well for large L, even for $L \sim 10^6$ on a standard PC. The results leading to Figure 3.7 were obtained by averaging the computation times for 100 experiments (with different random initializations) using a PC with Intel Core i5 CPU 750 @2.67 GHz, and 8 GB memory.

3.5 MATRIX PMLI DERIVATION FOR (3.71) AND (3.75)

In the following, we study the PMLI for designing $\boldsymbol{W}$ in (3.71). The extension of the results to the design of $\boldsymbol{S}$ in (3.75) is straightforward. For fixed $\boldsymbol{W}^{(t)}$, observe that the update matrix $\boldsymbol{W}^{(t+1)}$ is the minimizer of the criterion

$$\left\| \widetilde{\boldsymbol{W}}^{(t+1)} - \widetilde{\boldsymbol{C}} \widetilde{\boldsymbol{W}}^{(t)} \right\|_2^2 = \text{const} - 2\Re \left\{ \text{tr} \left(\widetilde{\boldsymbol{W}}^{(t+1)\,H} \widetilde{\boldsymbol{C}} \widetilde{\boldsymbol{W}}^{(t)} \right) \right\} \tag{3.84}$$

or, equivalently, the maximizer of the criterion

$$\Re\left\{\text{tr}\left(\widetilde{\boldsymbol{W}}^{(t+1)\,H}\widetilde{\boldsymbol{C}}\widetilde{\boldsymbol{W}}^{(t)}\right)\right\} \tag{3.85}$$

in the search space satisfying the given fixed-norm constraint on the rows of $\boldsymbol{W}$ (for $\boldsymbol{S}$, one should also consider the constraint set Ψ). Therefore, for the optimizer $\widetilde{\boldsymbol{W}}^{(t+1)}$ of (3.71), we must have

$$\Re\left\{\text{tr}\left(\widetilde{\boldsymbol{W}}^{(t+1)\,H}\widetilde{\boldsymbol{C}}\widetilde{\boldsymbol{W}}^{(t)}\right)\right\} \geq \text{tr}\left(\widetilde{\boldsymbol{W}}^{(t)\,H}\widetilde{\boldsymbol{C}}\widetilde{\boldsymbol{W}}^{(t)}\right) \tag{3.86}$$

Moreover, as $\widetilde{\boldsymbol{C}}$ is positive-definite:

$$\text{tr}\left(\left(\widetilde{\boldsymbol{W}}^{(t+1)} - \widetilde{\boldsymbol{W}}^{(t)}\right)^{H}\widetilde{\boldsymbol{C}}\left(\widetilde{\boldsymbol{W}}^{(t+1)} - \widetilde{\boldsymbol{W}}^{(t)}\right)\right) \geq 0 \tag{3.87}$$

which along with (3.86) implies

$$\text{tr}\left(\widetilde{\boldsymbol{W}}^{(t+1)\,H}\widetilde{\boldsymbol{C}}\widetilde{\boldsymbol{W}}^{(t+1)}\right) \geq \text{tr}\left(\widetilde{\boldsymbol{W}}^{(t)\,H}\widetilde{\boldsymbol{C}}\widetilde{\boldsymbol{W}}^{(t)}\right) \tag{3.88}$$

and, hence, a monotonic increase of the objective function in (3.71).

3.6 CONCLUSION

The PMLI approach was introduced to enable computationally efficient approximation of the solutions to signal-constrained quadratic optimization problems, which are commonly encountered in radar signal design. It was shown that PMLI can accommodate a wide range of signal constraints in addition to the regularly considered fixed-energy constraint. The application of PMLI in various radar signal design problems was thoroughly demonstrated.

3.7 EXERCISE PROBLEMS

Q1. In light of (3.10), discuss the importance of ensuring the positive definiteness of $\mathbf{R}$ in (3.5) for PMLI convergence.

Q2. Note that even if a Hermitian matrix $\mathbf{R}$ in (3.5) is not positive definite, it can be made so by diagonal loading:

$$\mathbf{R} \leftarrow \mathbf{R} + \lambda \mathbf{I} \tag{3.89}$$

with $\lambda > 0$. Discuss the appropriate amount of diagonal loading (λ) in terms of accuracy of solutions and convergence speed.

Q3. By drawing inspiration from the derivations (3.4) to (3.9), derive PMLI for signals $\mathbf{x}$ that are sparse, whose number of nonzero entries are bounded by a constant K (i.e., $\|\mathbf{x}\|_{\mathbf{0}} \leq \mathbf{K}$). This is particularly useful in radar problems involving antenna selection from an antenna array [62–69].

References

[1] M. Soltanalian and P. Stoica, "Designing unimodular codes via quadratic optimization," *IEEE Transactions on Signal Processing*, vol. 62, pp. 1221–1234, Mar. 2014.

[2] M. Soltanalian, B. Tang, J. Li, and P. Stoica, "Joint design of the receive filter and transmit sequence for active sensing," *IEEE Signal Processing Letters*, vol. 20, pp. 423–426, May 2013.

[3] M. Soltanalian, H. Hu, and P. Stoica, "Single-stage transmit beamforming design for MIMO radar," *Signal Processing*, vol. 102, pp. 132–138, 2014.

[4] M. M. Naghsh, M. Modarres-Hashemi, S. ShahbazPanahi, M. Soltanalian, and P. Stoica, "Unified optimization framework for multi-static radar code design using information-theoretic criteria," *IEEE Transactions on Signal Processing*, vol. 61, no. 21, pp. 5401–5416, 2013.

[5] M. M. Naghsh, M. Modarres-Hashemi, A. Sheikhi, M. Soltanalian, and P. Stoica, "Unimodular code design for MIMO radar using Bhattacharyya distance," in *2014 IEEE International Conference on Acoustics, Speech and Signal Processing (ICASSP)*, pp. 5282–5286, IEEE, 2014.

[6] G. Cui, X. Yu, G. Foglia, Y. Huang, and J. Li, "Quadratic optimization with similarity constraint for unimodular sequence synthesis," *IEEE Transactions on Signal Processing*, vol. 65, no. 18, pp. 4756–4769, 2017.

[7] C. Chen, H. Li, H. Hu, X. Zhu, and Z. Yuan, "Performance optimisation of multiple-input multiple-output radar for mainlobe interference suppression in a spectrum sharing environment," *IET Radar, Sonar & Navigation*, vol. 11, no. 8, pp. 1302–1308, 2017.

[8] J. Tranter, N. D. Sidiropoulos, X. Fu, and A. Swami, "Fast unit-modulus least squares with applications in beamforming," *IEEE Transactions on Signal Processing*, vol. 65, no. 11, pp. 2875–2887, 2017.

[9] J. Zhang, A. Wiesel, and M. Haardt, "Low rank approximation based hybrid precoding schemes for multi-carrier single-user massive MIMO systems," in *IEEE International Conference on Acoustics, Speech and Signal Processing (ICASSP)*, pp. 3281–3285, IEEE, 2016.

[10] X. Yu, G. Cui, J. Yang, J. Li, and L. Kong, "Quadratic optimization for unimodular sequence design via an ADPM framework," *IEEE Transactions on Signal Processing*, vol. 68, pp. 3619–3634, 2020.

[11] P. Gong, W.-Q. Wang, F. Li, and H. C. So, "Sparsity-aware transmit beamspace design for FDA-MIMO radar," *Signal Processing*, vol. 144, pp. 99–103, 2018.

[12] M. M. Naghsh, M. Modarres-Hashemi, S. ShahbazPanahi, M. Soltanalian, and P. Stoica, "Majorization-minimization technique for multi-static radar code design," in *21st European Signal Processing Conference (EUSIPCO 2013)*, pp. 1–5, IEEE, 2013.

[13] J. Zhang, C. Shi, X. Qiu, and Y. Wu, "Shaping radar ambiguity function by l-phase unimodular sequence," *IEEE Sensors Journal*, vol. 16, no. 14, pp. 5648–5659, 2016.

[14] B. Tang, Y. Zhang, and J. Tang, "An efficient minorization maximization approach for MIMO radar waveform optimization via relative entropy," *IEEE Transactions on Signal Processing*, vol. 66, no. 2, pp. 400–411, 2017.

[15] S. Imani, M. M. Nayebi, and M. Rashid, "Receive space-time filter and transmit sequence design in MIMO radar systems," *Wireless Personal Communications*, vol. 122, no. 1, pp. 501–522, 2022.

[16] X. Wei, Y. Jiang, Q. Liu, and X. Wang, "Calibration of phase shifter network for hybrid beamforming in mmWave massive MIMO systems," *IEEE Transactions on Signal Processing*, vol. 68, pp. 2302–2315, 2020.

[17] T. Liu, P. Fan, Z. Zhou, and Y. L. Guan, "Unimodular sequence design with good local auto-and cross-ambiguity function for MSPSR system," in *IEEE 89th Vehicular Technology Conference (VTC2019-Spring)*, pp. 1–5, IEEE, 2019.

[18] J. Mo, B. L. Ng, S. Chang, P. Huang, M. N. Kulkarni, A. AlAmmouri, J. C. Zhang, J. Lee, and W.-J. Choi, "Beam codebook design for 5G mmWave terminals," *IEEE Access*, vol. 7, pp. 98387–98404, 2019.

[19] S. Zhang and Y. Huang, "Complex quadratic optimization and semidefinite programming," *SIAM Journal on Optimization*, vol. 16, no. 3, pp. 871–890, 2006.

[20] M. Soltanalian and P. Stoica, "Design of perfect phase-quantized sequences with low peak-to-average-power ratio," in *2012 Proceedings of the 20th European Signal Processing Conference (EUSIPCO)*, pp. 2576–2580, IEEE, 2012.

[21] M. Soltanalian and P. Stoica, "On prime root-of-unity sequences with perfect periodic correlation," *IEEE Transactions on Signal Processing*, vol. 62, no. 20, pp. 5458–5470, 2014.

[22] A. Bose and M. Soltanalian, "Constructing binary sequences with good correlation properties: An efficient analytical-computational interplay," *IEEE Transactions on Signal Processing*, vol. 66, no. 11, pp. 2998–3007, 2018.

[23] J. Tropp, I. Dhillon, R. Heath, and T. Strohmer, "Designing structured tight frames via an alternating projection method," *IEEE Transactions on Information Theory*, vol. 51, pp. 188–209, January 2005.

[24] J. R. Hershey, J. L. Roux, and F. Weninger, "Deep unfolding: Model-based inspiration of novel deep architectures," *arXiv preprint arXiv:1409.2574*, 2014.

[25] S. Khobahi, A. Bose, and M. Soltanalian, "Deep radar waveform design for efficient automotive radar sensing," in *2020 IEEE 11th Sensor Array and Multichannel Signal Processing Workshop (SAM)*, pp. 1–5, 2020.

[26] H. He, J. Li, and P. Stoica, *Waveform Design for Active Sensing Systems: A Computational Approach*. Cambridge, UK: Cambridge University Press, 2012.

[27] N. Levanon and E. Mozeson, *Radar Signals*. New York: Wiley, 2004.

[28] H. He, P. Stoica, and J. Li, "On synthesizing cross ambiguity functions," in *IEEE International Conference on Acoustics, Speech and Signal Processing (ICASSP)*, (Prague, Czech Republic), pp. 3536–3539, May 2011.

[29] P. Stoica, H. He, and J. Li, "New algorithms for designing unimodular sequences with good correlation properties," *IEEE Transactions on Signal Processing*, vol. 57, pp. 1415–1425, April 2009.

[30] M. Soltanalian and P. Stoica, "Computational design of sequences with good correlation properties," *IEEE Transactions on Signal Processing*, vol. 60, pp. 2180–2193, May 2012.

[31] J. Benedetto, I. Konstantinidis, and M. Rangaswamy, "Phase-coded waveforms and their design," *IEEE Signal Processing Magazine*, vol. 26, pp. 22–31, Jan. 2009.

[32] A. De Maio, S. De Nicola, Y. Huang, S. Zhang, and A. Farina, "Code design to optimize radar detection performance under accuracy and similarity constraints," *IEEE Transactions on Signal Processing*, vol. 56, pp. 5618 –5629, Nov. 2008.

[33] A. De Maio and A. Farina, "Code selection for radar performance optimization," in *Waveform Diversity and Design Conference*, (Pisa, Italy), pp. 219–223, June 2007.

[34] M. Soltanalian, B. Tang, J. Li, and P. Stoica, "Joint design of the receive filter and transmit sequence for active sensing," *IEEE Signal Processing Letters*, vol. 20, no. 5, pp. 423–426, 2013.

[35] W. Dinkelbach, "On nonlinear fractional programming," *Management Science*, vol. 13, no. 7, pp. 492–498, 1967.

[36] P. Stoica, H. He, and J. Li, "Optimization of the receive filter and transmit sequence for active sensing," *IEEE Transactions on Signal Processing*, vol. 60, pp. 1730–1740, April 2012.

[37] M. M. Naghsh, M. Soltanalian, P. Stoica, and M. Modarres-Hashemi, "Radar code design for detection of moving targets," *IEEE Transactions on Aerospace and Electronic Systems*, vol. 50, no. 4, pp. 2762–2778, 2014.

[38] M. M. Naghsh, M. Soltanalian, P. Stoica, M. Modarres-Hashemi, A. De Maio, and A. Aubry, "A Doppler robust design of transmit sequence and receive filter in the presence of signal-dependent interference," *IEEE Transactions on Signal Processing*, vol. 62, no. 4, pp. 772–785, 2013.

[39] S. M. Kay, "Optimal signal design for detection of Gaussian point targets in stationary Gaussian clutter/reverberation," *IEEE Journal of Selected Topics in Signal Processing*, vol. 1, pp. 31–41, June 2007.

[40] S. Haykin, "Cognitive radars," *IEEE Signal Processing Magazine*, vol. 23, pp. 30–40, Jan. 2006.

[41] S. M. Kay, *Fundamentals of Statistical Signal Processing-Volume II: Detection Theory*. New Jersey: Prentice Hall, first ed., 1998.

[42] P. Stoica and R. Moses, *Spectral Analysis of Signals*. New Jersey: Prentice Hall, 2005.

[43] M. Skolnik, *Radar Handbook*. New York: McGraw-Hill, third ed., 2008.

[44] M. M. Naghsh and M. Modarres-Hashemi, "Exact theoretical performance analysis of optimum detector for statistical MIMO radars," *IET Journal on Radar, Sonar, and Navigation*, vol. 6, pp. 99–111, 2012.

[45] S. M. Kay, "Waveform design for multistatic radar detection," *IEEE Transactions on Aerospace and Electronic Systems*, vol. 45, pp. 1153–1165, July 2009.

[46] A. De Maio, M. Lops, and L. Venturino, "Diversity integration trade-off in MIMO detection," *IEEE Transactions on Signal Processing*, vol. 56, pp. 5051–5061, Oct. 2008.

[47] E. Grossi and M. Lops, "Space-time code design for MIMO detection based on Kullback-Leibler divergence," *IEEE Transactions on Information Theory*, vol. 58, no. 6, pp. 3989–4004, 2012.

[48] B. Tang, J. Tang, and Y. Peng, "MIMO radar waveform design in colored noise based on information theory," *IEEE Transactions on Signal Processing*, vol. 58, pp. 4684–4697, Sept. 2010.

[49] R. S. Blum and Y. Yang, "MIMO radar waveform design based on mutual information and minimum mean-square error estimation," *IEEE Transactions on Aerospace and Electronic Systems*, vol. 43, pp. 330–343, Jan. 2007.

[50] T. Kailath, "The divergence and Bhattacharyya distance measures in signal selection," *IEEE Transactions on Communications*, vol. 15, pp. 52–60, Feb. 1967.

[51] X. Song, P. Willett, S. Zhou, and P. Luh, "The MIMO radar and jammer games," *IEEE Transactions on Signal Processing*, vol. 60, pp. 687–699, Feb. 2012.

[52] A. Hassanien and S. A. Vorobyov, "Transmit energy focusing for DOA estimation in MIMO radar with colocated antennas," *IEEE Transactions on Signal Processing*, vol. 59, no. 6, pp. 2669–2682, 2011.

[53] A. Hassanien, M. W. Morency, A. Khabbazibasmenj, S. A. Vorobyov, J.-Y. Park, and S.-J. Kim, "Two-dimensional transmit beamforming for MIMO radar with sparse symmetric arrays," in *IEEE Radar Conference*, 2013.

[54] J. A. Tropp, I. S. Dhillon, R. W. Heath, and T. Strohmer, "Designing structured tight frames via an alternating projection method," *IEEE Transactions on Information Theory*, vol. 51, no. 1, pp. 188–209, 2005.

[55] P. Stoica, J. Li, and X. Yao, "On probing signal design for MIMO radar," *IEEE Transactions on Signal Processing*, vol. 55, no. 8, pp. 4151–4161, 2007.

[56] H. He, J. Li, and P. Stoica, *Waveform design for active sensing systems: a computational approach*. Cambridge University Press, 2012.

[57] M. Soltanalian, M. M. Naghsh, and P. Stoica, "A fast algorithm for designing complementary sets of sequences," *Signal Processing*, vol. 93, no. 7, pp. 2096–2102, 2013.

[58] M. Soltanalian and P. Stoica, "Computational design of sequences with good correlation properties," *IEEE Transactions on Signal Processing*, vol. 60, no. 5, pp. 2180–2193, 2012.

[59] H. He, P. Stoica, and J. Li, "Designing unimodular sequence sets with good correlations-including an application to MIMO radar," *IEEE Transactions on Signal Processing*, vol. 57, no. 11, pp. 4391–4405, 2009.

[60] J. Li, P. Stoica, and X. Zheng, "Signal synthesis and receiver design for MIMO radar imaging," *IEEE Transactions on Signal Processing*, vol. 56, no. 8, pp. 3959–3968, 2008.

[61] P. Stoica, J. Li, and X. Zhu, "Waveform synthesis for diversity-based transmit beampattern design," *IEEE Transactions on Signal Processing*, vol. 56, no. 6, pp. 2593–2598, 2008.

[62] M. Gkizeli and G. N. Karystinos, "Maximum-SNR antenna selection among a large number of transmit antennas," *IEEE Journal of Selected Topics in Signal Processing*, vol. 8, no. 5, pp. 891–901, 2014.

[63] X. Wang, A. Hassanien, and M. G. Amin, "Sparse transmit array design for dual-function radar communications by antenna selection," *Digital Signal Processing*, vol. 83, pp. 223–234, 2018.

[64] H. Nosrati, E. Aboutanios, and D. Smith, "Multi-stage antenna selection for adaptive beamforming in MIMO radar," *IEEE Transactions on Signal Processing*, vol. 68, pp. 1374–1389, 2020.

[65] Z. Xu, F. Liu, and A. Petropulu, "Cramér-Rao bound and antenna selection optimization for dual radar-communication design," in *IEEE International Conference on Acoustics, Speech and Signal Processing (ICASSP)*, pp. 5168–5172, IEEE, 2022.

[66] A. Bose, S. Khobahi, and M. Soltanalian, "Efficient waveform covariance matrix design and antenna selection for MIMO radar," *Signal Processing*, vol. 183, p. 107985, 2021.

[67] S. Villeval, J. Tabrikian, and I. Bilik, "Optimal antenna selection sequence for MIMO radar," in *53rd Asilomar Conference on Signals, Systems, and Computers*, pp. 1182–1185, 2019.

[68] A. Atalik, M. Yilmaz, and O. Arikan, "Radar antenna selection for direction-of-arrival estimations," in *2021 IEEE Radar Conference (RadarConf21)*, pp. 1–6, IEEE, 2021.

[69] A. M. Elbir and K. V. Mishra, "Joint antenna selection and hybrid beamformer design using unquantized and quantized deep learning networks," *IEEE Transactions on Wireless Communications*, vol. 19, no. 3, pp. 1677–1688, 2019.

Chapter 4

MM Methods

In this chapter, we discuss various sequence design techniques that are based on the principle of the MM framework. Before we start the discussion, let's highlight the importance of transmit sequences through various applications in active sensing systems. Active sensing systems like radar/sonar transmit and receive waveforms [1–4]. The signals reflected by different targets in the scene are then analyzed, and the target's location and strength are estimated [5, 6]. The distance (range) between the sensing system and a target can be estimated by measuring the round-trip time delay. Similarly other parameters like speed of a moving target can also be estimated by analyzing the Doppler shift in the received waveform. The resolution and the numerical precision in estimating the location and strength of the targets will depend on the autocorrelation property of transmitting sequences (or) waveforms.

4.1 SYSTEM MODEL

Let $\{x_n\}_{n=1}^{N}$ be a 'N' length discrete sequence with aperiodic autocorrelation $r(k)$, defined at any lag 'k' as:

$$r(k) = \sum_{n=1}^{N-k} x_{n+k} x_n^* = r^*(-k), \quad k = 0, ..., N-1 \tag{4.1}$$

To explain the importance of autocorrelation of the transmit sequence, we consider the example of parameter estimation in the active sensing

application. Let $y(t)$, be the continuous-time signal comprising M number of subpulses transmitted towards the target of interest, and $z(t)$, be the received signal by the system, which are given, respectively, by:

$$y(t) = \sum_{m=1}^{M} x_m r_m(t - (m-1)t_d) \tag{4.2}$$

where $r_m(t)$ is the shaping pulse (rectangular or sine) with duration t_d and

$$z(t) = \left(\sum_{k=1}^{K} \rho_k y(t - \tau_k) \right) + e(t) \tag{4.3}$$

where K denotes the total number of targets present in the scene, ρ_k, τ_k denote the strength and the round-trip time delay of the kth target, respectively and $e(t)$ denote the noise.

The strength of any kth target (ρ_k) can be calculated by filtering the received signal with a filter $f(t)$:

$$\bar{\rho_k} = \int_{-\infty}^{\infty} f^*(t) z(t) dt \tag{4.4}$$

By substituting (4.3) to (4.4), we have:

$$\begin{aligned} \bar{\rho_k} = \int_{-\infty}^{\infty} f^*(t) y(t - \tau_k) dt + \sum_{m=1, m \neq k}^{K} \left(\int_{-\infty}^{\infty} f^*(t) y(t - \tau_m) dt \right) \\ + \int_{-\infty}^{\infty} f^*(t) e(t) dt \end{aligned} \tag{4.5}$$

By taking a closer look at (4.5), one can see that the first term in (4.5) denotes the signal component returned from the kth target and the second term denotes the clutter, and the third term denotes the noise. Thus, the choice of $f(t)$ should be such that the first term in (4.5) should be amplified and the second, and third terms should be suppressed. A common choice of $f(t)$ is the matched filter that chooses $f(t)$ as $y(t - \tau_k)$; thus, (4.5) will become:

$$\bar{\rho_k} = \int_{-\infty}^{\infty} y^*(t-\tau_k)y(t-\tau_k)dt + \sum_{m=1,m\neq k}^{K}\left(\int_{-\infty}^{\infty} y^*(t-\tau_k)y(t-\tau_m)dt\right) + \int_{-\infty}^{\infty} y^*(t-\tau_k)e(t)dt \tag{4.6}$$

one can observe that the first term in (4.6) is nothing but the mainlobe of autocorrelation of $y(t)$ and similarly the second term denotes the autocorrelation sidelobes. Hence, it is clear that the transmit waveforms should possess good autocorrelation properties for better target detection [7–9].

Some modern radar systems such as automotive radar sensors continuously sense the environment. Through initial sensing of the environment, they would know rough target locations and, in the next step, they can use the initial sensing information to design pruned sequences that can give more accurate target locations. So, for continuously sensing the environment and assessing the target strengths, the automotive radars must have the capability to design the transmit sequences adaptively.

The ISL and PSL are the two metrics used to evaluate the quality of any sequence. Both are correlation-dependent metrics and are defined as:

$$\text{ISL} = \sum_{k=1}^{N-1} |r(k)|^2 \tag{4.7}$$

$$\text{PSL} = \underset{k=1,..,N-1}{\text{maximum}} |r(k)| \tag{4.8}$$

and an another closely related metric where only few lags are weighed more than the others is the weighted ISL (WISL) metric:

$$\text{WISL} = \sum_{k=1}^{N-1} w_k |r(k)|^2,\ w_k \geq 0 \tag{4.9}$$

However, in various practical scenarios, on top of the requirement of good autocorrelation properties, the applications mentioned earlier also pose different constraints on the transmit sequence, such as the power, spectral (range of operating frequencies), and constant-modulus constraints [10]. The power constraint is mainly due to the limited budget of transmitter power available in the system. The spectral limitation is imposed to not use

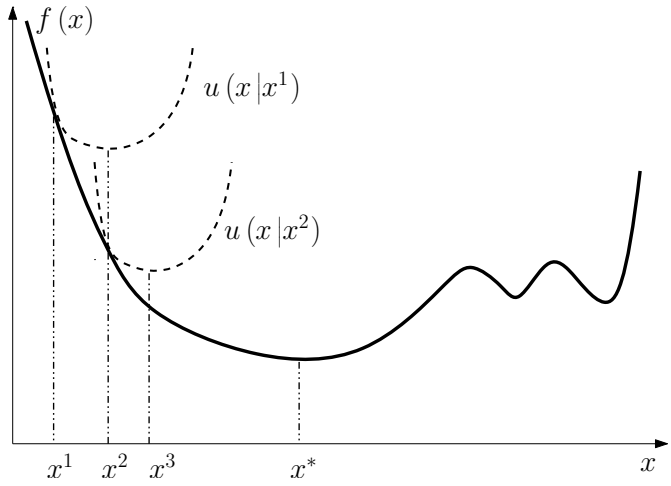

Figure 4.1. The MM procedure.

the frequency bands allocated for the defense (or) communication applications. Thus, to work on the power efficient region of hardware components such as power amplifiers and analog to digital converter (ADC), and digital to analog converter (DAC), the sequences are required to maintain the constant-modulus property [7, 8, 10, 11].

In this chapter, we will discuss the optimization technique of MM which can be used to design sequences with good autocorrelation properties. Before going directly into the sequence design methods, we will introduce the MM method, which plays a central role in the development of algorithms.

4.2 MM METHOD

4.2.1 MM Method for Minimization Problems

As previously stated in Chapter 2, MM is a two-step technique that is used to solve the hard (nonconvex or even convex) problems very efficiently [12, 13].

The MM procedure is given in the Figure 4.1. The first step of the MM method is to construct a majorization (upper-bound) function $u(.)$ to the original objective function $f(.)$ at any point $\boldsymbol{x}^t$ ($\boldsymbol{x}$ at t-th iteration) and the second step is to minimize the upper-bound function $u(.)$ to generate a next update $\boldsymbol{x}^{t+1}$. So, at every newly generated point, the abovementioned two steps will be applied repeatedly until the algorithm reaches a minimum of an original function $f(.)$. For any given problem, the construction of a majorization function is not unique and for the same problem, different types of majorization functions may exist. So, the performance will depend solely on the chosen majorization function and the different ways to construct a majorization function are shown in [13, 14].

The majorization function $u(\boldsymbol{x}|\boldsymbol{x}^t)$, which is constructed in the first step of the MM method, has to satisfy the following properties:

$$u(\boldsymbol{x}^t|\boldsymbol{x}^t) = f(\boldsymbol{x}^t), \quad \forall \boldsymbol{x} \in \boldsymbol{\chi} \tag{4.10}$$

$$u(\boldsymbol{x}|\boldsymbol{x}^t) \geq f(\boldsymbol{x}), \quad \forall \boldsymbol{x} \in \boldsymbol{\chi} \tag{4.11}$$

where $\boldsymbol{\chi}$ is the set consisting of all the possible values of $\boldsymbol{x}$. As the MM technique is an iterative process, it will generate the sequence of points $\{\boldsymbol{x}\} = \boldsymbol{x}^1, \boldsymbol{x}^2, \boldsymbol{x}^3, ..., \boldsymbol{x}^m$ according to the following update rule:

$$\boldsymbol{x}^{t+1} = \arg\min_{\boldsymbol{x} \in \boldsymbol{\chi}} u(\boldsymbol{x}|\boldsymbol{x}^t) \tag{4.12}$$

The cost function value evaluated at every point generated by (4.12) will satisfy the descent property, that is,

$$f(\boldsymbol{x}^{t+1}) \leq u(\boldsymbol{x}^{t+1}|\boldsymbol{x}^t) \leq u(\boldsymbol{x}^t|\boldsymbol{x}^t) = f(\boldsymbol{x}^t) \tag{4.13}$$

4.2.2 MM Method for Minimax Problems

Consider the minimax problem as follows:

$$\min_{\boldsymbol{x} \in \boldsymbol{\chi}} f(\boldsymbol{x}) \tag{4.14}$$

where $f(\boldsymbol{x}) = \underset{a=1,..,s}{\text{maximum}} f_a(\boldsymbol{x})$. Similar to the case of minimization problems, the majorization function for the objective in (4.14) can be constructed as follows:

$$u(\boldsymbol{x}|\boldsymbol{x}^t) = \underset{a=1,..,s}{\text{maximum}}\ \tilde{u}_a(\boldsymbol{x}|\boldsymbol{x}^t) \tag{4.15}$$

where each $\tilde{u}_a(\boldsymbol{x}|\boldsymbol{x}^t)$ is an upper bound for the respective $f_a(\boldsymbol{x})$ at any given $\boldsymbol{x}^t$, $\forall a$. Here, every majorization function $\tilde{u}_a(\boldsymbol{x}|\boldsymbol{x}^t)$, $\forall a$ will also satisfy the conditions mentioned in (4.10), and (4.11), that is,

$$\tilde{u}_a(\boldsymbol{x}^t|\boldsymbol{x}^t) = f_a(\boldsymbol{x}^t),\ \forall a, \boldsymbol{x} \in \boldsymbol{\chi} \tag{4.16}$$

$$\tilde{u}_a(\boldsymbol{x}|\boldsymbol{x}^t) \geq f_a(\boldsymbol{x}),\ \forall a, \boldsymbol{x} \in \boldsymbol{\chi} \tag{4.17}$$

It can be easily shown that the choice of $u(\boldsymbol{x}|\boldsymbol{x}^t)$ in (4.15) is a global upper-bound function of $f(\boldsymbol{x})$, that is,

$$u(\boldsymbol{x}^t|\boldsymbol{x}^t) = \underset{a=1,..,s}{\text{maximum}}\ \tilde{u}_a(\boldsymbol{x}^t|\boldsymbol{x}^t) = \underset{a=1,..,s}{\text{maximum}}\ f_a(\boldsymbol{x}^t) = f(\boldsymbol{x}^t) \tag{4.18}$$

$$\begin{aligned} \tilde{u}_a(\boldsymbol{x}|\boldsymbol{x}^t) \geq f_a(\boldsymbol{x}) \quad &\Leftrightarrow \underset{a=1,..,s}{\text{maximum}}\ \tilde{u}_a(\boldsymbol{x}|\boldsymbol{x}^t) \geq \underset{a=1,..,s}{\text{maximum}}\ f_a(\boldsymbol{x}) \\ &\Leftrightarrow u(\boldsymbol{x}|\boldsymbol{x}^t) \geq f(\boldsymbol{x}) \end{aligned} \tag{4.19}$$

Similar to the MM for minimization problems, here too the sequence of points $\{\boldsymbol{x}\} = \boldsymbol{x}^1, \boldsymbol{x}^2, \boldsymbol{x}^3, ..., \boldsymbol{x}^m$ obtained via the MM update rule will monotonically decrease the objective function.

4.3 SEQUENCE DESIGN ALGORITHMS

There are many MM-based sequence design algorithms that are developed in the literature to solve the following problems.

$$\begin{aligned} \underset{\boldsymbol{x}}{\text{minimize}} \quad & \text{ISL/PSL} \\ \text{subject to} \quad & |x_n| = 1,\ n = 1, ..., N \end{aligned} \tag{4.20}$$

where $\boldsymbol{x} = [x_1 x_2 .... x_N]^T_{1\times N}$. Here, we will discuss the ISL and PSL minimizers, which solve the following problems, respectively.

$$\begin{aligned} \underset{\boldsymbol{x}}{\text{minimize}} \quad & \text{ISL} = \sum_{k=1}^{N-1} |r(k)|^2 \\ \text{subject to} \quad & |x_n| = 1,\ n = 1, ..., N. \end{aligned} \tag{4.21}$$

$$\begin{aligned} \underset{\boldsymbol{x}}{\text{minimize}} \quad & \text{PSL} = \underset{k=1,..,N}{\text{maximum}} |r(k)| \\ \text{subject to} \quad & |x_n| = 1,\ n = 1, ..., N \end{aligned} \tag{4.22}$$

4.3.1 ISL Minimizers

In this subsection, we will discuss different MM based ISL minimization techniques (ISL minimizers), namely, the monotonic minimizer for integrated sidelobe level (MISL) [15] , ISL-NEW [16], FBMM [17], FISL [18], and UNIPOL [19].

4.3.1.1 MISL Algorithm

The MISL (monotonic minimizer for ISL) was originally published in [15]. In this subsection, we will briefly present the methodology involved in the derivation of the MISL algorithm. The cost function in (4.21) is expressed in terms of the autocorrelation values, by re-expressing it in the frequency domain (using the Parsevals theorem), we arrive at the following equivalent form:

$$\sum_{k=1}^{N-1} |r(k)|^2 = \frac{1}{4N} \sum_{a=1}^{2N} \left[\left| \sum_{n=1}^{N} x_n e^{-j\omega_a n} \right|^2 - N \right]^2 \tag{4.23}$$

where $\omega_a = \frac{2\pi}{2N} a$, $a = 1, ..., 2N$ are the Fourier grid frequencies. So, by using (4.23), the problem in (4.21) can be rewritten as (neglecting the constant multiplication term):

$$\begin{aligned} \underset{\boldsymbol{x}}{\text{minimize}} \quad & \sum_{a=1}^{2N} \left[\left| \sum_{n=1}^{N} x_n e^{-j\omega_a n} \right|^2 - N \right]^2 \\ \text{subject to} \quad & |x_n| = 1,\ n = 1, ..., N \end{aligned} \tag{4.24}$$

The cost function in the above problem can be rewritten as:

$$\sum_{a=1}^{2N} \left[\left| \sum_{n=1}^{N} x_n e^{-j\omega_a n} \right|^2 - N \right]^2 = \sum_{a=1}^{2N} \left[\boldsymbol{e}_a{}^H \boldsymbol{x}\boldsymbol{x}^H \boldsymbol{e}_a - N \right]^2 \tag{4.25}$$

where $\boldsymbol{e}_a = [e^{j\omega_a(1)}, e^{j\omega_a(2)}, ..., e^{j\omega_a(N)}]^T$. By expanding the above equivalent cost function, we have

$$\sum_{a=1}^{2N}\left[{\boldsymbol{e}_a}^H\boldsymbol{x}\boldsymbol{x}^H\boldsymbol{e}_a - N\right]^2 = \sum_{a=1}^{2N}\left[\left[{\boldsymbol{e}_a}^H\boldsymbol{x}\boldsymbol{x}^H\boldsymbol{e}_a\right]^2 + N^2 - 2N\left[{\boldsymbol{e}_a}^H\boldsymbol{x}\boldsymbol{x}^H\boldsymbol{e}_a\right]\right] \tag{4.26}$$

Due to the Parsevals theorem, the third term in (4.26), that is,

$$\left(\sum_{a=1}^{2N} 2N\left[{\boldsymbol{e}_a}^H\boldsymbol{x}\boldsymbol{x}^H\boldsymbol{e}_a\right] = 2N\left\|\boldsymbol{x}\right\|_2^2 = 2N^2\right) \tag{4.27}$$

is a constant and the second term $\left(N^2\right)$ is also a constant. Thereby ignoring the constant terms, the problem in (4.24) can be rewritten as:

$$\begin{aligned} \underset{\boldsymbol{x}}{\text{minimize}} \quad & \sum_{a=1}^{2N}\left[{\boldsymbol{e}_a}^H\boldsymbol{x}\boldsymbol{x}^H\boldsymbol{e}_a\right]^2 \\ \text{subject to} \quad & |x_n| = 1,\ n = 1, ..., N \end{aligned} \tag{4.28}$$

In terms of $\boldsymbol{x}$, the problem in (4.28) is quartic and it is very challenging to solve further. So, by defining $\boldsymbol{X} = \boldsymbol{x}\boldsymbol{x}^H$ and $\boldsymbol{C}_a = \boldsymbol{e}_a{\boldsymbol{e}_a}^H$, the problem in (4.28) can be rewritten as:

$$\begin{aligned} \underset{\boldsymbol{x},\boldsymbol{X}}{\text{minimize}} \quad & \sum_{a=1}^{2N}\text{Tr}\left(\boldsymbol{X}\boldsymbol{C}_a\right)^2 \\ \text{subject to} \quad & |x_n| = 1,\ n = 1, ..., N \\ & \boldsymbol{X} = \boldsymbol{x}\boldsymbol{x}^H \end{aligned} \tag{4.29}$$

Since $\text{Tr}\left(\boldsymbol{X}\boldsymbol{C}_a\right) = \text{vec}\left(\boldsymbol{X}\right)^H\text{vec}\left(\boldsymbol{C}_a\right)$, the problem in (4.29) can be rewritten as:

$$\begin{aligned} \underset{\boldsymbol{x},\boldsymbol{X}}{\text{minimize}} \quad & \text{vec}\left(\boldsymbol{X}\right)^H\boldsymbol{\Phi}\text{vec}\left(\boldsymbol{X}\right) \\ \text{subject to} \quad & |x_n| = 1,\ n = 1, ..., N \\ & \boldsymbol{X} = \boldsymbol{x}\boldsymbol{x}^H \end{aligned} \tag{4.30}$$

where $\boldsymbol{\Phi} = \sum_{a=1}^{2N}\text{vec}\left(\boldsymbol{C}_a\right)\text{vec}\left(\boldsymbol{C}_a\right)^H$. Now the cost function in (4.30) is quadratic in $\boldsymbol{X}$ and the MM approach can be used to effectively solve it. Let

us introduce the following lemma, which would be useful in developing the MM-based algorithms.

Lemma 4.1. *Let $\boldsymbol{Q}$ be an $n\times n$ Hermitian matrix and $\boldsymbol{R}$ be another $n\times n$ Hermitian matrix such that $\boldsymbol{R}\succeq\boldsymbol{Q}$. Then, for any point $\boldsymbol{x}^0\in\boldsymbol{C}^n$, the quadratic function $\boldsymbol{x}^H\boldsymbol{Q}\boldsymbol{x}$ is majorized by $\boldsymbol{x}^H\boldsymbol{R}\boldsymbol{x}+2Re\left(\boldsymbol{x}^H\left(\boldsymbol{Q}-\boldsymbol{R}\right)\boldsymbol{x}^0\right)+\left(\boldsymbol{x}^0\right)^H\left(\boldsymbol{R}-\boldsymbol{Q}\right)\boldsymbol{x}^0$ at $\boldsymbol{x}^0$.*

Proof: By using the second-order Taylor series expansion, the quadratic function $\boldsymbol{x}^H\boldsymbol{Q}\boldsymbol{x}$ can be expanded around a point $\boldsymbol{x}^0$ as:

$$\boldsymbol{x}^H\boldsymbol{Q}\boldsymbol{x}=\left(\boldsymbol{x}^0\right)^H\boldsymbol{Q}\boldsymbol{x}^0+2\text{Re}\left(\left(\boldsymbol{x}-\boldsymbol{x}^0\right)^H\boldsymbol{Q}\boldsymbol{x}^0\right)+\left(\boldsymbol{x}-\boldsymbol{x}^0\right)^H\boldsymbol{Q}\left(\boldsymbol{x}-\boldsymbol{x}^0\right) \tag{4.31}$$

As $\boldsymbol{R}\succeq\boldsymbol{Q}$, (4.31) can be upper-bounded as:

$$\boldsymbol{x}^H\boldsymbol{Q}\boldsymbol{x}\leq\left(\boldsymbol{x}^0\right)^H\boldsymbol{Q}\boldsymbol{x}^0+2\text{Re}\left(\left(\boldsymbol{x}-\boldsymbol{x}^0\right)^H\boldsymbol{Q}\boldsymbol{x}^0\right)+\left(\boldsymbol{x}-\boldsymbol{x}^0\right)^H\boldsymbol{R}\left(\boldsymbol{x}-\boldsymbol{x}^0\right) \tag{4.32}$$

which can be rearranged as:

$$\boldsymbol{x}^H\boldsymbol{Q}\boldsymbol{x}\leq\boldsymbol{x}^H\boldsymbol{R}\boldsymbol{x}+2\text{Re}\left(\boldsymbol{x}^H\left(\boldsymbol{Q}-\boldsymbol{R}\right)\boldsymbol{x}^0\right)+\left(\boldsymbol{x}^0\right)^H\left(\boldsymbol{R}-\boldsymbol{Q}\right)\boldsymbol{x}^0 \tag{4.33}$$

for any $\boldsymbol{x}\in\boldsymbol{C}^n$. ■

So, by using the Lemma 4.1, the cost function in (4.30) can be majorized as:

$$\begin{aligned}\text{vec}\left(\boldsymbol{X}\right)^H\boldsymbol{\Phi}\text{vec}\left(\boldsymbol{X}\right)\leq\text{vec}\left(\boldsymbol{X}\right)^H\boldsymbol{M}\text{vec}\left(\boldsymbol{X}\right)+2Re\Big(&\text{vec}\left(\boldsymbol{X}\right)^H\left(\boldsymbol{\Phi}-\boldsymbol{M}\right)\\&\text{vec}\left(\boldsymbol{X}^t\right)\Big)+\text{vec}\left(\boldsymbol{X}^t\right)^H\left(\boldsymbol{M}-\boldsymbol{\Phi}\right)\text{vec}\left(\boldsymbol{X}^t\right)\end{aligned} \tag{4.34}$$

where $\boldsymbol{M}=\lambda_{\max}(\boldsymbol{\Phi})\boldsymbol{I}_n$.

As $\boldsymbol{M}$ is a constant diagonal matrix and $\text{vec}\left(\boldsymbol{X}\right)^H\text{vec}\left(\boldsymbol{X}\right)=\left(\boldsymbol{x}^H\boldsymbol{x}\right)^2=N^2$, the first and the last terms in the majorized function (4.34) are constants. So, by neglecting the constant terms, the surrogate minimization problem for (4.30) can be written as:

$$\begin{aligned}\underset{\boldsymbol{x},\boldsymbol{X}}{\text{minimize}}\quad&Re\left(\text{vec}\left(\boldsymbol{X}\right)^H\left(\boldsymbol{\Phi}-\boldsymbol{M}\right)\text{vec}\left(\boldsymbol{X}^t\right)\right)\\\text{subject to}\quad&|x_n|=1,\ n=1,...,N\\&\boldsymbol{X}=\boldsymbol{x}\boldsymbol{x}^H\end{aligned} \tag{4.35}$$

The cost function in the above problem in (4.35) can be further expressed as:

$$Re\left(\text{vec}\left(\boldsymbol{X}\right)^{H}\left(\boldsymbol{\Phi}-\boldsymbol{M}\right)\text{vec}\left(\boldsymbol{X}^{t}\right)\right)=\sum_{a=1}^{2N}\text{Tr}\left(\boldsymbol{X}^{t}\boldsymbol{C}_{a}\right)\text{Tr}\left(\boldsymbol{C}_{a}\boldsymbol{X}\right)-2N^{2}\text{Tr}\left(\boldsymbol{X}^{t}\boldsymbol{X}\right) \tag{4.36}$$

By substituting back $\boldsymbol{X}=\boldsymbol{x}\boldsymbol{x}^{H}$, the cost function can be further obtained as:

$$\sum_{a=1}^{2N}\left|\boldsymbol{e}_{a}^{H}\boldsymbol{x}^{t}\right|^{2}\left|\boldsymbol{e}_{a}^{H}\boldsymbol{x}\right|^{2}-2N^{2}\left|\boldsymbol{x}^{H}\boldsymbol{x}^{t}\right|^{2} \tag{4.37}$$

By using (4.37), the problem in (4.35) can be rewritten more compactly as:

$$\begin{aligned}&\underset{\boldsymbol{x}}{\text{minimize}} \quad \boldsymbol{x}^{H}\left[\hat{\boldsymbol{E}}\text{Diag}(\boldsymbol{b}^{t})\hat{\boldsymbol{E}}^{H}-2N^{2}\boldsymbol{x}^{t}\left(\boldsymbol{x}^{t}\right)^{H}\right]\boldsymbol{x}\\&\text{subject to} \quad |x_{n}|=1,\ n=1,...,N\end{aligned} \tag{4.38}$$

where $\hat{\boldsymbol{E}}=[\boldsymbol{e}_{1},....,\boldsymbol{e}_{2N}]$ be an $N\times 2N$ matrix and $\boldsymbol{b}^{t}=\left|\hat{\boldsymbol{E}}^{H}\boldsymbol{x}^{t}\right|$. Now the resultant problem in (4.38) is quadratic in $\boldsymbol{x}$. So, by majorizing it again using the Lemma 4.1 with $\boldsymbol{R}=b_{max}^{t}\hat{\boldsymbol{E}}\hat{\boldsymbol{E}}^{H}$, the resultant surrogate function is given by:

$$b_{max}^{t}\boldsymbol{x}^{H}\hat{\boldsymbol{E}}\hat{\boldsymbol{E}}^{H}\boldsymbol{x}+2\text{Re}\left(\boldsymbol{x}^{H}\left[\tilde{\boldsymbol{C}}-2N^{2}\boldsymbol{x}^{t}\left(\boldsymbol{x}^{t}\right)^{H}\right]\boldsymbol{x}^{t}\right)+\left(\boldsymbol{x}^{t}\right)^{H}\left(2N^{2}\boldsymbol{x}^{t}\left(\boldsymbol{x}^{t}\right)^{H}-\tilde{\boldsymbol{C}}\right)\boldsymbol{x}^{t} \tag{4.39}$$

where $\tilde{\boldsymbol{C}}=\hat{\boldsymbol{E}}\left(\text{Diag}\left(\boldsymbol{b}^{2t}\right)-b_{max}^{t}\boldsymbol{I}\right)\hat{\boldsymbol{E}}^{H}$ and $b_{max}^{t}=\max_{a}\left\{(b_{a}^{t})^{2},\ a=1,2,.,2N\right\}$.

The first and last terms in (4.39) are constants, so by ignoring them, the final surrogate minimization problem is given by:

Algorithm 4.1: The MISL Algorithm Proposed in [15]

Require: sequence length 'N'
set $t = 0$, initialize $\boldsymbol{x}^0$
repeat
  $\boldsymbol{b}^t = \left|\hat{\boldsymbol{E}}^H \boldsymbol{x}^t\right|$
  $b^t_{\max} = \max_a \left\{(b^t_a)^2,\ a = 1, .., 2N\right\}$
  $\boldsymbol{d} = -\hat{\boldsymbol{E}}\left(\text{Diag}\left(\boldsymbol{b}^{2t}\right) - b^t_{\max}\boldsymbol{I} - N^2\boldsymbol{I}\right)\hat{\boldsymbol{E}}^H\boldsymbol{x}^t$
  $\boldsymbol{x}^{t+1} = \frac{\boldsymbol{d}}{|\boldsymbol{d}|}$
  $t \leftarrow t + 1$
until convergence

$$\begin{aligned} \underset{\boldsymbol{x}}{\text{minimize}} \quad & \text{Re}\left(\boldsymbol{x}^H\left[\tilde{\boldsymbol{C}} - 2N^2\boldsymbol{x}^t\left(\boldsymbol{x}^t\right)^H\right]\boldsymbol{x}^t\right) \\ \text{subject to} \quad & |x_n| = 1,\ n = 1, ..., N \end{aligned} \tag{4.40}$$

The problem in (4.40) can be compactly rewritten as:

$$\begin{aligned} \underset{\boldsymbol{x}}{\text{minimize}} \quad & \| \boldsymbol{x} - \boldsymbol{d} \|_2^2 \\ \text{subject to} \quad & |x_n| = 1,\ n = 1, ..., N \end{aligned} \tag{4.41}$$

where $\boldsymbol{d} = -\hat{\boldsymbol{E}}\left(\text{Diag}\left(\boldsymbol{b}^{2t}\right) - b^t_{max}\boldsymbol{I} - N^2\boldsymbol{I}\right)\hat{\boldsymbol{E}}^H\boldsymbol{x}^t$. The problem in (4.41) has a closed-form solution:

$$\boldsymbol{x}^{t+1} = \frac{\boldsymbol{d}}{|\boldsymbol{d}|} \tag{4.42}$$

Here $\left|\hat{\boldsymbol{E}}^H\boldsymbol{x}^t\right|$, $\frac{\boldsymbol{d}}{|\boldsymbol{d}|}$ are element-wise operations and the pseudocode of the MISL algorithm is summarized in Algorithm 4.1.

Convergence Analysis

As the derivation of MISL and other algorithms in this chapter are based on the MM technique, the convergence analysis of all the algorithms will be similar. However, for better understanding, here we will discuss the convergence of the MISL algorithm and the rest of the algorithms will have a similar proof of convergence. So, from (4.13), we have the descent property

$$f(\boldsymbol{x}^{t+1}) \leq u(\boldsymbol{x}^{t+1}|\boldsymbol{x}^{t}) \leq u(\boldsymbol{x}^{t}|\boldsymbol{x}^{t}) = f(\boldsymbol{x}^{t})$$

So, the MM technique is ensuring that the cost function value evaluated at every point $\{\boldsymbol{x}^t\}$ generated by the MISL algorithm will be monotonically decreasing and by the nature of the cost function of the problem in (4.21), one can observe that it is always bounded below by zero. So, the sequence of cost function values is guaranteed to converge to a finite value.

Now, we will discuss the convergence of points $\{\boldsymbol{x}^t\}$ generated by the MISL algorithm to a stationary point; so, starting with the definition of a stationary point.

Proposition 4.2. *Let $f : \boldsymbol{R}^n \rightarrow \boldsymbol{R}$ be any smooth function and let $\boldsymbol{x}^\star$ be a local minimum of f over a subset $\boldsymbol{\chi}$ of $\boldsymbol{R}^n$. Then*

$$\nabla f(\boldsymbol{x}^\star)\boldsymbol{y} \geq 0, \ \forall \boldsymbol{y} \in T_{\boldsymbol{\chi}}(\boldsymbol{x}^\star) \tag{4.43}$$

where $T_{\boldsymbol{\chi}}(\boldsymbol{x}^\star)$ denotes the tangent cone of $\boldsymbol{\chi}$ at $\boldsymbol{x}^\star$. Such any point $\boldsymbol{x}^\star$, which satisfies (4.43) is called as a stationary point [20–22].

Now, the convergence property of the MISL algorithm is explained as follows.

Theorem 4.3. *Let $\left\{\boldsymbol{x}^t\right\}$ be the sequence of points generated by the MISL algorithm. Then every point $\left\{\boldsymbol{x}^t\right\}$ is a stationary point of the problem in (4.21).*

Proof: Assume that there exists a converging subsequence $\boldsymbol{x}^{l_j} \rightarrow \boldsymbol{x}^\star$, then from the theory of MM technique, we have

$$u(\boldsymbol{x}^{(l_{j+1})}|\boldsymbol{x}^{(l_{j+1})}) = f(\boldsymbol{x}^{(l_{j+1})}) \leq f(\boldsymbol{x}^{(l_j+1)}) \leq u(\boldsymbol{x}^{(l_{j+1})}|\boldsymbol{x}^{(l_j)}) \leq u(\boldsymbol{x}|\boldsymbol{x}^{(l_j)})$$

$$u(\boldsymbol{x}^{(l_{j+1})}|\boldsymbol{x}^{(l_{j+1})}) \leq u(\boldsymbol{x}|\boldsymbol{x}^{(l_j)})$$

Letting $j \rightarrow +\infty$, we obtain

$$u(\boldsymbol{x}^{\infty}|\boldsymbol{x}^{\infty}) \leq u(\boldsymbol{x}|\boldsymbol{x}^{\infty}) \tag{4.44}$$

Replacing $\boldsymbol{x}^{\infty}$ with $\boldsymbol{x}^{\star}$, we have

$$u(\boldsymbol{x}^{\star}|\boldsymbol{x}^{\star}) \leq u(\boldsymbol{x}|\boldsymbol{x}^{\star}) \tag{4.45}$$

So, (4.45) conveys that $\boldsymbol{x}^{\star}$ is a stationary point and also a global minimizer of $u(.)$, that is,

$$\nabla u(\boldsymbol{x}^{\star})\boldsymbol{d} \geq 0, \ \forall \boldsymbol{d} \in T_{\boldsymbol{\chi}}(\boldsymbol{x}^{\star}) \tag{4.46}$$

From the majorization step, we know that the first-order behavior of majorized function $u(\boldsymbol{x}|\boldsymbol{x}^{t})$ is equal to the original cost function $f(\boldsymbol{x})$. So, we can show

$$u(\boldsymbol{x}^{\star}|\boldsymbol{x}^{\star}) \leq u(\boldsymbol{x}|\boldsymbol{x}^{\star}) \Leftrightarrow f(\boldsymbol{x}^{\star}) \leq f(\boldsymbol{x}) \tag{4.47}$$

and it leads to

$$\nabla f(\boldsymbol{x}^{\star})\boldsymbol{y} \geq 0, \forall \boldsymbol{y} \in T_{\boldsymbol{\chi}}(\boldsymbol{x}^{\star}) \tag{4.48}$$

So, the set of points generated by the MISL algorithm is a set of stationary points and $\boldsymbol{x}^{\star}$ is the minimizer of $f(\boldsymbol{x})$. This concludes the proof. ■

For efficient implementation of the MISL algorithm, the steps 3 and 5 of the algorithm (which form the core of the MISL algorithm) can be easily implemented by using the $2N$ point fast Fourier transform (FFT) and IFFT operations. Hence, the computational complexity of the MISL algorithm is given by $\mathcal{O}(2N\, log\, 2N)$. The space complexity is dominated by two vectors each of size $(2N \times 1)$ and a matrix of size $(N \times N)$ and thus the space complexity would be $\mathcal{O}(N^2)$.

4.3.1.2 ISL-NEW Algorithm

In this subsection, we will review another MM-based algorithm named ISL-NEW [16]. The derivations of ISL-NEW is very similar to that of MISL with only few minor differences. The original derivation of ISL-NEW algorithm was shown in the context of designing the set of sequences, where both the auto- and cross- correlation are taken into account. By particularizing it

for single sequence, the only difference between the MISL and ISL-NEW algorithms is in the way they arrive at their majorizing functions. After majorizing the objective function in (4.30) by using the Lemma 4.1 and then by removing the constant terms, the final surrogate minimization problem in terms of $\boldsymbol{x}$ is given by:

$$\begin{aligned} \underset{\boldsymbol{x}}{\text{minimize}} \quad & \boldsymbol{x}^H \left[\hat{\boldsymbol{E}} \text{Diag}(\boldsymbol{b}^t) \hat{\boldsymbol{E}}^H - N^2 \boldsymbol{x}^t \left(\boldsymbol{x}^t \right)^H \right] \boldsymbol{x} \\ \text{subject to} \quad & |x_n| = 1, \ n = 1, ..., N \end{aligned} \tag{4.49}$$

The resultant problem in (4.49) is quadratic in $\boldsymbol{x}$. So, by majorizing it using the Lemma 4.1 and then by removing the constant terms, the resultant problem is given by:

$$\begin{aligned} \underset{\boldsymbol{x}}{\text{minimize}} \quad & \text{Re}\left(\boldsymbol{x}^H \left[\bar{\boldsymbol{C}} - N^2 \boldsymbol{x}^t \left(\boldsymbol{x}^t \right)^H \right] \boldsymbol{x}^t \right) \\ \text{subject to} \quad & |x_n| = 1, \ n = 1, ..., N \end{aligned} \tag{4.50}$$

where $\bar{\boldsymbol{C}} = \hat{\boldsymbol{E}} \left(\text{Diag}(\boldsymbol{b}^{2t}) - 0.5 b_{max}^t \boldsymbol{I} \right) \hat{\boldsymbol{E}}^H$. The problem in (4.50) can be rewritten more compactly as:

$$\begin{aligned} \underset{\boldsymbol{x}}{\text{minimize}} \quad & \| \boldsymbol{x} - \hat{\boldsymbol{d}} \|_2^2 \\ \text{subject to} \quad & |x_n| = 1, \ n = 1, ..., N \end{aligned} \tag{4.51}$$

where $\hat{\boldsymbol{d}} = -\hat{\boldsymbol{E}} \left(\text{Diag}(\boldsymbol{b}^{2t}) - 0.5 b_{max}^t \boldsymbol{I} - 0.5 N^2 \boldsymbol{I} \right) \hat{\boldsymbol{E}}^H \boldsymbol{x}^t$. The problem in (4.51) has a closed-form solution:

$$\boldsymbol{x}^{t+1} = \frac{\hat{\boldsymbol{d}}}{|\hat{\boldsymbol{d}}|} \tag{4.52}$$

Here $\frac{\hat{\boldsymbol{d}}}{|\hat{\boldsymbol{d}}|}$ is an element-wise operation and the pseudocode of the ISL-NEW algorithm is summarized in Algorithm 4.2.

Hence, the MISL and ISL-NEW algorithms are very similar and they both share the same computational and space complexities.

Algorithm 4.2: The ISL-NEW Algorithm Proposed in [16]

Require: sequence length 'N'
1: set $t = 0$, initialize $\boldsymbol{x}^0$
2: **repeat**
3: $\boldsymbol{b}^t = \left|\boldsymbol{E}^H \boldsymbol{x}^t\right|$
4: $b^t_{\max} = \max_a \left\{(b^t_a)^2 : a = 1, .., 2N\right\}$
5: $\hat{\boldsymbol{d}} = -\hat{\boldsymbol{E}}\left(\text{Diag}\left(\boldsymbol{b}^{2t}\right) - 0.5 b^t_{\max}\boldsymbol{I} - 0.5N^2\boldsymbol{I}\right)\hat{\boldsymbol{E}}^H\boldsymbol{x}^t$
6: $\boldsymbol{x}^{t+1} = \frac{\hat{\boldsymbol{d}}}{|\hat{\boldsymbol{d}}|}$
7: $t \leftarrow t + 1$
8: **until** convergence

4.3.1.3 FBMM Algorithm

The above MISL and ISL-NEW algorithms have updated all the elements of a sequence vector simultaneously. However, in this subsection, we are going to review an algorithm named fast block majorization minimization (FBMM) [17]. The FBMM algorithm considers the elements of a sequence vector as blocks and updates them in a sequential manner. So, before discussing the FBMM algorithm, let us introduce the block MM algorithm, which plays a central role in the development of the FBMM algorithm.

Block MM Algorithm

If one can split an optimization variable into M blocks, then a combination of BCD and the MM procedure can be applied, that is, the optimization variable is split into blocks and then each block is treated as an independent variable and updated using the MM method by keeping the other blocks fixed [23]. Hence, the i-th block variable is updated by minimizing the surrogate function $u_i(x_i|\boldsymbol{x}^t)$, which majorizes $f(x_i)$ at a feasible point $\boldsymbol{x}^t$ on the i-th block. Such a surrogate function has to satisfy the following properties:

$$u_i(x^t_i|\boldsymbol{x}^t) = f(\boldsymbol{x}^t) \tag{4.53}$$

$$u_i(x_i|\boldsymbol{x}^t) \geq f(x_1^t, x_2^t, .., x_i, .., x_N^t) \tag{4.54}$$

The i-th block variable is updated by solving the following problem:

$$x_i^{t+1} \in \arg\min_{x_i} u_i(x_i|\boldsymbol{x}^t). \tag{4.55}$$

In Block MM method, every block is updated sequentially and the surrogate function is chosen in a way that it is easy to minimize and will follow the shape of the objective function.

FBMM Algorithm

The ISL minimization problem given in (4.21) is:

$$\begin{aligned} \underset{\boldsymbol{x}}{\text{minimize}} \quad & \sum_{k=1}^{N-1} |r(k)|^2 \\ \text{subject to} \quad & |x_n| = 1, \quad n = 1, ..., N \end{aligned}$$

After substituting for $r(k)$ given in (4.1), the above problem can be rewritten as

$$\begin{aligned} \underset{\boldsymbol{x}}{\text{minimize}} \quad & \left|\sum_{i=1}^{N-1} x_{i+1}x_i^*\right|^2 + ... + \left|\sum_{i=1}^{2} x_{i+N-2}x_i^*\right|^2 + \left|x_N x_1^*\right|^2 \\ \text{subject to} \quad & |x_n| = 1, \quad n = 1, ..., N \end{aligned} \tag{4.56}$$

Now, to solve the problem in (4.56), the FBMM algorithm uses the Block MM technique by considering $x_1, x_2, .., x_N$ as block variables. For the sake of clarity, in the following, a generic optimization problem in variable x_i has been considered, and optimization over any variable of "$\boldsymbol{x}$" would be very similar to the generic problem.

Let the generic problem be:

$$\begin{aligned} \underset{x_i}{\text{minimize}} \quad & f_i(x_i) \\ \text{subject to} \quad & |x_i| = 1 \end{aligned} \tag{4.57}$$

where x_i indicates the i-th block variable and its corresponding objective function $f_i(x_i)$ is defined as

$$f_i(x_i) = a_i \left[\sum_{k=1}^{l_1} \mid x_i m_{ki}^* + n_{ki} x_i^* + c_{ki} \mid^2 \right] + b_i \left[\sum_{k=l_2}^{l_3} \mid n_{ki} x_i^* + c_{ki} \mid^2 \right] \quad (4.58)$$

where a_i, b_i are some fixed multiplicative constants, l_1, l_2, l_3 are the summation limits, and m_{ki}, n_{ki}, c_{ki} are the constants associated with kth autocorrelation lag, which are given by

$$\begin{aligned} m_{ki} &= x_{i-k} \\ n_{ki} &= x_{i+k} \\ c_{ki} &= \sum_{q=k+1}^{N} (x_q x_{q-k}^*), \quad q \neq i,\, q \neq k+i \end{aligned} \quad (4.59)$$

The values that the variables a_i, b_i, l_1, l_2, l_3 take will depend on the variable index (x_i). They can be given as follows:

$$\begin{aligned} a_i &= \begin{cases} 0 & i = 1, N \\ 1 & else \end{cases} \quad ,\forall N \\ b_i &= \begin{cases} 0 & i = \lfloor N/2 \rfloor + 1, \forall N \in odd \\ 1 & \forall i,\, \forall N \end{cases} \end{aligned} \quad (4.60)$$

$$\begin{aligned} l_1 &= \begin{cases} i-1 & i = 2, .., \lfloor N/2 \rfloor, a_i \neq 0 \quad ,\forall N \\ i-1 & b_i = 0, a_i \neq 0 \\ N-i & i = \lfloor N/2 \rfloor + 1, a_i \neq 0 \quad ,\forall N \in even \\ N-i & i = \lfloor N/2 \rfloor + 2, .., N-1, a_i \neq 0 \quad ,\forall N \end{cases} \\ l_2 &= \begin{cases} i & a_i = 0 \\ l_1 + 1 & b_i \neq 0 \quad ,\forall N \end{cases} \\ l_3 &= \begin{cases} N-1 & a_i = 0 \\ N-i & i = 2, .., \lfloor N/2 \rfloor \quad ,\forall N \\ i-1 & b_i \neq 0 \end{cases} \end{aligned} \quad (4.61)$$

So, from (4.58), one has:

$$f_i(x_i) = a_i\left[\sum_{k=1}^{l_1} \mid x_i m_{ki}^* + n_{ki}x_i^* + c_{ki} \mid^2\right] + b_i\left[\sum_{k=l_2}^{l_3} \mid n_{ki}x_i^* + c_{ki} \mid^2\right]$$

which can be formulated as

$$f_i(x_i) = a_i\left[\sum_{k=1}^{l_1}\left|x_i m_{ki}^* + n_{ki}x_i^* + c_{ki}\right|^2\right] + b_i\left[\sum_{k=l_2}^{l_3}\left|n_{ki} + c_{ki}x_i\right|^2\right] \tag{4.62}$$

Further simplification yields:

$$f_i(x_i) = a_i\left[\sum_{k=1}^{l_1}\left|x_i m_{ki}^* + n_{ki}x_i^* + c_{ki}\right|^2\right] + b_i\left[\sum_{k=l_2}^{l_3} w_{ki}\left|x_i + d_{ki}\right|^2\right] \tag{4.63}$$

where

$$d_{ki} = \frac{n_{ki}}{c_{ki}},\ w_{ki} = |c_{ki}|^2$$

Expanding the square term in (4.63) and by ignoring the constant terms, (4.63) can be obtained as

$$\begin{aligned} f_i(x_i) = \sum_{k=1}^{l_1} a_i\Big[&(n_{ki}^* m_{ki}^*)(x_i^2) + (c_{ki}^* m_{ki}^* + n_{ki}^* c_{ki})(x_i) + (n_{ki}m_{ki})(x_i^2)^* \\ &+ (m_{ki}c_{ki} + c_{ki}^* n_{ki})(x_i)^*\Big] + \sum_{k=l_2}^{l_3} b_i w_{ki}\Big[x_i d_{ki}^* + d_{ki}x_i^*\Big] \end{aligned} \tag{4.64}$$

$$\begin{aligned} f_i(x_i) = \sum_{k=1}^{l_1} a_i\Big[&2\mathrm{Re}\Big((n_{ki}^* m_{ki}^*)(x_i^2)\Big) + 2\mathrm{Re}\Big((c_{ki}^* m_{ki}^* + n_{ki}^* c_{ki})(x_i)\Big)\Big] \\ &+ \sum_{k=l_2}^{l_3}\Big[b_i w_{ki} * 2\mathrm{Re}\Big(x_i d_{ki}^*\Big)\Big] \end{aligned} \tag{4.65}$$

Now by defining the following quantities:

$$\begin{aligned} &n_{ki}^* m_{ki}^* = \hat{a}_{1ki} + j\hat{a}_{2ki} \\ &(c_{ki}^* m_{ki}^* + n_{ki}^* c_{ki}) = \hat{b}_{1ki} + j\hat{b}_{2ki} \\ &d_{ki}^* = \hat{c}_{1ki} + j\hat{c}_{2ki} \\ &x_i = u_1 + ju_2 \end{aligned} \tag{4.66}$$

where $\hat{a}_{1ki}$, $\hat{a}_{2ki}$, $\hat{b}_{1ki}$, $\hat{b}_{2ki}$, $\hat{c}_{1ki}$, $\hat{c}_{2ki}$, u_1, u_2 are real-valued quantities.

Then $f_i(x_i)$ in (4.65) can be further simplified as:

$$\begin{aligned} f_i(u_1,u_2) = &\left[2a_i \sum_{k=1}^{l_1} \hat{a}_{1ki}\right](u_1)^2 - \left[4a_i \sum_{k=1}^{l_1} \hat{a}_{2ki}\right]u_1u_2 + \left[2a_i \sum_{k=1}^{l_1} \hat{b}_{1ki}\right. \\ &\left. + 2b_i \sum_{k=l_2}^{l_3} w_{ki}\hat{c}_{1ki}\right]u_1 - \left[\sum_{k=1}^{l_1} 2a_i\hat{b}_{2ki} + \sum_{k=l_2}^{l_3} 2b_i w_{ki}\hat{c}_{2ki}\right]u_2 \\ &- \left[2a_i \sum_{k=1}^{l_1} \hat{a}_{1ki}\right](u_2)^2 \end{aligned} \tag{4.67}$$

Again introducing,

$$\begin{aligned} a &= 2a_i \sum_{k=1}^{l_1} \hat{a}_{1ki} \\ b &= 4a_i \sum_{k=1}^{l_1} (\hat{a}_{2ki}) \\ c &= 2a_i \sum_{k=1}^{l_1} \hat{b}_{1ki} + 2b_i \sum_{k=l_2}^{l_3} w_{ki}\hat{c}_{1ki} \\ d &= 2a_i \sum_{k=1}^{l_1} \hat{b}_{2ki} + 2b_i \sum_{k=l_2}^{l_3} w_{ki}\hat{c}_{2ki} \end{aligned} \tag{4.68}$$

Then $f_i(u_1,u_2)$ in (4.67) is simplified as:

$$f_i(u_1,u_2) = au_1^2 - bu_1u_2 + cu_1 - du_2 - au_2^2 \tag{4.69}$$

Thus, the problem in (4.57) has become the following problem with real-valued variables.

$$\begin{aligned} \underset{u_1,u_2}{\text{minimize}} \quad & f_i(u_1,u_2) \\ \text{subject to} \quad & u_1^2 + u_2^2 = 1 \end{aligned} \tag{4.70}$$

Now, the problem in (4.70) can be rewritten in the matrix-vector form as:

$$\begin{aligned} \underset{\boldsymbol{v}}{\text{minimize}} \quad & \boldsymbol{v}^T \boldsymbol{A} \boldsymbol{v} + \boldsymbol{e}^T \boldsymbol{v} \\ \text{subject to} \quad & \boldsymbol{v}^T \boldsymbol{v} = 1 \end{aligned} \tag{4.71}$$

with

$$\begin{aligned} \boldsymbol{A} &= \begin{bmatrix} a & \frac{-b}{2} \\ \frac{-b}{2} & -a \end{bmatrix} \\ \boldsymbol{e} &= \begin{bmatrix} c \\ -d \end{bmatrix} \\ \boldsymbol{v} &= \begin{bmatrix} u_1 \\ u_2 \end{bmatrix} \end{aligned} \tag{4.72}$$

The problem in (4.71) has an objective function that is a nonconvex quadratic function in the variable $\boldsymbol{v}$ because of $(-a)$ in the diagonal of $\boldsymbol{A}$ and also the constraint is a quadratic equality constraint, so the problem in (4.71) is a nonconvex problem and hard to solve. So, the FBMM technique employs the MM technique to solve the problem in (4.71).

Now, by using the Lemma 4.1, the quadratic term in the objective function of the problem in (4.71) can be majorized at any feasible point $\boldsymbol{v} = \boldsymbol{v}^t$:

$$u_i(\boldsymbol{v}|\boldsymbol{v}^t) = \boldsymbol{v}^T \boldsymbol{A}_1 \boldsymbol{v} + 2[\boldsymbol{v}^T(\boldsymbol{A} - \boldsymbol{A}_1)\boldsymbol{v}^t] + (\boldsymbol{v}^t)^T(\boldsymbol{A}_1 - \boldsymbol{A})\boldsymbol{v}^t \tag{4.73}$$

where $\boldsymbol{A}_1 = \lambda_{\max}(\boldsymbol{A})\boldsymbol{I}_n$. Since $\lambda_{\max}(\boldsymbol{A})$ is a constant value and $\boldsymbol{v}^T\boldsymbol{v} = 1$, so the first and the last terms in the above surrogate function are constants. Hence, after ignoring the constant terms from (4.73), the surrogate becomes:

$$u_i(\boldsymbol{v}|\boldsymbol{v}^t) = 2[\boldsymbol{v}^T(\boldsymbol{A} - \boldsymbol{A}_1)\boldsymbol{v}^t] \tag{4.74}$$

Now the problem (4.71) is equal to

$$\begin{aligned} \underset{\boldsymbol{v}}{\text{minimize}} \quad & 2[\boldsymbol{v}^T(\boldsymbol{A} - \boldsymbol{A}_1)\boldsymbol{v}^t] + \boldsymbol{e}^T \boldsymbol{v} \\ \text{subject to} \quad & \boldsymbol{v}^T \boldsymbol{v} = 1 \end{aligned} \tag{4.75}$$

which can be formulated further as:

$$\begin{aligned} \underset{\boldsymbol{v}}{\text{minimize}} \quad & u_i(\boldsymbol{v}|\boldsymbol{v}^t) = \| \boldsymbol{v} - \boldsymbol{z} \|_2^2 \\ \text{subject to} \quad & \boldsymbol{v}^T \boldsymbol{v} = 1 \end{aligned} \tag{4.76}$$

where $\boldsymbol{z} = -[(\boldsymbol{A} - \boldsymbol{A}_1)\boldsymbol{v}^t + (\boldsymbol{e}/2)]$.

Now, the problem in (4.76) has a closed-form solution:

$$\boldsymbol{v} = \frac{\boldsymbol{z}}{||\boldsymbol{z}||_2} \tag{4.77}$$

Then the update x_i^{t+1} is given by:

$$x_i^{t+1} = u_1 + ju_2 \tag{4.78}$$

The constants $(c_{1i}, c_{2i}, ..., c_{(N-1)i})$ in (4.59) that are evaluated at every iteration form the bulk of the computations of the FBMM algorithm, and they can be computed via FFT and inverse FFT (IFFT) operations as follows. For example, the constant (c_{1i}) can be interpreted as the autocorrelation of a sequence (with $x_i = 0$), which, in turn, can be calculated by an FFT and IFFT operation. So, to calculate all the constants of N variables, one would require an N number of FFT, and N number of IFFT operations. To avoid implementing FFT and IFFT operations N number of times, a computationally efficient way to calculate the constants was proposed. To achieve this, the algorithm exploits the cyclic pattern in the expression of the constants. First, a variable $\boldsymbol{s}$ was defined that includes original variable $\boldsymbol{x}$ along with some predefined zero-padding structure as shown below:

$$\boldsymbol{s} = [\boldsymbol{0}_{1\times N-2}, \boldsymbol{x}^T, \boldsymbol{0}_{1\times N}]^T \tag{4.79}$$

Then the variables $\boldsymbol{b}_i$ and $\boldsymbol{D}_i$ are defined as:

$$\boldsymbol{b}_i = [-x_i^*, x_{i-1}^*, -x_i, x_{i-1}]^T \tag{4.80}$$

$$\boldsymbol{D}_i = \begin{bmatrix} \boldsymbol{s}_{(N+i-1)} & \cdot & \cdot & \boldsymbol{s}_{(2N+i-4)} & 0 \\ 0 & \boldsymbol{s}_{(N+i-1)} & \cdot & \cdot & \boldsymbol{s}_{(2N+i-4)} \\ 0 & \boldsymbol{s}^*_{(N+i-4)} & \cdot & \cdot & \boldsymbol{s}^*_{(i-1)} \\ \boldsymbol{s}^*_{(N+i-4)} & \cdot & \cdot & \boldsymbol{s}^*_{(i-1)} & 0 \end{bmatrix} \tag{4.81}$$

So, to calculate the i-th variable constants $(c_{1i}, c_{2i}, \ldots, c_{(N-1)i})$, the constants associated with the $(i-1)$-th variable $(c_{1(i-1)}, c_{2(i-1)}, \ldots, c_{(N-1)(i-1)})$ are used as follows:

$$\left[c_{1i}, \ldots, c_{(N-1)i}\right] = \left[c_{1(i-1)}, \ldots, c_{(N-1)(i-1)}\right] + \boldsymbol{b}_i^T \boldsymbol{D}_i, \;\; \forall\, i = 2, \ldots, N \tag{4.82}$$

Algorithm 4.3: The FBMM Algorithm Proposed in [17]

Require: sequence length 'N'
set $t = 0$, initialize $\boldsymbol{x}^0$
repeat
  set $i = 1$
    repeat
      calculate $\{c_{ki}\}_{k=1}^{N-1}$ using (4.82)
      calculate $d_{ki} = \frac{n_{ki}}{c_{ki}}$, $w_{ki} = |c_{ki}|^2$, $k = 1, ..., N-1$.
      $\boldsymbol{A}_1$=$\lambda_{\max}(\boldsymbol{A})\boldsymbol{I}_2$
      $\boldsymbol{z} = -[(\boldsymbol{A} - \boldsymbol{A}_1)\boldsymbol{v}^t + (\boldsymbol{e}/2)]$
      $\boldsymbol{v} = \frac{\boldsymbol{z}}{||\boldsymbol{z}||_2}$
      $x_i^{t+1} = u_1 + ju_2$
      $i \longleftarrow i + 1$
    until length of a sequence
  $t \longleftarrow t + 1$
until convergence

Therefore, all the $(N-1)$ number of constants associated with each of the N variables are implemented using only one FFT and IFFT operation. The steps of the FBMM algorithm is given in Algorithm 4.3.

Computational and Space Complexities

The per iteration computational complexity of the FBMM algorithm is dominated in the calculation of constants $c_{ki}, k = 1, \ldots, N-1, i = 1, \ldots, N$. These constants can be calculated using one FFT and IFFT operation and the approach as mentioned in the end of subsection (FBMM algorithm), where some cyclic pattern in the variable of the algorithm are exploited and the constants are calculated. The per iteration computational complexity of the FBMM algorithm would be $\mathcal{O}(N^2) + \mathcal{O}(2N\, log\, 2N)$. In each iteration of the FBMM algorithm, the space complexity is dominated by the three vectors each of size $(N-1) \times 1$, and one vector of size $N \times 1$; hence, the space complexity will be $\mathcal{O}(N)$.

4.3.1.4 FISL Algorithm

In this subsection, we are going to see the presentation of another MM-based algorithm for sequence design. The algorithms presented until now, namely MISL, ISL-NEW, and FBMM, all exploit only gradient information of the ISL cost function and do not exploit the Hessian information in the development of the algorithm. The FISL (faster integrated side-lobe level minimization) algorithm [18], which will be reviewed in this subsection, uses the Hessian information of the ISL cost function in its development. The ISL minimization problem in (4.21) is usually considered with only the positive lags, but now it is reframed such that the problem of interest consists of both the positive and negative lags along with the zeroth lag (which is always a constant value N due to the unimodular property). So, the problem of interest becomes:

$$\begin{aligned} \underset{\boldsymbol{x}}{\text{minimize}} \quad & f(\boldsymbol{x}) = \sum_{k=-(N-1)}^{N-1} |r(k)|^2 \\ \text{subject to} \quad & |x_n| = 1,\ n = 1, ..., N \end{aligned} \tag{4.83}$$

Let $r(k) = \boldsymbol{x}^H \boldsymbol{W}_k \boldsymbol{x}$, where $\boldsymbol{W}_k$ is a Toeplitz matrix of dimension $N \times N$, with entries given by:

$$[\boldsymbol{W}_k]_{i,j} = \begin{cases} 1 & ; j - i = k \\ 0 & ; else \end{cases} \tag{4.84}$$

i, j denote the row and column indexes of $\boldsymbol{W}_k$, respectively. So, the objective function of a problem in (4.83) can be rewritten as $f(\boldsymbol{x}) = \boldsymbol{x}^H \boldsymbol{R}(\boldsymbol{x}) \boldsymbol{x}$, where

$$\boldsymbol{R}(\boldsymbol{x}) \triangleq \sum_{k=1}^{N-1} r^*(k) \boldsymbol{W}_k + \sum_{k=1}^{N-1} r(k) \boldsymbol{W}_k^H + \text{Diag}(\boldsymbol{r}_c) \tag{4.85}$$

where $\boldsymbol{r}_c = [r(0), r(0), ..., r(0)]^T_{1\times N}$. So,

$$\boldsymbol{R}(\boldsymbol{x}) = \begin{bmatrix} r(0) & r^*(1) & . & . & r^*(N-2) & r^*(N-1) \\ r(1) & r(0) & r^*(1) & . & . & r^*(N-2) \\ . & r(1) & r(0) & r^*(1) & . & . \\ . & . & r(1) & . & . & . \\ r(N-2) & . & . & . & . & r^*(1) \\ r(N-1) & r(N-2) & . & . & r(1) & r(0) \end{bmatrix} \tag{4.86}$$

is a Hermitian Toeplitz matrix and to arrive at the elements of it, one can find the autocorrelation of $\boldsymbol{x}$ using the FFT and IFFT operations as:

$$\boldsymbol{r} = \hat{\boldsymbol{E}} \mid \hat{\boldsymbol{E}}^H \boldsymbol{x} \mid^2 \tag{4.87}$$

Here $\mid . \mid^2$ is an element-wise operation. Then the problem of interest (4.83) becomes:

$$\begin{aligned} \underset{\boldsymbol{x}}{\text{minimize}} \quad & f(\boldsymbol{x}) = \boldsymbol{x}^H \boldsymbol{R}(\boldsymbol{x}) \boldsymbol{x} \\ \text{subject to} \quad & |x_n| = 1,\ n = 1, ..., N \end{aligned} \tag{4.88}$$

According to the Lemma 4.1, by using the second-order Taylor series expansion, at any fixed point $\boldsymbol{x}^t$, the objective function of the problem in (4.88) can be majorized as:

$$\begin{aligned} \boldsymbol{x}^H \boldsymbol{R}(\boldsymbol{x}) \boldsymbol{x} \leq \quad & \Big((\boldsymbol{x}^t)^H \boldsymbol{R}(\boldsymbol{x}^t) \boldsymbol{x}^t + \text{Re}\Big(\big(\nabla f(\boldsymbol{x}^t)\big)^H (\boldsymbol{x} - \boldsymbol{x}^t) \Big) \\ & + \tfrac{1}{2} (\boldsymbol{x} - \boldsymbol{x}^t)^H (\boldsymbol{M}) (\boldsymbol{x} - \boldsymbol{x}^t) \Big) = u(\boldsymbol{x} | \boldsymbol{x}^t) \end{aligned} \tag{4.89}$$

where $\boldsymbol{M} \succeq \nabla^2 f(\boldsymbol{x}^t)$.

So, the construction of majorization function $u(\boldsymbol{x}|\boldsymbol{x}^t)$ requires the gradient and Hessian information of $f(\boldsymbol{x})$ and they can be derived as follows.

We have $f(\boldsymbol{x})$ as:

$$f(\boldsymbol{x}) = \sum_{k=-(N-1)}^{N-1} |r(k)|^2 = \sum_{k=-(N-1)}^{N-1} |\boldsymbol{x}^H \boldsymbol{W}_k \boldsymbol{x}|^2 \tag{4.90}$$

Now the gradient of $f(\boldsymbol{x})$ is given by:

$$\begin{aligned}\nabla f(\boldsymbol{x}) &= \sum_{k=-(N-1)}^{N-1} \begin{bmatrix} \frac{\partial}{\partial x_1}|\boldsymbol{x}^H \boldsymbol{W}_k \boldsymbol{x}|^2 \\ \cdot \\ \cdot \\ \frac{\partial}{\partial x_N}|\boldsymbol{x}^H \boldsymbol{W}_k \boldsymbol{x}|^2 \end{bmatrix} \\ &= 2 \sum_{k=-(N-1)}^{N-1} \boldsymbol{x}^H \boldsymbol{W}_k \boldsymbol{x} \left[\boldsymbol{W}_k + \boldsymbol{W}_k^H\right] \boldsymbol{x} \\ &= 2 \sum_{k=1}^{N-1} \left[\left(\boldsymbol{x}^H \boldsymbol{W}_k \boldsymbol{x}\right) \boldsymbol{W}_k \boldsymbol{x} + \left(\boldsymbol{x}^H \boldsymbol{W}_k \boldsymbol{x}\right) \boldsymbol{W}_k^H \boldsymbol{x}\right] \\ &\quad + 2 \sum_{k=-(N-1)}^{-1} \left[\left(\boldsymbol{x}^H \boldsymbol{W}_k \boldsymbol{x}\right) \boldsymbol{W}_k \boldsymbol{x} + \left(\boldsymbol{x}^H \boldsymbol{W}_k \boldsymbol{x}\right) \boldsymbol{W}_k^H \boldsymbol{x}\right] \\ &\quad + 4 \left(\boldsymbol{x}^H \boldsymbol{W}_0 \boldsymbol{x}\right) \boldsymbol{x}\end{aligned} \tag{4.91}$$

It is known that $r(k) = \boldsymbol{x}^H \boldsymbol{W}_k \boldsymbol{x}$, so

$$\begin{aligned}\nabla f(\boldsymbol{x}) &= 2 \sum_{k=1}^{N-1} \left[r(k) \boldsymbol{W}_k \boldsymbol{x} + r(k) \boldsymbol{W}_k^H \boldsymbol{x}\right] \\ &\quad + 2 \sum_{k=-(N-1)}^{-1} \left[r(k) \boldsymbol{W}_k \boldsymbol{x} + r(k) \boldsymbol{W}_k^H \boldsymbol{x}\right] + 4 r(0) \boldsymbol{x}\end{aligned} \tag{4.92}$$

By using the relations $r^*(k) = r(-k)$ and $\boldsymbol{W}_{-k} = \boldsymbol{W}_k^H$ and substituting them in (4.92), one can conclude that:

$$\begin{aligned}\nabla f(\boldsymbol{x}) &= 2 \sum_{k=1}^{N-1} \left[r(k) \boldsymbol{W}_k \boldsymbol{x} + r(k) \boldsymbol{W}_k^H \boldsymbol{x}\right] \\ &\quad + 2 \sum_{k=1}^{N-1} \left[r^*(k) \boldsymbol{W}_k^H \boldsymbol{x} + r^*(k) \boldsymbol{W}_k \boldsymbol{x}\right] + 4 r(0) \boldsymbol{x} \\ &= 2 \sum_{k=1}^{N-1} \left[r(k) \boldsymbol{W}_k \boldsymbol{x} + r^*(k) \boldsymbol{W}_k^H \boldsymbol{x}\right] \\ &\quad + 2 \sum_{k=1}^{N-1} \left[r(k) \boldsymbol{W}_k^H \boldsymbol{x} + r^*(k) \boldsymbol{W}_k \boldsymbol{x}\right] + 4 r(0) \boldsymbol{x}\end{aligned} \tag{4.93}$$

$$\nabla f(\boldsymbol{x}) = 2\left[\boldsymbol{R}^*(\boldsymbol{x}) + \boldsymbol{R}(\boldsymbol{x})\right]\boldsymbol{x} \tag{4.94}$$

Since $\boldsymbol{R}^*(\boldsymbol{x}) = \boldsymbol{R}(\boldsymbol{x})$,

$$\nabla f(\boldsymbol{x}) = 4\boldsymbol{R}(\boldsymbol{x})\boldsymbol{x} \tag{4.95}$$

Now the Hessian of $f(\boldsymbol{x})$ is given by:

$$\nabla^2 f(\boldsymbol{x}) = \nabla\left(4\boldsymbol{R}(\boldsymbol{x})\boldsymbol{x}\right) \tag{4.96}$$

By using $\boldsymbol{R}(\boldsymbol{x}) = \sum_{k=-(N-1)}^{N-1}\left[\boldsymbol{x}^H\boldsymbol{W}_k\boldsymbol{x}\right]\boldsymbol{W}_k$, the Hessian can be given as:

$$\begin{aligned}\nabla^2 f(\boldsymbol{x}) &= 4\sum_{k=-(N-1)}^{N-1}\left[\boldsymbol{W}_k + \boldsymbol{W}_k^H\right]\boldsymbol{x}^H\boldsymbol{W}_k\boldsymbol{x} \\ &= 4\sum_{k=-(N-1)}^{N-1}\left[\boldsymbol{W}_k\boldsymbol{x}^H\boldsymbol{W}_k\boldsymbol{x} + \boldsymbol{W}_k^H\boldsymbol{x}^H\boldsymbol{W}_k\boldsymbol{x}\right] \\ &= 4\left[\boldsymbol{R}(\boldsymbol{x}) + \boldsymbol{R}^*(\boldsymbol{x})\right]\end{aligned} \tag{4.97}$$

Thus,

$$\nabla^2 f(\boldsymbol{x}) = 8\boldsymbol{R}(\boldsymbol{x}) \tag{4.98}$$

There is more than one way to construct the matrix $\boldsymbol{M}$, such that (4.89) will always hold and some simple straightforward ways would be to choose:

$$\boldsymbol{M} = \mathrm{Tr}(8\boldsymbol{R}(\boldsymbol{x}^t))\boldsymbol{I}_N = 8N^2\boldsymbol{I}_N \tag{4.99}$$

or

$$\boldsymbol{M} = \lambda_{\max}(8\boldsymbol{R}(\boldsymbol{x}^t))\boldsymbol{I}_N \tag{4.100}$$

But in practice, for large dimension sequences, calculating the maximum eigenvalue is a computationally demanding procedure. So, in the original FISL paper [18], the authors try and employed various tighter upper bounds on maximum eigenvalue of the Hessian matrix, some of the ideas are listed below.

Theorem 4.4. *[Theorem 2.1 [24]]: Let $\boldsymbol{A}$ be an $N \times N$ Hermitian matrix with complex entries having real eigenvalues and let*

$$m = \frac{1}{N}Tr(\boldsymbol{A}), \quad s^2 = \left(\frac{1}{N}Tr(\boldsymbol{A}^2)\right) - m^2 \tag{4.101}$$

Then

$$m - s(N-1)^{1/2} \leq \lambda_{min}(\boldsymbol{A}) \leq m - \frac{s}{(N-1)^{1/2}} \tag{4.102}$$

$$m + \frac{s}{(N-1)^{1/2}} \leq \lambda_{max}(\boldsymbol{A}) \leq m + s(N-1)^{1/2} \tag{4.103}$$

So, by using the result from Theorem 4.4 one can find an upper bound on the maximum eigenvalue of $8\boldsymbol{R}(\boldsymbol{x}^t)$ and form $\boldsymbol{M}$ as:

$$\boldsymbol{M} = (m + s(N-1)^{1/2})\boldsymbol{I}_N \tag{4.104}$$

where $m = \frac{8}{N}\text{Tr}(\boldsymbol{R}(\boldsymbol{x}^t))$, $s^2 = (\frac{64}{N}\text{Tr}(\boldsymbol{R}(\boldsymbol{x}^t)^2)) - m^2$. Here on, the three approaches of obtaining $\boldsymbol{M}$ are named as TR (using TRace), EI (using EIgenvalue), and BEI (using Bound on the EIgenvalue). In the following an another approach to arrive at $\boldsymbol{M}$ was explored.

Lemma 4.5. *[Lemma 3 and Lemma 4 [25]]: Let $\boldsymbol{A}$ be an $N \times N$ Hermitian Toeplitz matrix defined as follows:*

$$\boldsymbol{A} = \begin{bmatrix} a(0) & a^*(1) & . & . & a^*(N-2) & a^*(N-1) \\ a(1) & a(0) & a^*(1) & . & . & a^*(N-2) \\ . & a(1) & a(0) & a^*(1) & . & . \\ . & . & a(1) & . & . & . \\ a(N-2) & . & . & . & . & a^*(1) \\ a(N-1) & a(N-2) & . & . & a(1) & a(0) \end{bmatrix}$$

Let $\boldsymbol{d} = [a_0, a_1, ..., a_{N-1}, 0, a_{N-1}^*, ..., a_1^*]^T$ and $\boldsymbol{s} = \hat{\boldsymbol{E}}^H \boldsymbol{d}$ be the discrete Fourier transform of $\boldsymbol{d}$.

(a) Then the maximum eigenvalue of the Hermitian Toeplitz matrix $\boldsymbol{A}$ can be bounded as

$$\lambda_{max}(\boldsymbol{A}) \leq \frac{1}{2}\left(\max_{1 \leq i \leq N} \boldsymbol{s}_{2i} + \max_{1 \leq i \leq N} \boldsymbol{s}_{2i-1} \right) \tag{4.105}$$

(b) The Hermitian Toeplitz matrix $\boldsymbol{A}$ can be decomposed as

$$\boldsymbol{A} = \frac{1}{2N} \hat{\boldsymbol{E}}_{:,1:N} Diag(\boldsymbol{s}) \hat{\boldsymbol{E}}_{:,1:N}^H \tag{4.106}$$

Proof: The proof can be found in [25]. ■

Using Lemma 4.5, one can also find the bound on the maximum eigenvalue of a Hermitian Toeplitz matrix $8\boldsymbol{R}(\boldsymbol{x}^t)$ using FFT and IFFT operations as:

$$\boldsymbol{M} = 4\left(\max_{1\leq i\leq N} \boldsymbol{s}_{2i} + \max_{1\leq i\leq N} \boldsymbol{s}_{2i-1}\right)\boldsymbol{I}_N. \tag{4.107}$$

where $\boldsymbol{d} = [r(0), r(1), .., r(N-1), 0, r(N-1)^*, .., r(1)^*]^T$ and $\boldsymbol{s} = \hat{\boldsymbol{E}}^H\boldsymbol{d}$. This approach is named as BEFFT (bound on eigenvalue using FFT).

So, from (4.89) the upper bound (majorization) function of the original objective function $f(\boldsymbol{x})$ at any fixed point $\boldsymbol{x}^t$ can be given as:

$$\begin{aligned} u(\boldsymbol{x}|\boldsymbol{x}^t) = \boldsymbol{x}^H(0.5\boldsymbol{M})\boldsymbol{x} + 4\text{Re}((\boldsymbol{x}^t)^H(\boldsymbol{R}(\boldsymbol{x}^t) - 0.25\boldsymbol{M})\boldsymbol{x}) \\ + (\boldsymbol{x}^t)^H(0.5\boldsymbol{M} - 3\boldsymbol{R}(\boldsymbol{x}^t))\boldsymbol{x}^t \end{aligned} \tag{4.108}$$

As the $\boldsymbol{M}$ (obtained by all four approaches described above) is a constant times a diagonal matrix, and since $\boldsymbol{x}^H\boldsymbol{x}$ is a constant, the first and last terms in the (4.108) are constants. So, after ignoring the constant terms, the surrogate minimization problem can be rewritten as:

$$\begin{aligned} \underset{\boldsymbol{x}}{\text{minimize}} \quad & u(\boldsymbol{x}|\boldsymbol{x}^t) = 4\text{Re}((\boldsymbol{x}^t)^H(\boldsymbol{R}(\boldsymbol{x}^t) - 0.25\boldsymbol{M})\boldsymbol{x}) \\ \text{subject to} \quad & |x_n| = 1,\ n = 1, ..., N \end{aligned} \tag{4.109}$$

The problem in (4.109) can be rewritten more compactly as:

$$\begin{aligned} \underset{\boldsymbol{x}}{\text{minimize}} \quad & u(\boldsymbol{x}|\boldsymbol{x}^t) = ||\boldsymbol{x} - \tilde{\boldsymbol{a}}||_2^2 \\ \text{subject to} \quad & |x_n| = 1,\ n = 1, ..., N \end{aligned} \tag{4.110}$$

where $\tilde{\boldsymbol{a}} = -(\boldsymbol{R}(\boldsymbol{x}^t) - 0.25\boldsymbol{M})\boldsymbol{x}^t$, which involves computing Hermitian Toeplitz matrix-vector multiplication. The matrix vector product $\boldsymbol{R}(\boldsymbol{x}^t)\boldsymbol{x}^t$ can be implemented via the FFT and IFFT operations as follows. By using the Fourier decomposition given in Lemma 4.5, the Toeplitz matrix can be expressed as $\boldsymbol{R}(\boldsymbol{x}^t) = \boldsymbol{E}\boldsymbol{D}\boldsymbol{E}^H$, where $\boldsymbol{E}$ is a partial Fourier matrix of dimension $N \times 2N$ and $\boldsymbol{D}$ is a diagonal matrix obtained by taking FFT of $\left[r(k)\right]_{k=-(N-1)}^{N-1}$. Thus, $\boldsymbol{R}(\boldsymbol{x}^t)\boldsymbol{x}^t$ can be implemented via the FFT and IFFT operations.

Algorithm 4.4: The FISL Algorithm Proposed in [18]

Require: sequence length 'N'
1:set $t = 0$, initialize $\boldsymbol{x}^0$
2: **repeat**
3: compute $\boldsymbol{R}(\boldsymbol{x}^t)$ using (4.86)
4: compute $\boldsymbol{M}$ using (4.107)
5: $\tilde{\boldsymbol{a}} = -(\boldsymbol{R}(\boldsymbol{x}^t) - 0.25\boldsymbol{M})\boldsymbol{x}^t$
6: $\boldsymbol{x}^{t+1} = \frac{\tilde{\boldsymbol{a}}_{1:N}}{|\tilde{\boldsymbol{a}}_{1:N}|}$
7: $t \longleftarrow t + 1$
8: **until** convergence

The problem in (4.110) has a closed-form solution of

$$\boldsymbol{x}^{t+1} = \frac{\tilde{\boldsymbol{a}}_{1:N}}{|\tilde{\boldsymbol{a}}_{1:N}|} \tag{4.111}$$

Here $\frac{\tilde{\boldsymbol{a}}_{1:N}}{|\tilde{\boldsymbol{a}}_{1:N}|}$ is the element-wise operation and the pseudo code of the FISL algorithm is given in the Algorithm 4.4.

Computational and Space Complexities

The per iteration computational complexity of the FISL algorithm is dominated by the calculation of Hermitian Toeplitz matrix $\boldsymbol{R}(\boldsymbol{x}^t)$, Diagonal matrix $\boldsymbol{M}$ and Hermitian Toeplitz matrix-vector multiplication to form $\tilde{\boldsymbol{a}}$. Using Lemma 4.5, all the operations can be replaced by FFT and IFFT operations, so to implement the FISL algorithm, one requires only 3-FFT and 2-IFFT operations, and the computational complexity would be $\mathcal{O}(2N\, log\, 2N)$. In each iteration of the FISL algorithm, the space complexity is dominated by the three different vectors of sizes $N \times 1$, $(2N-1) \times 1$, $2N \times 1$, respectively, and the space complexity would be $\mathcal{O}(N)$.

4.3.1.5 UNIPOL Algorithm

The algorithms discussed so far employs MM technique to construct surrogate for the ISL function. All the algorithms discussed until now constructs either first-order or second-order surrogate functions. However, the ISL cost

function is quartic in nature (in the design variable $\boldsymbol{x}$). In this subsection, we will review an algorithm named UNIPOL (UNImodular sequence design via a separable iterative POLynomial optimization), which is also based on MM framework but preserves the quartic nature in the surrogate function involved.

The cost function in the ISL minimization problem in (4.21) is expressed in terms of the autocorrelation values; by re-expressing it in the frequency domain (using the Parsevals theorem), the following equivalent form (a short proof of the same can be found in the appendix of [26]) is arrived:

$$\sum_{k=1}^{N-1} \left|r(k)\right|^2 = \frac{1}{4N} \sum_{a=1}^{2N} \left| \left| \sum_{n=1}^{N} x_n e^{-j\omega_a n} \right|^2 - N \right|^2 \tag{4.112}$$

where $\omega_a = \frac{2\pi}{2N} a$, $a = 1, .., 2N$.

By expanding the square in the equivalent objective function and using the fact that the energy of the signal is constant (i.e., $\sum\limits_{a=1}^{2N} \left| \sum\limits_{n=1}^{N} x_n e^{-j\omega_a n} \right|^2 = 2N^2$), the ISL minimization problem can be expressed as:

$$\underset{|x_n|=1,\, \forall n}{\text{minimum}} \quad \sum_{a=1}^{2N} \left| \sum_{n=1}^{N} x_n e^{-j\omega_a n} \right|^4 \tag{4.113}$$

Now using Jensen's inequality (see example 11 in [13]), at any given x_n^t, the cost function in the above problem can be majorized (or) upper-bounded as follows:

$$\sum_{a=1}^{2N} \left| \sum_{n=1}^{N} x_n e^{-j\omega_a n} \right|^4 \leq \sum_{a=1}^{2N} \sum_{n=1}^{N} \frac{1}{N} \left| N\left(x_n - x_n^t\right) e^{-j\omega_a n} + \sum_{n'=1}^{N} x_{n'}^t e^{-j\omega_a n'} \right|^4 \tag{4.114}$$

The above inequality is due to Jensen's inequality, more details of which can be found in the tutorial paper example 11 in [13]. One can observe that both the upper bound and the ISL function are quartic in nature. Hence, it confirms that, by using Jensen's inequality UNIPOL is able to construct a quartic majorization function to the original quartic objective function. After

pulling out the factor N and the complex exponential in the first and second terms the following equivalent upper bound function is obtained:

$$u(x_n|x_n^t) = \sum_{a=1}^{2N}\sum_{n=1}^{N}\left| x_n - x_n^t + \frac{1}{N}\sum_{n'=1}^{N} x_{n'}^t e^{-j\omega_a\left(n'-n\right)}\right|^4 \tag{4.115}$$

It's worth pointing out that the above majorization function is separable in x_n and a generic function (independent of n) will be given by:

$$u(x|x^t) = \sum_{a=1}^{2N}\left| x - x^t + \frac{1}{N}\sum_{n'=1}^{N} x_{n'}^t e^{-j\omega_a\left(n'-q\right)}\right|^4 \tag{4.116}$$

where q denotes the corresponding variable index of x. The majorization function in (4.116) can be rewritten more compactly as:

$$u(x|x^t) = \sum_{a=1}^{2N}|x-\alpha_a|^4 \tag{4.117}$$

where $\alpha_a = x^t - \frac{1}{N}\sum\limits_{n'=1}^{N} x_{n'}^t e^{-j\omega_a\left(n'-q\right)}$. So, any individual minimization problem would be as follows:

$$\min_{|x|=1}\ \sum_{a=1}^{2N}|x-\alpha_a|^4 \tag{4.118}$$

where α_a is a complex variable with $|\alpha_a| \neq 1$. The cost function in problem (4.118) can be rewritten furtherly as:

$$\begin{aligned}\sum_{a=1}^{2N}|x-\alpha_a|^4 &= \sum_{a=1}^{2N}\left(|x-\alpha_a|^2\right)^2 = \sum_{a=1}^{2N}\left(1-2\mathrm{Re}\left(\alpha_a^* x\right)+|\alpha_a|^2\right)^2 \\ &= \sum_{a=1}^{2N}\left(4\left(\mathrm{Re}\left(\alpha_a^* x\right)\right)^2 - 4\mathrm{Re}\left(\alpha_a^* x\right)\left(1+|\alpha_a|^2\right)+\mathrm{const}\right)\end{aligned} \tag{4.119}$$

By neglecting the constant terms, (4.119) simplifies as:

$$\begin{aligned}&\sum_{a=1}^{2N}\left(\left(\alpha_a^* x+x^*\alpha_a\right)^2-4\mathrm{Re}\left(\alpha_a^* x\right)\left(1+|\alpha_a|^2\right)\right)\\&=\sum_{a=1}^{2N}\left(\left[\left(\alpha_a^*\right)^2 x^2+\left(x^*\right)^2\alpha_a^2\right]-4\mathrm{Re}\left(\alpha_a^* x\right)\left(1+|\alpha_a|^2\right)+\text{const}\right)\end{aligned} \tag{4.120}$$

By neglecting the constant terms, (4.120) can be rewritten as:

$$\sum_{a=1}^{2N}\left(2\mathrm{Re}\left(\left(\alpha_a^*\right)^2 x^2\right)-4\mathrm{Re}\left(\alpha_a^* x\right)\left(1+|\alpha_a|^2\right)\right)=\mathrm{Re}\left(\hat{a}x^2\right)-\mathrm{Re}\left(\hat{b}x\right) \tag{4.121}$$

where $\hat{a}=\sum_{a=1}^{2N}2\left(\alpha_a^*\right)^2$ and $\hat{b}=\sum_{a=1}^{2N}4\alpha_a^*\left(1+|\alpha_a|^2\right)$. So the minimization problem would be:

$$\min_{|x|=1}\ \mathrm{Re}\left(\hat{a}x^2-\hat{b}x\right) \tag{4.122}$$

Although the above problem looks like a simple univariable optimization problem, it does not have any closed-form solution. So, to compute its minimizer, the constraint $|x|=1$ is expressed as $x=e^{j\theta}$ and then the first-order KKT condition of the above problem is given as:

$$\frac{d}{d\theta}(\mathrm{Re}\left(\hat{a}e^{2j\theta}-\hat{b}e^{j\theta}\right))=\mathrm{Re}\left(2\hat{a}je^{2j\theta}-j\hat{b}e^{j\theta}\right)=0 \tag{4.123}$$

By defining $2j\hat{a}=-2a_I+j2a_R$ and $j\hat{b}=-b_I+jb_R$, where a_R,b_R,a_I,b_I are the real and imaginary parts of $\hat{a}$ and $\hat{b}$, respectively, the KKT condition becomes:

$$2a_I\cos\left(2\theta\right)+2a_R\sin\left(2\theta\right)-b_I\cos\left(\theta\right)-b_R\sin\left(\theta\right)=0 \tag{4.124}$$

let $\beta=tan\left(\frac{\theta}{2}\right)$, and $sin\left(\theta\right)=\frac{2\beta}{1+\beta^2}$, $cos\left(\theta\right)=\frac{1-\beta^2}{1+\beta^2}$, $sin\left(2\theta\right)=\frac{4\beta\left(1-\beta^2\right)}{\left(1+\beta^2\right)^2}$, $cos\left(2\theta\right)=\frac{1+\beta^4-6\beta^2}{\left(1+\beta^2\right)^2}$, then the KKT condition can be rewritten as:

$$\frac{2a_I\left(1+\beta^4-6\beta^2\right)}{\left(1+\beta^2\right)^2}+\frac{2a_R\left(4\beta\left(1-\beta^2\right)\right)}{\left(1+\beta^2\right)^2}-\frac{b_I\left(1-\beta^2\right)}{1+\beta^2}-\frac{b_R 2\beta}{1+\beta^2}=0 \tag{4.125}$$

$$\frac{2a_I(1+\beta^4) - 12a_I\beta^2 + 8a_R(\beta-\beta^3) - b_I(1-\beta^4) - 2b_R(\beta+\beta^3)}{(1+\beta^2)^2} = 0 \tag{4.126}$$

which can be rewritten as:

$$\frac{p_4\beta^4 + p_3\beta^3 + p_2\beta^2 + p_1\beta + p_0}{(1+\beta^2)^2} = 0 \tag{4.127}$$

with

$$\begin{aligned} &p_4 = 2a_I + b_I,\ p_3 = -8a_R - 2b_R \\ &p_2 = -12a_I,\ p_1 = 8a_R - 2b_R,\ p_0 = 2a_I - b_I \end{aligned} \tag{4.128}$$

since $(1+\beta^2) \neq 0$, (4.127) is equivalent to:

$$p_4\beta^4 + p_3\beta^3 + p_2\beta^2 + p_1\beta + p_0 = 0 \tag{4.129}$$

which is a quartic polynomial. So, the roots of this quartic polynomial are calculated and the root that gives the least value of objective in (4.122) is chosen as the minimizer of surrogate minimization problem. The pseudo-code of the UNIPOL algorithm is given in Algorithm 4.5.

Algorithm 4.5: The UNIPOL Algorithm Proposed in [19]

Require: sequence length 'N'
1:set $t = 0$, initialize $\boldsymbol{x}^0$
2: **repeat**
3: set $n = 1$
4: **repeat**
5: compute α_a, $\forall a$.
6: compute $\hat{a}, \hat{b}$.
7: compute p_0, p_1, p_2, p_3, p_4 using (4.128).
8: compute optimal β_n by solving the KKT condition.
9: $n \longleftarrow n+1$
10: **until** $n = N$
11: $x_n^{t+1} = e^{j2\arctan(\beta_n)}$, $\forall n$.
12: $t \longleftarrow t+1$
13: **until** convergence

Some remarks on the UNIPOL algorithm are given next:

- The major chunk of the computational complexity comes from the calculation of α_p's, which can be done easily via the FFT operations (that is the second term in α_p can be written as $\frac{1}{N}\sum_{n'=1}^{N} x_{n'}^{t} e^{-j\omega_p n'} e^{j\omega_p q}$ where $\sum_{n'=1}^{N} x_{n'}^{t} e^{-j\omega_p n'}$ is FFT of $\boldsymbol{x}$). Hence, the computational complexity is $\mathcal{O}\left(2N\, log 2N\right)$ and the space complexity is $\mathcal{O}\left(N\right)$.
- It is worth pointing out that the original ISL objective function is quartic in x_n and the upper bounds employed by the methods like MISL, ISL-NEW, and FBMM are linear in x_n, FISL is quadratic in x_n, on the other hand, the surrogate function derived in UNIPOL algorithm (see (4.118)) is quartic in x_n . Thus, the proposed surrogate function would be a tighter upper bound for the ISL function than the surrogates of MISL, ISL-NEW, FBMM, and FISL algorithms. As the convergence of MM algorithms will depend mostly on the tightness of surrogate function, it is expected that the convergence of UNIPOL algorithm would be much better than rest of the ISL minimizers. Indeed, we will show in Section 4.4 that UNIPOL algorithm is faster than the MISL, ISL-NEW, FBMM, and FISL algorithms.

4.3.2 PSL Minimizers

Earlier we discussed different ISL minimization techniques (ISL minimizers), but here we will discuss the different MM-based PSL minimization techniques (PSL minimizers), namely, the MM-PSL [25] and SLOPE [27].

4.3.2.1 MM-PSL Algorithm

To obtain uniform sidelobe levels, the MM-PSL algorithm [25] solves the general l_p norm minimization problem, which is given as:

$$\begin{aligned} \underset{\boldsymbol{x}}{\text{minimize}} \quad & \left[\sum_{k=1}^{N-1} |r(k)|^p\right]^{\frac{1}{p}} \\ \text{subject to} \quad & |x_n| = 1,\ n = 1, ..., N \end{aligned} \tag{4.130}$$

where $2 \leq p < \infty$. An equivalent reformulation of (4.130) is:

$$\begin{aligned} \underset{\boldsymbol{x}}{\text{minimize}} \quad & \sum_{k=1}^{N-1} |r(k)|^p \\ \text{subject to} \quad & |x_n| = 1,\ n = 1, ..., N \end{aligned} \tag{4.131}$$

Since the MISL and ISL-NEW algorithms addressed the l_2 norm squared minimization problem, they are able to construct a global quadratic majorization function. But here when $p > 2$, it is impossible to construct a global majorization function. So, MM-PSL method approaches the problem by constructing the local majorization function using the following lemma.

Lemma 4.6. *Let $f(x) = x^p$ with $p \geq 2$ and $x \epsilon [0, q]$. Then for any given $x^0 \epsilon [0, q)$, $f(x)$ is majorized at x^0 over the interval $[0, q]$ by the following quadratic function*

$$cx^2 + \left(p\left(x^0\right)^{p-1} - 2cx^0\right)x + c\left(x^0\right)^2 - (p-1)\left(x^0\right)^p \tag{4.132}$$

where $c = \frac{q^p - \left(x^0\right)^p - p\left(x^0\right)^{p-1}\left(q - x^0\right)}{\left(q - x^0\right)^2}$.

Proof: The proof can be found in [25]. ■

So, by using Lemma 4.6, a local majorization function for $|r(k)|^p$ over $[0, q]$ can be obtained as shown below:

$$c_k \left|r(k)\right|^2 + d_k \left|r(k)\right| + c_k \left|\left(r(k)\right)^t\right|^2 - (p-1)\left|\left(r(k)\right)^t\right|^p \tag{4.133}$$

where

$$c_k = \frac{q^p - \left|\left(r(k)\right)^t\right|^p - p\left|\left(r(k)\right)^t\right|^{p-1}\left(q - \left|\left(r(k)\right)^t\right|\right)}{\left(q - \left|\left(r(k)\right)^t\right|\right)^2} \tag{4.134}$$

$$d_k = p\left|\left(r(k)\right)^t\right|^{p-1} - 2c_k\left|\left(r(k)\right)^t\right| \tag{4.135}$$

Here the interval q for (4.134) is selected based on the current sequence estimate. From (4.13), we have $f(\boldsymbol{x}^{t+1}) \leq f(\boldsymbol{x}^t)$, which ensures that at every iteration the cost function value will decrease. Hence, it is sufficient

to majorize $|r(k)|^p$ over the set on which the cost function value is smaller, that is, $\sum_{k=1}^{N-1}\left|\left(r(k)\right)\right|^p \leq \sum_{k=1}^{N-1}\left|\left(r(k)\right)^t\right|^p$, so the q has been chosen as $q=\left[\sum_{k=1}^{N-1}\left|\left(r(k)\right)^t\right|^p\right]^{\frac{1}{p}}$.

The third and fourth terms in the above constructed majorization function (4.133) are constants. Hence, by ignoring the constants, the surrogate minimization problem can be written as:

$$\begin{aligned} \underset{\boldsymbol{x}}{\text{minimize}} \quad & \sum_{k=1}^{N-1}\left(c_k\left|r(k)\right|^2+d_k\left|r(k)\right|\right) \\ \text{subject to} \quad & |x_n|=1,\ n=1,...,N \end{aligned} \tag{4.136}$$

The cost function in the problem in (4.136) consists of two different terms $c_k\left|r(k)\right|^2$ and $d_k\left|r(k)\right|$, and in the following they will be tackled independently.

The first term $\sum_{k=1}^{N-1} c_k\left|r(k)\right|^2$ (which looks like the weighted ISL function, so following the MISL derivation) can be rewritten as:

$$\sum_{k=1}^{N-1} c_k|r(k)|^2=\text{vec}\left(\boldsymbol{X}\right)^H\tilde{\boldsymbol{\Phi}}\text{vec}\left(\boldsymbol{X}\right) \tag{4.137}$$

where $\boldsymbol{X}=\boldsymbol{x}\boldsymbol{x}^H$, $\tilde{\boldsymbol{\Phi}}=\sum_{k=1-N}^{N-1} c_k\text{vec}(\boldsymbol{U}_k)\text{vec}(\boldsymbol{U}_k)^H$, $\boldsymbol{U}_k$ is the $N\times N$ Toeplitz matrix with the kth diagonal elements as 1 and 0 else.

Equation (4.137) is quadratic in $\text{vec}\left(\boldsymbol{X}\right)$, so it can be majorized by using Lemma 4.1:

$$\begin{aligned} \text{vec}\left(\boldsymbol{X}\right)^H\tilde{\boldsymbol{\Phi}}\text{vec}\left(\boldsymbol{X}\right) \leq \text{vec}\left(\boldsymbol{X}\right)^H\boldsymbol{M}\text{vec}\left(\boldsymbol{X}\right)+2\text{Re}\Big(\text{vec}\left(\boldsymbol{X}\right)^H\left(\tilde{\boldsymbol{\Phi}}-\boldsymbol{M}\right) \\ \text{vec}\left(\boldsymbol{X}^t\right)\Big)+\text{vec}\left(\boldsymbol{X}^t\right)^H\left(\boldsymbol{M}-\tilde{\boldsymbol{\Phi}}\right)\text{vec}\left(\boldsymbol{X}^t\right) \end{aligned} \tag{4.138}$$

where $\boldsymbol{M}=\lambda_{\max}\left(\tilde{\boldsymbol{\Phi}}\right)\boldsymbol{I}$.

The first and the last terms in the above surrogate function are constants. So, by neglecting them, the surrogate looks like:

$$2\text{Re}\left(\text{vec}\left(\boldsymbol{X}\right)^H\left(\tilde{\boldsymbol{\Phi}}-\boldsymbol{M}\right)\text{vec}\left(\boldsymbol{X}^t\right)\right) \tag{4.139}$$

which can also be rewritten in terms of $\boldsymbol{x}$ as:

$$\boldsymbol{x}^H\left(\boldsymbol{A}-\lambda_{\max}\left(\tilde{\boldsymbol{\Phi}}\right)\boldsymbol{x}^t\left(\boldsymbol{x}^t\right)^H\right)\boldsymbol{x} \tag{4.140}$$

where $\boldsymbol{A}=\sum\limits_{k=1-N}^{N-1}c_k\left(r(-k)\right)^t\boldsymbol{U}_k$ and $\left(r(-k)\right)^t=\text{Tr}\left(\boldsymbol{U}_{-k}\boldsymbol{X}^t\right)$.

The second term in the cost function of the problem in (4.136) is $\sum_{k=1}^{N-1}d_k|r(k)|$, and it can be majorized (using Cauchy-Schwartz inequality) as:

$$\begin{aligned}\sum_{k=1}^{N-1}d_k|r(k)| &\leq \sum_{k=1}^{N-1}d_k\text{Re}\left\{\left(r(k)\right)^*\frac{\left(r(k)\right)^t}{\left|\left(r(k)\right)^t\right|}\right\}\\ &=\sum_{k=1}^{N-1}d_k\text{Re}\left\{\text{Tr}\left(\boldsymbol{U}_{-k}\boldsymbol{x}\boldsymbol{x}^H\right)\frac{\left(r(k)\right)^t}{\left|\left(r(k)\right)^t\right|}\right\}\\ &=\frac{1}{2}\boldsymbol{x}^H\left(\sum_{k=1-N}^{N-1}d_k\frac{\left(r(k)\right)^t}{\left|\left(r(k)\right)^t\right|}\boldsymbol{U}_{-k}\right)\boldsymbol{x}\end{aligned} \tag{4.141}$$

where $d_{-k}=d_k,\ k=1,..,N-1$, and $d_0=0$.

Now, by using (4.140) and (4.141), the problem in (4.136) can be rewritten more compactly as:

$$\begin{aligned}\underset{\boldsymbol{x}}{\text{minimize}}\quad & \boldsymbol{x}^H\left(\tilde{\boldsymbol{A}}-\lambda_{\max}(\tilde{\boldsymbol{\Phi}})\boldsymbol{x}^t\left(\boldsymbol{x}^t\right)^H\right)\boldsymbol{x}\\ \text{subject to}\quad & |x_n|=1,\ n=1,...,N\end{aligned} \tag{4.142}$$

where $\tilde{\boldsymbol{A}}=\sum_{k=1-N}^{N-1}w_k\left(r(-k)\right)^t\boldsymbol{U}_k$ and $w_k=w_{-k}=c_k+\frac{d_k}{2\left|\left(r(k)\right)^t\right|}=\frac{p}{2}\left|\left(r(k)\right)^t\right|^{p-2}$.

The cost function in the problem in (4.142) is quadratic in $\boldsymbol{x}$, so by majorizing it again using the lemma (4.1) and by ignoring the constant terms, the final surrogate minimization problem is given by:

$$\begin{aligned} \underset{\boldsymbol{x}}{\text{minimize}} \quad & \| \boldsymbol{x} - \boldsymbol{s} \|_2^2 \\ \text{subject to} \quad & |x_n| = 1,\ n = 1, ..., N \end{aligned} \tag{4.143}$$

where $\boldsymbol{s} = (\lambda_P N + \lambda_{\text{u}})\, \boldsymbol{x}^t - \tilde{\boldsymbol{A}}\boldsymbol{x}^t$, $\lambda_P = \lambda_{\max}(\tilde{\boldsymbol{\Phi}})$, λ_{u} is the maximum eigenvalue of $\left(\tilde{\boldsymbol{A}} - \lambda_{\max}(\tilde{\boldsymbol{\Phi}})\boldsymbol{x}^t \left(\boldsymbol{x}^t\right)^H\right)$.

The problem in (4.143) has a closed-form solution:

$$\boldsymbol{x}^{t+1} = \frac{\boldsymbol{s}}{|\boldsymbol{s}|} \tag{4.144}$$

here $\frac{\boldsymbol{s}}{|\boldsymbol{s}|}$ is an element wise operation. The pseudocode (the efficient implementation using FFT and IFFT operations) of the MM-PSL algorithm is given in Algorithm 4.6.

4.3.2.2 SLOPE Algorithm

In the last subsection, we reviewed a PSL minimization algorithm named MM-PSL, which approximates the nondifferentiable PSL cost function in terms of l_p norm function (for $p > 2$, p being large), and used MM to arrive at a minimizer. In this section we will review an algorithm named SLOPE (Sequence with LOw Peak sidelobE level), which minimizes the PSL objective.

The PSL minimization problem in (4.22) is given as:

$$\begin{aligned} \underset{\boldsymbol{x}}{\text{minimize}} \quad & \text{PSL} = \underset{k=1,..,N}{\text{maximum}} |r(k)| \\ \text{subject to} \quad & |x_n| = 1,\ n = 1, ..., N \end{aligned}$$

For analytical convenience, the above problem is reformulated as:

$$\begin{aligned} \underset{\boldsymbol{x}}{\text{minimize}} \quad & \max_{k=1,..,N} 2\,|r(k)|^2 \\ \text{subject to} \quad & |x_n| = 1,\ n = 1, ..., N \end{aligned} \tag{4.145}$$

Please note that we have squared the objective function (as squaring the absolute valued objective will not change the optimum) and have also scaled the objective by a factor 2. Then the cost function in problem (4.145) can be rewritten as:

Algorithm 4.6: The MM-PSL Algorithm Proposed in [25]

Require: sequence length 'N', parameter $p \geq 2$

set $t = 0$, initialize $\boldsymbol{x}^0$

repeat

$\boldsymbol{f} = \boldsymbol{F}\ \left[\left(\boldsymbol{x}^t\right)^T, \boldsymbol{0}_{1\times N}\right]^T$

$\boldsymbol{r} = \frac{1}{2N}\boldsymbol{F}^H\left|\boldsymbol{f}\right|^2$

$q = \left\|\boldsymbol{r}_{2:N}\right\|_p$

$c_k = \frac{1+(p-1)\left(\frac{|r(k+1)|}{q}\right)^p - p\left(\frac{|r(k+1)|}{q}\right)^{p-1}}{\left(q-|r(k+1)|\right)^2},\ k = 1,..,N-1$

$w_k = \frac{p}{2q^2}\left(\frac{|r(k+1)|}{q}\right)^{p-2},\ k = 1,..,N-1$

$\lambda_P = \max_k \left\{c_k(N-k),\ k = 1,..,N-1\right\}$

$\boldsymbol{c} = \boldsymbol{r} \circ [0, w_1, .., w_{N-1}, 0, w_{N-1}, .., w_1]$

$\boldsymbol{\mu} = \boldsymbol{F}\boldsymbol{c}$

$\lambda_u = \frac{1}{2}\left(\max_{1\leq i\leq N}\boldsymbol{\mu}_{2i} + \max_{1\leq i\leq N}\boldsymbol{\mu}_{2i-1}\right)$

$\boldsymbol{s} = \boldsymbol{x}^t - \frac{\boldsymbol{F}_{1:N}^H(\boldsymbol{\mu}\circ\boldsymbol{f})}{2N(\lambda_P N+\lambda_u)}$

$\boldsymbol{x}^{t+1} = \frac{\boldsymbol{s}}{|\boldsymbol{s}|}$

$t \leftarrow t+1$

until convergence

$$2\left|r(k)\right|^2 = \left|\boldsymbol{x}^H\boldsymbol{W}_k\boldsymbol{x}\right|^2 + \left|\boldsymbol{x}^H\boldsymbol{W}_k^H\boldsymbol{x}\right|^2 \tag{4.146}$$

where $\boldsymbol{W}_k$ is given in (4.84). By defining $\boldsymbol{X} = \boldsymbol{x}\boldsymbol{x}^H$, (4.146) can be further rewritten as:

$$\begin{aligned}\left|\boldsymbol{x}^H\boldsymbol{W}_k\boldsymbol{x}\right|^2 + \left|\boldsymbol{x}^H\boldsymbol{W}_k^H\boldsymbol{x}\right|^2 = {}& \mathrm{Tr}\Big(\boldsymbol{W}_k\boldsymbol{X}\Big)\mathrm{Tr}\Big(\boldsymbol{W}_k^H\boldsymbol{X}\Big) \\ & + \mathrm{Tr}\Big(\boldsymbol{X}\boldsymbol{W}_k^H\Big)\mathrm{Tr}\Big(\boldsymbol{W}_k\boldsymbol{X}\Big)\end{aligned} \tag{4.147}$$

By using (4.147) and the relation $\mathrm{Tr}\Big(\boldsymbol{W}_k\boldsymbol{X}\Big) = \mathrm{vec}^H\Big(\boldsymbol{X}\Big)\mathrm{vec}\Big(\boldsymbol{W}_k\Big)$, the problem in (4.145) can be rewritten as:

$$\begin{aligned} \underset{\boldsymbol{x},\boldsymbol{X}}{\text{minimize}} \quad & \max_{k=1,..,N} \text{vec}^H\Big(\boldsymbol{X}\Big)\Big(\boldsymbol{\Phi}(k)\Big)\text{vec}\Big(\boldsymbol{X}\Big) \\ \text{subject to} \quad & \boldsymbol{X} = \boldsymbol{x}\boldsymbol{x}^H, \\ & |x_n| = 1,\ n = 1, \ldots, N \end{aligned} \tag{4.148}$$

where $\boldsymbol{\Phi}(k) = \text{vec}\Big(\boldsymbol{W}_k\Big)\text{vec}^H\Big(\boldsymbol{W}_k^H\Big) + \text{vec}\Big(\boldsymbol{W}_k^H\Big)\text{vec}^H\Big(\boldsymbol{W}_k\Big)$ is an $N^2 \times N^2$ dimensional matrix.

The problem in (4.148) is quadratic in $\boldsymbol{X}$ and by using the Lemma 4.1, at any given point $\boldsymbol{X}^t$, a tighter surrogate can be obtained as:

$$\begin{aligned} \text{vec}^H\Big(\boldsymbol{X}\Big)\Big(\boldsymbol{\Phi}(k)\Big)\text{vec}\Big(\boldsymbol{X}\Big) \leq & -\text{vec}^H\Big(\boldsymbol{X}^t\Big)\Big(\boldsymbol{\Phi}(k) - \boldsymbol{C}(k)\Big)\text{vec}\Big(\boldsymbol{X}^t\Big) \\ & + 2\text{Re}\Big(\text{vec}^H\Big(\boldsymbol{X}^t\Big)\Big(\boldsymbol{\Phi}(k) - \boldsymbol{C}(k)\Big)\text{vec}\Big(\boldsymbol{X}\Big)\Big) \\ & + \text{vec}^H\Big(\boldsymbol{X}\Big)\Big(\boldsymbol{C}(k)\Big)\text{vec}\Big(\boldsymbol{X}\Big) \end{aligned} \tag{4.149}$$

where $\boldsymbol{C}(k) = \lambda_{\max}\Big(\boldsymbol{\Phi}(k)\Big)\boldsymbol{I}_{N^2}$.

It can be noted that, for obtaining the upper-bound function, one has to calculate the maximum eigenvalue of $\boldsymbol{\Phi}(k)$. The following lemma presents the derivation of maximum eigenvalue of $\boldsymbol{\Phi}(k)$.

Lemma 4.7. *The maximum eigenvalue of the $N^2 \times N^2$ dimensional sparse matrix $\boldsymbol{\Phi}(k)$ is equal to $(N-k)$, $\forall k$.*

Proof: Since $\boldsymbol{\Phi}(k) = \text{vec}\Big(\boldsymbol{W}_k\Big)\text{vec}^H\Big(\boldsymbol{W}_k^H\Big) + \text{vec}\Big(\boldsymbol{W}_k^H\Big)\text{vec}^H\Big(\boldsymbol{W}_k\Big)$ which is an aggregation of two rank-1 matrices, its maximum possible rank is 2. Let μ_1, μ_2 are the two different eigenvalues of $\boldsymbol{\Phi}(k)$ and its corresponding characteristic equation is given by:

$$x^2 - (\mu_1 + \mu_2)x + (\mu_1\mu_2) = 0 \tag{4.150}$$

It is known that $\text{vec}\Big(\boldsymbol{W}_k\Big)\text{vec}^H\Big(\boldsymbol{W}_k^H\Big)$ is an $N^2 \times N^2$ dimensional sparse matrix filled with zeros along the diagonal. Hence,

$$\mu_1 + \mu_2 = \text{Tr}\big(\boldsymbol{\Phi}(k)\big) = 0 \tag{4.151}$$

The relation $\mu_1\mu_2 = \frac{1}{2}((\mu_1+\mu_2)^2 - (\mu_1^2+\mu_2^2))$, which, by using (4.151) becomes $\mu_1\mu_2 = -\frac{1}{2}(\mu_1^2+\mu_2^2)$. It is known that

$$\mu_1^2+\mu_2^2 = 2\text{Tr}\left(\text{vec}\Big(\boldsymbol{W}_k\Big)\text{vec}^H\Big(\boldsymbol{W}_k^H\Big)\text{vec}\Big(\boldsymbol{W}_k^H\Big)\text{vec}^H\Big(\boldsymbol{W}_k\Big)\right)$$
$$= 2\big\|\text{vec}\Big(\boldsymbol{W}_k\Big)\big\|_2^2\big\|\text{vec}\Big(\boldsymbol{W}_k^H\Big)\big\|_2^2$$

Since the vectors $\text{vec}\Big(\boldsymbol{W}_k\Big)$ and $\text{vec}\Big(\boldsymbol{W}_k^H\Big)$ have only $(N-k)$ number of ones and the remaining elements as zeros, it can be obtained that $\big\|\text{vec}\Big(\boldsymbol{W}_k\Big)\big\|_2^2 = N-k$ and $\big\|\text{vec}\Big(\boldsymbol{W}_k^H\Big)\big\|_2^2 = N-k$ then

$$\mu_1^2+\mu_2^2 = 2\big\|\text{vec}\Big(\boldsymbol{W}_k\Big)\big\|_2^2\big\|\text{vec}\Big(\boldsymbol{W}_k^H\Big)\big\|_2^2 = 2\big(N-k\big)^2 \tag{4.152}$$

By using (4.151) and (4.152), the characteristic equation (4.150) becomes $x^2-\big(N-k\big)^2=0$, which implies $x=\pm(N-k)$. Among the two possibilities, the maximum will be $(N-k)$, and this concludes the proof. ■

So, according to Lemma 4.7, the maximum eigenvalue of $\boldsymbol{\Phi}(k)$ is taken as $N-k$ $\Big(\lambda_{\max}\Big(\boldsymbol{\Phi}(k)\Big)=(N-k),\,\forall k\Big)$.

Since $\text{vec}^H(\boldsymbol{X})\text{vec}(\boldsymbol{X}) = (\boldsymbol{x}^H\boldsymbol{x})^2 = N^2$, the surrogate function in (4.149) can be rewritten as:

$$u_k\Big(\boldsymbol{X}|\boldsymbol{X}^t\Big) = -\,\text{vec}^H\Big(\boldsymbol{X}^t\Big)\Big(\boldsymbol{\Phi}(k)\Big)\text{vec}\Big(\boldsymbol{X}^t\Big) + 2\text{Re}\left(\text{vec}^H\Big(\boldsymbol{X}^t\Big)\Big(\boldsymbol{\Phi}(k)\Big)\right.$$
$$\left.\text{vec}\Big(\boldsymbol{X}\Big)\right) - 2\Big(N-k\Big)\text{Re}\Big(\text{vec}^H\Big(\boldsymbol{X}^t\Big)\text{vec}\Big(\boldsymbol{X}\Big)\Big) + 2\Big(N-k\Big)N^2 \tag{4.153}$$

By substituting back $\boldsymbol{X}=\boldsymbol{x}\boldsymbol{x}^H$, the surrogate function in (4.153) can be expressed in the original variable $\boldsymbol{x}$ as follows:

$$\begin{aligned} u_k\Big(\boldsymbol{x}|\boldsymbol{x}^t\Big) = &-2\left|\Big(\boldsymbol{x}^t\Big)^H\boldsymbol{W}_k\boldsymbol{x}^t\right|^2 \\ &+2\left(\Big(\boldsymbol{x}^t\Big)^H\boldsymbol{W}_k\boldsymbol{x}^t\left(\Big(\boldsymbol{x}\Big)^H\boldsymbol{W}_k\boldsymbol{x}\right)^H\right. \\ &\qquad\left.+\Big(\boldsymbol{x}\Big)^H\boldsymbol{W}_k\boldsymbol{x}\left(\Big(\boldsymbol{x}^t\Big)^H\boldsymbol{W}_k\boldsymbol{x}^t\right)^H\right) \\ &-2\Big(N-k\Big)\Big(\boldsymbol{x}^H\boldsymbol{x}^t\Big(\boldsymbol{x}^t\Big)^H\boldsymbol{x}\Big)+2\Big(N-k\Big)N^2 \end{aligned} \tag{4.154}$$

The surrogate function (4.154) can be rewritten more compactly as:

$$\begin{aligned} u_k\Big(\boldsymbol{x}|\boldsymbol{x}^t\Big) = &-2\left|\Big(\boldsymbol{x}^t\Big)^H \boldsymbol{W}_k \boldsymbol{x}^t\right|^2 + 2\Big(\boldsymbol{x}^H\Big(\boldsymbol{D}(k)\Big)\boldsymbol{x}\Big) \\ &-2\Big(N-k\Big)\Big(\boldsymbol{x}^H\boldsymbol{x}^t\Big(\boldsymbol{x}^t\Big)^H\boldsymbol{x}\Big) + 2\Big(N-k\Big)N^2 \end{aligned} \tag{4.155}$$

where

$$\boldsymbol{D}(k) = \quad \boldsymbol{W}_k\left(\Big(\boldsymbol{x}^t\Big)^H \boldsymbol{W}_k \boldsymbol{x}^t\right)^H + \boldsymbol{W}_k^H\left(\Big(\boldsymbol{x}^t\Big)^H \boldsymbol{W}_k \boldsymbol{x}^t\right)$$

The surrogate function in (4.155) is a quadratic function in the variable $\boldsymbol{x}$ which would be difficult to minimize (mainly due to the unimodular constraint on the variables), so the following lemma can be used to further majorize the surrogate.

Lemma 4.8. *Let $g : \mathbb{C}^N \to \mathbb{R}$ be any differentiable concave function, then at any fixed point $\boldsymbol{z}^t$, $g(\boldsymbol{z})$ can be upper-bounded (majorized) as,*

$$g(\boldsymbol{z}) \leq g(\boldsymbol{z}^t) + Re\left(\Big(\nabla g(\boldsymbol{z}^t)\Big)^H(\boldsymbol{z}-\boldsymbol{z}^t)\right) \tag{4.156}$$

Proof: For any bounded concave function $g(\boldsymbol{z})$, linearizing at a point $\boldsymbol{z}^t$ using first-order Taylor series expansion will result in the abovementioned upper-bounded function and it concludes the proof. ■

Let $\bar{\boldsymbol{D}}(k) = \Big(\Big(\boldsymbol{D}(k)\Big) - \Big(\lambda_{\max}\Big(\boldsymbol{D}(k)\Big)\boldsymbol{I}_N\Big)\Big)$; then (4.155) can be rewritten as:

$$\begin{aligned} u_k\Big(\boldsymbol{x}|\boldsymbol{x}^t\Big) = &-2\left|\Big(\boldsymbol{x}^t\Big)^H \boldsymbol{W}_k \boldsymbol{x}^t\right|^2 + 2\Big(\boldsymbol{x}^H\bar{\boldsymbol{D}}(k)\boldsymbol{x}\Big) + 2\lambda_{\max}\Big(\boldsymbol{D}(k)\Big)N \\ &-2\Big(N-k\Big)\Big(\boldsymbol{x}^H\boldsymbol{x}^t\Big(\boldsymbol{x}^t\Big)^H\boldsymbol{x}\Big) + 2\Big(N-k\Big)N^2 \end{aligned} \tag{4.157}$$

The surrogate function in (4.157) is a quadratic concave function and can be further majorized by Lemma 4.8. So, by majorizing (4.157) as in Lemma 4.8, the surrogate to the surrogate function can be obtained as:

$$\begin{aligned} \tilde{u}_k\Big(\boldsymbol{x}|\boldsymbol{x}^t\Big) = &-2\left|\Big(\boldsymbol{x}^t\Big)^H \boldsymbol{W}_k \boldsymbol{x}^t\right|^2 + 2\lambda_{\max}\Big(\boldsymbol{D}(k)\Big)N \\ &+2\Big(-\Big(\boldsymbol{x}^t\Big)^H\bar{\boldsymbol{D}}(k)\boldsymbol{x}^t + 2\mathrm{Re}\Big(\Big(\boldsymbol{x}^t\Big)^H\bar{\boldsymbol{D}}(k)\boldsymbol{x}\Big)\Big) \\ &-2\Big(N-k\Big)\Big(-N^2 + 2N\mathrm{Re}\Big(\boldsymbol{x}^H\boldsymbol{x}^t\Big)\Big) + 2\Big(N-k\Big)N^2 \end{aligned} \tag{4.158}$$

It can be noted that the surrogate in (4.158) is a tighter upper bound for the surrogate in (4.157), which is again a tighter upper bound for the PSL metric, so one can directly formulate (4.158) as a tighter surrogate for the PSL metric. Thus, using (4.158), the surrogate minimization problem is given as:

$$\begin{aligned} \underset{\boldsymbol{x}}{\text{minimize}} \quad & \underset{k=1,..,N}{\text{maximize}} \quad 4\text{Re}\Big(\boldsymbol{x}^H \boldsymbol{d}(k)\Big) + p(k) \\ \text{subject to} \quad & \big|x_n\big| = 1,\, n = 1,..,N, \end{aligned} \tag{4.159}$$

where

$$\begin{aligned} \boldsymbol{d}(k) &= \Big(\bar{\boldsymbol{D}}(k)\Big)\boldsymbol{x}^t - \Big(N-k\Big)N\boldsymbol{x}^t \\ &= \Big(\boldsymbol{W}_k\boldsymbol{x}^t\Big)r^*(k) + \Big(\boldsymbol{W}_k^H\boldsymbol{x}^t\Big)r(k) - \Big(\lambda_{\max}\Big(\boldsymbol{D}(k)\Big)\boldsymbol{I}_N\Big)\boldsymbol{x}^t \\ &\quad - \Big(N-k\Big)N\boldsymbol{x}^t \end{aligned} \tag{4.160}$$

$$\begin{aligned} p(k) = -2\Big|\Big(\boldsymbol{x}^t\Big)^H\boldsymbol{W}_k\boldsymbol{x}^t\Big|^2 + 4\Big(N-k\Big)N^2 - 2\Big(\Big(\boldsymbol{x}^t\Big)^H\Big(\boldsymbol{D}(k)\Big)\boldsymbol{x}^t\Big) \\ + 4\lambda_{\max}\Big(\boldsymbol{D}(k)\Big)N \end{aligned} \tag{4.161}$$

$$p(k) = -6\Big|r(k)\Big|^2 + 4\lambda_{\max}\Big(\boldsymbol{D}_{i,j}(k)\Big)N + 4\Big(N-k\Big)N^2 \tag{4.162}$$

Interior Point Solver-Based SLOPE

The problem in (4.159) is a nonconvex problem because of the presence of equality constraint. However, the constraint set can be relaxed and the optimal minimizer for the relaxed problem will lie on the boundary set [28]. The epigraph form of the relaxed problem can be given as:

$$\begin{aligned} \underset{\boldsymbol{x},\alpha}{\text{minimize}} \quad & \underset{k=1,..,N}{\text{maximize}}\ \alpha \\ \text{subject to} \quad & 4\text{Re}\Big(\boldsymbol{x}^H\boldsymbol{d}(k)\Big) + p(k) \le \alpha,\, \forall k \\ & \big|x_n\big| \le 1,\, n = 1,\ldots,N \end{aligned} \tag{4.163}$$

Algorithm 4.7: The Interior Point Solver Based SLOPE Proposed in [27]

Require: Sequence length 'N'

1: set $t = 0$, initialize $\boldsymbol{x}^0$

2: form $\boldsymbol{A}_k\,, k$ using (4.84)

3: $\boldsymbol{\Phi}(k) = \text{vec}\Big(\boldsymbol{W}_k\Big)\text{vec}^H\Big(\boldsymbol{W}_k^H\Big) + \text{vec}\Big(\boldsymbol{W}_k^H\Big)\text{vec}^H\Big(\boldsymbol{W}_k\Big)$

4: **repeat**

5: $\boldsymbol{D}(k) = \boldsymbol{W}_k\Big(\Big(\boldsymbol{x}^t\Big)^H\boldsymbol{W}_k^H\boldsymbol{x}^t\Big) + \boldsymbol{W}_k^H\Big(\Big(\boldsymbol{x}^t\Big)^H\boldsymbol{W}_k\boldsymbol{x}^t\Big), \forall k.$

6: $\bar{\boldsymbol{D}}(k) = \Big(\Big(\boldsymbol{D}(k)\Big) - \Big(\lambda_{\max}\Big(\boldsymbol{D}(k)\Big)\boldsymbol{I}_N\Big)\Big)\forall k.$

7: $\boldsymbol{d}(k) = \Big(\bar{\boldsymbol{D}}(k)\Big)\boldsymbol{x}^t - \Big(N-k\Big)N\boldsymbol{x}^t\,, \forall k.$

8:

$$p(k) = -2\left|\Big(\boldsymbol{x}^t\Big)^H\boldsymbol{W}_k\boldsymbol{x}^t\right|^2 - 2\Big(\Big(\boldsymbol{x}^t\Big)^H\boldsymbol{D}(k)\boldsymbol{x}^t\Big) + 4\lambda_{\max}\Big(\boldsymbol{D}(k)\Big)N + 4\Big(N-k\Big)N^2, \forall k.$$

9: get $\boldsymbol{x}^{t+1}$ by solving the problem in (4.163).

10: $t \leftarrow t+1$

11: **until** convergence

The problem in (4.163) is a convex problem and there exist many off-the-shelf interior point solvers [29] to solve the problem in (4.163). The pseudocode of the interior point solver based SLOPE is given in the Algorithm 4.7.

However, when dimension of the problem (N) increases, off-the-shelf solvers will become computationally expensive. To overcome this issue, in the following an efficient way to compute the solution of (4.163) is discussed. The problem in (4.159) is a function of complex variable $\boldsymbol{x}$ and we first convert in terms of real variables as follows:

$$\begin{aligned} \underset{\boldsymbol{y}}{\text{minimize}} \quad & \underset{k=1,..,N}{\text{maximize}} \quad 4\boldsymbol{y}^T\boldsymbol{d}_k + p_k \\ \text{subject to} \quad & |y_n|^2 + |y_{n+N}|^2 \leq 1,\ n = 1,\ldots,N \end{aligned} \tag{4.164}$$

where $\boldsymbol{x}_R = \text{Re}(\boldsymbol{x}), \boldsymbol{x}_I = \text{Im}(\boldsymbol{x}), \boldsymbol{y} = [\boldsymbol{x}_R^T, \boldsymbol{x}_I^T]^T, \boldsymbol{d}_{Rk} = \text{Re}\Big(\boldsymbol{d}(k)\Big), \boldsymbol{d}_{Ik} = \text{Im}\Big(\boldsymbol{d}(k)\Big), \boldsymbol{d}_k = [\boldsymbol{d}_{Rk}^T, \boldsymbol{d}_{Ik}^T]^T, p_k = p(k).$

By introducing a simplex variable $\boldsymbol{q}$, one can rewrite the discrete inner maximum problem as follows:

$$\begin{aligned} &\underset{\boldsymbol{q}\geq 0,\mathbf{1}^T\boldsymbol{q}=1}{\text{maximize}} \quad \sum_{k=1}^{N-1}\Big[q_k(4\boldsymbol{y}^T\boldsymbol{d}_k+p_k)\Big] \\ &\underset{\boldsymbol{q}\geq 0,\mathbf{1}^T\boldsymbol{q}=1}{\text{maximize}} \quad 4\boldsymbol{y}^T\tilde{\boldsymbol{D}}\boldsymbol{q}+\boldsymbol{q}^T\boldsymbol{p} \end{aligned} \tag{4.165}$$

where $\tilde{\boldsymbol{D}} = \Big[\boldsymbol{d}_1,\boldsymbol{d}_2,...,\boldsymbol{d}_k\Big], \boldsymbol{q} = \Big[q_1,q_2,...,q_k\Big]^T$, $\boldsymbol{p} = \Big[p_1,p_2,..,p_k\Big]^T$. By using (4.165) and (4.164), the problem in (4.159) can be rewritten as:

$$\begin{aligned} \underset{\boldsymbol{y}}{\text{minimize}} \quad & \underset{\boldsymbol{q}\geq 0,\mathbf{1}^T\boldsymbol{q}=1}{\text{maximize}} \quad 4\boldsymbol{y}^T\tilde{\boldsymbol{D}}\boldsymbol{q}+\boldsymbol{q}^T\boldsymbol{p} \\ \text{subject to} \quad & |y_n|^2+|y_{n+N}|^2\leq 1,\ n=1,\ldots,N \end{aligned} \tag{4.166}$$

The problem in (4.166) is bilinear in the variables $\boldsymbol{y}$ and $\boldsymbol{q}$. By using the minmax theorem [30], without altering the solution, one can swap minmax to maxmin as follows:

$$\begin{aligned} \underset{\boldsymbol{q}\geq 0,\mathbf{1}^T\boldsymbol{q}=1}{\text{maximize}} \quad & \underset{\boldsymbol{y}}{\text{minimize}}\ 4\boldsymbol{y}^T\tilde{\boldsymbol{D}}\boldsymbol{q}+\boldsymbol{q}^T\boldsymbol{p} \\ \text{subject to} \quad & |y_n|^2+|y_{n+N}|^2\leq 1,\ n=1,\ldots,N \end{aligned} \tag{4.167}$$

Problem in (4.167) can be rewritten as:

$$\underset{\boldsymbol{q}\geq 0,\mathbf{1}^T\boldsymbol{q}=1}{\text{maximize}} \quad g(\boldsymbol{q}) \tag{4.168}$$

where

$$\begin{aligned} g(\boldsymbol{q}) = \underset{\boldsymbol{y}}{\text{minimize}} \quad & 4\boldsymbol{y}^T\tilde{\boldsymbol{D}}\boldsymbol{q}+\boldsymbol{q}^T\boldsymbol{p} \\ \text{subject to} \quad & |y_n|^2+|y_{n+N}|^2\leq 1,\ n=1,\ldots,N \end{aligned} \tag{4.169}$$

MDA-Based SLOPE

The problem in (4.168) can be solved iteratively via the MDA, which is a very established algorithm to solve minimization/maximization problems

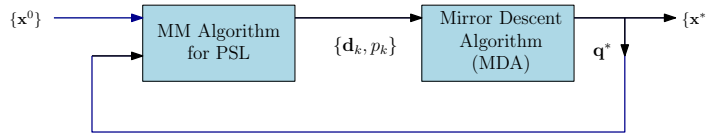

Figure 4.2. Block diagram for the MDA based SLOPE

with nondifferentiable objective. Without getting into details of the MDA algorithm (the interested reader can refer to [31]), the iterative steps of MDA for the problem in (4.168) can be given as:

Step 1: Get the subgradient of the objective $g(\boldsymbol{q})$, which is equal to $4\tilde{\boldsymbol{D}}^T\boldsymbol{z}^t + \boldsymbol{p}$, where $\boldsymbol{z}^t$ denote a sequence like variables (similar to $\boldsymbol{x}$) whose elements will have unit modulus.
Step 2: Update the simplex variable as $\boldsymbol{q}^{t+1} = \frac{\boldsymbol{q}^t \odot e^{\gamma_t 4\,\tilde{\boldsymbol{D}}^T\boldsymbol{z}^t + \boldsymbol{p}}}{\mathbf{1}^T(\boldsymbol{q}^t \odot e^{\gamma_t 4\,\tilde{\boldsymbol{D}}^T\boldsymbol{z}^t + \boldsymbol{p}})}$, where γ_t is a suitable step size.
Step 3: $t = t + 1$ and go to Step 1 unless convergence is achieved.

Once the optimal $\boldsymbol{q}^\star$ is obtained, the update for the variables $\boldsymbol{y}$ can be obtained as explained below:

$$\left[y_n, y_{n+MN}\right]^T = \frac{\boldsymbol{v}_n}{\|\boldsymbol{v}_n\|_2} \tag{4.170}$$

where $\boldsymbol{v}_n = \left[\tilde{c}_n, \tilde{c}_{n+MN}\right]^T$, $n = 1, ., MN$, and $\tilde{\boldsymbol{c}} = -\tilde{\boldsymbol{D}}\boldsymbol{q}^\star$. From the real variables $\boldsymbol{y}$, the complex variable $\boldsymbol{x}$ can be recovered. The pseudocode of the MDA-based SLOPE is given in Algorithm 4.8.

For the sake of better understanding, a birds-eye view of implementation of the MDA-based SLOPE is summarized in the following block diagram in Figure 4.2.

Computational and Space Complexities

SLOPE consists of two loops, in which the inner loop calculates $\boldsymbol{q}^\star$ using MDA and the outer loop will update the elements of a sequence. As shown

Algorithm 4.8: :The MDA-Based SLOPE Proposed in [27]

Require: Sequence length 'N'
1: set $t = 0$, initialize $\boldsymbol{x}^0$
2: form $\boldsymbol{A}_k$, k using (4.84)
3: $\boldsymbol{\Phi}(k) = \text{vec}\Big(\boldsymbol{W}_k\Big)\text{vec}^H\Big(\boldsymbol{W}_k^H\Big) + \text{vec}\Big(\boldsymbol{W}_k^H\Big)\text{vec}^H\Big(\boldsymbol{W}_k\Big)$
4: **repeat**
5: $\boldsymbol{D}(k) = \boldsymbol{W}_k\Big(\Big(\boldsymbol{x}^t\Big)^H\boldsymbol{W}_k^H\boldsymbol{x}^t\Big) + \boldsymbol{W}_k^H\Big(\Big(\boldsymbol{x}^t\Big)^H\boldsymbol{W}_k\boldsymbol{x}^t\Big), \forall k.$
6: $\bar{\boldsymbol{D}}(k) = \Big(\Big(\boldsymbol{D}(k)\Big) - \Big(\lambda_{\max}\Big(\boldsymbol{D}(k)\Big)\boldsymbol{I}_N\Big)\Big)\forall k.$
7: $\boldsymbol{d}(k) = \Big(\bar{\boldsymbol{D}}(k)\Big)\boldsymbol{x}^t - \Big(N-k\Big)N\boldsymbol{x}^t\,, \forall k.$
8:$p(k) =$
$-2\Big|\Big(\boldsymbol{x}^t\Big)^H\boldsymbol{W}_k\boldsymbol{x}^t\Big|^2 - 2\Big(\Big(\boldsymbol{x}^t\Big)^H\boldsymbol{D}(k)\boldsymbol{x}^t\Big) + 4\lambda_{\max}\Big(\boldsymbol{D}(k)\Big)N + 4\Big(N-k\Big)N^2, \forall k.$
9: evaluate $\boldsymbol{q}^\star$ using Mirror Descent Algorithm
10: $\tilde{\boldsymbol{c}} = -\tilde{\boldsymbol{D}}\boldsymbol{q}^\star$
11: $\boldsymbol{v}_n = \big[\tilde{c}_n, \tilde{c}_{n+N}\big]^T,\ n = 1, .., N.$
12: $\big[y_n, y_{n+N}\big]^T = \frac{\boldsymbol{v}_n}{\|\boldsymbol{v}_n\|_2}.$
13: Recover $\boldsymbol{x}^{t+1}$ from $\boldsymbol{y}^{t+1}$ and get required sequence from it.
14: $t \leftarrow t+1$
15: **until** convergence

in Algorithm 4.8, per iteration computational complexity of the outer loop is dominated by the calculation of $\boldsymbol{D}(k), \bar{\boldsymbol{D}}(k), \boldsymbol{d}(k), p(k), \tilde{\boldsymbol{c}}$. The quantity $\Big(\boldsymbol{x}^t\Big)^H\boldsymbol{W}_k\boldsymbol{x}^t$ which appears in some of the constants of the algorithm, is nothing but $r(k)$; which can be calculated using FFT and IFFT operations, one can implement the above quantities very efficiently. The optimal $\boldsymbol{q}^\star$ is obtained using MDA will be mostly sparse; then the quantity $\tilde{\boldsymbol{c}}$ can be calculated efficiently using a sparse matrix-vector multiplication. The per iteration computational complexity of the inner loop (i.e., MDA) is dominated by the calculation of subgradient, which can also be efficiently calculated via FFT operations. So, the per iteration computational complexity of the SLOPE algorithm is around $\mathcal{O}(3N\,log\,N)$. The space complexity is dominated by two $(N \times N)$ matrices, one $(N \times (N-1))$ matrix, two $((N-1) \times 1)$

Table 4.1
MM-Based Algorithms' Computational and Space Complexities for ISL and PSL Minimization

Algorithm	Computational Complexity per Iteration	Space Complexity
MISL	$\mathcal{O}(2N\,log\,2N)$	$\mathcal{O}(N^2)$
ISL-NEW	$\mathcal{O}(2N\,log\,2N)$	$\mathcal{O}(N^2)$
FBMM	$\mathcal{O}(N^2)+\mathcal{O}(2N\,log\,2N)$	$\mathcal{O}(N)$
FISL	$\mathcal{O}(2N\,log\,2N)$	$\mathcal{O}(N)$
UNIPOL	$\mathcal{O}(2N\,log\,2N)$	$\mathcal{O}(N)$
MM-PSL	$\mathcal{O}(2N\,log\,2N)$	$\mathcal{O}(N)$
SLOPE	$\mathcal{O}(3N\,log\,N)$	$\mathcal{O}(N^2)$

vectors, and one $(N \times 1)$ vector, and hence, total space complexity is around $\mathcal{O}(N(N-1))$.

For better comparison, the computational and space complexities of different MM-based algorithms are summarized in Table 4.1.

4.4 NUMERICAL SIMULATIONS

To evaluate the performance of MM-based algorithms (ISL and PSL minimizers), numerical experiments are conducted for different sequence lengths like $N = 64$, 100, 225, 400, 625, 900, 1000, 1300. In each experiment of the ISL minimizers (MISL, ISL-NEW, FBMM, FISL, UNIPOL), for each sequence length, the ISL value with respect to iterations and CPU time and the autocorrelation values of the converged sequence are computed. Here for both the MISL and ISL-NEW algorithms we have implemented the SQUAREM acceleration schemes mentioned in the original papers but named as normal MISL and ISL-NEW. For the PSL minimizers (MM-PSL, SLOPE), autocorrelations with respect to lags are computed. Experiments are conducted using different initialization sequences like the random sequence that is taken as $e^{j\theta_n}, n = 1, .., N$, where any θ_n follow the uniform distribution between $[0, 1]$, Golomb, and Frank sequences. For better comparison, all the algorithms are initialized using the same initial sequence and were run for 5000 iterations.

Figures 4.3, 4.4, and 4.5 consist of the ISL versus iterations, ISL versus time, and the autocorrelations versus lag plots for two different

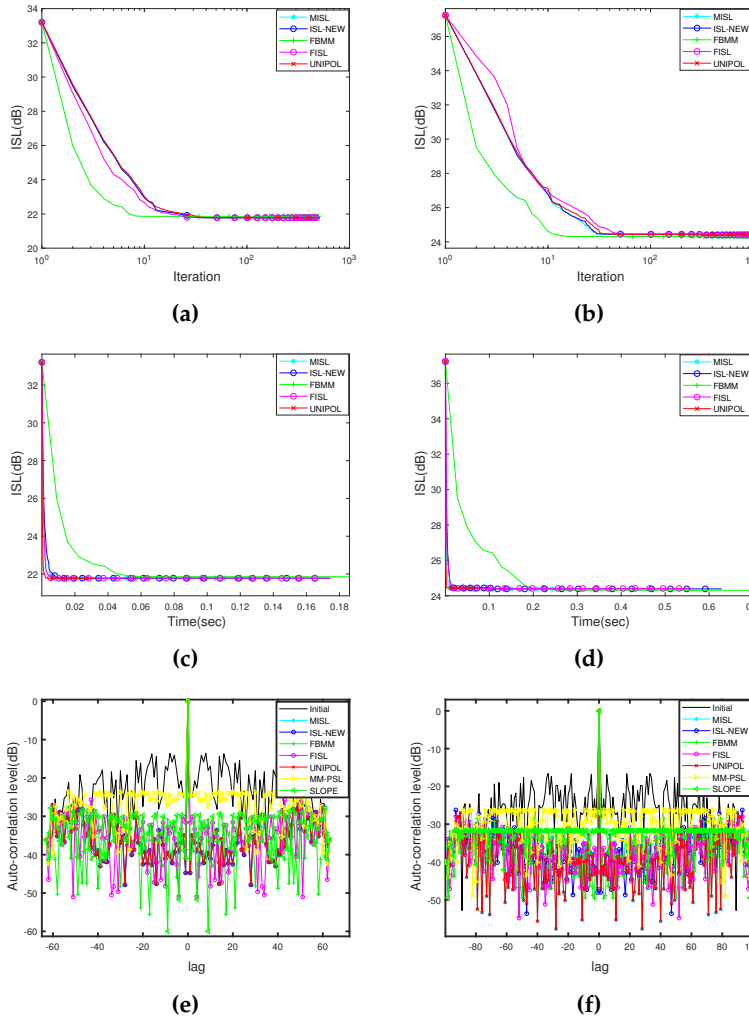

Figure 4.3. MM-based algorithms using the random initialization. (a) ISL vs iterations for $N = 64$ (b) ISL vs iterations for $N = 100$ (c) ISL vs time for $N = 64$ (d) ISL vs time for $N = 100$ (e) Autocorrelations vs lag for $N = 64$ (f) Autocorrelations vs lag for $N = 100$.

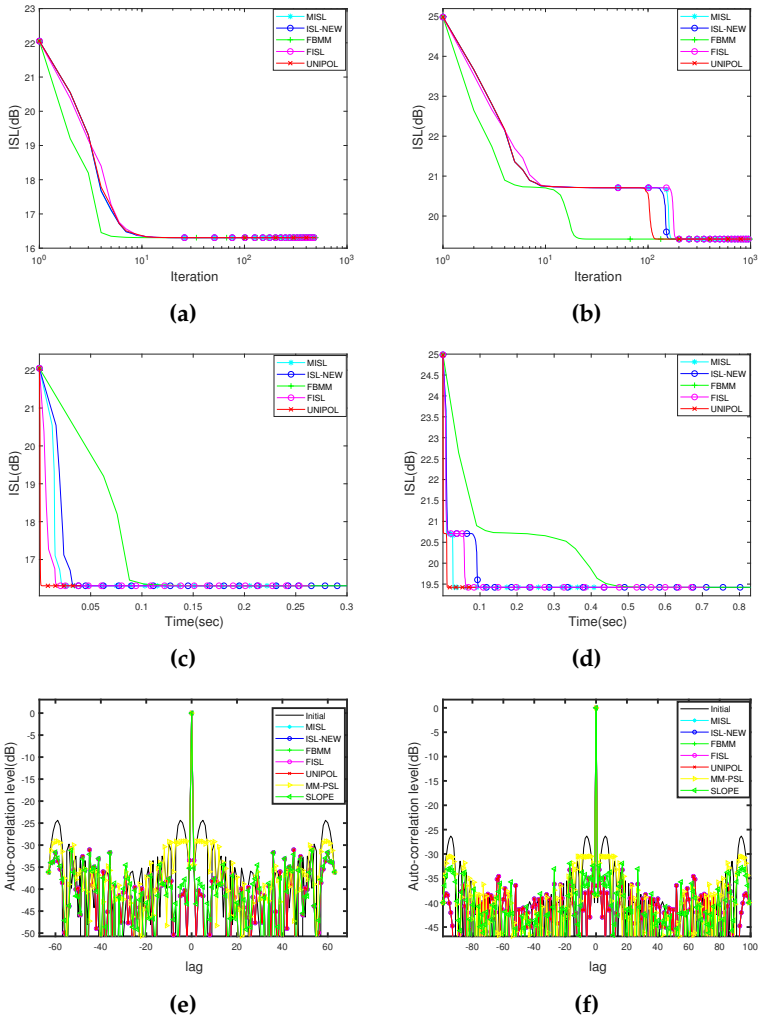

Figure 4.4. MM-based algorithms using the Golomb initialization. (a) ISL vs iterations for $N = 64$ (b) ISL vs iterations for $N = 100$ (c) ISL vs time for $N = 64$ (d) ISL vs time for $N = 100$ (e) Autocorrelations vs lag for $N = 64$ (f) Autocorrelations vs lag for $N = 100$

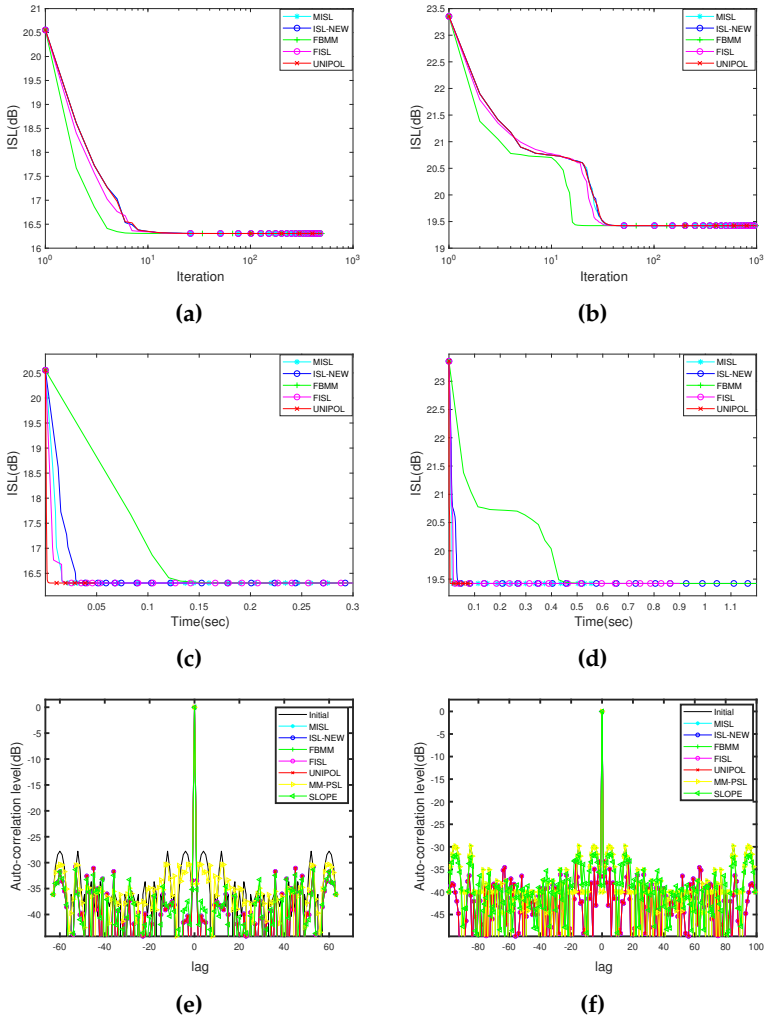

Figure 4.5. MM-based algorithms using the Frank initialization. (a) ISL vs iterations for $N = 64$ (b) ISL vs iterations for $N = 100$ (c) ISL vs time for $N = 64$ (d) ISL vs time for $N = 100$ (e) Autocorrelations vs lag for $N = 64$ (f) Autocorrelations vs lag for $N = 100$

sequence lengths $(N = 64, 100)$ using three different initializations. From the simulation plots, one can observe that all the algorithms have started at the same initial point and converged to the almost same minimum values but with different convergence rates. We noticed that in terms of the ISL minimizers the UNIPOL has converged to a better minimum in terms of CPU time. In terms of the autocorrelation sidelobe levels, irrespective of the sequence length and initialization, the SLOPE has obtained the better uniform side-lobe levels.

For fair comparisons, we also compare the UNIPOL algorithm with the SQUAREM accelerated MISL (ACC-MISL) and ISL-NEW (ACC-ISL-NEW) algorithms (here, for better understanding, we explicitly mention the accelerated algorithms as the ACC-MISL and ACC-ISL-NEW) and their corresponding simulation plots (ISL versus iterations) are given in Figure 4.6. Figure 4.6(a, b) shows the plots for a sequence length $N = 100$ and (c, d) show the plots for a sequence length $N = 1000$, respectively, where the convergence criteria selected to plot them is 1000 iterations. From the simulation plots we observed that irrespective of the sequence length, the UNIPOL is always attaining the local optimal minima and whereas the ACC-MISL, ACC-ISL-NEW algorithms are attaining the suboptimal minima. For instance from Figure 4.6(a) for a sequence length $N = 100$, the UNIPOL has reached an ISL value of 48 dB and the ACC-MISL, and ACC-ISL-NEW have reached an ISL value of 49.5 dB (suboptimal minimum). Since there is a difference of 1.5 dB which is not insignificant, we conclude that the UNIPOL is always arriving at the optimal minima with in fewer number of iterations.

The reason why ACC-MISL and ACC-ISL-NEW sometimes do not converge to a local minima can be explained as follows. The acceleration schemes, for instance, in SQUAREM acceleration, two MM iterates $\boldsymbol{x}^k$, $\boldsymbol{x}^{k+1}$ are computed by using the $\boldsymbol{x}^{k-1}$ and then by using a step size α, they would be combined to find a new iterate, that is, $\bar{\boldsymbol{x}} = \boldsymbol{x}^k - 2\alpha\boldsymbol{r} + \alpha^2\boldsymbol{v}$, where $\boldsymbol{r} = \boldsymbol{x}^k - \boldsymbol{x}^{k-1}$, $\boldsymbol{v} = \boldsymbol{x}^{k+1} - \boldsymbol{x}^k - \boldsymbol{r}$, but in our case $\bar{\boldsymbol{x}}$ may not be feasible (unimodular constraint), so in [15] they proposed to project $\bar{\boldsymbol{x}}$ back on to the unimodular constraint set. However, this projection may not ensure monotonicity, so the authors in [15] proposed decreasing the step size until the monotonicity is ensured, but this correction step is not proposed in the original SQUAREM paper [32], and this would be the reason behind the ACC-MISL and ACC-ISL-NEW algorithms getting stuck at a suboptimal

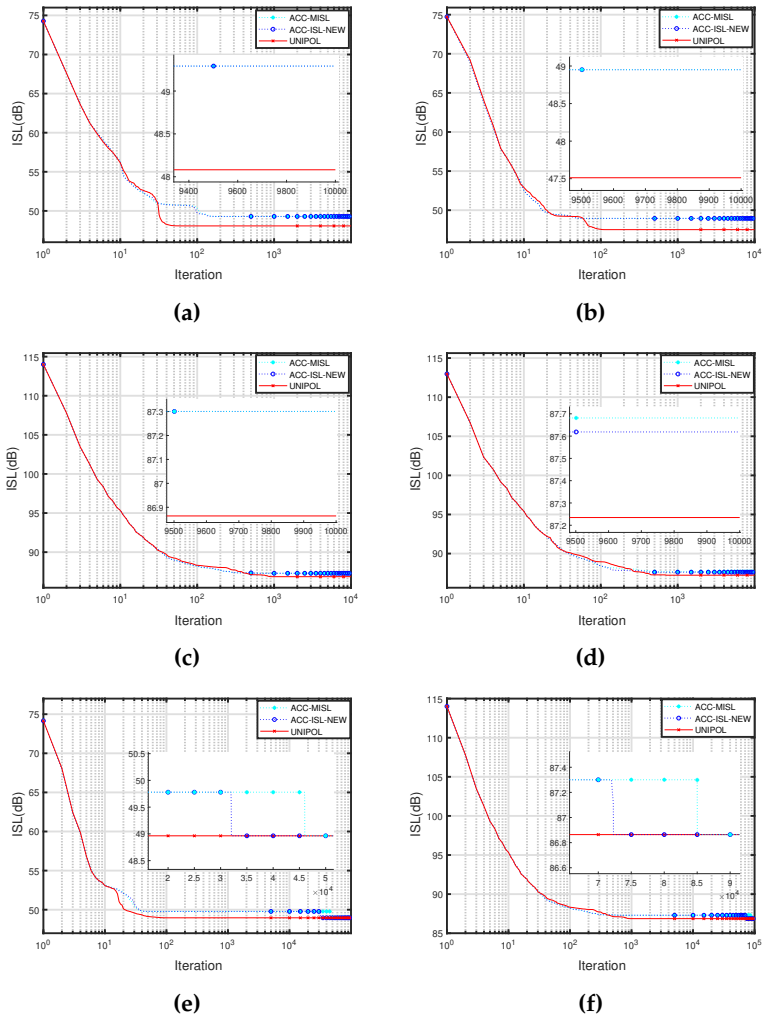

Figure 4.6. ISL versus iterations. (a) For a sequence length $N = 100$ (b) For a sequence length $N = 100$ (c) For a sequence length $N = 1000$ (d) For a sequence length $N = 1000$ (e) For a sequence length $N = 100$ (f) For a sequence length $N = 1000$

solution. So, if one considers the plain algorithmic convergence, the ACC-MISL and ACC-ISL-NEW algorithms are faster but they converge to a sub-optimal solution and, if one desires to find a local minimum, then they would require larger number of iterations to eventually converge to the local minimum.

To prove that even the ACC-MISL and ACC-ISL-NEW algorithms will also converge to the local optimal minima, we added $90,000$ more iterations and repeated the experiment for sequence lengths $N = 100, 1000$, and the resultant plots are given in Figure 4.6(e, f). From simulation plots we observed that both the ACC-MISL and ACC-ISL-NEW algorithms also converged to the same local minimum as UNIPOL. We have also implemented the approach to accelerate the MISL and ISL-NEW algorithms via a backtracking approach and observed the same phenomenon as above.

Figure 4.7 shows the comparison plots of different algorithms in terms of average running time versus different sequence lengths. To calculate the average running time, for each length the experiment is repeated over 30 Monte Carlo runs. All the algorithms are run until they converge to a local minima. From the simulation plots we observe that, irrespective of the sequence length, the UNIPOL has taken the least time to design sequences with better correlation properties.

4.5 CONCLUSION

In this chapter, we reviewed some of the MM-based sequence design algorithms. The algorithms MISL, FBMM, FISL, and UNIPOL monotonically minimize the ISL cost function, and the algorithms MM-PSL and SLOPE minimize the PSL cost function. Through brief numerical simulations, comparisons of the performance of all the methods were carried out.

4.6 EXERCISE PROBLEMS

Q1. The FBMM algorithm discussed in the chapter minimizes the ISL cost function, however, in some applications, there would be need to minimize only few selected squared lags of the autocorrelation, that is,

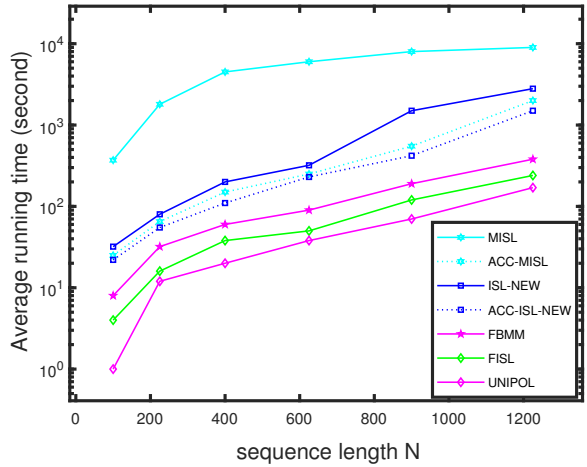

Figure 4.7. Average running time versus N.

$$\begin{aligned} \underset{\boldsymbol{x}}{\text{minimize}} \quad & \sum_{k=1}^{N-1} w_k |r(k)|^2 \\ \text{subject to} \quad & |x_n| = 1, \quad n = 1, \ldots, N \end{aligned} \tag{4.171}$$

where $w_k = \begin{cases} 1 & k \,\epsilon\, Z \\ 0 & \text{else} \end{cases}$, Z denotes the set of some prespecified indices.

How can the FBMM algorithm be adapted to solve the weighted ISL minimization problem?

Q2. The UNIPOL algorithm discussed in this chapter relies on the Parsevals theorem to express the ISL function in frequency domain. Exploring this, can the UNIPOL algorithm be adapted/changed to incorporate frequency domain constraints, like some band of frequencies are penalized more in the design?

Q3. The SLOPE algorithm discussed in this chapter minimizes the PSL cost function. Can the SLOPE algorithm be changed to minimize another useful criterion of the complementary autocorrelation function, which is given as:

$$\begin{aligned} &\underset{\{\boldsymbol{x}_1,\boldsymbol{x}_2,\ldots,\boldsymbol{x}_M\}}{\text{minimize}} \quad \underset{k=1,..,(N-1)}{\text{maximum}} \left| \sum_{m=1}^{M} r_m(k) \right| \\ &\text{subject to} \qquad \left|\boldsymbol{x}_m(n)\right| = 1,\ m = 1,\ldots,M,\ n = 1,\ldots,N \end{aligned} \tag{4.172}$$

where $\sum_{m=1}^{M} r_m(k)$ is the complementary autocorrelation function defined at lag k, $r_m(k)$ is the autocorrelation of the m-th sequence in the sequence set?

References

[1] M. A. Richards, *Fundamentals of Radar Signal Processing*. McGraw-Hill Professional, 2005. [Online]. Available: https://mhebooklibrary.com/doi/book/10.1036/0071444742

[2] W. C. Knight, R. G. Pridham, and S. M. Kay, "Digital signal processing for sonar," *Proceedings of the IEEE*, vol. 69, no. 11, pp. 1451–1506, Nov 1981.

[3] M. Skolnik, "Radar Handbook," *McGraw-Hill*, 1990.

[4] N. Levanon and E. Mozeson, "Basic Radar Signals," *John Wiley and Sons*, vol. 64, no. 11, pp. 53–73, 2004.

[5] I. Bekkerman and J. Tabrikian, "Target detection and localization using mimo radars and sonars," *IEEE Transactions on Signal Processing*, vol. 54, no. 10, pp. 3873–3883, 2006.

[6] J. Li, P. Stoica, and X. Zheng, "Signal synthesis and receiver design for mimo radar imaging," *IEEE Transactions on Signal Processing*, vol. 56, no. 8, pp. 3959–3968, 2008.

[7] W. Roberts, H. He, J. Li, and P. Stoica, "Probing waveform synthesis and receiver filter design," *IEEE Signal Processing Magazine*, vol. 27, no. 4, pp. 99–112, July 2010.

[8] P. Stoica, J. Li, and M. Xue, "Transmit codes and receive filters for radar," *IEEE Signal Processing Magazine*, vol. 25, no. 6, pp. 94–109, 2008.

[9] P. Stoica, H. He, and J. Li, "Optimization of the receive filter and transmit sequence for active sensing," *IEEE Transactions on Signal Processing*, vol. 60, no. 4, pp. 1730–1740, 2012.

[10] H. He, J. Li, and P. Stoica, *Wave form Design for Active Sensing Systems: A Computational Approach*. Cambridge University Press, 2012. [Online]. Available: https://books.google.co.in/books?id=syqYnQAACAAJ

[11] J. J. Benedetto, I. Konstantinidis, and M. Rangaswamy, "Phase-coded waveforms and their design," *IEEE Signal Processing Magazine*, vol. 26, no. 1, pp. 22–31, 2009.

[12] D. R. Hunter and K. Lange, "A tutorial on mm algorithms," *The American Statistician*, vol. 58, no. 1, pp. 30–37, 2004. [Online]. Available: https://doi.org/10.1198/0003130042836

[13] Y. Sun, P. Babu, and D. P. Palomar, "Majorization-minimization algorithms in signal processing, communications, and machine learning," *IEEE Transactions on Signal Processing*, vol. 65, no. 3, pp. 794–816, Feb 2017.

[14] L. Zhao, J. Song, P. Babu, and D. P. Palomar, "A unified framework for low autocorrelation sequence design via majorization-minimization," *IEEE Transactions on Signal Processing*, vol. 65, no. 2, pp. 438–453, Jan 2017.

[15] J. Song, P. Babu, and D. P. Palomar, "Optimization methods for designing sequences with low autocorrelation sidelobes," *IEEE Transactions on Signal Processing*, vol. 63, no. 15, pp. 3998–4009, Aug 2015.

[16] Y. Li and S. A. Vorobyov, "Fast algorithms for designing unimodular waveform(s) with good correlation properties," *IEEE Transactions on Signal Processing*, vol. 66, no. 5, pp. 1197–1212, March 2018.

[17] S. P. Sankuru and P. Babu, "Designing unimodular sequence with good auto-correlation properties via block majorization-minimization method," *Signal Processing*, vol. 176, p. 107707, 2020. [Online]. Available: https://www.sciencedirect.com/science/article/pii/S0165168420302504

[18] ——, "A fast iterative algorithm to design phase-only sequences by minimizing the isl metric," *Digital Signal Processing*, vol. 111, p. 102991, 2021. [Online]. Available: https://www.sciencedirect.com/science/article/pii/S1051200421000300

[19] S. P. Sankuru, P. Babu, and M. Alaee-Kerahroodi, "Unipol: Unimodular sequence design via a separable iterative quartic polynomial optimization for active sensing systems," *Signal Processing*, vol. 190, p. 108348, 2022. [Online]. Available: https://www.sciencedirect.com/science/article/pii/S0165168421003856

[20] D. Bertsekas, A. Nedić, and A. Ozdaglar, *Convex Analysis and Optimization*, ser. Athena Scientific optimization and computation series. Athena Scientific, 2003. [Online]. Available: https://books.google.co.in/books?id=DaOFQgAACAAJ

[21] MEISAM. RAZAVIYAYN, M. HONG, and ZHI-QUAN LUO, "A unified convergence analysis of block successive minimization methods for nonsmooth optimization," *SIAM Journal on Optimization*, vol. 23, no. 2, 2013.

[22] A. Aubry, A. De Maio, A. Zappone, M. Razaviyayn, and Z. Luo, "A new sequential optimization procedure and its applications to resource allocation for wireless systems," *IEEE Transactions on Signal Processing*, vol. 66, no. 24, pp. 6518–6533, 2018.

[23] A. Breloy, Y. Sun, P. Babu, and D. P. Palomar, "Block majorization-minimization algorithms for low-rank clutter subspace estimation," *2016 24th European Signal Processing Conference (EUSIPCO)*, pp. 2186–2190, Aug 2016.

[24] H. Wolkowicz and G. P. Styan, "Bounds for eigenvalues using traces," *Linear Algebra and its Applications*, vol. 29, pp. 471–506, 1980, special Volume Dedicated to Alson S. Householder. [Online]. Available: http://www.sciencedirect.com/science/article/pii/002437958090258X

[25] J. Song, P. Babu, and D. P. Palomar, "Sequence design to minimize the weighted integrated and peak sidelobe levels," *IEEE Transactions on Signal Processing*, vol. 64, no. 8, pp. 2051–2064, April 2016.

[26] P. Stoica, H. He, and J. Li, "New algorithms for designing unimodular sequences with good correlation properties," *IEEE Transactions on Signal Processing*, vol. 57, no. 4, pp. 1415–1425, April 2009.

[27] R. Jyothi, P. Babu, and M. Alaee-Kerahroodi, "SLOPE: A monotonic algorithm to design sequences with good autocorrelation properties by minimizing the peak sidelobe level," *Digital Signal Processing*, vol. 116, p. 103142, 2021. [Online]. Available: https://www.sciencedirect.com/science/article/pii/S1051200421001810

[28] S. Boyd, S. P. Boyd, and L. Vandenberghe, *Convex Optimization*. Cambridge university press, 2004.

[29] M. Grant and S. Boyd, "CVX: Matlab software for disciplined convex programming, version 2.1," http://cvxr.com/cvx, Mar. 2014.

[30] J. Von Neumann and O. Morgenstern, *Theory of Games and Economic Behavior*, ser. Science Editions. Princeton University Press, 1944. [Online]. Available: https://books.google.co.in/books?id=AUDPAAAAMAAJ

[31] A. Beck and M. Teboulle, "Mirror descent and nonlinear projected subgradient methods for convex optimization," *Oper. Res. Lett.*, vol. 31, no. 3, pp. 167–175, May 2003.

[32] R. Varadhan and C. Roland, "Simple and Globally Convergent Methods for Accelerating the Convergence of Any EM Algorithm," *Scandinavian Journal of Statistics*, vol. 35, no. 2, pp. 335–353, June 2008. [Online]. Available: https://ideas.repec.org/a/bla/scjsta/v35y2008i2p335-353.html

Chapter 5

BCD Method

BCD and block successive upper-bound minimization (BSUM) are two interesting optimization approaches that have gained a lot of attention in recent years in the context of waveform design and diversity. This chapter covers these simple yet effective strategies and illustrates how they might be used in real-world radar waveform design settings.

5.1 THE BCD METHOD

The BCD approach was among the first optimization schemes suggested for solving smooth unconstrained minimization problems because of its cheap iteration cost, minimal memory requirements, and excellent performance [1–3]. It is also a popular tool for big data optimization [4, 5].

The idea behind BCD is to partition the variable space into multiple variable blocks and then to alternatively solve the optimization problem with respect to one variable block at a time, while keeping the others fixed. This typically leads to subproblems that are significantly simpler than the original problem. If we optimize a single variable instead of a block of variables, the BCD method simplifies to the CD approach. Figure 5.1 illustrates the main idea of CD for minimizing a function of two variables, where we alternate between two search directions to minimize the objective function. The two-variable objective function is optimized in this way by looping through a set of possibly simpler uni-variate subproblems. This is the main advantage of the CD method, which endows simplicity to the optimization process.

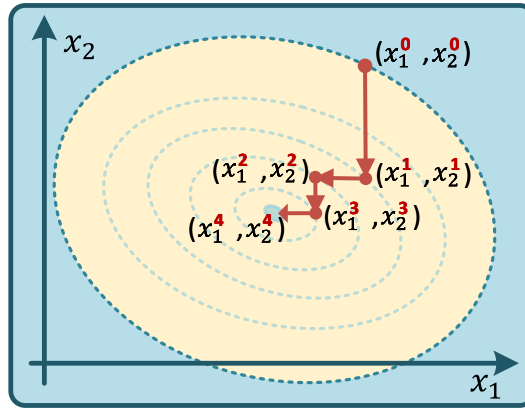

Figure 5.1. An illustration of the CD method for a two-dimensional problem. The contours of the objective function are shown by dashed curves, while the progress of the algorithm is represented by solid line arrows.

Consider the following block-structured optimization problem

$$\mathcal{P}_{\mathbf{x}} \begin{cases} \underset{\mathbf{x}_n}{\text{minimize}} & f(\mathbf{x}_1, \ldots, \mathbf{x}_N) \\ \text{subject to} & \mathbf{x}_n \in \mathcal{X}_n, \ \forall n = 1, \ldots, N \end{cases} \tag{5.1}$$

where $f(.) : \prod_{n=1}^{N} \mathcal{X}_n \to \mathbb{R}$ is a continuous function (possibly nonconvex, nonsmooth), each $\mathcal{X}_n$ is a closed convex set, and each $\mathbf{x}_n$ is a block variable, $n = 1, 2, \ldots, N$. The general idea of the BCD algorithm is to choose, at each iteration, an index n and change $\mathbf{x}_n$ such that the objective function decreases. Thus, by applying BCD to solve $\mathcal{P}_{\mathbf{x}}$, at every iteration i, N optimization problems, that is,

$$\mathcal{P}_{\mathbf{x}_n}^{(i+1)} \begin{cases} \underset{\mathbf{x}_n}{\text{minimize}} & f(\mathbf{x}_n; \mathbf{x}_{-n}^{(i)}) \\ \text{subject to} & \mathbf{x}_n \in \mathcal{X}_n \end{cases} \tag{5.2}$$

will be solved, where, at each $n \in \{1, \ldots, N\}$, $\mathbf{x}_n$ is the current optimization variable block, while $\mathbf{x}_{-n}^{(i)}$ denotes the rest of the variable blocks, whose its

definition (at a given iteration i) depends on the employed variable update rule, as detailed in the next subsection.

Choosing n can be as simple as cycling through the coordinates, or a more sophisticated coordinate selection rule can be employed. Using the cyclic selection rule, at the ith iteration the following subproblems will be solved iteratively,

$$
\begin{aligned}
\mathbf{x}_1^{(i+1)} &= \underset{\mathbf{x}_1 \in \mathcal{X}_1}{\arg\min} \; f(\mathbf{x}_1, \mathbf{x}_2^{(i)}, \mathbf{x}_3^{(i)}, \ldots, \mathbf{x}_N^{(i)}) \\
\mathbf{x}_2^{(i+1)} &= \underset{\mathbf{x}_2 \in \mathcal{X}_2}{\arg\min} \; f(\mathbf{x}_1^{(i+1)}, \mathbf{x}_2, \mathbf{x}_3^{(i)}, \ldots, \mathbf{x}_N^{(i)}) \\
\mathbf{x}_3^{(i+1)} &= \underset{\mathbf{x}_3 \in \mathcal{X}_3}{\arg\min} \; f(\mathbf{x}_1^{(i+1)}, \mathbf{x}_2^{(i+1)}, \mathbf{x}_3, \ldots, \mathbf{x}_N^{(i)}) \\
&\vdots \\
\mathbf{x}_N^{(i+1)} &= \underset{\mathbf{x}_N \in \mathcal{X}_N}{\arg\min} \; f(\mathbf{x}_1^{(i+1)}, \mathbf{x}_2^{(i+1)}, \mathbf{x}_3^{(i+1)}, \ldots, \mathbf{x}_N)
\end{aligned}
$$

Note that, in this case, updating the current block depends on the previously updated block. Algorithm 5.1 summarizes the BCD method where only a subset $\widetilde{N}$ of the variables are updated at each iteration. Precisely, at every iteration, the inner steps are performed until all entries of the set $\widetilde{N}$ are examined once, and then the set $\widetilde{N}$ can be updated/changed at each iteration. The entries of the set $\widetilde{N}$ are taken from $\{1, 2, \ldots, N\}$, with the

Algorithm 5.1: Sketch of the BCD Method

Result: Optimized decision vector $\mathbf{x}^\star$
Initialization;
for $i = 0, 1, 2, \ldots$ **do**
  Select indices order in the set $\widetilde{N}$;
  Optimize the nth coordinate $\forall n \in \widetilde{N}$, that is,
  $\mathbf{x}_n^{(i+1)} = \underset{\mathbf{x}_n \in \mathcal{X}_n}{\arg\min} \; f(\mathbf{x}_n; \mathbf{x}_{-n}^{(i)})$;
  Stop if convergence criterion is met;
end

indices-order chosen from the selection rules described next part.

5.1.1 Rules for Selecting the Index Set

Depending on the strategy used to create $\mathbf{x}_{-n}^{(i)}$ in Algorithm 5.1, there are two main classes for the updating rules: one-at-a-time and all-at-once [6, 7]. Several selection rules are introduced for the former; which are, generally, cyclic [2], randomized [4], and Greedy [8]. On the other end, the latter updates all the entries of the index set $\widetilde{N}$ in parallel, roughly with the same cost as a single variable update [9]. Below, more details for the aforementioned selection rules are given:

1. **One-at-a-time**: In this case, several ways are introduced to decide the indices order of the set $\widetilde{N}$ in every iteration, which are categorized in:

   (a) *Cyclic*: Through a fixed sort of coordinate block variables, the cyclic CD minimizes $f(.)$ repeatedly. As a result, if $\widetilde{N} = \{1, 2, \cdots, N\}$, x_1 changes first, then x_2, and so on through x_N. The procedure is then repeated, beginning with x_1[1] [2]. A variation of this is the Aitken double sweep method [12]. In this procedure, one searches over different x_n's back and forth, for example, set $\widetilde{N} = \{1, 2, \cdots, N\}$, in one iteration, and set $\widetilde{N} = \{N-1, N-2, \cdots, 1\}$, in the following iteration.

   (b) *Randomized*: In this case, the indices-order in $\widetilde{N}$ is picked according to a predefined probability distribution [13–15]. Choosing all blocks with equal probabilities should intuitively lead to similar results as the cyclic selection rule. However, it has been shown that CD with randomized selection rule can converge faster than cyclic selection rule, and hence, it might be preferable [15, 16].

   (c) *Greedy*:

      i. *Block coordinate gradient descent (CGD)*: If the gradient of the objective function is available, then it is possible to select the order of descent coordinates on the basis of the gradient. A popular technique is the *Gauss-Southwell (G-S)* method where at each stage the coordinate corresponding to the largest (in absolute value) component of the gradient vector is selected for descent, while the other blocks are fixed to the previous values [17].

1 If the block-wise minimizations are done using cyclic selection rule, then the BCD algorithm is known as the Gauss-Seidel algorithm [10], which is one of the oldest iterative algorithms and was proposed by Gauss and Seidel in the nineteenth century [11].

ii. *MBI*: It updates at each iteration only the variable block achieving the highest possible improvement on the objective function, while the other blocks are fixed to their previously computed values [8]. In general, the MBI rule is more expensive than the G-S rule because it involves the objective value computation. However, iterations of MBI are numerically more stable than gradient iterations, as observed in [18].

Before we end this section, it's worth noting that the cyclic and randomized rules have the advantage of not requiring any knowledge of the derivative or value of the objective function to identify the descent direction. However, greedy selection of variables is more expensive in the presence of a large number of variables, but it tends to be faster than cyclic or randomized selection of variables [19]. Furthermore, while the greedy updating rule can be implemented in parallel, cyclic and randomized rules cannot.

2. **All-at-once (Jacobi)**: When updating a specific coordinate, the Jacobi style fixes each of the other coordinates to be the corresponding solution at the previous iteration, that is, it does not account for intermediary steps until the complete update of all coordinates [9]. The major advantage of the Jacobi style is its intrinsic ability to perform coordinates update in parallel. However, convergence of the Jacobi algorithm is not guaranteed in general, even in the case when the objective function is smooth and convex, unless certain conditions are satisfied [7].

Remarkably, the CD method's complexity, convergence rate, and efficiency are all determined by the trade-off between the time spent selecting the variable to be updated in the current iteration and the quality of that selection in terms of function value improvement.

5.1.2 Convergence of BCD

The convergence of BCD is often analyzed when the one-at-a-time selection rule is chosen to update the variables [1, 2, 4, 6, 8, 10, 12, 16, 19–27]. In this case, the objective value is expected to decrease along iterations until convergence, as is specified below.

Convergence of the Objective Function $f(.)$

The monotonic property of the BCD technique illustrates that the objective function values are nondecreasing, that is,

$$f\left(\mathbf{x}^{(0)}\right) \geq f\left(\mathbf{x}^{(1)}\right) \geq f\left(\mathbf{x}^{(2)}\right) \geq \cdots \tag{5.3}$$

Thus, the sequence of objective values is guaranteed to converge as long as it is bounded below over the feasible set.

Convergence of the Decision Variables $\mathbf{x}_n$

Convergence of the variables in the coordinate descent method requires typically that $f(.)$ be strictly convex (or quasiconvex and hemivariate) differentiable [1, 2, 4, 6, 8, 10, 12, 16, 19–27]. In general, the strict convexity can be relaxed to pseudoconvexity, which allows $f(.)$ to have nonunique minimum along coordinate directions [21]. Indeed, this method can converge to the stationary point if the objective function is not convex, but satisfies some mild conditions itemized below:

- Using the MBI updating rule, which updates only the coordinate that provides the largest objective decrease at every iteration, the convergence of BCD to the stationary point can be guaranteed if the minimum with respect to each block of variables is unique [8].
- In cyclic and randomized selection rules, if the objective function:
  - is continuously differentiable over the feasible set;
  - has separable constraints;
  - has a unique minimizer at each step and for each coordinate;

  then BCD converges to the stationary point [21, 25].
- Assuming that $f(.)$ is continuous on a compact level set, the subsequence convergence of the iterates to a stationary point is shown when either $f(.)$ is pseudoconvex in every pair of coordinate blocks from among $N-1$ coordinate blocks or $f(.)$ has at most one minimum in each of $N-2$ coordinate blocks [21].

- If $f(.)$ is quasiconvex and hemivariate in every coordinate block, then the assumptions of continuity of $f(.)$ and compactness of the level set may be relaxed further [21].
- If $f(.)$ is continuous, and only two blocks are involved, then it does not require unique minimizer to converge to a stationary point [21].

Note that to guarantee the convergence in most of the aforementioned cases, $f(.)$ requires to be differentiable. If $f(.)$ is not differentiable, the BCD method may get stuck at a nonstationary point even when $f(.)$ is convex. Finally, if $f(.)$ is strictly convex and smooth, then the BCD algorithm converges to the global minimum (optimal solution) [21].

5.2 BSUM: A CONNECTION BETWEEN BCD AND MM

The BSUM framework provides a connection between BCD and MM[2], by successively optimizing a certain upper bound of the original objective in a coordinate-wise manner [3, 25]. The basic idea behind BSUM is to tackle a difficult problem by considering a sequence of approximate and easier problems, with objective and constraint functions that suitably upper-bound those of the original problem in the context of the minimization problems [28]. Let $f(.)$ be a multivariable continuous real function (possibly nonconvex, nonsmooth). The following optimization problem

$$\begin{cases} \underset{\mathbf{x}_n}{\text{minimize}} & f(\mathbf{x}_1, \mathbf{x}_2, \ldots, \mathbf{x}_N), \\ \text{subject to} & \mathbf{x}_n \in \mathcal{X}_n,\ n = 1, 2, \ldots, N \end{cases} \tag{5.4}$$

can be iteratively solved using the BSUM technique, by finding the solutions of the following subproblems for $i = 0, 1, 2, 3, \ldots$

$$\mathcal{P}_{\mathbf{x}_n}^{(i+1)} \begin{cases} \underset{\mathbf{x}_n}{\text{minimize}} & u_n(\mathbf{x}_n; \mathbf{x}_{-n}^{(i)}) \\ \text{subject to} & \mathbf{x}_n \in \mathcal{X}_n,\ \ n = 1, 2, \ldots, N \end{cases} \tag{5.5}$$

where $u_n(.)$ is the local approximation of the objective function, and $\mathbf{x}_{-n}^{(i)}$ represent all other variable blocks.

2 See Chapter 4 for further information about MM.

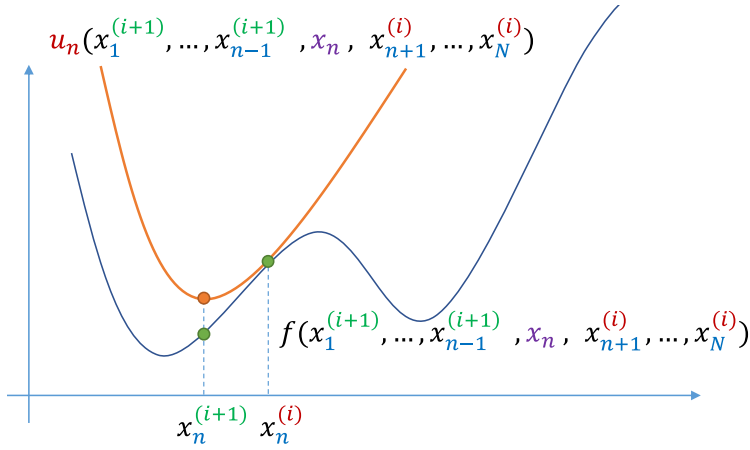

Figure 5.2. A pictorial illustration of the BSUM procedure.

The BSUM procedure is shown pictorially in Figure 5.2 and a sketch of the method is depicted in Algorithm 5.2, where only a subset $\widetilde{N}$ of the variables are updated at each iteration. The entries of the set $\widetilde{N}$ are taken from $\{1, 2, \cdots, N\}$, with the indices-order chosen from the selection rules described for the BCD method. The BSUM procedure consists of three main steps. In the first step, we select a variable block similar to the classical BCD. Next, we find a surrogate function that locally approximates the objective function, similar to the classical MM. Then, in the minimization step, we minimize the surrogate function.

5.3 APPLICATIONS

As discussed earlier, an interesting problem in radar waveform design is the design of sequences exhibiting small autocorrelation sidelobes that avoid masking weak targets and also mitigate the deleterious effects of distributed clutter. The well-known metrics that evaluate the goodness of waveform in this case (for radar pulse compression), are ISL and PSL. In the following we see how we can find the minimizer of ISL and PSL using the CD and successive upper-bound minimization (SUM) techniques. In addition to these examples, we further discuss on the effect of waveform design

Algorithm 5.2: Sketch of the BSUM Method

Result: Optimized code vector $\mathbf{x}^{\star}$
initialization;
for $i = 0, 1, 2, \ldots$ **do**
  Select indices-order in the set $\widetilde{N}$;
  Optimize the nth coordinate $\forall n \in \widetilde{n}$, that is,
  $$\mathbf{x}_n^{(i+1)} = \arg\min_{\mathbf{x}_n \in \mathcal{X}_n} u_n(\mathbf{x}_n; \mathbf{x}_{-n}^{(i)});$$
  Stop if convergence criterion is met;
end

for MIMO radar systems and show a trade-off via waveform correlation optimization between spatial- and range- ISLR.

5.3.1 Application 1: ISL Minimization

Let $\mathbf{x} = [x_1, x_2, \ldots, x_N]^T \in \mathbb{C}^N$ be the transmitted fast-time radar code vector with N being the number of coded subpulses (code length). By defining the operator $\circledast$ to denote the correlation, the aperiodic autocorrelation of $\mathbf{x}$ at lag k (e.g., matched filter output in pulse radars) is defined as,

$$(\mathbf{x} \circledast \mathbf{x})_k \equiv r_k = \sum_{n=1}^{N-k} x_n x_{n+k}^{*} \tag{5.6}$$

where $0 \leq k \leq N-1$, and $(.)^*$ denotes the complex conjugate. As discussed earlier in the previous chapter, the ISL can be mathematically defined by,

$$\text{ISL} = \sum_{k=1}^{N-1} |r_k|^2 \tag{5.7}$$

In many radar applications, it is desirable that the probing waveforms are constrained to be constant modulus to avoid distortions by the high-power amplifiers. Further, considering the implementation, we generally have no access to infinite precision numbers. Quantization of the optimized unimodular sequences to the discrete phase codes may be a solution, but bit truncation would distort the spectral shape and waveform envelope, which

will introduce amplitude fluctuations. Thus, a direct design of discrete phase sequences is required. In this case, the unimodular sequence design problem via ISL minimization can be formulated as:

$$\mathcal{P}_h \begin{cases} \underset{\mathbf{x}}{\text{minimize}} & \sum_{k=1}^{N-1} |r_k|^2 \\ \text{subject to} & x_n \in \Omega_h \end{cases} \tag{5.8}$$

where $h \in \{L, \infty\}$, and the constraints $\mathbf{x} \in \Omega_\infty$ and $\mathbf{x} \in \Omega_L$ identify continuous alphabet and finite alphabet codes, respectively. Precisely,

$$\Omega_\infty = \Big\{ \mathbf{x} \in \mathbb{C}^N | \; |x_n| = 1, \; n = 1, \ldots, N \Big\} \tag{5.9}$$

and

$$\Omega_L = \Big\{ \mathbf{x} \in \mathbb{C}^N | \; x_n \in \{1, e^{\mathrm{j}\frac{2\pi}{L}}, \ldots, e^{\mathrm{j}\frac{2\pi(L-1)}{L}}\}, \; n = 1, \ldots, N \Big\} \tag{5.10}$$

where L indicates the alphabet size for discrete phase sequence design problem. The above optimization problem is nonconvex and NP-hard in general. To find solution to this problem, one possible approach is to use the CD technique as described in this chapter.

5.3.1.1 Solution Using CD

According to the CD approach, the minimization of a multivariable function can be achieved by minimizing it along one direction at a time. In other words, we can sequentially optimize each element (e.g., x_n) by keeping the others fixed to monotonically decrease the objective value. This is the first step in the CD algorithm that converts a multivariable objective function to a sequence of single variable objective functions as described in Algorithm 5.1.

Let us assume that x_d is selected as the optimization variable in the code vector $\mathbf{x}$ at iteration $(i+1)$ of the CD algorithm. Then it can be shown that[3]

$$r_k(x_d) = a_{1k} x_d + a_{2k} x_d^* + a_{3k} \tag{5.11}$$

3 The dependency of r_k, x_d, and coefficients a_{1k}, a_{2k}, a_{3k} to iteration $(i+1)$ is omitted for simplicity of the notation.

where $a_{1k} = x^*_{d+k}\mathbf{I}_A(d+k)$, and $a_{2k} = x_{d-k}\mathbf{I}_A(d-k)$, with $\mathbf{I}_A(\nu)$ as the indicator function of the set $A = \{1, 2, \ldots, N\}$, that is,

$$\mathbf{I}_A(v) = \begin{cases} 1 & v \in A \\ 0 & \text{otherwise} \end{cases} \tag{5.12}$$

Also, by defining

$$\mathbf{x}_{-d} = \left[x_1^{(i+1)}, \ldots, x_{d-1}^{(i+1)}, 0, x_{d+1}^{(i)}, \ldots x_N^{(i+1)}\right]^T \in \mathbb{C}^N$$

we obtain $a_{3k} = (\mathbf{x}_{-d} \circledast \mathbf{x}_{-d})_k$. Thus, at iteration $(i+1)$ of the CD algorithm, the optimization problem is

$$\mathcal{P}_h^{(i+1)} \begin{cases} \underset{x_d}{\text{minimize}} & \displaystyle\sum_{k=1}^{N-1} \left|r_k(x_d)\right|^2 \\ \text{subject to} & x_d \in \Omega_h \end{cases}$$

To deal with the unimodularity constraint in the above problem, we can rewrite $r_k(x_d)$ as a function of ϕ_d, that is, $x_d = e^{j\phi_d}$:

$$\widetilde{r}_k(\phi_d) = a_{1k}e^{j\phi_d} + a_{2k}e^{-j\phi_d} + a_{3k} \tag{5.13}$$

As a result, the constraint can be incorporated in the optimization problem, and the optimal phase entry can be obtained by solving

$$\widetilde{\mathcal{P}}_h^{(i+1)} \begin{cases} \underset{\phi_d}{\text{minimize}} & \displaystyle\sum_{k=1}^{N-1} \left|\widetilde{r}_k(\phi_d)\right|^2 \\ \text{subject to} & \phi_d \in \arg(\Omega_h) \end{cases}$$

which is discussed in the following.

Solution to $\widetilde{\mathcal{P}}_\infty^{(i+1)}$

By performing the change of variable $\beta_d \triangleq \tan\left(\frac{\phi_d}{2}\right)$, we obtain

$$|\widetilde{r}_k(\phi_d)|^2 = \frac{\widetilde{p}_k(\beta_d)}{q(\beta_d)} \tag{5.14}$$

where

$$\widetilde{p}_k(\beta_d) = \mu_{1k}\beta_d^4 + \mu_{2k}\beta_d^3 + \mu_{3k}\beta_d^2 + \mu_{4k}\beta_d + \mu_{5k} \tag{5.15}$$

and

$$q(\beta_d) = (1+\beta_d^2)^2 \tag{5.16}$$

with μ_{ik}, $i = 1, 2, \ldots, 5$, as real-valued coefficients defined in Appendix 5A. Finally, the optimal $\beta_d^\star$ can be obtained by solving

$$\widetilde{\mathcal{P}}_{\infty,\beta_d}^{(i+1)} \begin{cases} \underset{\beta_d}{\text{minimize}} & \dfrac{\widetilde{p}_k(\beta_d)}{q(\beta_d)} \\ \text{subject to} & \beta_d \in \mathbb{R} \end{cases}$$

This problem can be solved by finding the real roots of a quartic function (related to the first-order derivative of the objective) and evaluating the objective function at these points as well as at infinity. Hence, the optimal phase code entry will be obtained by $x_d^\star = e^{j\phi_d^\star}$ where $\phi_d^\star = 2\tan^{-1}(\beta_d^\star)$.

Algorithm 5.3: CD-Based ISL Minimizer Under Continuous Phase Constraint

Result: Optimized code vector $\mathbf{x}^\star$
initialization;
for $i = 0, 1, 2, \ldots$ **do**
  for $d = 1, 2, \ldots, N$ **do**
    Set $a_{1k} = x_{d+k}^* \mathbf{I}_A(d+k)$, $a_{2k} = x_{d-k}\mathbf{I}_A(d-k)$;
    Set $a_{3k} = (\mathbf{x}_{-d} \circledast \mathbf{x}_{-d})_k$;
    Calculate μ_{tk}, $t = 1, 2, \ldots, 5$, according to Appendix 5A ;
    Find $\beta_d^\star$ by solving $\widetilde{\mathcal{P}}_{\infty,\beta_d}^{(i+1)}$;
    Set $\phi_d^\star = 2\tan^{-1}(\beta_d^\star)$, and $x_d^\star = e^{j\phi_d^\star}$;
  end
  Stop if convergence criterion is met;
end

Solution to $\widetilde{\mathcal{P}}_L^{(i+1)}$

In this case, by defining[4]

$$\boldsymbol{\zeta}_{dk} = \begin{cases} \left| \text{FFT}\left[a_{1k}, a_{3k}, a_{2k}, \mathbf{0}_{1\times(L-3)}\right]^T \right| \in \mathbb{R}^L & L \geq 3 \\ \left| \text{FFT}\left[a_{1k} + a_{2k}, a_{3k}\right]^T \right| \in \mathbb{R}^2 & L = 2 \end{cases} \tag{5.17}$$

and

$$\boldsymbol{\alpha}_{dk} = \sum_{k=1}^{N-1} \left(\boldsymbol{\zeta}_{dk} \odot \boldsymbol{\zeta}_{dk}\right) \in \mathbb{R}^L \tag{5.18}$$

the optimal $x_d^\star$ can be efficiently obtained by finding

$$\widetilde{l}^\star = \arg \min_{l=1,\ldots,L} \boldsymbol{\alpha}_{dk} \tag{5.19}$$

and setting $\phi_d^\star = \frac{2\pi(\widetilde{l}^\star - 1)}{L}$, $x_d^\star = e^{j\phi_d^\star}$.

Once the optimal code entry $x_d^\star$ is obtained (for either continuous phase or discrete phase cases), we repeat the procedure based on Algorithm 5.1, until all the entries of the code vector $\mathbf{x}$ are updated and a stopping criterion is met. A summary of the CD-based algorithms for ISL minimization under continuous and discrete phase constraints is, respectively, reported in Algorithm 5.3, and Algorithm 5.4.

5.3.1.2 Performance Analysis

We illustrate the performance of the CD-based method in ISL minimization via numerical experiments. Figure 5.3 shows the convergence curve of problems $\mathcal{P}_\infty$ and $\mathcal{P}_L$ for different initial sequences, including random sequence, Golomb,[5] and Frank;[6] at two different code lengths $N = 64$ and $N = 100$. It is clear to see that smaller values of alphabet size L lead to faster convergence but smaller sidelobes are obtained when the alphabet size is larger. Also, in all the cases, the algorithm converges monotonically to a local optimum.

4 The absolute is element-wise.

5 In case of sequence design with discrete phase constraint, we first quantize the initial sequence to the feasible alphabet set and then perform the optimization.

6 Frank sequence is only defined for perfect square lengths.

Algorithm 5.4: CD-Based ISL Minimizer Under Discrete Phase Constraint

Result: Optimized code vector $\mathbf{x}^\star$
initialization;
for $i = 0, 1, 2, \ldots$ **do**
  for $d = 1, 2, \ldots, N$ **do**
    Set $a_{1k} = x^*_{d+k}\mathbf{I}_A(d+k)$, $a_{2k} = x_{d-k}\mathbf{I}_A(d-k)$;
    Set $a_{3k} = (\mathbf{x}_{-d} \circledast \mathbf{x}_{-d})_k$;
    Calculate

$$\boldsymbol{\zeta}_{dk} = \begin{cases} \left|\text{FFT}\left[a_{1k}, a_{3k}, a_{2k}, \mathbf{0}_{1\times(L-3)}\right]^T\right| \in \mathbb{R}^L & L \geq 3, \\ \left|\text{FFT}\left[a_{1k} + a_{2k}, a_{3k}\right]^T\right| \in \mathbb{R}^2 & L = 2, \end{cases}$$

    Calculate $\boldsymbol{\alpha}_{dk} = \sum_{k=1}^{N-1} (\boldsymbol{\zeta}_{dk} \odot \boldsymbol{\zeta}_{dk})$;
    Find $\widetilde{l}^\star = \arg\min_{l=1,\ldots,L} \boldsymbol{\alpha}_{dk}$;
    Set $\phi^\star_d = \frac{2\pi(\widetilde{l}^\star - 1)}{L}$, and $x^\star_d = e^{j\phi^\star_d}$;
  end
  Stop if convergence criterion is met;
end

5.3.2 Application 2: PSL Minimization

PSL shows the maximum autocorrelation sidelobe of a transmit waveform and mathematically is defined as

$$\text{PSL} = \underset{k=1,2,\ldots,N-1}{\text{maximum}} |r_k| \tag{5.20}$$

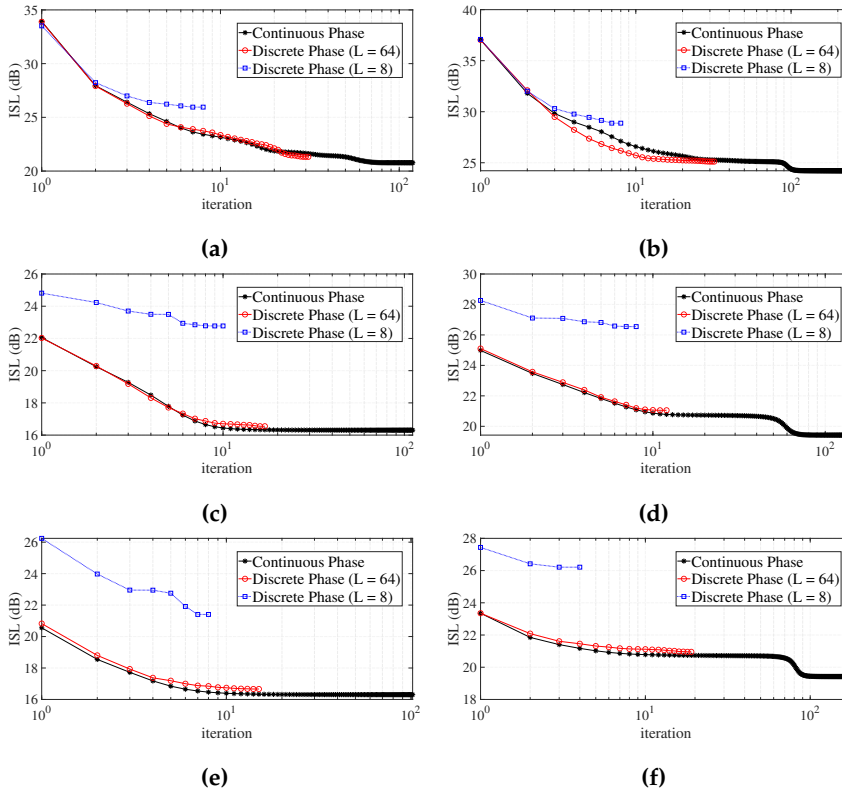

Figure 5.3. Convergence of CD-based algorithms for ISL minimization using different initialization. (a) Random initialization ($N = 64$), (b) Random initialization ($N = 100$), (c) Golomb initialization ($N = 64$), (d) Golomb initialization ($N = 100$), (e) Frank initialization ($N = 64$), (f) Frank initialization ($N = 100$).

For this case, the unimodular sequence design problem using PSL minimization can be formulated as

$$\mathcal{Q}_h \begin{cases} \underset{\mathbf{x}}{\text{minimize}} & \underset{k=1,2,\ldots,N-1}{\text{maximum}} |r_k| \\ \text{subject to} & x_n \in \Omega_h \end{cases} \tag{5.21}$$

where $h \in \{L, \infty\}$, and the constraints $\mathbf{x} \in \Omega_\infty$ and $\mathbf{x} \in \Omega_L$ are defined in (5.9) and (5.10), respectively. Similar to the previous example, Problem $\mathcal{Q}_L$ can be iteratively solved by modifying

$$\boldsymbol{\alpha}_{dk} = \underset{k=1,\ldots,N-1}{\text{maximum}} \left(\boldsymbol{\zeta}_{dk}\right) \in \mathbb{R}^L \tag{5.22}$$

calculating

$$\widetilde{l}^\star = \arg \min_{l=1,\ldots,L} \boldsymbol{\alpha}_{dk} \tag{5.23}$$

and setting $\phi_d^\star = \frac{2\pi(\widetilde{l}^\star - 1)}{L}$, and $x_d^\star = e^{j\phi_d^\star}$. However, a CD-based solution to problem $\mathcal{Q}_\infty$ needs additional steps like the procedure provided in [29] which deploys the bisection method. An alternative way is to minimize the ℓ_p-norm of autocorrelation sidelobes instead of directly minimizing the PSL, which is a very interesting design objective that by choosing different values of p trade-offs between good PSL or good ISL. Specifically, as $p \to +\infty$, the ℓ_p-norm metric boils down to an l_∞-norm of the autocorrelation sidelobes, which coincides with the PSL. In this case, unimodular sequence design problem can be formulated as

$$\widetilde{\mathcal{Q}}_h \begin{cases} \underset{\mathbf{x}}{\text{minimize}} & \displaystyle\sum_{k=1}^{N-1} |r_k|^p \\ \text{subject to} & x_n \in \Omega_h \end{cases} \tag{5.24}$$

The above optimization problem is nonconvex, and NP-hard in general. A possible solution for this problem is to find a surrogate function and then minimize it iteratively, an idea that was described in the SUM algorithm.

5.3.2.1 Solution Using SUM

In the following, we provide the solution to problem[7] $\widetilde{\mathcal{Q}}_\infty$. To this end, we use a quadratic majorizer as the surrogate function for $|r_k|^p$. Notice that, there is no quadratic majorizer of $|r_k|^p$ globally when $p > 2$. However, we can still majorize it by a quadratic function locally, by which the SUM framework still holds as long as the objective decreases along the iterations. The construction of the local majorizer is based on the following lemma [30].

Lemma 5.1. *Let $f(x) = x^p$ with $p \geq 2$ and $x \in [0, t]$. Then for any given $x_0 \in [0, t)$, $f(x)$ is majorized at x_0 over the interval $[0, t]$ by*

$$u(x) = ax^2 + \left(px_0^{p-1} - 2ax_0\right)x + ax_0^2 - (p-1)x_0^p \tag{5.25}$$

with

$$a = \frac{t^p - x_0^p - px_0^{p-1}(t - x_0)}{(t - x_0)^2} \tag{5.26}$$

Given $\left|r_k^{(\ell)}\right|$ at the ℓth iteration, according to Lemma 5.1, $|r_k|^p$ is majorized at $\left|r_k^{(\ell)}\right|$over $[0, t]$ by

$$u\left(|r_k|\right) = a_k |r_k|^2 + b_k |r_k| + \left(a\left|r_k^{(\ell)}\right|^2 - (p-1)\left|r_k^{(\ell)}\right|^p\right) \tag{5.27}$$

where

$$a_k = \frac{t^p - \left|r_k^{(\ell)}\right|^p - p\left|r_k^{(\ell)}\right|^{p-1}\left(t - \left|r_k^{(\ell)}\right|\right)}{\left(t - \left|r_k^{(\ell)}\right|\right)^2} \tag{5.28}$$

$$b_k = p\left|r_k^{(\ell)}\right|^{p-1} - 2a_k\left|r_k^{(\ell)}\right| \tag{5.29}$$

As illustrated above, (5.27) is the local majorizer over $[0, t]$, and we need to find a value of t so that the objective is guaranteed to decrease. Within the SUM framework, we have $\sum_{k=1}^{N-1}|r_k|^p \leq \sum_{k=1}^{N-1}\left|r_k^{(\ell)}\right|^p$, which implies

7 The solution to $\widetilde{\mathcal{Q}}_L$ can be directly obtained using the CD approach and a straightforward modification in (5.18).

$|r_k|^p \leq \left(\sum_{k=1}^{N-1} \left|r_k^{(\ell)}\right|^p\right)^{\frac{1}{p}}$. Therefore, we can choose $t = \left(\sum_{k=1}^{N-1} \left|r_k^{(\ell)}\right|^p\right)^{\frac{1}{p}}$ in (5.28). The majorized problem of $\widetilde{\mathcal{Q}}_\infty$ is given by, ignoring the constant term,

$$\mathcal{H}_\infty \begin{cases} \min\limits_{\mathbf{x}} & \sum\limits_{k=1}^{N-1} a_k |r_k|^2 + \sum\limits_{k=1}^{N-1} b_k |r_k| \\ s.t. & |x_n| = 1, n = 1, \ldots, N \end{cases} \tag{5.30}$$

As to the second term of the objective function in (5.30), since $b_k \leq 0$, we have

$$\sum_{k=1}^{N-1} b_k |r_k| \leq \sum_{k=1}^{N-1} b_k \Re\left\{ r_k^* \frac{r_k^{(\ell)}}{\left|r_k^{(\ell)}\right|} \right\} \tag{5.31}$$

where $b_{-k} = b_k$ for $k = 1, \ldots, N-1$ and $b_0 = 0$. Note that the equality of (5.31) holds when $\mathbf{x} = \mathbf{x}^{(\ell)}$, which shows that $\sum_{k=1}^{N-1} b_k \Re\left\{ r_k^* \frac{r_k^{(\ell)}}{\left|r_k^{(\ell)}\right|} \right\}$ is a majorizer of $\sum_{k=1}^{N-1} b_k |r_k|$. Thus, the optimization problem can be simplified to

$$\widetilde{\mathcal{H}}_\infty \begin{cases} \min\limits_{\mathbf{x}} & \sum\limits_{k=1}^{N-1} a_k |r_k|^2 + \sum\limits_{k=1}^{N-1} b_k \Re\left\{ r_k^* \frac{r_k^{(\ell)}}{\left|r_k^{(\ell)}\right|} \right\} \\ s.t. & |x_n| = 1, n = 1, \ldots, N \end{cases} \tag{5.32}$$

Let us assume that x_d is selected as the optimization variable in the code vector $\mathbf{x}$ at iteration $(i+1)$ of the SUM algorithm. Then, by using (5.11) and (5.13), the optimization problem under the unimodularity constraint is

$$\widetilde{\mathcal{H}}_\infty^{(i+1)} \begin{cases} \min\limits_{\phi_d} & \sum\limits_{k=1}^{N-1} a_k \left|\widetilde{r}_k(\phi_d)\right|^2 + \sum\limits_{k=1}^{N-1} b_k \Re\left\{ \widetilde{r}_k(\phi_d)^* \frac{r_k^{(\ell)}}{\left|r_k^{(\ell)}\right|} \right\} \\ s.t. & \phi_d \in [-\pi, \pi) \end{cases}$$

Thus, by making the change of the variable $\beta_d \triangleq \tan\left(\frac{\phi_d}{2}\right)$, we obtain

$$\Re\left\{\widetilde{r}_k^*(\beta_d)\frac{r_k^{(i)}}{\left|r_k^{(i)}\right|}\right\} = \frac{\bar{p}_k(\beta_d)}{q(\beta_d)} \tag{5.33}$$

where

$$\bar{p}_k(\beta_d) = \kappa_{1k}\beta_d^4 + \kappa_{2k}\beta_d^3 + \kappa_{3k}\beta_d^2 + \kappa_{4k}\beta_d + \kappa_{5k} \tag{5.34}$$

with κ_{ik}, $i = 1, 2, \ldots, 5$, being real-valued coefficients that are defined in Appendix 5B. By performing similar steps to *Solution to* $\widetilde{\mathcal{P}}_\infty^{(i+1)}$, the optimal $\beta_d^\star$ can be obtained by solving

$$\widetilde{\mathcal{H}}_{\infty,\beta_d}^{(i+1)} \begin{cases} \min\limits_{\beta_d} & \dfrac{1}{q(\beta_d)} \displaystyle\sum_{k=1}^{N-1} \left\{a_k\widetilde{p}_k(\beta_d) + b_k\bar{p}_k(\beta_d)\right\} \\ s.t. & \beta_d \in \mathbb{R} \end{cases}$$

Hence, the optimal phase code entry will be obtained by $x_d^\star = e^{j\phi_d^\star}$ where $\phi_d^\star = 2\tan^{-1}(\beta_d^\star)$.

Algorithm 5.5: SUM-Based PSL Minimizer Under Continuous Phase Constraint

Result: Optimized code vector $\mathbf{x}^\star$
initialization;
for $i = 0, 1, 2, \ldots$ **do**
  for $d = 1, 2, \ldots, N$ **do**
    Set $a_{1k} = x_{d+k}^*\mathbf{I}_A(d+k)$, $a_{2k} = x_{d-k}\mathbf{I}_A(d-k)$;
    Set $a_{3k} = (\mathbf{x}_{-d} \circledast \mathbf{x}_{-d})_k$;
    Calculate μ_{tk}, $t = 1, 2, \ldots, 5$, based on Appendix 5A;
    Calculate κ_{ik}, $i = 1, 2, \ldots, 5$, based on Appendix 5B;
    Find $\beta_d^\star$ by solving $\widetilde{\mathcal{H}}_{\infty,\beta_d}^{(i+1)}$;
    Set $\phi_d^\star = 2\tan^{-1}(\beta_d^\star)$, and $x_d^\star = e^{j\phi_d^\star}$;
  end
  Stop if convergence criterion is met;
end

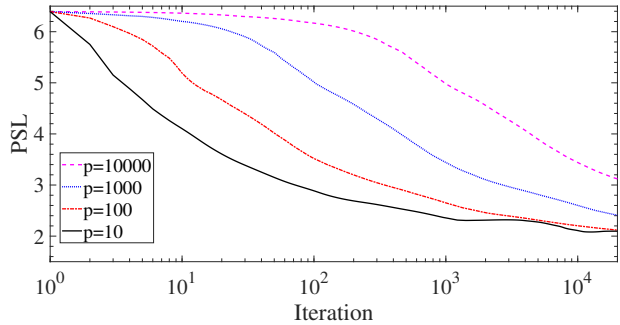

Figure 5.4. Convergence plot of the CD for designing a unimodular code at length $N = 400$ in different values of p. The algorithm is initialized by the Frank sequence.

5.3.2.2 Performance Analysis

Figure 5.4 shows the convergence behavior of problem $\mathcal{Q}_\infty$, for different values of p at the first 2×10^4 iterations. It is clear to see that smaller values of p lead to faster convergence and may not decrease the PSL at a later stage. This may be explained by the fact that the ℓ_p-norm with larger p approximates the ℓ_∞-norm better. Thus, gradually increasing the value of p and using the sequence for small p as the initial one for large p is probably a good approach to obtain very small PSL values.

Recall that problem $\mathcal{Q}_\infty$ is reduced to the ISL minimization and the PSL minimization when $p = 2$ and $+\infty$, respectively. In Figure 5.5, we compare the ISL and PSL minimization, where the PSL minimization is approximated by setting $p = 1000$. In this figure, we define the correlation level by

$$\text{Correlation level (dB)} = 20 \log_{10} \frac{|r_k|}{N} \tag{5.35}$$

The initial sequence is Frank, and the adopted code length is $N = 400$. The sidelobe level of the PSL minimization is flatter than the ISL minimization, as shown in this figure, which is consistent with the interpretation of the optimization metrics.

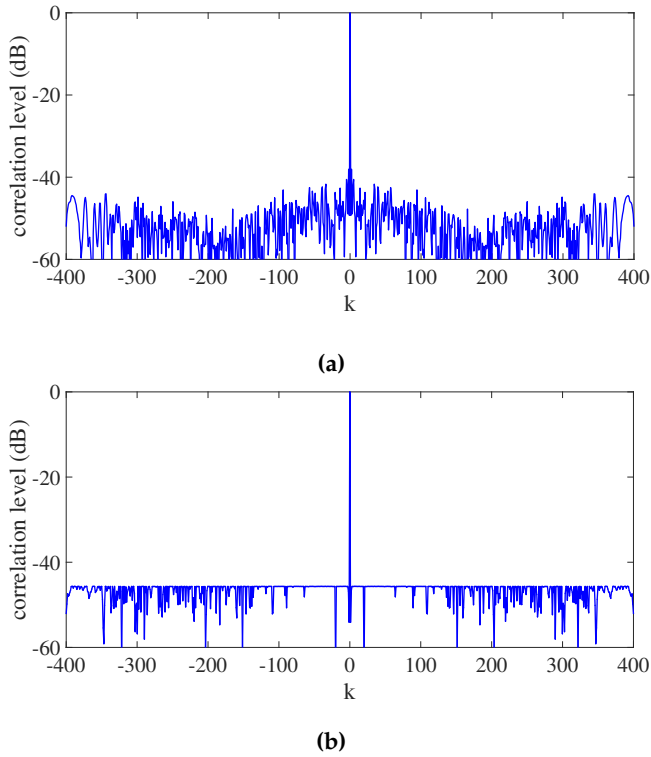

Figure 5.5. Autocorrelation comparison for designing unimodular codes at length $N = 400$. In the case of $p = 2$, the optimized sequences have small ISL and in the case of $p = 1000$ the optimized codes have low PSL. The algorithm is initialized by the Frank sequence. (a) SUM ($p = 2$), (b) SUM ($p = 1000$).

5.3.3 Application 3: Beampattern Matching in MIMO Radars

Waveform design in colocated MIMO radars can be split into two categories: uncorrelated and correlated waveform sets. In the first group, waveform optimization is being performed in order to provide a set of nearly orthogonal sequences to exploit the advantages of the largest possible virtual aperture. In this case, the sequences in the waveform set need to be orthogonal to one another in order to be separated on the received side [31]. In the second category, a correlated set of waveforms creates a directed probing beampattern [32]. Because just the waveform correlation matrix needs to be optimized in this case, phase shifters on both sides of the transmit and receive arrays can be removed, saving hardware costs, which is crucial in applications such as automotive where mass manufacturing is desired. As a result, the probing signal can be used to improve radar performance by enhancing the SINR through beampattern shaping. Beampattern matching, which is addressed in this section, is one way for controlling the directionality of the transmit waveforms with the purpose of minimizing the difference between the beampattern response and the desired beampattern.

5.3.3.1 System Model

Let the transmitted waveforms in a MIMO radar system with M transmit antennas be $\mathbf{X} \in \mathbb{C}^{M \times N}$, where every antenna is transmitting an arbitrary phase code of length N. At time sample n, we assume that the transmitted waveform across all M antennas is $\mathbf{x}_n$, precisely

$$\mathbf{x}_n = [x_{1,n}, x_{2,n}, \ldots, x_{M,n}]^T \in \mathbb{C}^M \tag{5.36}$$

where $x_{m,n}$ denotes the n^{th} sample of the m^{th} transmitted waveform. Let uniform linear array (ULA) be the configuration of the transmit antennas, where the distance between the elements are $d_t = \frac{\lambda}{2}$. Thus, the steering vector of the transmit array can be written as [33]:

$$\mathbf{a}(\theta) = [1, e^{j\pi \sin(\theta)}, \ldots, e^{j\pi(M-1)\sin(\theta)}]^T \in \mathbb{C}^M. \tag{5.37}$$

In this case, the radiated power in the spatial domain is given by [34]

$$p(\mathbf{X}, \theta) = \sum_{n=1}^{N} \left|\mathbf{a}^H(\theta)\mathbf{x}_n\right|^2 = \sum_{n=1}^{N} \mathbf{x}_n^H \mathbf{A}(\theta)\mathbf{x}_n \tag{5.38}$$

where $\mathbf{A}(\theta) \triangleq \mathbf{a}(\theta)\mathbf{a}^H(\theta)$. The problem of beampattern matching for MIMO radar systems under continuous and discrete phase constraints can be described as follows [35]

$$\begin{cases} \underset{\mathbf{X},\mu}{\text{minimize}} & f(\mathbf{X},\mu) \triangleq \sum_{k=1}^{K} |p(\mathbf{X},\theta_k) - \mu q_k|^2 \\ \text{subject to} & x_{m,n} = e^{j\phi}, \quad \phi \in \Phi_\infty \text{ or } \Phi_L \end{cases} \tag{5.39}$$

where q_k is the desired beampattern, μ is a scaling factor, and $\Phi_\infty = [0, 2\pi)$, and $\Phi_L = \left\{0, \frac{2\pi}{L}, \ldots, \frac{2\pi(L-1)}{L}\right\}$, which indicates the M-ary phase shift keying (MPSK) alphabet.

It is possible to conclude that the objective function in (5.39) is a quartic function with respect to variable $\mathbf{X}$ by substituting (5.38) in it. However, the equality constraint in (5.38) is not a affine set. Therefore, we encounter a nonconvex optimization problem with respect to variable $\mathbf{X}$. However, with respect to variable μ, the objective function is quadratic and the constraints do not depend on the variable. Thus, the optimization problem with respect to μ is convex. To address the above problem, one possible solution is to use the BCD algorithm with two blocks, such as the alternative optimization strategy [36], in which we alternate on the optimization variables μ and $\mathbf{X}$ while keeping the other fixed. This is described in the following.

Optimizing with Respect to Scaling Factor μ

The objective function in (5.39) has a quadratic form with respect to μ and is convex. Thus, the optimal value of μ can be obtained by finding the roots of the derivative of the objective function [35]:

$$\mu^\star = \frac{\sum_{k=1}^{K} q_k p(\mathbf{X},\theta_k)}{\sum_{k=1}^{K} q_k^2} \tag{5.40}$$

Optimizing with Respect to the Waveform Code Matrix $\mathbf{X}$

Using the CD framework presented earlier in this chapter, let us assume that $x_{t,d}^{(i)} = e^{j\phi_{t,d}^{(i)}}$ is the only variable in the code matrix $\mathbf{X}$ at ith iteration. The objective function of (5.39) with respect to $\phi_{t,d}^{(i)}$ can be written equivalently

as [37]:

$$f(\mu^\star, \phi_{t,d}^{(i)}) = \sum_{k=1}^{K} (b_{1,k}^{(i)} e^{j\phi_{t,d}^{(i)}} + b_{0,k}^{(i)} + b_{-1,k}^{(i)} e^{-j\phi_{t,d}^{(i)}} - \mu^\star q_k)^2 \tag{5.41}$$

Thus, the optimization variable with respect to $\phi_{t,d}^{(i)}$ at ith iteration is

$$\begin{cases} \underset{\phi_{t,d}^{(i)}}{\text{minimize}} & f(\mu^\star, \phi_{t,d}^{(i)}) \\ \text{subject to} & \phi_{t,d}^{(i)} \in \Phi_\infty \text{ or } \Phi_L \end{cases} \tag{5.42}$$

where

$$\begin{aligned} b_{1,k}^{(i)} &\triangleq \sum_{\substack{m=1 \\ m\neq t}}^{M} x_{m,d}^* a_{k_{m,t}}, \quad b_{-1,k}^{(i)} \triangleq b_{1,k}^*, \\ b_{0,k}^{(i)} &\triangleq a_{k_{t,t}} + \sum_{\substack{n=1 \\ n\neq d}}^{N} \mathbf{x}_n^H \mathbf{A}(\theta_k) \mathbf{x}_n + \sum_{\substack{m=1 \\ m\neq t}}^{M} \sum_{\substack{l=1 \\ l\neq t}}^{M} x_{m,d}^* a_{k_{m,l}} x_{l,d} \end{aligned} \tag{5.43}$$

and $a_{k_{m,l}}$ is the $(m,l)th$ entry of matrix $\mathbf{A}(\theta_k)$.

In the sequel, we use ϕ instead of $\phi_{t,d}$ for the convenience, without loss of the generality. To find the solution under Φ_∞ constraint , we expand $f(\mu^\star, \phi)$ according to Appendix 5C, and obtain

$$f(\mu^\star, \phi) = \sum_{n=-2}^{2} c_n^{(i)} e^{jn\phi} \tag{5.44}$$

The objective function in this case has at least two extrema (because it is periodic and real). As a result, its derivative has at least two true roots which can be obtained by

$$\frac{df(\mu^\star, \phi)}{d\phi} = j \sum_{n=-2}^{2} n c_n^{(i)} e^{jn\phi} \tag{5.45}$$

Using the slack variable $z \triangleq e^{-j\phi}$, the critical points can be obtained by calculating the roots of the polynomial $\frac{df(\mu^\star,\phi)}{d\phi}$. Let z_n, $n = \{-2, \ldots, 2\}$

be the roots of $\frac{df(\mu^\star,\phi)}{d\phi}$. Therefore, the critical points are $\phi_n = j \ln z_n$. Subsequently, the optimum $\phi^\star$ can be obtained by

$$\phi^\star = \arg\min_{\phi} \left\{ f(\mu^\star, \phi) \,|\, \phi \in \phi_n, n = \{-2, \ldots, 2\} \right\} \tag{5.46}$$

In the case of the discrete phase signal constraint, the phase values are limited to be drawn from a specific alphabet. The objective function in its discrete form can be expressed as

$$f(\mu^\star, l) = e^{j\frac{4\pi l}{L}} \sum_{n=0}^{4} v_n e^{-j\frac{2\pi n l}{L}} \tag{5.47}$$

where $l \in \{0, \ldots, L-1\}$. The summation part of (5.47) is the definition of L-points discrete Fourier transform (DFT) of sequence $[v_0, \ldots, v_4]^T$. Therefore, assuming $L \geqslant 5$, (5.47) can be rewritten equivalently as

$$f(\mu^\star, l) = \mathbf{h}_L \odot \mathcal{F}_L\{v_0, v_1, v_2, v_3, v_4\} \tag{5.48}$$

where $\mathbf{h}_L = [1, e^{j\frac{4\pi}{L}}, \ldots, e^{j\frac{4\pi(L-1)}{L}}]^T \in \mathbb{C}^L$, and $\mathcal{F}_L$ is $L-$point DFT operator. Due to the periodic property of the DFT, $f(\mu^\star, l)$ for $L = 2, 3, 4$ is given by

$$\begin{aligned}
L = 4 &\Rightarrow f(\mu^\star, l) = \mathbf{h}_L \odot \mathcal{F}_L\{v_0 + v_4, v_1, v_2, v_3\} \\
L = 3 &\Rightarrow f(\mu^\star, l) = \mathbf{h}_L \odot \mathcal{F}_L\{v_0 + v_3, v_1 + v_4, v_2\} \\
L = 2 &\Rightarrow f(\mu^\star, l) = \mathbf{h}_L \odot \mathcal{F}_L\{v_0 + v_2 + v_4, v_1 + v_3\}
\end{aligned}$$

Finally, the solution for discrete phase code design can be obtained by

$$l^\star = \arg\min_{l=1,\ldots,L} \left\{ f(\mu^\star, l) \right\} \tag{5.49}$$

Subsequently, the optimum phase is,

$$\phi^\star = \frac{2\pi(l^\star - 1)}{L} \tag{5.50}$$

Once $\phi^\star$ was obtained, we set $x^\star_{t,d} = e^{j\phi^\star}$ and repeat the procedure for all values of t and d. The design method is summarized in Algorithm 5.6.

Algorithm 5.6: CD Method for Beampattern Matching

Result: Optimized code vector $\mathbf{x}^\star$
initialization;
for $i = 0, 1, 2, \ldots$ **do**
  Find the optimum $\mu^\star$ using (5.40);
  for $d = 1, 2, \ldots, N$ **do**
    for $t = 1, 2, \ldots, M$ **do**
      Calculate the optimization coefficients using (5.43);
      Find the optimal $\phi^\star$ based on (5.46) or (5.50);
      Find the optimal code entry $x^\star_{t,d} = e^{j\phi^\star}$;
      Set $\mathbf{X}^{(i+1)} = \mathbf{X}^{(i)}|_{x_{t,d}=x^\star_{t,d}}$;
    end
  end
  Stop if convergence criterion is met;
end

5.3.3.2 Numerical Results

In this section, we present some representative numerical examples to demonstrate the capability of the CD method in shaping the transmit beampattern. We consider a ULA configuration with $M = 16$ transmitters and $N = 64$ pulses. We set $\Delta\mathbf{X}^{(i)} = \left\|\mathbf{X}^{(i)} - \mathbf{X}^{(i-1)}\right\|_F \leq \zeta = 10^{-3}$ as the stopping condition in Algorithm 5.6.

Figure 5.6 depicts convergence behavior of the CD-based algorithm in two aspects, namely, the objective function and the argument. In this figure, we assume that the desired angles are located at $[-15^o, 15^o]$ and the algorithm is initialized with random MPSK sequence with an alphabet size of $L = 4$. It can be observed that for all the alphabet sizes, the objective function decreases monotonically. By increasing the alphabet size of the waveform, the feasible set of the problem increases; therefore, the performance of the method improves.

The obtained beampattern in this case is illustrated in Figure 5.7. Observe that increasing the alphabet size causes the optimized beampattern to better match the desired response.

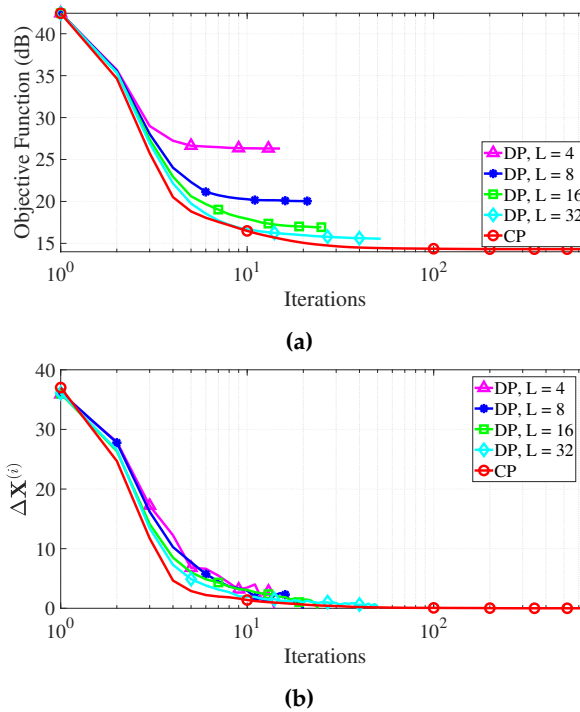

Figure 5.6. Convergence of CD-based algorithms for beampattern matching problem. (a) Convergence of the objective function, (b) Convergence of the argument.

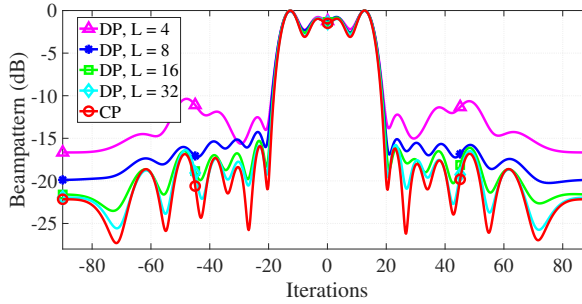

Figure 5.7. Comparison of the beampattern response of the CD-based method under continuous and discrete phase setting, with different alphabet sizes.

5.4 CONCLUSION

In this chapter, the principle behind CD and SUM with different flavors of the algorithms and different update rules was discussed. Further, three applications indicating the performance of the introduced optimization tools for different radar waveform design problems was described. In the first and second applications, synthesis of phase sequences exhibiting good aperiodic correlation features was addressed. Specifically, ISL and PSL were adopted as performance metrics and the design problem was formulated where either a continuous or a discrete phase constraint was imposed at the design stage. The emerging nonconvex and, in general, NP-hard problems were handled via CD and SUM methods; in each of their steps, we utilized an effective method to minimize the objective functions. In the third application, we considered the design of transmit waveforms for MIMO radar systems by considering shaping of the transmit beampattern. The problem formulation led to a nonconvex, multivariable and NP-hard optimization problem, and to tackle the problem, we used the CD technique.

5.5 EXERCISE PROBLEMS

Q1. In application 1 of this chapter, the waveform is designed by minimizing aperiodic correlation sidelobes.

- How can the coefficients a_{1k}, a_{2k}, and a_{3k} in (5.11) be adapted to optimize sequences with small periodic autocorrelation sidelobes?

Q2. In application 2 of this chapter, two problems $\mathcal{Q}_L$ and $\widetilde{\mathcal{Q}}_L$ are defined whose solutions are not given. However, following similar steps as those of the solution for $\mathcal{P}_L$, the aforementioned problems can also be solved.

- How will the solution to $\mathcal{Q}_L$ be different from the solution to $\widetilde{\mathcal{Q}}_L$? Which one will provide a smaller PSL value in general?
- Validate your response with a simulation for obtaining both the aforementioned solutions when the optimization starts with an identical initial sequence.

References

[1] D. P. Bertsekas, "Nonlinear programming," *Journal of the Operational Research Society*, vol. 48, no. 3, pp. 334–334, 1997.

[2] S. J. Wright, "Coordinate descent algorithms," *Mathematical Programming*, vol. 151, no. 1, pp. 3–34, 2015.

[3] M. Hong, M. Razaviyayn, Z. Luo, and J. Pang, "A unified algorithmic framework for block-structured optimization involving big data: With applications in machine learning and signal processing," *IEEE Signal Processing Magazine*, vol. 33, no. 1, pp. 57–77, 2016.

[4] Y. Nesterov, "Efficiency of coordinate descent methods on huge-scale optimization problems," *SIAM Journal on Optimization*, vol. 22, no. 2, pp. 341–362, 2012.

[5] P. Richtárik and M. Takáč, "Parallel coordinate descent methods for big data optimization," *Mathematical Programming*, vol. 156, pp. 433–484, Mar 2016.

[6] J. Friedman, T. Hastie, H. Höfling, and R. Tibshirani, "Pathwise coordinate optimization," *The Annals of Applied Statistics*, vol. 1, no. 2, pp. 302 – 332, 2007.

[7] G. Banjac, K. Margellos, and P. J. Goulart, "On the convergence of a regularized Jacobi algorithm for convex optimization," *IEEE Transactions on Automatic Control*, vol. 63, no. 4, pp. 1113–1119, 2018.

[8] B. Chen, S. He, Z. Li, and S. Zhang, "Maximum block improvement and polynomial optimization," *SIAM Journal on Optimization*, vol. 22, pp. 87–107, Jan 2012.

[9] O. Fercoq and P. Richtárik, "Accelerated, parallel, and proximal coordinate descent," *SIAM Journal on Optimization*, vol. 25, no. 4, pp. 1997–2023, 2015.

[10] H. Attouch, J. Bolte, and B. F. Svaiter, "Convergence of descent methods for semi-algebraic and tame problems: proximal algorithms, forward–backward splitting, and regularized Gauss–Seidel methods," *Mathematical Programming*, vol. 137, pp. 91–129, Feb 2013.

[11] A. Greenbaum, *Iterative Methods for Solving Linear Systems*. Society for Industrial and Applied Mathematics, 1997.

[12] Y. Y. David G. Luenberger, *Linear and Nonlinear Programming*. International series in operations research and management science, Springer, 2008.

[13] Y. Nesterov and S. U. Stich, "Efficiency of the accelerated coordinate descent method on structured optimization problems," *SIAM Journal on Optimization*, vol. 27, no. 1, pp. 110–123, 2017.

[14] D. Leventhal and A. S. Lewis, "Randomized methods for linear constraints: Convergence rates and conditioning," *Mathematics of operations research*, vol. 35, no. 3, pp. 641–654, 2010.

[15] R. Sun and Y. Ye, "Worst-case complexity of cyclic coordinate descent: $O(n^2)$ gap with randomized version," *Mathematical Programming*, vol. 185, pp. 487–520, Jan 2021.

[16] P. Richtárik and M. Takáč, "Iteration complexity of randomized block-coordinate descent methods for minimizing a composite function," *Mathematical Programming*, vol. 144, pp. 1–38, Apr 2014.

[17] P. Tseng and S. Yun, "A coordinate gradient descent method for nonsmooth separable minimization," *Mathematical Programming*, vol. 117, pp. 387–423, Mar 2009.

[18] D. P. Bertsekas, "Incremental proximal methods for large scale convex optimization," *Mathematical Programming*, vol. 129, p. 163, Jun 2011.

[19] J. Nutini, M. Schmidt, I. Laradji, M. Friedlander, and H. Koepke, "Coordinate descent converges faster with the gauss-southwell rule than random selection," in *International Conference on Machine Learning*, pp. 1632–1641, 2015.

[20] Z. Q. Luo and P. Tseng, "On the convergence of the coordinate descent method for convex differentiable minimization," *Journal of Optimization Theory and Applications*, vol. 72, pp. 7–35, Jan 1992.

[21] P. Tseng, "Convergence of a block coordinate descent method for nondifferentiable minimization," *Journal of Optimization Theory and Applications*, vol. 109, pp. 475–494, Jun 2001.

[22] A. Beck and L. Tetruashvili, "On the convergence of block coordinate descent type methods," *SIAM J. Optim.*, vol. 23, pp. 2037–2060, 2013.

[23] J. Nutini, I. Laradji, and M. Schmidt, "Let's make block coordinate descent go fast: Faster greedy rules, message-passing, active-set complexity, and superlinear convergence," *arXiv preprint arXiv:1712.08859*, 2017.

[24] J. C. Spall, "Cyclic seesaw process for optimization and identification," *Journal of Optimization Theory and Applications*, vol. 154, no. 1, pp. 187–208, 2012.

[25] M. Razaviyayn, M. Hong, and Z.-Q. Luo, "A unified convergence analysis of block successive minimization methods for nonsmooth optimization," *SIAM Journal on Optimization*, vol. 23, pp. 1126–1153, Sep 2013.

[26] D. Leventhal and A. S. Lewis, "Randomized methods for linear constraints: Convergence rates and conditioning," *Mathematics of Operations Research*, vol. 35, no. 3, pp. 641–654, 2010.

[27] M. Hong, X. Wang, M. Razaviyayn, and Z.-Q. Luo, "Iteration complexity analysis of block coordinate descent methods," *Mathematical Programming*, vol. 163, pp. 85–114, May 2017.

[28] A. Aubry, A. De Maio, A. Zappone, M. Razaviyayn, and Z.-Q. Luo, "A new sequential optimization procedure and its applications to resource allocation for wireless systems," *IEEE Transactions on Signal Processing*, vol. 66, no. 24, pp. 6518–6533, 2018.

[29] M. Alaee-Kerahroodi, A. Aubry, A. De Maio, M. M. Naghsh, and M. Modarres-Hashemi, "A coordinate-descent framework to design low PSL/ISL sequences," *IEEE Transactions on Signal Processing*, vol. 65, pp. 5942–5956, Nov. 2017.

[30] J. Song, P. Babu, and D. P. Palomar, "Sequence design to minimize the weighted integrated and peak sidelobe levels," *IEEE Transactions on Signal Processing*, vol. 64, no. 8, pp. 2051–2064, 2016.

[31] F. Engels, P. Heidenreich, M. Wintermantel, L. Stäcker, M. Al Kadi, and A. M. Zoubir, "Automotive radar signal processing: Research directions and practical challenges," *IEEE Journal of Selected Topics in Signal Processing*, vol. 15, no. 4, pp. 865–878, 2021.

[32] S. Ahmed and M. Alouini, "A survey of correlated waveform design for multifunction software radar," *IEEE Aerospace and Electronic Systems Magazine*, vol. 31, no. 3, pp. 19–31, 2016.

[33] J. Li and P. Stoica, *MIMO Radar Diversity Means Superiority*, ch. 1, pp. 1–64. Wiley-IEEE Press, 2009.

[34] A. Aubry, A. De Maio, and Y. Huang, "MIMO radar beampattern design via PSL/ISL optimization," *IEEE Transactions on Signal Processing*, vol. 64, pp. 3955–3967, Aug 2016.

[35] M. Alaee-Kerahroodi, K. V. Mishra, and B. S. M.R., "Radar beampattern design for a drone swarm," in *2019 53rd Asilomar Conference on Signals, Systems, and Computers*, pp. 1416–1421, 2019.

[36] U. Niesen, D. Shah, and G. W. Wornell, "Adaptive alternating minimization algorithms," *IEEE Transactions on Information Theory*, vol. 55, no. 3, pp. 1423–1429, 2009.

[37] E. Raei, M. Alaee-Kerahroodi, and M. B. Shankar, "Spatial- and range- ISLR trade-off in MIMO radar via waveform correlation optimization," *IEEE Transactions on Signal Processing*, vol. 69, pp. 3283–3298, 2021.

APPENDIX 5A

To calculate the coefficients in (5.15), we notice

$$\begin{aligned}|r_k(e^{j\phi_d})|^2 &= \left|a_{1k}e^{j\phi_d} + a_{2k}e^{-j\phi_d} + a_{3k}\right|^2 \\ &= \Big|\underbrace{\left(a_{dkr}e^{j\phi_d} + b_{dkr}e^{-j\phi_d} + c_{dkr}\right)}_{A_{dk}} \\ &\quad + \underbrace{j\left(a_{dki}e^{j\phi_d} + b_{dki}e^{-j\phi_d} + c_{dki}\right)}_{B_{dk}}\Big|^2\end{aligned}$$

where $a_{dkr} = \Re(a_{1k})$, $b_{dkr} = \Re(a_{2k})$, $c_{dkr} = \Re(a_{3k})$, $a_{dki} = \Im(a_{1k})$, $b_{dki} = \Im(a_{2k})$, and $c_{dki} = \Im(a_{3k})$. Also,

$$A_{dk} = \left((a_{dkr} + b_{dkr})\cos(\phi_d) + (b_{dki} - a_{dki})\sin(\phi_d) + c_{dkr}\right)^2 \tag{5A.1}$$

$$B_{dk} = \left((a_{dki} + b_{dki})\cos(\phi_d) + (a_{dkr} - b_{dkr})\sin(\phi_d) + c_{dki}\right)^2 \tag{5A.2}$$

Expanding (5A.1) and using the trigonometric relationships,

$$\sin\phi_d = \frac{2\tan\left(\frac{\phi_d}{2}\right)}{1+\tan^2\left(\frac{\phi_d}{2}\right)} \tag{5A.3}$$

$$\cos\phi_d = \frac{1-\tan^2\left(\frac{\phi_d}{2}\right)}{1+\tan^2\left(\frac{\phi_d}{2}\right)} \tag{5A.4}$$

and by defining $\beta_d = \tan\left(\frac{\phi_d}{2}\right)$, we obtain

$$A_{dk} = \frac{\mu'_{dk}\beta_d^4 + \kappa'_{dk}\beta_d^3 + \xi'_{dk}\beta_d^2 + \eta'_{dk}\beta_d + \rho'_{dk}}{(1+\beta_d^2)^2} \tag{5A.5}$$

with

$$\begin{aligned}
\mu'_{dk} =&(a_{dkr}+b_{dkr})^2-2c_{dkr}(a_{dkr}+b_{dkr})+c_{dkr}^2\\
\kappa'_{dk} =&-4(a_{dkr}+b_{dkr})(b_{dki}-a_{dki})+4c_{dkr}(b_{dki}-a_{dki})\\
\xi'_{dk} =&-2(a_{dkr}+b_{dkr})^2+2c_{dkr}^2+4(b_{dki}-a_{dki})^2\\
\eta'_{dk} =&4(a_{dkr}+b_{dkr})(b_{dki}-a_{dki})+4c_{dkr}(b_{dki}-a_{dki})\\
\rho'_{dk} =&(a_{dkr}+b_{dkr})^2+2(a_{dkr}+b_{dkr})c_{dkr}+c_{dkr}^2
\end{aligned} \tag{5A.6}$$

A similar procedure on B_{dk} yields,

$$B_{dk}=\frac{\mu''_{dk}\beta_d^4+\kappa''_{dk}\beta_d^3+\xi''_{dk}\beta_d^2+\eta''_{dk}\beta_d+\rho''_{dk}}{(1+\beta_d^2)^2} \tag{5A.7}$$

where

$$\begin{aligned}
\mu''_{dk} &= (a_{dki}+b_{dki})^2-2c_{dki}(a_{dki}+b_{dki})+c_{dki}^2\\
\kappa''_{dk} &= -4(a_{dki}+b_{dki})(a_{dkr}-b_{dkr})+4c_{dki}(a_{dkr}-b_{dkr}),\\
\xi''_{dk} &= -2(a_{dki}+b_{dki})^2+2c_{dki}^2+4(a_{dkr}-b_{dkr})^2,\\
\eta''_{dk} &= 4(a_{dki}+b_{dki})(a_{dkr}-b_{dkr})+4c_{dki}(a_{dkr}-b_{dkr}),\\
\rho''_{dk} &= (a_{dki}+b_{dki})^2+2(a_{dki}+b_{dki})c_{dki}+c_{dki}^2.
\end{aligned} \tag{5A.8}$$

Finally,

$$|\widetilde{r}_k(\beta_d)|^2=\frac{\mu_{1k}\beta_d^4+\mu_{2k}\beta_d^3+\mu_{3k}\beta_d^2+\mu_{4k}\beta_d+\mu_{5k}}{(1+\beta_d^2)^2} \tag{5A.9}$$

where $\mu_{1k}=\mu'_{dk}+\mu''_{dk}$, $\mu_{2k}=\kappa'_{dk}+\kappa''_{dk}$, $\mu_{3k}=\xi'_{dk}+\xi''_{dk}$, $\mu_{4k}=\eta'_{dk}+\eta''_{dk}$, and $\mu_{5k}=\rho'_{dk}+\rho''_{dk}$.

APPENDIX 5B

Note that

$$\begin{aligned}
\Re\left\{r_k^*(e^{-j\phi_d})\frac{r_k^{(n)}}{\left|r_k^{(n)}\right|}\right\} &= \Re\left\{\left[a_{1k}^*e^{-j\phi_d}+a_{2k}^*e^{j\phi_d}+a_{3k}^*\right]\frac{r_k^{(n)}}{\left|r_k^{(n)}\right|}\right\}\\
&= (\widetilde{a}_{dkr}+\widetilde{b}_{dkr})\cos(\phi_d)+(\widetilde{a}_{dki}-\widetilde{b}_{dki})\sin(\phi_d)+\widetilde{c}_{dkr},
\end{aligned} \tag{5B.1}$$

where $\widetilde{a}_{dkr} = \Re\left(a_{1k}^{*}\frac{r_k^{(n)}}{\left|r_k^{(n)}\right|}\right)$, $\widetilde{b}_{dkr} = \Re\left(a_{2k}^{*}\frac{r_k^{(n)}}{\left|r_k^{(n)}\right|}\right)$, $\widetilde{c}_{dkr} = \Re\left(a_{3k}^{*}\frac{r_k^{(n)}}{\left|r_k^{(n)}\right|}\right)$, $\widetilde{a}_{dki} = \Im\left(a_{1k}^{*}\frac{r_k^{(n)}}{\left|r_k^{(n)}\right|}\right)$, $\widetilde{b}_{dki} = \Im\left(a_{2k}^{*}\frac{r_k^{(n)}}{\left|r_k^{(n)}\right|}\right)$, $\widetilde{a}_{dk} = \widetilde{a}_{dkr} + j\widetilde{a}_{dki}$, and $\widetilde{b}_{dk} = \widetilde{b}_{dkr} + j\widetilde{b}_{dki}$. Using (5A.3) and (5A.4), we obtain

$$\begin{aligned}\Re\left\{\widetilde{r}_k^{*}(\beta_d)\frac{r_k^{(n)}}{\left|r_k^{(n)}\right|}\right\} =& \frac{1}{(1+\beta_d^2)^2}\{(\widetilde{a}_{dkr}+\widetilde{b}_{dkr})(1-\beta_d^4)\\ &+(\widetilde{a}_{dki}-\widetilde{b}_{dki})(2\beta_d)(1+\beta_d^2)\\ &+\widetilde{c}_{dkr}(1+\beta_d^2)^2\}.\end{aligned}$$

Finally, defining $\kappa_{1k} = \widetilde{c}_{dkr} - \widetilde{a}_{dkr} - \widetilde{b}_{dkr}$, $\kappa_{2k} = 2(\widetilde{a}_{dki} - \widetilde{b}_{dki})$, $\kappa_{3k} = 2\widetilde{c}_{dkr}$, $\kappa_{4k} = 2(\widetilde{a}_{dki} - \widetilde{b}_{dki})$, $\kappa_{5k} = \widetilde{a}_{dkr} + \widetilde{b}_{dkr} + \widetilde{c}_{dkr}$ yields

$$\Re\left\{\widetilde{r}_k^{*}(\beta_d)\frac{r_k^{(n)}}{\left|r_k^{(n)}\right|}\right\} = \frac{\kappa_{1k}\beta_d^4 + \kappa_{2k}\beta_d^3 + \kappa_{3k}\beta_d^2 + \kappa_{4k}\beta_d + \kappa_{5k}}{(1+\beta_d^2)^2}$$

APPENDIX 5C

By some mathematical manipulation, the objective function $f(\mu^{\star}, \phi)$ can be expanded as follows:

$$\begin{aligned}f(\mu^{\star},\phi) &= \sum_{k=1}^{K}(b_{1,k}^{(i)}e^{j\phi} + (b_{0,k}^{(i)} - \mu^{\star}q_k) + b_{-1,k}^{(i)}e^{-j\phi})^2\\ &= \sum_{k=1}^{K} {b_{1,k}^{(i)}}^2 e^{j2\phi} + 2b_{1,k}^{(i)}(b_{0,k}^{(i)} - \mu^{\star}q_k)e^{j\phi} + 2b_{1,k}^{(i)}b_{-1,k}^{(i)}\\ &+ (b_{0,k}^{(i)} - \mu^{\star}q_k)^2 + 2(b_{0,k}^{(i)}e^{-j\phi} - \mu^{\star}q_k)b_{-1,k}^{(i)} + {b_{-1,k}^{(i)}}^2 e^{-j2\phi}\end{aligned}$$

Defining $c_2^{(i)} \triangleq \sum_{k=1}^{K} {b_{1,k}^{(i)}}^2$, $c_1^{(i)} \triangleq \sum_{k=1}^{K} 2b_{1,k}^{(i)}(b_{0,k}^{(i)} - \mu^{\star}q_k)$, $c_0 \triangleq 2b_{1,k}^{(i)}b_{-1,k}^{(i)} + (b_{0,k}^{(i)} - \mu^{\star}q_k)^2$, $c_{-1} \triangleq c_1^{*}$, and $c_2 \triangleq c_{-2}^{*}$, the expansion in (5.44) can be obtained.

Chapter 6

Other Optimization Methods

Apart from the methods mentioned in earlier chapters, some alternative optimization approaches are also available for the optimal radar waveform design problem. Methods like semi-definite programming (SDP) and ADMM, among others, have also been used for waveform design to achieve the desired signal properties. This chapter will focus on using SDP to create unimodular waveforms with a desired beampattern and spectral occupancy.

6.1 SYSTEM MODEL

Consider a colocated narrow band MIMO radar system, with M transmit antennas, each transmitting a sequence of length N in the fast-time domain. Let the matrix $\mathbf{S} \in \mathbb{C}^{M \times N}$ denote the transmitted set of sequences as

$$\mathbf{S} \triangleq \begin{bmatrix} s_{1,1} & s_{1,2} & \dots & s_{1,N} \\ s_{2,1} & s_{2,2} & \dots & s_{2,N} \\ \vdots & \vdots & \vdots & \vdots \\ s_{M,1} & s_{M,2} & \dots & s_{M,N} \end{bmatrix}$$

We consider the row/column definitions $\mathbf{S} \triangleq [\bar{\mathbf{s}}_1, \dots, \bar{\mathbf{s}}_N] \triangleq [\tilde{\mathbf{s}}_1^T, \dots, \tilde{\mathbf{s}}_M^T]^T$, where the vector $\bar{\mathbf{s}}_n \triangleq [s_{1,n}, s_{2,n}, \dots, s_{M,n}]^T \in \mathbb{C}^M$ is composed of the n^{th} time sample ($n \in \{1, \dots, N\}$) across the M transmitters (the n^{th} column of matrix $\mathbf{S}$) while the $\tilde{\mathbf{s}}_m \triangleq [s_{m,1}, s_{m,2}, \dots, s_{m,N}]^T \in \mathbb{C}^N$ ($m \in \{1, \dots, M\}$) contains N samples collected from the m^{th} transmitter (the m^{th} row of

matrix $\mathbf{S}$). We aim to design $\mathbf{S}$ in the following while the transmit waveforms have good ISL in both the spatial and range domains, but also taking a spectral mask into consideration during the design stage [1, 2]. In order to achieve this, the system model is first presented in order to describe the system in the spectral and spatial domains. The similarity constraint is then imposed, requiring that the resulting waveforms match a predefined waveform set in terms of sidelobe level.

6.1.1 System Model in the Spatial Domain

Assume a colocated MIMO radar system with a ULA structure for the transmit array, characterized by the steering vector shown below [3]

$$\mathbf{a}(\theta) = [1, e^{j\frac{2\pi d}{\lambda}\sin(\theta)}, \ldots, e^{j\frac{2\pi d(M-1)}{\lambda}\sin(\theta)}]^T \in \mathbb{C}^M \tag{6.1}$$

where d is the distance between the transmitter antennas and λ is the signal wavelength. The beampattern in the direction of θ can be written as [3–5]

$$P(\mathbf{S},\theta) = \frac{1}{N}\sum_{n=1}^{N}\left|\mathbf{a}^H(\theta)\bar{\mathbf{s}}_n\right|^2 = \frac{1}{N}\sum_{n=1}^{N}\bar{\mathbf{s}}_n^H\mathbf{A}(\theta)\bar{\mathbf{s}}_n$$

where $\mathbf{A}(\theta) = \mathbf{a}(\theta)\mathbf{a}^H(\theta)$. Let Θ_d and Θ_u be the sets of desired and undesired angles in the spatial domain, respectively. These two sets satisfy $\Theta_d \cap \Theta_u = \varnothing$ and $\Theta_d \cup \Theta_u \subset [-90°, 90°]$. In this regard the spatial ISLR can be defined by the following expression [2]:

$$f(\mathbf{S}) \triangleq \frac{\sum_{\theta\in\Theta_u} P(\mathbf{S},\theta)}{\sum_{\theta\in\Theta_d} P(\mathbf{S},\theta)} = \frac{\sum_{n=1}^{N}\bar{\mathbf{s}}_n^H\mathbf{A}_u\bar{\mathbf{s}}_n}{\sum_{n=1}^{N}\bar{\mathbf{s}}_n^H\mathbf{A}_d\bar{\mathbf{s}}_n}, \tag{6.2}$$

where $\mathbf{A}_u \triangleq \frac{1}{N}\sum_{\theta\in\Theta_u}\mathbf{A}(\theta)$ and $\mathbf{A}_d \triangleq \frac{1}{N}\sum_{\theta\in\Theta_d}\mathbf{A}(\theta)$.

6.1.2 System Model in the Spectrum Domain

Let $\mathbf{F} \triangleq [\mathbf{f}_0, \ldots, \mathbf{f}_{\hat{N}-1}] \in \mathbb{C}^{\hat{N}\times\hat{N}}$ be the DFT matrix ($\hat{N} \geq N$), where

$$\mathbf{f}_k \triangleq \left[1, e^{-j\frac{2\pi k}{\hat{N}}}, \ldots, e^{-j\frac{2\pi k(\hat{N}-1)}{\hat{N}}}\right]^T \in \mathbb{C}^{\hat{N}},\ k \in \{0, \ldots, \hat{N}-1\}$$

Let $\mathcal{U} = \cup_{k=1}^{K}(u_{k,1}, u_{k,2})$ be the union of K normalized frequency stop-bands, where $0 \leq u_{k,1} < u_{k,2} \leq 1$ and $\cap_{k=1}^{K}(u_{k,1}, u_{k,2}) = \varnothing$. Thus, the undesired discrete frequency bands are given by $\mathcal{V} = \cup_{k=1}^{K}(\lfloor \hat{N}u_{k,1} \rceil, \lfloor \hat{N}u_{k,2} \rceil)$. In this regard, the absolute value of the spectrum at undesired frequency bins can be expressed as $|\mathbf{G}\hat{\mathbf{s}}_m|$, where $\hat{\mathbf{s}}_m$ is $\hat{N} - N$ zero-pad version of $\hat{\mathbf{s}}_m$, defined as

$$\hat{\mathbf{s}}_m \triangleq [\tilde{\mathbf{s}}_m; \underbrace{0; \ldots; 0}_{\hat{N}-N}] \tag{6.3}$$

the matrix $\mathbf{G} \in \mathbb{C}^{K \times \hat{N}}$ contains the rows of $\mathbf{F}$ corresponding to the frequencies in $\mathcal{V}$, and K is the number of undesired frequency bins [6].

6.2 PROBLEM FORMULATION

With spectrum compatibility and similarity constraints, waveform design for beampattern shaping and spectral masking (WISE) [1] aims to design a set of constant modulus sequences for MIMO radar such that the transmit beampattern is steered towards desired directions while having nulls at undesired directions. To that end, the optimization problem can be expressed as follows:

$$\begin{cases} \underset{\mathbf{S}}{\text{minimize}} & f(\mathbf{S}) = \dfrac{\sum_{n=1}^{N} \bar{\mathbf{s}}_n^H \mathbf{A}_u \bar{\mathbf{s}}_n}{\sum_{n=1}^{N} \bar{\mathbf{s}}_n^H \mathbf{A}_d \bar{\mathbf{s}}_n} & \text{(6.4a)} \\ \text{subject to} & \dfrac{1}{2} \leq \dfrac{\sum_{n=1}^{N} \bar{\mathbf{s}}_n^H \mathbf{A}(\theta_d) \bar{\mathbf{s}}_n}{\sum_{n=1}^{N} \bar{\mathbf{s}}_n^H \mathbf{A}(\theta_0) \bar{\mathbf{s}}_n} \leq 1 & \text{(6.4b)} \\ & |s_{m,n}| = 1 & \text{(6.4c)} \\ & \max\left\{|\mathbf{G}\hat{\mathbf{s}}_m|\right\} \leq \gamma,\ m \in \{1, \ldots, M\} & \text{(6.4d)} \\ & \dfrac{1}{\sqrt{MN}} \|\mathbf{S} - \mathbf{S}_0\|_F \leq \delta & \text{(6.4e)} \end{cases}$$

where (6.4b) indicates the 3-dB beamwidth constraint to guarantee the beampattern response at all desired angles is at least half the maximum power. In (6.4b), $\theta_d \in \{\theta | \forall \theta \in \Theta_d\}$. Also, θ_0 denotes the angle with maximum power, which is usually chosen to be at the center point of Θ_d. The constraint (6.4c) indicates the constant modulus property; this is attractive for radar system designers since its allows for the efficient and

uniform utilization of the limited transmitter power. The constraint (6.4d) indicates the spectrum masking and guarantees the power of spectrum in undesired frequencies not to be greater than γ. Finally, the constraint (6.4e) has been imposed on the waveform to control properties of the optimized code (such as orthogonality) similar to the reference waveform $\mathbf{S}_0$; for instance, this helps controlling ISLR in the range domain. If $\mathbf{S}$ and $\mathbf{S}_0$ are considered to be a constant modulus waveform, the maximum admissible value of the similarity constraint parameter would be $\delta = \sqrt{2}$ (i.e., $0 \leq \delta \leq \sqrt{2}$). Note that the bounds of the optimization problem's constraints must be carefully considered when determining the feasibility of the problem in (6.4). Some insight on how to identify a feasible solution to these problems can be found in [7, 8]. In (6.4), the objective function (6.4a) is a fractional quadratic function; also (6.4b) is a nonconvex inequality constraint. The (6.4c) is a nonaffine equality constraint while, the inequality constraint (6.4e) yields a convex set. Therefore, the problem is a nonconvex, multivariable and NP-hard optimization problem [2]. In order to solve the problem, WISE proposes an iterative method based on SDP to obtain an efficient local optimum, as follows.

6.3 OPTIMIZATION APPROACH

The maximum value of $P(\mathbf{S}, \theta)$ is M^2 and occurs when $\bar{\mathbf{s}}_n = \mathbf{a}(\theta)$, $n \in \{1, \ldots, N\}$. Therefore, the denominator of (6.4a) satisfies $\sum_{n=1}^{N} \bar{\mathbf{s}}_n^H \mathbf{A}_d \bar{\mathbf{s}}_n \leq K_d M^2$, where K_d is the number of desired angles. Thus, the problem (6.4) can be equivalently written as [9]:

$$
\begin{cases}
\underset{\mathbf{S}}{\text{minimize}} & \displaystyle\sum_{n=1}^{N} \bar{\mathbf{s}}_n^H \mathbf{A}_u \bar{\mathbf{s}}_n & \text{(6.5a)} \\
\text{subject to} & \displaystyle\sum_{n=1}^{N} \bar{\mathbf{s}}_n^H \mathbf{A}_d \bar{\mathbf{s}}_n \le K_d M^2 & \text{(6.5b)} \\
& \displaystyle\sum_{n=1}^{N} \bar{\mathbf{s}}_n^H \mathbf{A}(\theta_d) \bar{\mathbf{s}}_n \le \sum_{n=1}^{N} \bar{\mathbf{s}}_n^H \mathbf{A}(\theta_0) \bar{\mathbf{s}}_n & \text{(6.5c)} \\
& \displaystyle\sum_{n=1}^{N} \bar{\mathbf{s}}_n^H \mathbf{A}(\theta_0) \bar{\mathbf{s}}_n \le 2 \sum_{n=1}^{N} \bar{\mathbf{s}}_n^H \mathbf{A}(\theta_d) \bar{\mathbf{s}}_n & \text{(6.5d)} \\
& |s_{m,n}| = 1 & \text{(6.5e)} \\
& \|\mathbf{G}\hat{\mathbf{s}}_m\|_{p\to\infty} \le \gamma,\ m \in \{1, \ldots, M\} & \text{(6.5f)} \\
& \dfrac{1}{\sqrt{MN}} \|\mathbf{S} - \mathbf{S}_0\|_F \le \delta & \text{(6.5g)}
\end{cases}
$$

In (6.5), constraints (6.5c) and (6.5d) are obtained by expanding constraint (6.4b). Besides, the constraint $\max\{|\mathbf{G}\hat{\mathbf{s}}_m|\}$ (6.4d) is replaced with $\|\mathbf{G}\hat{\mathbf{s}}_m\|_{p\to\infty}$ (6.5f), which is a convex constraint for each finite p.

Remark 1. *Another possible solution to consider the constraint* (6.4d) *is direct implementation by individually bounding each frequency response at each undesired frequency bin. This reformulation makes the problem convex, but requires consideration of $M \times K$ constraints in total, which increases the complexity of the algorithm. As an alternative, this constraint is replaced with ℓ_p-norm, and leveraging the stability of the algorithm, choose a large p value to solve the problem.*

Problem (6.5) is still nonconvex with respect to $\mathbf{S}$ due to (6.5c), (6.5d), and (6.5e). To cope with this problem, defining $\mathbf{X}_n \triangleq \bar{\mathbf{s}}_n \bar{\mathbf{s}}_n^H$, (6.5) is recast as

follows:

$$\begin{cases} \underset{\mathbf{S},\mathbf{X}_n}{\text{minimize}} & \displaystyle\sum_{n=1}^{N} \text{Tr}(\mathbf{A}_u\mathbf{X}_n) & \text{(6.6a)} \\ \text{subject to} & \displaystyle\sum_{n=1}^{N} \text{Tr}(\mathbf{A}_d\mathbf{X}_n) \le K_d M^2 & \text{(6.6b)} \\ & \displaystyle\sum_{n=1}^{N} \text{Tr}(\mathbf{A}(\theta_d)\mathbf{X}_n) \le \sum_{n=1}^{N} \text{Tr}(\mathbf{A}(\theta_0)\mathbf{X}_n) & \text{(6.6c)} \\ & \displaystyle\sum_{n=1}^{N} \text{Tr}(\mathbf{A}(\theta_0)\mathbf{X}_n) \le 2\sum_{n=1}^{N} \text{Tr}(\mathbf{A}(\theta_d)\mathbf{X}_n) & \text{(6.6d)} \\ & \text{Diag}(\mathbf{X}_n) = \mathbf{1}_M & \text{(6.6e)} \\ & \text{(6.5f), (6.5g)} & \text{(6.6f)} \\ & \mathbf{X}_n \succcurlyeq \mathbf{0} & \text{(6.6g)} \\ & \mathbf{X}_n = \bar{\mathbf{s}}_n\bar{\mathbf{s}}_n^H & \text{(6.6h)} \end{cases}$$

It is readily observed that, in (6.6), the objective function and all the constraints but (6.6h) are convex in $\mathbf{X}_n$ and $\mathbf{S}$. In the following, an equivalent reformulation for (6.6) is presented, which paves the way for iteratively solving this nonconvex optimization problem.

Theorem 6.1. *Defining* $\mathbf{Q}_n \triangleq \begin{bmatrix} 1 & \bar{\mathbf{s}}_n^H \\ \bar{\mathbf{s}}_n & \mathbf{X}_n \end{bmatrix} \in \mathbb{C}^{(M+1)\times(M+1)}$ *and considering slack variables* $\mathbf{V}_n \in \mathbb{C}^{(M+1)\times M}$ *and* $b_n \in \mathbb{R}$*, the optimization problem* (6.6) *takes the following equivalent form:*

$$\begin{cases} \underset{\mathbf{S},\mathbf{X}_n,b_n}{\text{minimize}} & \displaystyle\sum_{n=1}^{N} Tr(\mathbf{A}_u\mathbf{X}_n) + \eta\sum_{n=1}^{N} b_n & \text{(6.7a)} \\ \text{subject to} & \text{(6.6b), (6.6c), (6.6d), (6.6e), (6.6f), (6.6g)} & \text{(6.7b)} \\ & \mathbf{Q}_n \succcurlyeq 0 & \text{(6.7c)} \\ & b_n\mathbf{I}_M - \mathbf{V}_n^H\mathbf{Q}_n\mathbf{V}_n \succcurlyeq \mathbf{0} & \text{(6.7d)} \\ & b_n \ge 0 & \text{(6.7e)} \end{cases}$$

where η *is a regularization parameter.*

Proof: See Appendix 6A. ■

The problem (6.7) can be solved iteratively by alternating between the parameters. Let $\mathbf{V}_n^{(i)}$, $\mathbf{Q}_n^{(i)}$, $\mathbf{S}^{(i)}$, $\mathbf{X}_n^{(i)}$, and $b_n^{(i)}$ be the values of $\mathbf{V}_n$, $\mathbf{Q}_n$, $\mathbf{S}$, $\mathbf{X}_n$, and b_n at i^{th} iteration, respectively. Given $\mathbf{V}^{(i-1)}$ and $b_n^{(i-1)}$, the optimization problem with respect to $\mathbf{S}^{(i)}$, $\mathbf{X}_n^{(i)}$, and $b_n^{(i)}$ at the i^{th} iteration becomes

$$
\begin{cases}
\underset{\mathbf{S}^{(i)},\mathbf{X}_n^{(i)},b_n^{(i)}}{\text{minimize}} & \displaystyle\sum_{n=1}^{N} \text{Tr}(\mathbf{A}_u \mathbf{X}_n^{(i)}) + \eta \sum_{n=1}^{N} b_n^{(i)} & \text{(6.8a)} \\
\text{subject to} & \displaystyle\sum_{n=1}^{N} \text{Tr}(\mathbf{A}_d \mathbf{X}_n^{(i)}) \leq K_d M^2 & \text{(6.8b)} \\
& \displaystyle\sum_{n=1}^{N} \text{Tr}(\mathbf{A}(\theta_d) \mathbf{X}_n^{(i)}) \leq \sum_{n=1}^{N} \text{Tr}(\mathbf{A}(\theta_0) \mathbf{X}_n^{(i)}) & \text{(6.8c)} \\
& \displaystyle\sum_{n=1}^{N} \text{Tr}(\mathbf{A}(\theta_0) \mathbf{X}_n^{(i)}) \leq 2 \sum_{n=1}^{N} \text{Tr}(\mathbf{A}(\theta_d) \mathbf{X}_n^{(i)}) & \text{(6.8d)} \\
& \text{Diag}(\mathbf{X}_n^{(i)}) = \mathbf{1}_M & \text{(6.8e)} \\
& \left\| \mathbf{G} \hat{\mathbf{s}}_m^{(i)} \right\|_{p \to \infty} \leq \gamma, \; m \in \{1, \ldots, M\} & \text{(6.8f)} \\
& \frac{1}{\sqrt{MN}} \left\| \mathbf{S}^{(i)} - \mathbf{S}_0 \right\|_F \leq \delta & \text{(6.8g)} \\
& \mathbf{X}_n^{(i)} \succcurlyeq \mathbf{0} & \text{(6.8h)} \\
& \mathbf{Q}_n^{(i)} \succcurlyeq \mathbf{0} & \text{(6.8i)} \\
& b_n^{(i)} \mathbf{I}_M - {\mathbf{V}_n^{(i-1)}}^H \mathbf{Q}_n^{(i)} \mathbf{V}_n^{(i-1)} \succcurlyeq \mathbf{0} & \text{(6.8j)} \\
& b_n^{(i-1)} \geq b_n^{(i)} \geq 0 & \text{(6.8k)}
\end{cases}
$$

Once $\mathbf{X}_n^{(i)}$, $\mathbf{S}_n^{(i)}$, and $b_n^{(i)}$ are found by solving (6.8), $\mathbf{V}_n^{(i)}$ can be obtained by seeking an $(M+1) \times M$ matrix with orthonormal columns such that $b_n^{(i)} \mathbf{I}_M \succcurlyeq {\mathbf{V}_n^{(i)}}^H \mathbf{Q}_n^{(i)} \mathbf{V}_n^{(i)}$. Choosing $\mathbf{V}_n^{(i)}$ to be equal to the matrix composed of the eigenvectors of $\mathbf{Q}_n^{(i)}$ corresponding to its M smallest eigenvalues, and following similar arguments provided after (6A.1), it can be concluded that [10, Corollary 4.3.16],

$$
\begin{aligned}
&{\mathbf{V}_n^{(i)}}^H \mathbf{Q}_n^{(i)} \mathbf{V}_n^{(i)} = \text{Diag}([\rho_1^{(i)}, \rho_2^{(i)}, \cdots, \rho_M^{(i)}]^T) \\
&\preccurlyeq \text{Diag}([\nu_1^{(i-1)}, \nu_2^{(i-1)}, \cdots, \nu_M^{(i-1)}]^T) \preccurlyeq b_n^{(i)} \mathbf{I}_M
\end{aligned}
\tag{6.9}
$$

where $\rho_1^{(i)} \leq \rho_2^{(i)} \leq \cdots \leq \rho_{M+N}^{(i)}$ and $\nu_1^{(i-1)} \leq \nu_2^{(i-1)} \leq \cdots \leq \nu_M^{(i-1)}$ denote the eigenvalues of $\mathbf{Q}_n^{(i)}$ and ${\mathbf{V}_n^{(i-1)}}^H \mathbf{Q}_n^{(i)} \mathbf{V}_n^{(i-1)}$, respectively. It follows from (6.9) that the matrix composed of the eigenvectors of $\mathbf{Q}_n^{(i)}$ corresponding to its M smallest eigenvalues is the appropriate choice for $\mathbf{V}_n^{(i)}$.

Accordingly, at each iteration of WISE, It is needed to solve a SDP followed by an eigenvalue decomposition (ED). Algorithm 6.1 summarizes the steps of the WISE approach for solving (6.4). In order to initialize the algorithm, $\mathbf{V}_n^{(0)}$ can be found through the eigenvalue decomposition of $\mathbf{Q}_n^{(0)}$ obtained from solving (6.8) without considering (6.8j) and (6.8k) constraints. Further, the algorithm is terminated when $\bar{\mathbf{s}}_n \bar{\mathbf{s}}_n^H$ converges to $\mathbf{X}_n$. In this regard, let us assume that

$$\xi_{n,1} \geq \xi_{n,2} \geq \cdots \geq \xi_{n,m} \geq \cdots \geq \xi_{n,M} \geq 0$$

are the eigenvalues of $\mathbf{X}_n$, $\xi \triangleq \frac{\max\{\xi_{n,2}\}}{\min\{\xi_{n,1}\}} < e_1$ (with $e_1 > 0$) is considered as the termination condition. In this case, the second largest eigenvalue of $\mathbf{X}_n$ is negligible compared to its largest eigenvalue and can be concluded that the solution is rank 1. In addition, $\max\left\{\frac{\left\|\bar{\mathbf{s}}_n \bar{\mathbf{s}}_n^H - \mathbf{X}_n\right\|_F}{\sqrt{MN}}\right\} < e_2$ (with $e_2 > 0$) is considered as the second termination condition. When either the first or second termination criteria occur, the algorithm stops. Note that the objective function of the problem is guaranteed to converge to at least a local minimum of (6.7) [11].

6.3.1 Convergence

It readily follows from (6.8k) that $\lim_{k\to\infty} \frac{|b_n^{(i)}|}{|b_n^{(i-1)}|} \leq 1$. This implies that $b_n^{(i)}$ converges at least sub linearly to zero [12]. Hence, there exist some $\mathcal{I}$ such that $b_n^{(i)} \leq \epsilon$ ($\epsilon \to 0$) for $i \geq \mathcal{I}$. Making use of this fact, it can be deduced from (6.8j) that

$${\mathbf{V}_n^{(i-1)}}^H \mathbf{Q}_n^{(i)} \mathbf{V}_n^{(i-1)} \preccurlyeq \epsilon \mathbf{I}_M, \quad \epsilon \to 0 \tag{6.10}$$

for $i \geq \mathcal{I}$. Then it follows from (6.10) and (6.9) that $\text{Rank}(\mathbf{Q}_n^{(i)}) \simeq 1$ for $i \geq \mathcal{I}$, thereby $\mathbf{X}_n^{(i)} = \bar{\mathbf{s}}_n^{(i)} \bar{\mathbf{s}}_n^{(i)H}$ for $i \geq \mathcal{I}$. This implies that $\mathbf{X}_n^{(i)}$, for any $i \geq \mathcal{I}$, is a feasible point for the optimization problem (6.7). However, considering the

Algorithm 6.1: MIMO Radar Waveform Design with a Desired Beampattern and Spectral Occupancy

Result: Optimized code vector $\mathbf{x}^\star$
Input: γ, δ, $\mathbf{S}_0$, $\mathcal{U}$ and $\hat{N}$;
Find $\mathbf{Q}_n^{(0)}$ using (6.8j) and (6.8k) then solving (6.8);
Find $\mathbf{V}_n^{(0)}$ which is the M eigenvectors of $\mathbf{Q}_n^{(0)}$, corresponding to the M lowest eigenvalues;
Find $b_n^{(0)}$ which is the second largest eigenvalue of $\mathbf{Q}_n^{(0)}$;
for $i = 0, 1, 2, \ldots$ **do**
  Find the optimum $\mu^\star$ using (5.40);
  Find $\mathbf{S}^{(i)}$, $\mathbf{X}_n^{(i)}$ and $b_n^{(i)}$ by solving (6.8);
  Find $\mathbf{V}_n^{(i)}$, which is the M eigenvectors of $\mathbf{Q}_n^{(i)}$, by dropping the eigenvector corresponding to the largest eigenvalue;
  Find $b_n^{(i)}$ which is the second largest eigenvalue of $\mathbf{Q}_n^{(i)}$. Stop if convergence criterion is met;
end

fact that $b_n^{(i)} \leq \epsilon$ for $i \geq \mathcal{I}$, it can be concluded that $\mathbf{X}_n^{(i)}$ for $i \geq \mathcal{I}$ is also a minimizer of the function $\sum_{n=1}^{N} \mathrm{Tr}(\mathbf{A}_u \mathbf{X}_n)$. These imply that $\mathbf{X}_n^{(i)}$ for $i \geq \mathcal{I}$ is at least a local minimizer of the optimization problem (6.7). The proves the convergence of the devised iterative algorithm.

6.3.2 Computational Complexity

In each iteration, Algorithm 6.1 performs the following steps:

- *Solving* (6.8): Needs the solution of a SDP, whose computational complexity is $\mathcal{O}(M^{3.5})$ [13].
- *Finding* $\mathbf{V}_n^{(i)}$ *and* $b_n^{(i)}$: Needs the implementation of a single value decomposition (SVD), whose computational complexity is $\mathcal{O}(M^3)$ [14].

Since there is N summation, the computational complexity of solving (6.8) is $\mathcal{O}(N(M^{3.5} + M^3))$. Let us assume that $\mathcal{I}$ iterations are required for the convergence; therefore, the overall computational complexity of Algorithm 6.1 is $\mathcal{O}(\mathcal{I}N(M^{3.5} + M^3))$.

6.4 NUMERICAL RESULTS

In this section, numerical results are provided for assessing the performance of the devised algorithm for beampattern shaping and spectral matching under constant modulus constraint. Toward this end, unless otherwise explicitly stated, the following setup is considered. For transmit parameters, the ULA configuration with $M = 8$ transmitters, with the spacing of $d = \lambda/2$ and each antenna transmits $N = 64$ samples, is considered. A uniform sampling of regions $\theta = [-90^\circ, 90^\circ]$ with a grid size of 5° is considered and the desired and undesired angles for beampattern shaping are $\Theta_d = [-55^\circ, -35^\circ]$ ($\theta_0 = -45^\circ$) and $\Theta_u = [-90^\circ, -60^\circ] \cup [-30^\circ, 90^\circ]$, respectively. The DFT point numbers is set as $\hat{N} = 5N$, the normalized frequency stop band is set at $\mathcal{U} = [0.3, 0.35] \cup [0.4, 0.45] \cup [0.7, 0.8]$ and the absolute spectral mask level is set as $\gamma = 0.01\sqrt{\hat{N}}$. As to the reference signal for similarity constraint, $\mathbf{S}_0$ is considered to be a set of sequences with a good range ISLR property, which is obtained by the method in [2]. For the optimization problem, $\eta = 0.1$ and $p = 1,000$ is set to approximate the (6.5f) constraint. The convex optimization problems are solved via the CVX toolbox [15] and the stop condition for Algorithm 6.1 are set at $e_1 = 10^{-5}$ and $e_2 = 10^{-4}$, with maximum iteration of $1,000$.

6.4.1 Convergence Analysis

Figure 6.1 depicts the convergence behavior of the devised method in different aspects. In this figure, the maximum admissible value for similarity parameter is considered (i.e., $\delta = \sqrt{2}$). Figure 6.1(a) shows the convergence of ξ to zero. This indicates that the second largest eigenvalue of $\mathbf{X}_n$ is negligible in comparison with the largest eigenvalue, therefore resulting in a rank 1 solution for $\bar{\mathbf{s}}_n$. Figure 6.1(b) shows that the solution of $\mathbf{X}_n$ converges to $\bar{\mathbf{s}}_n$, which confirms our claim about obtaining a rank 1 solution.

To indicate the performance of the devised method under constant modulus constraint, defining

$$s_{max} \triangleq \max\{|s_{m,n}|\}, \quad s_{min} \triangleq \min\{|s_{m,n}|\} \tag{6.11}$$

for $m \in \{1, \ldots, M\}$ and $n \in \{1, \ldots, N\}$. Figure 6.1(c) evaluates the maximum/minimum absolute values of the code entries in $\mathbf{S}$. The results indicate that the values of s_{max} and s_{min} are converging to a fixed value, which indicates the constant modulus solution of WISE.

In addition, Figure 6.1(d) depicts the devised method's peak-to-average power ratio (PAR) convergence. In the first step, the PAR value is high, and as the number of iterations increases, the PAR value converges to 1, indicating the constant modulus solution.

Please note that, the first iteration in Figure 6.1(a), Figure 6.1(b), and Figure 6.1(c), shows the semi-definite relaxation (SDR) solution of (6.8) by dropping (6.8j) and (6.8k). As can be seen, the SDR method does not provide a rank one or constant modulus solution. Since in the initial step (SDR) the constraints (6.8j) and (6.8k) are dropped, there are no lower bounds or equality energy constraints on variable $\mathbf{S}$. Considering those two constraints in the next steps of the algorithm (which are equivalent to (6.6h)), indeed impose the constraints $\mathbf{X}_n = \bar{\mathbf{s}}_n \bar{\mathbf{s}}_n^H$. However, the constraint $\mathbf{Diag}\, \mathbf{X}_n = \mathbf{1}_M$ forces the variable $\mathbf{S}$ to be constant modulus. Therefore, in the first iteration, the magnitude of the sequence in Figure 6.1(c) is close to zero.

6.4.2 Performance Evaluation

Figure 6.2 compares the devised method's performance in terms of beampattern shaping and spectral masking to that of the unimodular set of sequence design (UNIQUE) [2] method in spatial ISLR minimization mode ($\eta = 1$). The spectral masking (6.8f), 3-dB main beamwidth (6.8c), and (6.8d) constraints are excluded in this figure for fair comparison. As can be seen, the devised method performs almost identically (in some undesirable angles deeper nulls) to the UNIQUE method in this case. However, taking into account the spectral masking (6.8f), 3-dB main beamwidth (6.8c), and (6.8d) constraints, the devised method can simultaneously steer the beam towards the desired angles and steer the nulls at undesired angles.

The beampattern response of WISE at the desired angles region and the spectrum response of the devised method has better performance compared to UNIQUE method. Figure 6.2(b) shows the main beamwidth response of the devised method and UNIQUE. Since UNIQUE does not have the 3-dB main beamwidth constraint, it does not have a good main beamwidth response. However, the 3-dB main beamwidth constraint incorporated in our framework improves the main beamwidth response. Besides, the maximum beampattern response is located at -45° in the devised method while there is a deviation in the UNIQUE method. However, Figure 6.2(c) shows the spectrum response of the devised method. Observe that the waveform obtained by WISE masks the spectral power in the stop

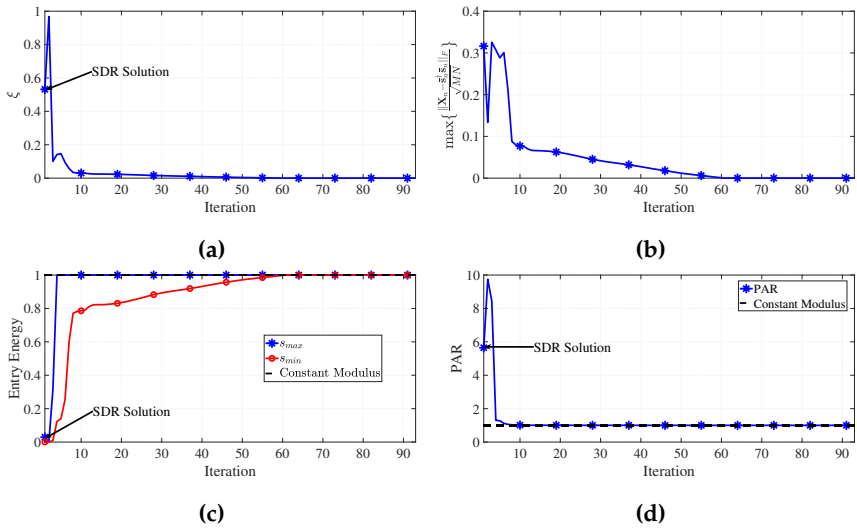

Figure 6.1. The convergence behavior of the devised method in different aspects: (a) $\xi = \frac{\max\{\xi_{n,2}\}}{\min\{\xi_{n,1}\}}$, (b) the constant modulus, (c) $\max\left\{\left\|\mathbf{X}_n - \mathbf{s}_n^H \mathbf{s}_n\right\|_F\right\}$, and (d) PAR ($M = 8$, $N = 64$, $\hat{N} = 5N$, $\delta = \sqrt{2}$, $\Theta_d = [-55°, -35°]$, $\Theta_u = [-90°, -60°] \cup [-30°, 90°]$, $\mathcal{U} = [0.12, 0.14] \cup [0.3, 0.35] \cup [0.7, 0.8]$, and $\gamma = 0.01\sqrt{\hat{N}}$).

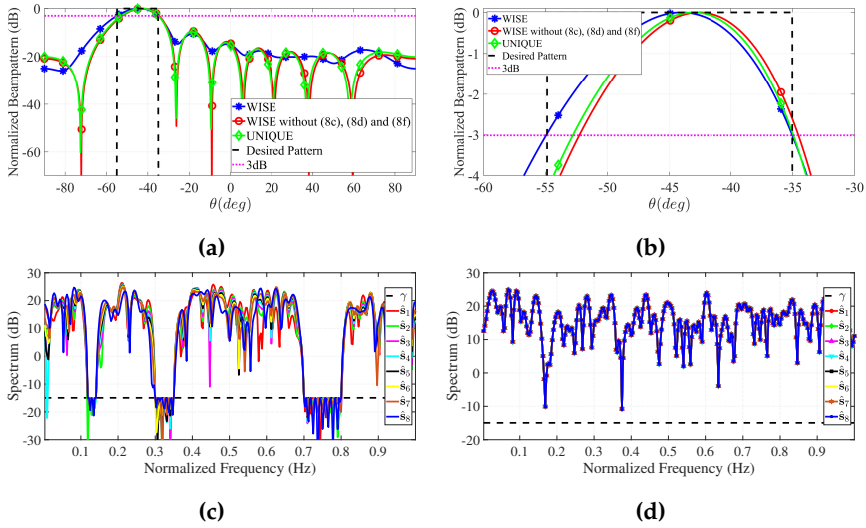

Figure 6.2. Comparing the performance of WISE and UNIQUE methods in several aspects ($M = 8$, $N = 64$, $\hat{N} = 5N$, $\delta = \sqrt{2}$, $\Theta_d = [-55°, -35°]$, $\Theta_u = [-90°, -60°] \cup [-30°, 90°]$, $\mathcal{U} = [0.3, 0.35] \cup [0.4, 0.55] \cup [0.7, 0.85]$, and $\gamma = 0.01\sqrt{N}$): (a) Beampattern response, (b) 3-dB main beamwidth, (c) Spectral of WISE, (d) Spectral of UNIQUE.

bands region ($\mathcal{U}$) below the γ value. However, the UNIQUE technique cannot notch the stop bands since it is not spectral-compatible. Additionally, as can be seen, the transmit waveforms in UNIQUE have the same spectrum. On the other extreme, the UNIQUE offers highly correlated waveforms to get a good beampattern response. This demonstrates how the steering beam pattern and orthogonality are incompatible.

6.4.3 The Impact of Similarity Parameter

In this subsection, the impact of choosing the similarity parameter δ on performance of the devised method is evaluated. Considering the maximum admissible value for similarity parameter, that is, $\delta = \sqrt{2}$, the similarity constraint is not included. However, by decreasing δ, there is a degree of

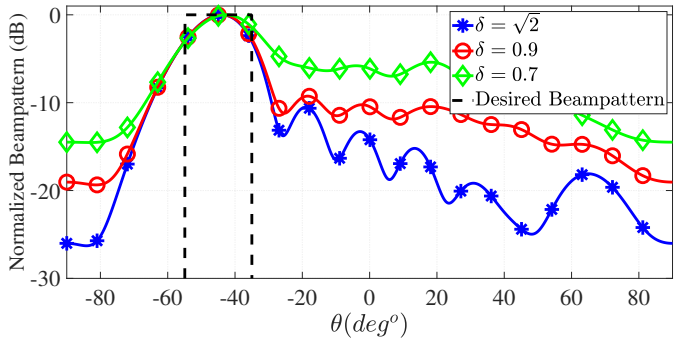

Figure 6.3. The impact of choosing δ in the devised method on the beampattern response ($M = 8$, $N = 64$, $\hat{N} = 5N$, $\Theta_d = [-55°, -35°]$ and $\Theta_u = [-90°, -60°] \cup [-30°, 90°]$, $\mathcal{U} = [0.12, 0.14] \cup [0.3, 0.35] \cup [0.7, 0.8]$, and $\gamma = 0.01\sqrt{\hat{N}}$).

freedom to enforce properties similar to the reference waveform on the optimal waveform. As mentioned earlier, $\mathbf{S}_0$ is considered to be a set of sequences with a good range ISLR property as the reference signal for similarity constraint, which is obtained by the UNIQUE method [2]. Therefore, by decreasing δ, a waveform set with good orthogonality among the sequences in the set is obtained, which leads to an omnidirectional beampattern.

Figure 6.3 shows the beampattern response of the devised method with different values of δ. As can be observed, an optimum beampattern is produced when $\delta = \sqrt{2}$, and as δ is decreased, the beampattern eventually tends to be omnidirectional.

In addition, the correlation level for various values of δ between the fourth transmit waveform created by the devised approach and other transmit sequences in the designed matrix $\mathbf{X}$ is illustrated in the figures Figure 6.4(a), Figure 6.4(c), and Figure 6.4(e). Observe that with $\delta = \sqrt{2}$ a fully correlated waveform is obtained and by decreasing δ the waveform gradually becomes uncorrelated. Besides Figure 6.4(b), Figure 6.4(d) and Figure 6.4(f) show the spectrum of the devised method with different values of δ. As can be seen in all cases. the devised method is able to perform the spectral masking. Additionally, notice that the transmit waveforms' spectral responses are more comparable for $\delta = \sqrt{2}$ than for lower values of δ in

the desired frequency range (e.g., in the range $[0.36, 0.69]$). This observation indicates that a more similar spectral response results in waveforms that are more correlated.

6.4.4 The Impact of Zero Padding

Figure 6.5 shows the impact of choosing $\hat{N}$ on the spectral response of the devised method. This figure indicates the DFT points as N_{FFT}. Figure 6.5(a) shows the spectrum response of WISE when zero padding is not applied, ($\hat{N} = N$) and $N_{\text{FFT}} = N$. In this case, the devised method is able to mask the spectral response on undesired frequencies. When the FFT resolution increases to $N_{\text{FFT}} = 5N$, some spikes appear in the $\mathcal{U}$ region (see Figure 6.5(b)). However, as can be observed from Figure 6.5(c) and Figure 6.5(d), when zero padding is applied to $\hat{N} = 5N$, the devised method is able to mask the spectral response on undesired frequencies for both $N_{\text{FFT}} = 5N$ and $N_{\text{FFT}} = 10N$.

6.5 CONCLUSION

This chapter discusses the problem of beampattern shaping with practical constraints in MIMO radar systems, namely, spectral masking, 3-dB beamwidth, as well as constant modulus and similarity constraints. Solving this problem, not considered hitherto, enables the control of the performance of MIMO radar in three domains of spatial, spectral, and orthogonality (by similarity constraints). Accordingly, a waveform design approach is considered for beampattern shaping, which is non convex and NP-hard in general. In order to obtain a local optimum of the problem, first by introducing a slack variable the optimization problem is converted to a linear problem with a rank 1 constraint. Then, to tackle the problem, an iterative method, referred to as WISE, is devised to obtain the rank 1 solution. Numerical results shows that the devised method is able to manage the resources efficiently to obtain the best performance.

References

[1] E. Raei, S. Sedighi, M. Alaee-Kerahroodi, and M. Shankar, "MIMO radar transmit beampattern shaping for spectrally dense environments," *arXiv preprint arXiv:2112.06670*, 2021.

[2] E. Raei, M. Alaee-Kerahroodi, and M. B. Shankar, "Spatial- and range- ISLR trade-off in MIMO radar via waveform correlation optimization," *IEEE Transactions on Signal Processing*, vol. 69, pp. 3283–3298, 2021.

[3] J. Li and P. Stoica, *MIMO Radar Signal Processing*. John Wiley & Sons, Inc., Hoboken, NJ, 2009.

[4] A. Aubry, A. De Maio, and Y. Huang, "MIMO radar beampattern design via PSL/ISL optimization," *IEEE Transactions on Signal Processing*, vol. 64, pp. 3955–3967, Aug 2016.

[5] P. Stoica, J. Li, and Y. Xie, "On probing signal design for MIMO radar," *IEEE Transactions on Signal Processing*, vol. 55, no. 8, pp. 4151–4161, 2007.

[6] M. Alaee-Kerahroodi, E. Raei, S. Kumar, and B. S. M. R. R. R., "Cognitive radar waveform design and prototype for coexistence with communications," *IEEE Sensors Journal*, pp. 1–1, 2022.

[7] A. Aubry, A. De Maio, M. Piezzo, and A. Farina, "Radar waveform design in a spectrally crowded environment via nonconvex quadratic optimization," *IEEE Transactions on Aerospace and Electronic Systems*, vol. 50, no. 2, pp. 1138–1152, 2014.

[8] A. Aubry, A. De Maio, Y. Huang, M. Piezzo, and A. Farina, "A new radar waveform design algorithm with improved feasibility for spectral coexistence," *IEEE Transactions on Aerospace and Electronic Systems*, vol. 51, no. 2, pp. 1029–1038, 2015.

[9] K. Shen and W. Yu, "Fractional programming for communication systems—part i: Power control and beamforming," *IEEE Transactions on Signal Processing*, vol. 66, no. 10, pp. 2616–2630, 2018.

[10] R. A. Horn and C. R. Johnson, *Matrix analysis*. Cambridge university press, 2012.

[11] J. C. Bezdek and R. J. Hathaway, "Convergence of alternating optimization," *Neural, Parallel & Scientific Computations*, vol. 11, no. 4, pp. 351–368, 2003.

[12] J. R. Senning, "Computing and estimating the rate of convergence," 2007.

[13] Z. Luo, W. Ma, A. M. So, Y. Ye, and S. Zhang, "Semidefinite relaxation of quadratic optimization problems," *IEEE Signal Processing Magazine*, vol. 27, pp. 20–34, May 2010.

[14] G. H. Golub and C. F. Van Loan, *Matrix Computations*. The Johns Hopkins University Press, third ed., 1996.

[15] "Cvx package." `http://cvxr.com/cvx/`. Accessed: 2021-06-07.

[16] M. S. Gowda and R. Sznajder, "Schur complements, Schur determinantal and Haynsworth inertia formulas in Euclidean Jordan algebras," *Linear Algebra Appl*, vol. 432, pp. 1553–1559, 2010.

APPENDIX 6A

It is readily confirmed that the constraint $\mathbf{X}_n = \bar{\mathbf{s}}_n\bar{\mathbf{s}}_n^H$ is equivalent to $\text{Rank}(\mathbf{X}_n - \bar{\mathbf{s}}_n\bar{\mathbf{s}}_n^H) = 0$. Further, it can be equivalently expressed as $1 + \text{Rank}(\mathbf{X}_n - \bar{\mathbf{s}}_n\bar{\mathbf{s}}_n^H) = 1$. Since 1 is positive-definite, it follows from the Guttman rank additivity formula [16] that $1 + \text{Rank}(\mathbf{X}_n - \bar{\mathbf{s}}_n\bar{\mathbf{s}}_n^H) = \text{Rank}(\mathbf{Q}_n)$. Moreover, it follows from $\mathbf{X}_n = \bar{\mathbf{s}}_n\bar{\mathbf{s}}_n^H$ and $1 \succ 0$ that $\mathbf{Q}_n$ has to be positive semidefinite. These imply that the constraint $\mathbf{X}_n = \bar{\mathbf{s}}_n\bar{\mathbf{s}}_n^H$ in (5.42) can be replaced with a rank and semidefinite constraints on matrix $\mathbf{Q}_n$. Hence, the optimization problem (5.42) can be recast as follows,

$$\begin{cases} \min\limits_{\mathbf{S},\mathbf{X}_n} & \sum\limits_{n=1}^{N} \text{Tr}(\mathbf{A}_u\mathbf{X}_n) & \text{(6A.1a)} \\ s.t. & \text{(6.6b), (6.6c), (6.6d), (6.6e), (6.6f), (6.6g)} & \text{(6A.1b)} \\ & \mathbf{Q}_n \succcurlyeq \mathbf{0} & \text{(6A.1c)} \\ & \text{Rank}(\mathbf{Q}_n) = 1 & \text{(6A.1d)} \end{cases}$$

Now, we show that the optimization problem (6.7) is equivalent to (6A.1). Let $\rho_{n,1} \leq \rho_{n,2} \leq \cdots \leq \rho_{n,M+1}$ and $\nu_{n,1} \leq \nu_{n,2} \leq \cdots \leq \nu_{n,M}$ denote the eigenvalues of $\mathbf{Q}_n$ and $\mathbf{V}_n^H\mathbf{Q}_n\mathbf{V}_n$, respectively. From the constraint $b_n\mathbf{I}_M - \mathbf{V}_n^H\mathbf{Q}_n\mathbf{V}_n \succcurlyeq 0$, we have $\nu_{n,i} \leq b_n, i = 1, 2, \cdots, M$ for any $\mathbf{V}_n$ and $\mathbf{Q}_n$ in the feasible set of (6.7). Additionally, it follows from [10, Corollary 4.3.16] that $0 \leq \rho_{n,i} \leq \nu_{n,i}, i = 1, 2, \cdots, M$ for any $\mathbf{V}_n$ and $\mathbf{Q}_n$ in the feasible set of (6.7). Hence, we observe that

$$\begin{aligned} \mathbf{0} &\preccurlyeq \text{Diag}([\rho_{n,1}, \cdots, \rho_{n,M}]^T) \\ &\preccurlyeq \text{Diag}([\nu_{n,1}, \cdots, \nu_{n,M}]^T) \preccurlyeq b_n\mathbf{I}_M \end{aligned} \tag{6A.2}$$

for any $\mathbf{V}_n$ and $\mathbf{Q}_n$ in the feasible set of (6.7). It is easily observed from (6.7) and (6A.2) that, by properly selecting η, the optimum value of $\mathbf{V}_n$ will be equal to the eigenvectors of $\mathbf{Q}_n$ corresponding to its M smallest eigenvalues and the optimum values of $b_n, \rho_{n,1}, \cdots, \rho_{n,M}, \nu_{n,1}, \cdots, \nu_{n,M}$ will be equal to zero. This implies that the optimum value of $\mathbf{Q}_n$ in (6A.2) possesses one nonzero and M zero eigenvalues. This completes the proof.

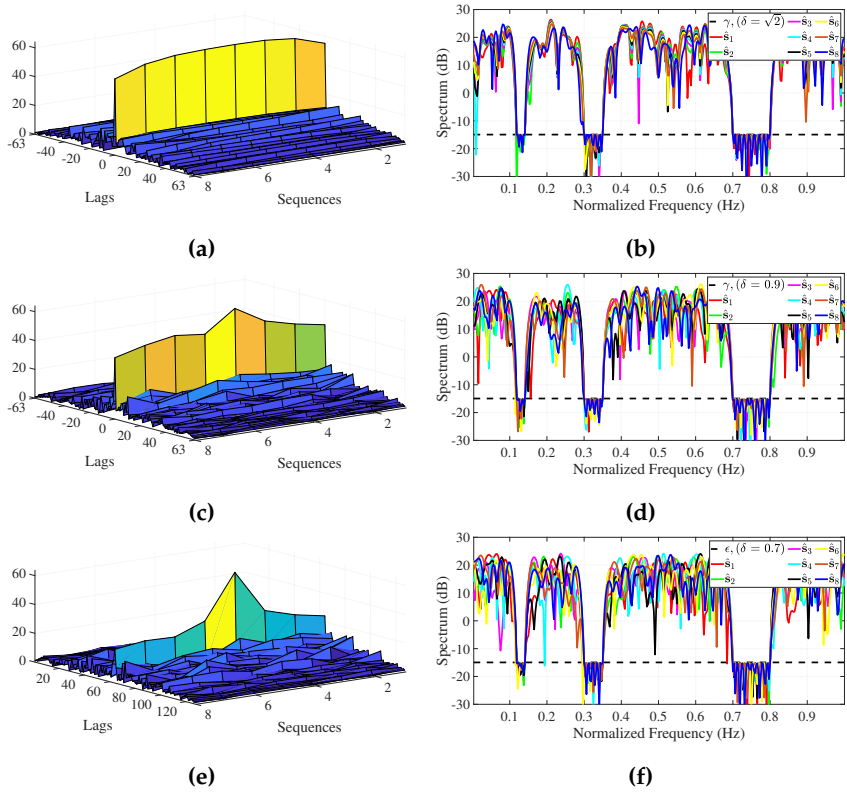

Figure 6.4. The impact of choosing δ on correlation level and spectral masking ($M = 8$, $N = 64$, $\hat{N} = 5N$, $\Theta_d = [-55°, -35°]$, and $\Theta_u = [-90°, -60°] \cup [-30°, 90°]$, $\mathcal{U} = [0.12, 0.14] \cup [0.3, 0.35] \cup [0.7, 0.8]$ and $\gamma = 0.01\sqrt{\hat{N}}$): (a) $\delta = \sqrt{2}$, (b) $\delta = \sqrt{2}$, (c) $\delta = 0.9$, (d) $\delta = 0.9$, (e) $\delta = 0.7$, (f) $\delta = 0.7$.

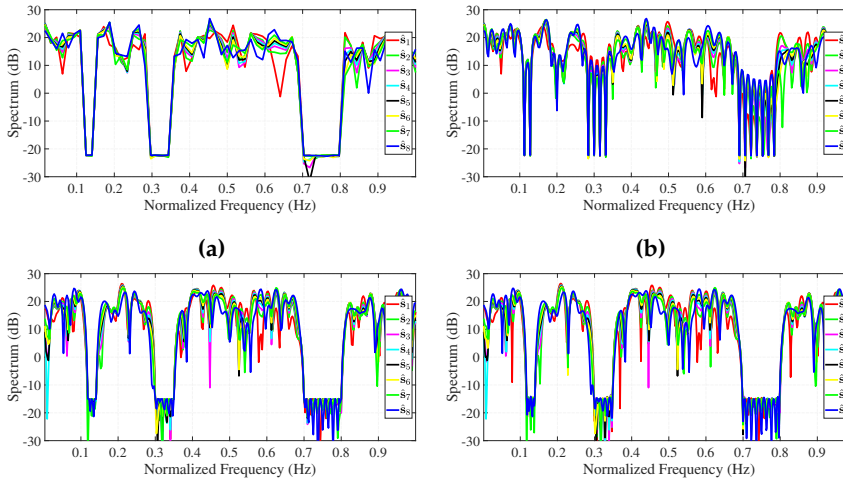

Figure 6.5. The impact of choosing $\hat{V}$ and N_{FFT} on the spectral response ($M = 8$, $N = 64$, $\Theta_d = [-55°, -35°]$ and $\Theta_u = [-90°, -60°] \cup [-30°, 90°]$, $\mathcal{U} = [0.12, 0.14] \cup [0.3, 0.35] \cup [0.7, 0.8]$, and $\gamma = 0.01\sqrt{\hat{N}}$): (a) $\hat{N} = N$ and $N_{\text{FFT}} = N$, (b) $\hat{N} = N$ and $N_{\text{FFT}} = 5N$, (c) $\hat{N} = 5N$ and $N_{\text{FFT}} = 5N$, (d) $\hat{N} = 5N$ and $N_{\text{FFT}} = 10N$.

Chapter 7

Deep Learning for Radar

Over the past decade, data-driven methods, specifically deep learning techniques, have attracted unprecedented attention from research communities across the board. The advent of low-cost specialized powerful computing resources and the continually increasing amount of data generated by the human population and machines, in conjunction with the new optimization and learning methods, have paved the way for deep neural networks (DNNs) and other machine learning-based models to prove their effectiveness in many engineering areas. Deterministic DNNs are constructed in a fashion that inference is straightforward, where the output of the network is obtained via consecutive matrix multiplications, resulting in a fixed computational complexity inference model.

The significant success of deep learning models in areas such as natural language processing (NLP) [1], life sciences [2], computer vision (CV) [3], and collaborative learning [4], among many others, has led to a surge of interest in employing deep learning models for radar signal processing. The exploitation of deep learning, however, is to be looked at through the specific lens of the critically and agility requirements that come with radar applications. To account for difficulties in the underlying signal processing tasks, most existing deep learning approaches resort to very large networks whose numbers of parameters are in the order of millions and billions [5]—making such models data and computing power hungry. Such bulky deep learning models further introduce nonignorable latency during inference which hinders in-time decision-making. More importantly, with all their repertoire of success, the existing data-driven tools typically lack the interpretability and trustability that comes with model-based signal processing.

They are particularly prone to be questioned further, or at least not fully trusted by the users, especially in critical applications such as autonomous vehicles or myriad of defense operations. Last but not least, the deterministic deep architectures are generic and it is unclear how to incorporate the existing domain knowledge on the problem in the processing stage. In contrast, many signal processing algorithms are backed by decades of theoretical development and research resulting in accurate, meaningful, and reliable models. Due to their theoretical foundations, model-based signal processing algorithms usually come with performance guarantees and bounds allowing for a robustness analysis of the output of the model and certifying the achievable performance required for the underlying task.

Despite the mentioned drawbacks of the generic deep learning models, there have been some attempts in adopting and repurposing such generic deep learning models for applications in radar signal processing, showing good performance. To name a few, [6] presented a general perspective on the application of deep learning in radar processing. The authors in [7] considered developing a data-driven methodology for the problem of joint design of transmitted waveform and detector in a radar system. The authors in [8] considered the problem of automatic waveform classification in the context of cognitive radar using generic convolutional auto-encoder models. Moreover, the research work [9] considered a deep learning-based radar detector. For a detailed treatment of the recent deep learning models for radar signal processing applications, we refer the reader to [10] and the references therein.

It has become apparent that a mere adoption or modification of generic deep neural networks designed for applications such as NLP and CV and ignoring years of theoretical developments mentioned earlier will result in inefficient networks. This is even more pronounced in the long-standing radar problems with a rich literature. Hence, it is to our belief that one needs to rethink the architectural design of deep neural models rather than repurposing them for adoption in critical fields such as radar signal processing.

The advantages associated with both model-based and data-driven methods show the need for developing frameworks that bridge the gap between the two approaches. The recent advent of the deep unfolding framework [11–18] has paved the way for a solution to the above problems by a game-changing fusion of models, and well-established signal processing approaches, with data-driven architectures. In this way, we not only exploit

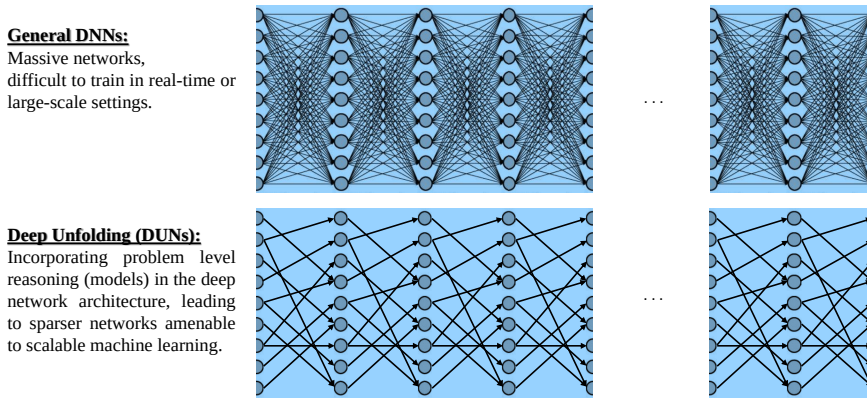

Figure 7.1. General DNNs versus DUNs. DUNs appear to be an excellent tool in reliable and real-time radar applications due to well-understood architecture as well as smaller degrees of freedom required for training and execution.

the vast amounts of available data but also integrate the prior knowledge of the system/inference model in the processing stage. Deep unfolding networks (DUNs) rely on the establishment of an optimization or inference iterative algorithm, whose iterations are then unfolded into the layers of a deep network, where each layer is designed to resemble one iteration of the optimization/inference algorithm. The proposed hybrid method benefits from the low computational cost (in execution stage) of deep neural networks and, at the same time, from the flexibility, versatility, and reliability of model-based methods. Moreover, the emerging networks appear to be an excellent tool in scalable or real-time machine learning applications due to the smaller degrees of freedom required for training and execution (afforded by the integration of the problem-level reasoning, or the model), see Figure 7.1.

In this chapter, we present our vision in developing interpretable, trustable, and model-driven neural networks for radar applications, starting from its theoretical foundations, to advance the state of the art in radar signal processing using machine learning. In contrast to generic deep neural networks, which cannot provide performance guarantees due to their black-box nature, the discussed deep network architectures allow for performing

a mathematical analysis of the performance of the model not only during the training of the network but also once the network is trained and is to be used for inference purposes. Last but not least, due to the incorporation of domain knowledge in the design of the network, the total number of parameters of the network are in the order of the signal dimension and the training can be performed very quickly with far less data samples—thus allowing for on-the-fly training in real-time radar applications.

7.1 DEEP LEARNING FOR GUARANTEED RADAR PROCESSING

As a central task in radar processing, we begin by looking at the problem of receive filter design for a given probing signal. Specifically, our goal is to design a filter to minimize the recovery MSE of the scattering coefficient of the target in the presence of clutter.

We take advantage of the same radar model as in Section 3.4.2. As mentioned above, a principal task and challenging problem for a radar signal processing unit is to obtain an estimation of the scattering coefficient α_0 given the acquired samples $\boldsymbol{y}$ in presence of clutter, to find the significantly contributing radar cross section (RCS). The RCS and the average clutter power are assumed to be constant during the observation interval. A useful methodology in obtaining an estimation of the scattering coefficient of interest α_0 is to use a mismatched filter (MMF) in the receiver side [19]. The deployment of mismatched filter in pulse compression has a great impact in clutter rejection and can be viewed as a linear estimator in which the estimate of α_0 is given by the MMF model $\hat{\alpha}_0 = \boldsymbol{w}^H \boldsymbol{y} / \boldsymbol{w}^H \boldsymbol{s}$, where $\boldsymbol{w} \in \mathbb{C}^N$ is the MMF vector. Under the aforementioned assumptions on the signal model and noise statistics, the optimal MMF filter $\boldsymbol{w}^\star$ can be formulated as the minimizer of the following objective function:

$$f(\boldsymbol{w}; \boldsymbol{s}) = \mathrm{MSE}(\hat{\alpha}_0; \boldsymbol{w}, \boldsymbol{s}) = \mathbb{E}\left\{ \left| \alpha_0 - \frac{\boldsymbol{w}^H \boldsymbol{y}}{\boldsymbol{w}^H \boldsymbol{s}} \right|^2 \right\} = \frac{\boldsymbol{w}^H \boldsymbol{R} \boldsymbol{w}}{|\boldsymbol{w}^H \boldsymbol{s}|^2} \tag{7.1}$$

where the interference covariance matrix $\boldsymbol{R}$ is given by:

$$\boldsymbol{R} = \gamma \sum_{0<|k|\leq(N-1)} \boldsymbol{J}_k \boldsymbol{s} \boldsymbol{s}^H \boldsymbol{J}_k^H + \boldsymbol{C} \tag{7.2}$$

and $\{\boldsymbol{J}_k\}$ are the same shift matrices that were introduced in (3.26). Specifically, the minimizer of the objective function $f(\boldsymbol{w};\boldsymbol{s})$ with respect to the MMF filter follows the well-known closed-form solution [20]:

$$\boldsymbol{w}^\star = \boldsymbol{R}^{-1}\boldsymbol{s} = \underset{\boldsymbol{w}\in\mathbb{C}^N}{\operatorname{argmin}} f(\boldsymbol{w};\boldsymbol{s}) \tag{7.3}$$

where the lower bound on the performance of the estimator (7.3) is given by $\mathrm{MSE}\,(\hat{\alpha}_0;\boldsymbol{w}^\star,\boldsymbol{s}) = (\boldsymbol{s}^H\boldsymbol{R}^{-1}\boldsymbol{s})^{-1}$. Note that, in practice, the covariance matrix $\boldsymbol{C}$ of the signal-independent interference is typically approximated via a sample covariance approach using the data gathered at prescan procedures during which the radar remains silent [21, 22].

Although the optimal MMF vector $\boldsymbol{w}^\star = \boldsymbol{R}^{-1}\boldsymbol{s}$ has a good performance in recovering the scattering coefficient in the presence of clutter, obtaining it requires inverting an $N \times N$ matrix $\boldsymbol{R}$, which may be computationally prohibitive in practice for large N, and present a critical computational bottleneck in real-time radar implementation. The inversion is not only computationally expensive, but also requires large data storage capabilities and is highly prone to numerical errors for ill-conditioned matrices. In the following, we propose a highly tailored model-based deep architecture based on the Neumann series inversion lemma, where the resulting network allows for: (1) controlling the computational complexity of the inference rule, (2) efficiently and quickly finding the optimal MMF vector, and (3) deriving performance bounds on the error of the estimator, upon training the network.

7.1.1 Deep Architecture for Radar Processing

In this section, we present the Deep Neural Matrix Inversion (DNMI) technique for radar processing. At the heart of our illustrative derivations in the following lies the Neumann power series expansion for matrix inversion [23]. As indicated earlier, in many signal detection and estimation tasks, including our radar problem, one usually encounters matrix inversion, whose computation may be prohibitive in large-scale settings. A similar problem arises, more broadly, in mathematical optimization techniques where a Hessian matrix is to be inverted. In such scenarios, truncated Neumann series (NS) expansions provide a low-cost alternative to approximate the inverted matrices. In the following, we first give a brief introduction to the Neumann series for matrix inversion, upon which we derive the architecture of our proposed DNN.

Theorem 1. (Neumann Series Theorem) [24]: Denote by $\{\lambda_1, \lambda_2, \cdots, \lambda_N\}$ *the set of eigenvalues of the augmented square matrix* $\bar{\boldsymbol{R}} = (\boldsymbol{I} - \boldsymbol{R})$. *If* $\rho\left(\bar{\boldsymbol{R}}\right) \triangleq \max_i |\lambda_i| < 1$, *the power series* $\bar{\boldsymbol{R}}^0 + \bar{\boldsymbol{R}}^1 + \bar{\boldsymbol{R}}^2 + \cdots$ *then converges to* $\boldsymbol{R}^{-1}$, *that is, we have* $\boldsymbol{R}^{-1} = \sum_{l=0}^{\infty} \left(\boldsymbol{I} - \boldsymbol{R}\right)^l$.

The above Neumann series theorem provides a powerful alternative for the exact matrix inversion by considering a truncation of the inversion series. Specifically, one may truncate the above expansion to only the K-term and use it as an approximation of the exact inversion. However, one can only rely on such an inversion technique if the underlying matrix satisfies the condition $\rho(\boldsymbol{I} - \boldsymbol{R}) < 1$. In many practical applications, the underlying matrix does not satisfy such a condition, which, in turn, renders the K-term Neumann series approximation inapplicable. To alleviate this problem, we further propose to augment the NS technique with a preconditioning matrix $\boldsymbol{W} \in \mathbb{C}^{N \times N}$, to obtain the following modified NS for matrix inversion:

$$\boldsymbol{R}^{-1} = (\boldsymbol{W}\boldsymbol{R})^{-1}\boldsymbol{W} = \left(\sum_{l=0}^{\infty} (\boldsymbol{I} - \boldsymbol{W}\boldsymbol{R})^l\right)\boldsymbol{W} \tag{7.4}$$

where the convergence is ensured if $\rho(\boldsymbol{I} - \boldsymbol{W}\boldsymbol{R}) < 1$. Note that, even with this augmentation, a judicious design of the preconditioning matrix is critical to the convergence of the above series. Constructing such matrices is an active area of research and is indeed a very difficult task [25, 26]. To the best of our knowledge, there exists no general methodology for designing the preconditioning matrices that ensure convergence and also result in an accelerated convergence of the underlying truncated NS. In the following, we present our proposed deep learning model that allows not only for tuning the preconditioning matrix in a data-driven manner but also an accelerated and accurate matrix inversion.

In light of the above, we propose to interpret the first K-term truncation of the Neumann series in (7.4) as a K-layer deep neural network, for which the matrix to be inverted $\boldsymbol{R}$ constitutes the input, and the preconditioning matrix the set of trainable parameters, given by $\phi = \{\boldsymbol{W} \in \mathbb{C}^{N \times N}\}$. Accordingly, let $\boldsymbol{G} = \boldsymbol{I} - \boldsymbol{W}\boldsymbol{R}$ and $\mathbb{L} = \{1, \cdots, K-2\}$. Then the mathematical operations carried out in the layers of the proposed deep architecture

are governed by the relations:

$$\begin{aligned}
&\boldsymbol{g}_0(\boldsymbol{R};\phi) = \boldsymbol{u}_0,\ \boldsymbol{u}_0 = \boldsymbol{I} \\
&\boldsymbol{g}_i(\boldsymbol{R};\phi) = \boldsymbol{G}\boldsymbol{u}_{i-1} + \boldsymbol{g}_{i-1}(\boldsymbol{R};\phi),\ \boldsymbol{u}_i = \boldsymbol{G}\boldsymbol{u}_{i-1},\ \forall\, i \in \mathbb{L} \\
&\boldsymbol{g}_{K-1}(\boldsymbol{R};\phi) = \boldsymbol{g}_{K-2}(\boldsymbol{R};\phi)\boldsymbol{W}
\end{aligned} \tag{7.5}$$

The overall mathematical expression of the proposed neural network can be given as

$$\mathcal{G}_\phi(\boldsymbol{R}) = \boldsymbol{g}_{K-1} \circ \cdots \circ \boldsymbol{g}_0(\boldsymbol{R};\phi). \tag{7.6}$$

It is not difficult to observe that the proposed neural network in (7.6) is equivalent to performing a K-term truncated version of (7.4), that is,

$$\mathcal{G}_\phi(\boldsymbol{R}) = \boldsymbol{R}_K^{-1}(\boldsymbol{W}) = \left(\sum_{l=0}^{K-1} (\boldsymbol{I} - \boldsymbol{W}\boldsymbol{R})^l\right)\boldsymbol{W} \tag{7.7}$$

yielding a matrix inversion operation with controllable computational cost, whose accuracy depends on the choice of the preconditioning matrix $\boldsymbol{W}$ and the total number of terms K. In particular, a judicious design of the preconditioning matrix $\boldsymbol{W}$ is expected to result in an accelerated Neumann series that provides higher accuracy while utilizing very few terms, as well as ensuring the convergence of the NS by guaranteeing $\rho(\boldsymbol{I} - \boldsymbol{W}\boldsymbol{R}) < 1$. In fact, the proposed deep architecture provides significant flexibility in learning the preconditioning matrix $\boldsymbol{W}$: one can impose a diagonal structure by defining $\boldsymbol{W} = \mathrm{diag}(w_1, \cdots, w_N)$, a tridiagonal structure, or a rank-constrained structure via parameterization $\boldsymbol{W} = \boldsymbol{A}\boldsymbol{B}$, where $\boldsymbol{A} \in \mathbb{C}^{N\times M}$ and $\boldsymbol{B} \in \mathbb{C}^{M\times N}$ ($M < N$), among many other useful structures depending on the application.

Recall that the optimal MMF vector, for a given covariance matrix $\boldsymbol{R}$ and probing signal $\boldsymbol{s}$, can be expressed as $\boldsymbol{w}^\star(\boldsymbol{R}, \boldsymbol{s}) = \boldsymbol{R}^{-1}\boldsymbol{s}$. The application of the proposed DNMI technique is thus immediate. Instead of using (7.3), we propose the following approximation of the MMF vector using the DNMI architecture:

$$\boldsymbol{w}_K^\star(\boldsymbol{R}, \boldsymbol{s};\phi) = \mathcal{G}_\phi(\boldsymbol{R})\boldsymbol{s} \tag{7.8}$$

where $\boldsymbol{w}_K^\star(\boldsymbol{R}, \boldsymbol{s};\phi)$ denotes the DNMI-based MMF vector. In the following, we briefly discuss the training stage of the DNMI network.

7.1.1.1 Training Procedure

The training of the proposed network can be carried out by using stochastic gradient descent optimizers commonly used for deep learning. Specifically, we consider the following scenario for training of the network depending on the available data. We assume the existence of a dataset of size B containing training tuples of the form $\{(\boldsymbol{w}^\star(\boldsymbol{R}^i, \boldsymbol{s}^i), \boldsymbol{R}^i)\}_{i=0}^{B-1}$. Such a dataset can be easily generated in an offline manner, via computing the optimal MMF vector through exact matrix inversion (a one-time cost), and upon training the network, one can employ the optimized DNMI network for inference purposes through (7.8). The training thus can be carried out according to:

$$\min_{\phi \in \mathbb{C}^{N \times N}} \frac{1}{B} \sum_i \|\boldsymbol{w}^\star(\boldsymbol{R}^i, \boldsymbol{s}^i) - \mathcal{G}_\phi(\boldsymbol{R}^i)\|_2^2 \tag{7.9}$$

7.1.1.2 Performance Guarantees

In contrast to generic DNNs, which may not provide performance guarantees due to their black-box nature, one can perform a mathematical analysis of the worst-case performance bound of the expansion series-based deep networks after the training is completed. As a case in point, one can verify that the accuracy of the K-layer DNMI network is bounded by the $(K+1)$-th power of the spectral norm of the matrix $\boldsymbol{I} - \boldsymbol{W}\boldsymbol{R}$. This provides an upper bound of the error that can guide the training in terms of the number of training epochs, training samples, and number of layers and, once the network is trained, provides an upper bound on the error of the network inference or optimization output—see below.

Let $\boldsymbol{G} = (\boldsymbol{I} - \boldsymbol{W}\boldsymbol{R})$. Then we define the error vector between the true MMF vector $\boldsymbol{w}^\star(\boldsymbol{R}, \boldsymbol{s})$ and the output of the DNMI network as follows:

$$\boldsymbol{e} = \boldsymbol{w}^\star(\boldsymbol{R}, \boldsymbol{s}) - \mathcal{G}_\phi(\boldsymbol{R})\boldsymbol{s} = \left(\boldsymbol{R}^{-1} - \boldsymbol{R}_K^{-1}(\boldsymbol{W})\right)\boldsymbol{s} \tag{7.10}$$

where we have that

$$\boldsymbol{R}^{-1} - \boldsymbol{R}_K^{-1}(\boldsymbol{W}) = \sum_{l=K}^{\infty} \boldsymbol{G}^l \boldsymbol{W} = \boldsymbol{G}^K \sum_{l=0}^{\infty} \boldsymbol{G}^l \boldsymbol{W} = \boldsymbol{G}^K \boldsymbol{R}^{-1} \tag{7.11}$$

Thus, from (7.10) to (7.11), we have the following upper bound on the error:

$$\|\boldsymbol{e}\|_2 = \|\boldsymbol{G}^K \boldsymbol{R}^{-1}\boldsymbol{s}\|_2 \leq \|\boldsymbol{G}^K\| \|\boldsymbol{R}^{-1}\boldsymbol{s}\|_2 \leq \rho^K(\boldsymbol{G}) \|\boldsymbol{R}^{-1}\boldsymbol{s}\|_2 \tag{7.12}$$

where the last inequality is obtained considering that $\|\boldsymbol{G}^K\| \leq \|\boldsymbol{G}\|^K = \rho^K(G)$. Note that such an error bound directly translates to a measure of closeness to the optimal MSE in the recovery of the target scattering coefficient α_0. It is clear from (7.12) that the spectral norm $\rho(\boldsymbol{G})$ provides a certificate for convergence. In addition, once can observe that a judicious design of $\boldsymbol{W}$ can result in the acceleration of the convergence (i.e., having a smaller $\rho(\boldsymbol{G})$).

The importance of the above upper bound is twofold. First, during the training of the network, one can check the convergence of the network and obtain a measure of success by looking into $\rho(\boldsymbol{G}^i = \boldsymbol{I} - \boldsymbol{W}\boldsymbol{R}^i)$ for training/testing data points. Second, once the network is trained, the obtained $\rho(\boldsymbol{G})$, for a specific covariance matrix, provides an upper bound on the expected error of the network, for the current number of layers, or as we introduce more layers. Indeed, once the network is certified for a specific $\boldsymbol{R}$ (meaning $\rho(\boldsymbol{G}) < 1$), one can aim to have $\|\boldsymbol{e}\|_2 \leq \epsilon$, for arbitrary $\epsilon > 0$, by employing more layers, for instance, K' layers of the trained network (without retraining) to meet such a bound via simply choosing $K' \geq \left(\ln \epsilon - \ln \|\boldsymbol{w}^\star(\boldsymbol{R}, \boldsymbol{s})\|_2\right) / \ln \rho(\boldsymbol{G})$.

7.1.2 Numerical Studies and Remarks

We investigate the performance of the proposed DNMI network through various numerical studies. We set $\beta = 1$, and $\sigma^2 = 1$, and fix the number of layers of the proposed DNMI to $K = 3$, and set the signal length to $N = 25$. We assume that the phases of the unimodular probing sequence $\boldsymbol{s}$ is independently and uniformly chosen from the range $[0, 2\pi)$. Accordingly, we generate a training dataset of size $B = 5,000$, and evaluate the performance of the network over a testing dataset of the same size. We train the network for a total of 100 epochs. Moreover, we define the probability of success as the percentage of datapoints for which we have $\rho(\boldsymbol{I} - \boldsymbol{W}\boldsymbol{R}^i) < 1$.

Figure 7.2 presents the empirical success rate of both training and testing points versus epoch number. Furthermore, Figure 7.2 presents the worst-case training and testing spectral norm versus the training epoch. We define the worst-case spectral norm as the maximum $\rho(\boldsymbol{G}^i)$ among the points in testing and training datasets. We note that the preconditioning matrix is initialized as $\boldsymbol{W} = \boldsymbol{I}$, and thus at the very first epoch the network boils down to a regular NS operator. However, it can be deduced from Figure 7.2 that merely using conventional NS for matrix inversion is not possible (the

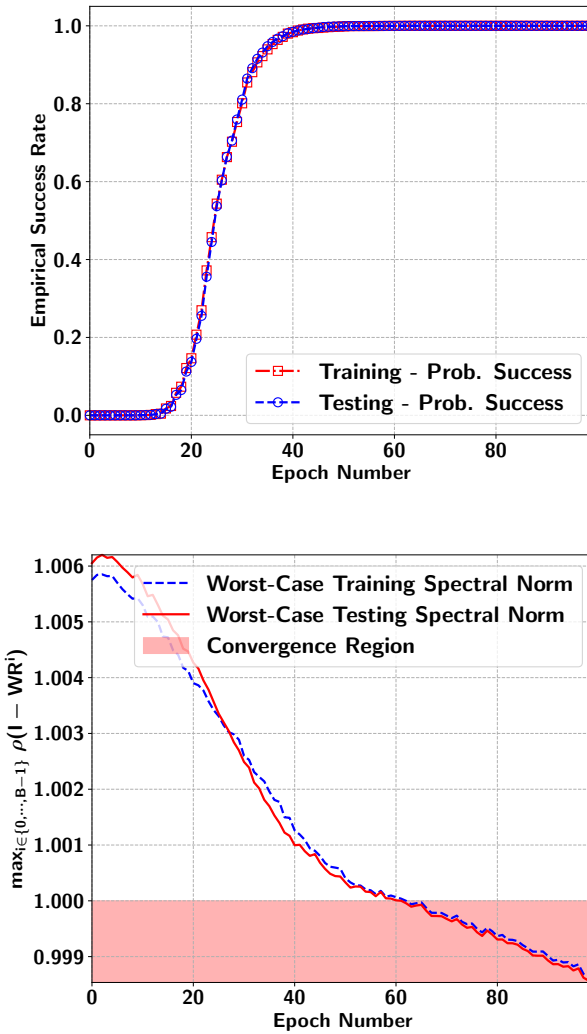

Figure 7.2. Examination of training and test success: (top) empirical success rate of training/test data versus training epoch number; (bottom) the worst-case spectral norm of the training and test data versus the epoch number.

series diverges) in that none of the data points satisfy the convergence criterion, as $\rho(\boldsymbol{G}^i) < 1$. This shows the importance of employing an optimized preconditioning matrix. However, as the training of the proposed DNMI continues, one can observe that, for epochs ≥ 60, the proposed methodology can successfully achieve $\rho(\boldsymbol{G}^i) < 1$ for all datapoints in both training and testing dataset. Furthermore, the training and testing curves in Figure 7.2 closely following each other indicates the highly significant generalization performance of the proposed methodology. This is in contrast to the conventional black-box data-driven methodologies for which the generalization gap is typically large.

Figure 7.3 demonstrates the theoretical upper bound on the error obtained in (7.12) for the proposed DNMI network versus the training epoch. Interestingly, one can observe that the network not only implicitly learns to reduce the theoretical upper bound (which is a function of the network parameter $\boldsymbol{W}$), but also keeps reducing it even after epochs ≥ 60 where the probability of success and worst-case spectral norm enter the convergence area. This implies that the learned preconditioning matrix is indeed resulting in an acceleration of the underlying NS (as the network keeps reducing the upper bound). This phenomenon is also in accordance with what we observe in Figure 7.2.

Figure 7.3 also demonstrates the MSE between the estimated scattering coefficient obtained via employing the exact MMF vector and the one obtained using the proposed DNMI network versus the number of layers of the DNMI network. First, we note that the MSE between the two methods is indeed very small, and one can obtain an accurate estimation even with K as low as 3. Second, we observe that as the number of layers increases, the accuracy of the DNMI network increases.

7.2 DEEP RADAR SIGNAL DESIGN

It would only be natural to consider the application of deep learning in radar signal design in conjunction with what we have already presented for radar signal procesing. As discussed earlier in Chapter 3, the PMLI approach paves the way for taking advantage of model-based deep learning in radar signal design. This is mainly due to its simple structure that relies on linear operations, followed by a nonlinear projection at each iteration, resembling one layer of a neural network.

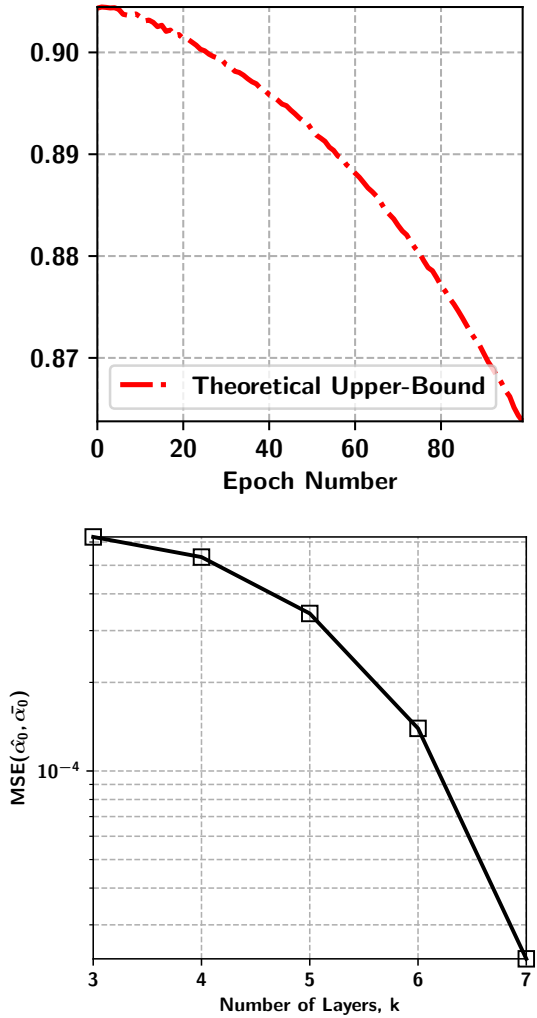

Figure 7.3. Numerical study of performance bounds: (top) the theoretical upper bound on the performance of the network versus the epoch number; (bottom) the MSE between the estimated scattering coefficient from the exact MMF and the DNMI-based MMF vector versus the number of layers of the DNMI network.

Note that, in model-based radar waveform design, the statistics of the interference and noise is usually assumed to be known (e.g., through pre-scan procedures [21, 22]). However, in many practical scenarios with a fast-changing radar engagement theater, such information may be difficult to collect and keep updated. While the previously considered radar metrics in this book would require knowledge of such information, herein we consider an alternative metric that helps to optimize the waveform's ability for resolvability along with clutter and noise rejection in a data-driven setting. Namely, using a matched filter (MF) in the pulse compression stage, one can look for waveforms that maximize the following criterion:

$$f(\boldsymbol{s}) = \frac{n(\boldsymbol{s})}{d(\boldsymbol{s})} \triangleq \frac{|\boldsymbol{s}^H \boldsymbol{y}|^2}{\sum_{k\neq 0} |\boldsymbol{s}^H \boldsymbol{J}_k \boldsymbol{y}|^2} = \frac{\boldsymbol{s}^H \boldsymbol{A} \boldsymbol{s}}{\boldsymbol{s}^H \boldsymbol{B} \boldsymbol{s}} \tag{7.13}$$

where $\boldsymbol{A} = \boldsymbol{y}\boldsymbol{y}^H$, $\boldsymbol{B} = \sum_{k\neq 0} \boldsymbol{J}_k \boldsymbol{A} \boldsymbol{J}_k^H$, and $\{\boldsymbol{J}_k\}$ are shift matrices satisfying $[\boldsymbol{J}_k]_{l,m} = [\boldsymbol{J}_{-k}^H]_{l,m} \triangleq \delta_{m-l-k}$, with $\delta_{(\cdot)}$ denoting the Kronecker delta function. Note that although $f(\mathbf{s})$ is not equal to the parametric SINR, it can be viewed as an oracle to SINR optimization using data. Considering the terms in its denominator, it promotes orthogonality of the signal with its shifted versions (thus rejecting signal dependent interference, or clutter), as well as any potential correlation with the noise within the environment (thus taking into account signal-independent interference). This makes the considered criterion more preferable to (weighted) ISL metrics that only facilitate clutter rejection.

Since both the numerator and denominator of $f(\mathbf{s})$ are quadratic in the waveform $\mathbf{s}$, an associated Dinkelbach objective for the maximization of $f(\mathbf{s})$ will take a quadratic form, say, $\mathbf{s}^H \boldsymbol{\chi} \mathbf{s}$, for given $\boldsymbol{\chi}$ that might vary as the Dinkelbach objectives vary through the optimization process. However, we readily know that the PMLI to maximize the quadratic objective $\mathbf{s}^H \boldsymbol{\chi} \mathbf{s}$ over unimodular waveforms $\mathbf{s}$ may be cast as

$$\mathbf{s}^{(t+1)} = \exp\left(j \arg\left(\boldsymbol{\chi} \mathbf{s}^{(t)}\right)\right) \tag{7.14}$$

where t denotes the iteration number and $\mathbf{s}^{(0)}$ is the current value of $\mathbf{s}$. One can continue updating $\boldsymbol{s}$ until convergence in the objective, or for a fixed number of steps, say L.

In the following, we discuss a hybrid data-driven and model-based approach that allows us to design adaptive transmit waveforms while indirectly learning the environmental parameters given the fact that such information is embedded into the observed received signal $\mathbf{y}$ of the radar. The neural network structure for the waveform design task is referred to as the Deep Evolutionary Cognitive Radar (DECoR). It will be created by considering the above PMLI approach as a baseline algorithm for the design of a model-based deep neural network [27]. Each layer of the resulting network is designed such that it imitates one iteration of the form (7.14). Consequently, the resulting deep architecture is model-aware, uses the same nonlinear operations as those in the power method, and hence, is interpretable as opposed to general deep learning models.

7.2.1 The Deep Evolutionary Cognitive Radar Architecture

The derivation begins by considering that in the vanilla PMLI algorithm, the matrix $\boldsymbol{\chi}$ is tied along all iterations. Hence, we enrich PMLI by introducing a tunable weight matrix $\boldsymbol{\chi}_i$ per iteration i. Considering the change of $\boldsymbol{\chi}$ as a result of applying the Dinkelbach's algorithm, such an over-parameterization of the iterations results in a deep architecture that is faithful to the original model-based waveform design method. This yields the following computational model for our proposed deep architecture (DECoR). Define g_{ϕ_i} as

$$g_{\phi_i}(\mathbf{z}) = \mathcal{S}(\mathbf{u}), \quad \text{where } \mathbf{u} = \boldsymbol{\chi}_i \mathbf{z} \tag{7.15}$$

where $\phi_i = \{\boldsymbol{\chi}_i\}$ denotes the set of parameters of the function g_{ϕ_i}, and observe that the nonlinear activation function of the deep network may be defined as $\mathcal{S}(\mathbf{x}) = \exp(j \arg(\mathbf{x}))$ applied element-wise on the vector argument. Then the dynamics of the proposed DECoR architecture with L layers can be expressed as:

$$\mathbf{s}_L = \mathcal{G}\left(\mathbf{s}_0; \boldsymbol{\Omega}\right) = g_{\phi_{L-1}} \circ g_{\phi_{L-2}} \circ \cdots \circ g_{\phi_0}(\mathbf{s}_0) \tag{7.16}$$

where $\mathbf{s}_0$ denotes some initial unimodular vector, and $\boldsymbol{\Omega} = \{\boldsymbol{\chi}_0, \ldots, \boldsymbol{\chi}_{L-1}\}$ denotes the set of trainable parameters of the network. The block diagram of the proposed architecture is depicted in Figure 7.4. The training of DeCoR occurs by using a random walk or random exploration strategy that is commonly used in reinforcement learning and online learning [28–32]. Such a strategy relies on continuously determining the best random perturbations

to the waveform in order to find (and possibly track) the optimum of the design criterion $f(\mathbf{s})$. More details on the training process can be found in [27].

7.2.2 Performance Analysis

We begin by evaluating the performance and effectiveness of the online learning strategy for optimizing the parameters of the DECoR architecture. For this experiment, we fix the total number of layers of the proposed DECoR architecture as $L = 30$. Throughout the simulations, we assume an environment with dynamics as in [33], with average clutter power of $\beta = 1$, and a noise covariance of $\mathbf{\Gamma} = \mathbf{I}$. This information was not made available to the DECoR architecture and we only use them for data generation purposes.

Figure 7.5 demonstrates the objective value $f(\mathbf{s}_L)$ for our experiment versus training iterations, for a waveform length of $N = 10$. It can be clearly seen that the proposed learning strategy and the corresponding DECoR architecture results in a monotonically increasing objective value $f(\mathbf{s}_L)$. It appears that the training algorithm optimizes the parameters of the proposed DECoR architecture very quickly. Next, we evaluate the performance of the presented hybrid model-based and data-driven architecture in terms of recovering the target coefficient $\alpha = \alpha_0$, in the case of a stationary target. In particular, we compare the performance of our method (DECoR) in designing unimodular codes with two state-of-the-art model-based algorithms: (1) CREW(cyclic) [34], a cyclic optimization of the transmit sequence and the receive filter; (2) CREW(MF) [34], a version of CREW(cyclic) that uses an MF as the receive filter; and (3) CREW(fre) [35], a frequency domain algorithm to jointly design transmit sequence and the receive filter.

Figure 7.5 also illustrates the empirical MSE of the estimated α_0 vs code lengths $N \in \{10, 25, 50, 100, 200\}$. The empirical MSE is defined as

$$\text{MSE}(\alpha_0) = \frac{1}{K} \sum_{k=0}^{K-1} \left| \alpha_0^{(k)} - \alpha_0 \right|^2 \tag{7.17}$$

where K denotes the total number of experiments, $\alpha_0^{(k)}$ denotes the recovered value of α_0 at the kth experiment, which is penalized based on its distance from the true α_0. For each N, we perform the optimization of DECoR architecture by allowing the radar agent to interact with the environment for 50 training epochs. After the training is completed, we use the optimized architecture to generate the unimodular code sequence $\mathbf{s}_L$ and use

Figure 7.4. The DECoR architecture for adaptive radar waveform design [27].

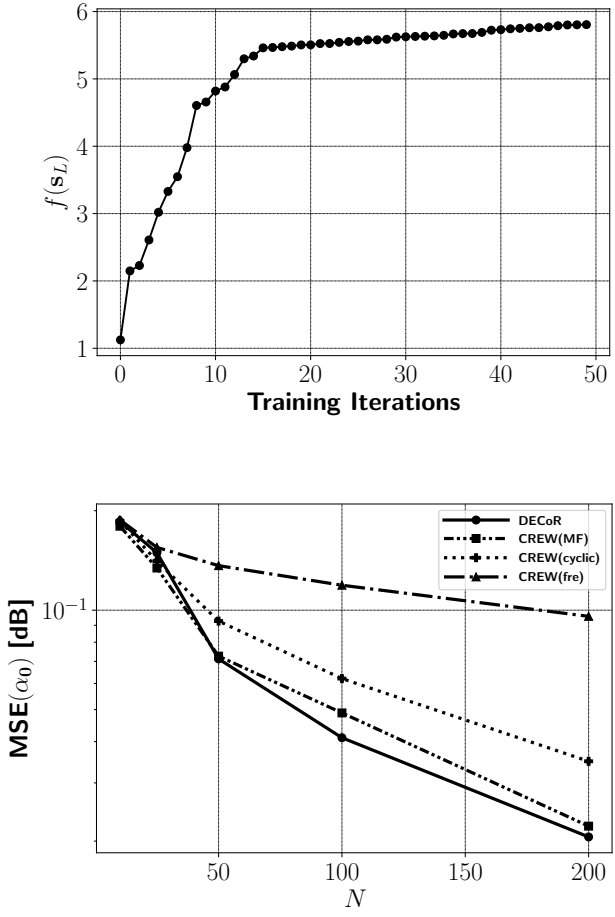

Figure 7.5. Illustration of (top) the design objective $f(\mathbf{s}_L)$ of the DECoR versus training iterations for a waveform length of $N = 10$, and (bottom) MSE values obtained by the different design algorithms for code lengths $N \in \{10, 25, 50, 100, 200\}$.

a matched filter to estimate α_0. We let the aforementioned algorithms perform the waveform design until convergence, while the presented DECoR architecture has been only afforded $L = 30$ layers (equivalent of $L = 30$ iterations). It is evident that DECoR significantly outperforms the other state-of-the-art approaches. Although the DECoR framework does not have access to the statistics of the environmental parameters (compared to the other algorithms), it is able to learn them by exploiting the observed data through interactions with the environment. A slightly better performance of DECoR can also be due to the commonly observed phenomenon in model-based deep learning that when the optimization objective is multimodal (i.e., it has many local optima), the data-driven nature of unfolded architectures, such as in DeCoR, provides them with a learning opportunity to avoid some poor local optima in their path. Such an opportunity, however, is not usually available to the considered model-based counterparts.

7.3 CONCLUSION

We discussed a reliable and interpretable deep learning approach for critical radar applications including methods for guaranteed radar signal processing and signal design. The proposed approach can take advantage of the traditional optimization algorithms as baselines, facilitating an enhanced radar performance by learning from the data.

7.4 EXERCISE PROBLEMS

Q1. Discuss how the nonlinear activation functions in the DeCoR architecture (Figure 7.4) would have been different if the desired signal was supposed to be binary, compared with the considered unimodularity constraint.

Q2. Discuss the choice of depth for the emerging DNNs by adopting a model-based perspective in network architecture determination. Would the number of layers be smaller or larger than the original iterative algorithm?

References

[1] A. Vaswani, N. Shazeer, N. Parmar, J. Uszkoreit, L. Jones, A. N. Gomez, L. Kaiser, and I. Polosukhin, "Attention is all you need," *Advances in Neural Information Processing Systems*, vol. 30, 2017.

[2] J. Jumper, R. Evans, A. Pritzel, T. Green, M. Figurnov, O. Ronneberger, K. Tunyasuvunakool, R. Bates, A. Žídek, A. Potapenko, *et al.*, "Highly accurate protein structure prediction with AlphaFold," *Nature*, vol. 596, no. 7873, pp. 583–589, 2021.

[3] M. Hassaballah and A. I. Awad, *Deep Learning in Computer Vision: Principles and Applications*. CRC Press, 2020.

[4] D. Silver, T. Hubert, J. Schrittwieser, I. Antonoglou, M. Lai, A. Guez, M. Lanctot, L. Sifre, D. Kumaran, T. Graepel, *et al.*, "Mastering chess and shogi by self-play with a general reinforcement learning algorithm," *arXiv preprint arXiv:1712.01815*, 2017.

[5] T. Brown, B. Mann, N. Ryder, M. Subbiah, J. D. Kaplan, P. Dhariwal, A. Neelakantan, P. Shyam, G. Sastry, A. Askell, *et al.*, "Language models are few-shot learners," *Advances in Neural Information Processing Systems*, vol. 33, pp. 1877–1901, 2020.

[6] E. Mason, B. Yonel, and B. Yazici, "Deep learning for radar," in *IEEE Radar Conference (RadarConf)*, pp. 1703–1708, 2017.

[7] W. Jiang, A. M. Haimovich, and O. Simeone, "Joint design of radar waveform and detector via end-to-end learning with waveform constraints," *IEEE Transactions on Aerospace and Electronic Systems*, 2021.

[8] A. Dai, H. Zhang, and H. Sun, "Automatic modulation classification using stacked sparse auto-encoders," in *2016 IEEE 13th International Conference on Signal Processing (ICSP)*, pp. 248–252, 2016.

[9] D. Brodeski, I. Bilik, and R. Giryes, "Deep radar detector," in *IEEE Radar Conference (RadarConf)*, pp. 1–6, IEEE, 2019.

[10] Z. Geng, H. Yan, J. Zhang, and D. Zhu, "Deep-learning for radar: A survey," *IEEE Access*, vol. 9, pp. 141800–141818, 2021.

[11] K. Gregor and Y. LeCun, "Learning fast approximations of sparse coding," in *Proceedings of the 27th International Conference on Machine Learning*, pp. 399–406, Omnipress, 2010.

[12] J. R. Hershey, J. L. Roux, and F. Weninger, "Deep unfolding: Model-based inspiration of novel deep architectures," *arXiv preprint arXiv:1409.2574*, 2014.

[13] J.-T. Chien and C.-H. Lee, "Deep unfolding for topic models," *IEEE Transactions on Pattern Analysis and Machine Intelligence*, vol. 40, no. 2, pp. 318–331, 2017.

[14] S. Wisdom, T. Powers, J. Pitton, and L. Atlas, "Building recurrent networks by unfolding iterative thresholding for sequential sparse recovery," in *2017 IEEE International Conference on Acoustics, Speech and Signal Processing (ICASSP)*, pp. 4346–4350, 2017.

[15] V. Monga, Y. Li, and Y. C. Eldar, "Algorithm unrolling: Interpretable, efficient deep learning for signal and image processing," *IEEE Signal Processing Magazine*, vol. 38, no. 2, pp. 18–44, 2021.

[16] S. Khobahi, N. Naimipour, M. Soltanalian, and Y. C. Eldar, "Deep signal recovery with one-bit quantization," in *IEEE International Conference on Acoustics, Speech and Signal Processing (ICASSP)*, pp. 2987–2991, IEEE, 2019.

[17] S. Wisdom, J. Hershey, J. Le Roux, and S. Watanabe, "Deep unfolding for multichannel source separation," in *IEEE International Conference on Acoustics, Speech and Signal Processing (ICASSP)*, pp. 121–125, IEEE, 2016.

[18] S. Ghungrad, B. Gould, M. Soltanalian, S. J. Wolff, and A. Haghighi, "Model-based deep learning for additive manufacturing: New frontiers and applications," *Manufacturing Letters*, vol. 29, pp. 94–98, 2021.

[19] P. Stoica, J. Li, and M. Xue, "Transmit codes and receive filters for radar," *IEEE Signal Processing Magazine*, vol. 25, no. 6, pp. 94–109, 2008.

[20] P. Stoica, H. He, and J. Li, "Optimization of the receive filter and transmit sequence for active sensing," *IEEE Transactions on Signal Processing*, vol. 60, no. 4, pp. 1730–1740, 2011.

[21] A. Aubry, A. DeMaio, A. Farina, and M. Wicks, "Knowledge-aided (potentially cognitive) transmit signal and receive filter design in signal-dependent clutter," *IEEE Transactions on Aerospace and Electronic Systems*, vol. 49, no. 1, pp. 93–117, 2013.

[22] S. Haykin, "Cognitive radar: A way of the future," *IEEE Signal Processing Magazine*, vol. 23, no. 1, pp. 30–40, 2006.

[23] G. W. Stewart, *Matrix Algorithms: Volume 1: Basic Decompositions*. SIAM, 1998.

[24] R. A. Horn and C. R. Johnson, *Matrix Analysis*. Cambridge University Press, 2012.

[25] O. Gustafsson, E. Bertilsson, J. Klasson, and C. Ingemarsson, "Approximate Neumann series or exact matrix inversion for massive MIMO?," in *2017 IEEE 24th Symposium on Computer Arithmetic (ARITH)*, pp. 62–63, 2017.

[26] D. Zhu, B. Li, and P. Liang, "On the matrix inversion approximation based on Neumann series in massive MIMO systems," in *2015 IEEE international conference on communications (ICC)*, pp. 1763–1769, IEEE, 2015.

[27] S. Khobahi, A. Bose, and M. Soltanalian, "Deep radar waveform design for efficient automotive radar sensing," in *2020 IEEE 11th Sensor Array and Multichannel Signal Processing Workshop (SAM)*, pp. 1–5, 2020.

[28] C. Szepesvári, "Algorithms for reinforcement learning," *Synthesis Lectures on Artificial Intelligence and Machine Learning*, vol. 4, no. 1, pp. 1–103, 2010.

[29] M. A. Wiering, *Explorations in Efficient Reinforcement Learning*. PhD thesis, University of Amsterdam, 1999.

[30] S. Thrun, "Exploration in active learning," *Handbook of Brain Science and Neural Networks*, pp. 381–384, 1995.

[31] L. M. Peshkin, *Reinforcement Learning by Policy Search*. Brown University, 2002.

[32] H. van Hoof, D. Tanneberg, and J. Peters, "Generalized exploration in policy search," *Machine Learning*, vol. 106, no. 9, pp. 1705–1724, 2017.

[33] P. Stoica, J. Li, and M. Xue, "Transmit codes and receive filters for radar," *IEEE Signal Processing Magazine*, vol. 25, no. 6, pp. 94–109, 2008.

[34] M. Soltanalian, B. Tang, J. Li, and P. Stoica, "Joint design of the receive filter and transmit sequence for active sensing," *IEEE Signal Processing Letters*, vol. 20, pp. 423–426, May 2013.

[35] P. Stoica, H. He, and J. Li, "New algorithms for designing unimodular sequences with good correlation properties," *IEEE Transactions on Signal Processing*, vol. 57, no. 4, pp. 1415–1425, 2009.

Chapter 8

Waveform Design in 4-D Imaging MIMO Radars

Imaging radars are conventionally referred as synthetic aperture radar (SAR) where the motion of the radar antenna over a target region is used to provide finer spatial resolution than conventional stationary beam-scanning radars [1]. As transmission and reception occur at different times, they map to different small positions. The coherent synthesis of the received signals creates a virtual aperture that is considerably wider than the physical antenna width. This is where the phrase "synthetic aperture," which allows for imaging using radar systems, comes from.

For colocated MIMO radars, waveform diversity and sparse antenna positioning produce a similar synthetic aperture property known as virtual aperture [2]. The development of automotive radar sensors, which focus on developing inexpensive sensors with high resolution and accuracy, has benefited greatly from this capacity of MIMO radars, which allows radar sensors to have high angular resolution while requiring a little quantity of physical components [3]. With a large virtual array in both azimuth and elevation, the recently developed automotive 4-D imaging MIMO radars have significant advantages over conventional automotive radars, especially when it comes to determining an object's height. This technology is necessary for the building of Level 4 and Level 5 automated vehicles as well as some Level 2 and Level 3 advanced driver-assistance systems (ADAS) features [3].

Traditional automotive radar systems are capable of scanning the roadway in a horizontal plane and determining an object's "3D's": distance,

direction, and relative velocity (Doppler). Newer 4-D imaging radar systems add a new dimension to the mix: vertical data. The term "imaging radar" refers to these devices' numerous virtual antenna elements, which contribute to the richness of the data that they return. Specifically, the radar can identify a variety of reflection points with both horizontal and vertical data, which, when mapped out, start to resemble a picture. In these emerging automotive radar sensors, short-range radar (SRR), mid-range radar (MRR), and long-range radar (LRR) applications are planned to be merged, to provide unique and high angular resolution in the entire radar detection range, as depicted in Figure 8.1. In Figure 8.1, both long-range property and fine angular resolution are combined to create a wide field of view for point cloud imaging. To achieve this property, the MIMO radar system should have the capability of transmit beampattern shaping to enhance the received SINR and the detection performance, while the orthogonality of the transmit waveforms is necessary in order to construct the MIMO radar virtual array in the receiver and achieve fine angular resolution. In this case, controlling a trade-off between beampattern shaping and orthogonality of the transmit waveforms in MIMO radar systems would be crucial because these two notions are incompatible [4].

8.1 BEAMPATTERN SHAPING AND ORTHOGONALITY

Transmit beampattern shaping, which was previously covered in Chapter 5, plays a significant role in enhancing the radar performance through increased power efficiency, improved target identification, improved interference mitigation, and other factors by controlling the spatial distribution of the transmit power. Transmit beampatterns are generally shaped by a variety of metrics (objective functions), such as spatial ISLR/peak sidelobe level ratio (PSLR) minimization; which the former is considered in this chapter.

In spatial ISLR and PSLR minimization approach, the aim is minimizing the ratio of summation of the beampattern response on undesired over desired angles, and minimizing the ratio of maximum beampattern response on undesired angles over minimum beampattern response on desired angles, respectively. This has recently been researched in a number of studies (see a few examples in [4–8]).

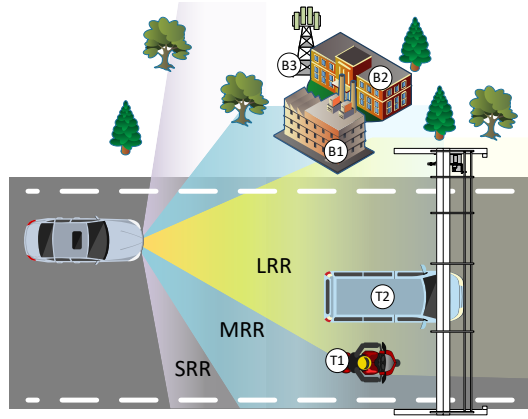

(a) Conventional automotive radars.

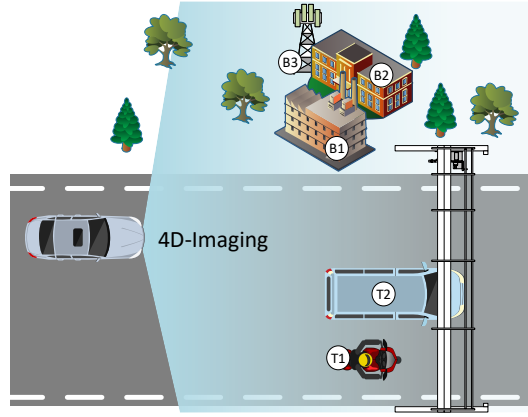

(b) 4-D imaging radars.

Figure 8.1. Coverage comparison between (a) conventional and (b) 4-D imaging MIMO radar systems. Radar will provide a broad beampattern and a precise angular resolution when it constructs a virtual array using orthogonal transmit waveforms. It can create a focused transmit beampattern using the correlated waveforms on the other side to boost SINR. When these two processes are carried out adaptively, it is possible to have a large coverage with a high spatial resolution.

While beampattern shaping directing the radiation intensity in a spatial region of desired angles, waveform orthogonality aims to increase spatial resolution by making use of the concept of virtual array. Waveforms with low ISLR in time domain, also known as range ISLR, are typically sought to enable an effective virtual array. This is achieved by designing a set of waveforms that are uncorrelated with each other (within and across antennas). Thus, a contradiction arises in achieving small spatial and range ISLR simultaneously, leading to a waveform design trade-off between spatial and range ISLR. This trade-off calls for a specific waveform design strategy, which is what the UNIQUE method [4] pursues and is covered in the following.

8.1.1 System Model

Let us consider a colocated narrow band MIMO radar system, with M_t transmit antennas, each transmitting a sequence of length N in the fast time domain. Let the matrix $\boldsymbol{S} \in \mathbb{C}^{M_t \times N}$ denotes the transmitted set of sequences in baseband. Let us assume that $\boldsymbol{S} \triangleq [\bar{\boldsymbol{s}}_1, \ldots, \bar{\boldsymbol{s}}_N] \triangleq [\tilde{\boldsymbol{s}}_1^T; \ldots; \tilde{\boldsymbol{s}}_{M_t}^T]^T$, where the vector $\bar{\boldsymbol{s}}_n \triangleq [s_{1,n}, s_{2,n}, \ldots, s_{M_t,n}]^T \in \mathbb{C}^{M_t}$ $(n = \{1, \ldots, N\})$ indicates the n^{th} time sample across the M_t transmitters (the n th column of matrix $\boldsymbol{S}$) while the $\tilde{\boldsymbol{s}}_m \triangleq [s_{m,1}, s_{m,2}, \ldots, s_{m,N}]^T \in \mathbb{C}^N$ $(m = \{1, \ldots, M_t\})$ indicates the N samples of m^{th} transmitter (the m^{th} row of matrix $\boldsymbol{S}$).

8.1.1.1 System Model in Spatial Domain

We assume a ULA form for the transmit array. The transmit steering vector takes the from,

$$\boldsymbol{a}(\theta) = [1, e^{j\frac{2\pi d_t}{\lambda}\sin(\theta)}, \ldots, e^{j\frac{2\pi d_t(M_t-1)}{\lambda}\sin(\theta)}]^T \in \mathbb{C}^{M_t} \tag{8.1}$$

In (8.1), d_t is the distance between the transmitter antennas and λ is the signal wavelength. The power of transmitted signal (beampattern) in the direction θ can be written as:

$$P(\boldsymbol{S}, \theta) = \frac{1}{N}\sum_{n=1}^{N} \left|\boldsymbol{a}^H(\theta)\bar{\boldsymbol{s}}_n\right|^2 = \frac{1}{N}\sum_{n=1}^{N} \bar{\boldsymbol{s}}_n^H \boldsymbol{A}(\theta)\bar{\boldsymbol{s}}_n \tag{8.2}$$

where $\boldsymbol{A}(\theta) = \boldsymbol{a}(\theta)\boldsymbol{a}^H(\theta)$. Let $\Theta_d = \{\theta_{d,1}, \theta_{d,2}, \ldots, \theta_{d,M_d}\}$ and $\Theta_u = \{\theta_{u,1}, \theta_{u,2}, \ldots, \theta_{u,M_u}\}$ denote the sets of M_d desired and M_u undesired angles in the spatial domain, respectively. This information can be obtained

from a cognitive paradigm. We define the spatial ISLR, $\bar{f}(\boldsymbol{S})$, as the ratio of beampattern response on the undesired directions (sidelobes) to those on the desired angles (mainlobes) by the following equation,

$$\bar{f}(\boldsymbol{S}) \triangleq \frac{\frac{1}{M_u}\sum_{r=1}^{M_u} P(\boldsymbol{S},\theta_{u,r})}{\frac{1}{M_d}\sum_{r=1}^{M_d} P(\boldsymbol{S},\theta_{d,r})} = \frac{\sum_{n=1}^{N} \bar{\boldsymbol{s}}_n^H \boldsymbol{A}_u \bar{\boldsymbol{s}}_n}{\sum_{n=1}^{N} \bar{\boldsymbol{s}}_n^H \boldsymbol{A}_d \bar{\boldsymbol{s}}_n} \tag{8.3}$$

where $\boldsymbol{A}_u \triangleq \frac{\sum_{r=1}^{M_u} \boldsymbol{A}(\theta_{u,r})}{NM_u}$ and $\boldsymbol{A}_d \triangleq \frac{\sum_{r=1}^{M_d} \boldsymbol{A}(\theta_{d,r})}{NM_d}$. Note that $\bar{f}(\boldsymbol{S})$ is a fractional quadratic function.

8.1.1.2 System Model in the Fast-Time Domain

The aperiodic cross-correlation of $\tilde{\boldsymbol{s}}_m$ and $\tilde{\boldsymbol{s}}_l$ is defined as

$$r_{m,l}(k) = \sum_{n=1}^{N-k} s_{m,n} s_{l,n+k}^* \tag{8.4}$$

where $m, l \in \{1, \ldots, M_t\}$ are the transmit antenna indices and $k \in \{-N+1, \ldots, N-1\}$ denotes the lag of cross-correlation. If $m = l$, (8.4) represents the aperiodic autocorrelation of signal $\tilde{\boldsymbol{s}}_m$. The zero lag of autocorrelation represents the peak of the matched filter output and contains the energy of the sequence , while the other lags ($k \neq 0$) are referred to the sidelobes. The range ISL can therefore be expressed by

$$\sum_{\substack{m,l=1 \\ l\neq m}}^{M_t} \sum_{k=-N+1}^{N-1} |r_{m,l}(k)|^2 + \sum_{m=1}^{M_t} \sum_{\substack{k=-N+1 \\ k\neq 0}}^{N-1} |r_{m,m}(k)|^2 \tag{8.5}$$

where the first and second terms represent the cross-correlation and auto-correlation sidelobes, respectively. For the sake of convenience, (8.5) can be written as

$$\text{ISL} = \sum_{m,l=1}^{M_t} \sum_{k=-N+1}^{N-1} |r_{m,l}(k)|^2 - \sum_{m=1}^{M_t} |r_{m,m}(0)|^2 \tag{8.6}$$

The range ISLR (time ISLR) is the ratio of range ISL over the mainlobe energy, that is

$$\tilde{f}(\boldsymbol{S}) = \frac{\sum\limits_{m,l=1}^{M_t} \sum\limits_{k=-N+1}^{N-1} \left\|\tilde{\boldsymbol{s}}_m^H \boldsymbol{J}_k \tilde{\boldsymbol{s}}_l\right\|_2^2 - \sum\limits_{m=1}^{M_t} \left\|\tilde{\boldsymbol{s}}_m^H \tilde{\boldsymbol{s}}_m\right\|_2^2}{\sum\limits_{m=1}^{M_t} \left\|\tilde{\boldsymbol{s}}_m^H \tilde{\boldsymbol{s}}_m\right\|_2^2} \tag{8.7}$$

where $\boldsymbol{J}_k = \boldsymbol{J}_{-k}^T$ denotes the $N \times N$ shift matrix with the following definition,

$$\boldsymbol{J}_k(u,v) = \begin{cases} 1, & u - v = k \\ 0, & u - v \neq k \end{cases} \tag{8.8}$$

Note that, when the transmit set of sequences are unimodular, then

$$\sum_{m=1}^{M_t} \left\| \tilde{\boldsymbol{s}}_m^H \tilde{\boldsymbol{s}}_m \right\|_2^2 = M_t N^2$$

and $\tilde{f}(\boldsymbol{S})$ is a scaled version of the range ISLR defined in [9]. As can be seen $\tilde{f}(\boldsymbol{S})$ is a fractional quartic function.

8.1.2 Problem Formulation

We aim to design sets of sequences that simultaneously possess good properties in terms of both spatial and range ISLR, under limited transmit power, bounded PAR, constant modulus and discrete phase constraints. The optimization problem can be represented as

$$\begin{cases} \underset{\boldsymbol{S}}{\text{minimize}} & \bar{f}(\boldsymbol{S}), \tilde{f}(\boldsymbol{S}) \\ \text{subject to} & s_{m,n} \in C_i \end{cases} \tag{8.9}$$

where $i \in \{1,2,3,4\}$, $m = \{1,\ldots,M_t\}$, $n = \{1,\ldots,N\}$, and

$$\begin{aligned} &C_1 : 0 < \|\boldsymbol{S}\|_F^2 \leqslant M_t N \\ &C_2 : 0 < \|\boldsymbol{S}\|_F^2 \leqslant M_t N \, \frac{\max |s_{m,n}|^2}{\frac{1}{M_t N}\|\boldsymbol{S}\|_F^2} \leqslant \gamma_p \\ &C_3 : s_{m,n} = e^{j\phi_{m,n}}, \ \phi \in \Phi_\infty \\ &C_4 : s_{m,n} = e^{j\phi_{m,n}}, \ \phi \in \Phi_L \end{aligned} \tag{8.10}$$

In (8.10), C_1 represents the limited transmit power constraint; C_2 is the PAR constraint with limited power, and γ_p indicates the maximum admissible PAR; C_3 is the constant modulus constraint with $\Phi_\infty = [-\pi, \pi)$; C_4 is the discrete phase constraint with $\Phi_L = \{\phi_0, \phi_1, \ldots, \phi_{L-1}\} \in \left\{0, \frac{2\pi}{L}, \ldots, \frac{2\pi(L-1)}{L}\right\}$;

and L is the alphabet size. The first constraint (C_1) is convex while the second constraint (C_2) is nonconvex due to the fractional inequality. Besides, the equality constraints C_3 and C_4 ($s_{m,n} = e^{j\phi}$ or $|s_{m,n}| = 1$)[1] are not affine. The aforementioned constraints can be sorted from the smallest to the largest feasible set as

$$C_4 \subset C_3 \subset C_2 \subset C_1 \tag{8.11}$$

Problem (8.9) is a bi objective optimization problem in which a feasible solution that minimizes both the objective functions may not exist [10]. Scalarization, a well-known technique converts the biobjective optimization problem to a single objective problem, by replacing a weighted sum of the objective functions. Using this technique, the following Pareto-optimization problem will be obtained:

$$\mathcal{P}\begin{cases}\underset{\boldsymbol{S}}{\text{minimize}} & f_o(\boldsymbol{S}) \triangleq \eta\bar{f}(\boldsymbol{S}) + (1-\eta)\tilde{f}(\boldsymbol{S}) \\ \text{subject to} & s_{m,n} \in C_i\end{cases} \tag{8.12}$$

The coefficient $\eta \in [0, 1]$ is a weight factor that affects the trade-off between spatial and range ISLR. In (8.12), $\bar{f}(\boldsymbol{S})$ is a fractional quadratic function of $\bar{\boldsymbol{s}}_n$, and $\tilde{f}(\boldsymbol{S})$ is fractional quartic function of $\tilde{\boldsymbol{s}}_m$. Consequently, we come into a multivariable, NP-hard optimization problem.

8.2 DESIGN PROCEDURE USING THE CD FRAMEWORK

The CD design framework was described earlier in Chapter 5. As indicated, the methodologies based on CD generally start with a feasible matrix $\boldsymbol{S} = \boldsymbol{S}^{(0)}$ as the initial waveform set. Then, at each iteration, the waveform set is updated entry by entry several times. In particular, an entry of $\boldsymbol{S}$ is considered as the only variable while others are held fixed and then the objective function is optimized with respect to this identified variable. Let us assume that $s_{t,d}$ ($t \in \{1, \ldots, M_t\}$ and $d \in \{1, \ldots, N\}$) is the only variable. We consider cyclic rule to update the waveform (see Chapter 5 for more details on selection rules). In this case, the fixed code entries are stored in

1 For convenience, we use ϕ instead of $\phi_{m,n}$ (8.10) in the rest of the chapter.

the matrix $\boldsymbol{S}^{(i)}_{-(t,d)}$ as the following,

$$\boldsymbol{S}^{(i)}_{-(t,d)} \triangleq \begin{bmatrix} s^{(i)}_{1,1} & \cdots & \cdots & \cdots & \cdots & \cdots & s^{(i)}_{1,N} \\ \vdots & \vdots & \vdots & \vdots & \vdots & \vdots & \vdots \\ s^{(i)}_{t,1} & \cdots & s^{(i)}_{t,d-1} & 0 & s^{(i-1)}_{t,d+1} & \cdots & s^{(i-1)}_{t,N} \\ \vdots & \vdots & \vdots & \vdots & \vdots & \vdots & \vdots \\ s^{(i-1)}_{M_t,1} & \cdots & \cdots & \cdots & \cdots & \cdots & s^{(i-1)}_{M_t,N} \end{bmatrix}$$

where the superscripts (i) and $(i-1)$ show the updated and nonupdated entries at iteration i. In this regard, the optimization problem with respect to variable $s_{t,d}$ can be written as follows (see Appendix 8A for details):

$$\mathcal{P}_{s_{t,d}} \begin{cases} \underset{s_{t,d}}{\text{minimize}} & f_o(s_{t,d}, \boldsymbol{S}^{(i)}_{-(t,d)}) \\ \text{subject to} & s_{m,n} \in C_i \end{cases} \tag{8.13}$$

where $f_o(s_{t,d}, \boldsymbol{S}^{(i)}_{-(t,d)})$ and the constraints are given by

$$f_o(s_{t,d}, \boldsymbol{S}^{(i)}_{-(t,d)}) \triangleq \eta \bar{f}(s_{t,d}, \boldsymbol{S}^{(i)}_{-(t,d)}) + (1-\eta)\tilde{f}(s_{t,d}, \boldsymbol{S}^{(i)}_{-(t,d)})$$

with

$$\bar{f}(s_{t,d}, \boldsymbol{S}^{(i)}_{-(t,d)}) \triangleq \frac{a_0 s_{t,d} + a_1 + a_2 s^*_{t,d} + a_3 |s_{t,d}|^2}{b_0 s_{t,d} + b_1 + b_2 s^*_{t,d} + b_3 |s_{t,d}|^2} \tag{8.14}$$

$$\tilde{f}(s_{t,d}, \boldsymbol{S}^{(i)}_{-(t,d)}) \triangleq \frac{c_0 s^2_{t,d} + c_1 s_{t,d} + c_2 + c_3 s^*_{t,d} + c_4 {s^*_{t,d}}^2 + c_5 |s_{t,d}|^2}{|s_{t,d}|^4 + d_1 |s_{t,d}|^2 + d_2} \tag{8.15}$$

$$\begin{aligned} &C_1 : |s_{t,d}|^2 \leqslant \gamma_e \\ &C_2 : |s_{t,d}|^2 \leqslant \gamma_e, \quad \gamma_l \leqslant |s_{t,d}|^2 \leqslant \gamma_u \\ &C_3 : s_{t,d} = e^{j\phi}, \quad \phi \in \Phi_\infty \\ &C_4 : s_{t,d} = e^{j\phi}, \quad \phi \in \Phi_L \end{aligned} \tag{8.16}$$

In (8.14), (8.15), and (8.16), the coefficients a_v, b_v, ($v \in \{0, \ldots, 3\}$), c_w ($w \in \{0, \ldots, 5\}$) and boundaries γ_l, γ_u, and γ_e, depend on $\boldsymbol{S}^{(i)}_{-(t,d)}$, all of which are defined in Appendix 8A.

At the (i)th iteration of the CD algorithm, for $t = 1, \ldots, M_t$, and $d = 1, \ldots, N$, the (t,d)th entry of $\boldsymbol{S}$ will be updated by solving (8.13). After updating all the entries, a new iteration will be started, provided that the stopping criteria are not met. This procedure will continue until the objective function converges to an optimal value. A pseudo-code summary of the method is reported in Algorithm 8.1.

Algorithm 8.1: Waveform Design for 4-D imaging MIMO Radars

Result: Optimized space-time code matrix $\boldsymbol{S}^{\star}$
initialization;
for $i = 0, 1, 2, \ldots$ **do**
  for $t = 1, 2, \ldots, M_t$ **do**
    for $d = 1, 2, \ldots, N$ **do**
      Find the optimal code entry $s^{\star}_{t,d}$ by solving $\mathcal{P}_{s_{t,d}}$;
      Set $s^{(i)}_{t,d} = s^{\star}_{t,d}$;
      Set $\boldsymbol{S}^{(i)} = \boldsymbol{S}^{(i)}_{-(t,d)}\big|_{s_{t,d}=s^{(i)}_{t,d}}$;
    end
  end
  Stop if convergence criterion is met;
end

To optimize the code entries, notice that the optimization variable is a complex number and can be expressed as $s_{t,d} = re^{j\phi}$, where $r \geqslant 0$ and $\phi \in [-\pi, \pi)$ are the amplitude and phase of $s_{t,d}$, respectively. By substituting $s_{t,d}$ with $re^{j\phi}$ and performing standard mathematical manipulations, problem $\mathcal{P}_{s_{t,d}}$ can be rewritten with respect to r and ϕ as follows:

$$\mathcal{P}_{r,\phi} \begin{cases} \underset{r,\phi}{\text{minimize}} & f_o\left(r,\phi\right) \\ \text{subject to} & s_{m,n} \in C_i \end{cases} \tag{8.17}$$

with $f_o\left(r,\phi\right) \triangleq \eta \bar{f}\left(r,\phi\right) + (1-\eta)\tilde{f}\left(r,\phi\right)$, where

$$\bar{f}\left(r,\phi\right) \triangleq \frac{a_0 re^{j\phi} + a_1 + a_2 re^{-j\phi} + a_3 r^2}{b_0 re^{j\phi} + b_1 + b_2 re^{-j\phi} + b_3 r^2} \tag{8.18}$$

$$\tilde{f}\left(r,\phi\right) \triangleq \frac{c_0 r^2 e^{j2\phi} + c_1 r e^{j\phi} + c_2 + c_3 r e^{-j\phi} + c_4 r^2 e^{-j2\phi} + c_5 r^2}{r^4 + d_1 r^2 + d_2} \tag{8.19}$$

$$\begin{aligned} C_1 &: 0 \leqslant r \leqslant \sqrt{\gamma_e} \\ C_2 &: 0 \leqslant r \leqslant \sqrt{\gamma_e}\sqrt{\gamma_l} \leqslant r \leqslant \sqrt{\gamma_u} \\ C_3 &: r = 1; \quad \phi \in \Phi_\infty \\ C_4 &: r = 1; \quad \phi \in \Phi_L \end{aligned} \tag{8.20}$$

Let $s^\star_{t,d} = r^\star e^{j\phi^\star}$ be the optimized solution of problem $\mathcal{P}_{r,\phi}$. Toward obtaining this solution, Algorithm 8.1 starts with a feasible set of sequences as the initial waveforms. It then chooses the (t,d) element of matrix $\boldsymbol{S}$ as the variable and updates it with the optimized value signified by $s^\star_{t,d}$ at each single variable update. Other entries are subjected to the same process, which is carried out until each entry has been optimized at least once. After optimizing the $M_t N^{th}$ entry, the algorithm examines the convergence metric for the objective function. If the stopping criterion is not met, the algorithm repeats the aforementioned steps.

With the defined methodology, it now remains to solve $\mathcal{P}_{r,\phi}$ for the different constraints. This is considered next.

8.2.1 Solution for Limited Power Constraint

Problem $\mathcal{P}_{r,\phi}$ under the C_1 constraint can be written as follows (see Appendix 8B for details),

$$\mathcal{P}_e \begin{cases} \underset{r,\phi}{\text{minimize}} & f_o\left(r,\phi\right) \\ \text{subject to} & C_1 : 0 \leqslant r \leqslant \sqrt{\gamma_e} \end{cases} \tag{8.21}$$

where $f_o\left(r,\phi\right) = \eta\bar{f}\left(r,\phi\right) + (1-\eta)\tilde{f}\left(r,\phi\right)$ and

$$\bar{f}\left(r,\phi\right) = \frac{a_3 r^2 + 2(a_{0r}\cos\phi - a_{0i}\sin\phi)r + a_1}{b_3 r^2 + 2(b_{0r}\cos\phi - b_{0i}\sin\phi)r + b_1} \tag{8.22}$$

$$\begin{aligned} \tilde{f}\left(r,\phi\right) = &[(2c_{0r}\cos 2\phi - 2c_{0i}\sin 2\phi + c_5)r^2 \\ &+ 2(c_{1r}\cos\phi - c_{1i}\sin\phi)r + c_2]\frac{1}{r^4 + d_1 r^2 + d_2} \end{aligned} \tag{8.23}$$

The solution to $\mathcal{P}_e$ will be obtained by finding the critical points of the objective function and selecting the one that minimizes the objective. As

$f_o(r,\phi)$ is a differentiable function, the critical points of $\mathcal{P}_e$ contain the solutions to $\nabla f_o(r,\phi) = 0$ and the boundaries $(0, \sqrt{\gamma_e})$, which satisfy the constraint $(0 \leqslant r \leqslant \sqrt{\gamma_e})$. To solve this problem, we use alternating optimization, where we first optimize for r keeping ϕ fixed and vice versa.

Optimization with respect to r Let us assume that the phase of the code entry $s_{t,d}^{(i-1)}$ is $\phi_0 = \tan^{-1}\left(\frac{\Im(s_{t,d}^{(i-1)})}{\Re(s_{t,d}^{(i-1)})}\right)$. By substituting ϕ_0 in $\frac{\partial f_o(r,\phi)}{\partial r}$, it can be shown that the solution to the condition $\frac{\partial f_o(r,\phi_0)}{\partial r} = 0$ can be obtained by finding the roots of the following degree 10 real polynomial (see Appendix 8C for details),

$$\sum_{k=0}^{10} p_k r^k = 0 \tag{8.24}$$

Further, since r is real, we seek only the real extrema points. Let us assume that the roots are r_v, $v = \{1,\dots,10\}$; therefore the critical points of problem $\mathcal{P}_e$ with respect to r can be expressed as

$$R_e = \left\{ r \in \{0, \sqrt{\gamma_e}, r_1, \dots, r_{10}\} | \Im(r) = 0, 0 \leqslant r \leqslant \sqrt{\gamma_e} \right\} \tag{8.25}$$

Thus, the optimum solution for r will be obtained by

$$r_e^\star = \arg\min_r \left\{ f_o(r,\phi_0) | r \in R_e \right\} \tag{8.26}$$

Optimization with respect to ϕ Let us keep r fixed and optimize the problem with respect to ϕ. Considering $\cos(\phi) = (1-\tan^2(\frac{\phi}{2}))/(1+\tan^2(\frac{\phi}{2}))$, $\sin(\phi) = 2\tan(\frac{\phi}{2})/(1+\tan^2(\frac{\phi}{2}))$ and using the change of variable $z \triangleq \tan(\frac{\phi}{2})$, it can be shown that finding the roots of $\frac{\partial f_o(r_e^\star,\phi)}{\partial \phi}$ is equivalent finding the roots of the following 8 degree real polynomial (see Appendix 8D for details),

$$\sum_{k=0}^{8} q_k z^k \tag{8.27}$$

Similar to (8.24), we only admit real roots. Let us assume that z_v, $v = \{1,\dots,8\}$ are the roots of (8.27). Hence, the critical points of $\mathcal{P}_e$ with respect to ϕ can be expressed as

$$\Phi = \left\{ 2\arctan(z_v) | \Im(z_v) = 0 \right\} \tag{8.28}$$

Therefore, the optimum solution for ϕ is

$$\phi_e^\star = \arg\min_\phi \left\{ f_o(r_e^\star,\phi) | \phi \in \Phi \right\} \tag{8.29}$$

Subsequently, the optimum solution for $s_{t,d}$ is, $s_{t,d}^{(i)} = r_e^\star e^{j\phi_e^\star}$.

Remark 2. *All the constraints in* (8.10) *satisfy* $\|\boldsymbol{S}\|_F > 0$. *Therefore, the denominator of* $\tilde{f}(\boldsymbol{S})$ *in* (8.7) *never become zero. However, since* $\boldsymbol{A}_d$ *is a positive definite matrix, the denominator of* $\bar{f}(\boldsymbol{S})$ *in* (8.3) *will not become zero. Since* $f_o(\boldsymbol{S})$ *is a linear combination of* $\bar{f}(\boldsymbol{S})$ *and* $\tilde{f}(\boldsymbol{S})$, *we do not have a singularity issue. According to* (8.18) *and* (8.19), $\bar{f}(r,\phi)$ *and* $\tilde{f}(r,\phi)$ *are polynomial fractional functions with respect to both* r *and* $e^{j\phi}$. *Therefore, the objective function is continuous and differentiable with respect to* $r \geq 0$ *and* $\phi \in [0, 2\pi)$. *With respect to* r, *since* 0 *and* $\sqrt{\gamma_e}$ *are members of* R_e, *two critical points always exist, and* R_e *is never a null set. Further, the functions* $\cos\phi$ *and* $\sin\phi$ *are periodic (*$\cos\phi = \cos(\phi + 2K\pi)$ *and* $\sin\phi = \sin(\phi + 2K\pi)$*). As* $f_o(r_0,\phi)$ *is function of* $\cos\phi$ *and* $\sin\phi$, *hence* $f_o(r_0,\phi) = f_o(r_0,\phi+2K\pi)$ *is a periodic function as well. Therefore, it has at least two extrema and, since it is differentiable, its derivative has at least two real roots; thus,* Φ_e *never becomes a null set. As a result, in each single variable update, the problem has a solution and never becomes infeasible.*

8.2.2 Solution for PAR Constraint

Problem $\mathcal{P}_{r,\phi}$ under C_2 constraint is a special case of C_1 and the procedures in subsection 8.2.1 are valid for limited power and PAR constraint. The only difference lies in the boundaries and critical points with respect to r. Considering the C_2 constraint, the critical points can be expressed as the following:

$$\begin{aligned} R_p = &\{r \in \{\max\{0,\sqrt{\gamma_l}\}, \min\{\sqrt{\gamma_u},\sqrt{\gamma_e}\}, r_1,\ldots,r_{10}\}| \\ &\Im(r) = 0, \max\{0,\sqrt{\gamma_l}\} \leqslant r \leqslant \min\{\sqrt{\gamma_u},\sqrt{\gamma_e}\}\} \end{aligned} \tag{8.30}$$

Therefore, the optimum solution for r and ϕ is

$$\begin{aligned} r_p^\star &= \arg\min_r \left\{ f_o(r,\phi_0) | r \in R_p \right\} \\ \phi_p^\star &= \arg\min_\phi \left\{ f_o(r_p^\star,\phi) | \phi \in \Phi \right\} \end{aligned} \tag{8.31}$$

and the optimum entry can be obtained by, $s_{t,d}^{(i)} = r_p^\star e^{j\phi_p^\star}$.

8.2.3 Solution for Continuous Phase

The continuous phase constraint (C_3) is a special case of limited power (C_1) constraint. In this case $r = 1$, and the optimum solution for ϕ is

$$\phi_c^\star = \arg\min_{\phi} \left\{ f_o(r, \phi) | \phi \in \Phi, r = 1 \right\} \tag{8.32}$$

The optimum entry can be obtained by $s_{t,d}^{(i)} = e^{j\phi_c^\star}$.

8.2.4 Solution for Discrete Phase

We consider the design of a set of MPSK sequences for the discrete phase problem. In this case, $\mathcal{P}_{r,\phi}$ can be written as follows (see Appendix 8E for details)

$$\mathcal{P}_d \begin{cases} \underset{\phi}{\text{minimize}} & f_d(\phi) = \dfrac{e^{j3\phi} \sum_{k=0}^{6} g_k e^{-jk\phi}}{e^{j\phi} \sum_{k=0}^{2} h_k^{-jk\phi}} \\ \text{subject to} & C_4 : \phi \in \Phi_L \end{cases} \tag{8.33}$$

As the problem under C_4 constraint is discrete, the optimization procedure is different compared with other constraints. In this case, all the discrete points lie on the boundary of the optimization problem; hence, all of them are critical points for the problem. Therefore, one approach for solving this problem is to obtain all the possibilities of the objective function $f_o(\phi)$ over the set $\Phi_L = \{\phi_0, \phi_1, \ldots, \phi_{L-1}\} = \left\{0, \frac{2\pi}{L}, \ldots, \frac{2\pi(L-1)}{L}\right\}$ and choose the phase that minimizes the objective function. It immediately occurs that such an evaluation could be cumbersome; however, for the MPSK alphabet, an elegant solution can be obtained as detailed below.

The objective function can be formulated with respect to the indices of Φ_L as follows:

$$f_d(\phi_l) = f_d(l) = \frac{e^{j3\frac{2\pi l}{L}} \sum_{k=0}^{6} g_k e^{-jk\frac{2\pi l}{L}}}{e^{j\frac{2\pi l}{L}} \sum_{k=0}^{2} h_k e^{-jk\frac{2\pi l}{L}}} \tag{8.34}$$

where $l \in \{0, \ldots, L-1\}$, and the summation terms on numerator and denominator exactly follow the definition of L-points DFT of sequences $\{g_0, \ldots, g_6\}$ and $\{h_0, h_1, h_2\}$ respectively. [2] Therefore, problem $\mathcal{P}_d$ can be

2 Let x_n be a sequence with a length of N. The K-point DFT of x_n can be obtained by $X_k = \sum_{n=0}^{N-1} x_n e^{-jn\frac{2\pi k}{K}}$ [11].

written as

$$\mathcal{P}_l \left\{ \underset{l}{\text{minimize}} \quad f_d(\phi_l) = \frac{\boldsymbol{w}_{L,3} \odot \mathcal{F}_L\{g_0, g_1, g_2, g_3, g_4, g_5, g_6\}}{\boldsymbol{w}_{L,1} \odot \mathcal{F}_L\{h_0, h_1, h_2\}} \right. \tag{8.35}$$

where $\boldsymbol{w}_{L,\nu} = \left[1, e^{-j\nu\frac{2\pi}{L}}, \ldots, e^{-j\nu\frac{2\pi(L-1)}{L}}\right]^T \in \mathbb{C}^L$ and $\mathcal{F}_L$ is L-point DFT operator. Due to the aliasing phenomena, when $L < 7$, the objective function would be changed. Let N_{f_d} and D_{f_d} be the summation terms in nominator and denominator of $f_d(\phi_l)$, respectively, it can be shown that

$$\begin{aligned}
L = 6 &\Rightarrow N_{f_d} = \mathcal{F}_L\{g_0 + g_6, g_1, g_2, g_3, g_4, g_5\} \\
L = 5 &\Rightarrow N_{f_d} = \mathcal{F}_L\{g_0 + g_5, g_1 + g_6, g_2, g_3, g_4\} \\
L = 4 &\Rightarrow N_{f_d} = \mathcal{F}_L\{g_0 + g_4, g_1 + g_5, g_2 + g_6, g_3\} \\
L = 3 &\Rightarrow N_{f_d} = \mathcal{F}_L\{g_0 + g_3 + g_6, g_1 + g_4, g_2 + g_5\},
\end{aligned}$$

and for $L = 2$, $N_{f_d} = \mathcal{F}_L\{g_0 + g_2 + g_4 + g_6, g_1 + g_3 + g_5\}$ and $D_{f_d} = \mathcal{F}_L\{h_0 + h_2, h_1\}$.

According to the aforementioned discussion, the optimum solution of (8.35) is

$$l^\star = \arg \min_{l=1,\ldots,L} \left\{ f_d(\phi_l) \right\} \tag{8.36}$$

Hence, $\phi_d^\star = \frac{2\pi(l^\star - 1)}{L}$ and the optimum entry is $s_{t,d}^{(i)} = e^{j\phi_d^\star}$.

8.3 NUMERICAL EXAMPLES

Now we assess the performance of the UNIQUE algorithm. For transmit and receive antennas, we consider ULA configuration with $M_t = M_r = 8$ elements and the antenna distance $d_t = d_r = \frac{\lambda}{2}$. We select the desired and undesired angular regions to be $\Theta_d = [-55°, -35°]$ and $\Theta_u = [-90°, -60°] \cup [-30°, 90°]$, respectively. For the purpose of simulation, we consider a uniform sampling of these regions with a grid size of $5°$. Since MPSK sequences are feasible for all the constraints, we consider a set of random MPSK sequences ($\boldsymbol{S}_0 \in \mathbb{C}^{M_t \times N}$) with an alphabet size of $L = 8$ as an initial waveform. Here, every code entry is given by

$$s_{m,n}^{(0)} = e^{j\frac{2\pi(l-1)}{L}} \tag{8.37}$$

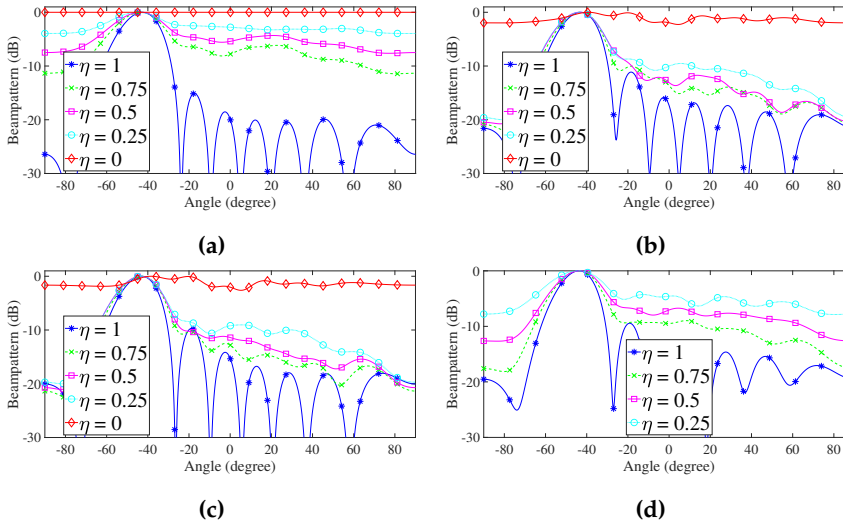

Figure 8.2. Transmit beampattern under different constraint and value of η ($M_t = 8$, $N = 64$, $\Theta_d = [-55°, -35°]$, and $\Theta_u = [-90°, -60°] \cup [-30°, 90°]$): (a) C_1 constraint, (b) C_2 constraint, $\gamma_p = 1.5dB$, (c) C_3 constraint, C_4 constraint, $L = 8$.

where l is the random integer variable uniformly distributed in $[1, L]$. We consider $(f_o(\boldsymbol{S}^{(i)}) - f_o(\boldsymbol{S}^{(i-1)}) \leq \zeta$, as the stopping criterion for Algorithm 8.1 and we set $\zeta = 10^{-6}$.

8.3.1 Contradictory Nature of Spatial and Range ISLR

We first assess the contradiction in waveform design for beampattern shaping and orthogonality; subsequently, we show the importance of making a trade-off between spatial and range ISLR to obtain a better performance. Figure 8.2 shows the beampattern of the proposed algorithm under $C_1, \ldots, C_4$ constraints for different values of η. Setting $\eta = 0$ results in an almost omnidirectional beam. By increasing η, radiation pattern takes the shape of a beam, with $\eta = 1$ offering the optimized pattern.

Table 8.1 shows a three-dimensional representation of the magnitude of correlation of the forth sequence with the other waveforms in the optimized set $\boldsymbol{S}^{\star}$. [3] In this regard, the fourth sequence in this figure shows the autocorrelation of that particular waveform. In this figure for constraint C_2, $\gamma_p = 1.5$ dB, and for constraint C_4 the alphabet size is $L = 8$. With $\eta = 1$ (last column in Table 8.1), yields an optimized beampattern, the cross-correlation with other sequences is rather large in all cases. This shows the transmission of scaled waveforms (phase-shifted) from all antennas is similar to the traditional phased array radar systems. In this case, it would not be possible to separate the transmit signals at the receiver (by matched filter) and the MIMO virtual array will not be formed, thereby losing in the angular resolution. When $\eta = 0$ (first column in Table 8.1), an orthogonal set of sequences is obtained as their cross-terms (autocorrelation and cross-correlation lags) are small under different design constraints. The resulting omnidirectional beampattern (see Figure 8.2), however, prevents steering of the transmit power toward the desired angles, while a strong signal from the undesired directions may saturate the radar receiver. The middle column in Table 8.1 depicts $\eta = 0.5$, a case when partially orthogonal waveforms are adopted, while some degree of transmit beampattern shaping can still be obtained.

Figure 8.2 and Table 8.1 show that having simultaneous beampattern shaping and orthogonality are contradictory and the choice of η affects a trade-off between the two and enhances the performance of the radar system.

8.3.2 Trade-Off Between Spatial and Range ISLR

The scenario shown in Figure 8.1, in which two desirable targets (T_1 and T_2) with identical radial speeds and relative ranges to radar are situated in $\theta_{T_1} = -40^{\circ}$ and $\theta_{T_2} = -50^{\circ}$, is used to demonstrate the efficiency of selecting $0 < \eta < 1$. The choice of identical speed and range was made in order to account for the worst-case scenario in which targets could not be retrieved from the range-Doppler profile. Additionally, we suppose that three other powerful objects, designated B_1, B_2, and B_3 (which may

3 In order to show the auto correlations and cross-correlations in this figure, we first sort the optimized waveforms based on their energy; then we move the waveform that has the maximum energy at the middle of the waveform set ($\lfloor \frac{M_t}{2} \rceil$). By this rearrangement, the peak of autocorrelation will be always located at the middle.

Table 8.1

Three Dimensional Representation of the autocorrelation and crosscorrelation of the Optimized Set of Sequences Under Different Constraints ($M_t = 8$, $N = 1,024$)

	$\eta = 0$	$\eta = 0.5$	$\eta = 1$
C_1	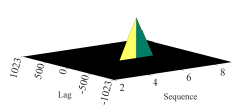	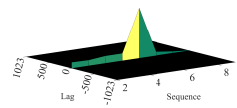	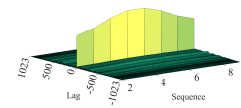
C_2	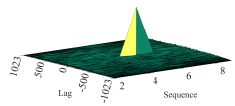	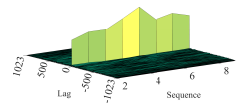	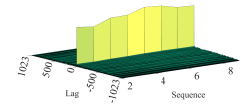
C_3	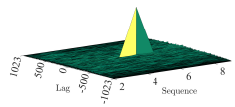	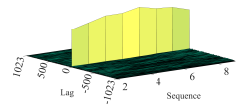	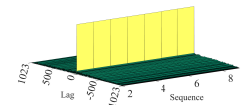
C_4	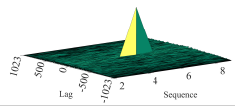	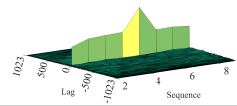	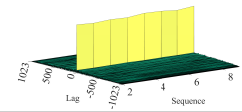

or may not be clutter), are positioned at different angles from the radar, $\theta_{B_1} = -9.5^\circ$, $\theta_{B_2} = 18.5^\circ$, and $\theta_{B_3} = 37^\circ$, but at the same speed and range. We aim to design a set of transmit sequences to be able to discriminate the two desired targets, but avoiding interference from the undesired directions.

Figure 8.3 shows the range-angle profile of the above scenario under the representative C_4 constraint with $L = 8$. When $\eta = 1$, we consider the conventional phased array receiver processing for Figure 8.3(a) and use one matched filter to extract the range-angle profile. To this end we assume $\lambda/2$ spacing for transmit and receive antenna elements (i.e., $d_t = d_r = \frac{\lambda}{2}$). Observe that, despite the mitigation of undesired targets, the two targets are not discriminated and are merged into a single target. The same scenario has been repeated in Figure 8.3(b) when $\eta = 0$. Since the optimized waveforms are orthogonal in this case, we consider MIMO processing to exploit the virtual array and improve the discrimination/identifiability. In this case, we use M_t matched filters in every receive chain, each corresponding to one of the M_t transmit sequences. The receive antennas have a sparse configuration with $d_r = M_t \frac{\lambda}{2}$ but the transmit antennas are a filled ULA with $d_t = \frac{\lambda}{2}$; this forms a MIMO virtual array with a maximum length. In this case, the optimized set of transmit sequences is able to discriminate the two targets, but it is contaminated by the strong reflections of the undesired targets. Also, some false targets (F_1, F_2, and F_3) have appeared due to the high sidelobe levels of the strong reflectors. By choosing $\eta = \frac{1}{2}$, we are able to discriminate the two targets and mitigate the signal of the undesired reflections in a same time. This fact is shown in Figure 8.3(c).

Table 8.2 shows the amplitude of the desired targets and undesired reflections in the scene (after the detection chain) at different Pareto weights (η). As can be seen from Table 8.2, the performance of target enhancement and interference mitigation reduces from $\eta = 1$ to $\eta = 0$. Nevertheless by choosing $\eta = 0.5$, the waveform achieves a trade-off between spatial and range ISLR, it can discriminate the two targets and mitigate the interference from the undesired locations.

8.3.3 The Impact of Alphabet Size and PAR

Figure 8.4 shows the impact of alphabet size and PAR value in transmit beampattern and auto correlation functions. In both cases, by increasing the alphabet size, the solution under C_4 constraint approaches that of obtained under C_3 constraint. This behavior is expected since the feasible set of C_4

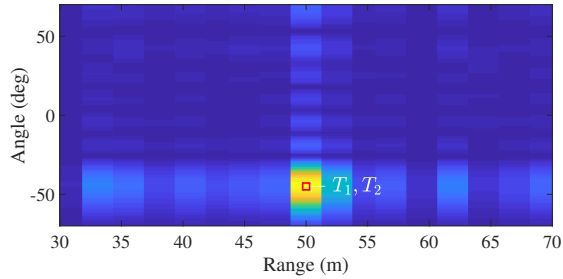

(a)

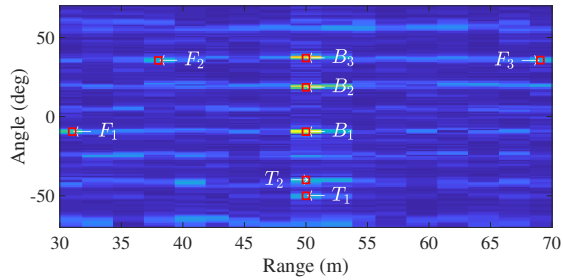

(b)

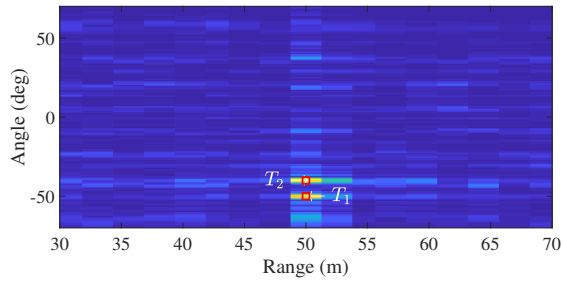

(c)

Figure 8.3. Illustration of the centrality of η (C_4 constraint, $M_t = M_r = 8$, $N = 64$, $L = 8$, $\theta_{T_1} = -50°$, $\theta_{T_2} = -40°$, $\theta_{B_1} = -9.5°$, $\theta_{B_2} = 18.5°$, and $\theta_{B_3} = 37°$): (a) Phased array processing $\eta = 1$, (b) MIMO processing $\eta = 0$, MIMO processing $\eta = \frac{1}{2}$.

Table 8.2
Amplitude of the Desired and Undesired Targets

η	T_1	T_2	B_1	B_2	B_3
1	9.54 dB	9.79 dB	-13.24 dB	-19.93 dB	-9.4 dB
0.5	8.78 dB	9.71 dB	-3.5 dB	-3.51 dB	-0.6 dB
0	-2.39 dB	-2.44 dB	3.68 dB	2.95 dB	2.87 dB

will be close to that of C_3, and the optimized solutions will behave the same. Further, by increasing the PAR threshold, the feasible set under C_2 constraint converges to the feasible set under C_1 constraint. By decreasing the PAR threshold to 1, the feasible set will be limited to that specified in C_3, and thus similar performance for the optimized sequences are obtained.

8.4 CONCLUSION

This chapter examined the challenge of designing waveforms for cutting-edge 4-D imaging automotive radar systems. To achieve this, we used the spatial and range ISLR as illustrative figures of merit to trade off beampattern adaptation and waveform orthogonality. Accordingly, we introduced a biobjective optimization problem to minimize the two metrics simultaneously, under power budget, PAR, and continuous and discrete phase constraints. The problem formulation led to a nonconvex, multivariable, and NP-hard optimization problem. We used the CD framework to solve the problem, where each step optimizes the objective with regard to one variable while holding the rest fixed. Simulation results have illustrated significant capability of effecting an optimal trade-off between the two ISLRs.

8.5 EXERCISE PROBLEMS

Q1. How would be the correlation matrix of the waveforms when a MIMO radar shapes its transmit beampattern to a desired direction? How the transmit waveforms will be separated in the receiver of MIMO radar in this case? Q2. What are the possible ways to make a trade-off between beampattern shaping and orthogonality in a MIMO radar system?

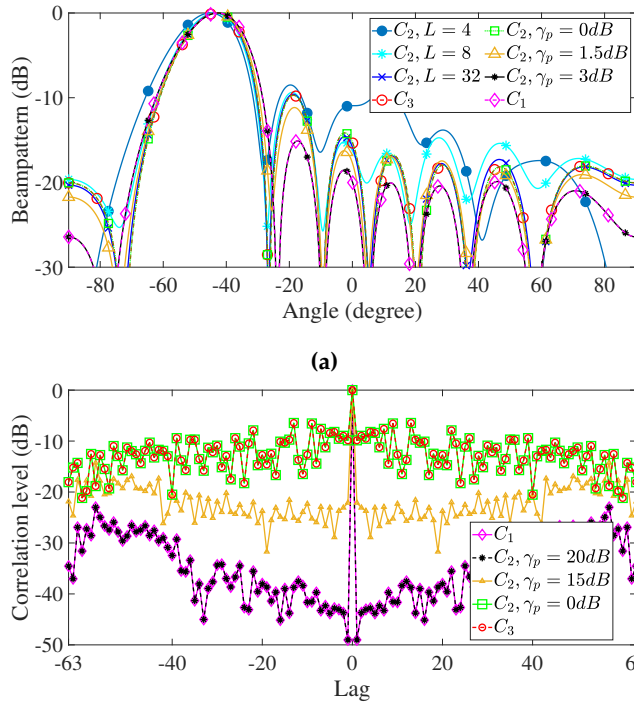

Figure 8.4. Impact of alphabet size and PAR value on the optimized (a) transmit beampattern and (b) autocorrelation ($M_t = 8$ and $N = 64$): (a) $\eta = 1$, $\Theta_d = [-55°, -35°]$ and $\Theta_u = [-90°, -60°] \cup [-30°, 90°]$, (b) $\eta = 0$.

References

[1] A. Moreira, P. Prats-Iraola, M. Younis, G. Krieger, I. Hajnsek, and K. P. Papathanassiou, "A tutorial on synthetic aperture radar," *IEEE Geoscience and Remote Sensing Magazine*, vol. 1, no. 1, pp. 6–43, 2013.

[2] J. Li and P. Stoica, "MIMO radar with colocated antennas," *IEEE Signal Processing Magazine*, vol. 24, no. 5, pp. 106–114, 2007.

[3] F. Engels, P. Heidenreich, M. Wintermantel, L. Stäcker, M. Al Kadi, and A. M. Zoubir, "Automotive radar signal processing: Research directions and practical challenges," *IEEE Journal of Selected Topics in Signal Processing*, vol. 15, no. 4, pp. 865–878, 2021.

[4] E. Raei, M. Alaee-Kerahroodi, and M. B. Shankar, "Spatial- and range- ISLR trade-off in MIMO radar via waveform correlation optimization," *IEEE Transactions on Signal Processing*, vol. 69, pp. 3283–3298, 2021.

[5] H. Xu, R. S. Blum, J. Wang, and J. Yuan, "Colocated MIMO radar waveform design for transmit beampattern formation," *IEEE Transactions on Aerospace and Electronic Systems*, vol. 51, no. 2, pp. 1558–1568, 2015.

[6] A. Aubry, A. De Maio, and Y. Huang, "MIMO radar beampattern design via PSL/ISL optimization," *IEEE Transactions on Signal Processing*, vol. 64, pp. 3955–3967, Aug 2016.

[7] W. Fan, J. Liang, and J. Li, "Constant modulus MIMO radar waveform design with minimum peak sidelobe transmit beampattern," *IEEE Transactions on Signal Processing*, vol. 66, no. 16, pp. 4207–4222, 2018.

[8] E. Raei, M. Alaee-Kerahroodi, and B. M. R. Shankar, "Waveform design for beampattern shaping in 4D-imaging MIMO radar systems," in *2021 21st International Radar Symposium (IRS)*, pp. 1–10, 2021.

[9] M. Alaee-Kerahroodi, M. Modarres-Hashemi, and M. M. Naghsh, "Designing sets of binary sequences for MIMO radar systems," *IEEE Transactions on Signal Processing*, vol. 67, pp. 3347–3360, July 2019.

[10] K. Deb, *Multi-Objective Optimization Using Evolutionary Algorithms*, vol. 16. John Wiley & Sons, 2001.

[11] A. V. Oppenheim and R. W. Schafer, *Discrete-Time Signal Processing*. Prentice Hall Press, 3rd ed., 2009.

APPENDIX 8A

Writing (8.12) with respect to $s_{t,d}$ can be done through the following steps:

Spatial ISLR Coefficients

The beampattern of undesired angles can be written as

$$\sum_{n=1}^{N} \bar{\boldsymbol{s}}_n^H \boldsymbol{A}_u \bar{\boldsymbol{s}}_n = \sum_{\substack{n=1 \\ n\neq d}}^{N} \bar{\boldsymbol{s}}_n^H \boldsymbol{A}_u \bar{\boldsymbol{s}}_n + \bar{\boldsymbol{s}}_d^H \boldsymbol{A}_u \bar{\boldsymbol{s}}_d \tag{8A.1}$$

where

$$\begin{aligned}\bar{\boldsymbol{s}}_d^H \boldsymbol{A}_u \bar{\boldsymbol{s}}_d = &\textstyle\sum_{\substack{m=1 \\ m\neq t}}^{M_t} \sum_{\substack{l=1 \\ l\neq t}}^{M_t} s_{m,d}^* a_{u_{m,l}} s_{l,d} \\ &+ s_{t,d} \textstyle\sum_{\substack{m=1 \\ m\neq t}}^{M_t} s_{m,d}^* a_{u_{m,t}} + s_{t,d}^* \sum_{\substack{l=1 \\ l\neq t}}^{M_t} a_{u_{t,l}} s_{l,d} + s_{t,d}^* a_{u_{t,t}} s_{t,d}\end{aligned}$$

with $a_{u_{m,l}}$ indicating $\{m, l\}$ entries of matrix $\boldsymbol{A}_u$. Thus, by defining,

$$\begin{aligned} a_0 &\triangleq \textstyle\sum_{\substack{m=1 \\ m\neq t}}^{M_t} s_{m,d}^* a_{u_{m,t}}, \quad a_3 \triangleq a_{u_{t,t}}, \quad a_2 \triangleq a_0^* \\ a_1 &\triangleq \textstyle\sum_{\substack{n=1 \\ n\neq d}}^{N} \bar{\boldsymbol{s}}_n^H \boldsymbol{A}_u \bar{\boldsymbol{s}}_n + \sum_{\substack{m=1 \\ m\neq t}}^{M_t} \sum_{\substack{l=1 \\ l\neq t}}^{M_t} s_{m,d}^* a_{u_{m,l}} s_{l,d} \end{aligned}$$

the beampattern response on undesired angles is equivalent to

$$\textstyle\sum_{n=1}^{N} \bar{\boldsymbol{s}}_n^H \boldsymbol{A}_u \bar{\boldsymbol{s}}_n = a_0 s_{t,d} + a_1 + a_2 s_{t,d}^* + a_3 |s_{t,d}|^2 \tag{8A.2}$$

Likewise the beampattern at desired angles is:

$$\textstyle\sum_{n=1}^{N} \bar{\boldsymbol{s}}_n^H \boldsymbol{A}_d \bar{\boldsymbol{s}}_n = b_0 s_{t,d} + b_1 + b_2 s_{t,d}^* + b_3 |s_{t,d}|^2 \tag{8A.3}$$

$$\begin{aligned} b_0 &\triangleq \textstyle\sum_{\substack{m=1 \\ m\neq t}}^{M_t} s_{m,d}^* a_{d_{m,t}}, \quad b_3 \triangleq a_{d_{t,t}}, \quad b_2 \triangleq b_0^*, \\ b_1 &\triangleq \textstyle\sum_{\substack{n=1 \\ n\neq d}}^{N} \bar{\boldsymbol{s}}_n^H \boldsymbol{A}_d \bar{\boldsymbol{s}}_n + \sum_{\substack{m=1 \\ m\neq t}}^{M_t} \sum_{\substack{l=1 \\ l\neq t}}^{M_t} s_{m,d}^* a_{d_{m,l}} s_{l,d}, \end{aligned}$$

where $a_{d_{m,l}}$ are the $\{m, l\}$ entries of $\boldsymbol{A}_d$.

Range ISLR Coefficients

We calculate range ISLR coefficients (see (8.6)) using following steps:

$$\begin{aligned}\text{ISL} =&\gamma_t + \textstyle\sum_{k=-N+1}^{N-1} |r_{t,t}(k)|^2 + |r_{t,t}(0)|^2 + \sum_{\substack{l=1\\l\neq t}}^{M_t} \sum_{k=-N+1}^{N-1} |r_{t,l}(k)|^2 \\ &+ \sum_{\substack{m=1\\m\neq t}}^{M_t} \sum_{k=-N+1}^{N-1} |r_{m,t}(k)|^2\end{aligned}$$

where $\gamma_t \triangleq \sum_{\substack{m=1\\m\neq t}}^{M_t} \sum_{\substack{l=1\\l\neq t}}^{M_t} \sum_{k=-N+1}^{N-1} |r_{m,l}(k)|^2 - \sum_{\substack{m=1\\m\neq t}}^{M_t} |r_{m,m}(0)|^2$ and

$$\begin{aligned}r_{m,t}(k) =& \textstyle\sum_{\substack{n=1\\n\neq d-k}}^{N-k} s_{m,n} s_{t,n+k}^* + s_{m,d-k} s_{t,d}^* I_A(d-k) \\ r_{t,l}(k) =& \textstyle\sum_{\substack{n=1\\n\neq d}}^{N-k} s_{t,n} s_{l,n+k}^* + s_{t,d} s_{l,d+k}^* I_A(d+k) \\ r_{t,t}(k) =& \textstyle\sum_{\substack{n=1\\n\neq d, n\neq d-k}}^{N-k} s_{t,n} s_{t,n+k}^* + s_{t,d} s_{t,d+k}^* I_A(d+k) \\ &+ s_{t,d}^* s_{t,d-k} I_A(d-k)\end{aligned}$$

where $I_A(p)$ is the indicator function of set $A = \{1, \ldots, N\}$, that is,

$$I_A(p) \triangleq \begin{cases} 1, & p \in A \\ 0, & p \notin A \end{cases}$$

Let us define

$$\begin{aligned}\gamma_{mtdk} &\triangleq \textstyle\sum_{\substack{n=1\\n\neq d-k}}^{N-k} s_{m,n} s_{t,n+k}^*, \beta_{mtdk} \triangleq s_{m,d-k} I_A(d-k) \\ \gamma_{tldk} &\triangleq \textstyle\sum_{\substack{n=1\\n\neq d}}^{N-k} s_{t,n} s_{l,n+k}^*, \alpha_{tldk} \triangleq s_{l,d+k}^* I_A(d+k) \\ \gamma_{ttdk} &\triangleq \textstyle\sum_{\substack{n=1\\n\neq d, n\neq d-k}}^{N-k} s_{t,n} s_{t,n+k}^*, \alpha_{ttdk} \triangleq s_{t,d+k}^* I_A(d+k) \\ \beta_{ttdk} &\triangleq s_{t,d-k} I_A(d-k)\end{aligned}$$

Thus, we obtain

$$\text{ISL} = c_0 s_{t,d}^2 + c_1 s_{t,d} + c_2 + c_3 s_{t,d}^* + c_4 {s_{t,d}^*}^2 + c_5 |s_{t,d}|^2 \tag{8A.4}$$

where

$$
\begin{aligned}
c_0 &\triangleq \sum_{\substack{k=-N+1\\k\neq 0}}^{N-1} \alpha_{ttdk}\beta^*_{ttdk}\\
c_1 &\triangleq \sum_{\substack{k=-N+1\\k\neq 0}}^{N-1} (\gamma^*_{ttdk}\alpha_{ttdk} + \gamma_{ttdk}\beta^*_{ttdk}) + \sum_{\substack{l=1\\l\neq t}}^{M_t}\sum_{k=-N+1}^{N-1}\gamma^*_{tldk}\alpha_{tldk}\\
&\quad + \sum_{\substack{m=1\\m\neq t}}^{M_t}\sum_{k=-N+1}^{N-1}\gamma_{mtdk}\beta^*_{mtdk}\\
c_2 &\triangleq \sum_{\substack{k=-N+1\\k\neq 0}}^{N-1} |\gamma_{ttdk}|^2 + \sum_{\substack{l=1\\l\neq t}}^{M_t}\sum_{k=-N+1}^{N-1}|\gamma_{tldk}|^2\\
&\quad + \sum_{\substack{m=1\\m\neq t}}^{M_t}\sum_{k=-N+1}^{N-1}|\gamma_{mtdk}|^2 + \gamma_t\\
c_3 &\triangleq c_1^*\\
c_4 &\triangleq c_0^*\\
c_5 &\triangleq \sum_{\substack{k=-N+1\\k\neq 0}}^{N-1} (|\alpha_{ttdk}|^2 + |\beta_{ttdk}|^2) + \sum_{\substack{l=1\\l\neq t}}^{M_t}\sum_{k=-N+1}^{N-1}|\alpha_{tldk}|^2\\
&\quad + \sum_{\substack{m=1\\m\neq t}}^{M_t}\sum_{k=-N+1}^{N-1}|\beta_{mtdk}|^2
\end{aligned}
$$

Since the coefficients $c_0 = c_4^*$, $c_1 = c_3^*$, and c_1, c_5 have real values, (8A.4) is a real and non-negative function. Also, for the mainlobe,

$$
\begin{aligned}
\sum_{m=1}^{M_t}|r_{m,m}(0)|^2 &= \sum_{\substack{m=1\\m\neq t}}^{M_t}\left(\sum_{n=1}^{N}|s_{m,n}|^2\right)^2 + \left(\sum_{\substack{n=1\\n\neq d}}^{N}|s_{t,n}|^2\right)^2\\
&\quad + 2|s_{t,d}|^2\sum_{\substack{n=1\\n\neq d}}^{N}|s_{t,n}|^2 + |s_{t,d}|^4
\end{aligned}
$$

Defining

$$
d_2 \triangleq \sum_{\substack{m=1\\m\neq t}}^{M_t}\left(\sum_{n=1}^{N}|s_{m,n}|^2\right)^2 + \left(\sum_{\substack{n=1\\n\neq d}}^{N}|s_{t,n}|^2\right)^2
$$

and $d_1 \triangleq 2\sum_{\substack{n=1\\n\neq d}}^{N}|s_{t,n}|^2$ we obtain

$$
\sum_{m=1}^{M_t}|r_{m,m}(0)|^2 = |s_{t,d}|^4 + d_1|s_{t,d}|^2 + d_2 \tag{8A.5}
$$

C_1 Constraint

In this case, we first notice that

$$
\|\boldsymbol{S}\|_F^2 = \sum_{\substack{m=1\\m\neq t}}^{M_t}\sum_{n=1}^{N}|s_{m,n}|^2 + \sum_{\substack{n=1\\n\neq d}}^{N}|s_{t,n}|^2 + |s_{t,d}|^2
$$

Thus, for the only variable, we obtain

$$\gamma_e \triangleq M_t N - \sum_{\substack{m=1 \\ m\neq t}}^{M_t} \sum_{n=1}^{N} |s_{m,n}|^2 - \sum_{\substack{n=1 \\ n\neq d}}^{N} |s_{t,n}|^2 \tag{8A.6}$$

C_2 Constraint

The PAR constraint can be written as $M_t N \max |s_{m,n}|^2 \leqslant \gamma_p \|\boldsymbol{S}\|_F^2$. Defining $P_{-(t,d)} \triangleq \max\{|s_{m,n}|^2; (m,n) \neq (t,d)\}$, we obtain

$$M_t N \max\{|s_{t,d}|^2, P_{-(t,d)}\} \leqslant \gamma_p \left(|s_{t,d}|^2 + \left\| \boldsymbol{S}_{-(t,d)} \right\|_F^2 \right)$$

We define

$$\gamma_l \triangleq \frac{M_t N P_{-(t,d)} - \gamma_p \left\| \boldsymbol{S}_{-(t,d)} \right\|_F^2}{\gamma_p}, \quad \gamma_u \triangleq \frac{\gamma_p \left\| \boldsymbol{S}_{-(t,d)} \right\|_F^2}{M_t N - \gamma_p}$$

Hence, $|s_{t,d}|^2 \geqslant \gamma_l$ when $|s_{t,d}|^2 \leqslant P_{-(t,d)}$, and $|s_{t,d}|^2 \leqslant \gamma_u$ when $|s_{t,d}|^2 \geqslant P_{-(t,d)}$.

APPENDIX 8B

Considering $a_2 = a_0^*$, $b_2 = b_0^*$, $c_4 = c_0^*$, and $c_3 = c_1^*$, (8.18) and (8.19) can be rewritten as [4]

$$\begin{aligned} \bar{f}(r,\phi) =& \frac{2\Re\{a_0 r e^{j\phi}\} + a_1 + a_3 r^3}{2\Re\{b_0 r e^{j\phi}\} + b_1 + b_3 r^3} \\ =& \frac{2\Re\{c_0 r^2 e^{j2\phi}\} + 2\Re\{c_1 r e^{j\phi}\} + c_2 + c_5 r^2}{r^4 + d_1 r^2 + d_2} \\ =& [(2c_{0r}\cos 2\phi - 2c_{0i}\sin 2\phi + c_5) r^2 \\ & + 2(c_{1r}\cos\phi - c_{1i}\sin\phi) r + c_2] \frac{1}{r^4 + d_1 r^2 + d_2} \end{aligned} \tag{8B.1}$$

where, $a_{0r} = \Re(a_0)$, $a_{0i} = \Im(a_0)$, $b_{0r} = \Re(b_0)$, $b_{0i} = \Im(b_0)$, $c_{0r} = \Re(c_0)$, $c_{0i} = \Im(c_0)$, $c_{1r} = \Re(c_1)$, and $c_{1i} = \Im(c_1)$.

4 It is possible to consider $e^{j\phi}$ as the variable and solve the problem. However, we reformulate the problem in the real variable to enable computations in the real domain to be closer to practical implementation.

APPENDIX 8C

As $f_o(r,\phi_0)$ is a fractional function, $\frac{\partial f_o(r,\phi_0)}{\partial r}$ is also a fractional function. Hence, to find the roots of $\frac{\partial f_o(r,\phi_0)}{\partial r}=0$, it is sufficient to find the roots of the numerator. By some mathematical manipulation, it can be shown that the numerator can be written as (8.24), and the coefficients are

$$
\begin{aligned}
p_0 &\triangleq 2\eta\Re\{\rho_0 e^{j\phi 0}\}\\
p_1 &\triangleq 2(\eta\rho_1+(\eta-1)b_3^2\rho_2)\\
p_2 &\triangleq 2(\eta\Re\{(\rho_3+2d_1\rho_0)e^{j\phi_0}\}+(\eta-1)(3b_3^2\rho_4+4b_3\rho_5\rho_2))\\
p_3 &\triangleq 4(\eta d_1\rho_1+(\eta-1)((2\rho_5^2+b_1b_3)\rho_2+c_2b_3^2+6b_3\rho_5\rho_4))\\
p_4 &\triangleq 2(\eta\Re\{(\rho_6\rho_0+2d_1\rho_3)e^{j\phi_0}\}\\
&\quad+(\eta-1)(\rho_4(12\rho_5^2+6b_1b_3+b_3^2d_1)+4\rho_5(b_1\rho_2+2b_3c_2)))\\
p_5 &\triangleq 2(\eta\rho_6\rho_1+(\eta-1)(\rho_2(b_1^2-d_2b_3^2)+b_3^2c_2d_1+4c_2(2\rho_5^2+b_1b_3)+\\
&\quad 4\rho_5\rho_4(3b_1+b_3d_1)))\\
p_6 &\triangleq 2(\eta\Re\{(\rho_6\rho_3+2d_1d_2\rho_0)e^{j\phi_0}\}+(\eta-1)(\rho_4(3b_1^2-b_3^2d_2\\
&\quad+2d_1(2\rho_5^2+b_1b_3))+4\rho_5(2b_1c_2-b_3(d_2\rho_2-c_2d_1))))\\
p_7 &\triangleq 4(\eta d_1d_2\rho_1+(\eta-1)(b_1^2c_2+2(b_1d_1-b_3d_2)\rho_5\rho_4\\
&\quad-(d_2\rho_2-c_2d_1)(2\rho_5^2+b_1b_3)))\\
p_8 &\triangleq 2(\eta\Re\{(d_2^2\rho_0+2d_1d_2\rho_3)e^{j\phi_0}\}+(\eta-1)(\rho_4(b_1^2d_1-2d_2(2\rho_5^2+b_1b_3))-\\
&\quad 4b_1\rho_5(d_2\rho_2-c_2d_1)))\\
p_9 &\triangleq 2(\eta d_2^2\rho_1-(\eta-1)(b_1^2(d_2\rho_2-c_2d_1)+4b_1d_2\rho_5\rho_4))\\
p_{10} &\triangleq 2(\eta d_2^2\Re\{\rho_3e^{j\phi_0}\}-(\eta-1)b_1^2d_2\rho_4)
\end{aligned}
$$

where $\rho_0 \triangleq a_3b_0-b_3a_0$, $\rho_1 \triangleq a_3b_1-a_1b_3$, $\rho_2 \triangleq c_5+2\Re\{c_0e^{j2\phi_0}\}$, $\rho_3 \triangleq b_1a_0-a_1b_0$, $\rho_4 \triangleq \Re\{c_1e^{j\phi_0}\}$, $\rho_5 \triangleq \Re\{b_0e^{j\phi_0}\}$, and $\rho_6 \triangleq d_1^2+2d_2$.

APPENDIX 8D

After substituting

$$\cos(\phi)=\frac{(1-\tan^2(\frac{\phi}{2}))}{(1+\tan^2(\frac{\phi}{2}))}$$

and

$$\sin(\phi) = \frac{2\tan(\frac{\phi}{2})}{(1+\tan^2(\frac{\phi}{2}))}$$

in $\frac{\partial f_o(r_e^\star,\phi)}{\partial \phi}$ and considering $z \triangleq \tan(\frac{\phi}{2})$, we encounter a fractional function. In this case, it is sufficient to find the roots of a nominator. It can be shown that the nominator can be written as (8.27), where

$$\begin{aligned}
q_0 \triangleq & 2r_e^\star(\eta\xi_0(2\xi_3-\xi_2)+(1-\eta)(c_{1i}-2\xi_9)(\xi_4^2-4\xi_6(\xi_4-\xi_6)))\\
q_1 \triangleq & 4r_e^\star(\eta\xi_0\xi_1+(1-\eta)(4\xi_7(2\xi_9-c_{1i})(\xi_4-2\xi_6)\\
& +(4\xi_8-c_{1r})(\xi_4^2-4\xi_6(\xi_4-\xi_6))))\\
q_2 \triangleq & 4r_e^\star(\eta\xi_0(4\xi_3-\xi_2)+(1-\eta)(-8\xi_7(4\xi_8-c_{1r})(\xi_4-2\xi_6)\\
& +\xi_4^2(4\xi_9+c_{1i})+4(r_e^{\star 2}\xi_5(2\xi_9-c_{1i})-6\xi_6\xi_9(\xi_4-\xi_6))))\\
q_3 \triangleq & 4r_e^\star(3\eta\xi_0\xi_1+(1-\eta)(\xi_4^2(4\xi_8-3c_{1r})+8\xi_{10}+4\xi_{11}+\\
& 4(\xi_5 r_e^{\star 2}(c_{1r}-8\xi_8)-2\xi_7^2c_{1r}-2\xi_6(2\xi_6\xi_8-\xi_7(14\xi_9-c_{1i})))))\\
q_4 \triangleq & 8r_e^\star(3\eta\xi_0\xi_3+(1-\eta)(\xi_9(5\xi_4^2-24r_e^{\star 2}\xi_5)\\
& +2\xi_4(4\xi_7c_{1r}+\xi_6c_{1i})-4\xi_6(16\xi_7\xi_8+\xi_9\xi_6)))\\
q_5 \triangleq & 4r_e^\star(3\eta\xi_0\xi_1+(1-\eta)(-\xi_4^2(4\xi_8+3c_{1r})+8\xi_{10}-4\xi_{11}+\\
& 4(\xi_5 r_e^{\star 2}(c_{1r}+8\xi_8)-2\xi_7^2c_{1r}+2\xi_6(2\xi_6\xi_8-\xi_7(14\xi_9+c_{1i})))))\\
q_6 \triangleq & 4r_e^\star(\eta\xi_0(4\xi_3+\xi_2)+(1-\eta)(8\xi_7(4\xi_8+c_{1r})(\xi_4+2\xi_6)\\
& +\xi_4^2(4\xi_9-c_{1i})+4(r_e^{\star 2}\xi_5(2\xi_9+c_{1i})+6\xi_6\xi_9(\xi_4+\xi_6))))\\
q_7 \triangleq & 4r_e^\star(\eta\xi_0\xi_1+(1-\eta)(4\xi_7(2\xi_9+c_{1i})(\xi_4+2\xi_6)\\
& -(4\xi_8+c_{1r})(\xi_4^2+4\xi_6(\xi_4+\xi_6))))\\
q_8 \triangleq & 2r_e^\star(\eta\xi_0(2\xi_3+\xi_2)-(1-\eta)(c_{1i}+2\xi_9)(\xi_4^2+4\xi_6(\xi_4+\xi_6)))
\end{aligned}$$

where, $\xi_0 \triangleq r_e^{\star 4}+r_e^{\star 2}d_1+d_2$, $\xi_1 \triangleq r_e^{\star 2}(a_3b_{0r}-a_{0r}b_3)+(a_1b_{0r}-a_{0r}b_1)$, $\xi_2 \triangleq r_e^{\star 2}(a_3b_{0i}-a_{0i}b_3)+(a_1b_{0i}-a_{0i}b_1)$, $\xi_3 \triangleq r_e^\star(a_{0r}b_{0i}-a_{0i}b_{0r})$, $\xi_4 \triangleq r_e^{\star 2}b_3+b_1$, $\xi_5 \triangleq b_{0r}^2-2b_{0i}^2$, $\xi_6 \triangleq r_e^\star b_{0r}$, $\xi_7 \triangleq r_e^\star b_{0i}$, $\xi_8 \triangleq r_e^\star c_{0r}$, $\xi_9 \triangleq r_e^\star r_{0i}$, $\xi_{10} \triangleq \xi_4(2\xi_6\xi_8-5\xi_7\xi_9)$, and $\xi_{11} \triangleq \xi_4(\xi_6c_{1r}-\xi_7c_{1i})$.

APPENDIX 8E

By substituting $r = 1$ into (8.22) and (8.23), the objective function under C_4 constraint can be rewritten as (8.33), where

$$\begin{aligned}
&h_0 \triangleq b_0 \quad h_1 \triangleq b_1 + b_3, \quad h_2 \triangleq b_2 \\
&g_0 \triangleq c_0 b_0 \frac{1-\eta}{M_t N^2} \\
&g_1 \triangleq (c_0 b_1 + c_1 b_0) \frac{1-\eta}{M_t N^2} \\
&g_2 \triangleq (c_0 b_2 + c_1 b_1 + c_2 b_0) \frac{1-\eta}{M_t N^2} + a_0 \eta \\
&g_3 \triangleq (c_1 b_2 + c_2 b_1 + c_3 b_0) \frac{1-\eta}{M_t N^2} + a_1 \eta \\
&g_4 \triangleq g_2^* \quad g_5 \triangleq g_1^* \quad g_6 \triangleq g_0^*
\end{aligned} \tag{8E.1}$$

Chapter 9

Waveform Design for Spectrum Sharing

Spectrum is a scarce resource that needs to be shared or reused judiciously to enable multiple radio-based services [1–11]. The focus of this chapter will be on the sharing of spectrum between radar and the ubiquitous wireless communications. In this context, sharing the spectrum among sensing systems and wireless communications has been considered in depth. This sharing could be in the radio-frequency RF domain (radar and cellular communications), optical (lidar and optical communications), or acoustical (sonar and acoustic). The investigation has focused on their unhindered operation while sharing the spectrum [12, 13]. This is a natural consequence of the interference among the different services reusing the spectrum as a consequence of the wireless nature of the operation.

Traditionally, spectrum allocation is guided by ITU policies that consider the need and impact of allocating a band to a particular service. Traditionally, the band allocation is static and, in this context, several portions of frequency bands (UHF to THz) have been allocated exclusively for different radar applications [3]. Radar systems are sparse geographically and a large fraction of these bands remain underutilized in allocated regions. However, when being used, radars need to maintain constant access to these bands for performing their tasks, which could encompass secondary surveillance, autonomous driving, and acquiring cognitive capabilities, among others. However, it is a known fact that the demand from the wireless industry for additional spectrum has been increasing over the last decade to accommodate the increasing number of users and data-hungry services. It has been indicated in [3, 12] that wireless systems such as commercial Long Term-Evolution (LTE) communications technology, fifth-generation (5G), Wi-Fi,

IEEE Radar band	VHF/UHF [30 MHz – 1 GHz]	L [1-2 GHz]	S [2-4 GHz]	C [4-8 GHz]	X [8-12 GHz]	Ku, K, Ka ,V, W [12-300 GHz]
Examples of radar usage	FOPEN	ARSR	ASR, NEXRAD	TDWR	CASA	Automotive radars, cloud radars
Co-existing comms	TV/broadcast/802.11ah/f	WiMAX, JTIDS	LTE	802.11a/ac	LTE	802.11ad, mmwave comm

Figure 9.1. Spectrum allocation among radar and communications.

Internet-of-Things (IoT), and Citizens Broadband Radio Services (CBRS) already cause spectral interference to legacy military, weather, astronomy, and aircraft surveillance radars.

Figure 9.1 gives an overview of the spectrum sharing between radar and communications that invariably leads to interference. Thus, it is necessary and meaningful for the two radio services to devise mutually beneficial coexistence strategies for spectrum sharing.

In this chapter, we focus on exploiting the degrees of design freedom to enable efficient spectrum sharing. Toward this, a scenario where a single waveform is used for both radar and communications is considered in this chapter. The problem is cast as an iterative optimization problem.

9.1 SCENARIO AND SIGNAL MODEL

Figure 9.2 shows the scenario where a Joint Radar Communication (JRC)-equipped vehicle (JRCV) intends to convey communication symbols to an active communicating vehicle (ACV) while also sensing the passive targets around ACV (e.g., bike, pedestrian). Toward this, the N antenna JRCV transmits a set of modulated sequences, known henceforth as the JRC waveform. This is a unified JRC waveform that aims at the dual functionality of sensing and communications.

The classical choices would be to select a well-known communication waveform like the orthogonal frequency division multiplexing (OFDM) or radar waveforms like FMCW or PMCW. When additional information about the propagation model is available, these single-functionality waveforms can be optimized to enhance their functionality. In this context, kindly recall the transmitter optimization schemes, for example, precoding, and

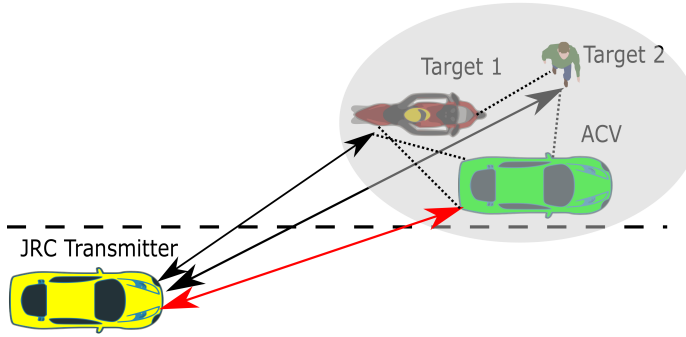

Figure 9.2. JRCV transmits a single waveform to communicate to an active communicating vehicle while intended to maximize the detection performance of passive targets (e.g., pedestrian and bike around it).

power allocation based on channel state information (CSI) in wireless communication systems. Further, in cognitive radar, the information about the environment (i.e., clutter), can be exploited to enhance target detection [14]. While the performance of these waveforms for their original application is guaranteed, the same cannot be said for the other application. In this context of channel-aware transmitter optimization, this book chapter focuses on the optimization of JRC waveform at the JRCV to simultaneously maximize SNR at the ACV and the SCNR (Signal to Clutter, and Noise Ratio) at the JRCV, in order to communicate efficiently with the ACV while sensing the passive target in the vicinity of ACV with high accuracy. As mentioned earlier, the optimization requires environment information; the novelty of the considered work also lies in the exploitation of the bidirectional communication link to provide information for enhancing the dual functionality.

In this chapter, for ease of comprehension, we assume a scene with a single passive target in the vicinity of the ACV; since ACV is also a target for the radar, we have 2 effective targets/scatterers. For a general situation, the reader can refer to [15]. Further, to elucidate the key concepts, these targets are modeled as point targets.

9.1.1 Communication Link and CSI

In the current scenario, CSI refers to the combination of antenna effects, path loss, and other radio propagation effects as well as fixed phase offsets. Knowledge of CSI is typically used to enhance transmitter and/or receiver operations in wireless communications. Following the classical communication receiver architecture, CSI can be measured at the ACV through the gain and phase of dedicated pilots in the JRCV transmissions. In a time-division duplexing (TDD) protocol for implementing bidirectional communication, the forward link (JRCV $\rightarrow$ ACV) and the return link (ACV$\rightarrow$ JRCV) are time-multiplexed. In TDD, the concept of reciprocity is utilized where the JRCV estimates the CSI on the return link pilot transmissions from the ACV and uses it for the JRCV$\rightarrow$ ACV transmission. Another popular protocol enabling bidirectional links is frequency-division duplexing (FDD), establishing CSI at the JRCV in FDD mode requires explicit feedback. For this work, we assume that the communication protocol enables the acquisition of bidirectional CSI at the JRCV. We further assume that the CSI remains unchanged during the coherent processing interval (CPI); this follows the well-known block fading model in communications.

9.1.2 Transmit Signal Model

The system model for the JRCV transmitter is abstracted in Figure 9.3. The figure also indicates the radar receiver operation of the JRCV.

This chapter considers a sequence-based radar and let $\{s(l)\}_{l=1}^{L}$ be the L length sequence with $s(l)$ denoting the lth chip. This sequence is padded using $2\hat{L}$ zeros to avoid inter symbol interference, whose need will be detailed in subsequent sections. The zero-padded sequence, $\mathbf{s} = [s(1), s(2), \ldots, s(L)], \tilde{\mathbf{s}} = [\mathbf{s}, \mathbf{0}_{2\hat{L}\times 1}]$, forms the transmit pulse that the JRCV continuously transmits from its N antennas after appropriate communication modulation and beamforming. With t_c being the chip duration, the transmit pulse has a duration of $(L + 2\hat{L})t_c$. Further, we consider a sampled system with t_s as the sampling interval. Typically, oversampling is considered with $t_s = \dfrac{t_c}{N_c}$, so that there are N_c samples per chip. However, without loss of generality, we assume $N_c = 1$ in this work.

JRC Waveform: The N antennas are assumed to be arranged in a uniform linear array configuration with a spacing of $\lambda/2$, where λ is the

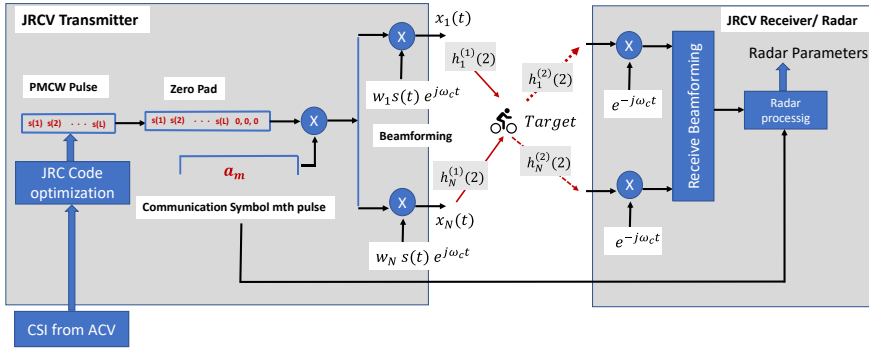

Figure 9.3. System model for the JRCV: depiction of the transmission of a JRCV waveform and the monostatic radar reception. The passive target is indexed with 2.

operational wavelength. Let $\tilde{s}_n(t)$ be the JRC waveform transmitted on the nth antenna at time t. Focusing on a particular pulse interval, $\tilde{s}_n(t)$ sampled at instances $t = lt_c = lt_s$, takes the form,

$$\tilde{s}_n(l) = aw_n s(l), \;\; 1 \leq l \leq L + 2\hat{L}, \;\; 1 \leq n \leq N \tag{9.1}$$

where $w_n = \frac{1}{\sqrt{N}} e^{-j2\pi n d \sin\theta/\lambda}$ denotes the complex beamforming weight associated with the nth antenna. Each pulse in (9.1) is modulated with a communication symbol, a, drawn from the predefined constellation of unit energy. From (9.1), one communication symbol is transmitted effectively from the N antennas in one pulse interval; communication symbols change every pulse interval. Transmission of a single symbol within a pulse interval arises from the fact that ACV has a single antenna and hence can receive only one communication stream.

The aim of the chapter lies in the design of the JRC waveform $\tilde{s}_n(l)$ for a given direction of transmission (i.e., given $\{w_n\}$). Since $\{a\}$ can be drawn from any arbitrary modulation and $\{w_n\}$ are given, the objective reduces to the design of the pulse sequence $\{s_n(l)\}$.

9.1.3 Signal Model at Targets

Referring to Figure 9.3, let $h_n^{(1)}(i)$ denote the channel on the forward (or transmit) path, modeling the link between the nth transmit antenna of JRCV to the ith target. This represents the cumulative effect of the antenna gains, small-scale fading and large-scale path loss between the nth JRCV antenna and the ith target. For simplicity, we assume one path per target leading to a total of 2 taps (recall the assumption of only two targets) for each n, that is, $\{h_n^{(1)}(i)\}_{i=1}^2$. For the convenience of notation, we assume the first target, that is, $i = 1$, corresponds to the ACV and $i = 2$ corresponds to the passive target (this channel is depicted in Figure 9.3). The superscript $^{(1)}$ refers to the forward path.

The noiseless received signal at the ith target sampled at $t = lt_s$ can be expressed as

$$y_i(l) = \sum_{n=1}^{N} h_n^{(1)}(i)\tilde{s}_n(l - l_i)e^{j2\pi l t_s f_{D_{(i)}}^{(1)}} \tag{9.2}$$

where l_i is the path delay normalized to t_s and $f_{D_{(i)}}^{(1)}$ is the relative Doppler experienced by the target i. In the considered scenario, different relative Doppler shifts corresponding to different targets are assumed (depicted with dashed lines in Figure 9.2) due to different relative velocities on the forward path, $\Delta v_i^{(1)}$, leading to $f_{D_i}^{(1)} = f_c \frac{\Delta v_i^{(1)}}{c}$ with c being the speed of light. Further, the delay l_i is assumed to be an integer with $l_i \leq \hat{L}$, where $\hat{L}$ considers the excess delay corresponding to the direct path and range bins of the targets (at sampling rate t_s). The fixed offset $e^{j2\pi l t_s \frac{c}{\lambda}}$ is absorbed into $h_n^{(1)}(i)$.

In the following, a simplification of (9.2) is undertaken. Towards this, define $g_{n,i}^{(1)}(l)$ to be a $\hat{L}$ length channel with $g_{n,i}^{(1)}(l) = h_n^{(1)}(i)$ when $l = l_i$ and $g_{n,i}^{(1)}(l) = 0$ otherwise; the channel taps $\{g_{n,i}^{(1)}\}$ now include the delay information unlike the $\{h_n^{(1)}(i)\}$. Recalling that $\mathbf{s}$ collects the L (nonzero-padded) entries of the sequence, that is, $\mathbf{s} = [s(l)]_{l=1}^{L} \in \mathbb{C}^L$, the convolution between the transmit waveform and the arbitrary channel in (9.2) can be represented in vector form using the transmit signal vector and the channel Toeplitz matrix [16]. Herein, the channel Toeplitz matrix, denoted as $\tilde{\mathbf{H}}_{n,i}^{(1)} \in$

$\mathbb{C}^{(\hat{L}+L-1)\times L}$, takes the form

$$\tilde{\mathbf{H}}_{n,i}^{(1)} \triangleq \text{Toep}(\mathbf{g}_{n,i}^{(1)}, \bar{\mathbf{g}}_{n,i}^{(1)}) \in \mathbb{C}^{(\hat{L}+L-1)\times L} \tag{9.3}$$

where

$$\mathbf{g}_{n,i}^{(1)} = [g_{n,i}^{(1)}(1), \ldots, g_{n,i}^{(1)}(\hat{L}), \mathbf{0}_{1\times L-1}]^T \in \mathbb{C}^{L+\hat{L}-1}$$

and $\bar{\mathbf{g}}_{n,i}^{(1)} = [g_{n,i}^{(1)}(1), \mathbf{0}_{1\times L-1}]^T \in \mathbb{C}^L$. Since each target has a single path from the JRCV transmitter, only one out of $\hat{L}$ coefficients of $[g_{n,i}^{(1)}(1), \ldots, g_{n,i}^{(1)}(\hat{L})]$ is nonzero; however, we pursue this notation to enable the reader to extend the discussion to multiple targets as presented in [15].

Assuming the samples of the Doppler shifts to be time and antenna-independent at the fast time processing, a valid assumption in automotive radar, the effective Doppler can be taken as $e^{j2\pi\hat{L}t_s f_{D_{(1)}}^{(1)}}$. Using this and the superposition of signals transmitted from different antennas (see (9.2)) enable us to describe the effective channel as

$$\mathbf{B}_i^{(1)} := \sum_{n=1}^{N} w_n e^{j2\pi(L+\hat{L}-1)t_s f_{D_{(i)}}^{(1)}} \tilde{\mathbf{H}}_{n,i}^{(1)} \in \mathbb{C}^{(\hat{L}+L-1)\times L} \tag{9.4}$$

Thus, the signal at the passive target for a generic pulse can then be compactly written as

$$\hat{\mathbf{y}}_2 = a\mathbf{B}_2^{(1)}\mathbf{s} \tag{9.5}$$

Recall that w_n in (9.4) denotes the beamforming weight for the nth antenna defined in (9.1).

9.1.4 Backscatter Signal Model

Referring to Figure 9.3, we define $h_n^{(2)}(i)$ and $f_{D_{(i)}}^{(2)}$, respectively, to be the channel and Doppler on the return path from the ith target to the nth antenna of JRCV. Here, the superscript $^{(2)}$ refers to the backscatter. To emphasize the RCS of targets for detection, let $\zeta(i)$ denote the impact of target i while $h_n^{(2)}(i)$ includes fixed phase offsets and radio propagation effects. Motivated by the Swerling-0 model for target RCS, we assume $\zeta(i)$ to be fixed during the CPI. Following a model similar to (9.2) and using the

principle of superposition, the noiseless and clutter-free received signal at the pth antenna of JRCV sampled at $t = lt_s$, can be modeled as

$$\begin{aligned} z_p(l) &= \sum_{i=1}^{2} \zeta(i) h_p^{(2)}(i) y_i(l - l_i) e^{j2\pi l t_s f_{D_{(i)}}^{(2)}} \\ &= \sum_{i=1}^{2} \sum_{n=1}^{N} a\zeta(i) h_p^{(2)}(i) h_n^{(1)}(i) w_n s(l - 2l_i) \\ &\quad \times e^{j2\pi l t_s \left(f_{D_{(i)}}^{(1)} + f_{D_{(i)}}^{(2)}\right)} e^{-j2\pi l_i t_s f_{D_{(i)}}^{(1)}},\ 1 \le p \le N \end{aligned} \tag{9.6}$$

Further, the delay of the forward and return paths to the ith target is assumed to be the same from/to all the antennas (this is reasonable due to the colocated nature of transmission and the far-field assumption of the targets). Clearly, the signal model at the targets, ACV, and the JRCV indicates multipath (excess delay of $2\hat{L}$) leading to inter pulse interference. However, as discussed in Section 9.1.2, each pulse is adequately zero-padded ($2\hat{L}$) to avoid interpulse interference and enable single pulse processing.

Similar to the previous discussion, define $g_{n,i}^{(2)}(l) = h_{n,i}^{(2)}(i)$ if $l = l_i$ and zero otherwise; the total support of $\{g_{n,i}^{(2)}(l)\}$ is still $\hat{L}$. Let $\tilde{\mathbf{H}}_{n,i}^{(2)} \in \mathbb{C}^{(2\hat{L}+L-1)\times(\hat{L}+L-1)}$ be the channel Toeplitz matrix formed in a manner similar to $\mathbf{H}_{n,i}^{(1)}$ of (9.3), but with a larger dimensions using $\{g_{n,i}^{(2)}(l)\}$ and $2\hat{L}$ zeros. It is assumed that the excess delay of the return paths is $\hat{L}$. Hence, the total excess delay on the two paths is $2\hat{L}$, motivating the zero pad of $2\hat{L}$.

To reconstruct the signal from the intended target at the JRCV receiver, define $\mathbf{H}_n^{(2)} = \left[\left(\tilde{\mathbf{H}}_{1,n}^{(2)}\right)^T, \left(\tilde{\mathbf{H}}_{2,n}^{(2)}\right)^T, \ldots, \left(\tilde{\mathbf{H}}_{N,n}^{(2)}\right)^T\right]^T \in \mathbb{C}^{N(2\hat{L}+L-1)\times(\hat{L}+L-1)}$. The noiseless received signal at JRCV from the qth target, denoted by $\mathbf{z}_q \in \mathbb{C}^{N(2\hat{L}+L-1)}$, can be expressed as

$$\mathbf{z}_q = \mathbf{B}_q^{(2)} \hat{\mathbf{y}}_q \tag{9.7}$$

$$\mathbf{B}_q^{(2)} := \zeta(q) e^{j2\pi(L+2\hat{L}-1)t_s f_{D_{(q)}}^{(2)}} \mathbf{H}_2^{(2)} \in \mathbb{C}^{(2\hat{L}+L-1)\times(\hat{L}+L-1)} \tag{9.8}$$

Typically, the target returns are contaminated by the ubiquitous clutter (reflections from unwanted targets including roads and trees) and the JRCV receiver noise. The superposition of the target returns (including ACV) and

clutter can be written as

$$\begin{aligned}\mathbf{r} &= \mathbf{z}_1 + \mathbf{z}_2 + \tilde{\boldsymbol{c}} + \boldsymbol{n} = a\left(\mathbf{Y}_1 + \mathbf{Y}_2\right)\mathbf{s} + \tilde{\mathbf{c}} + \mathbf{n} \in \mathbb{C}^{N(2\hat{L}+L-1)} \\ \mathbf{Y}_1 &= \mathbf{X}_1^{(2)}\mathbf{X}_1^{(1)} = \zeta(1)\mathbf{B}_1^{(2)}\mathbf{B}_1^{(1)} \\ \mathbf{Y}_2 &= \mathbf{X}_2^{(2)}\mathbf{X}_2^{(1)} = \zeta(2)\mathbf{B}_2^{(2)}\mathbf{B}_2^{(1)}\end{aligned} \tag{9.9}$$

where $\mathbf{n}$ is a complex-valued circular Gaussian noise with known variance σ_n^2 and $\tilde{\mathbf{c}}$ is the clutter signal is defined in Section 9.1.5.

9.1.5 Clutter Model

The model for the clutter follows [17] and takes the form

$$\begin{aligned}&\tilde{\mathbf{c}} = [\tilde{\mathbf{c}}_i]_{i=1}^{N} \in \mathbb{C}^{N(2\hat{L}+L-1)} \\ &\tilde{\mathbf{c}}_i = [\tilde{c}_i(l)]_{l=1}^{2\hat{L}+L-1},\ 1 \le i \le N \\ &\tilde{c}_i(l) = \sum_{n=1}^{N}\sum_{q=1}^{Q_c} \alpha_{q,n} e^{j2\pi f_{D_q} l t_s} s_n(l - r_q)\end{aligned} \tag{9.10}$$

where the parameters $\alpha_{q,n}$, f_{D_q}, and θ_q denote the complex amplitude, normalized Doppler frequency, and relative angle of the qth clutter for antenna n, respectively. The covariance matrix of $\tilde{\mathbf{c}}_i$ for given Doppler shifts, $\{f_{D_q}\}$, then takes the form

$$\mathbb{E}[\tilde{\mathbf{c}}_i\tilde{\mathbf{c}}_i^H|\{f_{D_q}\}] = \sum_{n=1}^{N}\sum_{k=1}^{N}\sum_{q=1}^{Q_c} \sigma_\alpha^2 \mathbf{s}_n(l - r_q)\mathbf{s}_k(m - r_q)^H\, e^{j2\pi f_{D_q}(l-m)t_s} \tag{9.11}$$

where $\mathbb{E}[\tilde{\mathbf{c}}_i\tilde{\mathbf{c}}_i^H|\{f_{D_q}\}] \in \mathbb{C}^{(2\hat{L}+L-1)\times(2\hat{L}+L-1)}$, $\sigma_\alpha^2 = \mathbb{E}[|\alpha_{q,n}^2|]$ and $\mathbf{s}_n(l - r_q)$ is the sequence of unknown object q corresponding to delay r_q transmitted from the nth antenna. We can further assume that Doppler shifts of the clutters are uniformly distributed around mean values $\bar{f}_{D_q}$, that is,

$$f_{D_q} \sim U(\bar{f}_{D_q} - \frac{\epsilon_q}{2}, \bar{f}_{D_q} + \frac{\epsilon_q}{2}) \tag{9.12}$$

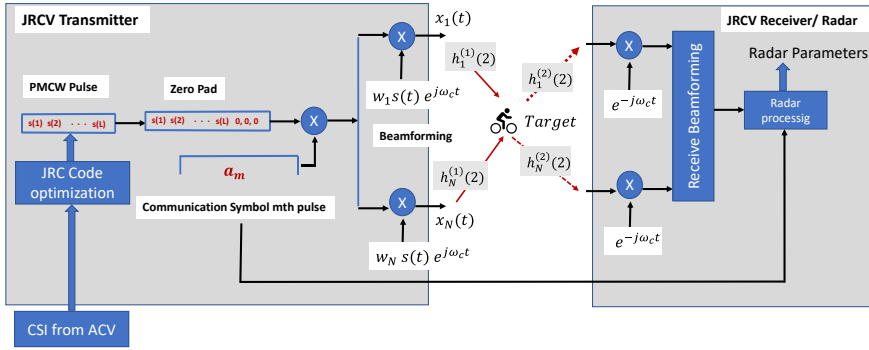

Figure 9.4. System model for the ACV. The channel is indexed by 1.

and ϵ_q accounts for the uncertainty on Doppler shifts. Thus, the unconditional covariance matrix becomes

$$\begin{aligned}
\mathbb{E}[\tilde{\mathbf{c}}_i\tilde{\mathbf{c}}_i^H] &= \mathbb{E}[\mathbb{E}[\tilde{\mathbf{c}}_i\tilde{\mathbf{c}}_i^H|\{f_{D_q}\}]] \\
&= \frac{1}{\epsilon_q}\int_{\bar{f}_{D_q}-\frac{\epsilon_q}{2}}^{\bar{f}_{D_q}+\frac{\epsilon_q}{2}} \sum_{n=1}^{N}\sum_{k=1}^{N}\sum_{q=1}^{Q_c} \sigma_\alpha^2 \mathbf{s}_n(l-r_q)\mathbf{s}_k(m-r_q)^H e^{j2\pi f_{D_q}(l-m)t_s} df_{D_q} \\
&= \sum_{n=1}^{N}\sum_{k=1}^{N}\sum_{q=1}^{Q_c} \sigma_{clt}^2 \mathbf{s}_n(l-r_q)\mathbf{s}_k(m-r_q)^H e^{j2\pi \bar{f}_{D,q}(l-m)t_s} \frac{\sin(\pi\epsilon_q(l-m))}{\pi\epsilon_q(l-m)}
\end{aligned} \tag{9.13}$$

Note that $\mathbb{E}[\tilde{\mathbf{c}}_i\tilde{\mathbf{c}}_i^H] \in \mathbb{C}^{(2\hat{L}+L-1)\times(2\hat{L}+L-1)}$. We further denote $\sigma_C^2 = trace\left(\mathbb{E}[\tilde{\mathbf{c}}_i\tilde{\mathbf{c}}_i^H]\right) = \mathbb{E}[\tilde{\mathbf{c}}_i^H\tilde{\mathbf{c}}_i]$ to denote the total clutter power; this quantity will be used later in Section 9.2.2.

9.1.6 Signal Model at ACV

The JRCV→ ACV communication link is presented in Figure 9.4. Toward determining the signal at the ACV, (9.5) is now specialized for $i = 1$.

Recall that w_n in (9.4) denotes the beamforming weight for the nth antenna defined in (9.1). With these notations, the signal received at ACV, that is, $i = 1$, can be expressed as

$$\mathbf{y}_{\text{com}} = a\mathbf{B}_1^{(1)}\mathbf{s} + \mathbf{n}_0 \in \mathbb{C}^{(\hat{L}+L-1)} \tag{9.14}$$

where $\mathbf{n}_0$ is the zero-mean complex-valued circular Gaussian noise at the communication receiver with known covariance matrix. Recall that a is the communication symbol and $\mathbf{s}$ is the vector representation of the L length sequence $s(l)$. In (9.14), we have exploited the fact that the transmissions from different antennas, $s_n(l)$ in (9.1), are zero-padded adequately.

9.1.7 CSI Exploitation

The channels for the passive target are assumed to be perturbed versions of the channel to the ACV. In particular, $h_n^{(k)}(2) = h_n^{(k)}(1) + \eta_n^{(k)}(1),\ k = 1, 2$ where $\eta_n^{(k)}(1)$ is a zero mean circularly symmetric additive Gaussian perturbation with variance $\sigma_2^{2^{(k)}}$. Thus, $\tilde{\mathbf{H}}_{n,2}^{(1)}$ is replaced by $\tilde{\mathbf{H}}_{n,1}^{(1)} + \tilde{\mathbf{\Delta}}_{n,1}^{(1)}$ where $\tilde{\mathbf{\Delta}}_{n,1}^{(1)} \in \mathbb{C}^{(\hat{L}+L-1)\times L}$ is a Toeplitz matrix given by $\tilde{\mathbf{\Delta}}_{n,1}^{(1)} := \text{Toep}(\boldsymbol{\eta}_n^{(1)}, \bar{\boldsymbol{\eta}}_n^{(1)})$, where $\boldsymbol{\eta}_n^{(1)} = [\eta_{n,i}^{(1)}(1), \ldots, \eta_{n,i}^{(1)}(\hat{L}), \mathbf{0}_{1\times L-1}]^T \in \mathbb{C}^{L+\hat{L}-1}$ and $\bar{\boldsymbol{\eta}}_n^{(1)} = [\eta_n^{(1)}(1), \mathbf{0}_{1\times L-1}]^T \in \mathbb{C}^L$. The entries of $\tilde{\mathbf{\Delta}}_{n,1}^{(1)}$ are independent for different n and $\mathbb{E}\left[\tilde{\mathbf{\Delta}}_{n,1}^{(1)}\left(\tilde{\mathbf{\Delta}}_{n,1}^{(1)}\right)^H\right] = \hat{L}\sigma_q^{2^{(1)}}\mathbf{I}_{(\hat{L}+L-1)}$. The applicability of the model is favored in scenarios offering spatial correlation; the beamformed transmission considered in this work and the presence of all targets in that beam offer a line-of-sight scenario motivating the use of the model. Nevertheless, the quantities, $\{\sigma_2^{2^{(i)}}\}$, can be set based on the scenario. Using these, the signal at the passive target can be specialized from (9.5) as

$$\begin{aligned}
\hat{\mathbf{y}}_2 &= e^{j2\pi\hat{L}t_s f_{D_{(2)}}^{(1)}}\left(\sum_{n=1}^{N} a w_n \tilde{\mathbf{H}}_{n,2}^{(1)}\right)\mathbf{s} \\
&= \left(\sum_{n=1}^{N} a w_n e^{j2\pi\hat{L}t_s f_{D_{(2)}}^{(1)}}\left(\tilde{\mathbf{H}}_{n,1}^{(1)} + \tilde{\mathbf{\Delta}}_{n,1}^{(1)}\right)\right)\mathbf{s} \qquad (9.15) \\
\mathbf{X}_2^{(1)} &= \left(\sum_{n=1}^{N} a w_n e^{j2\pi\hat{L}t_s f_{D_{(2)}}^{(1)}}\tilde{\mathbf{H}}_{n,1}^{(1)} + \mathbf{\Delta}_2^{(1)}\right)
\end{aligned}$$

where $\mathbf{\Delta}_2^{(1)} := \sum_{n=1}^{N} a w_n e^{j2\pi\hat{L}t_s f_{D_{(2)}}^{(1)}}\tilde{\mathbf{\Delta}}_{n,1}^{(1)}$. Given the Doppler shift estimate, w_n and a, the nonzero entries of $\mathbf{\Delta}_2^{(1)} = \sum_{n=1}^{N} a w_n e^{j2\pi\hat{L}t_s f_{D_{(2)}}^{(1)}}\tilde{\mathbf{\Delta}}_{n,1}^{(1)}$ can be shown to have statistical properties similar to $\tilde{\mathbf{\Delta}}_{n,1}^{(1)}$, except for variance.

Further, note that Doppler has a unit amplitude and w_n has an amplitude $1/\sqrt{N}$. For given Doppler shifts and a, the nonzero entries of $\mathbf{\Delta}_{n,2}^{(1)}$ has a variance $|a|^2\sigma_2^{2^{(1)}}$. The unconditional variance of the nonzero entries of $\tilde{\mathbf{\Delta}}_{n,q}^{(1)}$ will be $\sigma_q^{2^{(1)}}$ as a is drawn from a unit energy constellation.

Similarly, the backscatter model can be updated from (9.7) as

$$\begin{aligned}
\boldsymbol{z}_2 &= e^{j2\pi\hat{L}t_s f_{D_{(2)}}^{(1)}}\zeta(2)\boldsymbol{H}_2^{(2)}\hat{\boldsymbol{y}}_2 \\
&= e^{j2\pi\hat{L}t_s f_{D_{(2)}}^{(1)}}\zeta(2)\big(\boldsymbol{H}_1^{(2)} + \tilde{\mathbf{\Delta}}_2^{(2)}\big)\hat{\boldsymbol{y}}_2 \\
&= \zeta(2)\left(e^{j2\pi\hat{L}t_s f_{D_{(2)}}^{(1)}}\boldsymbol{H}_1^{(2)} + \mathbf{\Delta}_2^{(2)}\right)\hat{\boldsymbol{y}}_2 \\
\boldsymbol{X}_2^{(2)} &= \zeta(2)\left(e^{j2\pi\hat{L}t_s f_{D_{(2)}}^{(1)}}\boldsymbol{H}_1^{(2)} + \mathbf{\Delta}_2^{(2)}\right)
\end{aligned} \tag{9.16}$$

Using (9.16), the equation relating the transmit and receive signals can be updated from (9.9) can be simplified as

$$\begin{aligned}
\mathbf{r} = \mathbf{z}_1 + \mathbf{z}_2 + \tilde{\boldsymbol{c}} + \boldsymbol{n} &= a\left(\mathbf{Y}_1 + \mathbf{Y}_2\right)\mathbf{s} + \tilde{\mathbf{c}} + \mathbf{n} \in \mathbb{C}^{N(2\hat{L}+L-1)} \\
\mathbf{Y}_1 = \mathbf{X}_1^{(2)}\mathbf{X}_1^{(1)} &= \zeta(1)\mathbf{B}_1^{(2)}\mathbf{B}_1^{(1)} \\
\mathbf{Y}_2 = \mathbf{X}_2^{(2)}\mathbf{X}_2^{(1)} &= \zeta(2)\left(\mathbf{B}_1^{(2)} + \mathbf{\Delta}_2^{(2)}\right)\left(\mathbf{B}_1^{(1)} + \mathbf{\Delta}_2^{(1)}\right)
\end{aligned} \tag{9.17}$$

This section has developed models for the radar backscattered signal at the JRCV as well as the communication signal at ACV. These models provide the platform for developing performance analysis and is discussed in the next section.

9.2 PERFORMANCE INDICATORS

The key performance indicators considered in this chapter for waveform design are SNR at the ACV and SCNR at the JRCV. These metrics have been widely used in literature and in the following, we specialize these metrics to the signal model developed in Section 9.1.

9.2.1 ACV SNR Evaluation

The SNR at ACV is defined as

$$\text{SNR} = \frac{\mathbb{E}[\|a\mathbf{B}_1^{(1)}\mathbf{s}\|^2]}{\mathbb{E}[\mathbf{n}_0^H\mathbf{n}_0]} = \frac{\|\mathbf{B}_1^{(1)}\mathbf{s}\|^2}{\sigma_n^2} \tag{9.18}$$

Note that the averaging is over realizations of noise and communication symbols. Further, the communication symbols are assumed to have unit energy while $\mathbb{E}[\mathbf{n}_0^H\mathbf{n}_0] = \sigma_n^2$ refers to the total noise power.

In reality, $e^{j2\pi\hat{L}t_s f_{D_{(1)}}^{(1)}}$ and $\tilde{\mathbf{H}}_{n,1}^{(1)}$ are replaced by $e^{j2\pi\hat{L}t_s \hat{f}_{D_{(1)}}^{(1)}}$ and $\hat{\mathbf{H}}_{n,1}^{(1)}$, which are constructed using estimates of Doppler shifts and channel coefficients obtained by ACV during the CSI acquisition process (through appropriate pilots).

9.2.2 SCNR at JRCV

With the aforementioned discussion, the radar SCNR when using the perturbed channel can be defined as

$$\text{SCNR} = \frac{\mathbb{E}[P_{\text{rad}}]}{\mathbb{E}[P_{(C+N)}]} \tag{9.19}$$

where $\mathbb{E}[P_{\text{rad}}]$ denotes the power of the radar backscatter considering the partial exploitation of the channel, the uncertainty in the channel estimates, and the randomness of the communication signal. This metric is representative of an average received radar power and leads to a tractable analysis in waveform optimization. However, use of a filter matched to $\mathbf{s}$ would lead to quartic problems (of the form $\left|\mathbf{s}^H\mathbf{X}_2^{(2)}\mathbf{X}_2^{(1)}\mathbf{s}\right|^2$) unlike the quadratic form for SCNR to be detailed in the sequel.

Further, to compute the denominator of (9.19), the averaging is over the clutter, noise, and communication symbol statistics. It should also be noted that the channel of the link JRCV→ACV is perfectly known.

In this setting, the SCNR expression in (9.19) can be simplified as

$$\mathbb{E}[P_{\text{rad}}] = \mathbf{s}^H\mathbf{V}\mathbf{s} \tag{9.20}$$

$$\mathbb{E}[P_{(C+N)}] = \mathbf{s}^H\mathbf{W}\mathbf{s} + \sigma_n^2 \tag{9.21}$$

Using the derivation in Appendix 9A, it can be further shown that

$$\mathbf{V} = |\zeta^H(2)|^2 \mathbf{B}_2^{(1)H} \mathbf{B}_2^{(2)H} \mathbf{B}_2^{(2)} \mathbf{B}_2^{(1)} + |\zeta(2)|^2 \hat{L} \sigma_2^{2^{(2)}} \mathbf{R}_{B_2^{(1)}} + |\zeta(2)|^2 \hat{L} \sigma_2^{2^{(1)}} \mathrm{tr}\{\mathbf{R}_{B_2^{(2)}}\}\mathbf{I} + \hat{L}^2 |\zeta(2)|^2 \varrho_2^2 \sigma_2^{2^{(1)}} \sigma_2^{2^{(2)}} \mathbf{I} \tag{9.22}$$

$$\mathbf{W} = |\zeta^H(1)|^2 \mathbf{B}_1^{(1)H} \mathbf{B}_1^{(2)H} \mathbf{B}_1^{(2)} \mathbf{B}_1^{(1)} + (\sigma_C^2 + \sigma_n^2)\mathbf{I} \tag{9.23}$$

and $\mathbf{R}_{B_q^{(i)}} = \mathbf{B}_q^{(i)H} \mathbf{B}_q^{(i)}$, $i \in \{1, 2\}$, $\mathbb{E}[|a|^2] = 1$, and noting that the clutter power is computed by summing the diagonal elements of (9.13) over the antennas. We denote the power of clutter by σ_C^2 in (9.19). Kindly refer to Appendix 9A for the details of the derivation. Using these, the SCNR in (9.19) can be calculated.

9.3 WAVEFORM DESIGN AND OPTIMIZATION FORMULATION

This section presents the waveform design algorithm to enhance the performance of both radar and communications.

9.3.1 Design Methodology

In order to improve SCNR, it is essential to have knowledge about the $\zeta(k)$ and Doppler shifts of all targets at the JRCV to be able to reconstruct the matrices $\mathbf{V}$ and $\mathbf{W}$ in (9.19), (9.20), and (9.21). As a simple approach, we assume $\zeta(k)$ are known, possibly from a prescan, a priori information, or the use of appropriate estimates. Inspired by the use of matched filters at the receiver in the case of unknown Doppler shifts, we consider a grid of Doppler points and maximize the worst-case SCNR with regard to these possible Doppler shifts. This ensures that JRCV achieves a certain SCNR level irrespective of the Doppler.

It is further assumed that the Doppler of the ACV is known at the JRCV; this can be estimated at the ACV using the pilot symbols and fed back to JRCV. Perfect knowledge and feedback are assumed to obtain a benchmark in this case. This simplification is considered to ease the presentation of this chapter. A general treatment without this assumption is presented in [15].

In this context, we let $\Omega := [0, 1]$ and consider an n point grid on this domain, that is, $\mathbf{\Omega} := \mathrm{grid}(\Omega, n)$, to be able to find the worst-case Doppler

shifts. In particular, we obtain a series of SCNR values from (9.19), (9.20), and (9.21) for different grid points; the resulting expression is

$$\text{SCNR}_i = \frac{\mathbf{s}^H \mathbf{V}(f_D)\mathbf{s}}{\mathbf{s}^H \mathbf{W}\mathbf{s} + \sigma_n^2} = \frac{\mathbf{s}^H \mathbf{V}_i \mathbf{s}}{\mathbf{s}^H \mathbf{W}\mathbf{s} + \sigma_n^2},\ i \in \mathbf{\Omega} \tag{9.24}$$

where the matrix $\mathbf{V}_i$ is the realization of $\mathbf{V}(f_D)$ for Doppler shifts on a grid indexed by i. The worst-case SCNR is then computed from (9.24). Simultaneously, we design this sequence to satisfy a certain level of SNR for communications. The strategy is to obtain a sequence that maximizes the SNR at ACV first, and then we set a trade-off constraint to modify this sequence optimally to satisfy radar desired properties.

9.3.2 Optimization Problem for ACV

The communications scheme is based on modulating designed sequences with data; hence, its receiver carries out matched-filtering (correlator) with regards to $\{s(l)\}$ over the received signal to extract data. The output of the matched filter/correlator depends on the correlation properties of the sequence and its peak determines the performance of the communication system. Hence, a sequence with low correlation lags (low sidelobes) is desired to avoid spurious peaks in presence of noise. In this context, a low ISL assists the matched filter to increase the quality of demodulation/decoding and hence enhances the communication performance. To this end, we first define ISL mathematically. Recall that $s(n)$ and $s(n+l)$ are the nth and $(n+l)$th elements of the transmit sequence and that the sequences are zero-padded to length $2\hat{L} + L - 1$ to comply with the channel matrix with excess delay $\hat{L}$. As mentioned earlier, we focus on the non-padded part. For this sequence, we let

$$r(l) = \sum_{n=1}^{L-l} s(n)s^*(n+l) \tag{9.25}$$

denote the autocorrelation of a sequence, where $-L+1 \leq l \leq L-1$. Clearly, $r(l)$ is conjugate symmetric (i.e., $r(l) = r(-l)^*$). We define the ISL of

a sequence of length L as

$$\text{ISL} = \sum_{\substack{l=-L+1 \\ l\neq 0}}^{L-1} |r(l)|^2 \tag{9.26}$$

Finally, the ISL can be written in matrix form as

$$2\sum_{i=1}^{L-1} \left| \operatorname{tr}\left[\text{Diag}[\mathbf{s}\mathbf{s}^H, i]\right]\right|^2 = \sum_{\substack{l=-L+1 \\ l\neq 0}}^{L-1} |r(l)|^2 \tag{9.27}$$

where Diag$[\mathbf{S}, i]$ returns a diagonal matrix by taking the elements on the ith diagonal of $\boldsymbol{m}S$. Note that $i = 0$ represents the main diagonal, which is omitted in (9.26). To ensure the correlation quality of the sequence, we impose a constraint on ISL limiting it to a threshold level, namely, γ. Without loss of generality, we consider unit power transmission $\|\boldsymbol{s}\|^2 = 1$. In order to maximize communications SNR at ACV, that is, (9.18), with respect to ISL and power constraints, it suffices to solve the following optimization problem:

$$P_1^{\text{Comm.}} \begin{cases} \max\limits_{\mathbf{s}} & \|\mathbf{B}_1^{(1)}\mathbf{s}\|^2 \\ \text{subject to} & \|\mathbf{s}\|^2 = 1 \\ & \sum_{i=1}^{L-1} \left| \operatorname{tr}\left\{\text{Diag}\{\mathbf{s}\mathbf{s}^H, i\}\right\}\right|^2 \leq \gamma \end{cases}$$

To simplify $P_1^{\text{Comm.}}$, we write the objective function as

$$\|\mathbf{B}_1^{(1)}\mathbf{s}\|^2 = \langle \mathbf{R}_{\text{com}}^H, \boldsymbol{S}\rangle \tag{9.28}$$

where $\mathbf{R}_{\text{com}} = [B_1^{(1)}]^H\mathbf{B}_1^{(1)}$ and $\mathbf{S}$ is a rank one positive semidefinite (PSD) matrix. Recalling the definition of $\langle \mathbf{X}, \mathbf{Y}\rangle$, $P_1^{\text{Comm.}}$ can be reduced to

$$P_2^{\text{Comm.}} \begin{cases} \max\limits_{\mathbf{s}} & \langle \mathbf{R}_{\text{com}}^H, \mathbf{S}\rangle \\ \text{subject to} & \sum_{i=1}^{L-1} \left| \operatorname{tr}\left\{\text{Diag}\{\mathbf{S}, i\}\right\}\right|^2 \leq \gamma \\ & \text{rank}(\mathbf{S}) = 1 \\ & \mathbf{S} \succeq 0 \\ & \text{tr}\{\mathbf{S}\} = 1 \end{cases}$$

In order to solve $P_2^{\text{Comm.}}$, it is required to further relax it by removing the rank 1 constraint on $\mathbf{S}$,

$$P_3^{\text{Comm.}} \begin{cases} \max\limits_{\boldsymbol{ms}} & \langle \mathbf{R}_{\text{com}}^H, \mathbf{S} \rangle \\ \text{subject to} & \sum_{i=1}^{L-1} \left| \text{tr}\left\{ \text{Diag}\{\mathbf{S}, i\} \right\} \right|^2 \leq \gamma, \\ & \mathbf{S} \succeq 0, \\ & \text{tr}\{\mathbf{S}\} = 1 \end{cases}$$

Problem $P_3^{\text{Comm.}}$ is a convex optimization problem and can be solved by many solvers (e.g., CVX), in polynomial time [18]. It is worth noting that, by dropping the ISL condition, the maximum SNR value of the above objective function becomes $\max\limits_{\mathbf{s}} \|\mathbf{R}_{\text{com}}\mathbf{s}\|^2 = \lambda_{max}\{\mathbf{R}_{\text{com}}\}$, which is an upper bound for solution to $P_3^{\text{Comm.}}$. Let $\mathbf{S}^\dagger$ be the optimal solution of $P_3^{\text{Comm.}}$. In Appendix 9B, we explain how to extract a rank 1 solution of $\mathbf{S}^\dagger$.

9.3.3 Formulation of JRC Waveform Optimization

Here, the worst-case scenario is considered by minimizing the objective function with regard to a feasible normalized Doppler region (defined as Ω in Section 9.3.1). Let $\mathbf{c}_s$ denote the optimal communications sequence derived in Section 9.3.2; and this work considers the optimal JRC sequence in the δ vicinity of $\mathbf{c}_s$ (i.e., $\|\mathbf{s} - \mathbf{c}_s\|^2 \leq \delta$). Here, δ determines the trade-off between the communications and radar systems. A large δ offers additional flexibility in JRC waveform design (away from communications waveform). In contrast, a small δ provides little freedom for designing radar waveform. We consider the following formulation:

$$P_1^{\text{JRC}} \begin{cases} \max\limits_{\mathbf{s}} \min\limits_{i \in \Omega} & \dfrac{\mathbf{s}^H \mathbf{V}_i \mathbf{s}}{\mathbf{s}^H \mathbf{W} \mathbf{s} + \sigma_n^2} \\ \text{subject to} & \sum_{i=1}^{L-1} \left| \text{tr}\left\{ \text{Diag}\{\mathbf{s}\mathbf{s}^H, i\} \right\} \right|^2 \leq \gamma \\ & \text{tr}\{\mathbf{s}\mathbf{s}^H\} = 1 \\ & \|\mathbf{s} - \mathbf{c}_s\|^2 \leq \delta \end{cases}$$

By considering a power constraint equal to unity, we simplify the trade-off constraint of $P_1^{\text{seq.}}$ as $(\mathbf{s} - \mathbf{c}_s)^H (\mathbf{s} - \mathbf{c}_s) = 2 - 2\Re(\mathbf{s}^H \mathbf{c}_s) \leq \delta \Rightarrow \Re(\mathbf{s}^H \mathbf{c}_s) \geq \tilde{\beta}$, with $\tilde{\beta} = (1 - \frac{\delta}{2})$.

Since applying an arbitrary phase shift $e^{j\phi}$ to $\mathbf{s}^H\mathbf{c_s}$ does not alter the norm of the sequence and the ISL is unchanged, one can introduce a phase shift to make $\mathbf{s}^H\mathbf{c_s}$ a real value. Without loss of generality affecting this choice of phase and exploiting the real nature of the resulting product $e^{j\phi}\mathbf{s}^H\boldsymbol{c}$, it follows that

$$\Re^2(e^{j\phi}\mathbf{s}^H\boldsymbol{c}) = \text{tr}\{\mathbf{s}\mathbf{s}^H\mathbf{C}\} \geq \tilde{\beta}^2 = \beta \tag{9.29}$$

This results in

$$\begin{aligned} \text{SCNR}_i &= \frac{\mathbf{s}^H\mathbf{V}_i\mathbf{s}}{\mathbf{s}^H\mathbf{\Gamma}\mathbf{s}} \\ \mathbf{\Gamma} &= \Big(\mathbf{W} + (\sigma_n^2 + \sigma_C^2)\mathbf{I}\Big) \end{aligned} \tag{9.30}$$

Considering (9.29) and (9.30), we can write P_1^{JRC} as

$$P_2^{\text{JRC}} \begin{cases} \max\limits_{\mathbf{s}} \min\limits_{i\in\Omega} \dfrac{\mathbf{s}^H\mathbf{V}_i\mathbf{s}}{\mathbf{s}^H\mathbf{\Gamma}\mathbf{s}} \\ \text{subject to} \quad \sum_{i=1}^{L-1} \left| \text{tr}\left\{\text{Diag}\{\mathbf{s}\mathbf{s}^H, i\}\right\}\right|^2 \leq \gamma \\ \qquad\qquad \text{tr}\{\mathbf{s}\mathbf{s}^H\} = 1 \\ \qquad\qquad \text{tr}\{\mathbf{s}\mathbf{s}^H\mathbf{C}\} \geq \beta^2 \end{cases}$$

Lemma 9.1. *The objective function of problem $\{P_2^{JRC}\}$ is upper-bounded by*

$$\max_{\mathbf{s}} \min_{i} \frac{\mathbf{s}^H\mathbf{V}_i\mathbf{s}}{\mathbf{s}^H\mathbf{\Gamma}\mathbf{s}} \leq \lambda_{max}\{\mathbf{\Gamma}^{-1}\mathbf{V}_i\} \tag{9.31}$$

Proof: Kindly refer to Appendix 9C. ■

Since $\mathbf{W}$ is full rank, the objective function of P_2^{JRC} is upper-bounded, any optimization method that can yield a monotonically increasing sequence of the objective function P_2^{JRC} is convergent.

9.3.4 Solution to the Optimization Problem

The Grab-n-Pull (GnP) algorithm presented in [19] is used to solve the max-min fractional program in P_2^{JRC}. Herein, we specialize the algorithm for the considered problem and present it for completeness; the reader is kindly

referred to [19] for details. Toward this, a reformulation of P_2^{JRC} is first considered:

$$P_3^{\text{JRC}} \begin{cases} \max\limits_{\mathbf{s}} \ \min\limits_{i\in\Omega} \{\mu_i\} & \\ \text{subject to} \quad \mu_i = \dfrac{\mathbf{s}^H\mathbf{V}_i\mathbf{s}}{\mathbf{s}^H\mathbf{\Gamma}\mathbf{s}} & (c_1) \\ \sum_{i=1}^{L-1} \left|\operatorname{tr}\left\{\text{Diag}\{\mathbf{s}\mathbf{s}^H, i\}\right\}\right|^2 \leq \gamma & (c_2) \\ \text{tr}\{\mathbf{s}\mathbf{s}^H\} = 1 & (c_3) \\ \text{tr}\{\mathbf{s}\mathbf{s}^H\mathbf{C}\} \geq \beta^2 & (c_4) \end{cases}$$

Note that constraint c_1 holds if and only if $\|\mathbf{V}_i^{\frac{1}{2}}\mathbf{s}\| = \sqrt{\mu_i}\|\mathbf{\Gamma}^{\frac{1}{2}}\mathbf{s}\|$. Therefore, by defining slack variables $\{\mu_i\}$ and a penalty term $\eta > 0$, $\|\mathbf{V}_i^{\frac{1}{2}}\boldsymbol{s}\|$ can be made close to $\|\mathbf{\Gamma}^{\frac{1}{2}}\mathbf{s}\|$ as

$$P_4^{\text{JRC}} \begin{cases} \max\limits_{\mathbf{s},\{\mu_i\}} \min\limits_{i} & \{\mu_i\} - \eta\sum_{i=1}^{I}\left(\|\mathbf{V}_i^{\frac{1}{2}}\mathbf{s}\| - \sqrt{\mu_i}\|\mathbf{\Gamma}^{\frac{1}{2}}\mathbf{s}\|\right)^2 \\ \text{subject to} & c_k,\ \forall k \in [2,4] \\ & \mu_i \geq 0 \end{cases}$$

In a manner similar to [19], the problem is further relaxed by introducing a new slack variable $\mathbf{Q}$ as a unitary rotation matrix to align the vector $\mathbf{\Gamma}^{\frac{1}{2}}\mathbf{s}$ in the same direction of $\mathbf{V}_i^{\frac{1}{2}}\mathbf{s}$ without changing its norm $\|\mathbf{V}_i^{\frac{1}{2}}\mathbf{s}\|$. Thus, an alternative problem to P_4^{JRC} is

$$P_5^{\text{JRC}} \begin{cases} \max\limits_{\mathbf{s},\{\mu_i\},\{\mathbf{Q}_i\}} \min\limits_{i} \{\mu_i\} - \eta\sum_{i=1}^{I}\|\mathbf{V}_i^{\frac{1}{2}}\mathbf{s} - \sqrt{\mu_i}\mathbf{Q}_i\mathbf{\Gamma}^{\frac{1}{2}}\mathbf{s}\|^2 \\ \text{subject to} \quad c_k,\ \forall k \in [2,4] \\ \qquad\qquad \mu_{i,j} \geq 0 \\ \qquad\qquad \mathbf{Q}_i^H\mathbf{Q}_i = \mathbf{I}_N \end{cases}$$

In the following, we solve P_5^{JRC} by an iterative optimization framework by partition of variables $\mathbf{s}$, $\mathbf{Q}_i$, and μ_i.

9.3.4.1 Optimization with Respect to $\mathbf{s}$

We begin by defining the optimization problem with respect to $\mathbf{s}$. To this end, we fixed $\{\mathbf{Q}_i\}$ and $\{\mu_i\}$ to solve P_5^{JRC} with respect to $\mathbf{s}$. We can write

the objective function of P_5^{JRC} as

$$\sum_{i=1}^{I} \|\mathbf{V}_i^{\frac{1}{2}}\mathbf{s} - \sqrt{\mu_i}\mathbf{Q}_i\mathbf{\Gamma}^{\frac{1}{2}}\mathbf{s}\|^2 = \mathbf{s}^H\mathbf{R}\mathbf{s} \tag{9.32}$$

where

$$\mathbf{R} = \sum_{i=1}^{I}\left\{(\mathbf{V}_i + \mu_i\mathbf{\Gamma}) - \sqrt{\mu_i}(\mathbf{V}_i^{\frac{1}{2}}\mathbf{Q}_i\mathbf{\Gamma}^{\frac{1}{2}} + \mathbf{\Gamma}^{\frac{1}{2}}\mathbf{Q}_i^H\mathbf{V}_i^{\frac{1}{2}})\right\}$$

We define $\hat{\mathbf{R}} = \kappa\mathbf{I} - \mathbf{R}$ wherein κ is larger than the maximum eigenvalue of $\mathbf{R}$. We relax the problem by dropping rank 1 constraint to formulate the following optimization problem:

$$P_1^{\boldsymbol{m}S}\begin{cases} \max\limits_{\mathbf{S}} & \text{tr}\{\mathbf{S}\hat{\mathbf{R}}\} \\ \text{subject to} & \sum_{i=1}^{L-1}\left|\,\text{tr}\left\{\text{Diag}\{\mathbf{s}\mathbf{s}^H, i\}\right\}\right|^2 \le \gamma \\ & \mathbf{S} \succeq 0 \\ & \text{tr}\{\mathbf{S}\} = 1 \\ & \text{tr}\{\mathbf{S}\mathbf{C}\} \ge \beta^2 \end{cases}$$

$P_1^{\mathbf{S}}$ is convex and it can be solved using normal convex programming methods. Then it is required to use Appendix B to derive a rank 1 approximation vector, (i.e., $\boldsymbol{m}s\dagger$ of the answer of $P_1^{\mathbf{S}}$).

9.3.4.2 Optimization with Respect to $\{\mathbf{Q}_i\}$

Suppose $\{\mu_i\}$ and $\mathbf{s}$ are fixed. Let us define

$$\boldsymbol{\psi}_i = \frac{\mathbf{V}_i^{\frac{1}{2}}\mathbf{s}}{\|\mathbf{V}_i^{\frac{1}{2}}\mathbf{s}\|} \tag{9.33}$$

$$\boldsymbol{\omega}_i = \frac{\mathbf{\Gamma}^{\frac{1}{2}}\mathbf{s}}{\|\mathbf{\Gamma}^{\frac{1}{2}}\mathbf{s}\|} \tag{9.34}$$

then $\mathbf{Q}_i$ can be found as

$$\mathbf{Q}_i = \boldsymbol{\psi}_i\boldsymbol{\omega}_i^H \tag{9.35}$$

9.3.4.3 Optimization with Respect to $\{\mu_i\}$

We assume that the optimal $\mathbf{s}$ and $\mathbf{Q}_i$ are derived from (9.35) and $P_1^{\mathbf{s}}$. Then the new optimization problem becomes

$$P_1^{\mu_i} \begin{cases} \max\limits_{\{\mu_i\}} \min\limits_{i} \{\mu_i\} - \eta \sum_{i=1}^{I} \left(\|\mathbf{V}_i^{\frac{1}{2}} \boldsymbol{s}\| - \sqrt{\mu_i} \|\boldsymbol{\Gamma}^{\frac{1}{2}} \mathbf{s}\| \right)^2 \\ \text{subject to} \quad c_k, \ \forall k \in [2,4] \\ \qquad\qquad\quad \mu_i \geq 0 \end{cases}$$

To obtain $\{\mu_i\}$, we employ the Grab-and-pull (GnP) method [19]. The solution to $P_1^{\mu_i}$ is selection of a set of $\{\mu_i\}, \forall i, j$ and reporting the minimum value of the set as the optimal solution. Intuitively, one can have two perspectives about the optimal solution of $P_1^{\mu_i}$. The following observations made in [19] are worth recalling in this current context.

Observation 1: Let $\alpha_i = \|\mathbf{V}_i^{\frac{1}{2}} \mathbf{s}\|$, $\varepsilon = \|\boldsymbol{\Gamma}^{\frac{1}{2}} \mathbf{s}\|$ and $\sqrt{\gamma_i} = \frac{\alpha_i}{\varepsilon}$. Intuitively, given the fact that $\{\mu_i\}$ and $\eta \sum_{i=1}^{I} \left(\alpha_i - \sqrt{\mu_i} \varepsilon \right)^2$ are both positive, the maximizer of $\{\mu_i\} - \eta \sum_{i=1}^{I} \left(\alpha_i - \sqrt{\mu_i} \varepsilon \right)^2$ should make the second term (i.e., $\eta \sum_{i=1}^{I} \left(\alpha_i - \sqrt{\mu_i} \varepsilon \right)^2$) close to zero. This term completely vanishes when

$$\{\mu_i\} = \gamma_i, \ \forall i \tag{9.36}$$

These values are appropriate starting points for the GnP method.

Observation 2: However, one can assume only one degree of freedom for the problem by limiting all choices of $\{\mu_i\}$ to only one variable μ. Thus, the $P_1^{\mu_i}$ boils down to the following problem

$$\max_{\mu} f(\mu)$$

where

$$f(\mu) = \mu - \eta \sum_{i \in \mathcal{S}_1} \left(\alpha_i - \sqrt{\mu} \varepsilon \right)^2 \tag{9.37}$$

and the maximum occurs as a weighted average of $\sqrt{\gamma_i}$ as

$$\sqrt{\mu^{\dagger}} = \frac{\sum_{i \in \mathcal{S}_1} \sqrt{\gamma_i} \varepsilon^2}{\varepsilon^2 - \frac{1}{\eta}} \tag{9.38}$$

The original problem has more degrees of freedom by choosing different values for $\{\mu_i\}$. Thus, one can intuitively suggest to set all $\{\mu_i\}$ equal to $\mu^{\dagger}$. This is not the optimum choice because it generates some offsets in the second term by deviating from (9.36), that is, having nonzero terms in $\eta \sum_{i=1}^{I} \left(\alpha_i - \sqrt{\mu_i} \varepsilon \right)^2$.

Eventually, the GnP method leverages both conjectures by making a connection between (9.36) and (9.38). It first sorts out all elements in ascending order (i.e., $0 \leq \gamma_1 \leq \gamma_2 \leq \cdots \leq \gamma_I$) and then iteratively grabs the lowest values of $\{\mu_i\} = \gamma_i, \ \forall i$ and pulls them toward higher values with respect to (9.38).

To solve the optimization problem with regard to $\{\mu_i\}$, first we define $\mathcal{S} = \{1\}$; Then we compute $\mu^{\dagger}$ from (9.38), given the current index set of minimal variables. Let $\{h\} \subset [K]$ denote the indices for which $h \notin \mathcal{S}$, then while $\gamma_h \leq \mu^{\dagger}$, we include h in $\mathcal{S}$, update the $\mu^{\dagger}$ from (9.38), and repeat this procedure until $\gamma_h \geq \mu^{\dagger}$.

9.3.5 JRC Algorithm Design

The considered waveform design algorithm is summarized in Table 9.1. It is composed of three main steps. In the first step, we solve the problem $P_3^{\text{Comm.}}$ for communications. In the second step, we recover the optimal communications sequence, and in the final step we run the GnP algorithm.

9.3.6 Complexity Analysis

The complexity of the proposed JRC algorithm is now considered. This complexity is determined by the GnP algorithm, which forms Step 3 of Table 9.1. The complexity order of Step 1 of Table 9.1 for solving $P_3^{\text{Comm.}}$ to obtain an optimal communication matrix $\mathbf{S} \in \mathcal{C}^{N(\hat{L}+L-1) \times N(\hat{L}+L-1)}$ is $\mathcal{O}((N(\hat{L}+L-1))^5)$. The complexity order of Step 2 of the JRC algorithm is $\mathcal{O}((N(\hat{L}+L-1))^3)$ for the recovering vector $\mathbf{s}$ from the SVD of $\mathbf{S}$. Solving

Table 9.1
JRC Algorithm

Step 1: Solve problem $P_3^{\text{Comm.}}$ to obtain optimal communications matrix $\mathbf{S}$.
Step 2: Recover vector $\mathbf{s}$ from SVD of PSD matrix $\mathbf{S}$ as follows:
- **2.1:** Define $\mathbf{d}$, $\tilde{\mathbf{d}}$, $\mathbf{D}$, $\tilde{\mathbf{D}}$ according to (9B.1)-(9B.4), Appendix B.
- **2.2:** Draw a random vector $\xi \in \mathbb{C}^{NL}$ from the complex normal distribution $\mathcal{N}(0, \tilde{\mathbf{D}}\tilde{\mathbf{S}}^{\dagger}\tilde{\mathbf{D}})$.
- **2.3:** Let $\mathbf{c} = [\frac{\sqrt{[C]_{ii}^{\dagger}}\xi_i}{|\xi_i|}]_{i=1}^{N}$.

Step 3: Solve the problem P_1^{JRC} as:
- **3.1:** Fix the sequence $\mathbf{s}$ by selecting a random one.
- **3.2:** Given $\mathbf{s}$, calculate rotation matrices $\{\mathbf{Q}_i\}$ from (9.35).
- **3.3:** Obtain $\{\mu_i\}$ and $\mu^{\dagger}$ by solving problem $P_1^{\mu_i}$, the following instruction,
  - **3.3.1:** Set $\mathcal{S} = \{1\}$,
  - **3.3.2:** Compute $\mu^{\dagger}$ from (9.38), given the current index set of minimal variables.
  - **3.3.3:** Let $\{h\} \subset [K]$ denote the indices for which $h \notin \mathcal{S}$. If $\gamma_h \leq \mu^{\dagger}$, include h in $\mathcal{S}$, and go to step 3.3.2; otherwise, go to 3.3.
- **3.4:** Given $\{\mu_i\}$, $\mu_i^{\dagger}$ and $\{\mathbf{Q}_i\}$ from previous steps, solve problem $p_1^{\mathbf{s}}$ to get the optimal sequence $\boldsymbol{m}s^{\dagger}$.
- **3.5:** If $\text{SCNR}^{(\text{t})} - \text{SCNR}^{(\text{t}-1)} > \epsilon$ where ϵ is an arbitrary positive small number and t is the iteration number, go to step 3.2; otherwise, stop.

problem $p_1^{\mathbf{s}}$ to determine the optimal sequence $\mathbf{s}^{\dagger}$ requires $\mathcal{O}((N(\hat{L}+L-1))^5)$ operations per iteration. The number of iterations depend on the scenario settings and is studied numerically. Interested readers should refer to [19] for more details about the GnP algorithm.

In the considered numerical simulations with the computer with the CPU of Intel Core $i7-6820$ HQ @2.7 GHz and memory RAM of 8 GB, 1.2 seconds were needed to carry out the JRC algorithm. We consider an urban automotive scenario with a carrier frequency of 24 GHz, and the maximum relative velocity of $\triangle v_r = 86.4$ Km/h or, equivalently, 24 m/s. Coherence

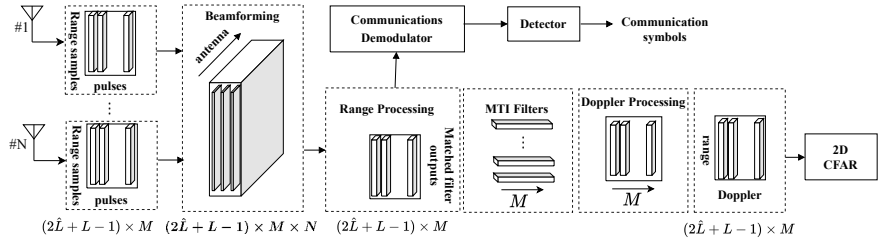

Figure 9.5. Block diagram of the radar receiver; the baseband signal is matched filtered to estimate the range of the targets followed by a moving target indication (MTI) filter to mitigate the effect of clutter. Eventually, the FFT-beam-scanner is applied to detect the Doppler shifts of the targets.

time is inversely proportional to the maximum Doppler frequency, which is related to the carrier frequency by $f_D = \dfrac{2f_c \triangle v_r}{c}$. For the considered situation, the maximum Doppler frequency is $f_D = 3.84$ KHz and the coherence time will be $C_T = \dfrac{1}{f_D} \approx 0.25$ ms. Assuming a bandwidth of $B = 1$ GHz, the chip rate will be $t_c = 1/B = 1$ ns; further assuming a code length of $L = 50$, the system offers a symbol rate of $1/(Lt_c) = 20$ MSymb/s. Even under a symmetric time division multiplexing, transmissions are about 2500 symbols on each link during the coherence time. This tends to offer adequate pilots for channel estimation. With faster processors and efficient implementation of the algorithm, it seems realistic to change the transmitted waveform in the considered scenario.

9.3.7 Range-Doppler Processing

Figure 9.5 shows the block diagram of the receiver processing. We stack the received sequences (9.9) and store the M JRC repetition frames of one CPI. Subsequently, we estimate the range in fast time and Doppler in slow time. To this end, a beamforming operation using the same weights as the transmit counterpart is implemented. This reduces the required number of range matched filters from N to 1. The range matched filter then estimates the range information hidden in the received signal. Let $r_m(k)$ be the result of the matched filter for the mth pulse; we obtain the delay (range) of the

targets by

$$\hat{\tau}_q = \arg\max_{\boldsymbol{m}k} |r_m(k)|,\ 1 \leq m \leq M \tag{9.39}$$

where $\boldsymbol{m}k$ is a vector with $Q+1$ elements corresponding to the time index of each target (including ACV). Range and delay are interconnected by $R_q = \tau_q c$, hence, range can be easily obtained from (9.39).

In accordance to Figure 9.5, the output of the range matched filter is processed by a bank of MTI to eliminate the effect of clutter. We store the result of the matched filter in the matrix $\mathbf{V} \in \mathbb{C}^{M \times 2\hat{L}+L-1}$. Since the Doppler values are roughly constant in fast time processing, we perform FFT in slow time over $\mathbf{V}$. This provides us with an estimate of the Doppler shifts of the targets. Towards this, we denote the FFT matrix as $\mathbf{F} = [e^{-j\frac{2kl\pi}{M}}]_{k=0,l=0}^{M,M}$. Then we apply the FFT matrix (Doppler matched filters) as $\mathbf{B} = \mathbf{F}\mathbf{V} \in \mathbb{C}^{M \times 2\hat{L}+L-1}$ where $\mathbf{B}$ contains $M-2$ close to zeros and two nonzero elements at each range bin (columns of $\mathbf{B}$), where positions of nonzero elements correspond to the two Doppler frequency indices. Subsequently, a beamforming operation using the same weights as the transmit counterpart is undertaken to obtain the final range Doppler map.

While the information gleaned from the communication link (e.g., Doppler estimate) can be used to identify ACV, in the ensuing simulations, we assume a genie-aided identification of ACV and focus only on the range-Doppler processing of the Q targets.

9.4 NUMERICAL RESULTS

In this section, we provide several numerical examples to investigate the performance of the JRC algorithm. We compare the designed waveform with random and pure communication waveforms to show the superiority of the JRC waveform. Focusing on algorithmic design, we first demonstrate the convergence of the JRC algorithm. Subsequently, we consider the radar performance; we compare the histogram of target absent/present hypotheses to intuitively illustrate the gain achieved by improving SCNR at the JRC vehicle leading to an enhancement of detection performance. Further, a ROC is plotted to show the performance comparison of different waveforms for radar. Moreover, the communication performance regarding the JRC algorithm is presented in terms of bit error rate (BER). More importantly, we

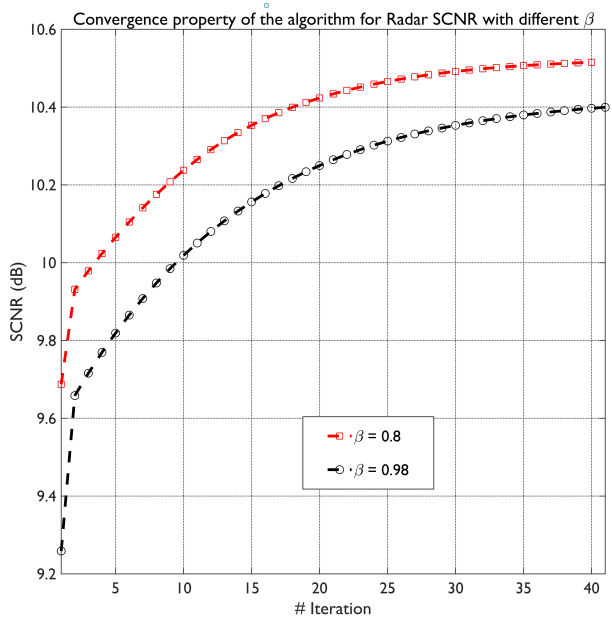

Figure 9.6. Convergence plot for radar SCNR based on the number of iterations for various values of β. When β is small, higher values of SCNR are achieved. The convergence trends are similar for different values of β chosen.

then discuss the radar and communications performance obtained through our algorithm by sweeping the trade-off factor β and illustrate the existing trade-off between communications and radar in terms of BER and P_D considering β.

For sake of simplicity, Table 9.2 summarizes simulation parameters.

9.4.1 Convergence Behavior of the JRC Algorithm

We assess the convergence behavior of the algorithm in Figure 9.6. To this end, we initialize the algorithm with the obtained optimal sequence for the communications, that is, the solution of $P_3^{\text{Comm.}}$, and enhance the radar

performance under the similarity threshold β. We observe that the SCNR increases monotonically, even when the threshold β is chosen to be very tight ($\beta = 0.98$). A minimum improvement of 1 dB is observable in all cases. Further, Figure 9.6 also shows the number of iterations required to reach a steady SCNR for different β. The figure plots SCNR dependence on the number of iteration for $\beta = 0.8$ and $\beta = 0.98$. Figure 9.6 shows that lower values of β yield higher values of SCNR. It also demonstrates that, the convergence of the JRC algorithm to the final SCNR has a similar trend for the choice of β.

9.4.2 Performance Assessment at the Radar Receiver

9.4.2.1 Histogram of the Received Signal

To illustrate the advantages of the designed waveform, the optimal communications waveform and a random waveform are considered as the benchmarks. In particular, Figure 9.7 depicts the histogram of the reflected signal in the case of target-present and target-absent for three cases:

1. Figure 9.7(a), when the JRC waveform is the optimal communications waveform.
2. Figure 9.7(b), when the JRC waveform is a random sequence with normal distribution with zero mean and unit variance.
3. Figure 9.7(c) employing the optimized JRC waveform.

To obtain this figure, the complete processing block diagram as indicated in Figure 9.5 is implemented on the received signal for different probing waveforms. Precisely, after range, Doppler, and spatial processing, the histogram of the received signal for the cell under test is plotted in Figure 9.7. We set the range of histogram values from the weakest signal to the strongest signal and use N_b bins to obtain a rough estimate of the spread of signal values. The value of these bins is shown in the histogram of Figure 9.7.

From Figure 9.7(a), we can observe that that the overlap percentage of two probability density functions (pdfs) are about 9%. Similarly, Figure 9.7(b) shows the overlap percentage of pdfs is about 50%, demonstrating a poor probability of detection in the case of using a random sequence as the transmit waveform. In contrast to these, the histogram of the JRC waveform in Figure 9.7(c) reveals the merits of our algorithm in terms of

Table 9.2
Simulation Parameters

Remark	Symbol	Quantity
Code length	L	22, 1000
Bandwidth	BW	100 MHz
Range resolution	-	1.5 m
No. of targets	Q	1
No. of simulated pulses	N_s	10^6
No. of integrated pulses	M	256
No. of Monte Carlo experiments	-	10^6
ISL threshold level	γ	0.6
Similarity threshold	β	$0.8, 0.9, 0.98$
Optimization penalty factor	η	0.1
Variance of CSI perturbation	$\sigma_q^{2(1)}$,$\sigma_q^{2(2)}$	1
RCS	$\zeta(q)$	1 dB/m^2, $\forall q$
No. of antennas	N	2
Modulation index	M_I	4

separation of two pdfs. We observe the distance between target-absent and target-present pdfs in Figure 9.7(c) is greater than those for the other cases (i.e., around 2% overlap). This leads to the superiority of JRC waveform in target detection performance with higher probability compared to other waveforms. This will be shown in Figure 9.8.

9.4.2.2 Radar ROC Curve

ROC curves of various waveforms are shown in Figure 9.8 to demonstrate the gain achieved by utilizing the JRC algorithm. We performed numerical simulations for the JRC algorithm at various values of β and for different sequences. Further, we plotted Monte Carlo simulation as well as the closed-form analytical formula relating the probability of detection (P_d) and the probability of false alarm (P_{fa}) for the case of nonfluctuating RCS under coherent integration. This closed-form relationship between P_d, P_{fa} and the

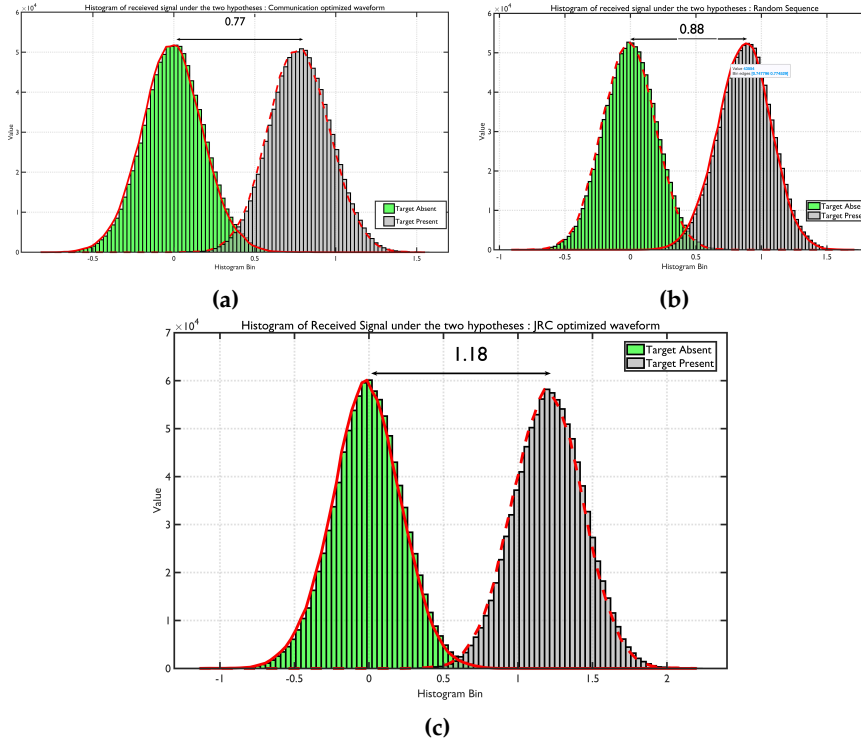

Figure 9.7. Histogram of the received signal in case of target absent/present with three different probing waveforms. The distance between the means of the two histograms (or the scaled empirical probability density function) determines the detection probability: (a) Histogram of the received signal where transmit waveform is the optimal communications sequence, $\beta = 1$, (b) Histogram of the received signal where transmit when waveform is a random sequence, (c) Histogram of the received signal where transmit waveform is the optimized JRC sequence with $\beta = 0.8$. The best performance is achieved by using a JRC waveform where the distance about 1.18.

achieved SCNR and integrating M number of pulses, is given by [20]:

$$P_d = \frac{1}{2}\,\mathrm{erfc}\left[\mathrm{erfc}^{-1}[2P_{fa}] - \sqrt{M \times \mathrm{SCNR}}\right] \tag{9.40}$$

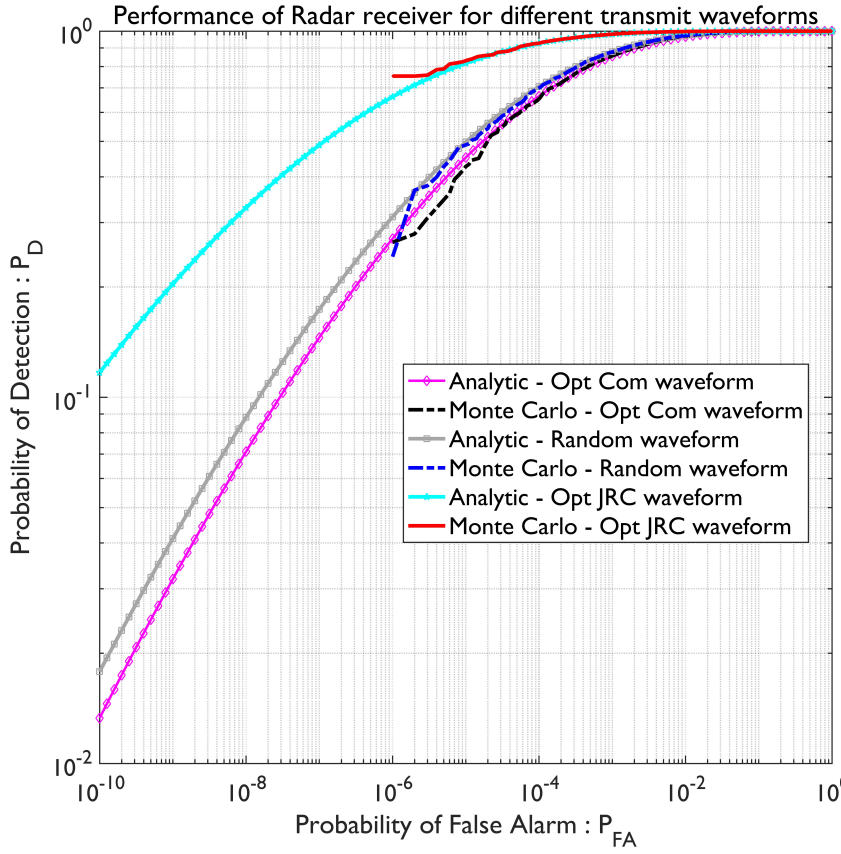

Figure 9.8. Receiver operating curves comparing the performance of radar for different waveforms and similarity threshold level $\beta = 0.8$ and $\gamma = 0.6$. An optimized JRC sequence provides a much higher P_D with a fixed P_{FA}.

where erfc is the complementary error function. The Monte Carlo simulation validates the results obtained analytically by numerically changing a threshold over a grid and determining the number of true and false detections.

Figure 9.8 shows higher values of P_d can be obtained by using the sequences designed by our JRC algorithm. It is worth noting that the performance trade-off between communications and radar is adjustable by setting β. For β far from unity, the similarity between the JRC waveform and an optimum communications waveform diminishes. Consequently, it provides more freedom for radar waveform design leading to a waveform that is suitable for radar-only purposes. In contrast, by choosing values near unity, the similarity between the radar waveform and the optimal communications waveform increases. It is obvious that an optimal JRC waveform enhances the detection capability significantly compared to other waveforms, since it achieves a higher SCNR level at the JRC-equipped receiver.

9.4.3 Performance Assessment at the Communications Receiver

Figure 9.9 shows the BER of the communication link for various waveforms as a function of SNR. The JRC car transmits N_s QPSK symbols enabling us to plot the BER curves for different SNR. At the ACV, matched filtering is carried out to determine the arrival time of the sequence in the received signal. Then the demodulation of the symbol is performed for BER calculation. One can observe that the optimal communications sequence has the best BER compared to other sequences and offers a lower bound. For large β, BER of optimal JRC sequence is naturally close to this bound. However, the radar performance degrades in this case. A similar trend occurs for optimal communications waveform when considering radar performance; it has a poor P_d in Figure 9.8. Finally, by adjusting the trade-off factor β one can find a waveform that satisfies a desired BER and the probability of detection.

9.4.4 Trade-Off Between Radar and Communications

Figure 9.10 shows the trade-off between the obtained SCNR at JRC and SNR at ACV. As β increases towards unity, the achieved SNR for communications improves; however, the achieved SCNR at JRCV decreases, indicating a trade-off. For instance, an SCNR of 10.4 dB and SNR of 6.1 dB can be obtained for $\beta = 0.8$ at JRCV and ACV, respectively. However, a decrease of 1 dB in SCNR and an increase of 0.9 dB SCNR is attained for $\beta = 0.99$.

Figure 9.11 shows a better perspective of radar and communications trade-off performance. We plot the achieved SCNR and SNR for the joint system. This curve shows a SCNR of 10.4 dB and SNR of 6.3 dB for $\beta = 0.5$.

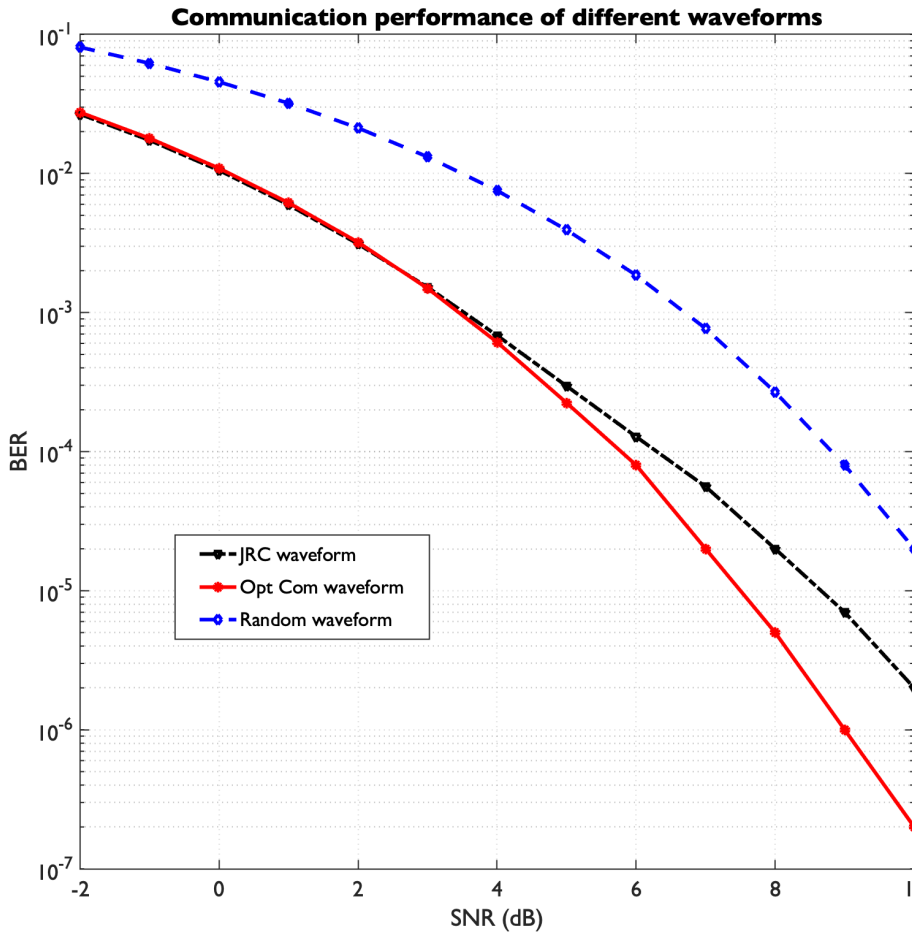

Figure 9.9. Communication performance in terms of bit error rate (BER) for different waveforms.

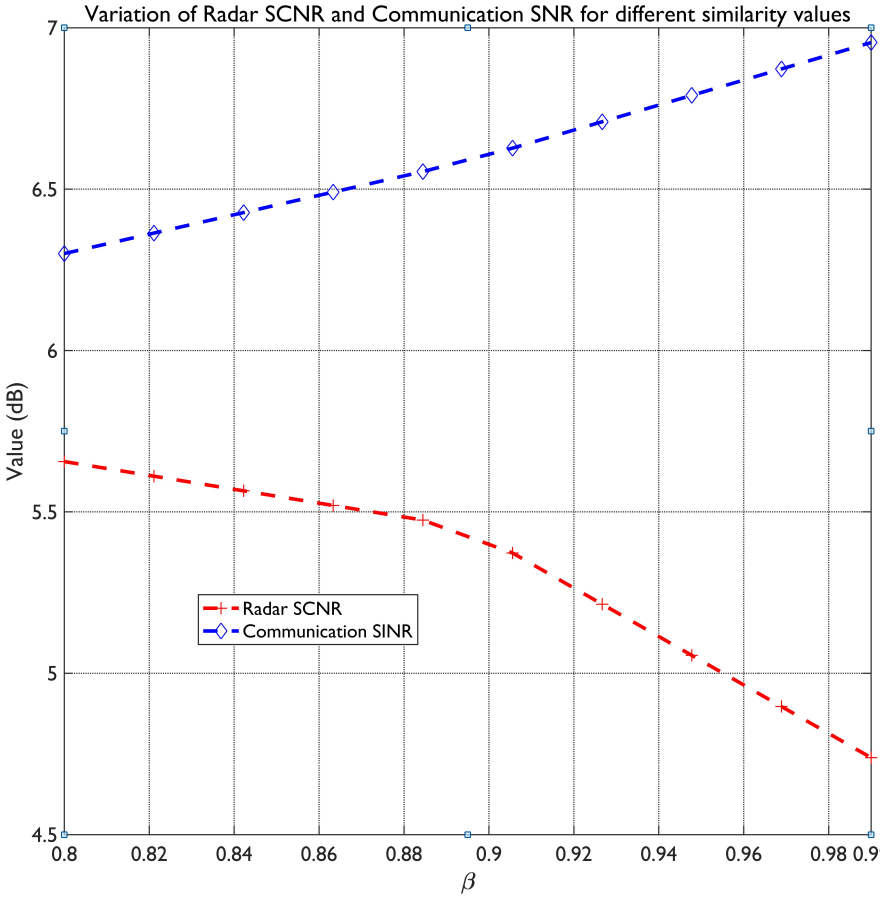

Figure 9.10. Achieved SCNR and SNR values at JRCV and ACV receiver, respectively as a function of the similarity/trade-off factor β. As $\beta \to 1$, the designed waveform is closer to optimal communication waveform.

However, by increasing β close to 1, SNR at ACV increases while we observe a decrease of around 1 dB in SCNR at JRCV. Further, Figure 9.11 also illustrates the impact of lower ISL on achieved SNR and SCNR. The quantity γ indicates the ISL limit and it is clear that lower γ achieves a better performance.

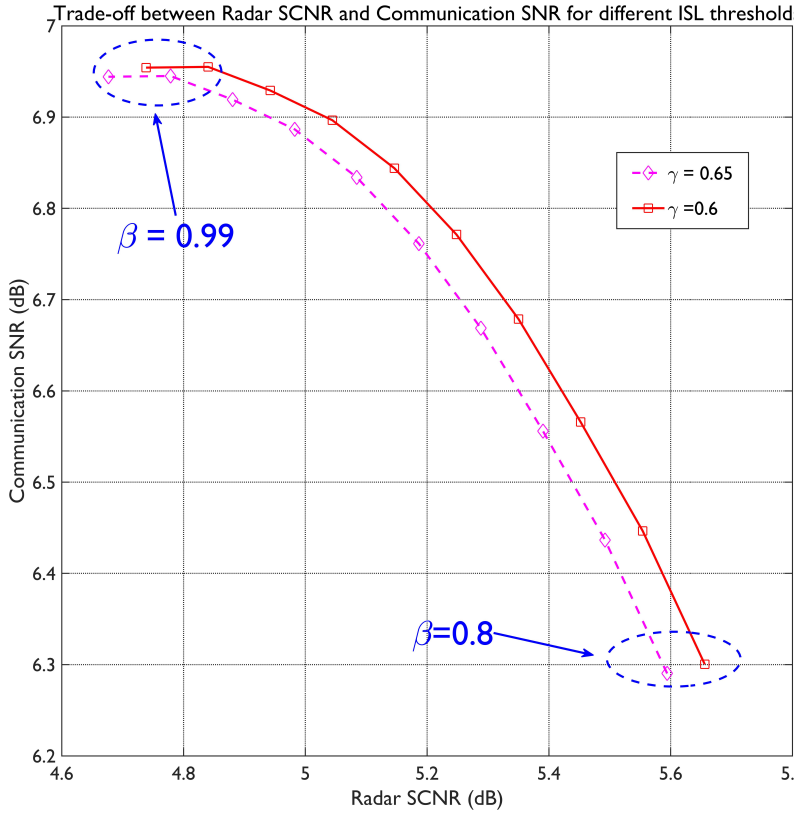

Figure 9.11. Trade-off between radar SCNR and communication SNR achieved for different β and ISL threshold γ.

9.5 CONCLUSION

A new approach for unified waveform design in automotive JRC system was discussed in this chapter to maximize simultaneously the SCNR at the JRC-equipped vehicle and the SNR of a concurrent communication link. After a detailed modeling of the system, the waveform design is formulated as an optimization problem considering performance of both systems and including a trade-off factor. The JRC-algorithm is developed to solve the aforementioned problem exploiting the channel information. The devised

JRC algorithm is able to shape the transmit waveform to maximize the performance of radar and communications with regard to a desired trade-off level between two systems. Finally, the chapter highlight the benefits of codesign of radar and communications through channel information exchange and attaining optimal performance trade-offs.

References

[1] A. Khawar, A. Abdelhadi, and C. Clancy, *MIMO radar waveform design for spectrum sharing with cellular systems: a MATLAB based approach*. Springer, 2016.

[2] H. Griffiths, L. Cohen, S. Watts, E. Mokole, C. Baker, M. Wicks, and S. Blunt, "Radar spectrum engineering and management: Technical and regulatory issues," *Proceedings of the IEEE*, vol. 103, no. 1, 2015.

[3] D. Cohen, K. V. Mishra, and Y. C. Eldar, "Spectrum sharing radar: Coexistence via xampling," *IEEE Transactions on Aerospace and Electronic Systems*, vol. 54, no. 3, pp. 1279–1296, 2018.

[4] J. Qian, M. Lops, L. Zheng, X. Wang, and Z. He, "Joint system design for coexistence of MIMO radar and MIMO communication," *IEEE Transactions on Signal Processing*, vol. 66, no. 13, pp. 3504–3519, 2018.

[5] B. Kang, O. Aldayel, V. Monga, and M. Rangaswamy, "Spatio-spectral radar beampattern design for coexistence with wireless communication systems," *IEEE Transactions on Aerospace and Electronic Systems*, vol. 55, no. 2, pp. 644–657, 2019.

[6] A. Aubry, A. De Maio, A. Zappone, M. Razaviyayn, and Z.-Q. Luo, "A new sequential optimization procedure and its applications to resource allocation for wireless systems," *IEEE Transactions on Signal Processing*, vol. 66, no. 24, pp. 6518–6533, 2018.

[7] L. Zheng, M. Lops, Y. C. Eldar, and X. Wang, "Radar and communication coexistence: An overview: A review of recent methods," *IEEE Signal Processing Magazine*, vol. 36, no. 5, pp. 85–99, 2019.

[8] C. Aydogdu, M. F. Keskin, N. Garcia, H. Wymeersch, and D. W. Bliss, "Radchat: Spectrum sharing for automotive radar interference mitigation," *IEEE Transactions on Intelligent Transportation Systems*, vol. 22, no. 1, pp. 416–429, 2021.

[9] A. Aubry, V. Carotenuto, A. De Maio, M. A. Govoni, and A. Farina, "Experimental analysis of block-sparsity-based spectrum sensing techniques for cognitive radar," *IEEE Transactions on Aerospace and Electronic Systems*, vol. 57, no. 1, pp. 355–370, 2021.

[10] A. F. Martone, K. D. Sherbondy, J. A. Kovarskiy, B. H. Kirk, R. M. Narayanan, C. E. Thornton, R. M. Buehrer, J. W. Owen, B. Ravenscroft, S. Blunt, A. Egbert, A. Goad, and C. Baylis, "Closing the loop on cognitive radar for spectrum sharing," *IEEE Aerospace and Electronic Systems Magazine*, vol. 36, no. 9, pp. 44–55, 2021.

[11] M. Alaee-Kerahroodi, E. Raei, S. Kumar, and B. S. M. R. R. R., "Cognitive radar waveform design and prototype for coexistence with communications," *IEEE Sensors Journal*, pp. 1–1, 2022.

[12] B. Paul, A. R. Chiriyath, and D. W. Bliss, "Survey of RF communications and sensing convergence research," *IEEE Access*, vol. 5, pp. 252–270, 2017.

[13] A. Hassanien, M. Amin, Y. Zhang, and F. Ahmad, "Signaling strategies for dual-function radar communications: An overview," *IEEE Aerosp. Electron. Syst. Mag.*, vol. 83, no. 10, pp. 36–45, 2017.

[14] S. Z. Gurbuz, H. D. Griffiths, A. Charlish, M. Rangaswamy, M. S. Greco, and K. Bell, "An overview of cognitive radar: Past, present, and future," *IEEE Aerospace and Electronic Systems Magazine*, vol. 34, no. 12, pp. 6–18, 2019.

[15] S. H. Dokhanchi, M. R. B. Shankar, M. Alaee-Kerahroodi, and B. Ottersten, "Adaptive waveform design for automotive joint radar-communication systems," *IEEE Transactions on Vehicular Technology*, vol. 70, no. 5, pp. 4273–4290, 2021.

[16] J. Metcalf, C. Sahin, S. Blunt, and M. Rangaswamy, "Analysis of symbol-design strategies for intrapulse radar-embedded communications," *IEEE Transactions on Aerospace and Electronic Systems*, vol. 51, no. 4, pp. 2914–2931, 2015.

[17] J. Qian, M. Lops, L. Zheng, X. Wang, and Z. He, "Joint system design for coexistence of MIMO radar and MIMO communication," *IEEE Transactions on Signal Processing*, vol. 66, pp. 3504–3519, Jul. 2018.

[18] M. Grant, S. Boyd, and Y. Ye, "CVX: Matlab software for disciplined convex programming," 2008.

[19] A. Gharanjik, M. Soltanalian, M. B. Shankar, and B. Ottersten, "Grab-n-pull: A max-min fractional quadratic programming framework with applications in signal and information processing," *Signal Processing*, vol. 160, pp. 1–12, 2019.

[20] M. A. Richards, *Fundamentals of radar signal processing*. Tata McGraw-Hill Education, 2005.

[21] A. De Maio, Y. Huang, M. Piezzo, S. Zhang, and A. Farina, "Design of optimized radar codes with a peak to average power ratio constraint," *IEEE Transactions on Signal Processing*, vol. 59, no. 6, pp. 2683–2697, 2011.

APPENDIX 9A

Toward computing SCNR at JRCV, it is required first to calculate $\mathbf{Y}_2^H\mathbf{Y}_2$

$$\mathbf{Y}_2^H\mathbf{Y}_2 = = |\zeta^H(2)|^2\Big(\mathbf{B}_2^{(1)H}\mathbf{B}_2^{(2)H} + \mathbf{B}_2^{(1)H}\boldsymbol{\Delta}_2^{(2)H} + \boldsymbol{\Delta}_2^{(1)H}\mathbf{B}_2^{(2)H} + \boldsymbol{\Delta}_2^{(1)H}\boldsymbol{\Delta}_2^{(2)H}\Big) \times\Big(\mathbf{B}_2^{(2)}\mathbf{B}_2^{(1)} + \mathbf{B}_2^{(2)}\boldsymbol{\Delta}_2^{(1)} + \boldsymbol{\Delta}_2^{(2)}\mathbf{B}_2^{(1)} + \boldsymbol{\Delta}_2^{(2)}\boldsymbol{\Delta}_2^{(1)}\Big) \quad (9A.1)$$

Noting that $\mathbf{s}$ is a deterministic variable, while $\mathbf{Y}_2$ is random due to a and the channel uncertainty, it follows from (9A.1) that

$$\mathbb{E}\{|a|^2\mathbf{s}^H\mathbf{Y}_2^H\mathbf{Y}_2\mathbf{s}\} = \mathbf{s}^H\mathbb{E}\Big\{|\zeta^H(2)|^2\Big(\mathbf{B}_2^{(1)H}\mathbf{B}_2^{(2)H}\mathbf{B}_2^{(2)}\mathbf{B}_2^{(1)} + \mathbf{B}_2^{(1)H}\boldsymbol{\Delta}_2^{(2)H}\boldsymbol{\Delta}_2^{(2)}\mathbf{B}_2^{(1)} + \boldsymbol{\Delta}_q^{(1)H}\mathbf{B}_q^{(2)H}\mathbf{B}_p^{(2)}\boldsymbol{\Delta}_p^{(1)} + \boldsymbol{\Delta}_q^{(1)H}\boldsymbol{\Delta}_q^{(2)H}\boldsymbol{\Delta}_p^{(2)}\boldsymbol{\Delta}_p^{(1)}\Big)\Big\}\mathbf{s} \quad (9A.2)$$

wherein we have used the independence of communication symbols and the channel uncertainties as well as $\mathbb{E}\{|a|^2 = 1$. In deriving (9A.2), we explore the facts: $\Delta_*^{(1)}$ and $\Delta_*^{(2)}$ are circularly symmetric and independent; further, the statistical modeling of the uncertainties leads to $E\left(\Delta_2^{(1)}\right) = E\left(\Delta_2^{(2)}\right) = \mathbf{0}$. Assuming $\hat{L}$ effective nonzero entries for each column of $\boldsymbol{\Delta}_q^{(i)}, i = 1, 2$ and letting $\mathbf{R}_{B_q^{(i)}} = \mathbf{B}_q^{(i)H}\mathbf{B}_q^{(i)},\ i \in \{1, 2\}$, we now evaluate each of the terms

$$\mathbb{E}\Big\{\zeta^H(2)\zeta(2)\mathbf{B}_2^{(1)H}\mathbf{B}_2^{(2)H}\mathbf{B}_2^{(2)}\mathbf{B}_2^{(1)}\Big\} = \zeta^H(2)\zeta(2)\mathbf{B}_2^{(1)H}\mathbf{B}_2^{(2)H}\mathbf{B}_2^{(2)}\mathbf{B}_2^{(1)} \quad (9A.3)$$

$$\mathbb{E}\Big\{\zeta^H(2)\zeta(2)\mathbf{B}_2^{(1)H}\boldsymbol{\Delta}_2^{(2)H}\boldsymbol{\Delta}_2^{(2)}\mathbf{B}_2^{(1)}\Big\} = \hat{L}|\zeta(2)|^2\mathbf{B}_2^{(1)H}\sigma_2^{2^{(2)}}\mathbf{B}_2^{(1)} = \hat{L}|\zeta(2)|^2\sigma_2^{2^{(2)}}\mathbf{R}_{B_2^{(1)}} \quad (9A.4)$$

$$\mathbb{E}\Big\{\zeta^H(2)\zeta(2)\boldsymbol{\Delta}_2^{(1)H}\mathbf{B}_2^{(2)H}\mathbf{B}_2^{(2)}\boldsymbol{\Delta}_2^{(1)}\Big\} = \hat{L}|\zeta(2)|^2\sigma_2^{2^{(1)}}\mathrm{tr}\{\mathbf{R}_{B_2^{(2)}}\}\mathbf{I} \quad (9A.5)$$

$$\mathbb{E}\Big\{\zeta^H(2)\zeta(2)\boldsymbol{\Delta}_2^{(1)H}\boldsymbol{\Delta}_2^{(2)H}\boldsymbol{\Delta}_2^{(2)}\boldsymbol{\Delta}_2^{(1)}\Big\} = \hat{L}^2|\zeta(2)|^2\sigma_2^{2^{(1)}}\sigma_2^{2^{(2)}}\mathbf{I} \quad (9A.6)$$

Thus, from (9A.4) to (9A.6), $\mathbb{E}(P_{\text{com}})$ can be written as

$$\begin{aligned}\mathbb{E}\{\mathbf{s}^H\mathbf{Y}_2^H\mathbf{Y}_2\mathbf{s}\} = \mathbf{s}^H\Big(&|\zeta(2)|^2\mathbf{B}_2^{(1)H}\mathbf{B}_2^{(2)H}\mathbf{B}_2^{(2)}\mathbf{B}_2^{(1)} \\ &+ \hat{L}|\zeta(2)|^2\sigma_2^{2^{(2)}}\mathbf{R}_{B_2^{(1)}} + \hat{L}|\zeta(2)|^2\sigma_2^{2^{(1)}}\text{tr}\{\mathbf{R}_{B_2^{(2)}}\})\mathbf{I} \\ &+ \hat{L}^2|\zeta(2)|^2\sigma_2^{2^{(1)}}\sigma_2^{2^{(2)}}\mathbf{I}\Big)\mathbf{s} = \mathbf{s}^H V\mathbf{s} \end{aligned} \tag{9A.7}$$

APPENDIX 9B

Let $\mathbf{S}^\dagger$ be the optimal solution of $P_3^{\text{Comm.}}$. Here, we intend to extract a rank-1 solution of $\mathbf{S}^\dagger$. If the rank of $\mathbf{S}^\dagger$ happens to be 1, then the radar code design problem is optimally solved under the SDP relaxation. Here, we solve this problem by Gaussian randomization method [21]. To this end, first $\mathbf{d}$, $\tilde{\mathbf{d}}$, $\mathbf{D}$, $\tilde{\mathbf{D}}$, should be generated as

$$\mathbf{d} = \sqrt{\text{diag}(\mathbf{S}^\dagger)} \tag{9B.1}$$

$$(\tilde{\mathbf{d}})_i = \begin{cases} \frac{1}{d_i}, & \text{if } d_i > 0 \\ 1, & \text{if } d_i = 0 \end{cases} \tag{9B.2}$$

$$\mathbf{D} = \text{Diag}(\mathbf{d}) \tag{9B.3}$$

$$\tilde{\mathbf{D}} = \text{Diag}(\tilde{\mathbf{d}}) \tag{9B.4}$$

Then we create matrix $\tilde{\mathbf{S}}^\dagger$ as

$$\tilde{\mathbf{S}}^\dagger = \mathbf{S}^\dagger + (\mathbf{I} - \tilde{\mathbf{D}}\mathbf{D})$$

where the entries of this matrix are

$$[\tilde{\mathbf{S}}^\dagger]_{i,k} = \begin{cases} [\mathbf{S}^\dagger]_{i,k}, & \text{if } i \neq k \\ [\mathbf{S}^\dagger]_{i,i}, & \text{if } [\mathbf{S}^\dagger]_{i,i} > 0 \\ 1, & \text{if } [\mathbf{S}^\dagger]_{i,i} = 0 \end{cases}$$

It can be proved that $\tilde{\mathbf{D}}\tilde{\mathbf{S}}^\dagger\tilde{\mathbf{D}} \succeq 0$ and the diagonal elements of $\tilde{\mathbf{D}}\tilde{\mathbf{S}}^\dagger\tilde{\mathbf{D}}$ are 1, so it is a suitable choice of covariance matrix of a Gaussian distribution for

randomized rank-one approximation. We take Gaussian random vectors ξ from the distribution $\mathcal{N}(0, \tilde{\mathbf{D}}\tilde{\mathbf{S}}^{\dagger}\tilde{\mathbf{D}})$. It can be verified that with probability 1, $[\frac{\sqrt{[\mathbf{S}^{\dagger}]_{ii}}\xi_i}{|\xi_i|}]_{i=1}^{N}$ is a rank-1 decomposition of matrix $\mathbf{S}^{\dagger}$. The randomization can be repeated many times to obtain a high-quality solution.

APPENDIX 9C

Proof of Lemma 9.1:

$$\begin{aligned}\max_{\mathbf{s}} \min_{i} \frac{\mathbf{s}^H \mathbf{V}_i \mathbf{s}}{\mathbf{s}^H \mathbf{\Gamma} \mathbf{s}} &\overset{A}{\leq} \min_{i} \max_{\mathbf{s}} \frac{\mathbf{s}^H \mathbf{V}_i \mathbf{s}}{\mathbf{s}^H \mathbf{\Gamma} \mathbf{s}} \\ &\overset{B}{\leq} \min_{i} \lambda_{max}\{\mathbf{\Gamma}^{-1}\mathbf{V}_i\} \leq \lambda_{max}\{\mathbf{\Gamma}^{-1}\mathbf{V}_i\} \end{aligned} \tag{9C.1}$$

A: Let $k := [i]$ and $\mathcal{L}(\mathbf{s}, k) := \dfrac{\mathbf{s}^H \mathbf{V}_i \mathbf{s}}{\mathbf{s}^H \mathbf{\Gamma} \mathbf{s}}$. For all $\mathbf{s} \in \mathcal{S}$ and $i \in \Omega^2$, we have the following relationship

$$\min_{\boldsymbol{m}\acute{k} \in \mathcal{K}} \mathcal{L}(\mathbf{s}, \boldsymbol{m}\acute{k}) \leq \max_{\acute{\mathbf{s}} \in \mathcal{S}} \mathcal{L}(\acute{\mathbf{s}}, k) \tag{9C.2}$$

by taking the minimum over $\mathbf{k} \in \mathcal{K}$ on the right-hand side and the maximum over $\mathbf{s} \in \mathcal{S}$ on the left-hand side, the proof is complete.
B: We want to find the maximum, that is, ρ_i,

$$\begin{aligned} \frac{\mathbf{s}^H \mathbf{V}_i \mathbf{s}}{\mathbf{s}^H \mathbf{\Gamma} \mathbf{s}} &\leq \rho_i \\ \mathbf{s}^H(\rho_i \mathbf{I}_n - \mathbf{\Gamma}^{-1}\mathbf{V}_i)\mathbf{s} &\geq 0 \end{aligned} \tag{9C.3}$$

Equation (9C.3) means that $(\rho_i \mathbf{I}_n - \mathbf{\Gamma}^{-1}\mathbf{V}_i)$ must be PSD, that is, $(\rho_i \mathbf{I}_n - \mathbf{\Gamma}^{-1}\mathbf{V}_i) \succeq 0$, which means all eigenvalues of it must be positive or equal to zero, so

$$\lambda_{max}\{\mathbf{\Gamma}^{-1}\mathbf{V}_i\} \leq \rho_i$$

The above equation shows that the minimum of ρ_i is $\lambda_{max}\{\mathbf{\Gamma}^{-1}\mathbf{V}_i\}$, which completes the proof.

Chapter 10

Doppler-Tolerant Waveform Design

When fast target speeds and high-resolution requirements are combined in radar applications, the waveform distortions seriously degrade the performance. To make up for the loss in SNR in this situation, either the target's Doppler shift should be known, or a bank of mismatched filters on the receive side should be taken into account [1]. However, using so-called Doppler-tolerant waveforms on the transmit side is a simpler alternative approach to dealing with high Doppler shifts [2]. In this case, even in the presence of an arbitrarily large Doppler shift, the received signal remains matched to the filter, but a range-Doppler coupling may occur as an unintended consequence [3].

It is known that linear frequency modulated (LFM) waveform has the Doppler-tolerant property by its nature [4, 5]. One approach to creating phase sequences with Doppler-tolerant qualities is to mimic the behavior of the LFM waveform by employing the phase history of a pulse with linearly variable frequency, which produces polyphase sequences that resemble chirps [6]. In fact, because frequency is the derivative of phase, polyphase sequences must have a quadratic phase variation over the whole sequence in order to exhibit linear frequency features such as LFM. This is shown in Figure 10.1 for Frank, Golomb, and P1 sequences of a length $N = 16$.

Interestingly, chirplike polyphase sequences such as Frank [7], P1, P2, P3, and P4 [8], Golomb [9], Chu [10], and PAT [11] are known to have good autocorrelation properties, in terms of PSL and ISL, the metrics that are strictly related to the sharpness of the code autocorrelation function [1, 12–22].

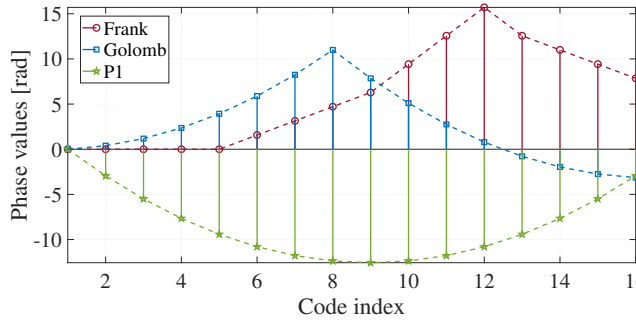

Figure 10.1. The unwrapped phase values of three polyphase codes of length $N = 16$: Frank, Golomb, and P1.

Table 10.1 specifies three classes of chirplike phase codes and indicates their ambiguity function (AF). Note that Frank code is derived from the phase history of a linearly frequency stepped pulse. The main drawback of the Frank code is that it only applies for codes of perfect square length ($M = L^2$) [4]. P1, P2, and Px codes are all modified versions of the Frank code, with the DC frequency term in the middle of the pulse instead of at the beginning. Unlike Frank, P1, P2, and Px codes, which are only applicable for perfect square lengths ($M = L^2$), the Zadoff code is applicable for any length. Chu codes are important variant of the Zadoff code, and Golomb, P3, and P4 codes are specific cyclically shifted and decimated versions of the Zadoff-Chu code. Indeed, as P1, P2 and Px codes were linked to the original Frank code, similarly, P3, P4, and Golomb polyphase codes are linked to the Zadoff-Chu code and are given for any length.

Several studies have recently focused on the analytical design of polyphase sequences with good Doppler tolerance properties, which is the focus of this chapter [23–31].

10.1 PROBLEM FORMULATION

Let $\{x_n\}_{n=1}^{N}$ be the transmitted complex unit-modulus radar code sequence of length N. The aperiodic autocorrelation of the transmitting waveform at

Table 10.1
Code Expression and AF of Frank, Zadoff, and Golomb Sequences [4]

Code	Phase Expression	AF
Frank	$\phi_{n,k} = 2\pi\dfrac{(n-1)(k-1)}{L}$ for $1 \le n \le L,\ \ 1 \le k \le L$	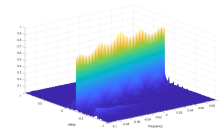
Zadoff	$\phi_m = \dfrac{2\pi}{M}(m-1)\left[r\left(\dfrac{M-1-m}{2}\right) - q\right]$ for $1 \le m \le M,\ \ 0 \le q \le M$ where M is any integer and r is any integer relatively prime to M	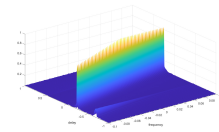
Golomb	$\phi_m = \dfrac{2\pi}{M}\widetilde{r}\left[\dfrac{(m-1)(m)}{2}\right]$ for $1 \le m \le M$ where M is any integer and $\widetilde{r}$ is any integer relatively prime to M	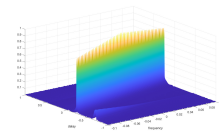

lag k (e.g., matched filter output at the radar receiver) is defined as

$$r_k = \sum_{n=1}^{N-k} x_n x_{n+k}^* = r_{-k}^*, \quad k = 0, \ldots, N-1 \tag{10.1}$$

The ISL and PSL can be mathematically defined by

$$\text{ISL} = \sum_{k=1}^{N-1} |r_k|^2 \tag{10.2}$$

$$\text{PSL} = \underset{k=1,2,\ldots,N-1}{\text{maximum}} |r_k| \tag{10.3}$$

It is clear that the ISL metric is the squared ℓ_2 norm of the autocorrelation sidelobes. Further, the ℓ_∞ norm of autocorrelation sidelobes of a sequence is the PSL metric. These can be generalized by considering the ℓ_p norm, $p \geq 2$, which offers additional flexibility in design while subsuming ISL and PSL. In general, the ℓ_p norm metric of the autocorrelation sidelobes is defined as

$$\left(\sum_{k=1}^{N-1} |r_k|^p \right)^{1/p}, \quad 2 \leq p < \infty \tag{10.4}$$

Many works in the literature consider sequence design via minimizing the ℓ_p norm of autocorrelation sidelobes as the objective function [13, 15, 32–34]. However, only a few have addressed the design of sequences with Doppler-tolerant properties, or polynomial phase behavior in code segments in general [23], which is the focus of this chapter. Further, because of the smaller number of variables involved in their construction, as well as their simple structure, designing polyphase sequences with multiple segments is advantageous for long sequence design and real-time implementations.

Let the sequence $\{x_n\}_{n=1}^N$ be partitioned into L subsequences each having a length of $M_l \leq N$, where $l \in 1, 2, \ldots, L$ such that every subsequence of it, say,

$$\widetilde{\mathbf{x}}_l = [x_{\{1,l\}}, \cdots, x_{\{m,l\}}, \cdots, x_{\{M_l,l\}}]^T \in \mathbb{C}^{M_l}, \tag{10.5}$$

has a polynomial phase, which can be expressed as

$$\arg(x_{\{m,l\}}) = \sum_{q=0}^{Q} a_{\{q,l\}} m^q \tag{10.6}$$

where $m \in \{1, 2, \ldots, M_l\}$ and $a_{\{q,l\}}$ is the Qth degree polynomial coefficient for the phase of the lth subsequence with $q \in \{0, 1, 2, \ldots, Q\}$. It can be

observed that the length of each subsequence can be arbitrarily chosen. The problem of interest is to design the code vector $\{x_n\}_{n=1}^{N}$ with a generic polynomial phase of a degree Q in its subsequences while having impulse-like autocorrelation function. Therefore, by considering $\sum_{k=1}^{N-1} |r_k|^p$ as the objective function, the optimization problem can be compactly written as

$$\mathcal{P}_1 \begin{cases} \underset{a_{\{q,l\}}}{\text{minimize}} & \displaystyle\sum_{k=1}^{N-1} |r_k|^p \\ \text{subject to} & \arg(x_{\{m,l\}}) = \displaystyle\sum_{q=0}^{Q} a_{\{q,l\}} m^q \\ & |x_{\{m,l\}}| = 1 \end{cases} \tag{10.7}$$

where $l = 1, \ldots, L$.

Figure 10.2 depicts the workflow of the Polynomial phase Estimate of Coefficients for unimodular Sequences (PECS) method, in which the code sequence $\{x_n\}_{n=1}^{N}$ is divided into different segments, which are designed to have a polynomial phase behavior during its code entries. The polynomial phase constraint in general provides a new design degree for the waveform set. In the case $Q = 2$, the design problem creates waveforms with linear frequency properties in its segment (LFM). The LFM signal is recognized as a waveform that maintains a constant compression factor (for small time-bandwidth products) in the matched filter output of the received signal, even when there is a Doppler shift in the received signal [4, 35]. Due to this property, LFM is known as a Doppler-tolerant waveform [36]. In this context, by defining the optimization problem $\mathcal{P}_1$, our goal is to offer a general framework for the analytical design of polyphase sequences that replicate the behavior of the LFM waveform. Based on the MM framework that was discussed in Chapter 4, we create an effective algorithm called PECS in the next section to construct a code vector with polynomial phase relationships of degree Q among its subsequences [23].

10.2 OPTIMIZATION METHOD

The optimization problem mentioned in (10.7) is hard to solve as each r_k is quadratically related to $\{x_n\}_{n=1}^{N}$ and each $\{x_n\}_{n=1}^{N}$ is nonlinearly

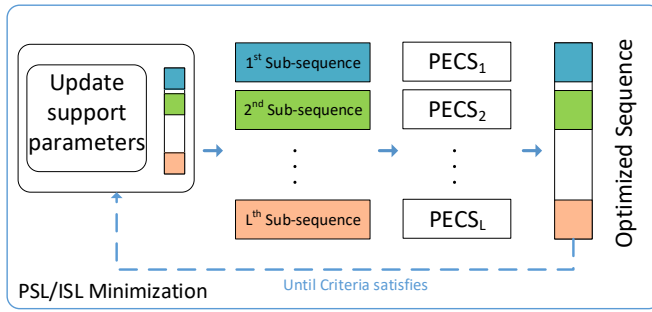

Figure 10.2. Workflow of PECS for sequence design based on ℓ_p norm minimization of the autocorrelation sidelobes.

related to $a_{\{q,l\}}$. Furthermore, when using direct solutions such as GD, it becomes difficult to minimize the ℓ_p norm of autocorrelation sidelobes typically because of numerical issues in calculating gradient for large p values [15]. As a result, the MM solution based on [13] is considered, which, after several majorization steps (refer Appendix 10A), it simplifies to the following optimization problem

$$\mathcal{P}_2 \begin{cases} \underset{a_{\{q,l\}}}{\text{minimize}} & ||\mathbf{x}-\mathbf{y}||_2 \\ \text{subject to} & \arg(x_{\{m,l\}}) = \displaystyle\sum_{q=0}^{Q} a_{\{q,l\}} m^q \\ & |x_{\{m,l\}}| = 1 \end{cases} \tag{10.8}$$

where

$$\mathbf{y} = \left(\lambda_{\max}(\boldsymbol{L})N + \lambda_u\right)\mathbf{x}^{(i)} - \widetilde{\boldsymbol{R}}\mathbf{x}^{(i)} \in \mathbb{C}^N$$

with $\lambda_{\max}, \boldsymbol{L}, \lambda_u$, and $\widetilde{\boldsymbol{R}}$ defined in Appendix 10A. Note that in [13] the polynomial phase constraint was not considered. As the objective in (10.8) is separable in the sequence variables, the minimization problem can now be split into L subproblems (each of which can be solved in parallel). Let us define

$$\boldsymbol{\rho} = |\mathbf{y}| = \left[|y_1|, |y_2| \cdots, |y_N|\right]^T \tag{10.9}$$

$$\boldsymbol{\psi} = \arg(\mathbf{y}) = \left[\arg(y_1), \arg(y_2), \cdots, \arg(y_N)\right]^T, \tag{10.10}$$

where ρ_n and ψ_n, $n = 1, 2, \ldots, N$, are the magnitude and phase of every entry of $\mathbf{y}$, respectively. Also, for ease of notation, let us assume that the polynomial phase coefficients and subsequence length of the lth subsequence, say, $a_{\{q,l\}}$ and M_l are indicated as $\widetilde{a}_q$ and $\widetilde{M}$, respectively. Thus, dropping the subscript l, each of the subproblem, can be further defined as

$$\mathcal{P}_3 \left\{ \underset{\widetilde{a}_q}{\text{minimize}} \quad \sum_{m=1}^{\widetilde{M}} \left| e^{j(\sum_{q=0}^{Q} \widetilde{a}_q m^q)} - \rho_m e^{j\psi_m} \right|^2 \right. \tag{10.11}$$

where we have considered the unimodular and polynomial phase constraints of problem $\mathcal{P}_2$ directly in the definition of the code entries in problem $\mathcal{P}_3$. Further, the above problem can be simplified as

$$\left\{ \underset{\widetilde{a}_q}{\text{minimize}} \quad - \left[\sum_{m=1}^{\widetilde{M}} \rho_m \cos\left(\sum_{q=0}^{Q} \widetilde{a}_q m^q - \psi_m \right) \right] \right. \tag{10.12}$$

The ideal step would be to minimize the majorized function in (10.12) for $\widetilde{a}_q$ given the previous value of $\widetilde{a}_q^{(i)}$. However, as the optimization variables are in the argument of the cosine function in the objective of (10.12), the solution to this problem is not straightforward. Hence, we resort to a second MM step. Towards this, let us define[1]

$$\theta_m = \sum_{q=0}^{Q} \widetilde{a}_q m^q - \psi_m$$

a majorizer ($g(\theta_m, \theta_m^{(i)})$) of the function $f(\theta_m) = -\rho_m \cos(\theta_m)$ can be obtained by

$$\begin{aligned} g(\theta_m, \theta_m^{(i)}) = &-\rho_m \cos(\theta_m^{(i)}) + (\theta_m - \theta_m^{(i)}) \rho_m \sin(\theta_m^{(i)}) + \\ &\frac{1}{2}(\theta_m - \theta_m^{(i)})^2 \rho_m \cos(\theta_m^{(i)}) \geq -\rho_m cos(\theta_m) \end{aligned} \tag{10.13}$$

where θ_m is the variable and $\theta_m^{(i)}$ is the phase value of the last iteration. This follows from exploiting the fact that if a function is continuously differentiable with a Lipschitz continuous gradient, then second-order Taylor

1 Note that θ_m depends on the optimization variables $\{\widetilde{a}_q\}$.

expansion can be used as a majorizer [33]. Using the aforementioned majorizer function, at the ith iteration of the MM algorithm, the optimization problem

$$\mathcal{P}_4 \begin{cases} \underset{\widetilde{a}_q}{\text{minimize}} \displaystyle\sum_{m=1}^{\widetilde{M}} & \Bigg[-\rho_m \cos(\theta_m^{(i)}) + \left(\theta_m - \theta_m^{(i)}\right) \rho_m \sin(\theta_m^{(i)}) \\ & \qquad + \frac{1}{2}\left(\theta_m - \theta_m^{(i)}\right)^2 \rho_m \cos(\theta_m^{(i)}) \Bigg] \end{cases} \tag{10.14}$$

The objective function in (10.14) can be rewritten into perfect square form and the constant terms independent to the optimization variable $\widetilde{a}_q$ can be ignored. Thus, a surrogate optimization problem deduced from (10.14) is given here

$$\mathcal{P}_5 \left\{ \underset{\widetilde{a}_q}{\text{minimize}} \quad \sum_{m=1}^{\widetilde{M}} \left[\rho_m \cos(\theta_m^{(i)}) \left(\sum_{q=0}^{Q} \widetilde{a}_q m^q \right) - \widetilde{b}_m \right]^2 \right. \tag{10.15}$$

where $\widetilde{b}_m = \rho_m \cos(\theta_m^{(i)}) \left(\psi_m + \theta_m^{(i)}\right) - \rho_m \sin(\theta_m^{(i)})$. Now, considering a generic subsequence index l, we define

$$\boldsymbol{\eta} = [1, 2, 3, \cdots, \widetilde{M}]^T \in \mathbb{Z}_+^{\widetilde{M}}$$

$\boldsymbol{\eta}^q$ implying each element of $\boldsymbol{\eta}$ is raised to the power of q, $q = 0, 1, \ldots, Q$. Further,

$$\begin{aligned} \boldsymbol{\gamma} &= \rho_m \cos(\theta_m^{(i)}) \odot [1, \cdots, 1]^T \in \mathbb{R}^{\widetilde{M}} \\ \widetilde{\boldsymbol{A}} &= \mathbf{Diag}\,(\boldsymbol{\gamma})[\boldsymbol{\eta}^0, \boldsymbol{\eta}^1, \cdots, \boldsymbol{\eta}^Q] \in \mathbb{R}^{\widetilde{M} \times Q+1} \\ \mathbf{z} &= [\widetilde{a}_0, \widetilde{a}_1, \cdots, \widetilde{a}_Q]^T \in \mathbb{R}^{Q+1} \\ \widetilde{\mathbf{b}} &= [\widetilde{b}_1, \widetilde{b}_2, \cdots, \widetilde{b}_{\widetilde{M}}]^T \in \mathbb{R}^{\widetilde{M}} \end{aligned} \tag{10.16}$$

the optimization problem in (10.15) can be rewritten as

$$\underset{\mathbf{z}}{\text{minimize}} \quad ||\widetilde{\boldsymbol{A}}\mathbf{z} - \widetilde{\mathbf{b}}||_2^2 \tag{10.17}$$

Algorithm 10.1: Designing Doppler-Tolerant Sequences Based on the PECS Method [23]

Data: Seed sequence $\mathbf{x}^{(0)}$, N, $\widetilde{M}$, L and p
Result: $\mathbf{x}$
Set $i = 0$, initialize $\mathbf{x}^{(0)}$;
while *stopping criterion is not met* **do**
  Calculate $\boldsymbol{F}, \widetilde{\boldsymbol{\mu}}, \mathbf{f}, \lambda_L, \lambda_u$ from Table 10.2;
  $\mathbf{y} = \mathbf{x}^{(i)} - \frac{\boldsymbol{F}_{:,1:N}(\widetilde{\boldsymbol{\mu}} \circ \mathbf{f})}{2N(\lambda_L N + \lambda_u)}$;
  $\boldsymbol{\psi} = \arg(\boldsymbol{y}) \mid \boldsymbol{\psi} = [\widetilde{\boldsymbol{\psi}}_1^T, \cdots, \widetilde{\boldsymbol{\psi}}_L^T]^T \in \mathbb{R}^N$;
  $\boldsymbol{\rho} = |\mathbf{y}| \mid \boldsymbol{\rho} = [\widetilde{\boldsymbol{\rho}}_1^T, \cdots, \widetilde{\boldsymbol{\rho}}_L^T]^T \in \mathbb{R}^N$;
  for $l \leftarrow 1$ *to* L **do**
    $\widetilde{\boldsymbol{\psi}}_l = [\psi_1, \cdots, \psi_{\widetilde{M}}]^T \in \mathbb{R}^{\widetilde{M}}$;
    $\widetilde{\boldsymbol{\rho}}_l = [\rho_1, \cdots, \rho_{\widetilde{M}}]^T \in \mathbb{R}^{\widetilde{M}}$;
    $\theta_m^{(i)} = \sum_{q=0}^{Q} \widetilde{a}_q m^q - \psi_m,\ m = 1, \ldots, \widetilde{M}$;
    $\widetilde{b}_m = \rho_m \cos\theta_m^{(i)} \left(\psi_m + \theta_m^{(i)}\right) - \rho_m \sin\theta_m^{(i)}$;
    $\boldsymbol{\eta} = [1, 2, 3, \cdots, \widetilde{M}]^T \in \mathbb{Z}_+^{\widetilde{M}}$;
    $\boldsymbol{\gamma} = \rho_m \cos(\theta_m^{(i)}) \odot [1, \cdots, 1]^T \in \mathbb{R}^{\widetilde{M}}$;
    $\widetilde{\boldsymbol{A}} = \mathbf{Diag}\,(\boldsymbol{\gamma})[\boldsymbol{\eta}^0, \boldsymbol{\eta}^1, \cdots, \boldsymbol{\eta}^Q] \in \mathbb{R}^{\widetilde{M} \times Q+1}$;
    $\mathbf{z} = [\widetilde{a}_0, \widetilde{a}_1, \cdots, \widetilde{a}_Q]^T \in \mathbb{R}^{Q+1}$;
    $\widetilde{\mathbf{b}} = [\widetilde{b}_1, \widetilde{b}_2, \cdots, \widetilde{b}_{\widetilde{M}}]^T \in \mathbb{R}^{\widetilde{M}}$;
    $\mathbf{z}^\star = \widetilde{\boldsymbol{A}}^{(\dagger)}\widetilde{\mathbf{b}}$;
    $\widetilde{\mathbf{x}}_l = e^{(j(\widetilde{\boldsymbol{A}}\mathbf{z}^\star))}$;
  end
  $\mathbf{x}^{(i+1)} = [\widetilde{\mathbf{x}}_1^T, \widetilde{\mathbf{x}}_2^T, \cdots, \widetilde{\mathbf{x}}_L^T]^T \in \mathbb{C}^N$;
  $i \leftarrow i + 1$;
end
return $\mathbf{x}^{(i+1)}$

which is a standard least squares (LS) problem. As a result, the optimal $\mathbf{z}^\star = \widetilde{\boldsymbol{A}}^{(\dagger)}\widetilde{\mathbf{b}} = [\widetilde{a}_0^\star, \widetilde{a}_1^\star, \cdots, \widetilde{a}_Q^\star]^T$ would be calculated[2] and the optimal sequence will be synthesized.

2 One can use "lsqr" in the *Sparse Matrices Toolbox* of MATLAB 2021a to solve (10.17).

Table 10.2
Supporting Parameters for Algorithm 10.1 [37]

No	Parameter	Relation
1	$\boldsymbol{F}$	$2N \times 2N$ FFT Matrix with $F_{m,n} = e^{-j\frac{2mn\pi}{2N}}$
2	f	$\boldsymbol{F}[\mathbf{x}^{(i)T}, \mathbf{0}_{1\times N}]$
3	$\mathbf{r}$	$\frac{1}{2N}\boldsymbol{F}^H\|\mathbf{f}\|^2$
4	t	$\|\|\mathbf{r}_{2:N}\|\|_p$
5	a_k	$\frac{1+(p-1)\left(\frac{\|r_{k+1}\|}{t}\right)^p - p\left(\frac{\|r_{k+1}\|}{t}\right)^{p-1}}{(t-\|r_{k+1}\|)^2}$
6	$\hat{w}_k$	$\frac{p}{2t^2}\left(\frac{\|r_{k+1}\|}{t}\right)^{p-2}, k = 1, \ldots, N-1$
7	$\tilde{\mathbf{c}}$	$\mathbf{r} \circ [\hat{w}_1, \ldots, \hat{w}_{N-1}, 0, \hat{w}_{N-1}, \ldots, \hat{w}_1]^T$
8	$\widetilde{\boldsymbol{\mu}}$	$\boldsymbol{F}\tilde{\mathbf{c}}$
9	λ_L	$\max_k\{\tilde{\alpha}_k(N-k) \| k = 1, \ldots, N\}$
10	λ_u	$\frac{1}{2}(\max_{(1\leq\tilde{i}\leq N)}\tilde{\mu}_{2\tilde{i}} + \max_{(1\leq\tilde{i}\leq N)}\tilde{\mu}_{2\tilde{i}-1})$

Using the aforementioned setup for a generic subsequence index l, we calculate all the $\widetilde{\mathbf{x}}_l$s pertaining to different subsequences and derive $\{x_n\}_{n=1}^N$ by concatenating all the $\widetilde{\mathbf{x}}_l$s. The algorithm successively improves the objective and an optimal value of $\mathbf{x}$ is achieved. Details of the implementation for the developed method in the form of pseudo code are summarized in Algorithm 10.1 and would be referred to further as PECS.

Remark 3. *Computational Complexity*
Assuming L subsequences are processed in parallel, the computational load of Algorithm 10.1 is dependent on deriving 1- the supporting parameters: $\mathbf{f}$, $\mathbf{r}$, t, $\mathbf{a}$, *and* $\hat{\mathbf{w}}$ *mentioned in Table 10.2, and 2- the least squares operation in every iteration of the algorithm. In 1, the order of computational complexity is* $\boldsymbol{O}(2N)$ *real additions/subtractions,* $\boldsymbol{O}(Np)$ *real multiplications,* $\boldsymbol{O}(N)$ *real divisions, and* $\boldsymbol{O}(N\log_2 N)$ *for FFT. In 2, assume* $M_1 = M_2 = \cdots = M_l = M$ *for simplicity, therefore, the complexity of the least squares operation:* $\boldsymbol{O}(M^2Q)$ + $\boldsymbol{O}(Q^2M)$ + $\boldsymbol{O}(QM)$ *real matrix multiplications and* $\boldsymbol{O}(Q^3)$ *real matrix inversion [38, 39]. Therefore, the overall computational complexity is* $\boldsymbol{O}(M^2Q)$ *(provided* $M > Q$*, which is true in general). In case the L subsequences are processed sequentially, the complexity is* $\boldsymbol{O}(M^2LQ)$.

10.3 EXTENSION OF OTHER METHODS TO PECS

In the previous section, by applying a constraint of the Qth degree polynomial phase variation on the subsequences, we have addressed the problem of minimizing the autocorrelation sidelobes to obtain optimal ISL/PSL of the complete sequence using the ℓ_p norm minimization using a method called the Monotonic Minimizer for the ℓ_p-norm of autocorrelation sidelobes (MM-PSL). In this section, we extend other methods, such as the MISL [32] and the cyclic algorithm new (CAN) [12], to enable us to design sequences with polynomial phase constraints.

10.3.1 Extension of MISL

The ISL minimization problem under piece-wise polynomial phase constraint of degree Q can be written as follows

$$\mathcal{M}_1 \begin{cases} \underset{a_{\{q,l\}}}{\text{minimize}} & \displaystyle\sum_{k=1}^{N-1} |r_k|^2 \\ \text{subject to} & \arg(x_{\{m,l\}}) = \displaystyle\sum_{q=0}^{Q} a_{\{q,l\}} m^q \\ & |x_{\{m,l\}}| = 1, \;\; m = 1, \ldots, M \\ & \qquad\qquad l = 1, \ldots, L \end{cases} \tag{10.18}$$

where $a_{\{q,l\}}$ indicate the coefficients of lth segment of the optimized sequence whose phase varies in accordance to the degree of the polynomial Q. It has been shown in [12] that the ISL metric of the aperiodic autocorrelations can be equivalently expressed in the frequency domain as

$$\text{ISL} = \frac{1}{4N} \sum_{g=1}^{2N} \left[\left| \sum_{n=1}^{N} x_n e^{-j\omega_g (n-1)} \right|^2 - N \right]^2 \tag{10.19}$$

where $\omega_g = \frac{2\pi}{2N}(g-1)$, $g = 1, ..., 2N$. Let us define $\mathbf{x} = [x_1, x_2, \ldots, x_N]^T$, $\mathbf{b}_g = [1, e^{j\omega_g}, ..., e^{j\omega_g (N-1)}]^T$, where $g = 1, \ldots, 2N$.

Therefore, rewriting (10.19) in a compact form

$$\text{ISL} = \sum_{g=1}^{2N} \left(\mathbf{b}_g^H \mathbf{x}\mathbf{x}^H \mathbf{b}_g \right)^2 \tag{10.20}$$

The ISL in (10.20) is quartic with respect to $\mathbf{x}$ and its minimization is still difficult. The MM-based algorithm (MISL) developed in [32] computes a minimizer of (10.20). So given any sequence $\mathbf{x}$, the surrogate minimization problem in MISL algorithm is given by

$$\mathcal{M}_2 \begin{cases} \underset{a_{\{q,l\}}}{\text{minimize}} & \Re\left(\mathbf{x}^H \left(\grave{\boldsymbol{A}} - 2N^2 \mathbf{x}^{(i)} \left(\mathbf{x}^{(i)^H} \right) \right) \mathbf{x}^{(i)} \right) \\ \text{subject to} & \arg\left(x_{\{m,l\}} \right) = \sum_{q=0}^{Q} a_{\{q,l\}} m^q \\ & \left| x_{\{m,l\}} \right| = 1 \end{cases} \tag{10.21}$$

where $\boldsymbol{A} = [b_1, \ldots, b_{2N}]$, $\mathbf{f}^{(i)} = \left| \boldsymbol{A}^H \mathbf{x}^{(i)} \right|^2$, $f_{max}^{(i)} = \max_f \left\{ f_g^{(i)} : g = 1, \ldots, 2N \right\}$, $\grave{\boldsymbol{A}} = \mathbf{A} \left(\mathbf{Diag} \left(\mathbf{f}^{(i)} \right) - f_{\max}^{(i)} \mathbf{I} \right) \mathbf{A}^H$. The problem in (10.21) is majorized once again and the surrogate minimization problem is given as

$$\mathcal{M}_3 \begin{cases} \underset{a_{\{q,l\}}}{\text{minimize}} & \|\mathbf{x} - \mathbf{y}\|_2 \\ \text{subject to} & \arg(x_{\{m,l\}}) = \sum_{q=0}^{Q} a_{\{q,l\}} m^q \\ & |x_{\{m,l\}}| = 1 \end{cases} \tag{10.22}$$

where $\mathbf{y} = -\mathbf{A}(\mathbf{Diag}\,(\mathbf{f}^{(i)}) - f_{\max}^{(i)} \mathbf{I}) \mathbf{A}^H \mathbf{x}^{(i)}$. Once the optimization problem in (10.22) has been solved, that is, $\mathcal{M}_3$, it is exactly equal to the problem in (10.8), that is, $\mathcal{P}_2$ and hence its solution can be pursued further. The details of the implementation can be found in Algorithms 10.2 and 10.3.

10.3.2 Extension of CAN

In addition to the aforementioned procedure using MISL, the optimization problem in (10.18) can also be solved using CAN method [12]. As opposed

Algorithm 10.2: PECS Subroutine

Data: $\mathbf{y}^{(i)}, L, \widetilde{M}, a_{q,l}^{(i)}$
Result: $\mathbf{x}^{(i+1)}$
$\boldsymbol{\psi} = \arg(\boldsymbol{y}) \mid \boldsymbol{\psi} = [\widetilde{\boldsymbol{\psi}}_1^T, \cdots, \widetilde{\boldsymbol{\psi}}_L^T]^T \in \mathbb{R}^N$;
$\boldsymbol{\rho} = |\mathbf{y}| \mid \boldsymbol{\rho} = [\widetilde{\boldsymbol{\rho}}_1^T, \cdots, \widetilde{\boldsymbol{\rho}}_L^T]^T \in \mathbb{R}^N$;
for $l \leftarrow 1$ *to* L **do**
  $\widetilde{\boldsymbol{\psi}}_l = [\psi_1, \cdots, \psi_{\widetilde{M}}]^T \in \mathbb{R}^{\widetilde{M}}$;
  $\widetilde{\boldsymbol{\rho}}_l = [\rho_1, \cdots, \rho_{\widetilde{M}}]^T \in \mathbb{R}^{\widetilde{M}}$;
  $\theta_m^{(i)} = \sum_{q=0}^{Q} \widetilde{a}_q m^q - \psi_m,\ m = 1, \ldots, \widetilde{M}$;
  $\widetilde{b}_m = \rho_m \cos\theta_m^{(i)} \left(\psi_m + \theta_m^{(i)}\right) - \rho_m \sin\theta_m^{(i)}$;
  $\boldsymbol{\eta} = [1, 2, 3, \cdots, \widetilde{M}]^T \in \mathbb{Z}_+^{\widetilde{M}}$;
  $\boldsymbol{\gamma} = \rho_m \cos(\theta_m^{(i)}) \odot [1, \cdots, 1]^T \in \mathbb{R}^{\widetilde{M}}$;
  $\widetilde{\boldsymbol{A}} = \mathbf{Diag}\,(\boldsymbol{\gamma})[\boldsymbol{\eta}^0, \boldsymbol{\eta}^1, \cdots, \boldsymbol{\eta}^Q] \in \mathbb{R}^{\widetilde{M} \times Q+1}$;
  $\mathbf{z} = [\widetilde{a}_0, \widetilde{a}_1, \cdots, \widetilde{a}_Q]^T \in \mathbb{R}^{Q+1}$;
  $\widetilde{\mathbf{b}} = [\widetilde{b}_1, \widetilde{b}_2, \cdots, \widetilde{b}_{\widetilde{M}}]^T \in \mathbb{R}^{\widetilde{M}}$;
  $\mathbf{z}^\star = \widetilde{\boldsymbol{A}}^{(\dagger)}\widetilde{\mathbf{b}}$;
  $\widetilde{\mathbf{x}}_l = e^{(j(\widetilde{\boldsymbol{A}}\mathbf{z}^\star))}$;
end
$\mathbf{x}^{(i+1)} = [\widetilde{\mathbf{x}}_1^T, \widetilde{\mathbf{x}}_2^T, \cdots, \widetilde{\mathbf{x}}_L^T]^T \in \mathbb{C}^N$;
return $\mathbf{x}^{(i+1)}$

to the approach pursued in [32] of directly minimizing a quartic function, in [12] the solution of the objective function in (10.18) is assumed to be almost equivalent to minimizing a quadratic function [40]

$$\underset{\{x_n\}_{n=1}^N;\{\psi_g\}_{g=1}^{2N}}{\text{minimize}} \sum_{g=1}^{2N} \left| \sum_{n=1}^{N} x_n e^{-j\omega_g n} - \sqrt{N} e^{j\psi_g} \right|^2 \tag{10.23}$$

It can be written in a more compact form (to within a multiplicative constant)

$$||\boldsymbol{A}^H \bar{\mathbf{x}} - \mathbf{v}||^2 \tag{10.24}$$

Algorithm 10.3: Optimal Sequence with Minimum ISL and Polynomial Phase Parameters $a_{\{q,l\}}$ using MISL

Data: N, L and $\widetilde{M}$
Result: $\mathbf{x}$
Set $i = 0$, initialize $\mathbf{x}^{(0)}$;
while *stopping criterion is not met* **do**
$\mathbf{f} = \left|\mathbf{A}^H \mathbf{x}^{(i)}\right|^2$;
$f_{\max} = \max(\mathbf{f})$;
$\mathbf{y}^{(i)} = -\mathbf{A}\left(\mathbf{Diag}(\mathbf{f}) - f_{\max}\mathbf{I} - N^2\mathbf{I}\right)\mathbf{A}^H\mathbf{x}^{(i)}$;
$\mathbf{x}^{(i+1)} = \text{PECS}(\mathbf{y}^{(i)}, L, \widetilde{M}, a^{(i)}_{\{q,l\}})$;
end
return $\mathbf{x} = \mathbf{x}^{(i+1)}$

where $\mathbf{a}_g^H = [e^{-j\omega_g}, \cdots, e^{-j2N\omega_g}]$ and $\boldsymbol{A}^H$ is the following unitary $2N \times 2N$ DFT matrix

$$\boldsymbol{A}^H = \frac{1}{\sqrt{2N}} \begin{bmatrix} \mathbf{a}_1^H \\ \vdots \\ \mathbf{a}_{2N}^H \end{bmatrix} \tag{10.25}$$

$\bar{\mathbf{x}}$ is the sequence $\{x_n\}_{n=1}^N$ padded with N zeros, that is,

$$\bar{\mathbf{x}} = [x_1, \cdots, x_N, 0, \cdots, 0]^T_{2N\times 1} \tag{10.26}$$

and $\mathbf{v} = \frac{1}{\sqrt{2}}[e^{j\psi_1}, \cdots, e^{j\psi_{2N}}]^T$. For given $\{x_n\}$, CAN minimizes (10.24) by alternating the optimization between $\bar{\mathbf{x}}$ and $\mathbf{v}$. Let

$$\bar{\mathbf{x}}^{(i)} = [x_1^{(i)}, \cdots, x_N^{(i)}, 0, \cdots, 0]^T_{2N\times 1} \tag{10.27}$$

and let D_i represent the value of $||\boldsymbol{A}^H\bar{\mathbf{x}}^{(i)} - \mathbf{v}^{(i)}||$ at iteration i. Then we have $D_{i-1} \geq D_i$. Further in the i^{th} iteration, the objective can be minimized using the technique proposed for solving (10.8) by assuming

$$\begin{aligned} &\mathbf{x} = \bar{\mathbf{x}}^{(i)}, \\ &\mathbf{y} = e^{j\arg(\mathbf{d})}, \;\; \mathbf{d} = \boldsymbol{A}\mathbf{v}^{(i)} \end{aligned} \tag{10.28}$$

Algorithm 10.4: Optimal Sequence with Minimum ISL and Polynomial Phase Parameters $a_{\{q,l\}}$ using CAN

Data: N, L and $\widetilde{M}$
Result: $\mathbf{x}$
Set $i = 0$, initialize $\mathbf{x}^{(0)}$;
while *stopping criterion is not met* **do**
  $\mathbf{f} = \mathbf{A}^H \mathbf{x}^{(i)}$;
  $v_g = e^{j(\arg(f_g))},\ g = 1, \ldots, 2N$;
  $\mathbf{d} = \mathbf{A}\mathbf{v}^{(i)}$;
  $y_n^{(i+1)} = e^{j(\arg(d_n))},\ n = 1, \ldots, N$;
  $\mathbf{x}^{(i+1)} = \text{PECS}(\mathbf{y}^{(i)}, L, \widetilde{M}, a_{\{q,l\}}^{(i)})$;
end
return $\mathbf{x} = \mathbf{x}^{(i+1)}$

in the objective function of (10.8). The details of the implementation can be found in Algorithm 10.4.

10.4 PERFORMANCE ANALYSIS

In this section, we assess the performance of the PECS algorithm and compare it with prior work in the literature.

10.4.1 ℓ_p Norm Minimization

At first, we evaluate the performance of Algorithm 10.1 in terms of ℓ_p norm minimization by several examples. For the initialization, we chose a random seed sequence and $Q = 2$.

Figure 10.3 shows the convergence behavior of Algorithm 10.1 when the simulation is mandatorily run for 10^6 iterations. We chose different values of p (i.e., $p = 2$, 5, 10, 100, and 1000), which allow to trade-off between good PSL and ISL. For this figure, we keep the values of sequence length, subsequence length, and polynomial degree fixed, by setting $N = 300$, $M = 5$, and $Q = 2$. Nevertheless, we observed similar behavior in the convergence for the different values of N, M, and Q.

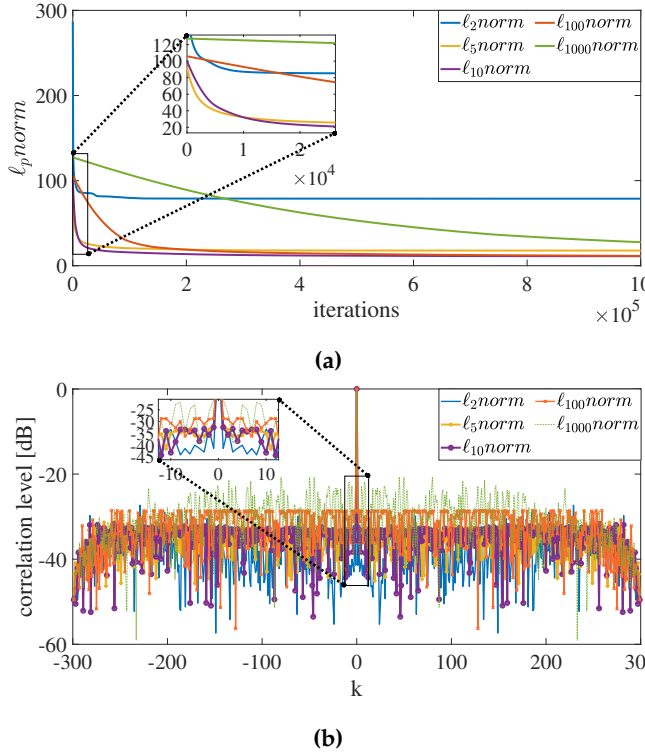

Figure 10.3. (a,b) ℓ_p norm convergence and autocorrelation comparison with varying p in ℓ_p norm for a sequence with input parameters $N = 300, M = 5, Q = 2$, and iterations $= 10^6$: (a) Objective convergence, (b) Autocorrelation response.

As evident from Figure 10.3, the objective function is reduced rapidly for $p = 2$ and this rate reduces with the objective saturating after 10^5 iterations, whereas by increasing the value of p to $5, 10$, and 100, we achieve similar convergence rate as observed earlier. Uniquely, while computing the ℓ_{1000} norm,[3] the objective converges slowly and continues to decrease until 10^6 iterations.

3 Computationally, we cannot use $p = \infty$, but by setting p to a tractable value (e.g., $p \geq 10$), we find that the peak sidelobe is effectively minimized.

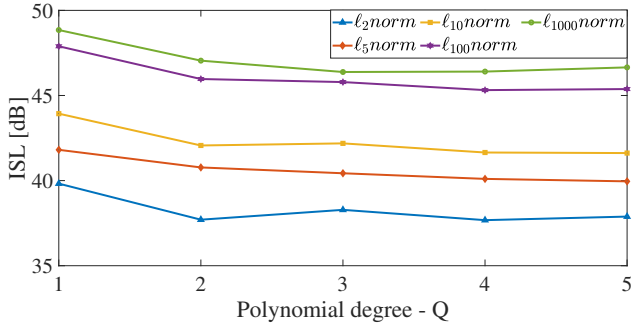

(a)

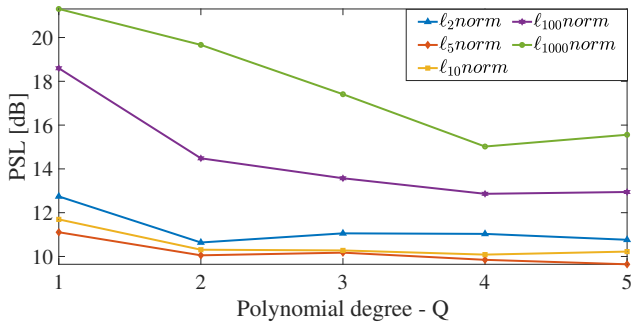

(b)

Figure 10.4. (a) ISL and (b) PSL variation with increasing Q.

Further, while analyzing the autocorrelation sidelobes in Figure 10.3 for the same set of input parameters of p, N, M and maximum number of iterations, we numerically observe that the lowest PSL values[4] are observed for the ℓ_{10} norm and other PSL values are higher for $p \neq 10$.

In Figure 10.4, we assess the relationship of the polynomial phase of degree Q as a tuning parameter with PSL and ISL. The parameter Q can be considered as another degree of freedom available for the design problem. Other input parameters are kept fixed (i.e., $N = 300$ and $M = 5$) and the same seed sequence is fed to the algorithm. As the value of Q is increased, we observe a decrement in the optimal PSL and ISL values generated from

4 $\text{PSL}_{dB} \triangleq 10\log_{10}(\text{PSL})$, $\text{ISL}_{dB} \triangleq 10\log_{10}(\text{ISL})$.

PECS for different norms (i.e., $p = 2, 5, 10, 100$, and 10^3). Therefore, the choice of the input parameters would vary depending upon the application.

10.4.2 Doppler-Tolerant Waveforms

Figure 10.5 illustrates the capability of Algorithm 10.1 for designing a sequence with quadratic phase in its segments. We consider $N = 300$, $M = 5$, $Q = 2$, and $p = 10$ and intentionally run the algorithm up to iterations $= 10^6$. The results clearly shows that every segment of optimized waveform has quadratic shape, while the entire AF is still thumbtack.

In Table 10.3, we show that by increasing M for a fixed N and Q, the PECS is able to design waveforms with high Doppler-tolerant properties.

For the plots shown here, the input parameters are $N = 300$, varying subsequence lengths of $M = 5, 50, 150$, and 300, $Q = 2$, and p limited to $2, 10$, and 100. In the unwrapped phase plots of the sequences, the quadratic nature of the subsequence is retained for all values of M and p. As evident, the AF achieves the thumbtack type shape for $M = 5$ keeping quadratic behavior in its phase and as the value of M increases, it starts evolving into a ridge-type shape, say, Doppler-tolerant waveform. For $M = N = 300$ (i.e., only one subsequence, $L = 1$), it achieves a perfect ridge-shaped AF. Further, the sharpness of the ridge shape is observed as the value of p increases (i.e., $p = 10, 100$).

10.4.3 Comparison with the Counterparts

In [41], an approach was presented for designing polyphase sequences with piecewise linearity and impulse such as autocorrelation properties (further referred to as "linear phase method"). In order to compare the performance of the linear phase method with the proposed PECS, we use both the algorithms to design a piecewise linear polyphase sequence with the input parameters defined in [41], say, length $N = 128$ with subsequence length 8 and thereby the total number of subsequences is 16. Normalized autocorrelation of the optimized sequences from both the approaches is shown in Figure 10.6(a) and it shows lower PSL values of the autocorrelation for PECS as compared to the linear phase method.

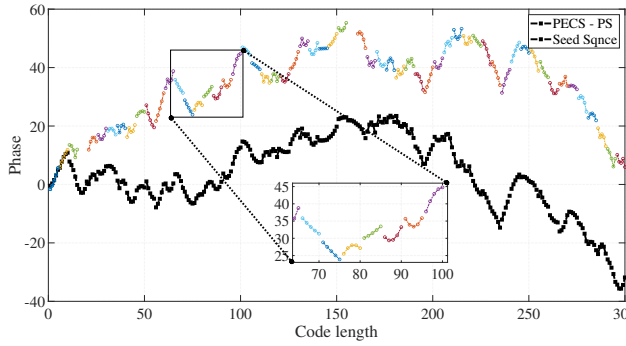

(a)

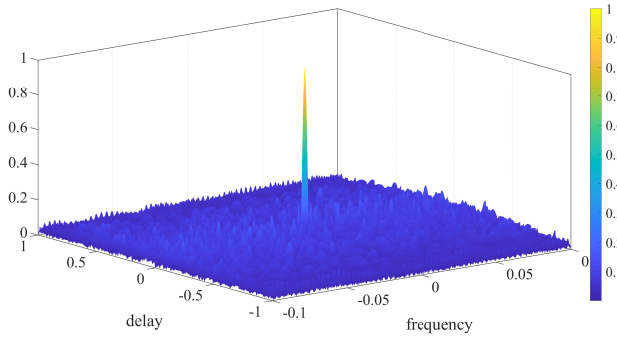

(b)

Figure 10.5. Optimal sequence generation using Algorithm 10.1 with input parameters $N = 300, M = 5, Q = 2$, and $p = 10$ and the number of iterations set to 10^6: (a) Phase of the sequence before and after optimization, (b) Ambiguity Function.

The unwrapped phase of the optimized sequences is shown in Figure 10.6(b)[5]. Linear Phase Method generates an optimal sequence whose

5 The phase unwrapping operation can be expressed mathematically as

$$\mathbf{x}_U = \mathcal{F}[\mathbf{x}_W] = \arg(\mathbf{x}_W) + 2k\pi$$

where $\mathcal{F}$ is the phase unwrapping operation, k is an integer,and $\mathbf{x}_W$ and $\mathbf{x}_U$ are the wrapped and unwrapped phase sequences, respectively.

Table 10.3

Unwrapped Phase and AF Comparison for Optimized waveforms with $N = 300$, and $Q = 2$.

	ℓ_2 **norm**	ℓ_{10} **norm**	ℓ_{100} **norm**
Phase	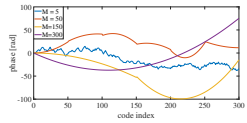	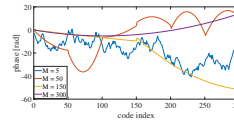	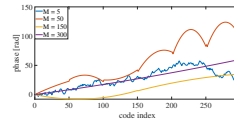
AF ($M = 5$)	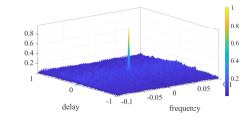	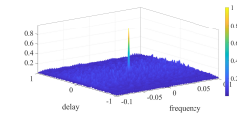	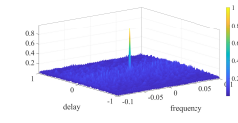
AF ($M = 50$)	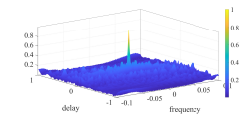	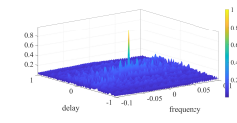	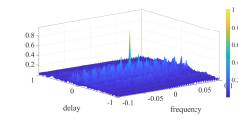
AF ($M = 150$)	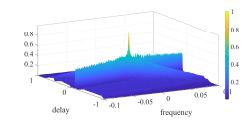	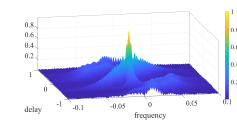	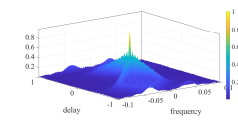
AF ($M = 300$)	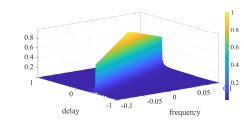	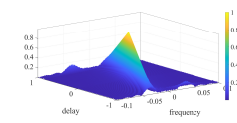	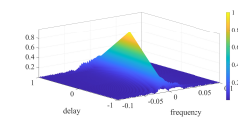

ISL and PSL values are 36.47 dB and 12.18 dB, respectively, whereas PECS results in an optimal sequence whose ISL and PSL values are 32.87 dB and 9.09 dB. Therefore, better results are obtained using the PECS approach.

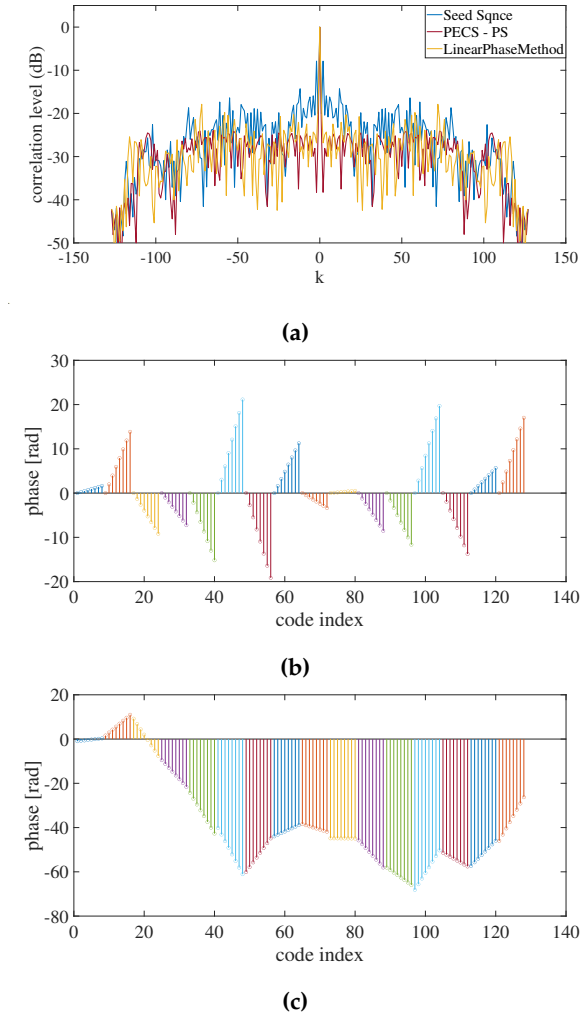

Figure 10.6. Comparison of linear phase method and PECS to design linear polyphase sequence with good autocorrelation properties: (a) autocorrelation response comparison, (b) unwrapped phase of linear phase method, (c) unwrapped phase of PECS.

In [28], an approach to shape the AF of a given sequence with respect to a desired sequence was proposed (later referred to as "AF shape method"). Here, we consider an example where the two approaches (i.e., AF shaping method and PECS) strive to achieve the desired AF of a Golomb sequence of length $N = 64$. The performance of the two approaches would be assessed by comparing the autocorrelation responses and ISL/PSL values of the optimal sequences. Both the algorithms are fed with the same seed sequence and the convergence criterion is kept the same for better comparison. As evident from Figure 10.7, the autocorrelation function of the optimal sequence derived from PECS shows improvement as compared to the optimal sequence of benchmark approach. The initial ISL of the seed sequence was 49.30 dB and the desired Golomb sequence was 22.050 dB. After the optimization was performed, the optimal ISL using the AF shaping approach was 22.345 dB and using PECS was 22.002 dB. In addition, the ridge shape of the AF generated using both the approaches is equally matched to the desired AF of Golomb sequence. The noteworthy point here is that the monotonic convergence of ISL is absent in the AF shape method as it optimizes a different objective function rather than ISL using the CD approach, whereas in the PECS method, monotonic convergence is achieved. As a result, PECS has the capability of achieving better ISL values than the Golomb sequence as it aims to minimize the objective in (10.7) and its proof can be seen from the optimal ISL value quoted above (i.e., 0.048 dB improvement with respect to ISL of Golomb sequence). To calculate the run time of the algorithm, we used a PC with the following specifications: 2.6 GHz i$9 - 11950$H CPU and 32 GB RAM. No acceleration schemes (including the Parallel Computing Toolbox in MATLAB) are used to generate the results and are evaluated from purely sequential processing.

For a sequence length of $N = 300$, computational time was derived by varying two input parameters: subsequence length $M = 5, 50, 150$, and 300 and $Q = 2, 3, 4, 5$, and 6. The results reported in Table 10.4 indicate that the computation time increases in proportion to the increasing values of Q keeping M fixed. However, computation time decreases as we keep Q fixed and increase M.

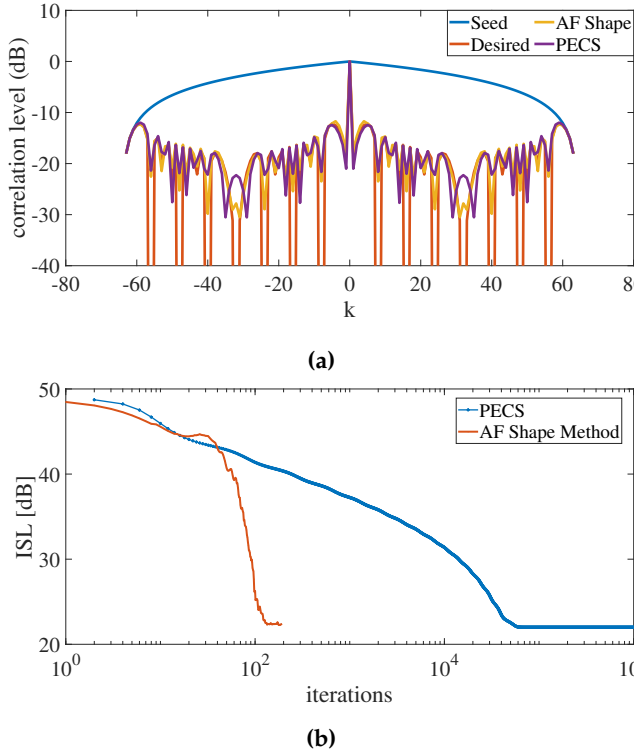

Figure 10.7. Performance comparison of AF Shape method and PECS algorithms: (a) autocorrelation response comparison, (b) ISL convergence of PECS.

10.5 CONCLUSION

A stable design procedure has been discussed for obtaining polyphase sequences synthesized with a constraint of polynomial phase behavior optimized for minimal PSL/ISL for any sequence length. Results shown in the text indicate the robustness of the method for various scenarios that offers additional degrees of freedom to adapt the input parameters in order to design unique waveforms with Doppler-tolerant properties. The algorithm performance was tested in comparison to the other techniques present in the

Table 10.4
PECS Run Time - Sequence Length $N = 300$

	$M = 5$	$M = 50$	$M = 150$	$M = 300$
$Q = 2$	429.25s	84.26s	52.53s	45.15s
$Q = 3$	521.41s	88.32s	55.03s	47.42s
$Q = 4$	562.04s	97.20s	64.55s	56.54s
$Q = 5$	573.72s	108.37s	73.47s	65.47s
$Q = 6$	620.90s	118.82s	83.39s	74.06s

literature and convincing results were observed. In addition, the technique can be used to improve the performance of the state of the art algorithms by extending them with the inclusion of PECS, which offers additional design parameters for waveform design. The algorithm is implemented by means of FFT and least squares operations and therefore is computationally efficient.

References

[1] P. Stoica, J. Li, and M. Xue, "Transmit codes and receive filters for radar," *IEEE Signal Processing Magazine*, vol. 25, no. 6, pp. 94–109, 2008.

[2] P. Setlur, J. Hollon, K. T. Arasu, and M. Rangaswamy, "On a formal measure of Doppler Tolerance," in *2017 IEEE Radar Conference (RadarConf)*, 2017, pp. 1751–1756.

[3] A. Rihaczek, "Doppler-tolerant signal waveforms," *Proceedings of the IEEE*, vol. 54, no. 6, pp. 849–857, 1966.

[4] M. E. Levanon Nadav, *Radar Signals*. John Wiley & Sons, Inc., Publication, 2004.

[5] M. A. Richards, *Fundamentals of radar signal processing*. Tata McGraw-Hill Education, 2005.

[6] N. Levanon and B. Getz, "Comparison between linear fm and phase-coded cw radars," *IEE Proceedings-Radar, Sonar and Navigation*, vol. 141, no. 4, pp. 230–240, 1994.

[7] R. Frank, "Polyphase codes with good nonperiodic correlation properties," *IEEE Transactions on Information Theory*, vol. 9, no. 1, pp. 43–45, 1963.

[8] B. L. Lewis and F. F. Kretschmer, "Linear frequency modulation derived polyphase pulse compression codes," *IEEE Transactions on Aerospace and Electronic Systems*, vol. AES-18, no. 5, pp. 637–641, 1982.

[9] N. Zhang and S. Golomb, "Polyphase sequence with low autocorrelations," *IEEE Transactions on Information Theory*, vol. 39, no. 3, pp. 1085–1089, 1993.

[10] D. Chu, "Polyphase codes with good periodic correlation properties (corresp.)," *IEEE Transactions on Information Theory*, vol. 18, no. 4, pp. 531–532, 1972.

[11] D. Petrolati, P. Angeletti, and G. Toso, "New piecewise linear polyphase sequences based on a spectral domain synthesis," *IEEE Transactions on Information Theory*, vol. 58, no. 7, pp. 4890–4898, 2012.

[12] P. Stoica, H. He, and J. Li, "New algorithms for designing unimodular sequences with good correlation properties," *IEEE Transactions on Signal Processing*, vol. 57, no. 4, pp. 1415–1425, 2009.

[13] J. Song, P. Babu, and D. P. Palomar, "Sequence design to minimize the weighted integrated and peak sidelobe levels," *IEEE Transactions on Signal Processing*, vol. 64, no. 8, pp. 2051–2064, 2016.

[14] M. Alaee-Kerahroodi, A. Aubry, A. De Maio, M. M. Naghsh, and M. Modarres-Hashemi, "A coordinate-descent framework to design low PSL/ISL sequences," *IEEE Transactions on Signal Processing*, vol. 65, no. 22, pp. 5942–5956, Nov. 2017.

[15] J. M. Baden, B. O'Donnell, and L. Schmieder, "Multiobjective sequence design via gradient descent methods," *IEEE Transactions on Aerospace and Electronic Systems*, vol. 54, no. 3, pp. 1237–1252, 2018.

[16] E. Raei, M. Alaee-Kerahroodi, and M. B. Shankar, "Spatial- and range- ISLR trade-off in MIMO radar via waveform correlation optimization," *IEEE Transactions on Signal Processing*, vol. 69, pp. 3283–3298, 2021.

[17] Q. Liu, W. Ren, K. Hou, T. Long, and A. E. Fathy, "Design of polyphase sequences with low integrated sidelobe level for radars with spectral distortion via majorization-minimization framework," *IEEE Transactions on Aerospace and Electronic Systems*, vol. 57, no. 6, pp. 4110–4126, 2021.

[18] S. P. Sankuru, P. Babu, and M. Alaee-Kerahroodi, "UNIPOL: Unimodular sequence design via a separable iterative quartic polynomial optimization for active sensing systems," *Signal Processing*, vol. 190, p. 108348, 2022. [Online]. Available: https://www.sciencedirect.com/science/article/pii/S0165168421003856

[19] R. Jyothi, P. Babu, and M. Alaee-Kerahroodi, "Slope: A monotonic algorithm to design sequences with good autocorrelation properties by minimizing the peak sidelobe level," *Digital Signal Processing*, vol. 116, p. 103142, 2021.

[20] M. Piezzo, A. Aubry, S. Buzzi, A. D. Maio, and A. Farina, "Non-cooperative code design in radar networks: a game-theoretic approach," *EURASIP Journal on Advances in Signal Processing*, vol. 2013, no. 1, p. 63, Mar 2013. [Online]. Available: https://doi.org/10.1186/1687-6180-2013-63

[21] M. Piezzo, A. De Maio, A. Aubry, and A. Farina, "Cognitive radar waveform design for spectral coexistence," in *2013 IEEE Radar Conference (RadarCon13)*, 2013, pp. 1–4.

[22] A. Aubry, V. Carotenuto, A. De Maio, and L. Pallotta, "High range resolution profile estimation via a cognitive stepped frequency technique," *IEEE Transactions on Aerospace and Electronic Systems*, vol. 55, no. 1, pp. 444–458, 2019.

[23] R. Amar, M. Alaee-Kerahroodi, P. Babu, and B. S. M. R, "Designing interference-immune Doppler-tolerant waveforms for automotive radar applications," 2022. [Online]. Available: https://arxiv.org/abs/2204.02236

[24] X. Feng, Y. nan Zhao, Z. quan Zhou, and Z. feng Zhao, "Waveform design with low range sidelobe and high Doppler tolerance for cognitive radar," *Signal Processing*, vol. 139, pp. 143–155, 2017.

[25] W.-Q. Wang, "Large time-bandwidth product mimo radar waveform design based on chirp rate diversity," *IEEE Sensors Journal*, vol. 15, no. 2, pp. 1027–1034, 2015.

[26] J. Zhang, C. Shi, X. Qiu, and Y. Wu, "Shaping radar ambiguity function by l -phase unimodular sequence," *IEEE Sensors Journal*, vol. 16, no. 14, pp. 5648–5659, 2016.

[27] O. Aldayel, T. Guo, V. Monga, and M. Rangaswamy, "Adaptive sequential refinement: A tractable approach for ambiguity function shaping in cognitive radar," in *2017 51st Asilomar Conference on Signals, Systems, and Computers*, 2017, pp. 573–577.

[28] M. Alaee-Kerahroodi, S. Sedighi, B. Shankar M.R., and B. Ottersten, "Designing (in)finite-alphabet sequences via shaping the radar ambiguity function," in *ICASSP 2019 - 2019 IEEE International Conference on Acoustics, Speech and Signal Processing (ICASSP)*, 2019, pp. 4295–4299.

[29] Z.-J. Wu, Z.-Q. Zhou, C.-X. Wang, Y.-C. Li, and Z.-F. Zhao, "Doppler resilient complementary waveform design for active sensing," *IEEE Sensors Journal*, vol. 20, no. 17, pp. 9963–9976, 2020.

[30] I. A. Arriaga-Trejo, "Design of constant modulus sequences with Doppler shift tolerance and good complete second order statistics," in *2020 IEEE International Radar Conference (RADAR)*, 2020, pp. 274–279.

[31] X. Feng, Q. Song, Z. Zhang, and Y. Zhao, "Novel waveform design with low probability of intercept and high Doppler tolerance for modern cognitive radar," in *2019 IEEE International Conference on Signal, Information and Data Processing (ICSIDP)*, 2019, pp. 1–6.

[32] J. Song, P. Babu, and D. Palomar, "Optimization methods for designing sequences with low autocorrelation sidelobes," *IEEE Transactions on Signal Processing*, vol. 63, no. 15, pp. 3998–4009, Aug 2015.

[33] Y. Sun, P. Babu, and D. P. Palomar, "Majorization-minimization algorithms in signal processing, communications, and machine learning," *IEEE Transactions on Signal Processing*, vol. 65, no. 3, pp. 794–816, Feb 2017.

[34] E. Raei, M. Alaee-Kerahroodi, P. Babu, and M. R. B. Shankar, "Design of mimo radar waveforms based on lp-norm criteria," 2021.

[35] M. A. Richards, J. Scheer, W. A. Holm, and W. L. Melvin, *Principles of modern radar*. Citeseer, 2010.

[36] A. W. Rihaczek, *Principles of High-Resolution Radar*. Artech House, 1969, ch. 12, Waveforms for Simplified Doppler Processing, pp. 420–422.

[37] S. P. Sankuru, R. Jyothi, P. Babu, and M. Alaee-Kerahroodi, "Designing sequence set with minimal peak side-lobe level for applications in high resolution radar imaging," *IEEE Open Journal of Signal Processing*, vol. 2, pp. 17–32, 2021.

[38] F. L. Gall and F. Urrutia, "Improved rectangular matrix multiplication using powers of the Coppersmith-Winograd tensor," in *Proceedings of the Twenty-Ninth Annual ACM-SIAM Symposium on Discrete Algorithms*, ser. SODA '18. USA: Society for Industrial and Applied Mathematics, 2018, p. 1029–1046.

[39] G. H. Golub and C. F. Van Loan, *Matrix Computations*, 3rd ed. The Johns Hopkins University Press, 1996.

[40] R. Lin, M. Soltanalian, B. Tang, and J. Li, "Efficient design of binary sequences with low autocorrelation sidelobes," *IEEE Transactions on Signal Processing*, vol. 67, no. 24, pp. 6397–6410, 2019.

[41] M. Soltanalian, P. Stoica, M. M. Naghsh, and A. De Maio, "Design of piecewise linear polyphase sequences with good correlation properties," in *2014 22nd European Signal Processing Conference (EUSIPCO)*, 2014, pp. 1297–1301.

APPENDIX 10A

We aim to obtain a minimizer of (10.7) iteratively using the MM algorithm. We can majorize $|r_k|^p$ by a quadratic function locally [13]. From the literature (see [13, 14] for more details), it is known that given $|r_k^{(i)}|$ at iteration i, $|r_k|^p$ (where $p \geq 2$) can be majorized at $|r_k^{(i)}|$ over $[0, t]$ by

$$\tilde{\alpha}_k |r_k|^2 + \tilde{\beta}_k |r_k| + \tilde{\alpha}_k \left| r_k^{(i)} \right|^2 - (p-1) \left| r_k^{(i)} \right|^p \tag{10A.1}$$

where

$$t = \left(\sum_{k=1}^{N-1} |r_k^{(i)}|^p \right)^{\frac{1}{p}}$$
$$\tilde{\alpha}_k = \frac{t^p - \left|r_k^{(i)}\right|^p - p\left|r_k^{(i)}\right|^{p-1}(t - \left|r_k^{(i)}\right|)}{(t - \left|r_k^{(i)}\right|)^2} \tag{10A.2}$$
$$\tilde{\beta}_k = p\left|r_k^{(i)}\right|^{p-1} - 2\tilde{\alpha}_k \left|r_k^{(i)}\right|$$

The majorizer is then given by (ignoring the constant terms)

$$\sum_{k=1}^{N-1} (\tilde{\alpha}_k |r_k|^2 + \tilde{\beta}_k |r_k|) \tag{10A.3}$$

The first term in the objective function is just the weighted ISL metric with weights $w_k = \tilde{\alpha}_k$, which can be majorized at $\mathbf{x}^{(i)}$ by (with constant terms ignored) [13],

$$\mathbf{x}^H \left(\boldsymbol{R} - \lambda_{max}(\boldsymbol{L}) \mathbf{x}^{(i)} (\mathbf{x}^{(i)})^H \right) \mathbf{x} \tag{10A.4}$$

$$\boldsymbol{R} = \sum_{k=1-N}^{N-1} w_k r_{-k}^{(i)} \boldsymbol{U}_k, \ \boldsymbol{L} = \sum_{k=1-N}^{N-1} w_k \text{vec}(\boldsymbol{U}_k) \text{vec}(\boldsymbol{U}_k)^H$$
$$\lambda_{max}(\boldsymbol{L}) = \max_k \{ w_k (N-k) | k = 1, \ldots, N-1 \}$$

$\lambda_{max}(\boldsymbol{L})$ is the maximum eigenvalue of $\boldsymbol{L}$, $r_k^{(i)}$ are the autocorrelations of the sequence $x_n^{(i)}$, and $\boldsymbol{U}_k$, $k = 0, \ldots, N-1$ to be the $N \times N$ Toeplitz matrix with the kth diagonal elements being 1 and 0 elsewhere. Here, the matrix $\boldsymbol{R}$ is a Hermitian Toeplitz matrix and the upper bound of $\lambda_{max}(\boldsymbol{R})$ is denoted by λ_u (refer to Lemma 3 in [13]).

For the second term, since it can be shown that $\tilde{\beta}_k \leq 0$, we have

$$\sum_{k=1}^{N-1} \tilde{\beta}_k |r_k| \leq \frac{1}{2} \mathbf{x}^H \left(\sum_{k=1-N}^{N-1} \tilde{\beta}_k \frac{r_k^{(i)}}{|r_k^{(i)}|} \boldsymbol{U}_{-k} \right) \mathbf{x} \tag{10A.5}$$

By adding the two majorization functions, that is, (10A.4) and (10A.5), and other simplifications as given in [13], we derive the majorizer of (10A.3) as

$$\mathbf{x}^H \left(\widetilde{\boldsymbol{R}} - \lambda_{max}(\boldsymbol{L}) \mathbf{x}^{(i)} (\mathbf{x}^{(i)})^H \right) \mathbf{x} \tag{10A.6}$$

where

$$\hat{w}_{-k} = \hat{w}_k = \tilde{\alpha}_k + \frac{\tilde{\beta}_k}{2|r_k^{(i)}|} = \frac{p}{2} |r_k^{(i)}|^{p-2}, \; k = 1, \ldots, N-1 \tag{10A.7}$$

and $\widetilde{\boldsymbol{R}} = \sum_{k=1-N}^{N-1} \hat{w}_k r_{-k}^{(i)} \boldsymbol{U}_k$. Finally, after performing one more majorization step as mentioned in [13], we derive another majorizer as

$$||\mathbf{x} - \mathbf{y}||_2 \tag{10A.8}$$

where $\mathbf{y} = \left(\lambda_{\max}(\boldsymbol{L}) N + \lambda_u \right) \mathbf{x}^{(i)} - \widetilde{\boldsymbol{R}} \mathbf{x}^{(i)}$, which forms the basis of our problem in (10.8).

Chapter 11

Waveform Design for STAP in MIMO Radars

The detrimental effects of ground clutter returns and jamming on the detection of moving targets must also be minimized by radar placed on flying platforms. STAP benefits radar signal processing in these scenarios, where the radar platform is mobile and ground clutter or jamming causes performance degradation [1]. It is possible to achieve order-of-magnitude sensitivity improvements in the received SINR and, consequently, target detection performance through careful waveform design and application of STAP. In this chapter, we formulate the STAP waveform design optimization problem and provide a solution based on the BCD framework, which was described in Chapter 5.

11.1 PROBLEM FORMULATION

Let us consider a narrowband MIMO radar system with N_t transmit and N_r receive antennas as illustrated in Figure 11.1 [2]. At the time sample (l), the transmitted waveform by the N_t transmit antenna elements can be represented as

$$\widetilde{\mathbf{x}}(l) = [x_1(l), x_2(l), \ldots, x_{N_t}(l)]^T \in \mathbb{C}^{N_t} \tag{11.1}$$

Thus, the transmitted waveform for L time samples can be represented equivalently as follows

$$\mathbf{X} = [\widetilde{\mathbf{x}}(1), \ldots, \widetilde{\mathbf{x}}(L)] \in \mathbb{C}^{N_t \times L} \tag{11.2}$$

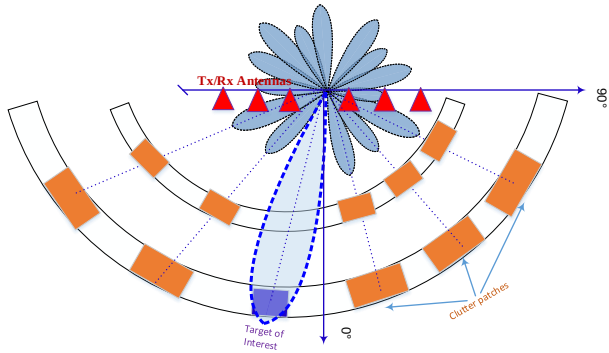

Figure 11.1. Range-azimuth bins for the colocated MIMO radar system.

Let us assume that both transmit and receive antenna arrays are ULA with half wavelength inter-element spacing. Therefore, the steering vectors of the transmit and receive arrays can be considered as

$$\mathbf{a}_i(\theta) = \frac{1}{\sqrt{N_i}} \left[1, e^{-j\pi \sin(\theta)}, \ldots, e^{-j\pi(N_i-1)\sin(\theta)}\right]^T \tag{11.3}$$

where $i \in \{t, r\}$. As a result, the signal received from a moving target at time sample (l) can be written as [3]

$$\widetilde{\mathbf{y}}(l) = \alpha_0 e^{j2\pi f_{d,0}(l-1)} \mathbf{a}_r^*(\theta_0)\mathbf{a}_t^H(\theta_0)\widetilde{\mathbf{x}}(l) + \widetilde{\mathbf{c}}(l) + \widetilde{\mathbf{n}}(l) \tag{11.4}$$

where α_0 is the complex path loss, $f_{d,0}$ indicates the actual target normalized Doppler frequency in hertz, $\theta = \theta_0$ is the target spatial angle, $\widetilde{\mathbf{c}}(l) \in \mathbb{C}^{N_r}$ represents the signal-dependent interference (clutter) at time sample (l), and $\widetilde{\mathbf{n}}(l) \in \mathbb{C}^{N_r}$ denotes white Gaussian noise at time sample (l) with distribution $\mathcal{N}(0, \sigma_n^2 \mathbf{I}_{N_r})$.

Now, suppose that

$$\mathbf{Y} = [\widetilde{\mathbf{y}}(1), \ldots, \widetilde{\mathbf{y}}(L)] \in \mathbb{C}^{N_r \times L} \tag{11.5}$$

$$\mathbf{C} = [\widetilde{\mathbf{c}}(1), \ldots, \widetilde{\mathbf{c}}(L)] \in \mathbb{C}^{N_r \times L} \tag{11.6}$$

$$\mathbf{N} = [\widetilde{\mathbf{n}}(1), \ldots, \widetilde{\mathbf{n}}(L)] \in \mathbb{C}^{N_r \times L} \tag{11.7}$$

where $\mathbf{y} = \text{vec}(\mathbf{Y}) \in \mathbb{C}^{N_r L}$, $\mathbf{c} = \text{vec}(\mathbf{C}) \in \mathbb{C}^{N_r L}$, and $\mathbf{n} = \text{vec}(\mathbf{N}) \in \mathbb{C}^{N_r L}$. By defining the Doppler steering vector

$$\mathbf{p}(f_{d,0}) = \left[1, e^{j2\pi f_{d,0}}, \ldots, e^{j2\pi f_{d,0}(L-1)}\right]^T \in \mathbb{C}^L \tag{11.8}$$

and

$$\mathbf{A}(\theta_0) = \mathbf{a}_r^*(\theta_0)\mathbf{a}_t^H(\theta_0) \tag{11.9}$$

we obtain

$$\mathbf{V}(f_{d,0}, \theta_0) = \text{diag}(\mathbf{p}(f_{d,0})) \otimes \mathbf{A}(\theta_0) \tag{11.10}$$

Therefore, the received baseband signals can be expressed as follows

$$\mathbf{y} = \alpha_0 \mathbf{V}(f_{d,0}, \theta_0)\mathbf{s} + \mathbf{c} + \mathbf{n} \tag{11.11}$$

where $\mathbf{s} = \text{vec}(\mathbf{X}) \in \mathbb{C}^{N_t L}$, and α_0 represents the complex path loss, which includes propagation loss and reflection coefficients related to the target within the range-azimuth bin of interest, and $\mathbf{c}$ represents the clutter vector, which contains the filtered signal-dependent interfering echo samples. Indeed, as illustrated in Figure 11.1, we consider a homogeneous clutter range-azimuth environment that interferes with the range-azimuth bin of interest $(0, 0)$. The vector $\mathbf{c}$ is the superposition of the echoes from different uncorrelated scatterers located at diverse range-azimuth bins, and can be written as

$$\mathbf{c} = \sum_{r=0}^{L_0-1} \sum_{q=0}^{Q_0-1} \alpha_{r,q} \mathbf{J}_r \mathbf{s} \odot \mathbf{p}(f_d) \tag{11.12}$$

where $\alpha_{r,q}$ indicates the complex amplitude echo of the scatterer in the range-azimuth cell (r, q) and f_d represents the clutter normalized Doppler frequency in hertz with uniform distribution over the mean values $\overline{f}_d$, that is

$$f_d \sim U(\overline{f}_d - \frac{\varepsilon}{2}, \overline{f}_d + \frac{\varepsilon}{2})$$

and ε as the uncertainty of clutter Doppler frequency [4]. The above clutter model is generic and considers a moving platform for radar, which cause to the average Doppler shift $\bar{f}_d$ for the static clutter. However, ϵ uncertainty is considered on the estimation of the clutter Doppler shift. Also, $L_0 \leq L$ is the number of range rings that interfere with the range-azimuth bin of interest and Q_0 represents the number of discrete azimuth cells. Considering

all $r \in \{0, 1, ..., L-1\}$, we have

$$\mathbf{J}_r(m_1, m_2) = \begin{cases} 1 & m_1 - m_2 = r \\ 0 & m_1 - m_2 \neq r \end{cases} \quad m_1, m_2 \in \{1, ..., L\}^2 \tag{11.13}$$

where $\mathbf{J}_r$ denotes the shift matrix with $\mathbf{J}_r = (\mathbf{J}_{-r})^T$ [3, 5, 6].

Consequently, the covariance matrix of the clutter can be defined as

$$\begin{aligned} \mathbf{R}_c(\mathbf{s}) &= \sum_{r=0}^{L_0-1} \sum_{q=0}^{Q_0-1} \sigma_c^2 (\mathbf{J}_r \otimes \mathbf{A}(\theta_{r,q})) \Psi(\mathbf{s}) (\mathbf{J}_r \otimes \mathbf{A}(\theta_{r,q}))^H \\ &= \sum_{r=0}^{L_0-1} \sum_{q=0}^{Q_0-1} \sigma_c^2 (\mathbf{J}_r \otimes \mathbf{A}(\theta_{r,q})) \left[\left(\mathbf{s}\mathbf{s}^H \right) \odot \left(\Phi_{\varepsilon}^{\overline{f}_d} \otimes \Upsilon \right) \right] (\mathbf{J}_r \otimes \mathbf{A}(\theta_{r,q}))^H \end{aligned} \tag{11.14}$$

where $\Upsilon = \mathbf{1}\mathbf{1}^T$, and $\mathbf{1} = [1, 1, \ldots, 1]^T$ being an N_t-length vector. Also, $\sigma_c^2 = \mathbb{E}\left[\left| \alpha_{r,q} \right|^2 \right]$,

$$\Psi(\mathbf{s}) = \mathrm{diag}(\mathbf{s}) \Phi_{\varepsilon}^{\overline{f}_d} \mathrm{diag}(\mathbf{s})^H$$

and

$$\Phi_{\varepsilon}^{\overline{f}_d} = \begin{cases} 1 & m_1 = m_2 \\ e^{j2\pi \overline{f}_d (m_1 - m_2)} \frac{\sin(\pi\varepsilon(m_1 - m_2))}{\pi\varepsilon(m_1 - m_2)} & m_1 \neq m_2 \end{cases} \quad m_1, m_2 \in \{1, ..., L\}^2 \tag{11.15}$$

denotes the covariance matrix of $\mathbf{p}(f_d)$.

It should be noted that the adopted clutter model has previously been presented in the literature (see [4, 5] for example). Further, clutter knowledge is assumed to be obtained via a cognitive paradigm by utilizing a site specific (possibly dynamic) environment database containing a geographical information system (GIS), meteorological data, previous scans, tracking files, and some electromagnetic reflectivity and spectral clutter models [5–8].

The received signal at the MIMO radar after passing through a linear filter $\mathbf{w}$ can be expressed as follows

$$\alpha_0 \mathbf{w}^H \mathbf{V}(f_{d,0}, \theta_0) \mathbf{s} + \mathbf{w}^H \mathbf{c} + \mathbf{w}^H \mathbf{n} \tag{11.16}$$

whereby the output SINR can be defined as

$$\text{SINR} \equiv f(\mathbf{s}, \mathbf{w}) = \frac{\alpha_0^2 \left| \mathbf{w}^H \mathbf{V}(f_{d,0}, \theta_0) \mathbf{s} \right|^2}{\mathbf{w}^H \mathbf{R}_c(\mathbf{s}) \mathbf{w} + \mathbf{w}^H \mathbf{R}_n \mathbf{w}} \tag{11.17}$$

where $\mathbf{R}_c(\mathbf{s})$ and $\mathbf{R}_n$ are the covariance matrix of clutter and noise, respectively. It is here assumed that $\mathbf{R}_n = \sigma_n^2 \mathbf{I}_{N_r}$.

Since the SINR in (11.17) is related to both $\mathbf{s}$ and $\mathbf{w}$, the transmit space-time waveform and receive filter should be jointly optimized. By defining $\Omega_\infty = \{\mathbf{s} \in \mathbb{C}^{N_t L} | \, |s_n| = 1, n = 1, \ldots, N_t L\}$ and $\Omega_M = \{\mathbf{s} | s_n \in \Psi_M, n = 1, \ldots, N_t L\}$, where $\Psi_M = \{1, \bar{\omega}, \ldots, \bar{\omega}^{M-1}\}$, $\bar{\omega} = e^{j\frac{2\pi}{M}}$ and M be the size of discrete constellation alphabet, the optimization problem for designing $\mathbf{s} = [s_1, s_2, \ldots, s_{N_t L}]^T$, and $\mathbf{w} = [w_1, w_2, \ldots, w_{N_r L}]^T$, under continuous and discrete phase constraints can be expressed as

$$\mathcal{P}^h_{\mathbf{s},\mathbf{w}} \begin{cases} \max\limits_{\mathbf{s},\mathbf{w}} & f(\mathbf{s}, \mathbf{w}) \\ \text{s.t.} & \mathbf{s} \in \Omega_h \end{cases}$$

where $h \in \{M, \infty\}$ in which the constraints $\mathbf{s} \in \Omega_\infty$, and $\mathbf{s} \in \Omega_M$ identify continuous alphabet and finite alphabet codes, respectively. Notice that continuous phase means the phase values can get any arbitrary value within $[0, 2\pi)$. The feasible set for the discrete phase is limited to a finite number of equi-spaced points on the unit circle. It should be noted that the aforementioned optimization problems are nonconvex, multivariable, constrained, and NP-hard in general [7]. We use the CD-based algorithm to solve these problems. Precisely, the continuous phase design problem is solved using a closed-form solution and the discrete phase optimization problem is solved using the FFT technique.

11.2 TRANSMIT SEQUENCE AND RECEIVE FILTER DESIGN

In this section, using alternating optimization [9], we provide the solution to problems $\mathcal{P}^\infty_{\mathbf{s},\mathbf{w}}$ and $\mathcal{P}^M_{\mathbf{s},\mathbf{w}}$. By doing so, we design $\mathbf{w}$ for a fixed $\mathbf{s}$ and then design $\mathbf{s}$ for a fixed $\mathbf{w}$.

11.2.1 Optimum Filter Design

Consider that $\mathbf{s}^{(k)}$ is a feasible radar code at iteration (k) for either $\mathcal{P}^\infty_{\mathbf{s},\mathbf{w}}$ or $\mathcal{P}^M_{\mathbf{s},\mathbf{w}}$. The optimal space-time receive filter $\mathbf{w}^{(k)}$ can be obtained solving the

following optimization problem:

$$\mathcal{P}_{\mathbf{w}} \begin{cases} \max\limits_{\mathbf{w}} & \dfrac{\alpha_0^2 \left| \mathbf{w}^H \mathbf{V}(f_{d,0}, \theta_0) \mathbf{s}^{(k)} \right|^2}{\mathbf{w}^H \mathbf{R}_c(\mathbf{s}^{(k)}) \mathbf{w} + \mathbf{w}^H \mathbf{w} \sigma_n^2} \end{cases} \tag{11.18}$$

An exploration of $\mathcal{P}_{\mathbf{w}}$ reveals that it is a classic SINR maximization problem, whose optimal solution $\mathbf{w}^{(k)}$ is minimum variance distortionless response (MVDR) [10] and can be obtained by

$$\widetilde{\mathbf{w}} = \mathbf{w}^{(k)} = \left(\mathbf{R}_c(\mathbf{s}^{(k)}) + \sigma_n^2 \mathbf{I}_{N_r} \right)^{-1} \mathbf{V}(f_{d,0}, \theta_0) \mathbf{s}^{(k)} \tag{11.19}$$

11.2.2 Code Optimization Algorithm

In this section, we consider the waveform optimization for a fixed $\widetilde{\mathbf{w}}$. In particular, we resort to the following optimization problem,

$$\mathcal{P}_{\mathbf{s}}^h \begin{cases} \max\limits_{\mathbf{s}} & \dfrac{\alpha_0^2 \left| \widetilde{\mathbf{w}}^H \mathbf{V}(f_{d,0}, \theta_0) \mathbf{s} \right|^2}{\widetilde{\mathbf{w}}^H \mathbf{R}_c(\mathbf{s}) \widetilde{\mathbf{w}} + \widetilde{\mathbf{w}}^H \mathbf{R}_n \widetilde{\mathbf{w}}} \\ \text{s.t.} & \mathbf{s} \in \Omega_h \end{cases} \tag{11.20}$$

Since in both problems $|s_n| = 1$, it is easy to show the objective in $\mathcal{P}_{\mathbf{s}}^h$ can be written as [7]

$$\frac{\alpha_0^2 \left| \widetilde{\mathbf{w}}^H \mathbf{V}(f_{d,0}, \theta_0) \mathbf{s} \right|^2}{\widetilde{\mathbf{w}}^H \mathbf{R}_c(\mathbf{s}) \widetilde{\mathbf{w}} + \widetilde{\mathbf{w}}^H \mathbf{R}_n \widetilde{\mathbf{w}}} = \frac{\mathbf{s}^H \Theta(\widetilde{\mathbf{W}}) \mathbf{s}}{\mathbf{s}^H \Sigma(\widetilde{\mathbf{W}}) \mathbf{s}} = f(\mathbf{s}, \widetilde{\mathbf{w}}) \tag{11.21}$$

where $\widetilde{\mathbf{W}} = \widetilde{\mathbf{w}} \widetilde{\mathbf{w}}^H$, with

$$\Theta(\widetilde{\mathbf{W}}) = \sigma_0^2 \mathbb{E} \left[\left(\operatorname{diag}(\mathbf{p}(f_{d,0}))^H \otimes \mathbf{A}^H(\theta_0) \right) \widetilde{\mathbf{W}} \left(\operatorname{diag}(\mathbf{p}(f_{d,0})) \otimes \mathbf{A}(\theta_0) \right) \right] \tag{11.22}$$

and

$$\begin{aligned} \Sigma(\widetilde{\mathbf{W}}) = & \sum_{r=0}^{L_0} \sum_{q=0}^{Q_0} \sigma_c^2(\mathbf{J}_r \otimes \mathbf{A}(\theta_{r,q})) \left[\widetilde{\mathbf{W}} \odot \left(\Phi_{\varepsilon}^{\overline{f}_d} \otimes \Upsilon \right) \right] (\mathbf{J}_r \otimes \mathbf{A}(\theta_{r,q}))^H \\ & + \sigma_n^2 \operatorname{tr}(\widetilde{\mathbf{W}}) \mathbf{I}_{NtL} \end{aligned} \tag{11.23}$$

Consequently, the optimization problems (11.20) can be rewritten as

$$\mathcal{P}_{\mathbf{s}}^{h} \begin{cases} \max\limits_{\mathbf{s}} & \dfrac{\mathbf{s}^H \Theta(\widetilde{\mathbf{W}})\mathbf{s}}{\mathbf{s}^H \Sigma(\widetilde{\mathbf{W}})\mathbf{s}} \\ \text{s.t.} & \mathbf{s} \in \Omega_h \end{cases} \tag{11.24}$$

To tackle problem (11.20), we resort to the CD framework [11–13] by sequentially optimizing each code entry in $\mathbf{s}$, keeping fixed the remaining $N_t L - 1$ code entries. Indeed, at each iteration, the algorithm finds a coordinate that maximizes the SINR over the corresponding coordinate while keeping all other coordinates constant. Let us assume that s_d is the only variable of the code vector $\mathbf{s}$, and $\mathbf{s}_{-d}^{(k)}$ refers to the remaining code entries that are assumed to be known and fixed at iteration $(k+1)$, that is

$$\widetilde{\mathbf{s}} = [s_1^{(k)}, \ldots, s_{d-1}^{(k)}, s_d, s_{d+1}^{(k)}, \ldots, s_{N_t L}^{(k)}]^T \in \mathbb{C}^{N_t L}$$

and

$$\widetilde{\mathbf{s}}_{-d}^{(k)} = [s_1^{(k)}, \ldots, s_{d-1}^{(k)}, s_{d+1}^{(k)}, \ldots, s_{N_t L}^{(k)}]^T \in \mathbb{C}^{N_t L - 1}$$

Thus, the nonconvex constrained optimization problems (11.24) at iteration $(k+1)$ can be recast as

$$\widetilde{\mathcal{P}}_{d,\mathbf{s}^{(k)}}^{\infty} \begin{cases} \max\limits_{s_d} & f_{\mathbf{w}}(s_d, \mathbf{s}_{-d}^{(k)}) \\ \text{s.t.} & |s_d| = 1 \end{cases} \tag{11.25}$$

$$\widetilde{\mathcal{P}}_{d,\mathbf{s}^{(k)}}^{M} \begin{cases} \max\limits_{s_d} & f_{\mathbf{w}}(s_d, \mathbf{s}_{-d}^{(k)}) \\ \text{s.t.} & s_d \in \Omega_M \end{cases} \tag{11.26}$$

where

$$f_{\mathbf{w}}(s_d, \mathbf{s}_{-d}^{(k)}) \equiv \frac{\sigma_0^2 \left| {\mathbf{w}^{(k)}}^H \mathbf{V}(f_{d,0}, \theta_0)\widetilde{\mathbf{s}} \right|^2}{{\mathbf{w}^{(k)}}^H \mathbf{R}_c(\widetilde{\mathbf{s}})\mathbf{w}^{(k)} + {\mathbf{w}^{(k)}}^H \mathbf{w}^{(k)} \sigma_n^2} = \frac{\widetilde{\mathbf{s}}^H \Theta(\mathbf{W}^{(k)})\widetilde{\mathbf{s}}}{\widetilde{\mathbf{s}}^H \Sigma(\mathbf{W}^{(k)})\widetilde{\mathbf{s}}} \tag{11.27}$$

whenever $s_d^\star$ is found, we set $\mathbf{s}^{(k+1)} = \widetilde{\mathbf{s}}$, where

$$\widetilde{\mathbf{s}}^\star = [s_1^{(k)}, \ldots, s_{d-1}^{(k)}, s_d^\star, s_{d+1}^{(k)}, \ldots, s_{N_t L}^{(k)}]^T \in \mathbb{C}^{N_t L}$$

A summary of the developed approach can be found in Algorithm 11.1.[1]

Algorithm 11.1: Waveform Design for STAP in MIMO Radar Systems

Result: The optimal $\mathbf{s}^{\star}$ and $\mathbf{w}^{\star}$
initialization;
for $k = 0, 1, 2, \ldots$ **do**
  for $d = 1, 2, \ldots, N_t L$ **do**
    Set $\widetilde{\mathbf{w}} = \mathbf{w}^{(k)} = \left(\mathbf{R}_c(\mathbf{s}^{(k)}) + \sigma_n^2 \mathbf{I}_{N_r}\right)^{-1} \mathbf{V}(f_{d,0}, \theta_0)\mathbf{s}^{(k)}$;
    Find $s_d{}^{\star}$ by solving (11.25) or (11.26) ;
    Set $\widetilde{\mathbf{s}} = \mathbf{s}^{(k)} = [s_1^{(k)}, \ldots, s_{d-1}^{(k)}, s_d^{\star}, s_{d+1}^{(k)}, \ldots, s_{N_t L}^{(k)}]^T$;
  end
  Set $\mathbf{w}^{(k+1)} = \widetilde{\mathbf{w}}$;
  Set $\mathbf{s}^{(k+1)} = \widetilde{\mathbf{s}}$;
  Stop if convergence criterion is met;
end

It should be noted that the developed method increases the SINR value with each iteration and can ensure convergence to a stationary point by employing the MBI [8, 14] rule. To tackle $\widetilde{\mathcal{P}}^{\infty}_{d,\mathbf{s}^{(k)}}$ or $\bar{\mathcal{P}}^{M}_{d,\mathbf{s}^{(k)}}$, first notice that the numerator of $f_{\mathbf{w}}(s_d, \mathbf{s}_{-d}^{(k)})$ can be written as

$$\begin{aligned} \sigma_0^2 \left| \mathbf{w}^{(k)H} \mathbf{V}(f_{d,0}, \theta_0) \widetilde{\mathbf{s}} \right|^2 &= \widetilde{\mathbf{s}}^H \Theta(\mathbf{W}^{(k)}) \widetilde{\mathbf{s}} \\ &= \sigma_0^2 \widetilde{\mathbf{s}}^H \mathbf{G}^{(k)}_{\theta_0, \mathbf{w}} \widetilde{\mathbf{s}} \end{aligned} \tag{11.28}$$

where

$$\mathbf{G}^{(k)}_{\theta_0, \mathbf{w}} = \mathbb{E}\left[\left(\mathrm{diag}(\mathbf{p}(f_{d,0}))^H \otimes \mathbf{A}^H(\theta_0) \right) \mathbf{W}^{(k)} \left(\mathrm{diag}(\mathbf{p}(f_{d,0})) \otimes \mathbf{A}(\theta_0) \right) \right]$$

1 (k) is the iteration number of entries and (i) is the cycle corresponding to the update of $N_t L$ iterations.

Given the structure of the constraints on s_d in either $\widetilde{\mathcal{P}}^{\infty}_{d,\mathbf{s}^{(k)}}$ or $\bar{\mathcal{P}}^{M}_{d,\mathbf{s}^{(k)}}$, we can benefit from the change of variable $s_d = e^{\jmath\phi_d}$ to show that[2]

$$f_{\mathbf{w}}(\phi_d, \mathbf{s}^{(k)}_{-d}) = \sigma_0^2 \frac{\nu_{\mathbf{w}}(\phi_d, \mathbf{s}^{(k)}_{-d})}{\zeta_{\mathbf{w}}(\phi_d, \mathbf{s}^{(k)}_{-d})} \tag{11.29}$$

where

$$\nu_{\mathbf{w}}(\phi_d, \mathbf{s}^{(k)}_{-d}) = (a_1^{(k)} + a_2^{(k)} e^{-\jmath\phi_d} + a_3^{(k)} e^{\jmath\phi_d}) \tag{11.30}$$

is corresponding to the signal power. We obtain coefficients $a_1^{(k)}, a_2^{(k)}$, and $a_3^{(k)}$ as follows

$$\begin{aligned} a_1^{(k)} =& \sum_{\substack{t=1\\ t\neq d}}^{N_t L} \sum_{\substack{q=1\\ q\neq d}}^{N_t L} \mathbf{G}^{(k)}_{\theta_0,\mathbf{w}}(t,q)\, s_q^{(k)} {s_t^{(k)}}^* + \mathbf{G}^{(k)}_{\theta_0,\mathbf{w}}(d,d) \\ a_2^{(k)} =& \sum_{\substack{t=1\\ t\neq d}}^{N_t L} \mathbf{G}^{(k)}_{\theta_0,\mathbf{w}}(t,d)\, {s_t^{(k)}}^* = \left(a_3^{(k)}\right)^* \end{aligned} \tag{11.31}$$

In addition, the denominator can be defined as

$$\zeta_{\mathbf{w}}(\phi_d, \mathbf{s}^{(k)}_{-d}) = b_1^{(k)} + b_2^{(k)} e^{-\jmath\phi_d} + b_3^{(k)} e^{\jmath\phi_d} \tag{11.32}$$

which is related to the clutter and noise power. The coefficients $b_1^{(k)}, b_2^{(k)}$ and $b_3^{(k)}$ can be obtained as follows

$$\begin{aligned} b_1^{(k)} =& \sum_{\substack{t=1\\ t\neq d}}^{N_t L} \sum_{\substack{q=1\\ q\neq d}}^{N_t L} \Sigma(\mathbf{W}^{(k)})(t,q)\, s_q^{(k)} {s_t^{(k)}}^* + \Sigma(\mathbf{W}^{(k)})(d,d) + \sigma_n^2 \mathbf{I}_{NtL} \\ b_2^{(k)} =& \sum_{\substack{t=1\\ t\neq d}}^{N_t L} \Sigma(\mathbf{W}^{(k)})(t,d)\, {s_t^{(k)}}^* = (b_3^{(k)})^* \end{aligned} \tag{11.33}$$

In the sequel, we tackle the problem in terms of the variable ϕ_d.

2 We assume to have normalized receive space time filter (${\mathbf{w}^{(k)}}^H \mathbf{w}^{(k)} = 1$).

11.2.3 Discrete Phase Code Optimization

The discrete phase optimization problem with explicit dependence on ϕ_d can be written as

$$\bar{\mathcal{P}}^{M}_{d,\phi_d{}^{(k)}} = \begin{cases} \max\limits_{\phi_d} & \sigma_0^2 \dfrac{\nu_{\mathbf{w}}(\phi_d, \mathbf{s}_{-d}^{(k)})}{\zeta_{\mathbf{w}}(\phi_d, \mathbf{s}_{-d}^{(k)})} \\ \text{s.t.} & \phi_d \in \left\{0, \dfrac{2\pi}{M}, \dfrac{4\pi}{M}, \ldots, \dfrac{2\pi(M-1)}{M}\right\} \end{cases}$$

where the objective function may simplified as

$$f_{\mathbf{w}}(\phi_d, \mathbf{s}_{-d}^{(k)}) = \sigma_0^2 \frac{\nu_{\mathbf{w}}(\phi_d, \mathbf{s}_{-d}^{(k)})}{\zeta_{\mathbf{w}}(\phi_d, \mathbf{s}_{-d}^{(k)})} = \sigma_0^2 \frac{(a_1^{(k)} + a_2^{(k)} e^{-\jmath\phi_d} + a_3^{(k)} e^{\jmath\phi_d})}{(b_1^{(k)} + b_2^{(k)} e^{-\jmath\phi_d} + b_3^{(k)} e^{\jmath\phi_d})} \tag{11.34}$$

In (11.34), the nominator and denominator can be efficiently calculated using the DFT technique and based on the lemma proposed in [12], which is also presented below

Lemma 11.1. *Let* $\boldsymbol{\rho}(\phi_m) = \left|\alpha_1 e^{-\jmath\phi_m} + \alpha_2 + \alpha_3 e^{\jmath\phi_m}\right|$, *with* $\phi_m = \frac{2\pi(m-1)}{M}$, $m = 1, \ldots, M$, *and* $\boldsymbol{\rho}(\phi) \in \mathbb{R}^M$. *Then*

$$\boldsymbol{\rho}(\phi) = \left| DFT\left[\alpha_3, \alpha_2, \alpha_1, \mathbf{0}_{1\times(M-3)}\right]^T \right| \tag{11.35}$$

Proof: The M-point DFT of $\left[\alpha_3, \alpha_2, \alpha_1, \mathbf{0}_{1\times(M-3)}\right]$ is

$$\begin{bmatrix} \alpha_3 + \alpha_2 + \alpha_1 \\ \alpha_3 + \alpha_2 e^{-\jmath\frac{2\pi}{M}} + \alpha_1 e^{-\jmath\frac{4\pi}{M}} \\ \vdots \\ \alpha_3 + \alpha_2 e^{-\jmath\frac{2\pi(M-1)}{M}} + \alpha_1 e^{-\jmath\frac{4\pi(M-1)}{M}} \end{bmatrix}$$

Next, observe that

$$\left| \left(\alpha_1 e^{-\jmath\phi_m} + \alpha_2 + \alpha_3 e^{\jmath\phi_m}\right) e^{-\jmath\phi_m} \right| = \alpha_3 + \alpha_2 e^{-\jmath\phi_m} + \alpha_1 e^{-\jmath 2\phi_m} \tag{11.36}$$

which completes the proof. ■

Inspired by Lemma 11.1, we can calculate all the possible M values of $f_{\mathbf{w}}(\phi_d, \mathbf{s}_{-d}^{(k)})$ using the FFT technique. By replacing these values into $\bar{\mathcal{P}}_{d,\phi_d{}^{(k)}}^{M}$, we obtain $\phi_d^\star = \frac{2\pi(m^\star-1)}{M}$, with

$$m^\star = \arg\max \frac{\sigma_0^2 \left| (a_1^{(k)} + a_2^{(k)} e^{-\jmath\phi_d} + a_3^{(k)} e^{\jmath\phi_d}) \right|}{\left| (b_1^{(k)} + b_2^{(k)} e^{-\jmath\phi_d} + b_3^{(k)} e^{\jmath\phi_d}) \right|} \tag{11.37}$$

Finally, the optimized code entry can be calculated by $s_d^\star = e^{\jmath\phi_d^\star}$.

11.2.4 Continuous Phase Code Optimization

The continuous phase optimization problem with explicit dependence to ϕ_d can be written as

$$\widetilde{\mathcal{P}}_{d,\phi_d{}^{(k)}}^{\infty} = \begin{cases} \max\limits_{\phi_d} & \sigma_0^2 \dfrac{\nu_{\mathbf{w}}(\phi_d, \mathbf{s}_{-d}^{(k)})}{\zeta_{\mathbf{w}}(\phi_d, \mathbf{s}_{-d}^{(k)})} \\ \text{s.t.} & \phi_d \in [0, 2\pi) \end{cases} \tag{11.38}$$

Note that $a_1^{(k)}$ and $b_1^{(k)}$ are real-valued coefficients, with $a_2^{(k)} = a_3^{(k)^*}$ and $b_2^{(k)} = b_3^{(k)^*}$; thus, the continuous phase optimization problem can be recast as

$$\widetilde{\mathcal{P}}_{d,\phi_d{}^{(k)}}^{\infty} = \begin{cases} \max\limits_{\phi_d} & \sigma_0^2 \dfrac{a_1^{(k)} + 2\Re(a_2^{(k)} e^{-\jmath\phi_d})}{b_1^{(k)} + 2\Re(b_2^{(k)} e^{-\jmath\phi_d})} \\ \text{s.t.} & \phi_d \in [0, 2\pi) \end{cases} \tag{11.39}$$

Considering $a_2 = c_1 + jc_2$ and $b_2 = d_1 + jd_2$, (11.39) can be further recast as

$$\begin{cases} \max\limits_{\phi_d} & \sigma_0^2 \dfrac{a_1^{(k)} + 2c_1^{(k)} \cos(\phi_d) + 2c_2^{(k)} \sin(\phi_d)}{b_1^{(k)} + 2d_1^{(k)} \cos(\phi_d) + 2d_2^{(k)} \sin(\phi_d)} \\ \text{s.t.} & \phi_d \in [0, 2\pi) \end{cases} \tag{11.40}$$

Let us assume that $\mu = \tan(\phi_d/2)$, then $\sin(\phi_d) = \frac{2\mu}{1+\mu^2}$ and $\cos(\phi_d) = \frac{1-\mu^2}{1+\mu^2}$. By replacing $\sin(\phi_d)$ and $\cos(\phi_d)$ in (11.40), and multiplying $1+\mu^2$ in

the numerator and denominator, the objective in (11.40) can be obtained by

$$\sigma_0^2 \frac{\alpha_1^{(k)}\mu^2 + \beta_1^{(k)}\mu + \gamma_1^{(k)}}{\alpha_2^{(k)}\mu^2 + \beta_2^{(k)}\mu + \gamma_2^{(k)}} \tag{11.41}$$

where $\alpha_1^{(k)} = (a_1^{(k)} - 2c_1^{(k)})$, $\beta_1^{(k)} = 4c_2^{(k)}$, $\gamma_1^{(k)} = (a_1^{(k)} + 2c_1^{(k)})$, $\alpha_2^{(k)} = (b_1^{(k)} - 2d_1^{(k)})$, $\beta_2^{(k)} = 4d_2^{(k)}$, $\gamma_2^{(k)} = (b_1^{(k)} + 2d_1^{(k)})$. Finally, the optimal solution $\mu^\star$ can be obtained by finding the real roots of the first-order derivative of the objective function, and evaluating it in these points. Thus, $\phi_d^\star = 2\tan^{-1}(\mu^\star)$, and $s_d^\star = e^{j\phi_d^\star}$. ■

11.3 NUMERICAL RESULTS

In this section, we provide some numerical examples to evaluate the performance of the developed method for the joint design of the radar code and the space-time receive filter. Let us assume a MIMO radar system with N_t transmit and N_r and receive antenna elements, which is assumed to be ULA with a half-wavelength interelement spacing. Unless otherwise stated, we consider the following scenario: $N_t = N_r = 5$, $L = 28$, $L_0 = 2$, $Q_0 = 1$, $\varepsilon = 0.05$. A moving target is also considered at $\theta_0 = 0^\circ$ with SNR $= 20$ dB and normalized Doppler $f_{d_0} = 0.25$ Hz, where the clutter to noise ratio (CNR) $= 20$ dB. For the stopping threshold, we define $z_k = f(\mathbf{s}^{(k)}, \mathbf{w}^{(k)})$, and we stop if $|z_{k+1} - z_k| < \tau$, where $\tau = 10^{-3}$. We assess the performance of the developed algorithm initializing by random phase and LFM. The term random-phase is used to indicate the family of the unimodular sequences that are defined by

$$x_{(n_t,l)} = e^{j\phi_{(n_t,l)}},\ n_t \in \{1, 2, \ldots, N_t\},\ l \in \{1, 2, \ldots, L\} \tag{11.42}$$

where $\phi_{(n_t,l)}$ are independent and identically distributed random variables with a uniform probability density function over $[0, 2\pi]$. For the LFM waveform, $\phi_{(n_t,l)}$ is also considered as follows

$$\phi_{(n_t,l)} = \pi \left(\frac{2n_t\,(l-1) + (l-1)^2}{N_t} \right) \tag{11.43}$$

where $n_t \in \{1, 2, \ldots, N_t\}$, $l \in \{1, 2, \ldots, L\}$ and the amplitude is divided to $\sqrt{LN_t}$.

In Figure 11.2, we assess the convergence behavior and constellation of the optimized sequences in the case of designing continuous and discrete phase waveforms ($M \in \{2, 8, 16\}$) versus the iteration number (k). Figure 11.2(a) depicts that the SINR values are monotonically increasing over the iterations, obtaining a value close to that defined by the target SNR without contaminating with clutter. Indeed, the optimized waveform and the corresponding receive filter could effectively remove the signal dependent interference effect while enhancing the SINR. More than 6 dB-improvement is observable in all the cases from the initial point, at this figure.

Figure 11.2(b) depicts the real and imaginary parts of the obtained obtained sequences of Figure 11.2(a), which indicates the devised algorithm has the advantage of designing M-ary phase shift keying (PSK) with high SINR values.

Figure 11.3 shows the performance of the developed algorithm for various values of target Doppler shift and spatial location. In this simulation, we assume that the normalized target Doppler shift is uniformly increased from 0 to 0.5 ($f_d \in [0, 0.5]$ Hz). Figure 11.3(a) indicates that when target and clutter are separated in the Doppler shift regions, the SINR improves. Indeed, for Doppler shifts greater than 0.1 Hz, the obtained SINR values are close to the upper bound. The clutter and noise covariance matrices in this figure are built for each of the Doppler shifts considered. As a result, different Doppler shifts cause a variation in the obtained SINR values. The proposed method, as shown in the figure, is a space-time adaptive filter that can eliminate clutter while increasing the SINR.

The same analysis is performed in Figure 11.3(b), but the target is located in $\theta_0 \in [0°, 25°]$. This graph shows that when $M = 8, 16$, the SINR values are almost constant and close to the upper bound.

In Figure 11.4, we evaluate the algorithm's performance in the presence of imperfect knowledge about the clutter covariance matrix. Let us assume that the uncertain clutter covariance matrix is $\widehat{\mathbf{R}}_c(\mathbf{s}) = \mathbf{R}_c(\mathbf{s}) + \beta \mathbf{U} \odot \mathbf{R}_c(\mathbf{s})$, where the entries of $\mathbf{U} \in \mathbb{C}^{N_r}$ are random variables uniformly distributed with zero mean and variance 1, and β is the uncertainty coefficient. We initialize the developed algorithms with 10 independent random phase sequences and report the averaged obtained SINR values. Figure 11.4 depicts that when $\beta \leq 0.02$, the loss in the obtained SINR values is less than 2.3 dB, for all the cases.

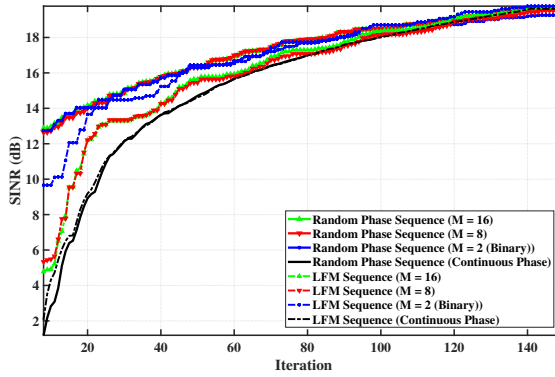
SINR (dB)
Iteration
Random Phase Sequence (M = 16)
Random Phase Sequence (M = 8)
Random Phase Sequence (M = 2 (Binary))
Random Phase Sequence (Continuous Phase)
LFM Sequence (M = 16)
LFM Sequence (M = 8)
LFM Sequence (M = 2 (Binary))
LFM Sequence (Continuous Phase)

(a)

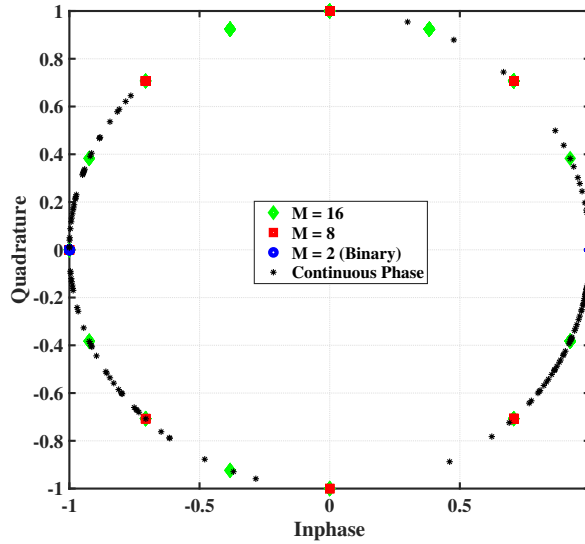

(b)

Figure 11.2. (a) Convergence behavior of the developed algorithm per iteration and (b) constellation of the optimized sequences.

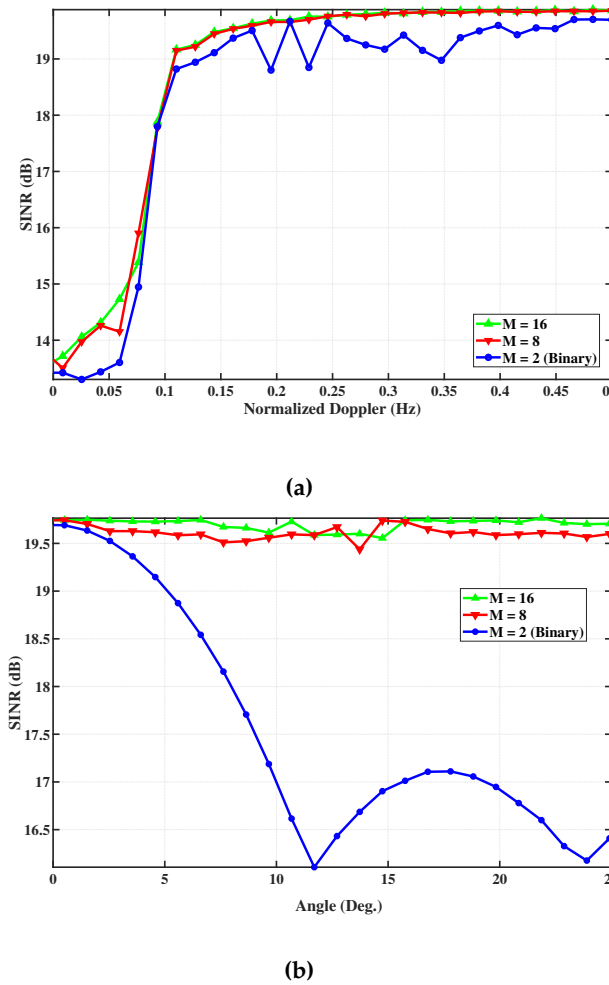

Figure 11.3. Behavior of the developed algorithm: (a) $f_{d_0} \in (0, 0.5)$Hz, (b) $\theta_0 \in (0°, 25°)$.

The performance of the developed algorithm is depicted by changing the alphabet size in Figure 11.5. This graph shows that the larger the alphabet, the better the performance in terms of SINR values. When compared to

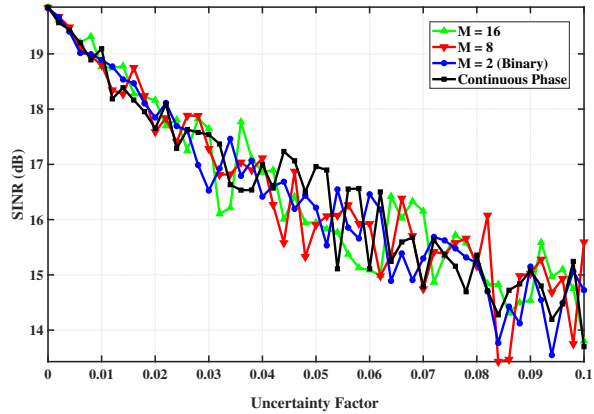

Figure 11.4. Obtained SINR for different uncertainty value (averaged over 10 independent trials).

Table 11.1
SINR Values, Required Number of Iterations for Convergence, and Run Time.

Method	**SINR** [dB]	**Cycle** (i)	**Run Time** (s)
CD (Binary)	8.66	2	0.33
CD (8-PSK)	8.58	2	1.23
CD (16-PSK)	8.72	3	3.75
CD (Continuous)	8.98	5	1.56
CA2 [7]	8.80	82	15.87
SOA2 [15]	8.80	24	35.08

the codes designed by the continuous phase algorithm, the loss is less than 0.04 (dB) when $M = 8$, and it is less than 0.07 (dB) in the worst case when $M = 2$ (binary case), indicating the quality of the devised algorithm for designing the discrete phase sequences. The results show that the developed algorithm is extremely capable in practical use cases where small alphabet size is required due to the implementation constraints.

Finally, comparing with the state of the art, Table 11.1 provides the SINR values, the number of required iterations for convergence, and the

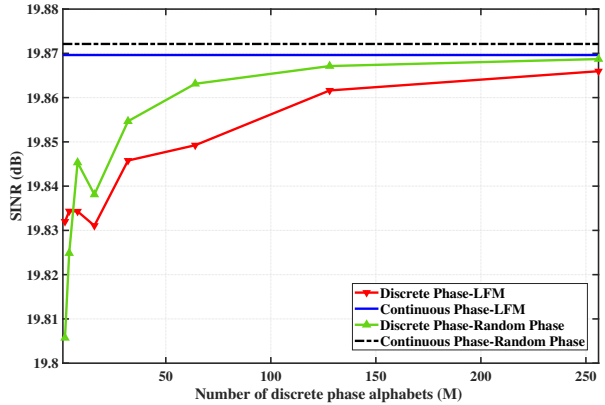

Figure 11.5. Obtained SINR values for different alphabet sizes.

run time when $N_t = 4$, $N_r = 8$, $L = 13$, $N_c = 1$, $A_c = 50$, $\varepsilon = 0.08$, SNR $= 10$ dB, CNR $= 25$ dB and moving target is located at $-\pi/180 \leq \theta_0 \leq \pi/180$ with $0.36 \leq f_{d_0} \leq 0.44$. We adopt the proposed method in [7], called CA2, and the method in [15], called SOA2, as the benchmarks. The initial sequence is the LFM waveform and the clutter distribution is similar to that of addressed in [7]. Further, to be fair in the comparison, we remove the similarity constraint from CA2 in [7]. The computation time reported in Table 11.1 was computed using a standard PC with a 3.3 GHz Core-i5 CPU and 8 GB RAM. The results indicate that the developed method achieves almost similar performance in terms of SINR values with the counterparts, while converges faster and has smaller computational time.

11.4 CONCLUSION

In this chapter, we developed an efficient algorithm based on the CD framework to address the nonconvex optimization problem of designing a continuous/discrete phase sequence and a space-time receive filter in cognitive MIMO radar systems. The obtained problem is nonconvex, but the developed algorithm can handle it efficiently. In the simulations, the developed algorithm's performance was evaluated in terms of convergence, target Doppler shift and direction, clutter uncertainty, different alphabet sizes, and computational time. The results indicated that even when the alphabet size is limited to binary, the obtained set of discrete phase sequences can improve monotonically SINR values.

References

[1] W. Melvin, "A STAP overview," *IEEE Aerospace and Electronic Systems Magazine*, vol. 19, no. 1, pp. 19–35, 2004.

[2] M. M. Feraidooni, D. Gharavian, S. Imani, and M. Alaee-Kerahroodi, "Designing M-ary sequences and space-time receive filter for moving target in cognitive MIMO radar systems," *Signal Processing*, vol. 174, p. 107620, 2020.

[3] J. Qian, M. Lops, L. Zheng, X. Wang, and Z. He, "Joint system design for coexistence of MIMO radar and MIMO communication," *IEEE Transactions on Signal Processing*, vol. 66, no. 13, pp. 3504–3519, 2018.

[4] A. Aubry, A. De Maio, and M. M. Naghsh, "Optimizing radar waveform and Doppler filter bank via generalized fractional programming," *IEEE Journal of Selected Topics in Signal Processing*, vol. 9, no. 8, pp. 1387–1399, 2015.

[5] A. Aubry, A. DeMaio, A. Farina, and M. Wicks, "Knowledge-aided (potentially cognitive) transmit signal and receive filter design in signal-dependent clutter," *IEEE Transactions on Aerospace and Electronic Systems*, vol. 49, no. 1, pp. 93–117, 2013.

[6] S. M. Karbasi, A. Aubry, V. Carotenuto, M. M. Naghsh, and M. H. Bastani, "Knowledge-based design of space–time transmit code and receive filter for a multiple-input–multiple-output radar in signal-dependent interference," *IET Radar, Sonar Navigation*, vol. 9, no. 8, pp. 1124–1135, 2015.

[7] G. Cui, X. Yu, V. Carotenuto, and L. Kong, "Space-time transmit code and receive filter design for colocated MIMO radar," *IEEE Transactions on Signal Processing*, vol. 65, pp. 1116–1129, Mar. 2017.

[8] A. Aubry, A. De Maio, B. Jiang, and S. Zhang, "Ambiguity function shaping for cognitive radar via complex quartic optimization," *IEEE Transactions on Signal Processing*, vol. 61, no. 22, pp. 5603–5619, 2013.

[9] U. Niesen, D. Shah, and G. W. Wornell, "Adaptive alternating minimization algorithms," *IEEE Transactions on Information Theory*, vol. 55, no. 3, pp. 1423–1429, 2009.

[10] J. Capon, "High-resolution frequency-wavenumber spectrum analysis," *Proceedings of the IEEE*, vol. 57, no. 8, pp. 1408–1418, 1969.

[11] M. Alaee-Kerahroodi, M. Modarres-Hashemi, and M. M. Naghsh, "Designing sets of binary sequences for MIMO radar systems," *IEEE Transactions on Signal Processing*, vol. 67, pp. 3347–3360, July 2019.

[12] M. Alaee-Kerahroodi, A. Aubry, A. De Maio, M. M. Naghsh, and M. Modarres-Hashemi, "A coordinate-descent framework to design low PSL/ISL sequences," *IEEE Transactions on Signal Processing*, vol. 65, pp. 5942–5956, Nov. 2017.

[13] M. Alaee-Kerahroodi, M. Modarres-Hashemi, M. M. Naghsh, B. Shankar, and B. Ottersten, "Binary sequences set with small ISL for MIMO radar systems," in *2018 26th European Signal Processing Conference (EUSIPCO)*, pp. 2395–2399, 2018.

[14] B. Chen, S. He, Z. Li, and S. Zhang, "Maximum block improvement and polynomial optimization," *SIAM Journal on Optimization*, vol. 22, pp. 87–107, Jan 2012.

[15] G. Cui, H. Li, and M. Rangaswamy, "MIMO radar waveform design with constant modulus and similarity constraints," *IEEE Transactions on Signal Processing*, vol. 62, no. 2, pp. 343–353, 2014.

Chapter 12

Cognitive Radar: Design and Implementation

Spectrum congestion has become an imminent problem with a multitude of radio services like wireless communications, active RF sensing, and radio astronomy vying for the scarce usable spectrum. Within this conundrum of spectrum congestion, radars need to cope with simultaneous transmissions from other RF systems. Given the requirement for large bandwidth in both systems, spectrum sharing with communications is a scenario that is very likely to occur [1–3]. While elaborate allocation policies are in place to regulate the spectral usage, the rigid allocations result in inefficient spectrum utilization when the subscription is sparse. In this context, smart spectrum utilization offers a flexible and a fairly promising solution for improved system performance in the emerging smart sensing systems [4].

Two paradigms, cognition and MIMO have been central to the prevalence of smart sensing systems. Herein, the former concept offers ability to choose intelligent transmission strategies based on prevailing environmental conditions and a prediction of the behavior of the emitters in the scene, in addition to the now-ubiquitous receiver adaptation [5–16]. The second approach, by including spatial diversity, provides the cognition manager with a range of transmission strategies to choose from; these strategies exploit waveform diversity and the available degrees of freedom [17, 18]. Smart sensing opens up the possibility of coexistence of radar systems with incumbent communication systems in the earlier mentioned spectrum sharing instance. A representative coexistence scenario is illustrated in Figure 12.1,

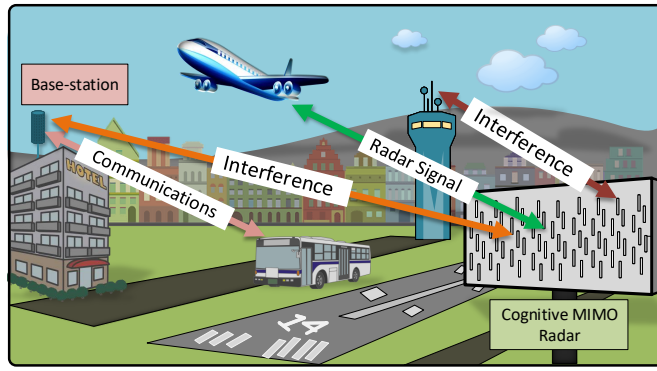

Figure 12.1. An illustration of coexistence between radar and communications. The radar aims at detecting the airplane, without creating interference to the communication links, and similarly avoiding interference from the communication links.

where an understanding of the environment is essential for seamless operation of radar systems while opportunistically using the spectrum allocated to communication [19–21].

In this chapter, we design a cognitive MIMO radar system towards fostering coexistence with communications; it involves spectrum sensing and transmission strategies adapted to the sensed spectrum while accomplishing the radar tasks and without degrading the performance of the communications. Particularly, a set of transmit sequences is designed to focus the emitted energy in the bands suggested by the spectrum sensing module while limiting the out-of-band interference. The waveforms, along with the receive processing, are designed to enhance the radar detection performance. The designed system is then demonstrated for the representative scenario of Figure 11.1 using a custom-built software-defined radio (SDR)-based prototype developed on USRPs[1] from national instruments (NI) [22, 23]. These USRPs operate at sub-6-GHz frequencies with a maximum instantaneous bandwidth of 160 MHz.

1 USRPs are inexpensive programmable radio platforms used in wireless communications and sensing prototyping, teaching, and research.

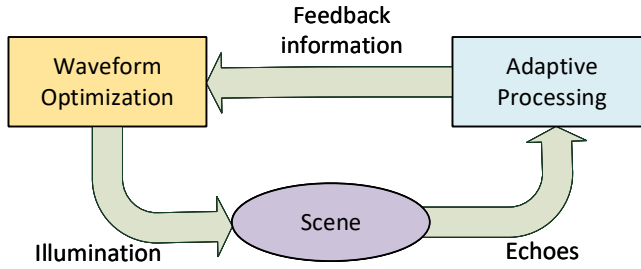

Figure 12.2. Sequence of operation in a cognitive radar system: receiving echoes from the scene and calculating environmental characteristics, performing adaptive processing, and then waveform optimization.

12.1 COGNITIVE RADAR

The scenario under consideration in this chapter is one where a radar system desires to operate in the presence of interfering signals that are generated by communication systems. The radar system will benefit from using as much bandwidth as possible. This will improve the systems range resolution and accuracy, but requires the radar system to avoid the frequency band occupied by communication signals for two reasons:

1. To enhance the performance of the communications that requires the radar system does not interfere with the communication signals.
2. To improve the sensitivity of the radar system for detecting targets with very small SINR values. Indeed, by removing the communications interference, the radar SINR will be enhanced and thus the sensitivity of the radar system will be improved.

Given the scenario under consideration, the cognitive radar requires scanning the environment, estimating the environmental parameters, and adapting the transceiver accordingly. These three steps are the high-level structure for a cognitive loop or perception/action cycle (PAC) that are indicated in Figure 12.2. Thus, the first important step is to sense the RF spectrum. Once RF spectral information has been collected, then the interfering signals needs to be characterized and some specifications such as their center frequencies and bandwidths needs to be extracted. After that, radar must choose how to adapt given the obtained information from the

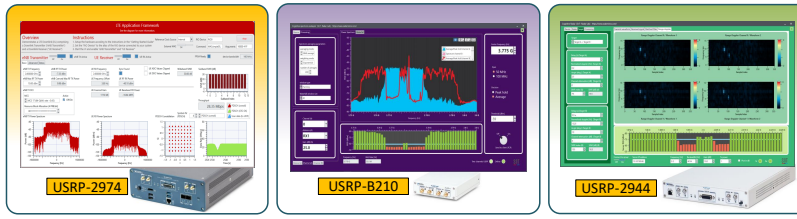

(a) (b) (c)

Figure 12.3. Application frameworks forming the prototype (a) LTE application developed by NI (b) spectrum sensing, and (c) cognitive MIMO radar applications developed in this chapter.

interference. In this step, waveform optimization can be a solution, which provides the optimal solution for the given constraints, provided that it can be performed before any new change in the environmental parameters. RF spectrum sensing, interference detection, and optimization of the radar transmit waveform correspond directly to steps 1, 2 and 3 of the basic PAC outlined in Figure 12.2.

12.2 THE PROTOTYPE ARCHITECTURE

The prototype consists of three application frameworks as depicted in Figure 12.3: (a) Long-Term evolution (LTE) application framework, (b) spectrum sensing application, and (c) cognitive MIMO radar application). A photograph of the proposed coexistence prototype is depicted in Figure 12.4. The hardware (HW) consists of three main modules: (1) USRP 2974 for LTE communications, (2) USRP B210 for spectrum sensing, and, (3) USRP 2944R for cognitive MIMO radar with specifications given in Table 12.1. USRPs are used for the transmission and reception of the wireless RF signals and the Rohde and Schwarz spectrum analyzer is used for the validation of the transmission.

12.2.1 LTE Application Framework

The LabVIEW LTE Application Framework (Figure 12.3(a)) is an add-on software that provides a real-time physical layer LTE implementation in the

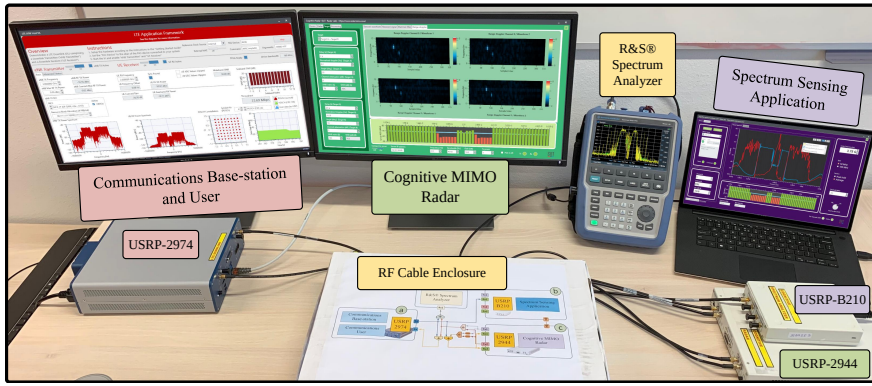

Figure 12.4. A photograph of the proposed coexistence prototype. The photo shows communication base station (BS) and user, spectrum sensing, and cognitive MIMO radar systems.

form of an open and modifiable source code [24]. The framework complies with a selected subset of the 3GPP LTE which includes a closed-loop over-the-air (OTA) operation with channel state and ACK/NACK feedback, 20-MHz bandwidth, physical downlink shared channel (PDSCH), and physical downlink control channel (PDCCH), up to 75-Mbps data throughput, FDD and TDD configuration 5-frame structure, QPSK, 16-QAM, and 64-QAM modulation, channel estimation, and zero-forcing channel equalization. The framework also has a basic MAC implementation to enable packet-based data transmission along with a MAC adaptation framework for rate adaptation. Since the NI-USRP 2974 has two independent RF chains and the application framework supports single antenna links, we emulated both the BS and communications user on different RF chains of the same USRP.

12.2.2 Spectrum Sensing Application

To perform the cognition and continuously sensing the environment, we developed an application based on LabView NXG 3.1 that connects to Ettus USRP B2xx (Figure 12.3(b)). The developed application is flexible in terms of changing many parameters on the fly, for example, averaging modes, window type, energy detection threshold, and the USRP configurations (gain, channel, start frequency). In the developed application, the center

Table 12.1
Hardware Characteristics of the Proposed Prototype

Parameters	2974/2944R	B210
Frequency range	10 MHz -6 GHz	70 MHz -6 GHz
Max. output power	20 dBm	10 dBm
Max. input power	$+10$ dBm	-15 dBm
Noise figure	$5-7$ dB	8 dB
Bandwidth	160 MHz	56 MHz
DACs	200 MS/s, 16 bits	61.44 MS/s, 12 bits
ADCs	200 MS/s, 14 bits	61.44 MS/s, 12 bits

frequency can be adjusted to any arbitrary value in the interval 70 MHz to 6 GHz, and the span bandwidth can be selected from the two values of 50 MHz and 100 MHz.[2] The obtained frequency chart is being transferred through a network connection (LAN/Wi-Fi) to the cognitive MIMO radar application.

12.2.3 MIMO Radar Prototype

Figure 12.5 depicts a snapshot of the developed cognitive MIMO radar application framework, when the licensed band 3.78 GHz with 40 MHz bandwidth was used for transmission.[3] All the parameters related to the radar waveform, processing units, and targets can be changed and adjusted during the operation of the radar system. The MIMO radar application was developed based on LabView NXG 3.1 and was connected to the HW platform NI-USRP 2944R. This USRP consists of a 2×2 MIMO RF transceiver with a programmable Kintex-7 field programmable gate array (FPGA). The developed application is flexible in terms of changing the transmit waveform on-the-fly, such that it can adapt with the environment. Table 12.2 details the features and flexibilities of the developed application. The center frequency can be adjusted to any arbitrary value in the interval

2 Note that USRP B2xx provides 56 MHz of real-time bandwidth by using AD9361 RFIC direct-conversion transceiver. However, the developed application can analyze larger bandwidths by sweeping the spectrum with efficient implementation.

3 SnT has an experimental license to use 3.75 to 3.8 GHz for 5G research in Luxembourg.

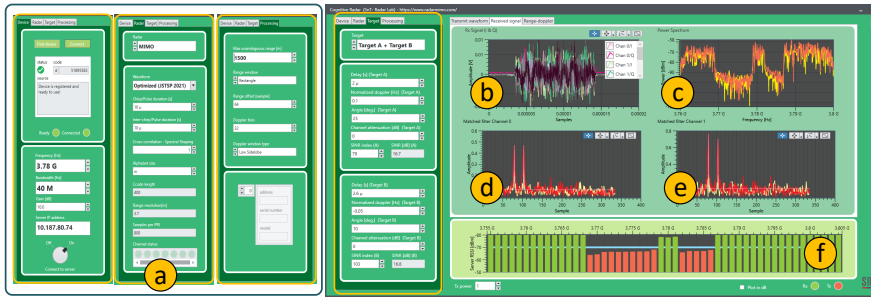

Figure 12.5. A snapshot of the developed cognitive MIMO radar application. (a) Settings for device, radar, and processing parameters. (b) I and Q signals of two receive channels. (c) Spectrum of the received signals in two receive channels. (d) Matched filters to two transmitting waveforms at the first receive channel. (e) Matched filters to two transmitting waveforms at the second receive channel. (f) Received information from the energy detector of the spectrum sensing application.

70 MHz to 6 GHz, and the radar bandwidth can be adjusted to any arbitrary value in the interval 1 MHz to 80 MHz.

The block diagram of the transmit units of the developed cognitive MIMO radar is depicted in Figure 12.6. Note that the application is connected through a network (LAN/Wi-Fi) to the spectrum sensing application to receive a list of occupied frequency bands. Based on this information, the radar optimizes the transmitting waveforms. The design algorithm for the waveform optimization is described next.

12.2.3.1 Waveform Optimization

To perform waveform optimization in our developed cognitive radar prototype, we utilize the CD framework wherein a multi variable optimization problem can be sequentially solved as a sequence of (potentially easier) single variable optimization problems (see Chapter 5 for more details). The benefits of using a CD framework for this prototype are listed as follows:

1. CD provides a sequential solution for the optimization problem, which typically converges fast (comparing with the other optimization frameworks). Further, initial iterations of the CD algorithm generally provide a

Table 12.2
Characteristics of the Developed Cognitive MIMO Radar

Parameters	**MIMO radar**
Operating bandwidth	$1-80$ MHz
Window type	Rectangle, Hamming, Blackman, etc.
Averaging mode	Coherent integration (FFT)
Processing units	Matched filtering, range-Doppler processing
Transmitting waveforms	Random-polyphase, Frank, Golomb, random-binary, Barker, m-sequence, Gold, Kasami, up-LFM, down-LFM, and the optimized sequences

deep decrement in the objective value. Consequently, based on the limited available time for having a stationary environment, CD can be terminated after a few numbers of iterations.

2. CD converts a multivariable objective function to a sequence of single-variable objective functions. As a result, the solutions of single-variable problems are generally less complex than the original problem. This is helpful for real-time implementation of the optimization algorithm, where the algorithm does not need to do complex operations in every iteration.

Using the advantages of the CD framework, we perform the waveform optimization given the limited time available for the scene to remain stationary. This time in principle can be as small as one CPI time or it can be adjusted depending on the dynamic of the scene and the decision of the designer.

Let us now discuss in detail the waveform design problem related to the scenario we pursued in this chapter. We consider a colocated narrowband MIMO radar system, with M transmit antennas, each transmitting a sequence of length N in the fast time domain. Let the matrix $\boldsymbol{X} \in \mathbb{C}^{M\times N} \triangleq [\mathbf{x}_1^T, \ldots, \mathbf{x}_M^T]^T$ denote the transmitted set of sequences in baseband, where the vector $\mathbf{x}_m \triangleq [x_{m,1}, \ldots, x_{m,N}]^T \in \mathbb{C}^N$ indicates the N samples of the m^{th} transmitter ($m \in \{1, \ldots, M\}$). We aim to design a transmit set of sequences that have small cross-correlation among each other, while each of the sequences has a desired spectral behavior. To this end, in the following, we introduce the spectral integrated level ratio (SILR) and integrated cross

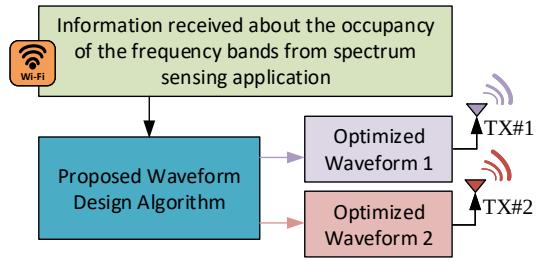

Figure 12.6. Block diagram of the transmitter in the developed cognitive MIMO radar application. A list of occupied frequency bands will be determined by the spectrum sensing application. Based on this information, the proposed design algorithm optimizes the transmit waveforms.

correlation level (ICCL) metrics and subsequently the optimization problem to handle them.

Let $\boldsymbol{F} \triangleq [\mathbf{f}_0, \ldots, \mathbf{f}_{N-1}] \in \mathbb{C}^{N\times N}$ denote the DFT matrix, where $\mathbf{f}_k \triangleq [1, e^{j\frac{2\pi k}{N}}, \ldots, e^{j\frac{2\pi k(N-1)}{N}}]^T \in \mathbb{C}^N,\ k = \{0, \ldots, N-1\}$. Let $\mathcal{V}$ and $\mathcal{U}$ be the desired and undesired discrete frequency bands for MIMO radar, respectively. These two sets satisfy $\mathcal{V} \cup \mathcal{U} = \{0, \ldots, N-1\}$ and $\mathcal{V} \cap \mathcal{U} = \emptyset$. We define SILR as

$$g_s(\boldsymbol{X}) \triangleq \frac{\sum_{m=1}^{M} \left\| \mathbf{f}_k^{\dagger} \mathbf{x}_m \right\|^2 | k \in \mathcal{U}}{\sum_{m=1}^{M} \left\| \mathbf{f}_k^{\dagger} \mathbf{x}_m \right\|^2 | k \in \mathcal{V}} \tag{12.1}$$

which is the energy of the radar waveform interfering with other incumbent services (like communications) relative to the energy of transmission in the desired bands. Optimizing the above objective function may shape the spectral power of the transmitting sequence and satisfy a desired mask in the spectrum. However, in a MIMO radar, it is necessary to separate the transmitting waveforms in the receiver to investigate the waveform diversity, which ideally requires orthogonality among the transmitting sequences. To make this orthogonality feasible by CDM, we need to transmit a set of sequences that have small cross-correlations among each other. The aperiodic

cross-correlation[4] of $\mathbf{x}_m$ and $\mathbf{x}_{m'}$ is defined as

$$r_{m,m'}(l) = \sum_{n=1}^{N-l} x_{m,n} x^*_{m',n+l} \tag{12.2}$$

where $m \neq m' \in \{1, \ldots, M\}$ are indices of the transmit antennas and $l \in \{-N+1, \ldots, N-1\}$ denotes the cross-correlation lag. We define ICCL as

$$\widetilde{g}_c(\boldsymbol{X}) \triangleq \sum_{m=1}^{M} \sum_{\substack{m'=1 \\ m' \neq m}}^{M} \sum_{l=-N+1}^{N-1} |r_{m,m'}(l)|^2 \tag{12.3}$$

which can be used to promote the orthogonality among the transmitting sequences.

Problem Formulation

We aim to design set of sequences with small SILR and ICCL values. To this end, we consider the following optimization problem,

$$\begin{cases} \underset{\boldsymbol{X}}{\text{minimize}} & g_s(\boldsymbol{X}), g_c(\boldsymbol{X}) \\ \text{subject to} & C_1 \text{ or } C_2 \end{cases} \tag{12.4}$$

where $g_c(\boldsymbol{X}) = \frac{1}{(2MN)^2} \widetilde{g}_c(\boldsymbol{X})$ is the scaled version of the ICCL, defined in (12.3). By defining $\Omega_\infty = [0, 2\pi)$, and $\Omega_L = \left\{0, \frac{2\pi}{L}, \ldots, \frac{2\pi(L-1)}{L}\right\}$, then

$$C_1 \triangleq \{\boldsymbol{X} \mid x_{m,n} = e^{j\phi_{m,n}}, \phi_{m,n} \in \Omega_\infty\} \tag{12.5}$$

and

$$C_2 \triangleq \{\boldsymbol{X} \mid x_{m,n} = e^{j\phi_{m,n}}, \phi_{m,n} \in \Omega_L\} \tag{12.6}$$

indicate constant modulus constraint and discrete phase constraints, respectively.

Problem (12.4) is a biobjective optimization problem in which a feasible solution that minimizes both objective functions may not exist [26, 27].

4 In this chapter, we provide the solution to the design of sequences with good aperiodic correlation functions. However, following the same steps as indicated in [25], the design procedure can be extended to obtain sequences with good periodic correlation properties.

Scalarization is a well-known technique that converts the biobjective optimization problem to a single objective problem by replacing a weighted sum of the objective functions. Using this technique, the following Pareto-optimization problem will be obtained

$$\mathcal{P}\begin{cases}\min\limits_{\boldsymbol{X}} & g(\boldsymbol{X}) \triangleq \theta g_s(\boldsymbol{X}) + (1-\theta) g_c(\boldsymbol{X}) \\ s.t. & C_1 \text{ or } C_2\end{cases} \tag{12.7}$$

The coefficient $\theta \in [0,1]$ is a weight factor that effects trade-off between SILR and ICCL. In (12.7), $g_s(\boldsymbol{X})$ is a fractional quadratic function while $g_c(\boldsymbol{X})$ is quartic function, both with multiple variables. Further, both C_1 and C_2 constraints are not an affine set, besides C_2 is noncontinuous and nondifferentiate set. Therefore, we encounter a nonconvex, multivariable optimization problem [26, 28].

The Optimization Method

Let us assume that $x_{t,d}$ is the only variable in code matrix $\mathbf{X}$ at (i)th iteration of the CD algorithm, where the other entries are kept fixed and stored in the matrix $\boldsymbol{X}^{(i)}_{-(t,d)}$ defined by

$$\boldsymbol{X}^{(i)}_{-(t,d)} \triangleq \begin{bmatrix} x^{(i)}_{1,1} & \cdots & \cdots & \cdots & \cdots & \cdots & x^{(i)}_{1,N} \\ \vdots & \vdots & \vdots & \vdots & \vdots & \vdots & \vdots \\ x^{(i)}_{t,1} & \cdots & x^{(i)}_{t,d-1} & 0 & x^{(i-1)}_{t,d+1} & \cdots & x^{(i-1)}_{t,N} \\ \vdots & \vdots & \vdots & \vdots & \vdots & \vdots & \vdots \\ x^{(i-1)}_{M_t,1} & \cdots & \cdots & \cdots & \cdots & \cdots & x^{(i-1)}_{M_t,N} \end{bmatrix}$$

The resulting single-variable objective function can be written as (see Appendix 12A)

$$g(x_{t,d}, \boldsymbol{X}^{(i)}_{-(t,d)}) = \theta \frac{a_0 x_{t,d} + a_1 + a_2 x^*_{t,d}}{b_0 x_{t,d} + b_1 + b_2 x^*_{t,d}} + (1-\theta)\left(c_0 x_{t,d} + c_1 + c_2 x^*_{t,d}\right) \tag{12.8}$$

where the coefficients a_i, b_i, and c_i depend on $\boldsymbol{X}^{(i)}_{-(t,d)}$ (with $t \in \{1,\ldots,M\}$ and $d \in \{1,\ldots,N\}$) and are specified in Appendix 12A. By considering

$g(x_{t,d}, \boldsymbol{X}^{(i)}_{-(t,d)})$ as the objective function of the single variable optimization problem, and substituting[5] $x_{t,d} = e^{j\phi}$, the optimization problem at the i^{th} iteration of the CD algorithm is

$$\mathcal{P}^{(i)}_{\phi} \begin{cases} \min\limits_{\phi} & \theta \dfrac{a_0 e^{j\phi} + a_1 + a_2 e^{-j\phi}}{b_0 e^{j\phi} + b_1 + b_2 e^{-j\phi}} + (1-\theta)\left(c_0 e^{j\phi} + c_1 + c_2 e^{-j\phi}\right) \\ s.t. & C_1 \text{ or } C_2 \end{cases} \tag{12.9}$$

Assume that the optimal phase value for the (t,d)th element of $\boldsymbol{X}$ is $\phi^{\star}$. By resolving (12.9), we find this value, leading to the optimal code entry $x^{\star}_{t,d} = e^{j\phi^{\star}}$. We then perform this optimization for all the entries in the code matrix $\boldsymbol{X}$. After optimizing all the code entries ($t = 1, \ldots, M$, and $d = 1, \ldots, N$), a new iteration will be started, provided that the stopping criteria are not met. A summary of the devised optimization method is reported in Algorithm 12.1.

Algorithm 12.1: Waveform Design for Spectral Shaping with Small Cross-Correlation Values

Result: Optimized code matrix $\boldsymbol{X}^{\star}$
initialization;
for $i = 0, 1, 2, \ldots$ **do**
  for $t = 1, 2, \ldots, M$ **do**
    for $d = 1, 2, \ldots, N$ **do**
      Find $\phi^{\star}$ by solving $\mathcal{P}^{(i)}_{\phi}$;
      Set $x^{\star}_{t,d} = e^{j\phi^{\star}}$;
      Set $\boldsymbol{X}^{(i)} = \boldsymbol{X}^{(i)}_{-(t,d)}|_{x_{t,d}=x^{(i)}_{t,d}}$;
    end
  end
  Stop if convergence criterion is met;
end

5 For the sake of notational simplicity, we use ϕ instead of $\phi_{t,d}$ in the rest of this chapter.

Solution Under Continuous Phase Constraint

The next step to finalize the waveform design part is to provide a solution to problem $\mathcal{P}_{\phi}^{(i)}$. Let us define

$$g(\phi) = \theta \frac{a_0 e^{j\phi} + a_1 + a_2 e^{-j\phi}}{b_0 e^{j\phi} + b_1 + b_2 e^{-j\phi}} + (1-\theta)\left(c_0 e^{j\phi} + c_1 + c_2 e^{-j\phi}\right) \tag{12.10}$$

Since $g(\phi)$ is a differentiable function with respect to the variable ϕ, the critical points of (12.9) contain the solutions to $\frac{d}{d\phi} g(\phi) = 0$. By standard mathematical manipulations, the derivative of $g(\phi)$ can be obtained as

$$g'(\phi) = \frac{e^{j3\phi} \sum_{p=0}^{6} q_p e^{jp\phi}}{(b_0 e^{j\phi} + b_1 + b_2 e^{-j\phi})^2} \tag{12.11}$$

where the coefficients q_p are given in Appendix 12B. Using the slack variable $z \triangleq e^{-j\phi}$, the critical points can be obtained by obtaining the roots of a six-degree polynomial of $g'(z) \triangleq \sum_{p=0}^{6} q_p z^p = 0$. Let us assume that z_p, $p = \{1, \ldots, 6\}$ are the roots of $g'(z)$. Hence, the critical points of (12.9) can be expressed as $\phi_p = j \ln z_p$. Since ϕ is a real variable, we seek only the real extrema points. Therefore, the optimum solution for ϕ is

$$\phi_c^{\star} = \arg\min_{\phi} \left\{ g(\phi) | \phi \in \phi_p, \Im(\phi_p) = 0 \right\} \tag{12.12}$$

Subsequently, the optimum solution for is $x_{t,d} = e^{j\phi_c^{\star}}$.[6]

Solution Under Discrete Phase Constraint

In this case, the feasible set is limited to a set of L phases. Thus, the objective function with respect to the indices of Ω_L can be written as

$$g(l) = \theta \frac{\sum_{n=0}^{2} a_n e^{-j\frac{2\pi nl}{L}}}{\sum_{n=0}^{2} b_n e^{-j\frac{2\pi nl}{L}}} + (1-\theta) e^{\frac{j2\pi l}{L}} \sum_{n=0}^{2} c_n e^{-j\frac{2\pi nl}{L}} \tag{12.13}$$

6 Since $g(\phi)$ is a function of $\cos\phi$ and $\sin\phi$, it is periodic, real, and differentiable. Therefore, it has at least two extrema, and hence its derivative has at least two real roots. As a result, in each single variable update, the problem has a solution and never becomes infeasible.

where $l \in \{0, \ldots, L-1\}$. The summation term in the numerator and denominator in (12.13) is exactly the definition of the L-point DFT of sequences $[a_0, a_1, a_2]$, $[b_0, b_1, b_2]$, and $[b_0, b_1, b_2]$, respectively. Therefore, $g(l)$ can be written as

$$g(l) = \theta \frac{\mathcal{F}_L\{a_0, a_1, a_2\}}{\mathcal{F}_L\{b_0, b_1, b_2\}} + (1-\theta)\boldsymbol{h} \odot \mathcal{F}_L\{c_0, c_1, c_2\} \tag{12.14}$$

where $\boldsymbol{h} = [1, e^{-j\frac{2\pi}{L}}, \ldots, e^{-j\frac{2\pi(L-1)}{L}}]^T \in \mathbb{C}^L$, and $\mathcal{F}_L$ is the L-point DFT operator. The current function is valid only for $L > 2$. According to the periodic property of DFT, for binary $g(l)$ can be written as

$$g(l) = \theta \frac{\mathcal{F}_L\{a_0 + a_2, a_1\}}{\mathcal{F}_L\{b_0 + b_2, b_1\}} + (1-\theta)\boldsymbol{h} \odot \mathcal{F}_L\{c_0 + c_2, c_1\} \tag{12.15}$$

Finally, $l^\star = \arg \min_{l=1,\ldots,L} \{g(l)\}$, and $\phi_d^\star = \frac{2\pi(l^\star - 1)}{L}$.

12.2.3.2 Adaptive Receive Processing

The block diagram of the receive units of the developed cognitive MIMO radar is depicted in Figure 12.7. The receiver starts sampling by a trigger that is received by transmitter, indicating the start of transmission (possibility of working in continuous wave (CW) mode is supported). In each receive channel, two filters matched to each of the transmitting waveforms is implemented using the fast convolution technique. Four range-Doppler plots corresponding to the receive channels and transmitting waveforms are obtained by implementing FFT in the slow-time dimension.

12.3 EXPERIMENTS AND RESULTS

In this section, we present experiments conducted using the developed prototype and analyze the HW results. For the practical applicability of our methods and verification of the simulation, we established all the connections shown in Figure 12.8 using RF cables and splitters/combiners, and measured the performance in a controlled environment.

Passing the transmitting waveforms through the 30-dB attenuators as indicated in Figure 12.8, a reflection will be generated; this will be used to

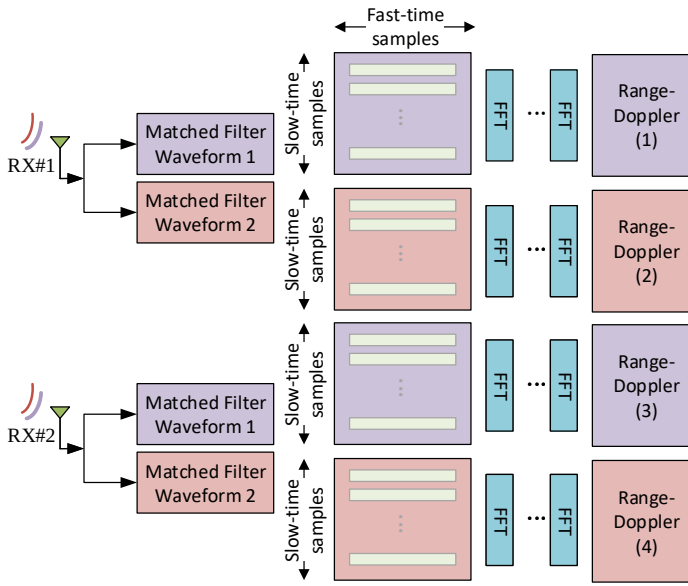

Figure 12.7. Block diagram of the receiver of the developed cognitive MIMO radar application. The coefficients of the matched filter will be updated for appropriate matched filtering in the fast time dimension. Consequently, the modulus of the range-Doppler plots will be calculated after taking FFT in the slow time dimension.

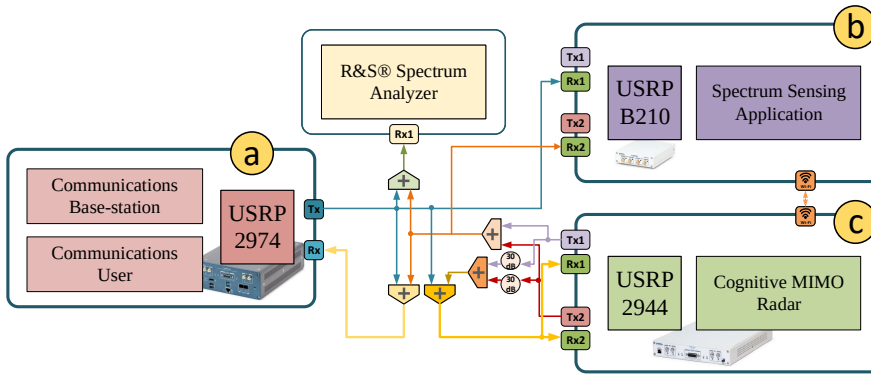

Figure 12.8. The connection diagram of the proposed coexistence prototype. In (a), a downlink communication between the BS and the user was established using the USRP 2974. The custom-built spectrum sensing program was operated on the USRP B210 which is indicated in (b). The custom-built cognitive radar application was run on the USRP 2944R in (c). In order to establish a connected connection and ensure repeatability of the experiment results, splitters and combiners are utilized.

Table 12.3
Radar Experiment Parameters

Parameters	**Value**
Center frequency	2 GHz
Real-time bandwidth	40 MHz
Transmit and receive channels	2×2
Transmit power	10 dBm
Duty cycle	50%
Transmit code length	400
Pulse repetition interval	20 μs

Table 12.4
Target Experiment Parameters

Parameters	**Target 1**	**Target 2**
Range delay	$2\mu s$	$2.6\mu s$
Normalized Doppler	0.2 Hz	-0.25 Hz
Angle	25 deg	15 deg
Attenuation	30 dB	35 dB

generate the targets, contaminated with the communications interference. The received signal in this way will be further shifted in time, frequency, and spatial direction to create the simulated targets. These targets will be detected after calculating the absolute values of the range-Doppler maps.

The transmitting waveforms can be selected based on the options in Table 12.2 or obtained based on Algorithm 12.1. When executing the application, input parameters to optimize the waveforms pass from the graphical user interface (GUI) to MATLAB, and the optimized set of sequences are passed to the application through the GUI. The other processing blocks of the radar system including matched filtering, Doppler processing, and scene generation are developed in the LabView G dataflow application. Tables 12.3 and 12.4 summarize the parameters used for radar and targets in this experiment.

For the LTE communications, we established the downlink between a BS and one user. Nonetheless, the experiments can be also be performed

Table 12.5
Communications Experiment Parameters

Parameters	**Value**
Communication MCS	MCS0 (QPSK 0.12) MCS10 (16QAM 0.33) MCS17 (64QAM 0.43)
Center frequency (Tx and Rx)	2 GHz
Bandwidth	20 MHz

with uplink LTE as well as a bidirectional LTE link. LabVIEW LTE framework offers the possibility to vary the modulation and coding schemes (MCS) of PDSCH from 0 to 28 where the constellation size goes from QPSK to 64QAM [29]. LTE uses PDSCH for the transport of data between the BS and the user. Table 12.5 indicates the experimental parameters used in our test set-up for the communications.

In Figure 12.9, we assess the convergence behavior of the proposed algorithm in the cases $M = 4$ and $N = 64$ for the first 100 iterations. It can be observed that, given a few number of iterations, the objective value decreases significantly. This behavior is the same for different values of θ and also under C_1 or C_2 constraints. Note that the optimized solution under C_1 constraints obtain lower objective values compared to the solution of the C_2 constraint, due to more degrees of freedom in selecting the alphabet size.

Let us now terminate the optimization procedure at iteration 10 and see the performance of the obtained waveform at this iteration, compared with SHAPE [30], which is an algorithm for shaping the spectrum of the waveforms using spectral-matching framework. Figure 12.10 shows spectral behavior and cross-correlation levels of the optimized waveforms in the cases $M = 2$, $N = 400$, and $\mathcal{S} = [0.25, 0.49] \cup [0.63, 0.75]$ Hz. It is observable that by choosing $\theta = 0$, the optimized waveforms are not able to put notches on the undesired frequencies. By increasing θ, the notches will appear gradually and in case of $\theta = 1$, we obtain the deepest notches. However, when $\theta = 1$, the cross-correlation is at the highest level, which decreases with θ. In the case of $\theta = 0$, we obtain the best orthogonality. Therefore, by choosing an appropriate value of θ, one can make a good trade-off between spectral shaping and orthogonality. For instance, choosing $\theta = 0.75$ is able to put a

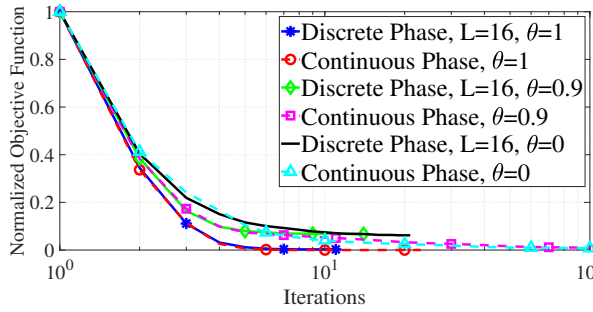

Figure 12.9. Convergence behavior of the proposed method under continuous and discrete phase constraints for different θ values ($M = 4$, $N = 64$, and $L = 16$).

null level around 50 dB (see Figure 12.10(a)), while having a relatively good cross-correlation level (see Figure 12.10(b)).

Based on the aforementioned analysis, we set $\theta = 0.75$ and always terminate the algorithm after 10 iterations for optimizing radar waveform. In this case, we show the impact of optimized radar waveform on a coexistence with a communications scenario with the experiment. We use the experiment parameters reported in Tables 12.3 and 12.5 for radar and communications, respectively. According to these tables, we utilize the radar with a 50% duty cycle. By transmitting a set of $M = 2$ waveforms with length $N = 400$, radar transmissions will occupy a bandwidth of 40-MHz with some nulls that will be obtained adaptively based on the received feedback from the spectrum sensing application. On the other side, the LTE communications framework utilizes 20-MHz bandwidth for transmission. To have some nulls that can be utilized by radar in the spectrum of communications, we select the allocation 111111111111000000111111 for the LTE resource blocks (4 physical resource blocks/bit), where the entry 1 indicates the use of the corresponding time-bandwidth resources in the LTE application framework. The spectrum of this LTE downlink is measured with the developed spectrum sensing application as depicted in Figure 12.11. This figure serves two purposes, (1) focusing on the LTE downlink spectrum, it validates the spectrum analyzer application with a commercial product, and (2) it clearly indicates that the desired objective of spectrum shaping is met.

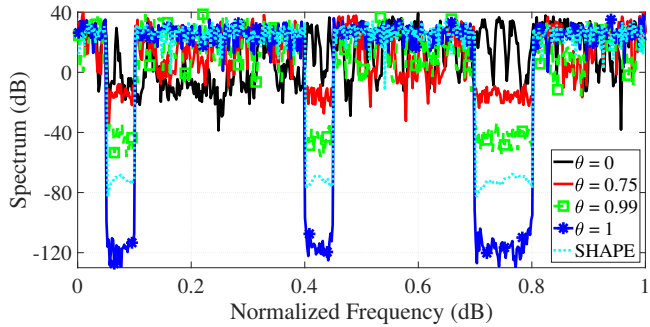

(a)

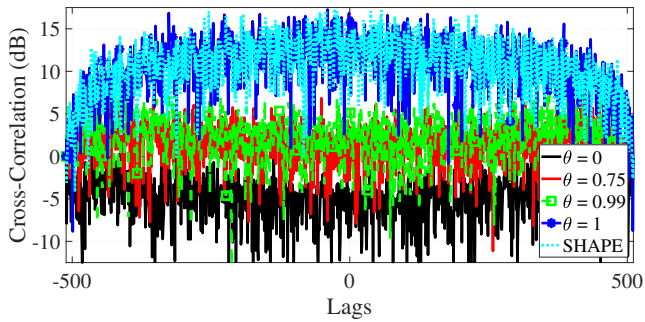

(b)

Figure 12.10. The impact of θ value on the trade-off between (a) spectral shaping, and (b) cross-correlation levels in comparison with SHAPE [30] ($M = 2$ and $N = 512$).

The impact of this matching on performance of radar and communications is presented next.

When the radar is not aware of the presence of communications, it transmits optimized sequences when $\theta = 0$. In this case, radar utilizes the entire bandwidth and the two systems mutually interfere. In fact, the operations of both radar and communications are disrupted as depicted in Figure 12.12(a) and Figure 12.12(b), thereby creating difficulties for their coexistence. In this case, by utilizing the optimized waveforms obtained by $\theta = 0.75$, the performance of both systems are enhanced as indicated pictorially in Figure 12.12(c) and Figure 12.12(d).

12.4 PERFORMANCE ANALYSIS

To measure the performance of the proposed prototype, we calculate the SINR of the two targets for radar, while on the communication side, we report the PDSCH throughput calculated by the LTE application framework. We perform our experiments in the following steps:

- Step 1: In the absence of radar transmission, we collect the LTE PDSCH throughput for MCS0, MCS10, and MCS 17. For each MCS, we use LTE transmit power of 5 dBm, 10 dBm, 15 dBm, and 20 dBm.
- Step 2: In the absence of LTE transmission, we obtain the received SNR for the two targets. In this case, radar utilizes its optimized waveform by setting $\theta = 0$. The SNR is calculated as the ratio of the peak power of the detected targets to the average power of the cells close to the target location in the range-Doppler map.
- Step 3: We transmit a set of optimized radar waveforms by setting $\theta = 0$. At the same time, we transmit the LTE waveform and let the two waveforms interfere with each other. We log the PDSCH throughput as well as the SINR of Targets 1 and Targets 2. We perform this experiment for MCS0, MCS10, and MCS17 and for each MCS, we increase the LTE transmit power from 5 dBm to 20 dBm in steps of 5 dBm. Throughout the experiment, we keep the radar transmit power fixed. For each LTE MCS and LTE transmit power combination, we average over 5 experiments before logging the PDSCH throughput and target SINRs.

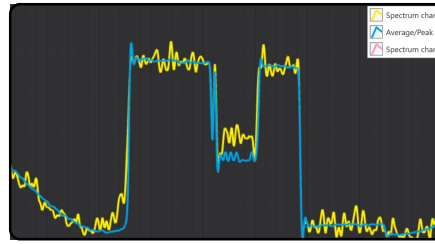

(a)

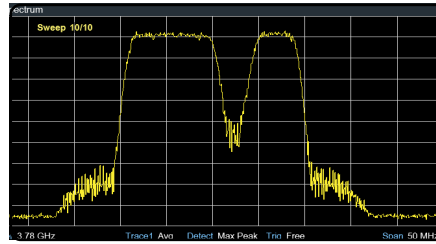

(b)

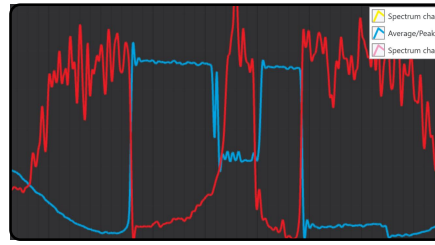

(c)

Figure 12.11. Screen captures of the resulting spectrum occupied by the LTE communications and optimized radar signals ($\theta = 0.75$) at the developed two-channel spectrum sensing application and R&H spectrum analyzer. The spectrum of the LTE downlink in (a) is validated by a commercial product in (b), and (c) indicates the the resulting spectrum of both communications (blue) and radar (red) at the developed two-channel spectrum sensing application.

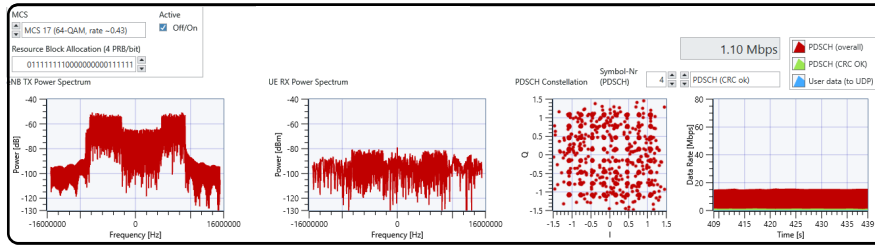

(a)

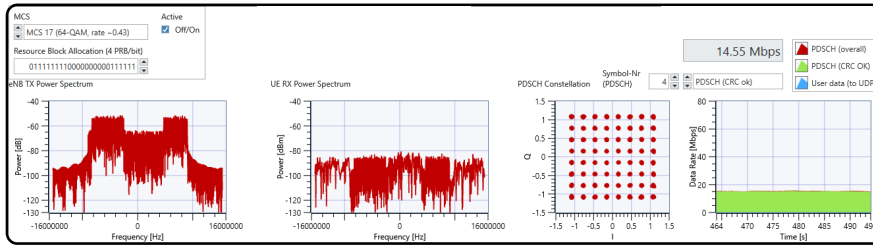

(b)

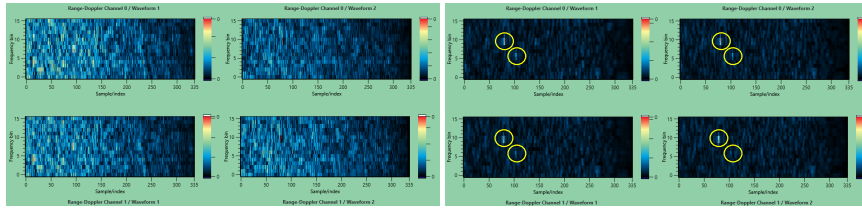

(c) **(d)**

Figure 12.12. LTE application framework in the presence of radar signal. In the case of transmitting random-phase sequences in radar at the same frequency band of communications, the throughput of communications decreases drastically, which is depicted in (a). In this case, radar also cannot detect the targets as depicted in (c). In case of transmitting the optimized waveforms ($\theta = 0.75$), the throughput of communications enhances in (b), and radar performance also improves in (d).

- Step 4: We repeat step 3, but using the optimized waveforms with $\theta = 0.75$ at the radar transmitter.

To evaluate the performance of the communication data rate, we reported PDSCH throughput in Figure 12.13. Indeed, the PDSCH throughput value matches the theoretical data rate for the combination of MCS and resource block allocation set for the UE TX. This value indicates the number of payload bits per received transport block that could be decoded successfully in every second. Mathematically it can be written as

$$\text{Throughput} = \sum_{1\text{second}} n_{\text{payload bits}} \tag{12.16}$$

In Figure 12.13, we first notice that, in the presence of radar interference, the link's throughput degrades. Because the SINR requirement for obtaining a clean constellation for larger modulations is also high, the degradation becomes more noticeable at higher MCS. Subsequently, the LTE throughput improves when the radar optimizes its waveform with $\theta = 0.75$. Again we see that the improvement is prominent in the higher MCS. This is due to the fact that the lower MCS exhibits no symbol error after a certain SINR since the constellation points are already far apart. However, as the distance between the constellation points decreases, even a small increase in SINR leads to improved error vector magnitude (EVM), which leads to improved decoding and thus a significant increase in throughput.

In Figure 12.14, in the presence of LTE interference, we observe that the SINRs of Target 1 and Target 2 degrade. These quantities improve when the radar optimizes the transmitting waveforms by setting $\theta = 0.75$. Interestingly, when the LTE transmission power is high (15 dBm, and 20 dBm), higher improvement results from the avoidance of the used LTE bands. Precisely, when the communication system is transmitting with a power of 20 dBm, use of the optimized waveforms enhances the SINR of Target 1, and Target 2 in excess of 7 dB in all the MCS values. Note that, due to the different attenuation paths that are considered for the two targets (see Table 12.3), the measured SINRs for these targets are different. Also, in the absence of the LTE interference, the achieved SINR of Target 1, and Target 2 is 22 dB and 17 dB, respectively, which is the upper bound for the achievable SINR through the optimized waveforms in presence of the communications interference.

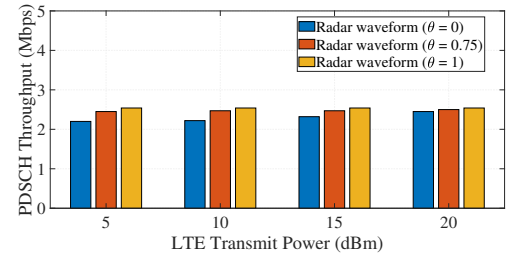

(a)

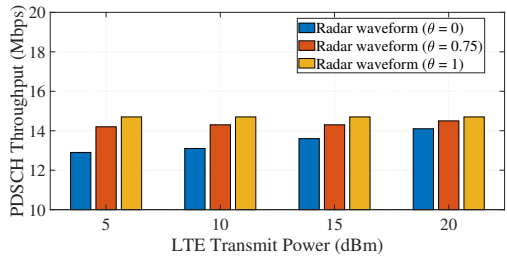

(b)

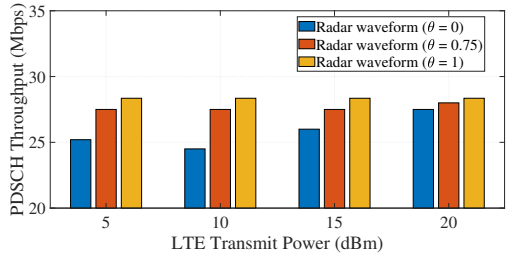

(c)

Figure 12.13. PDSCH throughput of LTE under radar interference. We observe that with radar interference reduces the PDSCH throughput but, with cognitive spectrum sensing followed by spectral shaping of the radar waveform, PDSCH throughput improves for all the LTE MCS. (a) MCS 0 (QPSK 0.12), (b) MCS 10 (16QAM 0.33), (c) MCS 17 (64QAM 0.43).

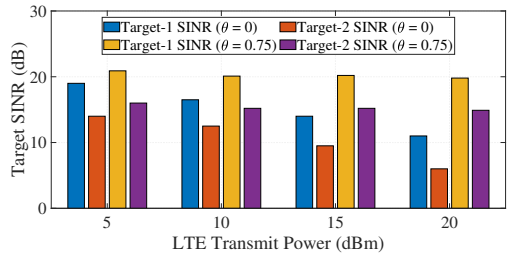

(a)

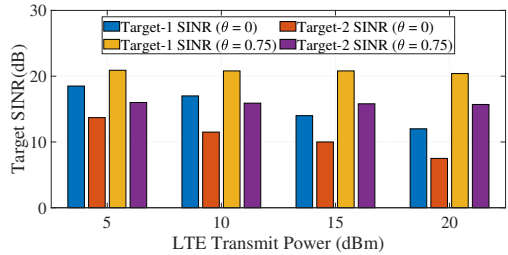

(b)

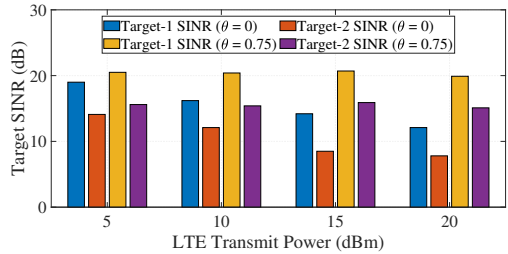

(c)

Figure 12.14. SINR of targets under interference from downlink LTE link. We observe that by optimizing the transmitting waveforms, the SNR of both the targets improves. (a) MCS 0 (QPSK 0.12), (b) MCS 10 (16QAM 0.33), (c) MCS 17 (64QAM 0.43). Note that in this experiment the SNR upper bound for the first and second targets in the absence of communications interference was 22 dB, and 17 dB, respectively.

12.5 CONCLUSION

In this chapter, we developed an SDR-based cognitive MIMO radar prototype using USRP devices that coexist with LTE communications. To enable seamless operation of incumbent LTE links and smart radar sensing, this chapter relied on cognition achieved through the implementation of a spectrum sensing followed by the development of a MIMO waveform design process. An algorithm based on the CD approach was considered to design a set of sequences, where the optimization was based on real-time feedback received from the environment through the spectrum sensing application. The developed prototype was tested in a controlled environment to validate its functionalities. The experimental results indicated adherence to system requirements and performance enhancement were presented.

References

[1] L. Zheng, M. Lops, Y. C. Eldar, and X. Wang, "Radar and communication coexistence: An overview: A review of recent methods," *IEEE Signal Processing Magazine*, vol. 36, no. 5, pp. 85–99, 2019.

[2] K. V. Mishra, M. R. Bhavani Shankar, V. Koivunen, B. Ottersten, and S. A. Vorobyov, "Toward millimeter-wave joint radar communications: A signal processing perspective," *IEEE Signal Processing Magazine*, vol. 36, no. 5, pp. 100–114, 2019.

[3] S. H. Dokhanchi, B. S. Mysore, K. V. Mishra, and B. Ottersten, "A mmwave automotive joint radar-communications system," *IEEE Transactions on Aerospace and Electronic Systems*, vol. 55, no. 3, pp. 1241–1260, 2019.

[4] H. Griffiths, L. Cohen, S. Watts, E. Mokole, C. Baker, M. Wicks, and S. Blunt, "Radar spectrum engineering and management: Technical and regulatory issues," *Proceedings of the IEEE*, vol. 103, no. 1, 2015.

[5] J. R. Guerci, R. M. Guerci, M. Ranagaswamy, J. S. Bergin, and M. C. Wicks, "CoFAR: Cognitive fully adaptive radar," in *2014 IEEE Radar Conference*, pp. 0984–0989, 2014.

[6] P. Stinco, M. Greco, F. Gini, and B. Himed, "Cognitive radars in spectrally dense environments," *IEEE Aerospace and Electronic Systems Magazine*, vol. 31, no. 10, pp. 20–27, 2016.

[7] M. S. Greco, F. Gini, P. Stinco, and K. Bell, "Cognitive radars: On the road to reality: Progress thus far and possibilities for the future," *IEEE Signal Processing Magazine*, vol. 35, no. 4, pp. 112–125, 2018.

[8] A. Aubry, V. Carotenuto, A. De Maio, and M. A. Govoni, "Multi-snapshot spectrum sensing for cognitive radar via block-sparsity exploitation," *IEEE Transactions on Signal Processing*, vol. 67, no. 6, pp. 1396–1406, 2019.

[9] S. Z. Gurbuz, H. D. Griffiths, A. Charlish, M. Rangaswamy, M. S. Greco, and K. Bell, "An overview of cognitive radar: Past, present, and future," *IEEE Aerospace and Electronic Systems Magazine*, vol. 34, no. 12, pp. 6–18, 2019.

[10] A. Aubry, A. De Maio, M. A. Govoni, and L. Martino, "On the design of multi-spectrally constrained constant modulus radar signals," *IEEE Transactions on Signal Processing*, vol. 68, pp. 2231–2243, 2020.

[11] J. Yang, A. Aubry, A. De Maio, X. Yu, and G. Cui, "Design of constant modulus discrete phase radar waveforms subject to multi-spectral constraints," *IEEE Signal Processing Letters*, vol. 27, pp. 875–879, 2020.

[12] A. F. Martone, K. D. Sherbondy, J. A. Kovarskiy, B. H. Kirk, C. E. Thornton, J. W. Owen, B. Ravenscroft, A. Egbert, A. Goad, A. Dockendorf, R. M. Buehrer, R. M. Narayanan, S. D. Blunt, and C. Baylis, "Metacognition for radar coexistence," in *2020 IEEE International Radar Conference (RADAR)*, pp. 55–60, 2020.

[13] A. De Maio and A. Farina, "The role of cognition in radar sensing," in *2020 IEEE Radar Conference (RadarConf20)*, pp. 1–6, 2020.

[14] A. F. Martone, K. D. Sherbondy, J. A. Kovarskiy, B. H. Kirk, J. W. Owen, B. Ravenscroft, A. Egbert, A. Goad, A. Dockendorf, C. E. Thornton, R. M. Buehrer, R. M. Narayanan, S. Blunt, and C. Baylis, "Practical aspects of cognitive radar," in *2020 IEEE Radar Conference (RadarConf20)*, pp. 1–6, 2020.

[15] A. F. Martone and A. Charlish, "Cognitive radar for waveform diversity utilization," in *2021 IEEE Radar Conference (RadarConf21)*, pp. 1–6, 2021.

[16] A. F. Martone, K. D. Sherbondy, J. A. Kovarskiy, B. H. Kirk, R. M. Narayanan, C. E. Thornton, R. M. Buehrer, J. W. Owen, B. Ravenscroft, S. Blunt, A. Egbert, A. Goad, and C. Baylis, "Closing the loop on cognitive radar for spectrum sharing," *IEEE Aerospace and Electronic Systems Magazine*, vol. 36, no. 9, pp. 44–55, 2021.

[17] J. Li and P. Stoica, *MIMO radar signal processing*. John Wiley & Sons, 2008.

[18] A. Khawar, A. Abdelhadi, and C. Clancy, *MIMO radar waveform design for spectrum sharing with cellular systems: a MATLAB based approach*. Springer, 2016.

[19] B. H. Kirk, K. A. Gallagher, J. W. Owen, R. M. Narayanan, A. F. Martone, and K. D. Sherbondy, "Cognitive software defined radar: A reactive approach to rfi avoidance," in *2018 IEEE Radar Conference (RadarConf18)*, pp. 0630–0635, 2018.

[20] M. Alaee-Kerahroodi, K. V. Mishra, M. R. Bhavani Shankar, and B. Ottersten, "Discrete-phase sequence design for coexistence of MIMO radar and MIMO communications," in *2019 IEEE 20th International Workshop on Signal Processing Advances in Wireless Communications (SPAWC)*, pp. 1–5, 2019.

[21] D. Ma, N. Shlezinger, T. Huang, Y. Liu, and Y. C. Eldar, "Joint radar-communication strategies for autonomous vehicles: Combining two key automotive technologies," *IEEE Signal Processing Magazine*, vol. 37, no. 4, pp. 85–97, 2020.

[22] "Ettus research." https://www.ettus.com/. Accessed: 2021-01-19.

[23] "National instruments." https://www.ni.com/en-gb.html. Accessed: 2021-01-19.

[24] "Overview of the LabVIEW communications application frameworks." https://www.ni.com/en-gb/innovations/white-papers/14/overview-of-the-labview-communications-application-frameworks.html. Accessed: 2021-01-21.

[25] M. Alaee-Kerahroodi, M. R. Bhavani Shankar, K. V. Mishra, and B. Ottersten, "Meeting the lower bound on designing set of unimodular sequences with small aperiodic/periodic isl," in *2019 20th International Radar Symposium (IRS)*, pp. 1–13, 2019.

[26] M. Alaee-Kerahroodi, M. Modarres-Hashemi, and M. M. Naghsh, "Designing sets of binary sequences for MIMO radar systems," *IEEE Transactions on Signal Processing*, vol. 67, pp. 3347–3360, July 2019.

[27] K. Deb, *Multi-Objective Optimization Using Evolutionary Algorithms*, vol. 16. John Wiley & Sons, 2001.

[28] M. Alaee-Kerahroodi, A. Aubry, A. De Maio, M. M. Naghsh, and M. Modarres-Hashemi, "A coordinate-descent framework to design low PSL/ISL sequences," *IEEE Transactions on Signal Processing*, vol. 65, pp. 5942–5956, Nov. 2017.

[29] "NI labview LTE framework." https://www.ni.com/en-us/support/documentation/supplemental/16/labview-communications-lte-application-framework-2-0-and-2-0-1.html. Accessed: 2021-01-24.

[30] W. Rowe, P. Stoica, and J. Li, "Spectrally constrained waveform design [SP tips tricks]," *IEEE Signal Processing Magazine*, vol. 31, no. 3, pp. 157–162, 2014.

APPENDIX 12A

SILR Coefficients

Let us assume that

$$\boldsymbol{F}_{\mathcal{U}} \triangleq \sum_{k \in \mathcal{U}} \mathbf{f}_k \mathbf{f}_k^{\dagger} \in \mathbb{C}^{N \times N}$$

and $u_{n,l}$ indicates (n,l)th element ($n = 1, 2, \ldots, N$, $l = 1, 2, \ldots, N$) of matrix $\boldsymbol{F}_{\mathcal{U}}$. The nominator in (12.1) can be rewritten as

$$\begin{aligned}\sum_{m=1}^{M}\left\|\mathbf{f}_k^{\dagger}\mathbf{x}_m\right\|^2 |k\in\mathcal{U} &= \sum_{m=1}^{M}\sum_{k\in\mathcal{U}}\mathbf{x}_m^{\dagger}\mathbf{f}_k\mathbf{f}_k^{\dagger}\mathbf{x}_m = \textstyle\sum_{m=1}^{M}\mathbf{x}_m^{\dagger}\boldsymbol{F}_{\mathcal{U}}\mathbf{x}_m \\ &= \sum_{m=1}^{M}\sum_{n=1}^{N}\sum_{l=1}^{N}x_{m,n}^{*}u_{n,l}x_{m,l} \\ &= a_0x_{t,d} + a_1 + a_2x_{t,d}^{*}\end{aligned} \tag{12A.1}$$

where

$$\begin{aligned}a_0 &= \sum_{\substack{n=1\\n\neq d}}^{N}x_{t,n}^{*}u_{n,d} \\ a_1 &= \sum_{\substack{n=1\\n\neq d}}^{N}\sum_{n,l=1}^{N}x_{m,n}^{*}u_{n,l}x_{m,l} + \sum_{\substack{n,l=1\\n,l\neq d}}^{N}x_{t,n}^{*}u_{n,l}x_{t,l} + u_{d,d}\end{aligned} \tag{12A.2}$$

and $a_2 = a_0^{*}$. Similarly, by defining

$$\boldsymbol{F}_{\mathcal{V}} \triangleq \sum_{k\in\mathcal{V}}\mathbf{f}_k\mathbf{f}_k^{\dagger} \in \mathbb{C}^{N\times N}$$

the denominator in (12.1) is

$$\sum_{m=1}^{M}\left\|\mathbf{f}_k^{\dagger}\mathbf{x}_m\right\|^2 |k\in\mathcal{V} = b_0x_{t,d} + b_1 + b_2x_{t,d}^{*} \tag{12A.3}$$

where

$$\begin{aligned}b_0 &= \sum_{\substack{n=1\\n\neq d}}^{N}x_{t,n}^{*}v_{n,d} \\ b_1 &= \sum_{\substack{n=1\\n\neq d}}^{N}\sum_{n,l=1}^{N}x_{m,n}^{*}v_{n,l}x_{m,l} + \sum_{\substack{n,l=1\\n,l\neq d}}^{N}x_{t,n}^{*}v_{n,l}x_{t,l} + v_{d,d}\end{aligned} \tag{12A.4}$$

where $b_2 = b_0^{*}$ and $v_{n,l}$ are the elements of $\boldsymbol{F}_{\mathcal{V}}$.

ICCL Coefficients

For (12.3), it can be shown that

$$\sum_{m=1}^{M}\sum_{\substack{m'=1\\m'\neq m}}^{M}\sum_{l=-N+1}^{N-1}|r_{m,m'}(l)|^2=\gamma_t+2\sum_{\substack{m=1\\m\neq t}}^{M}\sum_{l=-N+1}^{N-1}|r_{m,t}(l)|^2 \tag{12A.5}$$

where

$$\gamma_t\triangleq\sum_{\substack{m=1\\m\neq t}}^{M}\sum_{\substack{m'=1\\m'\neq m,t}}^{M}\sum_{l=-N+1}^{N-1}|r_{m,m'}(l)|^2$$

Further, it would be easy to show

$$r_{m,t}(l)=\alpha_{mtdl}x_{t,d}+\gamma_{mtdl} \tag{12A.6}$$

where $\alpha_{mtdl}=x_{m,d-l}I_A(d-l)$ and

$$\gamma_{mtdl}=\sum_{\substack{n=1\\n\neq d-l}}^{N-l}x_{m,n}x_{t,n+l}^{*} \tag{12A.7}$$

where $I_A(p)$ is the indicator function of set $A=\{1,\ldots,N\}$, defined by

$$I_A(p)=\begin{cases}1, & p\in A\\ 0, & p\notin A\end{cases} \tag{12A.8}$$

Thus,

$$\sum_{m=1}^{M}\sum_{\substack{m'=1\\m'\neq m}}^{M}\sum_{l=-N+1}^{N-1}|r_{m,m'}(l)|^2=c_0x_{t,d}+c_1+c_2x_{t,d}^{*} \tag{12A.9}$$

where

$$c_0=\frac{2}{(2MN)^2}\sum_{\substack{m=1\\m\neq t}}^{M}\sum_{l=-N+1}^{N-1}\alpha_{mtdl}\gamma_{mtdl}^{*} \tag{12A.10}$$

$$c_1 = \frac{1}{(2MN)^2}(\gamma_t + 2\sum_{\substack{m=1\\m\neq t}}^{M}\sum_{l=-N+1}^{N-1}|\alpha_{mtdl}|^2 + 2\sum_{\substack{m=1\\m\neq t}}^{M}\sum_{l=-N+1}^{N-1}|\gamma_{mtdl}|^2) \quad (12A.11)$$

and $c_2 = c_0^*$.

APPENDIX 12B

Equation (12.10) can be re-expressed as

$$g(\phi) = \theta\frac{g_a(\phi)}{g_b(\phi)} + (1-\theta)g_c(\phi) \quad (12B.1)$$

where

$$g_a(\phi) = a_0e^{j\phi} + a_1 + a_2e^{-j\phi}$$
$$g_b(\phi) = b_0e^{j\phi} + b_1 + b_2e^{-j\phi}$$
$$g_c(\phi) = c_0e^{j\phi} + c_1 + c_2e^{-j\phi}$$

The derivative of $g(\phi)$ can be written as

$$g'(\phi) = \theta\frac{g_a'(\phi)g_b(\phi) - g_b'(\phi)g_a(\phi)}{g_b^2(\phi)} + (1-\theta)g_c'(\phi) \quad (12B.2)$$

By some standard mathematical manipulation, $g'(\phi)$ can be written as

$$g'(\phi) = \frac{e^{j3\phi}\sum_{p=0}^{6}q_pe^{jp\phi}}{(b_0e^{j\phi} + b_1 + b_2e^{-j\phi})^2} \quad (12B.3)$$

where

$$\begin{aligned}
q_0 &= j(1-\theta)c_0b_0^2\\
q_1 &= j2(1-\theta)c_0b_0b_1\\
q_2 &= j(\theta(a_0b_1 - b_0a_1) + (1-\theta)(2c_0b_0b_2 + c_0b_1^2 - c_2b_0^2))\\
q_3 &= j2(\theta(a_0b_2 - a_2b_0) + (1-\theta)b_1(c_0b_2 - c_2b_0))\\
q_4 &= q_2^*, \quad q_5 \triangleq q_1^*, \quad q_6 \triangleq q_0^*
\end{aligned} \quad (12B.4)$$

Chapter 13

Conclusion

Radar sensing has moved from niche military applications to utilitarian, impacting day-to-day life including applications in automotive, building security, vital sign monitoring, and weather sensing, among others. The potential of sensing has also been realized in the context of wireless communication where integrated sensing and communications (ISAC) have been considered in 6G, towards exploiting the communication systems beyond their original objective and rendering their design and operation more effective. Such a shift is highly welcome and leads to a wider proliferation of advanced radar signal processing techniques in academia and industry that will pave the way for novel research avenues and cross-fertilization of ideas. However, these novel applications bring in their own nuances rendering the sensing problems more challenging and motivating research beyond the state of the art. Indoor sensing brings in the complexities of the near-field scenario with extended targets, significant clutter, and management of number of targets, often occluding each other. Automotive sensing also brings with itself the need for simultaneous long- and short-range applications, point and extended targets, interference, and a highly dynamic scenario. In addition, the new applications come with restrictions on resources: commercial use limits the transmit power and processing capabilities while the proliferation of wireless communications imposes constraints on the use of spectrum. Many times, the aesthetics, combined with the processing limitation, also impose constraints on the aperture of the radar sensor. In summary, new applications accelerate the proliferation of radar sensing, but the novel challenges need to be surmounted.

To navigate the aforementioned canvas, it is essential for modern radar systems to dig deeper into the degrees of freedom available and exploit them to the fullest. In this context, the radar systems benefit from the design of waveforms at the transmitter based on the application. Research has led to the development of new waveforms that are now implemented using novel technologies. Traditional radars have used continuous wave or linear ramps and variants of therein as waveforms; with the emergence of digital technology, the pulse coded waveforms, which were difficult to conceive and implement earlier, are a reality. These waveforms offer significant degrees of freedom that can be exploited to meet the objectives of the radar task. This is the platform, a fertile ground, on which this book is built.

This book considered exploitation of the waveform structures and proposed various ways to optimize them to render them effective in meeting the objective of the new applications while surmounting the challenges. However, the radar tasks are numerous (detection, estimation, classification, tracking) and there exist a plethora of scenarios (indoor, outdoor, clutter-free, static, etc.). Optimization of a waveform for one scenario may not be optimal in other and, hence, scenario-specific optimization needs to be performed. Central to the optimization is the problem formulation which involves the objective and the constraints.

A well-designed waveform can allow for more accurate target detection and parameter estimation. However, we are facing several challenges when designing radar waveform, a few of which are highlighted below.

13.1 COMPUTATIONAL EFFICIENCY

Radar signal processing and design are an application with extreme emphasis on real-time operation, which requires a fast implementation of waveform design. Moreover, compared to traditional radars that only require one matched filter, the independent transmit waveforms of a MIMO radar requires more processing resources for matched filtering. In addition, if the radar system runs in a cognitive manner, the adaptability is achieved by redesigning the waveform before the next transmission, which means a short time window for the design phase.

13.2 WAVEFORM DIVERSITY

With the consideration of hardware configuration and application scenarios, some waveform constraints are necessarily incorporated. High-power amplifiers, for example, are utilized in the saturation region in many real-world applications. It is desirable that the probing waveforms are constrained to be constant modulus to avoid distortions by the high-power amplifiers. However, including this constraint in the optimization problems will likely increase the design difficulty.

13.3 PERFORMANCE TRADE-OFF

Different objectives may have contradictory natures but need to be tuned simultaneously. For example, emitted probing waveforms in a MIMO radar should have small cross-correlation properties to provide the possibility of separating waveforms in the receiver matched filter and building the virtual array for a finer angular resolution. However, SINR can be maximized when correlated waveforms are transmitted, which form a focused beampattern in the direction of target. Another example is small autocorrelation sidelobes of the transmitting waveform to detect weak targets from adjacent range bins of a strong target. However, small autocorrelation sidelobes in the time domain correspond to a flat spectrum in the frequency domain, which is inconsistent with spectral shaping that eliminates narrowband interferences.

With regard to the objectives, one could consider them in range, angle and Doppler domains, or combinations thereof. In this context, this book explored a wide variety of objective functions after translating from the system requirements to mathematical formulations that can be handled. Some applications necessitate a set of optimized interpulse waveforms and receive filters to improve SINR, which was considered in Chapter 3 using PMLI. With regard to the range, toward discerning multiple targets, the design of a waveform with good PSL and ISL characteristics was considered in chapters 4 and 5, using MM and CD techniques, respectively. Apart from the aforementioned methods, some alternate optimization approaches are also available for optimal radar waveform design problem. Methods such as SDP can also be employed to arrive at optimized radar waveforms with desired correlation properties. Chapter 6 put emphasis on this optimization

method in the context where spectral and spatial behavior of the transmit waveform needs to be controlled simultaneously.

Chapter 7 introduced the application of data-driven approaches for radar signal design and processing. In particular, this chapter illustrated novel hybrid model-driven and data-driven architectures stemming from the deep unfolding framework that unfolds the iterations of well-established model-based radar signal design algorithms into the layers of deep neural networks. This approach lays the groundwork for developing extremely low-cost waveform design and processing frameworks for radar systems deployed in real-world applications.

With regard to the angular properties, enhancing the resolvability of sources using the virtual array concept from MIMO literature has led to the design of waveforms with low cross-correlation in addition to the low PSL or ISL metrics mentioned above. While MIMO offers theoretical guarantees on resolvability, it suffers in practice due to lower SINR arising out of the isotropic radiation. Objectives to improve SINR have focused on beampattern shaping and beampattern matching in the spatial domain. This involves steering the radiation power in a spatial region of desired angles, while reducing interference from sidelobe returns to improve the SINR and consequently target detection. Many works have also brought out the inherent contradiction between spatial uncorrelateness for MIMO and the correlation requirement of beamforming to create novel objectives effecting efficient trade-off. These have been explored in Chapter 8.

With regard to the Doppler perturbations, the idea has been to ensure resilience over a wide range of Doppler frequencies. By considering l_p norm of the autocorrelation sidelobes as a generalized metric to PSL and ISL, the design of waveforms that are constrained to have polynomial phase behavior in their segments and with high Doppler tolerant properties is explored in Chapter 10. Further, since spectrum is a scarce resource, it needs to be shared or reused judiciously to enable multiple radio-based services. This radio-based coexistence, particularly with communications, imposes constraints on the use of the spectrum (spectral shaping) as well as the space (spatial beampattern shaping) to avoid interference. This has been explored in Chapter 9, with a prototype for the coexistence of communications and radar designed and implemented in Chapter 12.

All in all, for radar waveform design, an algorithmic framework is desired that it is not only computationally efficient but also flexible so that various waveform constraints can be handled. Subsequently, this book

looked at various methodologies to solve the problems mentioned above. These problems are typically nonlinear, nonconvex and, in most cases, NP-hard. This opens up the possibility to consider multiple approaches to the same problem, and the selection of a particular approach depending on its performance, ease of implementation, and complexity. This book explored several optimization frameworks, like BCD, MM, BSUM, and PMLI, which have been successfully applied in the design and implementation of radar waveforms under practical constraints. It detailed the fundamentals of each approach, brought out the nuances, and discussed their performance and complexity, as well as applications to realize the practiced radars.

About the Authors

Mohammad Alaee-Kerahroodi received a PhD in telecommunication engineering from the Department of Electrical and Computer Engineering at Isfahan University of Technology, Iran, in 2017. During his doctoral studies and in 2016, he worked as a visiting researcher at the University of Naples "Federico II" in Italy. After receiving his doctorate, he began working as a research associate at Interdisciplinary Centre for Security, Reliability, and Trust (SnT), at the University of Luxembourg, Luxembourg. At present, he works as a research scientist at SnT and leads the prototyping and lab activities for the SPARC (Signal Processing Applications in Radar and Communications) research group. Along with conducting academic research in the field of radar waveform design and array signal processing, he is working on novel solutions for millimeter wave MIMO radar systems. Dr. Alaee has more than 12 years of experience working with a variety of radar systems, including automotive, ground surveillance, air surveillance, weather, passive, and marine.

Mojtaba Soltanalian received a PhD degree in electrical engineering (with specialization in signal processing) from the Department of Information Technology, Uppsala University, Sweden, in 2014. He is currently with the faculty of the Electrical and Computer Engineering Department, University of Illinois at Chicago (UIC), Chicago, Illinois. Before joining UIC, he held research positions with the Interdisciplinary Centre for Security, Reliability, and Trust (SnT, University of Luxembourg), and California Institute of Technology, Pasadena, California. His research interests include interplay of signal processing, learning and optimization theory, and specifically different ways that the optimization

theory can facilitate better processing and design of signals for collecting information and communication, and also to form a more profound understanding of data, whether it is in everyday applications or in large-scale, complex scenarios. Dr. Soltanalian serves as an associate editor for the *IEEE Transactions on Signal Processing* and as the chair of the IEEE Signal Processing Society Chapter in Chicago. He was the recipient of the 2017 IEEE Signal Processing Society Young Author Best Paper Award and the 2018 European Signal Processing Association Best PhD Award.

Dr. Prabhu Babu received his B. Tech degree from Madras Institute of Technology in Electronics in 2005. He then obtained his M. Tech degree in radio frequency design technology (RFDT) from Centre for Applied Research in Electronics (CARE), IIT Delhi in 2007. He finished his doctor of philosophy from Uppsala University, Sweden in 2012. From January 2013 to December 2015, he was at Hong Kong University of Science and Technology (HKUST), Hong Kong doing his postdoctoral research. In January 2016, he joined CARE, IIT Delhi as an Associate Professor.

M. R. Bhavani Shankar received his master's and PhD in Electrical Communication Engineering from the Indian Institute of Science, Bangalore, in 2000 and 2007 respectively. He was a postdoctoral candidate at the ACCESS Linnaeus Centre, Signal Processing Lab, Royal Institute of Technology (KTH), Sweden from 2007 to September 2009. He joined SnT in October 2009 as a Research Associate and is currently a Senior Research Scientist/Assistant Professor at SnT leading the Radar signal processing activities. He was with Beceem Communications, Bangalore, from 2006 to 2007 as a Staff Design Engineer working on physical layer algorithms for WiMAX compliant chipsets. He was a visiting student at the Communication Theory Group, ETH Zurich, headed by Professor Helmut Bölcskei during 2004. Prior to joining the PhD program, he worked on audio coding algorithms in Sasken Communications, Bangalore, as a design engineer from 2000 to 2001. His research interests include design and optimization of MIMO communication systems, automotive radar and array

processing, polynomial signal processing, satellite communication systems, resource allocation, and fast algorithms for structured matrices. He is currently on the Executive Committee of the IEEE Benelux joint chapter on communications and vehicular technology, serves as handling editor for the *Elsevier Signal Processing* journal and is member of the EURASIP Technical Area Committee on Theoretical and Methodological Trends in Signal Processing. He was a corecipient of the 2014 Distinguished Contributions to Satellite Communications Award from the Satellite and Space Communications Technical Committee of the IEEE Communications Society.

Index

4-D Imaging, 201

ADMM, 25
alternating projection (AP), 23

BCD, 22, 26, 125, 132, 306, 327
  Beampattern matching in MIMO radars, 146
  Beampattern shaping and orthogonality, 202
  Block CGD, 128
  Cyclic, 128
  ISL minimization, 133
  Jacobi, 129
  MBI, 129
  PSL minimization, 139
  Randomized, 128
BPM, 3
BSUM, 131, 132

CAN, 282
CCP, 22, 27
CD, 23, 132, 307, 327
CDM, 3
Cognitive radar, 323
Convex optimization, 8, 17
Cross ambiguity function, 35

DC programming, 22
DDM, 3
DNN, 179
  DECoR, 192
Doppler-tolerant, 271
  Chu, 271
  Frank, 271
  Golomb, 271
  P1, 271
  P2, 271
  P3, 271
  P4, 271
  PAT, 271
  Px, 272
  Zadoff-Chu, 272

EM, 22, 27

FFT, 41, 79, 87, 88, 94, 137, 173, 255, 280, 294, 305, 311, 334

GD, 18, 26

ICCL, 329
IFFT, 79, 87, 88, 94
ISAC, 353
ISL, 6, 69, 132, 271
ISLR, 202, 220

JRCV, 231, 234

LFM, 271, 275
LTE, 324

MDA, 19, 26
MIMO Radar, 48, 50, 146
MIMO radar, 3, 159, 326, 354
MM, 20, 67, 70, 275
  FBMM, 81

FISL, 89
ISL-NEW algorithm, 79
MDA, 111
minimax problems, 71
minimization problems, 70
MISL, 73, 281
MM-PSL, 100, 297
SLOPE, 104
UNIPOL, 95
MSE, 39
MTI, 255

Newton's method, 18, 26
Nonconvex optimization, 8, 18

PMLI, 20, 31, 49, 189
fractional programming, 39
information-theoretic criteria, 48
transmit beamforming, 50
POCS, 23
Prototype, 324
PSL, 6, 69, 132, 139, 271
PSLR, 202

ROC, 49

SAR, 201
SDP, 159
SILR, 329
SINR, 7, 203, 305
SNR, 39, 44
STAP, 301
SUM, 132

TDM, 3

ULA, 146, 160, 302
USRP, 324

WISL, 69